

5-2017

## Tuning the pKa of Fluorescent Rhodamine pH Probes via Substituent Effects

Sarah G. Stratton  
*College of William and Mary*

Follow this and additional works at: <https://scholarworks.wm.edu/honorsthesis>

 Part of the [Physical Chemistry Commons](#)

---

### Recommended Citation

Stratton, Sarah G., "Tuning the pKa of Fluorescent Rhodamine pH Probes via Substituent Effects" (2017). *Undergraduate Honors Theses*. Paper 1105.  
<https://scholarworks.wm.edu/honorsthesis/1105>

This Honors Thesis is brought to you for free and open access by the Theses, Dissertations, & Master Projects at W&M ScholarWorks. It has been accepted for inclusion in Undergraduate Honors Theses by an authorized administrator of W&M ScholarWorks. For more information, please contact [scholarworks@wm.edu](mailto:scholarworks@wm.edu).

## **Tuning the pKa of Fluorescent Rhodamine pH Probes via Substituent Effects**

A thesis submitted in partial fulfillment of the requirement for the  
degree of Bachelors of Science in Chemistry from The College of  
William and Mary

By

Sarah Graham Stratton

Accepted for \_\_\_\_\_

\_\_\_\_\_  
**Dr. Elizabeth J. Harbron, Director**

\_\_\_\_\_  
**Dr. Robert J. Hinkle**

\_\_\_\_\_  
**Dr. John C. Poutsma**

\_\_\_\_\_  
**Dr. John Conlee**

## Table of Contents

<b>List of Tables and Figures</b> .....	i
<b>Abstract</b> .....	1
Introduction .....	2
Results and Discussion .....	11
Section I. Synthesis of di- <i>ortho</i> RB and R6G derivatives.....	11
Section II. pK <sub>a</sub> studies of <i>ortho</i> -substituted RB and R6G derivatives.....	24
Section III. Crystal structure and Gaussian modeling .....	61
Section IV. Nano incorporation of RB-DIA dyes .....	82
Conclusions .....	94
Experimental.....	95
Acknowledgements .....	114
References .....	116
Appendix A.....	119
Appendix B.....	188
Appendix C.....	248
Appendix D .....	275

## List of Tables and Figures

Figure 1. Jablonski diagram depicting absorption in blue and fluorescence in red	4
Figure 2. Absorption (left) and fluorescence (right) spectra.	4
Figure 3. Rhodamine dye structures (RB and R6G)	5
Scheme 1. Rhodamine spirolactam ring opening	5
Figure 4. Rhodamine <i>para</i> substituents	8
Figure 5. Rhodamine B-adamantanamine	8
Figure 6. RB and R6G di- <i>ortho</i> substituents and RB mono- <i>ortho</i> substituents	9
Scheme 2. Rhodamine 6G synthesis and derivatives	13
Scheme 3. Rhodamine 6G synthesis and derivatives	19
Table 1. Comparison of syntheses for RB and R6G di- <i>ortho</i> substituted derivatives	23
Figure 7. A fluorescence spectra of R6G-DMA	25
Figure 8. Graph of fluorescence peak intensity versus pH for R6G-DMA	26
Table 2. Average pK <sub>a</sub> values for the RB and R6G di- <i>ortho</i> series.	26
Table 3. Average pK <sub>a</sub> values for the additional titrations	28
Table 4. Average pK <sub>a</sub> values for the RB mono- <i>ortho</i> series	31
Table 5. Steric parameters for modeling di- <i>ortho</i> series	34
Table 6. Electronic parameters for modeling di- <i>ortho</i> series	35
Figure 9. RB and R6G pK <sub>a</sub> data for di- <i>ortho</i> substituents versus their A values	36
Figure 10. RB and R6G pK <sub>a</sub> data for electron withdrawing di- <i>ortho</i> substituents versus their A values	36
Figure 11. RB and R6G pK <sub>a</sub> data for electron donating di- <i>ortho</i> substituents versus their A values	37
Figure 12. R6G A value predicted pK <sub>a</sub> versus experimental pK <sub>a</sub>	38
Table 7. R6G regression analysis	39
Figure 13. R6G E <sub>s</sub> predicted pK <sub>a</sub> versus experimental pK <sub>a</sub>	45
Figure 14. R6G E <sub>s</sub> -σ <sub>I</sub> -F regression predicted pK <sub>a</sub> versus pK <sub>a</sub> of di- <i>ortho</i> derivatives	47
Figure 15. RB E <sub>s</sub> -σ <sub>p</sub> -F regression predicted pK <sub>a</sub> versus pK <sub>a</sub> of di- <i>ortho</i> derivatives	47
Table 8. Analysis of VIFs of R6G three-parameter regression models	47
Figure 16. R6G E <sub>s</sub> -σ <sub>p</sub> -R regression predicted pK <sub>a</sub> versus pK <sub>a</sub> of di- <i>ortho</i> derivatives	48
Figure 17. R6G E <sub>s</sub> -σ <sub>p</sub> -F-R regression predicted pK <sub>a</sub> versus pK <sub>a</sub> of di- <i>ortho</i> derivatives	49
Table 9. Analysis of VIFs of RB three-parameter regression models	50
Table 10 RB regression analysis	51
Figure 18. RB E <sub>s</sub> -σ <sub>p</sub> -R regression predicted pK <sub>a</sub> versus pK <sub>a</sub> of di- <i>ortho</i> derivatives	54
Table 12. Electronic parameters for modeling mono- <i>ortho</i> series	56
Figure 19. RB pK <sub>a</sub> data for mono- <i>ortho</i> substituents versus their σ <sub>p</sub> values	57
Table 11. Mono- <i>ortho</i> regression analysis	58
Figure 20. RB pK <sub>a</sub> data for mono- <i>ortho</i> substituents versus their σ <sub>o</sub> values	59
Figure 21. RB σ <sub>o</sub> regression predicted pK <sub>a</sub> versus pK <sub>a</sub> of mono- <i>ortho</i> derivatives	60

Figure 22. RB-DIA aliphatic region	61
Table 12. Crystal growing experiment results based on solution	62
Figure 23. Crystal structure of RB-DIA	63
Figure 24. Optimized structure of R6G-A (left) front view and (right) bird's eye view	64
Figure 25. Optimized structure of R6G-DFA (left) front view and (right) bird's eye view	64
Figure 26. Optimized structure of R6G-DCA (left) front view and (right) bird's eye view	65
Figure 27. Optimized structure of R6G-DEA (left) front view and (right) bird's eye view	65
Figure 28. Optimized structure of R6G-DMA	65
Figure 29. Optimized structure of R6G-DIA	66
Figure 30. Crystal structure of RB-A	66
Figure 32. Optimized structure of RB-DCA	67
Figure 33. Optimized structure of RB-DEA	67
Figure 34. Optimized structure of RB-DMA	67
Figure 35. Optimized structure of RB-DIA	68
Table 13. RB and R6G derivatives by $pK_a$ , xanthene ring twist, A value, $\sigma_p$ value, and $E_s$	68
Figure 36. The angles measured to calculate the xanthene twist	69
Figure 37. Xanthene ring torsion for RB and R6G derivatives versus the $E_s$ parameter	69
Figure 38. Xanthene ring torsion for RB and R6G derivatives versus the A value parameter	70
Figure 39. Xanthene ring torsion for RB and R6G derivatives versus the $\sigma_p$ parameter	71
Figure 40. RB and R6G derivatives $pK_a$ values versus their respective xanthene ring torsion	71
Table 14. Regression analysis on R6G and RB using xanthene twist as a parameter	72
Figure 41. The angle between C20-N3-C21-C22	73
Figure 42. $pK_a$ versus RB and R6G derivatives measure of coplanarity with the carbonyl	73
Table 15. RB and R6G derivatives by $pK_a$ and coplanarity with the carbonyl	73
Figure 43. RB and R6G derivatives measure of coplanarity with the carbonyl versus the $E_s$ parameter	74
Figure 44. RB and R6G derivatives measure of coplanarity with the carbonyl versus the $\sigma_p$ parameter	75
Figure 45. Optimized structure of RB-2CA	76
Figure 46. Optimized structure of RB-2MA	76
Figure 47. Optimized structure of RB-2IA	76
Table 16. RB mono- <i>ortho</i> derivatives by $pK_a$ , xanthene ring twist, A value, $\sigma_p$ value, and $E_s$	77
Figure 48. Xanthene ring torsion for RB mono- <i>ortho</i> derivatives versus A values	77
Figure 49. Xanthene ring torsion for RB mono- <i>ortho</i> derivatives versus the $E_s$ parameter	78
Figure 50. Xanthene ring torsion for RB mono- <i>ortho</i> derivatives versus the $\sigma_p$ parameter	78
Table 17. RB mono- <i>ortho</i> derivatives by $pK_a$ and coplanarity with the carbonyl	79
Figure 51. RB mono- <i>ortho</i> derivatives measure of coplanarity with the carbonyl versus $E_s$ parameter	80
Figure 52. RB mono- <i>ortho</i> derivatives measure of coplanarity with the carbonyl versus $\sigma_p$ parameter	80

Figure 53. Structure of PFBT	82
Figure 55. The addition of acid switches the fluorescence of the CPNs from the green region to the red as FRET occurs between PFBT and RB-DIA	83
Figure 56. PFBT UV-Vis spectrum	85
Figure 57. Post-argon bubbling addition of dye fluorescence, excitation at 450 nm	86
Figure 58. Post-argon bubbling addition of dye fluorescence, excitation at 535 nm	86
Figure 59. Pre-argon bubbling addition of dye fluorescence, excitation at 450 nm	88
Figure 60. Pre-argon bubbling addition of dye fluorescence, excitation at 535 nm	88
Figure 61. Post-argon bubbling addition of dye UV-Vis spectra	89
Figure 62. Pre-argon bubbling addition of dye UV-Vis spectra	89
Figure 63. Two-day old nanos addition of acid fluorescence, excitation at 450 nm	90
Figure 64. Two-day old nanos addition of base fluorescence, excitation at 450 nm	90
Figure 65. PFBT and PVCoCo with no dye, addition of acid fluorescence, excitation at 450 nm (pH range of 6.60 to 3.93; red to pink line)	92
Figure 66. PFBT and PVCoCo with no dye, addition of acid UV-Vis spectra	93
Figure 67. Sample particle sizing of the dye-doped nanoparticle	93
Table 18. Structures and abbreviations for the rhodamine derivatives and precursors	99
Figure A1: $^1\text{H}$ NMR Spectrum of RB-DCA	119
Figure A2: $^1\text{H}$ NMR Spectrum of RB-DCA (6.0-8.5 ppm)	120
Figure A3: $^1\text{H}$ NMR Spectrum of RB-DCA (0-4.5 ppm)	121
Figure A4: $^{13}\text{C}$ NMR Spectrum of RB-DCA	122
Figure A5: $^1\text{H}$ NMR Spectrum of RB-DFA	123
Figure A6: $^1\text{H}$ NMR Spectrum of RB-DFA (6.0-8.5 ppm)	124
Figure A7: $^1\text{H}$ NMR Spectrum of RB-DFA (0-4.5 ppm)	125
Figure A8: $^{13}\text{C}$ NMR Spectrum of RB-DFA	126
Figure A9: $^1\text{H}$ NMR Spectrum of RB-DEA	127
Figure A10: $^1\text{H}$ NMR Spectrum of RB-DEA (6.0-8.5 ppm)	128
Figure A11: $^1\text{H}$ NMR Spectrum of RB-DEA (0-4.5 ppm)	129
Figure A12: $^{13}\text{C}$ NMR Spectrum of RB-DEA	130
Figure A13: $^1\text{H}$ NMR Spectrum of RB-DMA	131
Figure A14: $^1\text{H}$ NMR Spectrum of RB-DMA (6.0-8.5 ppm) <sup>15</sup>	132
Figure A15: $^1\text{H}$ NMR Spectrum of RB-DMA (0-4.5 ppm) <sup>15</sup>	133
Figure A16: $^{13}\text{C}$ NMR Spectrum of RB-DMA	134
Figure A17: $^1\text{H}$ NMR Spectrum of RB-DIA	135
Figure A18: $^1\text{H}$ NMR Spectrum of RB-DIA (6.0-8.5 ppm)	136
Figure A19: $^1\text{H}$ NMR Spectrum of RB-DIA (0-4.5 ppm)	137
Figure A20: $^{13}\text{C}$ NMR Spectrum of RB-DIA	138
Figure A21: $^1\text{H}$ NMR Spectrum of R6G-A	139
Figure A22: $^1\text{H}$ NMR Spectrum of R6G-A (6.0-8.5 ppm)	140
Figure A23: $^1\text{H}$ NMR Spectrum of R6G-A (0-4.5 ppm)	141

Figure A24: $^{13}\text{C}$ NMR Spectrum of R6G-A	142
Figure A25: $^1\text{H}$ NMR Spectrum of R6G-DCA	143
Figure A26: $^1\text{H}$ NMR Spectrum of R6G-DCA (6.0-8.5 ppm)	144
Figure A27: $^1\text{H}$ NMR Spectrum of R6G-DCA (0-4.5 ppm)	145
Figure A28: $^{13}\text{C}$ NMR Spectrum of R6G-DCA	146
Figure A29: $^1\text{H}$ NMR Spectrum of R6G-DFA	147
Figure A30: $^1\text{H}$ NMR Spectrum of R6G-DFA (6.0-8.5 ppm)	148
Figure A31: $^1\text{H}$ NMR Spectrum of R6G-DFA (0-4.5 ppm)	149
Figure A32: $^{13}\text{C}$ NMR Spectrum of R6G-DFA	150
Figure A33: $^1\text{H}$ NMR Spectrum of R6G-DEA	151
Figure A34: $^1\text{H}$ NMR Spectrum of R6G-DEA (6.0-8.5 ppm)	152
Figure A35: $^1\text{H}$ NMR Spectrum of R6G-DEA (0-4.5 ppm)	153
Figure A36: $^{13}\text{C}$ NMR Spectrum of R6G-DEA	154
Figure A37: $^1\text{H}$ NMR Spectrum of R6G-DMA	155
Figure A38: $^1\text{H}$ NMR Spectrum of R6G-DMA (6.0-8.5 ppm)	156
Figure A39: $^1\text{H}$ NMR Spectrum of R6G-DMA (0-4.5 ppm)	157
Figure A40: $^{13}\text{C}$ NMR Spectrum of R6G-DMA	158
Figure A41: $^1\text{H}$ NMR Spectrum of R6G-DIA	159
Figure A42: $^1\text{H}$ NMR Spectrum of R6G-DIA (6.0-8.5 ppm)	160
Figure A43: $^1\text{H}$ NMR Spectrum of R6G-DIA (0-4.5 ppm)	161
Figure A44: $^{13}\text{C}$ NMR Spectrum of R6G-DIA	162
Figure A45: $^1\text{H}$ NMR Spectrum of RB-DCPA	163
Figure A46: $^1\text{H}$ NMR Spectrum of RB-DCPA (6.0-8.5 ppm)	164
Figure A47: $^1\text{H}$ NMR Spectrum of RB-DCPA (0-4.5 ppm)	165
Figure A48: $^1\text{H}$ NMR Spectrum of RB-DNA	166
Figure A49: $^1\text{H}$ NMR Spectrum of RB-DNA (6.0-8.5 ppm) <sup>16</sup>	167
Figure A50: $^1\text{H}$ NMR Spectrum of RB-DNA (0-4.5 ppm) <sup>16</sup>	168
Figure A51: $^{13}\text{C}$ NMR Spectrum of RB-DNA <sup>16</sup>	169
Figure A52: $^1\text{H}$ NMR Spectrum of RB-2CA	170
Figure A53: $^1\text{H}$ NMR Spectrum of RB-2CA (6.0-8.5 ppm)	171
Figure A54: $^1\text{H}$ NMR Spectrum of RB-2CA (0-4.5 ppm)	172
Figure A55: $^{13}\text{C}$ NMR Spectrum of RB-2CA	173
Figure A56: $^1\text{H}$ NMR Spectrum of RB-2FA	174
Figure A57: $^1\text{H}$ NMR Spectrum of RB-2FA (6.0-8.5 ppm)	175
Figure A58: $^1\text{H}$ NMR Spectrum of RB-2FA (0-4.5 ppm)	176
Figure A59: $^{13}\text{C}$ NMR Spectrum of RB-2FA	177
Figure A60: $^1\text{H}$ NMR Spectrum of RB-2MA	178
Figure A61: $^1\text{H}$ NMR Spectrum of RB-2MA (6.0-8.5 ppm)	179
Figure A62: $^1\text{H}$ NMR Spectrum of RB-2MA (0-4.5 ppm)	180
Figure A63: $^{13}\text{C}$ NMR Spectrum of RB-2MA	181

Figure A64: $^1\text{H}$ NMR Spectrum of RB-2IA	182
Figure A65: $^1\text{H}$ NMR Spectrum of RB-2IA (6.0-8.5 ppm)	183
Figure A66: $^1\text{H}$ NMR Spectrum of RB-2IA (0-4.5 ppm)	184
Figure A67: $^{13}\text{C}$ NMR Spectrum of RB-2IA	185
Figure A68: Stock solution of $\text{CDCl}_3$	186
Figure A69: Purified $\text{CDCl}_3$	187
Figure B1: Sample fluorescence spectra for RB-A	188
Figure B2: Sample titration curve for RB-A	189
Figure B3: Sample UV-Vis spectra for RB-A	189
Table B1: $\text{pK}_a$ values for RB-A	190
Figure B4: Sample fluorescence spectra for RB-DFA	191
Figure B5: Sample titration curve for RB-DFA	192
Figure B6: Sample UV-Vis spectra for RB-DFA	192
Table B2: $\text{pK}_a$ values for RB-DFA	193
Figure B7: Sample fluorescence spectra for RB-DCA	194
Figure B8: Sample titration curve for RB-DCA	195
Figure B9: Sample UV-Vis spectra for RB-DCA	195
Table B3: $\text{pK}_a$ values for RB-DCA	196
Figure B10: Sample fluorescence spectra for RB-DEA	197
Figure B11: Sample titration curve for RB-DEA	198
Figure B12: Sample UV-Vis spectra for RB-DEA	198
Table B4: $\text{pK}_a$ values for RB-DEA	199
Figure B13: Sample fluorescence spectra for RB-DMA	200
Figure B14: Sample titration curve for RB-DMA	201
Figure B15: Sample UV-Vis spectra for RB-DMA	201
Table B5: $\text{pK}_a$ values for RB-DMA	202
Figure B16: Sample fluorescence spectra for RB-DIA	203
Figure B17: Sample titration curve for RB-DIA	204
Figure B18: Sample UV-Vis spectra for RB-DIA	204
Table B6: $\text{pK}_a$ values for RB-DIA	205
Figure B19: Sample fluorescence spectra for RB-DCPA	206
Figure B20: Sample titration curve for RB-DCPA	207
Figure B21: Sample UV-Vis spectra for RB-DCPA	207
Table B7: $\text{pK}_a$ values for RB-DCPA	208
Figure B22: Sample fluorescence spectra for R6G-A	209
Figure B23: Sample titration curve for R6G-A	210
Figure B24: Sample UV-Vis spectra for R6G-A	210
Table B8: $\text{pK}_a$ values for R6G-A	211
Figure B25: Sample fluorescence spectra for R6G-DFA	212
Figure B26: Sample titration curve for R6G-DFA	213



Figure B27: Sample UV-Vis spectra for R6G-DFA	213
Table B9: pKa values for R6G-DFA	214
Figure B28: Sample fluorescence spectra for R6G-DCA	215
Figure B29: Sample titration curve for R6G-DCA	216
Figure B30: Sample UV-Vis spectra for R6G-DCA	216
Table B10: pKa values for R6G-DCA	217
Figure B31: Sample fluorescence spectra for R6G-DEA	218
Figure B32: Sample titration curve for R6G-DEA	219
Figure B33: Sample UV-Vis spectra for R6G-DEA	219
Table B11: pKa values for R6G-DEA	220
Figure B34: Sample fluorescence spectra for R6G-DMA	221
Figure B35: Sample titration curve for R6G-DMA	222
Figure B36: Sample UV-Vis spectra for R6G-DMA	222
Table B12: pKa values for R6G-DMA	223
Figure B37: Sample fluorescence spectra for R6G-DIA	224
Figure B38: Sample titration curve for R6G-DIA	225
Figure B39: Sample UV-Vis spectra for R6G-DIA	225
Table B13: pKa values for R6G-DIA	226
Figure B40: Sample fluorescence spectra for RB-4CA	227
Figure B41: Sample titration curve for RB-4CA	228
Figure B42: Sample UV-Vis spectra for RB-4CA	228
Table B14: pKa values for RB-4CA	229
Figure B43: Sample fluorescence spectra for RB-3,5CA	230
Figure B44: Sample titration curve for RB-3,5CA	231
Figure B45: Sample UV-Vis spectra for RB-3,5CA	231
Table B15: pKa values for RB-3,5CA	232
Figure B46: Sample fluorescence spectra for RB-DCNA	233
Figure B47: Sample titration curve for RB-DCNA	234
Figure B48: Sample UV-Vis spectra for RB-DCNA	234
Table B16: pKa values for RB-DCNA	235
Figure B49: Sample fluorescence spectra for RB-2FA	236
Figure B50: Sample titration curve for RB-2FA	237
Figure B51: Sample UV-Vis spectra for RB-2FA	237
Table B17: pKa values for RB-2FA	238
Figure B52: Sample fluorescence spectra for RB-2CA	239
Figure B53: Sample titration curve for RB-2CA	240
Figure B54: Sample UV-Vis spectra for RB-2CA	240
Table B18: pKa values for RB-2CA	241
Figure B55: Sample fluorescence spectra for RB-2MA	242
Figure B56: Sample titration curve for RB-2MA	243

Figure B57: Sample UV-Vis spectra for RB-2MA	243
Table B19: pK <sub>a</sub> values for RB-2MA	244
Figure B58: Sample fluorescence spectra for RB-2IA	245
Figure B59: Sample titration curve for RB-2IA	246
Figure B60: Sample UV-Vis spectra for RB-2IA	246
Table B20: pK <sub>a</sub> values for RB-2IA	247
Figure C1. RB and R6G pK <sub>a</sub> data for di- <i>ortho</i> substituents versus their Taft-Kutter-Hansch's E <sub>s</sub> values	248
Figure C2. RB and R6G pK <sub>a</sub> data for di- <i>ortho</i> substituents versus their Charton $\nu$ values	248
Figure C3. RB and R6G pK <sub>a</sub> data for di- <i>ortho</i> substituents versus their I <sup>X-H</sup> kJ/mol values	249
Figure C4. RB and R6G pK <sub>a</sub> data for di- <i>ortho</i> substituents versus their Meyer's V <sup>a</sup> values	249
Figure C5. RB and R6G pK <sub>a</sub> data for di- <i>ortho</i> substituents versus their $\sigma_p$ values	250
Figure C6. RB and R6G pK <sub>a</sub> data for di- <i>ortho</i> substituents versus their Traynham's $\sigma_o$ values	250
Figure C7. RB and R6G pK <sub>a</sub> data for di- <i>ortho</i> substituents versus their Swain-Lupton-Hansch's F values	251
Figure C8. RB and R6G pK <sub>a</sub> data for di- <i>ortho</i> substituents versus their Swain-Lupton's R values	251
Figure C9. RB and R6G pK <sub>a</sub> data for di- <i>ortho</i> substituents versus their $\sigma_I$ values	252
Figure C10. R6G A- $\sigma_p$ regression predicted pK <sub>a</sub> versus pK <sub>a</sub> of di- <i>ortho</i> derivatives	252
Figure C11. R6G E <sub>s</sub> - $\sigma_p$ regression predicted pK <sub>a</sub> versus pK <sub>a</sub> of di- <i>ortho</i> derivatives	253
Figure C12. R6G $\nu$ - $\sigma_p$ regression predicted pK <sub>a</sub> versus pK <sub>a</sub> of di- <i>ortho</i> derivatives	253
Figure C13. R6G I <sup>X-H</sup> - $\sigma_p$ regression predicted pK <sub>a</sub> versus pK <sub>a</sub> of di- <i>ortho</i> derivatives	254
Figure C14. R6G V <sup>a</sup> - $\sigma_p$ regression predicted pK <sub>a</sub> versus pK <sub>a</sub> of di- <i>ortho</i> derivatives	254
Figure C15. R6G A- $\sigma_o$ regression predicted pK <sub>a</sub> versus pK <sub>a</sub> of di- <i>ortho</i> derivatives	255
Figure C16. R6G E <sub>s</sub> - $\sigma_o$ regression predicted pK <sub>a</sub> versus pK <sub>a</sub> of di- <i>ortho</i> derivatives	255
Figure C17. R6G $\nu$ - $\sigma_o$ regression predicted pK <sub>a</sub> versus pK <sub>a</sub> of di- <i>ortho</i> derivatives	256
Figure C18. R6G I <sup>X-H</sup> - $\sigma_o$ regression predicted pK <sub>a</sub> versus pK <sub>a</sub> of di- <i>ortho</i> derivatives	256
Figure C20. R6G A-F regression predicted pK <sub>a</sub> versus pK <sub>a</sub> of di- <i>ortho</i> derivatives	257
Figure C21. R6G E <sub>s</sub> -F regression predicted pK <sub>a</sub> versus pK <sub>a</sub> of di- <i>ortho</i> derivatives	258
Figure C22. R6G $\nu$ -R regression predicted pK <sub>a</sub> versus pK <sub>a</sub> of di- <i>ortho</i> derivatives	258
Figure C23. R6G I <sup>X-H</sup> -R regression predicted pK <sub>a</sub> versus pK <sub>a</sub> of di- <i>ortho</i> derivatives	259
Figure C24. R6G V <sup>a</sup> -R regression predicted pK <sub>a</sub> versus pK <sub>a</sub> of di- <i>ortho</i> derivatives	259
Figure C25. R6G A- $\sigma_I$ regression predicted pK <sub>a</sub> versus pK <sub>a</sub> of di- <i>ortho</i> derivatives	260
Figure C26. R6G E <sub>s</sub> - $\sigma_I$ regression predicted pK <sub>a</sub> versus pK <sub>a</sub> of di- <i>ortho</i> derivatives	260
Figure C27. R6G E <sub>s</sub> -F-R regression predicted pK <sub>a</sub> versus pK <sub>a</sub> of di- <i>ortho</i> derivatives	261
Figure C28. R6G E <sub>s</sub> - $\sigma_I$ -R regression predicted pK <sub>a</sub> versus pK <sub>a</sub> of di- <i>ortho</i> derivatives	261
Figure C29. R6G E <sub>s</sub> - $\sigma_I$ -F-R regression predicted pK <sub>a</sub> versus pK <sub>a</sub> of di- <i>ortho</i> derivatives	262
Figure C30. R6G E <sub>s</sub> - $\sigma_I^{\text{mod}}$ -F-R regression predicted pK <sub>a</sub> versus pK <sub>a</sub> of di- <i>ortho</i> derivatives	262
Figure C31. RB A- $\sigma_p$ regression predicted pK <sub>a</sub> versus pK <sub>a</sub> of di- <i>ortho</i> derivatives	263
Figure C32. RB E <sub>s</sub> - $\sigma_p$ regression predicted pK <sub>a</sub> versus pK <sub>a</sub> of di- <i>ortho</i> derivatives	263

Figure C33. RB $I^{X-H}-\sigma_p$ regression predicted $pK_a$ versus $pK_a$ of di- <i>ortho</i> derivatives	264
Figure C34. RB $A-\sigma_o$ regression predicted $pK_a$ versus $pK_a$ of di- <i>ortho</i> derivatives	264
Figure C35. RB $E_s-\sigma_o$ regression predicted $pK_a$ versus $pK_a$ of di- <i>ortho</i> derivatives	265
Figure C36. RB $I^{X-H}-\sigma_o$ regression predicted $pK_a$ versus $pK_a$ of di- <i>ortho</i> derivatives	265
Figure C37. RB $\nu-R$ regression predicted $pK_a$ versus $pK_a$ of di- <i>ortho</i> derivatives	266
Figure C38. RB $I^{X-H}-R$ regression predicted $pK_a$ versus $pK_a$ of di- <i>ortho</i> derivatives	266
Figure C39. RB $E_s-\sigma_p-F$ regression predicted $pK_a$ versus $pK_a$ of di- <i>ortho</i> derivatives	267
Figure C40. RB $E_s-F-R$ regression predicted $pK_a$ versus $pK_a$ of di- <i>ortho</i> derivatives	267
Figure C41. RB $E_s-\sigma_I-R$ regression predicted $pK_a$ versus $pK_a$ of di- <i>ortho</i> derivatives	268
Figure C42. RB $E_s-\sigma_I-F-R$ regression predicted $pK_a$ versus $pK_a$ of di- <i>ortho</i> derivatives	268
Figure C43. RB $pK_a$ data for mono- <i>ortho</i> substituents versus their $\sigma_I$ values	269
Figure C44. RB $pK_a$ data for mono- <i>ortho</i> substituents versus their $F$ values	269
Figure C45. RB $pK_a$ data for mono- <i>ortho</i> substituents versus their $R$ values	270
Figure C46. RB $pK_a$ data for mono- <i>ortho</i> substituents versus their $V^a$ values	270
Figure C47. RB $pK_a$ data for mono- <i>ortho</i> substituents versus their $E_s$ values	271
Figure C48. RB $pK_a$ data for mono- <i>ortho</i> substituents versus their $A$ values	271
Figure C49. RB $pK_a$ data for mono- <i>ortho</i> substituents versus their $\nu$ values	272
Figure C50. RB $pK_a$ data for mono- <i>ortho</i> substituents versus their $I^{X-H}$ values	272
Figure C51. RB $\sigma_p$ regression predicted $pK_a$ versus $pK_a$ of mono- <i>ortho</i> derivatives	273
Figure C52. RB $\sigma_I$ regression predicted $pK_a$ versus $pK_a$ of mono- <i>ortho</i> derivatives	273
Figure C53. RB $\sigma_I^{mod}-R$ regression predicted $pK_a$ versus $pK_a$ of mono- <i>ortho</i> derivatives	274
Figure C54. RB $F$ regression predicted $pK_a$ versus $pK_a$ of mono- <i>ortho</i> derivatives	274
Table D1. Atomic coordinates ( x 104) and equivalent isotropic displacement parameters ( $\text{\AA}^2 \times 103$ ) for RB-DIA	275
Table D3. Torsion angles [ $^\circ$ ] for RB-DIA	285

**Abstract**

Rhodamine based dyes have grown in popularity for use as pH sensors in biological systems due to their sensitive and rapid response to changes in pH. However, these rhodamine dyes typically fluoresce at levels which are too acidic for most biological system. Since the pH at which the dyes fluoresce is a function of the steric and electronic effects of different substituents, different *di-ortho* Rhodamine B (RB) and Rhodamine 6G (R6G) derivatives were synthesized.

Computational models were also used in order to develop a better understanding of the steric and electronic interactions which drive the pH-dependent fluorescence of rhodamine dyes. As a result of titrations of the RB and R6G series, a working equation for use in predicting the pKa of a derivative based on the substituents was drafted using both steric and electronic parameters.

Ultimately, the pH response was tuned enough to allow for the development of a rhodamine pH probe capable of responding at a high enough pH for biological applicability. This pH probe was incorporated into conjugated polymer nanoparticles as proof of concept for a possible vector pathway for future biological studies.

## Introduction

pH expression in biological systems varies based on the location within the cell as different organelles require different pH levels for optimum function. A disruption in this pH level can cause cell death or a change in the function of the cellular system.<sup>1</sup> As a result of these changes, pH plays an important role in certain cell dysfunctions as occurs when pH regulation in the lysosome fails. Autophagy, the process by which cells degrade waste and dispose of damaged organelles, requires an acidic pH; a problem in the regulation of lysosomal pH can contribute to neurodegeneration.<sup>2</sup> Presenilin 1 assists in the acidification of the lysosome which enables the digestive enzymes to work.<sup>3</sup> Mutations in this gene and other lysosomal proteins can all contributed to an abnormal increase of pH. Lysosomes typically have a pH of about 4.7 as opposed to the typical cellular environment, which is firmly in the neutral region around 7. This pH regulation plays an important role in several disease states such as Alzheimer's disease, Parkinson disease, and prototypical lysosomal storage diseases.<sup>2</sup>

While diseases involving the lysosome are usually characterized by an increase in pH, another cellular dysfunction characterized by unusual pH levels is cancer, in which the pH of the cell and surroundings is abnormally low. Due to the large demand for energy needed for continuous growth and division, cancerous cells rely upon anaerobic metabolic processes, even when in the presence of oxygen. This reliance upon glycolysis is called the "Warburg effect." A byproduct of glycolysis is lactic acid which, in addition to the poor blood flow, results in a decrease in extracellular pH from 7.5 to approximately 6.4-7.1. Less of a change is observed in the intracellular pH. The decrease in the extracellular pH benefits the cancer cell in two ways: one, the lower pH allows the cell to pass relatively unnoticed by the body's immune system<sup>4</sup>, and two, the acidic environment further encourages the spread of cancerous cells throughout the

body, a process known as metastasis. Studies have found that correcting the pH can inhibit cancerous growth and increase the effectiveness of some chemotherapeutic drugs.<sup>5</sup>

Fluorescent pH probes are growing increasingly common for studying cancerous cells as they are easy to use, highly specific, and highly selective.<sup>6</sup> Since they can respond quickly to pH changes within a cell and the fluorescent imaging techniques are nondestructive, fluorescent pH probes are particularly well suited for studying cellular systems.<sup>7</sup> However, while there are several fluorescent pH probes designed for a neutral pH range (pH 7), there are fewer for use in the acidic region (pH 4.5-6).<sup>8</sup> Many probes that do work in this region are not well suited to *in vivo* imaging. For example, some are hydrophobic. Probes designed for *in vivo* imaging can be used in the detection of cancers by attaching to cancer-targeting antibody and activating in the lysosome, where the fluorescence is triggered by the more acidic pH. Here, a reversible probe is particularly beneficial as when cell death occurs the pH becomes more neutral and the probe loses the fluorescence signal. As a result, the probe could be used to monitor the effect of treatment on cancer cell death in real-time.<sup>9</sup>

Another method which uses pH-sensitive probes in cancer detection is the injection of the probe into the body. In this process, the fluorescence is most intense on the edges of the tumor as a result of the decreased extracellular pH and possible difficulties encountered by the probe in penetrating deeper into the tumor. Such a distribution would aid surgeons in determining the boundaries of cancerous tumors to ensure the removal of the entire tumor, thereby reducing the chance of remission. Though, as stated above, the extracellular pH of cancerous cells is about 6.4-7.1, dyes that fluoresce at lower pH values still had good fluorescence in and around tumors which makes our goal of a probe in the 4.5-6 range still valid.<sup>4</sup> Rhodamine spirolactams (RSLs) have all the properties needed for *in vivo* imaging, but they typically have pKa values below the

acidic region. One common RSL, rhodamine B, has a pKa of 3.2.<sup>10</sup> Therefore, we developed several new probes by modifying rhodamine dyes through the addition of various substituent groups.

Fluorescence is best explained through use of a Jablonski diagram (**Figure 1**). The blue line demonstrates the excitation of the electron into an excited singlet state. This excitation is caused by the absorption of energy in the form of light. The electron can then relax within the excited singlet state as shown by the dashed line. When the molecule returns to the ground state, as shown by the red line, it emits a photon, releasing the absorbed energy as light. This process is known as fluorescence. Not all compounds are fluorescent; the return to the ground state must be spin allowed. In other words, the excited state electron must be paired to a ground state electron of opposite spin.<sup>11</sup> The absorption of the light produces absorption spectra (**Figure 2**). Both these spectra and the fluorescence spectra typically mirror each other but the latter are observed at higher wavelengths. This means that the emission energy is less than the excitation energy, with the difference between them called the Stokes' shift. Energy can be lost by internal conversion, the transition of the electron from one electronic energy level to another (shown by the first dotted line in **Figure 1**), or by vibrational relaxation within the excited state when the electron

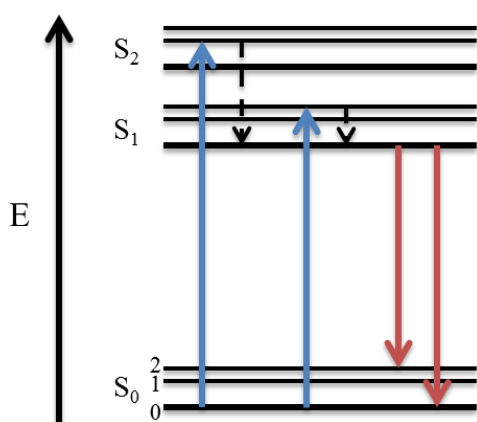


**Figure 1.** Jablonski diagram depicting absorption in blue and fluorescence in red.

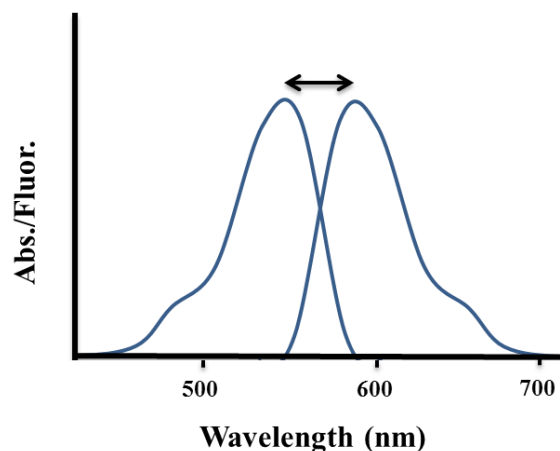


**Figure 2.** Absorption (left) and fluorescence (right) spectra.

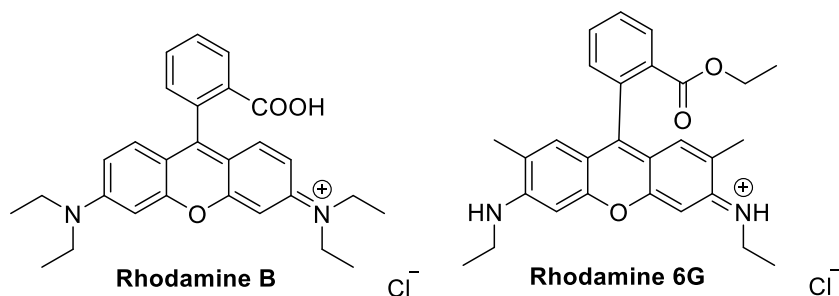
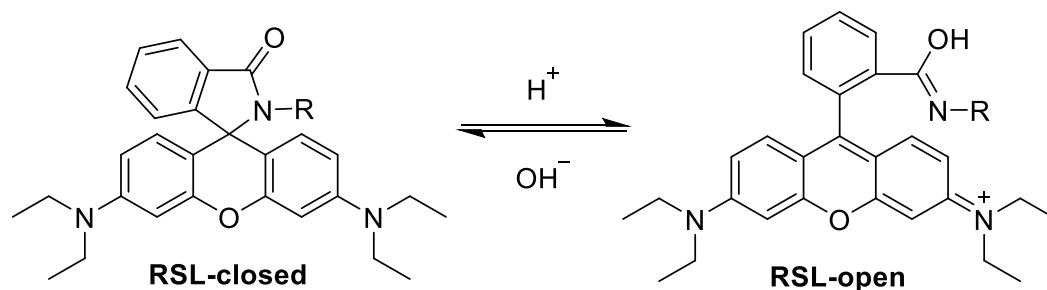


**Figure 3.** Rhodamine dye structures (RB and R6G)



**Scheme 1.** Rhodamine spirolactam ring opening mechanism in rhodamine B.

loses energy to other vibrational states such as the kinetic state (shown by the second dotted line). This process occurs more quickly than fluorescence. Stokes' shifts can also be affected by solvent effects and other interactions.<sup>11</sup>

RSLs are amino isologs of fluorescein dyes.<sup>7</sup> Whereas fluoresceins fluoresce under basic conditions, RSLs are fluorescent in acidic environments, which make them ideal for the purposes outlined earlier in the paper.<sup>12</sup> The specific RSLs used to develop the pH probes described in the following paper were rhodamine B (RB) and rhodamine 6G (R6G) (**Figure 3**). These dyes consist of two planes, one containing the xanthene ring and the other containing the spirolactam ring. The addition of acid protonates the carbonyl on the spirolactam ring, thereby opening the ring and extending the conjugation of the molecule.<sup>6</sup> It is this conjugation which results in fluorescence. Since rhodamines also possess colorimetric properties this ring opening also marks the change of the compound from colorless to bright pink. Since the opening of the spirolactam ring controls the fluorescence it is the ring modified in order to influence the  $pK_a$  of the rhodamine derivative.<sup>6</sup>



Since RSL probes have a second colorless form in addition to the two forms, one colorless and one colored, assumed by the Henderson-Hasselbach equation (1), the Henderson-Hasselback-type mass action equation (2) is instead used to determine  $pK_a$  values.<sup>13</sup>

$$pH = pK_a + \log\left(\frac{[In]}{[HIn^+]}\right) \quad (1)$$

$$pK_a = pH - \log\left(\frac{I_{max}-I}{I-I_{min}}\right) \quad (2)$$

The  $pK_a$  is based on the fluorescence intensity (I), with  $I_{max}$  and  $I_{min}$  as the maximum and minimum fluorescence intensities respectively.<sup>6</sup> This intensity is based on the pH but also depends on the molecule used and the solvent. RSL derivatives demonstrate more intense fluorescence in polar protic solvents, like the ethanol-water mixture used in the fluorescence titrations described later. Protic solvents provide a more stable environment for the ring opening due to their H-bonding interactions with the acyclic amino groups. The polar properties of the protic solvents are also important to the intensity, as greater polarity favors an open-ring structure by separating the intramolecular charges.<sup>14</sup> These solvents effects are less important for pH probes used in cellular environments, where the solvents cannot be varied. Thus, substituents would have the most impact on the fluorescence intensity of those probes. I will discuss the effects of the substituents on the intensity later in the paper, however it is important to note that rhodamine 6G has a more intense fluorescence than rhodamine B.<sup>12</sup> This difference in intensity is explained by R6G's larger quantum yield, 0.95, as compared to RB's quantum yield of 0.65 when measured in ethanol at room temperature.<sup>15</sup> Quantum yields are the number of emitted photons compared to the number of absorbed photons<sup>11</sup>:

$$Q = \frac{\# \text{ photons emitted from } S_1}{\# \text{ photons absorbed}} = \frac{\Gamma}{\Gamma + k_{nr}} \quad (3)$$

$\Gamma$  represents the fluorescence rate constant while  $k_{nr}$  is the rate constant for all nonradiative decay, the return to the ground state by emitting energy in the form of heat instead of as a

photon. Thus, the quantum yield is large if the rate of nonradiative decay is less than the rate of fluorescence. Substances with the largest quantum yields, those near 1, therefore have the most intense fluorescence.<sup>11</sup>

As mentioned previously, RSLs have the properties needed for use in living cells. They possess high photostability with a high quantum yield and long excitation wavelength, so that their use as a sensor in biological systems is sensitive and specific. That means their fluorescence is a response based solely on the pH of the environment.<sup>6</sup> They are also capable of crossing the cell membrane without requiring the use of cell loading techniques that might damage the cell.<sup>1</sup> Once in the cell, rhodamine based sensors are selective for lysosomes as a result of the lysosomal acidic environment.<sup>14</sup> Additionally, several experiments have shown that rhodamine probes are not prone to interference with biologically important species in the cell system and therefore have low cytotoxicities when used at low concentrations.<sup>1,12</sup>

Within this paper, I will examine the effects of substituents on the  $pK_a$  of rhodamine B and rhodamine 6G derivatives. We are interested in determining what types of substituents will raise the  $pK_a$  of these molecules into the desired acidic region so that these probes can then be used in living cells. The key properties of the substituents we are varying are their steric and electronic properties. Prior experiments conducted on RB derivatives with *para* substituted R groups (**Figure 4**) by Will Czaplyski, a former member of the Harbron lab group, demonstrated that the electronic substituent effects did not influence the  $pK_a$ ; the substituent electronics only affected the kinetics of the spirolactam ring opening.<sup>13</sup> Electron-withdrawing substituents had the fastest reaction rate with a more intense fluorescence. All *para* derivatives had similar  $pK_a$  values with an average of  $4.14 \pm 0.04$ . However, we later determined that switching pH probes

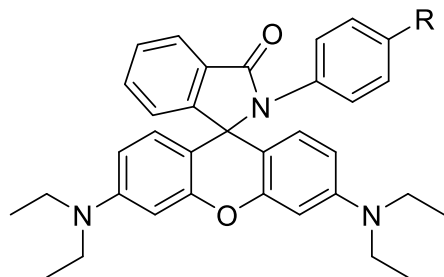


**Figure 4.** Rhodamine *para* substituents (R= -OCH<sub>3</sub>, -*t*-C<sub>4</sub>H<sub>9</sub>, -CH<sub>3</sub>, -H, -Cl, -CF<sub>3</sub>, -C≡N, -NO<sub>2</sub>)

attached to the pH meter without calibrating the instrument had contributed to error in some cases. This lack of calibration in addition to the fact that only one titration trial was used to determine pK<sub>a</sub> resulted in some uncertainty with regards to the results recorded in this paper. A repeat set of four titrations of RB-4Cl gave a pK<sub>a</sub> of 4.21 ± 0.01 as opposed to the previously reported 4.10 value. In addition, RB-A was retitrated for an increased pK<sub>a</sub> value as discussed later in the paper. We may be able to assume that all the data points are still within a narrow distribution, just slightly shifted due to inaccurate pH readings during the titration.

In comparison, the single titration of RB-2,6-Cl<sub>2</sub>-4-NO<sub>2</sub> (RB-DCNA) had a value of 5.43 which was far more consistent with the three additional titrations for a final pK<sub>a</sub> of 5.46 ± 0.03. This particular probe was developed to test the theory that sterically bulky groups would increase the pH and was consistent with Lin Yuan's findings.<sup>12,13</sup> Yuan supported his theory by attaching 1-adamantanamine to the amide moiety of both R6G and RB for pK<sub>a</sub> values of 6.5 and 5.6

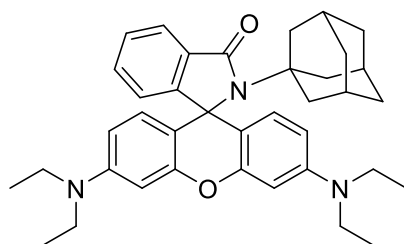


**Figure 5.** Rhodamine B-adamantanamine

respectively.<sup>12</sup> The RB version of this compound is depicted in **Figure 5**. R6G derivatives tend to derivatives tend to fluoresce at higher  $pK_a$ s because the additional methyl group on the xanthene ring creates greater steric strain, making the spirolactam ring more likely to open. Another set of Yuan's compounds involved a *para* substituted R group of -OH (using the same model as in **Figure 4**). This R6G-4OH had a  $pK_a$  value of 3.2. Unfortunately, the  $pK_a$  for the RB version of this derivative was not reported but if it is less than the R6G-4OH, as is generally the case, than there is a *para* substituent which is inconsistent with Czaplowski's data. Thus, either R6G compounds react differently when *para* substituted or else the theory that only steric bulk influences ring opening in *para* substituted compounds begins to break down. I will discuss the possibility of both these options and the consequences later in this paper in reference to my titrations of di-*ortho* substituted RB and R6G derivatives as well as Mona Rasooly's titrations of mono-*ortho* substituted RB derivatives (**Figure 6**). Grace Purnell synthesized several of the RB di-*ortho* compounds and Grace Taumoefolau synthesized the majority of the R6G versions. Additionally, I will use Purnell's calculations of the optimized structure for the RB di-*ortho* derivatives with the exception of RB-diethoxyaniline (RB-DEA), which I calculated.

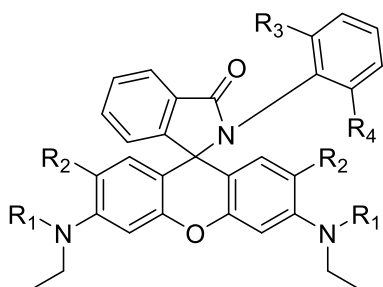


**Figure 6.** RB and R6G di-*ortho* substituents and RB mono-*ortho* substituents  
 Rhodamine B di-*ortho* compounds ( $R_1$ =Et,  $R_2$ =H,  $R_3$ = $R_4$ = -H, -Cl, -F, -OEt, -Me, -*i*-Pr),  
 rhodamine 6G di-*ortho* compounds ( $R_1$ =H,  $R_2$ =Me,  $R_3$ = $R_4$ = -H, -Cl, -F, -OEt, -Me, -*i*-Pr), and  
 rhodamine B mono-*ortho* compounds ( $R_1$ =Et,  $R_2$ = H,  $R_3$ = H,  $R_4$ = -Cl, -F, -Me, -*i*-Pr)

The goal of this project was to determine the influence of the steric and electronic properties of di-*ortho* substituents on the opening of the spirolactam ring. We tested several different numerical measurements of steric bulk and electronics to determine the best model for the system. Our original hypothesis based on Czaplyski's data from the *para*-substituted RB set was that steric bulk would increase the  $pK_a$  but that the electronic properties of the substituent would not impact the  $pK_a$  in any way. We hoped to be able to successfully synthesize a dye with a  $pK_a$  in the acidic region and then be able to incorporate that dye onto a conjugated polymer nanoparticle (CPN). CPNs can serve as a vector for transporting drugs, and in this case dyes, into a cell. They have low cytotoxicity and the combination of their large quantum yield and photostability makes them ideal for *in vivo* imaging.<sup>16</sup> CPNs have been used in imaging cancer tumors previously and can be conjugated to attach antibodies targeting cancer cells as a means of transporting the rhodamine dyes to those cells for imaging as otherwise our dyes would not specifically target them.<sup>17</sup>

## Results and Discussion

### Section I. Synthesis of di-*ortho* RB and R6G derivatives

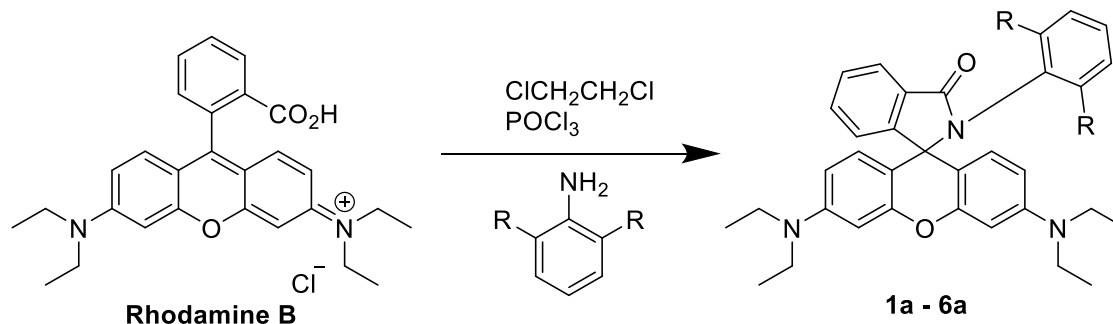
Synthesis of di-*ortho* substituted RSL derivatives is challenging due to the steric interactions. The yields of RB reactions are substantially lower (8-57%) than Czaplyski's percent yields for his *para*-substituted RB compounds (40-94%). R6G derivatives have even lower yields (5-18%) due to their increased reactivity, the result of the hydrogen groups off of the xanthene nitrogens and the increased steric hindrance provided by the xanthene ring methyl groups. R6G based compounds also tended to interact more with the silica type column due to their greater sensitivity to the acidic column and therefore increased streaking, which caused more product to be lost during separation due to bands running together and product remaining on the column. Hereafter the RSL derivatives with the di-*ortho* R groups -H, -F, -Cl, -Me, -OEt, and -*i*-Pr will be abbreviated as RB-A, RB-DFA, RB-DCA, RB-DMA, RB-DEA, and RB-DIA respectively with the RB replaced by R6G for those versions of the derivatives. These specific side groups were chosen for their range of steric values.

The synthesis procedure used in the creation of the RB di-*ortho* substituents was developed by Grace Purnell. It is similar in nature to the procedure outlined in Czaplyski's paper, but with variations in the duration of reflux, atmosphere, and ratio of reactants.<sup>13</sup> These differences could have also contributed to the small percent yields and would be worth investigating further for future synthesis reactions. The synthesis procedure developed for the R6G di-*ortho* substituents was optimized by Grace Taumoefolau based in part on the synthesis described by Quinn Best and colleagues in their paper on Anilinomethylrhodamines.<sup>18,19</sup>

This section contains a basic summary of the synthesis procedures used to make di-*ortho* substituted RB and R6G derivatives as well as a discussion of their purification. Additionally, I

will detail the differences between the previous procedure used for RB derivative synthesis and the current procedure as well as possible modifications and investigations.

A. *RB di-ortho derivatives synthesis and purification*



**Scheme 2.** Rhodamine 6G synthesis and derivatives  
 R= H(**1a**), F (**2a**), Cl (**3a**), Me (**4a**), OEt (**5a**), iPr (**6a**)

A single pot reaction was used for the synthesis of RB di-*ortho* derivatives, detailed above in **Scheme 2**. RB reacts best under reflux. The phosphoryl chloride ( $\text{POCl}_3$ ) and 1,2-dichloroethane ( $\text{ClCH}_2\text{CH}_2\text{Cl}$ ) reacted with the RB to create RB-acid chloride, in which the OH group was replaced with Cl. This reaction set up the second step, in which the acid halide's C-Cl bond is broken by the formation of HCl, leaving the amide attached to the RB base. These reactions can clearly be split into a multi-step reaction, and indeed we found that splitting up the process worked best when synthesizing RB-dinitroaniline (RB-DNA). However, generally the RB synthesis worked well with just one step.

In a one-step reaction, RB was dissolved in dichloroethane. Next,  $\text{POCl}_3$  was slowly added drop-wise, while swirling. A 3:1 ratio of the aniline derivative to RB was used (1.25 mmol of aniline derivative). The aniline was also slowly added drop-wise, while swirling. These chemicals formed the mixture to be refluxed. The reaction was run under reflux until a thin-layer chromatography (TLC) plate showed evidence of product formation, which typically took about twenty-four hours. This product was usually found as a pink band just under a yellow band which indicated the presence of unreacted aniline. A UV lamp provided further proof of product as the band containing product glowed when the TLC plate was placed under the UV light. In



particular, the product band glowed under the long wave UV light of 365 nm. The solvent used for the TLC plates was a mixture of ethyl acetate and hexanes, with ethyl acetate being polar and hexanes being non-polar. At times the product band was difficult to discern due to the presence of other byproducts. In these cases, the reaction was run until there was no noticeable change in the TLC plate from the day prior. A reaction was rarely run longer than three days.

Unfortunately, starting material was always present so monitoring for the disappearance of the starting material was ineffective. The continued presence of starting material does suggest that the synthesis could be further streamlined to minimize waste.

In the case of the two-step reaction for RB-DNA, RB was dissolved in dichloroethane.  $\text{POCl}_3$  was then added dropwise to the mixture over the course of several minutes. This mixture was then refluxed for four hours to produce RB-acid chloride. After reflux, the solution was rotovapped until no solvent remained before being redissolved in dichloroethane. A 6:1 molar ratio was used of DNA (2.51 mmol) to RB. This ratio was larger than the 3:1 ratio of aniline derivative to RB typically used in this type of synthesis. DNA was particularly difficult to attach to the RB base, hence the greater excess of aniline to ensure a good conversion. Once the DNA was added slowly drop-wise, it was refluxed until the TLC plate showed product (ca. 24 h). This two-step reaction was most similar to the synthesis procedure used in the Best paper mentioned previously.<sup>18</sup>

Czaplyski ran his *para*-substituted reactions in an argon atmosphere.<sup>13</sup> This argon is intended to keep the reaction dry so as to minimize side reactions, which is of particular importance in the R6G derivative synthesis. RB is not as reactive, which is presumably why the use of argon atmosphere was unnecessary. Instead, the rubber stopper was used to cover the round bottom to reduce exposure to contaminants but this step appeared to have little effect on

the yield. Another difference between the prior procedure and current procedure is the time of reflux. Czaplyski only ran his reflux reaction for five hours.<sup>13</sup> While Yuan and Best both performed two-step reactions in their respective papers, Yuan refluxed both steps for six hours while Best refluxed the first step for four hours and the second step for twenty-four hours.<sup>12,18</sup> The shorter duration of reflux could minimize the chance for byproduct formation, assuming that the RB di-*ortho* derivative is preferentially and rapidly formed. The Best paper still reported high yields, however.<sup>18</sup> Given these findings, I might suggest an investigation comparing a one-step to a two-step reaction, particularly since RB-DNA was best synthesized through use of the later procedure. It therefore stands to reason that the two-step reaction might have an increased yield; addition of the aniline post acid halide formation might also minimize possible interactions between the POCl<sub>3</sub> and aniline. Additionally, an investigation of reflux duration should be done ranging from five hours to twenty-four while monitoring the percent yield and byproduct formation. As mentioned above, monitoring the reaction through the presence of the starting material is not effective with the current procedure but should the synthesis be improved to the point where all the starting material is interacting with the reagents then the disappearance of starting material would be the best indication that the reaction has run to completion.

The final key difference in Czaplyski's synthesis procedure was the amounts of reactants used. In my synthesis procedure I used 0.42 mmol of RB, 3.22 mmol of POCl<sub>3</sub>, and 1.25 mmol of the aniline derivative except for the RB-DNA synthesis where 2.51 mmol was used. Czaplyski used 0.21 mmol of RB, 0.25 mmol of POCl<sub>3</sub>, and 0.63 mmol of the aniline derivative.<sup>13</sup> While both procedures typically have an excess of aniline at a 3:1 ratio compared to RB, with the exception of the RB-DNA synthesis, the ratio of POCl<sub>3</sub> to RB is significantly different. Czaplyski's synthesis had a 1.19:1 ratio of POCl<sub>3</sub> to RB, an approximately equivalent ratio. My

synthesis on the other hand had a greater excess of  $\text{POCl}_3$  for a 2.68:1 ratio. I believe that Czaplyski's ratio makes more sense synthetically as  $\text{POCl}_3$  is highly reactive and so could be causing byproduct formation when in an excess. Such formations could contribute to our lower product yields. Theoretically, one mole of  $\text{POCl}_3$  should react with one mole of RB to form RB-acid chloride so a 1:1 ratio would be best. This aspect of our synthetic procedure should be modified. Czaplyski also added the  $\text{POCl}_3$  after the addition of the aniline to the RB solution but I feel that, based on the preference for the two-step reaction in the literature, the formation of RB-acid chloride prior to the addition of the aniline was best.<sup>13</sup> However, this change in the order of reactant addition may be worth investigating.

The workup for RB derivatives after the solution was removed from reflux involved diluting with chloroform before washing with acid, base, and brine in a separatory funnel. Anhydrous magnesium sulfate was added to the organic layer. Magnesium sulfate clumps in the presence of water so it was added to the mixture until the mixture gained a snow globe effect when swirled, that is it was added until the magnesium sulfate stopped clumping when added. Then the mixture was filtered and concentrated under reduced pressure to form the crude product. A  $^1\text{H}$  NMR spectrum of this mixture was used to confirm the presence of product.

Flash column chromatography was used to separate the desired product from the byproducts and starting material. Prior to beginning a column, a ratio of ethyl acetate to hexanes was decided upon by testing several proportions to determine which gave the best separation of bands on the TLC plate. A ratio of 80:20 of ethyl acetate to hexanes (EtOAc:Hexanes) provided the quickest retrieval of the product, that is the highest retention factor ( $R_f$ ) value. However, it also tended to have the least amount of separation. The lower the ratio of EtOAc:Hexanes, the greater the separation but the longer it took for the product band to exit the column. Therefore a

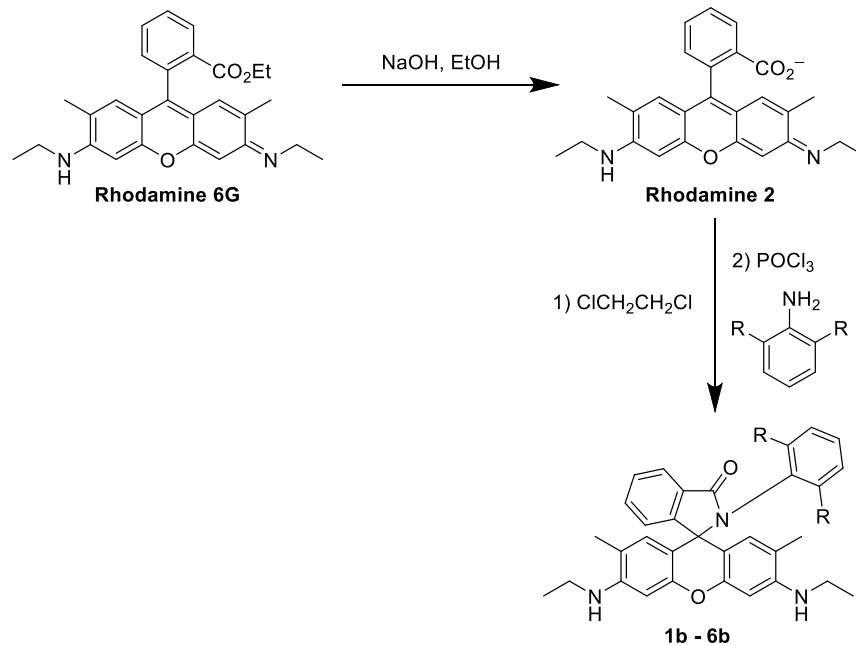
ratio between 40:60 EtOAc:Hexanes and 60:40 EtOAc:Hexanes was usually selected as the starting eluent for the column. This gradient could be increased gradually once a good degree of separation had been achieved within the column in order to speed the elution. Thus, the gradient was usually increased once the excess aniline, which had the highest  $R_f$  value of all the bands, was eluted from the column. The product band was generally the band immediately following the aniline band, but this was not always the case.

The stationary phase of the column chromatography was silica gel. Since silica gel is somewhat acidic, product would open on the column, which could result in the product band getting 'stuck'. The interactions between the silica and acid-sensitive RB derivative could slow the band to the point where it would not move through the column or would 'smear' which would draw out the width of the band and therefore increase the risk of byproduct bands running into the product band. The regular addition of triethylamine, a base, was needed to keep the product closed and therefore moving smoothly through the column. The column was then packed using a slurry method in which the EtOAc:Hexane solvent was added to dry silica in an Erlenmeyer flask. This slurry was then added to the column. Extra solvent was added before air was run through the column to increase the flow rate. Just when the solvent was about to enter the stationary phase, the air was stopped and the stop-cock closed. About a millimeter of sand was added to the top of the column. The crude product was dissolved in chloroform and pipetted into the column in a manner which ensured that the sand layer was evenly saturated with the product containing solution. Solvent could then be added, taking care not to disturb the sand layer. Air was an effective means of pushing the solvent through the stationary phase at a faster rate but it was necessary to watch the column carefully to make sure that no parts of the stationary phase began to dry out. The bands exiting the column were collected in test tubes,

which were then tested on TLC plates to ensure there was only one compound present in the band. Product usually appeared as a pink dot on the TLC plate and glowed under UV light as mentioned above. TLC was used to confirm the start and end of each band. The test tubes containing that band were combined into a round bottom flask and rinsed with acetone into that same round bottom in order to gather as much product as possible. The round bottom was then concentrated *in vacuo* to form a powder so that an NMR could be used to confirm that the band was indeed product. Sometimes multiple columns needed to be run on a compound to obtain a pure product. I found that the high vacuum line worked better than the rotovap to further dry the product at this stage.

Best used an alumina column, which is more basic in nature than silica gel, in order to prevent reactions between the desired product and stationary material.<sup>18</sup> However, Grace Taumoefolau found that, at least in the case of R6G di-*ortho* derivatives, the alumina column interacted with the product in such a manner that it changed the structure, possibly as a result of oxidizing an amine on the xanthene rings.<sup>19</sup> While this process is less likely to occur with RB derivatives due to the lack hydrogen on the amines of the xanthene ring plane and alumina columns were successfully used with R6G derivatives by Best, I would still continue to use silica gel. As long as the product is kept in the closed form, RB does not appear to interact too much with the silica gel and Czaplyski was still able to get high product yields using this type of column.<sup>13</sup>

### B. R6G di-ortho derivatives synthesis and purification



**Scheme 3.** Rhodamine 6G synthesis and derivatives  
 R= H(**1b**), F (**2b**), Cl (**3b**), Me (**4b**), OEt (**5b**), iPr (**6b**)

As shown in **Scheme 3** above, the synthesis for R6G derivatives was somewhat more involved than for their RB counterparts. RB needs the energy from heat during reflux to react; an attempted synthesis of an RB di-*ortho* derivative at room temperature revealed no product formation after a day. Unlike RB, R6G-acid is sensitive to heat and water in the air, therefore it has to be run under room temperature or cold conditions with measures taken to ensure the entire process remains as dry as possible. Grace Taumoefolau optimized the R6G synthesis procedure into the following process to minimize byproduct formation.<sup>19</sup>

In the first step of the reaction, R6G-acid was synthesized. R6G, NaOH, EtOH (ethanol), and de-ionized water (DI H<sub>2</sub>O) were combined in a round bottom and refluxed for approximately twenty-four hours before leaving to stir for two days. The round bottom was then placed in an ice bath where 6 M HCl was slowly added to the solution before the mixture underwent Buchner filtration. R6G-acid was obtained in the form of a sticky red solid. During this synthesis the

condenser should be kept greased for the reflux stage as otherwise the round bottom will stick to the condenser.

For the next step in the procedure, molecular sieves were added to a round bottom. The top was then covered with rubber stopper and needle to vent after adding a stir bar. The round bottom was then flame dried while connected to argon gas. The heat from the flame activated the molecular sieves. The round bottom was left to cool as R6G-acid from step one was massed out into a small Erlenmeyer. The R6G-acid was crushed with a spatula and anhydrous dichloroethane was added before sonicating. 10 mL of anhydrous dichloroethane was added to the round bottom while stirring, before the 20 mL from the Erlenmeyer was added. Another 20 mL of dichloroethane was added to the Erlenmeyer and once again the R6G-acid was crushed prior to sonicating. This solution was then added to the round bottom. The remaining R6G-acid was crushed as much as possible, then 10 mL dichloroethane was added to it and the mixture was sonicated. This final batch was added to round bottom. Since R6G-acid is so sticky, there was always some left over in the Erlenmeyer so it was best to err on the side of too much R6G-acid than too little for the sake of product yield. It was also important to attempt to dissolve as much R6G-acid as possible into the dichloroethane, not just so that there was more R6G to react with the aniline later but also so the needle would not be clogged when attempting to transfer the dichloroethane into the round bottom. R6G works best under more dilute circumstances, hence why the quantities of dichloroethane used in this reaction are far greater than in the RB reaction where dilution is not as important.

The dissolved R6G-acid was in the round bottom to stir overnight under argon. After approximately twenty-four hours, the solution was placed in an ice bath. While still stirring and under argon, 3.29 mmol of an aniline derivative was added and left to stir for thirty minutes.

After thirty minutes, 0.05 ml of  $\text{POCl}_3$  (0.54 mmol) was added drop-wise. The formation of product upon this addition of  $\text{POCl}_3$  is almost instantaneous. If the reaction with  $\text{POCl}_3$  occurs too quickly, the R6G-acid will form a byproduct that will precipitate out of the solution so the reaction is slowed by use of the ice bath. A suggestion for future synthesis reactions with R6G would be the possible use of a dry ice and acetone bath to further slow the reaction, which might reduce the number of byproducts.

Though I recommended adding  $\text{POCl}_3$  first in the RB derivative synthesis procedure, I feel that given the rapid formation of product it is best added last here. The high reactivity and R6G's tendency to form byproducts would suggest that adding  $\text{POCl}_3$  first would increase the number of byproducts. The ratio of aniline derivative to R6G-acid here is 6.85:1, which is appropriate given the already low product yields. In this manner, the synthesis of RB-DNA is similar to the synthesis of R6G di-*ortho* derivatives. The ratio of  $\text{POCl}_3$  to R6G-acid here is 1.13:1, which is much closer to the 1:1 ratio I recommended earlier than the ratio used in the RB di-*ortho* synthesis.

The mixture was stirred overnight under argon in the ice bath. The next day, the melted ice bath was removed and the solution left to stir for another twenty-four hours, with TLC confirming the presence of product. The solution was then removed from the stir plate and taken off the argon gas before setting up a Buchner filtration. At this stage, anhydrous dichloroethane was no longer needed so the filter was washed with non-anhydrous dichloroethane until the filtrate was clear. The liquid was then transferred to a large separatory funnel, rinsing the flask with more dichloroethane until the liquid in the flask was clear to ensure all possible product was retrieved. The work up consisted of four washes with small amounts of chilled base and one wash with brine. The organic layer contained product, just as with the RB workup, but particular



care was taken with the R6G to be gentle when swirling the separatory funnel. Violent shaking encourages emulsion formation while acid protonates the R6G, forming a salt which is difficult to dry, hence the lack of an acid wash. Once the solution had been collected from the separatory funnel, anhydrous sodium sulfate was used to remove water from the mixture. Once the sodium sulfate stopped clumping, another Buchner filtration was performed, including scooping the wet sodium sulfate onto the filter and rinsing with chloroform to ensure the greatest transfer of product. This solution was then condensed *in vacuo* before obtaining a  $^1\text{H}$  NMR spectrum to determine if the synthesis was successful.

The purification process for R6G was basically the same as for RB, discussed in detail previously in this paper. Of note though, is that R6G was more prone to getting ‘stuck’ in a column due to its reactions with the acidic silica so less silica gel should be used in columns for R6G and triethylamine is of particular importance in the solvent. Smaller diameter columns with small amounts of silica gel are best for use with R6G compounds. R6G derivative synthesis also tends to produce more byproducts so these derivatives typically have to go through more columns than the RB series compounds. Additionally, due to the large number of bands, a smaller ratio of EtOAc to Hexanes is recommended to promote separation over speed. The heat from the rotovap did not appear to have an adverse effect on the R6G derivatives but generally the high vacuum line is better for drying the R6G compounds due to the colder environment.

C. Conclusions and Future Directions for RSL Synthesis Pathways

**Table 1.** Comparison of syntheses for RB and R6G di-*ortho* substituted derivatives

	<b>RB di-<i>ortho</i> derivatives</b>	<b>R6G di-<i>ortho</i> derivatives</b>
Number of Steps in Reaction	One step	Multi-step
Reaction Time/Condition (post aniline and POCl <sub>3</sub> addition)	Refluxed for 24 hrs	Stirred in cold environment for 12 hours Stirred at room temperature for 24 hours
Atmosphere	Open to air	Argon atmosphere
Order of addition of POCl <sub>3</sub> and aniline	1) POCl <sub>3</sub> 2) Aniline	1) Aniline 2) POCl <sub>3</sub>
Ratio of rhodamine to POCl <sub>3</sub>	1:2.68	1:1.13
Ratio of rhodamine to aniline	1:3	1:6.85
Percent Yield	8-57%	5-18%

While Grace Taumoefolau's optimized synthesis for R6G derivatives proved efficient, as the compounds had relatively high yields for the difficult steric environment, the RB derivative synthesis was less efficient. Obviously, the ratio of POCl<sub>3</sub> to rhodamine needs to be adjusted downwards. The change to an argon atmosphere might be worthwhile in particularly difficult syntheses, like the synthesis of RB-DNA; however, overall RB is not as reactive as R6G and so maintaining a dry environment would not increase the yield significantly. Certainly the two-step procedure seems to be effective at boosting the yield, as it did for RB-DNA; however, I was unable to replicate this synthesis after repeated attempts and the RB-acid chloride formed would have to be very stable and not particularly likely to react with its environment. A two-step procedure creating RB-acid chloride and then adding aniline under argon might be worth investigation though. Such a procedure would more closely model the R6G derivative synthesis, except with the use of reflux as opposed to an ice bath. Increasing the ratio of rhodamine to aniline would help in sterically complex molecules but in a simple RB derivative synthesis it would simply be a waste of aniline. These modifications should help in optimizing the synthesis procedure for RB di-*ortho* derivatives and thereby improve the yield.

## Section II. pK<sub>a</sub> studies of *ortho*-substituted RB and R6G derivatives

### A. Titrations of RB and R6G di-ortho compounds

Both series of compounds needed to be titrated in order to determine the pK<sub>a</sub> of each compound. Titrations were performed a minimum of four times to determine if the results were replicable. The standard deviation of the experimental pK<sub>a</sub>s was used to verify the four titrations- if the standard deviation was below 0.1, the titrations were considered accurate and reproducible. Compounds were titrated no more than eight times. An overview of the literature reveals that it is relatively common to do one titration; however, a minimum of four titrations, with additional trials needed if the standard deviation is high, provides greater accuracy.<sup>12,13</sup>

The general titration procedure began by massing out approximately 1 mg of the compound. This 1 mg ( $\pm 0.0003$  g) was then dissolved in 25 mL of ethanol (EtOH) in a volumetric flask. 10 mL of this solution was then placed in a 100 mL volumetric flask. 40 mL of EtOH and 50 mL of de-ionized water (DI H<sub>2</sub>O) was added to create a 1:1 solution of EtOH to water. Since the quantum yield of R6G is greater than for RB, all the R6G compounds and some RB compounds had to go through a further dilution, with 10 mL of the 1:1 solution of EtOH detailed above placed in a volumetric flask and diluted with another 40 mL of EtOH and 50 mL of DI H<sub>2</sub>O.<sup>15</sup> RB-DCA and RB-DMA were the only RB compounds which needed to undergo the second dilution. These dilutions were stirred for a least 1 hour prior to the titration, which was done with 0.1 M HCl acid. The use of acid meant that small quantities of 0.1 M NaOH had to be added to the solution before titration in order to raise the pH to a reasonable point where none of the compound was in the open form. An example of the fluorescence data obtained from a titration is shown in **Figure 7**.

The fluorescence of the compounds as viewed with a fluorimeter increased as the

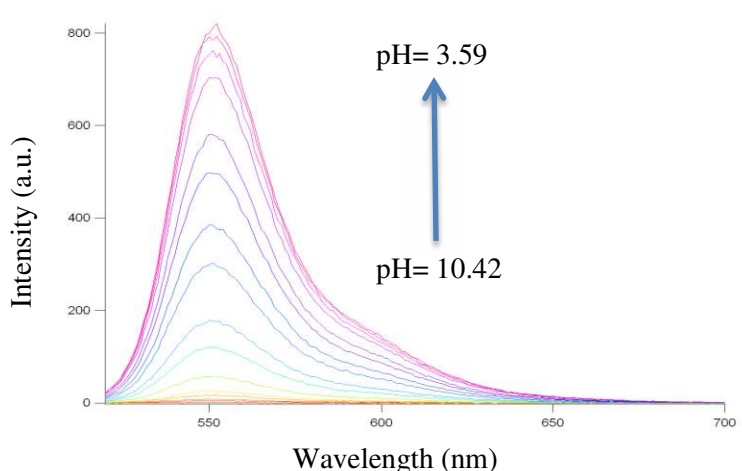


**Figure 7.** A fluorescence spectra of R6G-DMA throughout the course of a titration.

addition of acid induced a ring opening, transforming the closed and non-fluorescent RSL to the fluorescent form. Similarly, the absorbance of the compounds as noted on the UV-Visible spectrometer increased with the addition of acid as the compounds changed from the colorless forms to the pink ones. However, there was an additional stage at which both the fluorescence and absorbance stopped increasing and in fact began to decrease. This loss of fluorescence demonstrates the transformation of the fluorescent form of the dye into a second colorless and non-fluorescent form<sup>13</sup>. At what pH the ring started opening and when the fluorescence reached its peak was dependent upon the compound. R6G compounds had a  $\lambda_{\text{max,fl}}$  in the 551-555 nm range while RB compounds had their peaks from 581-583 nm, depending on the attached substituent.

The peak fluorescence intensity of the compounds was graphed against the pH to develop a titration curve, as shown in **Figure 8**. In this particular graph, the maximum fluorescent intensity was 495 at 552 nm and the fluorescence intensities were normalized so that 495 was 1.0 on the fluorescent intensity axis in the figure. The midpoint of the titration curve, that is the pH at which the fluorescence intensity is 0.5 on the normalized graph, is the  $\text{pK}_a$  of the compound. A

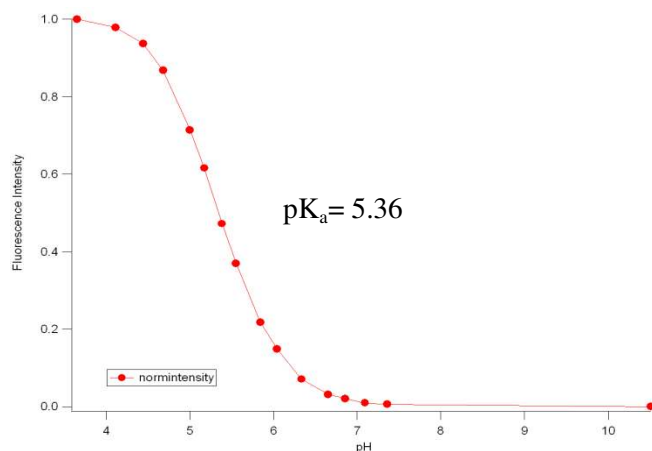


**Figure 8.** Graph of fluorescence peak intensity versus pH for R6G-DMA.

**Table 2.** Average  $pK_a$  values for the RB and R6G di-*ortho* series.

Substituent	RB $pK_a$	R6G $pK_a$
H	$4.31 \pm 0.02$	$3.81 \pm 0.02$
F	$4.52 \pm 0.08$	$4.30 \pm 0.04$
Cl	$5.38 \pm 0.08$	$5.62 \pm 0.04$
OEt	$4.03 \pm 0.07$	$4.15 \pm 0.05$
Me	$4.90 \pm 0.11$	$5.32 \pm 0.07$
iPr	$5.72 \pm 0.13$	$5.87 \pm 0.06$

more exact method of determining the  $pK_a$  was through the use of a modified Henderson-Hasselbalch equation to account for the two colorless and non-fluorescent forms of the RSL, as mentioned in the introduction.<sup>13</sup> For the R6G-DMA titration from **Figure 8**, the  $pK_a$  was 5.33.

R6G typically fluoresces at a higher  $pK_a$  than RB. This general trend is observed in most of the collected data, with the exceptions being R6G-A and R6G-DFA. As a result, R6G covered the greatest pH range for a total range of 2.06 as compared to RB's range of 1.69. Given that the substituents H and F have the smallest steric bulk, these observations can be interpreted as being due to steric interactions. R6G compounds tend to have higher  $pK_a$ s because their additional methyl group on the xanthene ring creates greater steric strain, which makes the spiro lactam ring more likely to open. It appears that this steric interaction only drives the opening of the spiro lactam ring when the di-*ortho* substituents on the attached aniline ring have a greater steric bulk. This explanation does not explain why the  $pK_a$  for these compounds is lower than the RB

versions. One possible explanation is that conformationally flexible nature of the ethyl groups off of the xanthene ring nitrogens in RB compounds results in an ethyl group flipping back to interact with the RB substituents.

Yuan and colleagues hypothesized that steric effects were what determined the  $pK_a$  of a compound and that larger groups would increase the  $pK_a$ .<sup>12</sup> Their findings were supported by Czaplyski's own RB *para*-substituted derivatives, which had a narrow range of  $pK_a$  values. The narrow range indicated that electronics did not play a role in the spiro lactam ring opening.<sup>13</sup> We did find that bulkier substituents tended to increase the  $pK_a$  as in the case of RB-DCNA ( $pK_a$  of 5.46) and both the RB and R6G di-*ortho* isopropyl aniline substituted derivatives. However, the narrow range mentioned for the *para*-substituted compounds ( $4.14 \pm 0.04$ ) cannot be entirely trusted as repeated titrations on RB-A and RB-4Cl resulted in values of 4.31 and 4.21 respectively.<sup>13</sup> Both are increases from their previously reported values. We can assume that the remainder of the compounds still remain within a relatively narrow distribution of  $pK_a$  values, albeit slightly higher ones than originally thought; however, there is some evidence contradicting this assumption.

As mentioned in the introduction, Yuan's R6G-4OH had a  $pK_a$  value of 3.2.<sup>12</sup> If the  $pK_a$  for the RB version of this derivative is less than the R6G-4OH, as RB compounds tend to be lower in  $pK_a$  than their R6G counterparts, the *para*-substituent is significantly different from the narrow range suggested by Czaplyski's results. The hydroxyl group is strongly electron donating when attached to an aromatic system, more so than the  $-OCH_3$  *para*-substituent in Czaplyski's paper.<sup>13</sup> Otherwise, it does not have a greater steric bulk than the other *para*-substituted RB derivatives Czaplyski tested. Thus, if the  $pK_a$  is lower, it is due to electronic effects.

The protonated intermediate form of the rhodamine has a positive charge (see **Scheme 1**).

**Table 3.** Average pK<sub>a</sub> values for the additional titrations. RB-2,6 DCPA is RB-2,6-(C<sub>5</sub>H<sub>4</sub>)<sub>2</sub>, RB-3,5-DCA is RB-3,5-Cl<sub>2</sub>, RB-4CA is RB-4-Cl, and RB-DCNA is RB-2,6-Cl<sub>2</sub>-4-NO<sub>2</sub>.

Compound	pK <sub>a</sub>
RB-2,6DCPA	4.97 ± 0.06
RB-3,5DCA	4.34 ± 0.05
RB-4CA	4.21 ± 0.01
RB-DCNA	5.46 ± 0.03

This charge can be stabilized by electron donating groups so that the intermediate is more favorable. Only when the steric bulk is great enough can it overcome this stabilizing effect, as seen with both RB-DIA and R6G-DIA. In comparison, the electron withdrawing groups destabilize the intermediate, making it less favorable and thereby raising the pK<sub>a</sub> of the derivative. Since –OH is electron donating, it is possible that the *para*-substituent can still stabilize the intermediate, which could explain the possibly lower pK<sub>a</sub>.

Steric effects did not appear to influence the ring opening in the case of the *para*-substituents. The pK<sub>a</sub> value does not increase significantly as the steric bulk of the substituent increases. Presumably, the *para*-substituents are located far enough away from the spirolactam ring that both their steric and electronic properties do not play nearly as great a role as they do in the *ortho*-substituted derivatives.

Returning to the R6G-4OH, it is quite possible that this R6G compound has a lower pK<sub>a</sub> than its hypothetical RB counterpart. Remember that R6G-A and R6G-DFA had smaller pK<sub>a</sub>s as compared to RB-A and RB-DFA. While –OH has a larger steric bulk than both of these substituents, the fact that the substituents are di-*ortho* doubles their steric bulk so that –OH is closer in size to them. Additionally, it is possible that it is removed enough from the spirolactam ring that it effects the ring system as would a smaller substituent, in that the R6G versions have a smaller pK<sub>a</sub> than the RB ones. This latter explanation for the inconsistent pK<sub>a</sub> is one I found more believable than the idea that RB-4OH would have a pK<sub>a</sub> of less than 3.2 when we know

that the *para*-substituted compounds generally have a small range of  $pK_a$  values. To be fully confident that *para*-substituted derivatives are not impacted by electronic effects, the compounds would need to be tested again. Until that time, we will assume that, given the distance of the *para*-substituents from the spirolactam ring, our original deduction that the electronics do not play much of a role in their  $pK_a$  values is accurate.

The di-*meta* RB chloroaniline (see **Table 3**) had a  $pK_a$  much lower than the di-*ortho* substitution which suggests that, like the *para* position, substituents on the *meta* position are not in a position of steric strain such that the  $pK_a$  would be increased. The fact that the  $pK_a$ s for the *para* and di-*meta* chloroanilines are very similar supports this hypothesis. The di-*meta* position was slightly higher than the *para*, which makes sense as the double substitution on the slightly closer positions would make the spirolactam ring slightly more strained. Unfortunately, we cannot tell what the role of electronics in this particular ring opening is based off of these titrations alone.

Titration attempts were made on RB-DCPA. However, the compound did not dissolve well in the titration solvent of ethanol and de-ionized water. Since RB-DCPA was not visible on the UV-Vis, the titration values obtained cannot be considered completely accurate results. However, the higher  $pK_a$  for the compound is as expected for a slightly more bulky substituent. RB-DNA was also titrated, but it would only close when dissolved in pure triethylamine, a range above which our pH probe covered. While clearly possessing a  $pK_a$  in the more basic region and therefore not suited for our purposes of developing a pH probe for the acidic region, this does provide some interesting information regarding the role of sterics and electronics.  $-\text{NO}_2$  is not very sterically bulky but it is extremely electron withdrawing. We can already see from the trend of the other electron withdrawing groups ( $-\text{H}$ ,  $-\text{F}$ ,  $-\text{Cl}$ ) that the  $pK_a$  rises with increasing steric



bulk.  $\text{NO}_2$  does have a higher A value than the other electron withdrawing groups tested here. The most electron donating group (-OEt) has a lower  $\text{pK}_a$  than the least electron donating (-iPr). For the RB series, -OEt has a lower  $\text{pK}_a$  than the least electron withdrawing substituent (-H). As explained above, electron donating groups can stabilize the protonated intermediate which would explain their comparatively lower  $\text{pK}_a$  values. Thus it appears that the more electron withdrawing and bulky a substituent is, the higher the  $\text{pK}_a$ . However, as I mentioned before, at some point we exit the acidic region we want to study so increasing the  $\text{pK}_a$  as far as it will go was not the purpose of this research.

Czaplyski's study of the *para*-substituted RB derivatives also demonstrated that electron withdrawing substituents had the highest intensity of fluorescence.<sup>13</sup> These findings were not supported by my experiments. Both RB-DCA and RB-DMA had to be diluted a second time because their fluorescence intensity was too great for the instrument at their peak intensity. R6G-DMA was also comparably bright versus the R6G derivatives with electron withdrawing substituents.

### B. Titrations of RB mono-ortho compounds

**Table 4.** Average pK<sub>a</sub> values for the RB mono-ortho series.

Substituent	RB pK <sub>a</sub>
F	4.33 ± 0.01
Cl	4.43 ± 0.08
Me	4.31 ± 0.02
iPr	4.28 ± 0.02

In order to determine the role of mono versus di substitutions on ring opening, Mona Rasooly and I performed titrations on several RB mono-ortho versions of the di-ortho series discussed previously. Though the majority of this paper involves modeling and discussions of the di-ortho series, these results are useful as an additional piece of evidence proving that di-ortho substitutions place the spiro lactam ring under greater stress, causing it to open at higher pK<sub>a</sub> values than mono-ortho substitutions. The goal was a minimum of four titrations, done using the same procedure mentioned previously. However, at the time this paper was written only RB-2MA had four complete titrations with all the others having three trials. None of these compounds needed an additional dilution from the original one.

The mono-ortho compounds had lower pK<sub>a</sub> values than their di-ortho counterparts. Since the mono-ortho variations can rotate so as to reduce the strain generated by the substituent, the ring was not popped open as easily. Like the *para*-substituted compounds, the mono-ortho compounds were in a relatively narrow range of values close to the pK<sub>a</sub> of RB-A (4.31). The modeling of this data will be discussed in the next section, in addition to the modeling of the di-ortho derivatives. However, it is already clear that sterics effects are not as present in these compounds as electronic. The mono-iPr compound has a lower pK<sub>a</sub> in comparison to the RB-2CA, which suggests that the pK<sub>a</sub> in the mono-ortho derivatives is primarily determined by electronic effects.

### C. Mathematical prediction of R6G and RB di-ortho pKa

There are multiple means of measuring sterics and electronics mathematically in a system. Steric parameters include A values, Taft  $E_s$ , Charton's  $\nu$ , Meyer's  $V^a$  values, and  $I^{X-H}$  (kJ/mol). A values are a numerical measurement of the preference for an equatorial as opposed to axial oriented substituent in a mono-substituted cyclohexane.<sup>20</sup> The steric substituent  $E_s$  is taken from the Taft equation, a measure of rates<sup>20</sup>:

$$\log k = \log k_0 + \rho^* \sigma^* + \delta E_s \quad (4)$$

Given this equation, when polar effects are not present ( $\sigma^*$ ), we can thereby reduce the equation to<sup>21</sup>:

$$\log \frac{k}{k_0} = E_s \quad (5)$$

Thus, Taft defined  $E_s$  as a steric parameter, however it could also include effects that do not originate from the polar effect, the combination of field and resonance effects, given by  $\sigma^*$ . Research has shown that  $E_s$  is impacted by solvent effects.<sup>21</sup> Kutter and Hansch derived a variation of these  $E_s$  values, improving upon Taft's work and correcting the scale.<sup>22</sup> While these  $E_s$  values, at least for groups fitting the formula of  $\text{CH}_2\text{X}$ ,  $\text{CHX}_2$ , and  $\text{CX}_3$ , correlate with the van der Waals radii, Charton's  $\nu$  values are entirely derived from the van der Waals radii. As such, they are based solely on the size of the substituent. Meyer's  $V^a$  values are a measurement of the volume of the substituent within a designated distance of 0.3 nm from the reaction site.<sup>21</sup>  $I^{X-H}$  was derived from the free energies of activation.<sup>23</sup>

The values used as electronic parameters included the Hammett sigma constant  $\sigma_{\text{para}}$ ,  $\sigma_{\text{I}}$ , Traynham's  $\sigma_{\text{o}}$ , and Swain-Lupton-Hansch's F and R. Electronic parameters can consist of a combination of an inductive effect, resonance effect, and field effect.<sup>24</sup> While the Hammett equation is commonly used to model these interactions, it is typically applied to cases where

*meta*- or *para*-substituents impact the reactivity of a functional group in a benzene derivative so Hammett constants only account for the electronics of the *meta* and *para* substitutions ( $\sigma_{\text{meta}}$  and  $\sigma_{\text{para}}$  respectively).<sup>20</sup>

$$\log \frac{k}{k_0} = \sigma \rho \quad (6)$$

However, several papers have studied the applicability of these constants to *ortho*-substituents and found that the  $\sigma_{\text{para}}$ , or  $\sigma_{\text{p}}$ , can be used to model these series.<sup>25,26</sup> Since  $\sigma_{\text{p}}$  was defined based on whether the substituents increased the acidity of benzoic acid or not, electron withdrawing groups have a positive  $\sigma_{\text{p}}$  while electron donating groups have a negative  $\sigma_{\text{p}}$ .<sup>20</sup> The  $\sigma_{\text{I}}$  was once again determined by Taft as a measure of the field effect, which was not included in the Taft equation listed above. If field effects are measured independently than resonance effects must be as well<sup>21</sup>.

$$\log \frac{k}{k_0} = \rho_{\text{I}} \sigma_{\text{I}} + \rho_{\text{R}} \sigma_{\text{R}} \quad (7)$$

Traynham's  $\sigma_{\text{o}}$  constant was developed as an improvement upon Taft's  $\sigma_{\text{o}}^*$ , which only included polar effects. In comparison, Traynham's constant was based off of chemical shifts. The reliability of this measurement was based off of good correlation with the *para*-substituted phenols tested and reactivity data. This constant is not necessarily independent of sterics though.<sup>21</sup>

Swain and Lupton developed F, field effect, and R, resonance, constants. As demonstrated in the below equation, F and R split  $\sigma$  into two different contributions, just like the  $\sigma_{\text{I}}$  and  $\sigma_{\text{R}}$ .<sup>21</sup>

$$\sigma = fF + rR \quad (8)$$

The F values determined by Swain and Lupton were later modified by Hansch to improve the scale. These values for field effect were combined with Taft-Kutter-Hansch's steric parameter,  $E_{\text{s}}$ , and the Hammett constant,  $\sigma_{\text{p}}$ , to form the Fujita-Nishioka equation. This equation serves as a

model for *ortho* compounds in circumstances where proximity polar and steric effects are independent of polar effects.

$$\log k = \rho\sigma_p + \delta E_s + fF + c \quad (9)$$

However, Fujita and Nishioka recognized that  $\sigma_p$  was not the greatest estimate for *ortho* compounds, as resonance and inductive effects differ between *para* and *ortho* substituents.<sup>22</sup>

Additionally, this equation, like others mentioned previously, is based on kinetics, whereas we are looking to model  $pK_a$ . Therefore, a variety of parameters were tested.

When modeling the  $pK_a$  data by the steric and electronic effect, we multiplied the constants by two to account for the di-*ortho* substitution.<sup>26,27</sup> However, since all the data in this set are di-*ortho*, this change doesn't particularly matter in the regressions themselves as the coefficients would adjust the intensity of the effect as needed. The parameters for the steric and

**Table 5.** Steric parameters for modeling di-*ortho* series

Substituent	A <sup>1</sup>	E <sub>s</sub> <sup>2</sup>	v <sup>3</sup>	V <sup>a3</sup>	I <sup>X-H</sup> kJ/mol <sup>4</sup>
H	0.00	0.00	0.00	0.00	8.00
F	0.30	-0.92	0.54	2.44	38.4
Cl	0.86	-1.94	1.10	5.08	76.2
OEt	1.80	-1.10	0.96 <sup>5</sup>	6.78*	53.2*
Me	3.40	-2.48	1.04	5.68	80.8
iPr	4.30	-3.42	1.52	11.48	105.2

<sup>1</sup> <http://chem.wisc.edu/areas/organic/index-chem.htm>

<sup>2</sup> Fujita, T. and Nishioka, T. The Analysis of the Ortho Effect. *Prog. Phys. Org. Chem.* **1976**, *12*, 49-89.

<sup>3</sup> Smith, M. B. and March, J. March's Advanced Organic Chemistry: Reactions, Mechanisms, and Structure. *John Wiley & Sons.* **2007**.

\*No value for OEt so substituted in OMe

<sup>4</sup> Bott, G.; Field, L. D.; and Sternhell, S. Steric Effects. A Study of a Rationally Designed System. *J. Am. Chem. Soc.* **1980**, *102*, 5618-5626.

<sup>5</sup> <http://www.wiredchemist.com/data/hammett-sigma-constants>

**Table 6.** Electronic parameters for modeling di-*ortho* series

Substituent	$\sigma_p^2$	$\sigma_o^6$	F <sup>2</sup>	R <sup>2</sup>	$\sigma_I^2$	$\sigma_I^{\text{mod}7}$
H	0.00	0.00	0.00	0.00	0.00	0.00
F	0.12	0.58	0.86	-0.68	1.04	1.04
Cl	0.46	1.00	0.82	-0.30	0.94	0.94
OEt	-0.48	-0.60	0.44	-0.88	0.54	0.54
Me	-0.34	-0.26	-0.08	-0.26	-0.10	0.00
iPr	-0.30	-0.30	-0.10	-0.20	-0.12	0.00

electronic models are given in **Tables 5** and **6** respectively.

First, I graphed the pK<sub>a</sub> data against both steric and electronic measures. All these graphs can be found in **Appendix C** but I will discuss some significant ones in depth here. When the pK<sub>a</sub> data was graphed versus the A values, there was notable distinction between the electron withdrawing substituents and the electron donating ones, a trait that is also present in the pK<sub>a</sub> versus  $\sigma_p$  graph (see **Figures 9, 10, and 11**). This trend implied that A values were not simply a steric measure but possibly had an electronic component. Since A values are measures of the preference for an equatorial as opposed to axial oriented substituent it makes sense that electronics properties of substituents could play some role in this preference.<sup>20</sup> A regression testing the collinearity, that is how much the independent variables are related to each other, between A values and  $\sigma_p$  resulted in a variance inflation factor (VIF) of 1.729 for RB derivatives and 1.790 in R6G ones. These values are not exceedingly large but they do indicate there is some

<sup>6</sup> Tribble, M. T. and Traynham, J. G. Nuclear Magnetic Resonance Studies of ortho-Substituted Phenols in Dimethyl Sulfoxide Solutions. Electronic Effects of ortho-Substituents. *Journal of the American Chemical Society*. 1969, 91(1), 379-388.

<sup>7</sup> Bijloo, G. J. and Rekker, R. F. Some Critical Remarks Concerning the Inductive Parameter  $\sigma_I$  Part IV: Parametrization of the Ortho Effect in Anilines and Pyridines. *Quant. Struct. Act. Relat.* **1984**, 3, 111-115.

relationship between A values and  $\sigma_p$ . They were also higher than the VIF factors for  $\sigma_p$  and  $E_s$  (1.085 for R6G and 1.081 for RB).

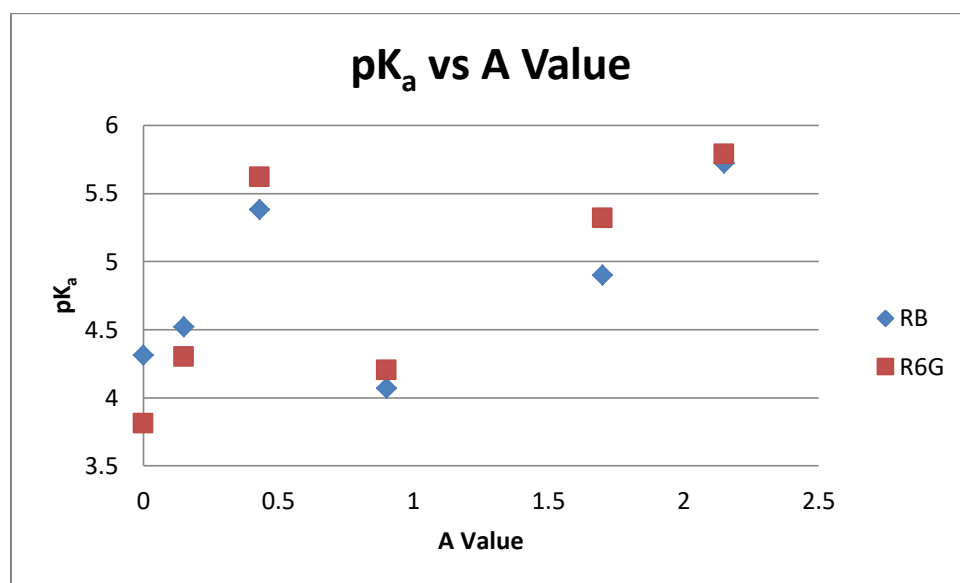


**Figure 9.** RB and R6G  $pK_a$  data for di-*ortho* substituents versus their A values

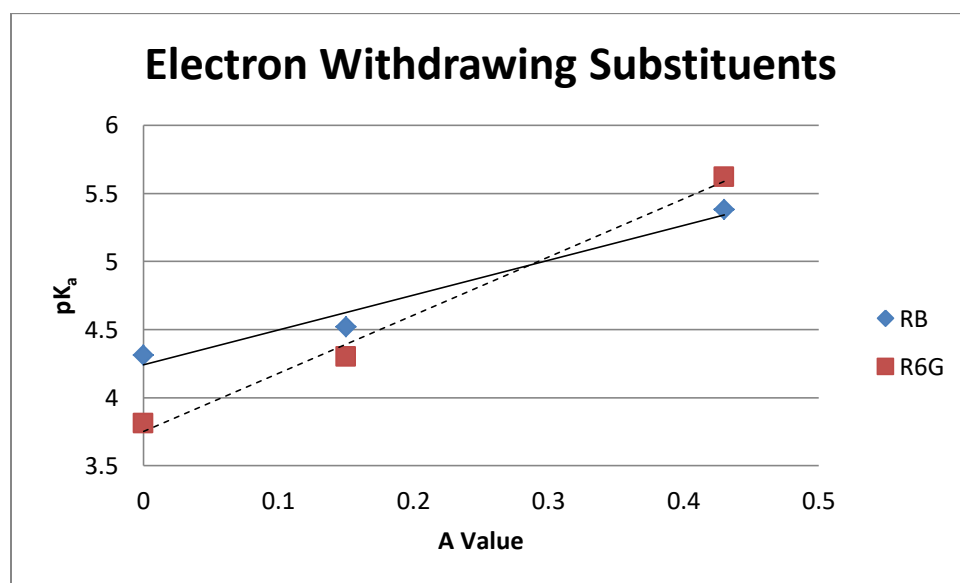


**Figure 10.** RB and R6G  $pK_a$  data for electron withdrawing di-*ortho* substituents versus their A values

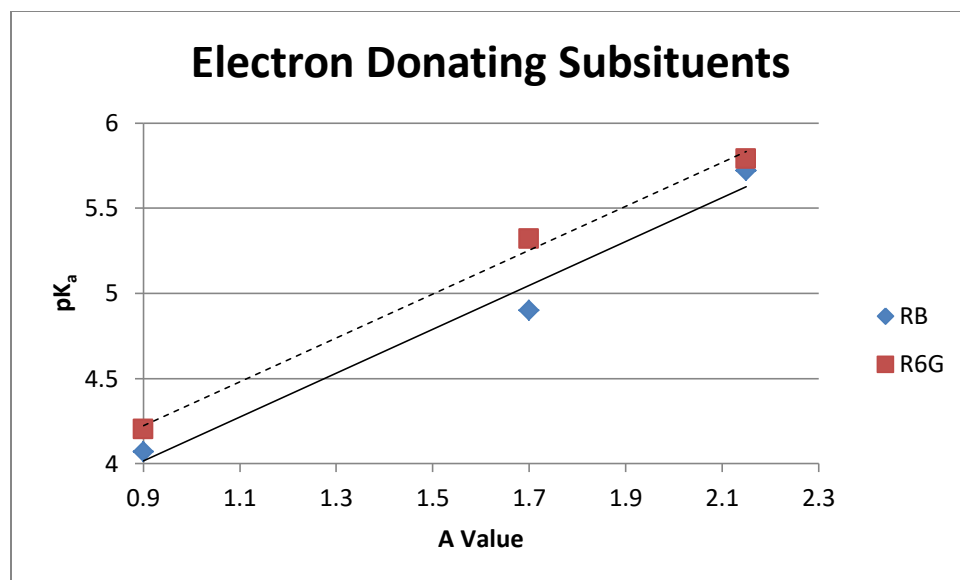


**Figure 11.** RB and R6G pK<sub>a</sub> data for electron donating di-*ortho* substituents versus their A values

In comparison, the graphs of pK<sub>a</sub> versus E<sub>s</sub> and I<sup>X-H</sup> were much more linear in appearance, suggesting that those models are a better measure of solely steric parameters as opposed to electronic. The Meyer's V<sup>a</sup> graph also showed some linearity, broken by the data points for RB-DEA and R6G-DEA. This discrepancy might be a result of the substitution of the V<sup>a</sup> of -OMe for -OEt.

Among the electronic parameters versus pK<sub>a</sub> graphs, σ<sub>p</sub> showed the best linearity within electronic withdrawing and donating groups. While σ<sub>o</sub>, F, and σ<sub>I</sub> were also split into different groups based on whether they were electron withdrawing or electron donating, their linearity within those categories was not as good, which led me to believe that σ<sub>p</sub> was in fact the best model for the *ortho* substituents. However, R versus the pK<sub>a</sub> showed good linearity without any distinction between electron withdrawing or donating. The Fujita-Nishioka assumes that there is no proximity resonance effect and while the changes in pK<sub>a</sub> for R are not massive, it does appear



that the resonance has a distinct effect. This effect could mean that the Fujita-Nishioka equation might have to be modified to include an R parameter.<sup>22</sup>

$$\log k = \rho\sigma_p + \delta E_s + fF + rR + c \quad (10)$$

The RB and R6G derivatives could not be modeled together as the coefficients are too different across the derivatives. Such variation is likely due to the different interactions created by the methyl group in R6G. **Table 7** contains the R6G regressions, while **Table 10** contains the RB regressions. Based on the trend for the A values graphed versus the  $\text{pK}_a$  a regression was run on solely on A and  $E_s$  values to see what, if any trend, they demonstrated. Once again, in both RB and R6G, the A values seemed to have a notable electronic effect, as evidenced by the two distinct lines (top is electron donating while bottom is electron withdrawing) corresponding to the electron withdrawing and donating substituents (**Figure 12**). In comparison,  $E_s$  appeared to be a much better model of sterics given the linear shape (**Figure 13**). The fact that the points are already mostly linear implies a strong reliance on sterics with electronic parameters required solely to fit the line better. Additionally, the  $A-\sigma_p$  regression has clear patterns in the residuals, which implies that there is another variable needed to explain the  $\text{pK}_a$  trends.

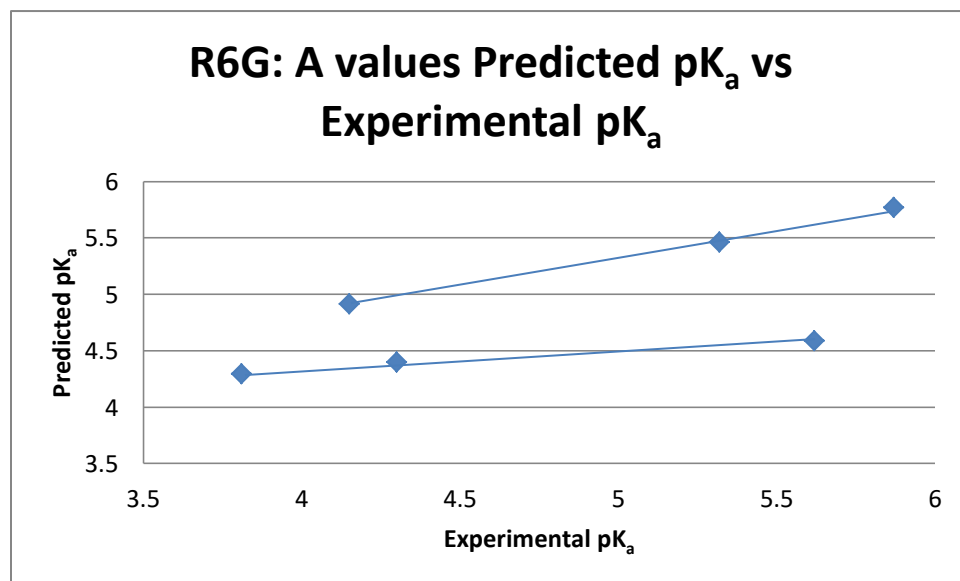


**Figure 12.** R6G A value predicted  $\text{pK}_a$  versus experimental  $\text{pK}_a$

	$A-\sigma_p$	$E_s-\sigma_p$	$v-\sigma_p$	$I^{X-H}-\sigma_p$	$V^a-\sigma_p$	$A-\sigma_o$
Intercept	3.893 ( $\pm$ 0.028)	3.736 ( $\pm$ 0.034)	3.637 ( $\pm$ 0.088)	3.453 ( $\pm$ 0.0515)	3.866 ( $\pm$ 0.101)	3.713 ( $\pm$ 0.049)
P-value	2.43e-54	4.72e-50	9.05e-34	6.53e-42	1.56e-32	5.64e-44
Steric	0.647 ( $\pm$ 0.014)	-0.723 ( $\pm$ 0.018)	1.530 ( $\pm$ 0.094)	0.024 ( $\pm$ 0.001)	0.218 ( $\pm$ 0.018)	0.584 ( $\pm$ 0.021)
P-value	2.43e-54	2.59e-33	5.7e-19	2.76e-29	8.57e-15	1.95e-27
Electronic	2.337 ( $\pm$ 0.074)	0.853 ( $\pm$ 0.064)	0.643 ( $\pm$ 0.147)	0.658 ( $\pm$ 0.080)	1.166 ( $\pm$ 0.202)	1.215 ( $\pm$ 0.062)
P-value	2.99e-35	4.55e-16	8.73e-05	4.64e-10	1.1e-06	8.53e-22
Field/Other						
P-value						
Other						
P-value						
Adjusted R <sup>2</sup>	0.980	0.975	0.865	0.960	0.780	0.951
df	41	41	41	41	41	41
n	42	42	42	42	42	42
F	1018.1	805.937	132.688	493.763	73.655	399.504
P-value	2.2e-34	1.91e-32	3.96e-18	2.01e-28	5.7e-14	1.05e-26

<b>R6G</b>	<b>E<sub>s</sub>-σ<sub>o</sub></b>	<b>v- σ<sub>o</sub></b>	<b>I<sup>X-H</sup>- σ<sub>o</sub></b>	<b>V<sup>a</sup>- σ<sub>o</sub></b>	<b>A-F</b>	<b>E<sub>s</sub>-F</b>
Intercept	3.679 (± 0.046)	3.602 (± 0.094)	3.420 (± 0.061)	3.758 (± 0.106)	3.714 (± 0.161)	3.646 (± 0.085)
P-value	7.25e-45	1.54e-32	7.13e-39	2.87e-31	2.51e-24	2.04e-34
Steric	-0.694 (± 0.023)	1.479 (± 0.097)	0.024 (± 0.001)	0.209 (± 0.017)	0.498 (± 0.055)	-0.688 (± 0.037)
P-value	8.71e-29	4.54e-18	1.58e-26	7.08e-15	4.83e-11	6.31e-21
Electronic	0.445 (± 0.047)	0.329 (± 0.088)	0.333 (± 0.053)	0.662 (± 0.112)	0.980 (± 0.210)	0.327 (± 0.098)
P-value	1.21e-11	0.000561	2.18e-07	6.65e-07	3.5e-05	0.0018
Field/Other						
P-value						
Other						
P-value						
R <sup>2</sup> Adjusted	0.958	0.853	0.946	0.785	0.660	0.893
df	41	41	41	41	41	41
n	42	42	42	42	42	42
F	471.852	119.501	356.973	76.021	40.723	172.639
P-value	4.72e-28	2.33e-17	8.49e-26	3.5e-14	2.82e-10	4.22e-20

<b>R6G</b>	<b>v-F</b>	<b>I<sup>X-H</sup>-F</b>	<b>V<sup>a</sup>-F</b>	<b>A-R</b>	<b>E<sub>S</sub>-R</b>	<b>v-R</b>
Intercept	3.706 (± 0.117)	3.459 (± 0.093)	3.915 (± 0.157)	4.405 (± 0.176)	3.934 (± 0.095)	3.941 (± 0.078)
P-value	1.73e-29	4.87e-32	1.5e-25	1.21e-25	7.72e-34	4.27e-37
Steric	1.440 (± 0.112)	0.023 (± 0.001)	0.181 (± 0.023)	0.339 (± 0.055)	-0.6509 (± 0.039)	1.533 (± 0.074)
P-value	1.33e-15	5.8e-21	7.87e-10	3.56e-07	1.53e-19	1.27e-22
Electronic	-0.066 (± 0.129)	0.102 (± 0.095)	0.232 (± 0.187)	0.292 (± 0.322)	0.340 (± 0.156)	0.957 (± 0.131)
P-value	0.612	0.291	0.222	0.370	0.035	8.92e-09
Field/Other						
P-value						
Other						
P-value						
R <sup>2</sup> Adjusted	0.800	0.894	0.608	0.480	0.878	0.915
df	41	41	41	41	41	41
n	42	42	42	42	42	42
F	83.240	173.467	32.784	19.924	147.951	221.172
P-value	8.45e-15	3.88e-20	4.44e-09	1.09e-06	6.16e-19	5.22e-22

<b>R6G</b>	<b>I<sup>X-H</sup>-R</b>	<b>V<sup>a</sup>-R</b>	<b>A-<math>\sigma_I</math></b>	<b>E<sub>s</sub>-<math>\sigma_I</math></b>	<b>v-<math>\sigma_I</math></b>	<b>I<sup>X-H</sup>-<math>\sigma_I</math></b>
Intercept	3.700 ( $\pm$ 0.075)	4.259 ( $\pm$ 0.143)	3.744 ( $\pm$ 0.166)	3.654 ( $\pm$ 0.087)	3.714 ( $\pm$ 0.117)	3.465 ( $\pm$ 0.094)
P-value	9.79e-37	2.05e-28	5.81e-24	4.39e-34	1.64e-29	6.46e-32
Steric	0.0233 ( $\pm$ 0.001)	0.181 ( $\pm$ 0.020)	0.491 ( $\pm$ 0.057)	-0.688 ( $\pm$ 0.038)	1.438 ( $\pm$ 0.112)	0.023 ( $\pm$ 0.001)
P-value	5.88e-25	5.12e-11	1.64e-10	1.32e-20	1.3e-15	7.42e-21
Electronic	0.586 ( $\pm$ 0.113)	0.763 ( $\pm$ 0.258)	0.784 ( $\pm$ 0.183)	0.260 ( $\pm$ 0.084)	-0.0738 ( $\pm$ 0.109)	0.072 ( $\pm$ 0.081)
P-value	6.86e-06	0.0052	0.000114	0.00366	0.502	0.376
Field/Other						
P-value						
Other						
P-value						
R <sup>2</sup> Adjusted	0.935	0.667	0.639	0.890	0.801	0.893
df	41	41	41	41	41	41
n	42	42	42	42	42	42
F	297.428	42.097	37.317	166.276	83.758	171.800
P-value	2.44e-24	1.82e-10	8.78e-10	8.14e-20	7.66e-15	4.59e-20

<b>R6G</b>	<b>V<sup>a</sup>-<math>\sigma_I</math></b>	<b>E<sub>s</sub>-<math>\sigma_p</math>-F-R</b>	<b>E<sub>s</sub>-<math>\sigma_p</math>-F</b>	<b>E<sub>s</sub>-<math>\sigma_p</math>-R</b>	<b>E<sub>s</sub>-F-R</b>	<b>E<sub>s</sub>-<math>\sigma_I</math>-R</b>
Intercept	3.931 ( $\pm$ 0.158)	3.831 ( $\pm$ 0.026)	3.822 ( $\pm$ 0.038)	3.822 ( $\pm$ 0.038)	3.822 ( $\pm$ 0.038)	3.824 ( $\pm$ 0.040)
P-value	1.69e-25	8.68e-53	1.03e-47	9.39e-48	6.58e-48	4.68e-47
Steric	0.181 ( $\pm$ 0.023)	-0.640 ( $\pm$ 0.016)	-0.7179 ( $\pm$ 0.016)	-0.718 ( $\pm$ 0.016)	-0.716 ( $\pm$ 0.016)	-0.721 ( $\pm$ 0.017)
P-value	1.06e-09	3.84e-32	9.08e-35	8.62e-35	6.1e-35	4.34e-34
Electronic	0.167 ( $\pm$ 1.59)	-47.231 ( $\pm$ 7.280)	1.052 ( $\pm$ 0.078)	0.828 ( $\pm$ 0.056)	0.775 ( $\pm$ 0.052)	0.665 ( $\pm$ 0.048)
P-value	0.300	1.38e-07	4.17e-016	2.74e-17	1.92e-17	1.42e-16
Field/Other		44.941 ( $\pm$ 6.808)	-0.209 ( $\pm$ 0.057)	0.227 ( $\pm$ 0.061)	1.062 ( $\pm$ 0.077)	1.097 ( $\pm$ 0.083)
P-value		9.68e-08	0.00075	0.000677	2.65e-16	1.03e-15
Other		48.657 ( $\pm$ 7.336)				
P-value		8.8e-08				
R <sup>2</sup> Adjusted	0.604	0.991	0.981	0.981	0.982	0.980
df	41	41	41	41	41	41
n	42	42	42	42	42	42
F	32.217	1150.979	713.172	716.851	730.585	656.677
P-value	5.49e-09	2.93e-38	1.96e-33	1.78e-33	1.25e-33	9.11e-33

<b>R6G</b>	<b>E<sub>s</sub>-σ<sub>I</sub>-F</b>	<b>E<sub>s</sub>-σ<sub>I</sub>-F-R</b>	<b>E<sub>s</sub>-σ<sub>I</sub><sup>mod</sup>-F-R</b>			
Intercept	3.791 (± 0.024)	3.816 (± 0.017)	3.828 (± 0.024)			
P-value	6.42e-55	9.94e-60	2.47e-54			
Steric	-0.600 (± 0.011)	-0.639 (± 0.009)	-0.814 (± 0.016)			
P-value	1.11e-37	1.87e-40	8.09e-36			
Electronic	-14.673 (± 0.672)	-10.065 (± 0.816)	-4.083 (± 0.532)			
P-value	4.22e-23	1.14e-14	3.66e-09			
Field/Other	17.642 (± 0.794)	12.384 (± 0.942)	5.191 (± 0.576)			
P-value	2.22e-23	1.62e-15	7.34e-11			
Other		0.4236 (± 0.062)	0.720 (± 0.066)			
P-value		5.36e-08	4.29e-13			
R <sup>2</sup> Adjusted	0.992	0.996	0.993			
df	41	41	41			
n	42	42	42			
F	1676.98	2763.502	1397.373			
P-value	2.09e-40	2.94e-45	8.31e-40			

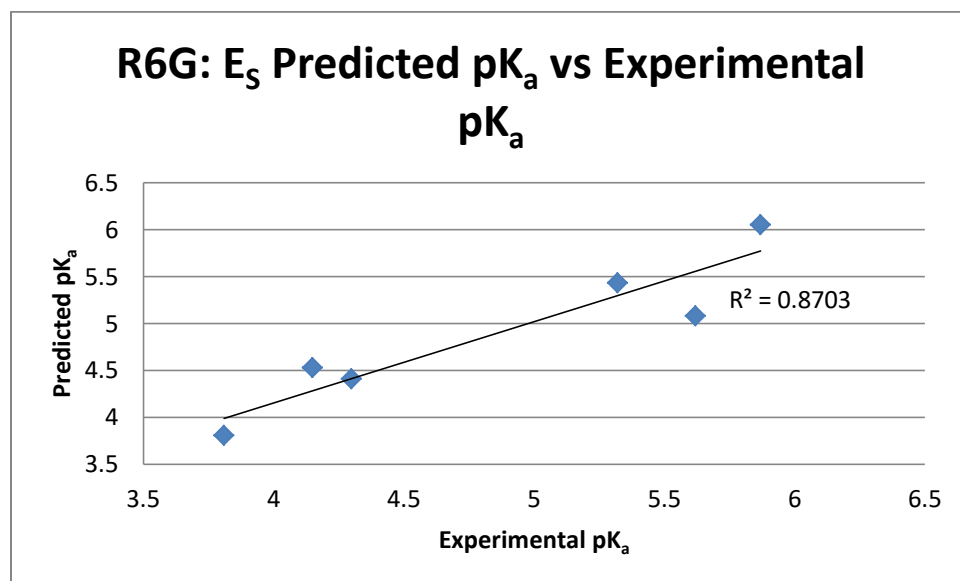


**Figure 13.** R6G  $E_s$  predicted  $pK_a$  versus experimental  $pK_a$

As expected the Fujita-Nishioka equation produced good correlation (adjusted  $R^2$  of 0.981 and 0.950 for R6G and RB respectively). However, the modified version of the equation with the addition of the resonance factor,  $R$ , produced even better correlations for R6G. It appears that  $\sigma_{para}$  does not fully account for the field and resonance effects in di-*ortho* substituted compounds, at least in R6G. Since RB had such large p-values for the modified Fujita-Nishioka equation it would seem that  $\sigma_{para}$  does account more for these effects. For the regressions with  $\sigma_I$ , RB seemed to be much more dependent upon resonance than R6G derivatives, which had best results with resonance and field effects added to the regression. As suggested by Bijloo and colleagues, the substitution of  $\sigma_I$  for  $\sigma_p$  resulted in stronger correlations but the change was not especially large. The modified  $\sigma_I$  did not produce better results, which suggests the spiro lactam ring significantly changes the properties of the compound from just the plain anilines Bijloo examined.<sup>26</sup>



To summarize, for the R6G derivatives, the best three parameter correlation was with  $E_s$ - $\sigma_I$ -F (**Figure 14**).

$$pK_a = 3.791(\pm 0.024) - 0.600(\pm 0.011)E_s - 14.673(\pm 0.672)\sigma_I + 17.642(\pm 0.794)F$$

The electronic parameters are surprisingly the most weighted, even with R6G's added steric strain. In other words, the percent weight of each parameter is 4.309, 47.495, and 48.196 for  $E_s$ ,  $\sigma_I$ , and F respectively. These weights are calculated as the percent contribution from each coefficient after standardizing the parameters, in other words by taking the beta. The beta is given at the value of the parameter minus the mean all divided by the standard deviation. Once a regression is run on these new standardized values you can take one coefficient for a parameter and divide it by the total sum of the coefficients for your parameters. This process tells you approximately how much the coefficients contribute; if your coefficient for the steric parameter is comparatively large then it is weighted more in the regression. As expected, the parameters were correlated with each other, particularly  $\sigma_I$  and F with a VIF of 811.429. This is an extremely high correlation which could contribute to inaccurate parameter estimates and could explain the oddly high reliance on electronics. This correlation was also present with the modified  $\sigma_I$  values. If we return to the Fujita-Nishioka equation parameters, we find that  $\sigma_p$  is much less correlated with F (VIF of 2.057) (**Figure 15**).

$$pK_a = 3.822(\pm 0.038) - 0.718(\pm 0.016)E_s + 1.052(\pm 0.078)\sigma_p - 0.209(\pm 0.057)F$$

This equation generates a much more believable weighting for the electronic and steric parameters; F contributes 7.282%,  $\sigma_p$  contributes 27.030%, and  $E_s$  contributes 65.689%. Given the steric strain in the R6G compounds, I find this equation more trustworthy. Therefore, even though  $\sigma_I$  has the greatest fit, I find that  $\sigma_p$  is more accurate in describing the effects of the electronic and steric parameters.

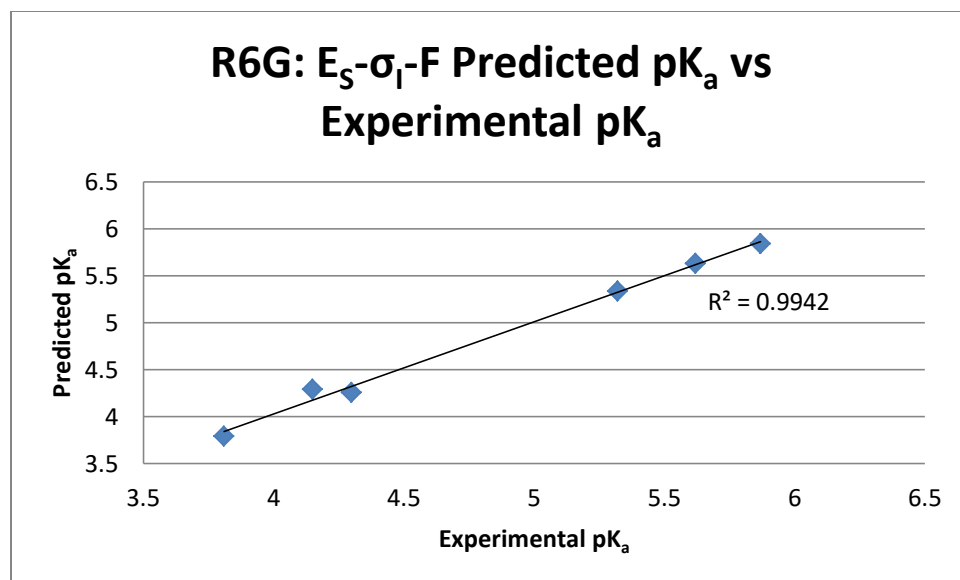


**Figure 14.** R6G  $E_s$ - $\sigma_I$ -F regression predicted  $pK_a$  versus  $pK_a$  of di-*ortho* derivatives

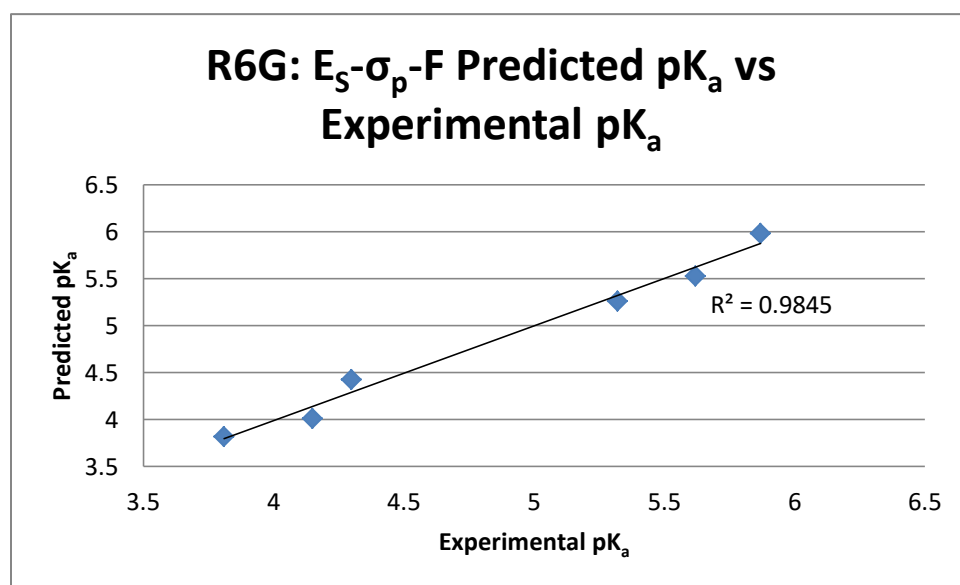


**Figure 15.** RB  $E_s$ - $\sigma_p$ -F regression predicted  $pK_a$  versus  $pK_a$  of di-*ortho* derivatives

**Table 8.** Analysis of VIFs of R6G three-parameter regression models

<b>R6G</b>	<b><math>E_s</math>-<math>\sigma_I</math>-R</b>	<b><math>E_s</math>-<math>\sigma_p</math>-R</b>	<b><math>E_s</math>-F-R</b>
$E_s$ -R	1.004	1.004	1.004
$E_s$ - $\sigma_I$ / $\sigma_p$ /F	1.079	1.085	1.072
R- $\sigma_I$ / $\sigma_p$ /F	1.691	1.011	1.624

As shown in the table above (**Table 8**), even though  $E_s$ - $\sigma_I$ -R and  $E_s$ -F-R have the better fits of the values predicted by the regression with the actual data points, the VIF of R- $\sigma_I$  and R-F is significantly larger than R- $\sigma_p$ . Therefore, for a three parameter model, a modified version of the Fujita-Nishioka is best, substituting R for F (**Figure 16**).

$$pK_a = 3.822(\pm 0.038) - 0.718(\pm 0.016)E_s + 0.828(\pm 0.056)\sigma_p + 0.227(\pm 0.061)R$$

R has less correlation with  $\sigma_p$  than F (VIF of 1.01 versus 2.06) as well as slightly less correlation with  $E_s$  (VIF of 1.00 versus 1.07). Though the electronic values do show some correlation with  $E_s$  the effects are not significant enough to interfere with the coefficient values. The weightings in this equation are 23.104%, 71.309%, and 5.567% contribution from  $\sigma_p$ ,  $E_s$ , and R respectively.

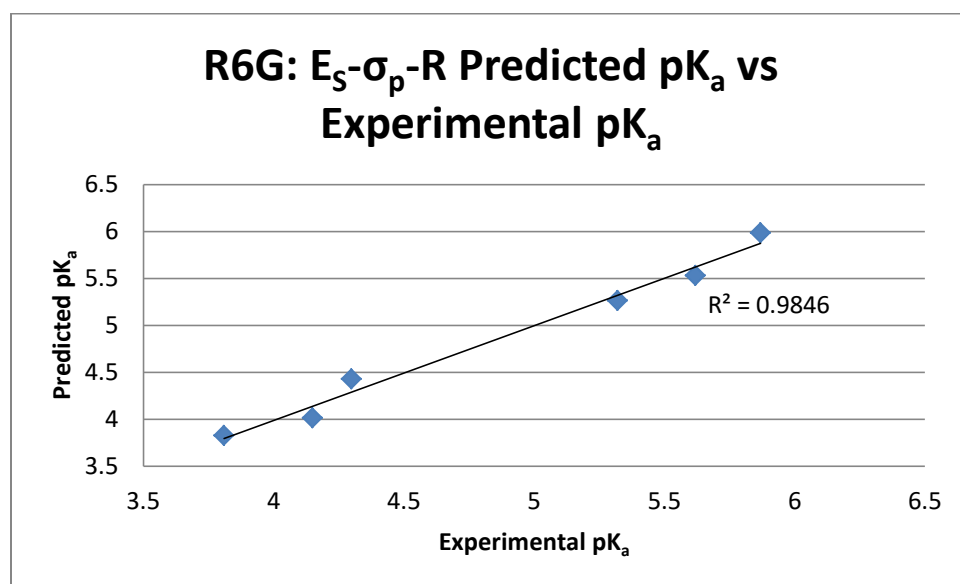


**Figure 16.** R6G  $E_s$ - $\sigma_p$ -R regression predicted pK<sub>a</sub> versus pK<sub>a</sub> of di-*ortho* derivatives

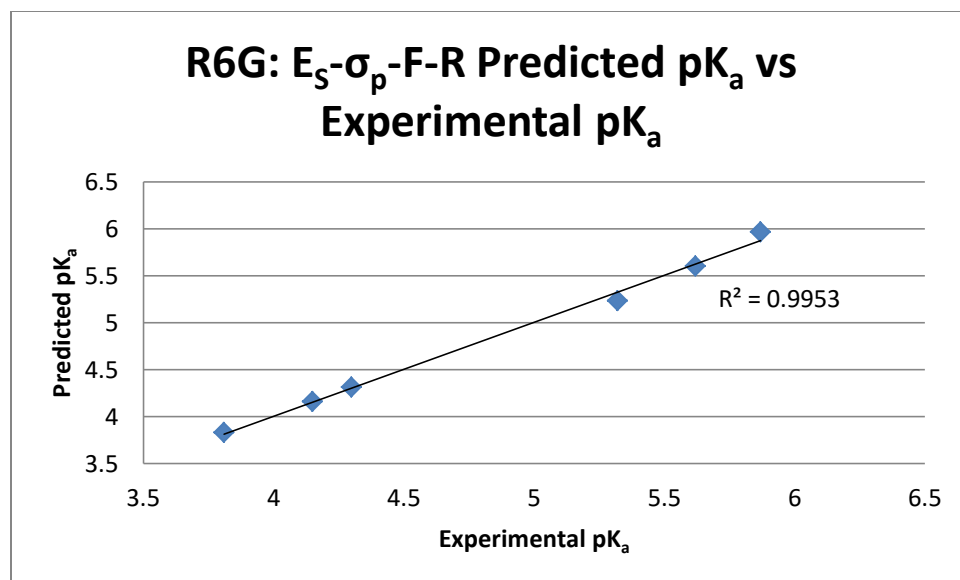


**Figure 17.** R6G  $E_s$ - $\sigma_p$ -F-R regression predicted  $pK_a$  versus  $pK_a$  of di-*ortho* derivatives

Given what we now know about  $\sigma_I$  correlation with F, the best four parameter model would be based on the Fujita-Nishioka equation (**Figure 17**).

$$pK_a = 3.831(\pm 0.026) - 0.640(\pm 0.016)E_s - 47.231(\pm 7.280)\sigma_p + 44.941(\pm 6.808)F + 48.657(\pm 7.336)R$$

However, the weighting for the steric and electronic components are drastically changed by the addition of another electronic parameter. The steric parameter now contributes 1.488% to the  $pK_a$  which cannot be accurate given the steric strain present in R6G. Therefore we must conclude that four parameters are not accurate for the estimation of the contributions of steric and electronic effects, most likely due to the addition of correlations between the independent variables.

The parameters for the R6G regressions with adjusted  $R^2$  values of 0.9 or greater were used as the parameters for the RB regressions. Overall, RB derivative were less mathematically sound. That is to say that they did not fit the mathematical model as well as the R6G derivatives. It was also evident from the regressions that there were significant differences in the steric and

electronic contributions. With  $E_s\text{-}\sigma_p\text{-R}$ ,  $E_s\text{-F-R}$ ,  $E_s\text{-}\sigma_p\text{-F}$ , and  $E_s\text{-}\sigma_I\text{-R}$  having the best fits in the regression analysis, their VIF values were compared to determine which would be the best model. As shown in **Table 9** below, the significant differences in VIF came from the 2<sup>nd</sup> and 3<sup>rd</sup> terms.  $\sigma_p\text{-R}$  had less correlation than  $\sigma_p\text{-F}$ , which was expected given the high p-values for  $\sigma_I\text{-F}$ . The greater correlation with F was also found in the R6G model, so  $\sigma_p$  most accurately represents the field effects of *ortho*-substitution in our rhodamine models. Once again,  $\sigma_p\text{-R}$  also had less correlation than  $\sigma_I\text{-R}$  so as was the case with the R6G derivatives,  $E_s\text{-}\sigma_p\text{-R}$  is the best model (**Figure 18**).

**Table 9.** Analysis of VIFs of RB three-parameter regression models

<b>RB</b>	<b><math>E_s\text{-}\sigma_p\text{-R}</math></b>	<b><math>E_s\text{-}\sigma_p\text{-F}</math></b>	<b><math>E_s\text{-F-R}</math></b>	<b><math>E_s\text{-}\sigma_I\text{-R}</math></b>
1 <sup>st</sup> -2 <sup>nd</sup> Term	1.081	1.081	1.108	1.095
1 <sup>st</sup> -3 <sup>rd</sup> Term	1.016	1.108	1.016	1.016
2 <sup>nd</sup> -3 <sup>rd</sup> Term	1.032	1.861	1.566	1.637

	<b>A-<math>\sigma_p</math></b>	<b>E<sub>s</sub>-<math>\sigma_p</math></b>	<b>I<sup>X-H</sup>-<math>\sigma_p</math></b>	<b>A-<math>\sigma_o</math></b>	<b>E<sub>s</sub>-<math>\sigma_o</math></b>	<b>I<sup>X-H</sup>-<math>\sigma_o</math></b>
Intercept	4.184 (±	4.077 (±	3.901 (±	4.049 (±	4.018 (±	3.862 (±
P-value	0.036)	0.050)	0.082)	0.062)	0.063)	0.092)
	1.65e-55	9.84e-49	8.26e-39	1.38e-44	2.67e-44	1.75e-36
Steric	0.449 (±	-0.499 (±	0.016 (±	0.395 (±	-0.470 (±	0.016 (±
P-value	0.018)	0.026)	0.001)	0.026)	0.031)	0.001)
	2.93e-27	6.9e-23	4.83e-17	1.03e-18	4.84 e-19	5.55e-15
Electronic	1.883 (±	0.871 (±	0.757 (±	0.941 (±	0.432 (±	0.370 (±
P-value	0.092)	0.092)	2.72e-07)	0.078)	0.064)	0.078)
	1.01e-23	4.84e-12	2.72e-07	2.65e-15	2.73e-08	2.55e-05
Field/Other						
P-value						
Other						
P-value						
Adjusted R <sup>2</sup>	0.936	0.897	0.808	0.842	0.847	0.765
df	45	45	45	45	45	45
n	46	46	46	46	46	46
F	327.856	197.449	95.848	120.791	125.847	74.120
P-value	9.27e-27	2.14e-22	1.42e-16	2.26e-18	1.07e-18	1.16e-14

<b>RB</b>	<b>v-R</b>	<b>I<sup>X-H</sup>-R</b>	<b>E<sub>s</sub>-σ<sub>p</sub>-F-R</b>	<b>E<sub>s</sub>-σ<sub>p</sub>-F</b>	<b>E<sub>s</sub>-σ<sub>p</sub>-R</b>	<b>E<sub>s</sub>-F-R</b>
Intercept	4.414 (±	4.260 (±	4.282 (±	4.282 (±	4.282 (±	4.283 (±
P-value	0.086)	0.094)	0.047)	0.046)	0.046)	0.046)
	3.9e-40	5.75e-38	5.69e-49	3.71e-50	3.76e-50	3.79e-50
Steric	0.967 (±	0.015 (±	-0.479 (±	-0.476 (±	-0.476 (±	-0.475 (±
P-value	0.078)	0.001)	0.026)	0.018)	0.018)	0.018)
	1.06e-15	5.36e-16	2.47e-21	1.43e-27	1.59e-27	1.66e-27
Electronic	1.089 (±	0.832 (±	2.690 (±	1.246 (±	0.771 (±	0.721 (±
P-value	0.134)	0.130)	12.296)	0.085)	0.066)	0.062)
	2.97e-10	1.02e-07	0.828	3.98e-18	9.4e-15	9.52e-15
Field/Other			-1.796 (±	-0.444 (±	0.479 (±	1.257 (±
P-value			11.504)	0.065)	0.071)	0.086)
			0.876	2.96e-08	2.98e-08	4.05e-18
Other			-1.458 (±			
P-value			12.406)			
			0.907			
Adjusted R <sup>2</sup>	0.811	0.817	0.949	0.950	0.950	0.950
df	45	45	45	45	45	45
n	46	46	46	46	46	46
F	97.38.384	101.1789	208.568	284.772	284.696	284.525
P-value	1.08e-16	5.48e-17	1.15e-26	6.28e-28	6.31e-28	6.39e-28

<b>RB</b>	<b><math>E_s-\sigma_I-R</math></b>	<b><math>E_s-\sigma_I-F-R</math></b>	<b><math>E_s-\sigma_I-F</math></b>	<b><math>E_s-\sigma_I^{\text{mod}}-F-R</math></b>		
Intercept	4.283 ( $\pm$ P-value 0.044) 4.58e-51	4.297 ( $\pm$ P-value 0.038) 1.32e-52	4.075 ( $\pm$ P-value 0.100) 2.59e-35	4.281 ( $\pm$ P-value 0.047) 4.32e-49		
Steric	-0.471 ( $\pm$ P-value 0.017) 2.49e-28	-0.445 ( $\pm$ P-value 0.016) 9.51e-28	-0.496 ( $\pm$ P-value 0.045) 5.88e-14	-0.456 ( $\pm$ P-value 0.031) 4.9e-18		
Electronic	0.645 ( $\pm$ P-value 0.052) 1.18e-15	4.211 ( $\pm$ P-value 0.926) 4.78e-05	-5.272 ( $\pm$ P-value 2.052) 0.0138	0.735 ( $\pm$ P-value 0.984) 0.459		
Field/Other	1.302 ( $\pm$ P-value 0.083) 4.26e-19	-4.051 ( $\pm$ P-value 1.051) 0.000402	6.288 ( $\pm$ P-value 2.380) 0.0115	-0.0769 ( $\pm$ P-value 1.071) 0.943		
Other		1.502 ( $\pm$ P-value 0.089) 4.6e-20		1.307 ( $\pm$ P-value 0.110) 6.84e-15		
Adjusted $R^2$	0.954	0.966	0.734	0.949		
df	45	45	45	45		
n	46	46	46	46		
F P-value	315.577 8.01e-29	318.447 2.79e-30	42.472 8.77e-13	211.285 8.94e-27		



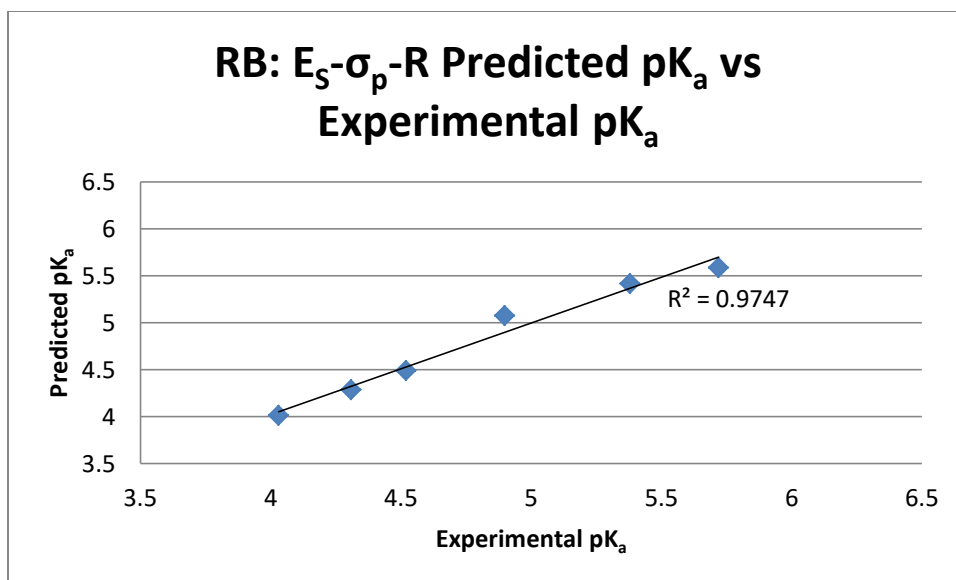


**Figure 18.** RB  $E_s$ - $\sigma_p$ -R regression predicted  $pK_a$  versus  $pK_a$  of di-*ortho* derivatives

$$pK_a = 4.282(\pm 0.046) - 0.476(\pm 0.018)E_s + 0.771(\pm 0.066)\sigma_p + 0.479(\pm 0.071)R$$

Unlike for R6G derivatives where sterics were almost 3/4<sup>th</sup>s of the contribution to the  $pK_a$ , with RB derivatives  $E_s$  only contributed 58.597%. With  $\sigma_p$  and R supplying the remaining 26.472% and 14.931% respectively, RB has almost equivalent contributions from sterics and electronics. The weighting of the R, resonance effect, was also greater for RB derivatives which matches the regressional preference for R over F in the RB series given that that preference was not so distinct in the R6G series.

In conclusion, as expected R6G derivatives demonstrated a greater dependence upon steric parameters than RB derivatives. Our regressions did have a greater fit with the  $\sigma_I$  model suggested by Bijloo for use with anilines; however, the correlation between the  $\sigma_I$  and F as well as with R made the coefficients inaccurate, thereby overstating the role of electronics in the  $pK_a$ .<sup>26</sup> It does not appear that Bijloo checked the VIFs or the expected contributions of steric and electronic parameters in his work so he might have inadvertently sacrificed accuracy in the coefficient weighting for fit.<sup>26</sup> While the Fujita-Nishioka equation did have good correlation, the

coefficients for R substituted for F are likely more accurate in these models.<sup>22</sup> A kinetics test would assist in confirming the accuracy of the proposed modification, as the Fujita-Nishioka equation is based on kinetics. A three parameter model is best as four parameter models add up the multicollinearity within the proposed equation, making it less accurate.

Though RB derivatives are easier to synthesize and have higher yields, R6G derivatives have more intense fluorescence and respond better to mathematical modeling. Therefore, R6G derivatives should be the preferred focus of future rhodamine pH probes. Though the models had high adjusted  $R^2$  values of 0.981 and 0.950 for R6G and RB derivatives respectively, these values are lower than the  $R^2$  values found by Fujita and Nishioka for their system and Bijloo for his.<sup>22,26</sup> As stated above, these high correlations between predicted and experimental values might be at the cost of accuracy in the coefficients but regardless there is still room for improvement in the rhodamine models. A further study of electronic and steric parameters could assist, though I suspect that no present parameter would completely fit our data without affecting our coefficients in a negative manner.

#### D. Mathematical prediction of RB mono-ortho pK<sub>a</sub>

Since the mono-ortho compounds only have one ortho group, their electronic and steric parameters were not doubled as was done with the di-ortho derivatives. The parameters for the mono-ortho series are shown in **Tables 11** and **12**. As mentioned in the discussion of the pK<sub>a</sub>

**Table 11.** Steric parameters for modeling mono-ortho series

Substituent	A <sup>8</sup>	E <sub>s</sub> <sup>9</sup>	v <sup>10</sup>	V <sup>a10</sup>	I <sup>X-H</sup> kJ/mol <sup>11</sup>
H	0.00	0.00	0.00	0.00	4.00
F	0.15	-0.46	0.27	1.22	19.2
Cl	0.43	-0.97	0.55	2.54	38.1
Me	1.70	-1.24	0.52	2.84	40.4
iPr	2.15	-1.71	0.76	5.74	52.6

**Table 12.** Electronic parameters for modeling mono-ortho series

Substituent	σ <sub>p</sub> <sup>9</sup>	σ <sub>o</sub> <sup>12</sup>	F <sup>9</sup>	R <sup>9</sup>	σ <sub>I</sub> <sup>9</sup>	σ <sub>I</sub> <sup>mod13</sup>
H	0.00	0.00	0.00	0.00	0.00	0.00
F	0.06	0.29	0.43	-0.34	0.52	0.52
Cl	0.23	0.50	0.41	-0.15	0.47	0.47
Me	-0.17	-0.13	-0.04	-0.13	-0.05	0.00
iPr	-0.15	-0.15	-0.05	-0.10	-0.06	0.00

<sup>8</sup> <http://chem.wisc.edu/areas/organic/index-chem.htm>

<sup>9</sup> Fujita, T. and Nishioka, T. The Analysis of the Ortho Effect. *Prog. Phys. Org. Chem.* **1976**, 12, 49-89.

<sup>10</sup> Smith, M. B. and March, J. March's Advanced Organic Chemistry: Reactions, Mechanisms, and Structure. *John Wiley & Sons.* **2007**.

<sup>11</sup> Bott, G.; Field, L. D.; and Sternhell, S. Steric Effects. A Study of a Rationally Designed System. *J. Am. Chem. Soc.* **1980**, 102, 5618-5626.

<sup>12</sup> Tribble, M. T. and Traynham, J. G. Nuclear Magnetic Resonance Studies of ortho-Substituted Phenols in Dimethyl Sulfoxide Solutions. Electronic Effects of ortho-Substituents. *Journal of the American Chemical Society.* 1969, 91(1), 379-388.

<sup>13</sup> Bijloo, G. J. and Rekker, R. F. Some Critical Remarks Concerning the Inductive Parameter σ<sub>I</sub> Part IV: Parametrization of the Ortho Effect in Anilines and Pyridines. *Quant. Struct. Act. Relat.* **1984**, 3, 111-115.

values previously, the mono-*ortho* series does not seem to be as impacted by sterics. This was confirmed through regressions as all of the regressions containing a steric parameter had large p-values for that parameter. Regressions were run instead using only electronic parameters. Only those regressions with p-values of less than 0.01 were included in **Table 11**.

The graphs of the mono-*ortho*  $pK_a$  values versus  $\sigma_p$  and  $\sigma_o$  showed the closest to linear fit (**Figures 19 and 20**). In both graphs though, it appears as though the electron donating and electron withdrawing groups have different slopes. The graph versus  $\sigma_o$  shows the best linear shape as a result, though it is less linear overall as compared to the electron withdrawing groups in the graph versus  $\sigma_p$ . This observation is supported by the regression analysis since the regression against  $\sigma_o$  successfully places RB-2MA at a higher  $pK_a$  than RB-2IA as was observed.  $\sigma_p$  did not; in that regression, RB-2MA and RB-2IA were predicted to be essentially the same, with RB-2IA slightly larger. Though the experimental values for the two compounds were still very similar, the regression for  $\sigma_o$  had more points on the line, a better fit overall, and smaller p-values.

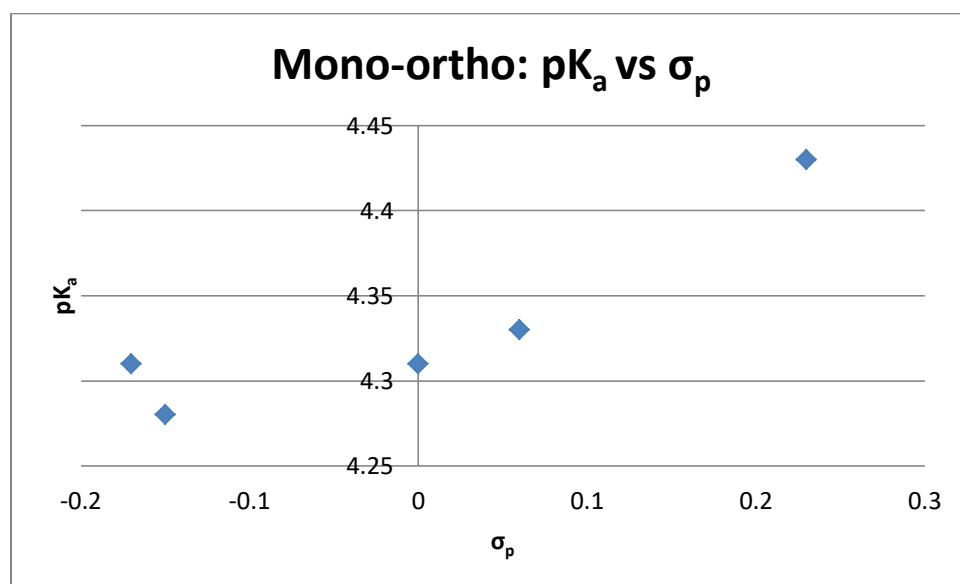


**Figure 19.** RB  $pK_a$  data for mono-*ortho* substituents versus their  $\sigma_p$  values

<b>Table 11.</b> Mono-ortho regression analysis						
	$\sigma_p$	$\sigma_I$	$\sigma_I^{\text{mod-R}}$	F	$\sigma_o$	
Intercept	4.332 ( $\pm$ 0.008)	4.311 ( $\pm$ 0.011)	4.328 ( $\pm$ 0.012)	4.310 ( $\pm$ 0.011)	4.316 ( $\pm$ 0.009)	
P-value	8.47e-41	2.27e-38	3.39e-36	1.77e-38	1.38e-40	
Electronic	0.316 ( $\pm$ 0.065)	0.140 ( $\pm$ 0.042)	0.297 ( $\pm$ 0.062)	0.170 ( $\pm$ 0.049)	0.185 ( $\pm$ 0.037)	
P-value	0.000115	0.00371	0.000155	0.00271	8.32e-05	
Field/Other			0.386 ( $\pm$ 0.125)			
P-value			0.00632			
Other						
P-value						
Adjusted R <sup>2</sup>	0.528	0.332	0.524	0.352	0.543	
df	20	20	20	20	20	
n	21	21	21	21	21	
F	23.382	10.938	12.008	11.868	24.795	
P-value	0.00115	0.00371	0.000486	0.00271	8.32e-05	

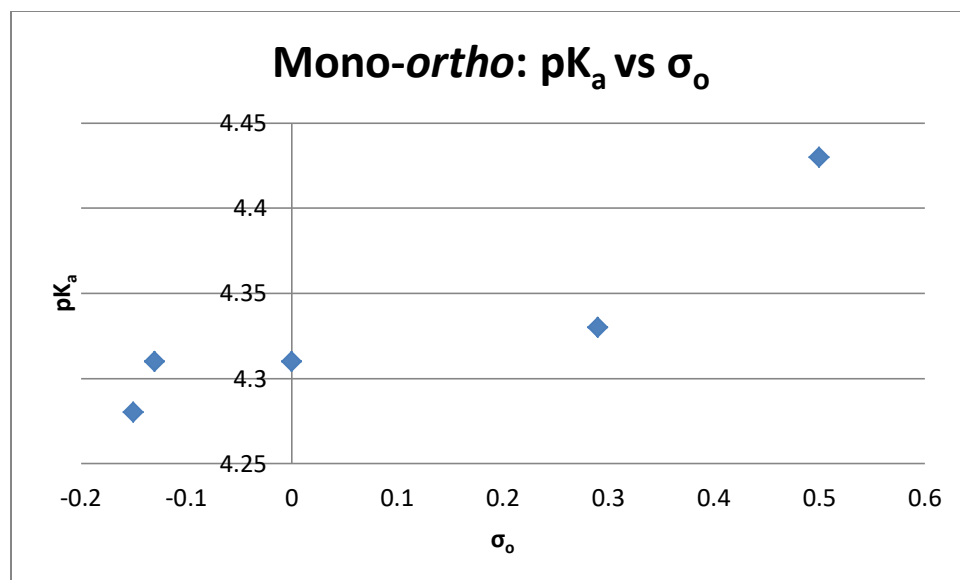


**Figure 20.** RB  $pK_a$  data for mono-*ortho* substituents versus their  $\sigma_o$  values

$$pK_a = 4.316(\pm 0.009) + 0.185(\pm 0.037)\sigma_o$$

This equation contradicts Bijloo's analysis of mono-*ortho* anilines as having an electronic and steric component.<sup>26</sup> Most likely this is because the mono-*ortho* substituted aniline is in a position where it can twist to reduce steric strain on the spiro lactam and xanthene rings, unlike what would occur in a plain aniline. The next section contains further evidence for this hypothesis through computational models. While the fit of this regression was best overall, RB-2FA and RB-2MA are noticeably off the line of best fit (**Figure 21**). There is most likely another factor which would improve the regression analysis, though it would be particularly hard to identify it without more data points to strengthen the regression. A further study of electronic parameters would be best for determining a better regression, though a kinetics study might also prove useful by providing another parameter with which to analyze the regression.

In conclusion, the mono-*ortho* substituted compounds have only an electronic component for the RB series, due to the aniline ring's ability to twist to relieve steric strain. It would be interesting to see if this remains the case for mono-*ortho* R6G derivatives given their methyl

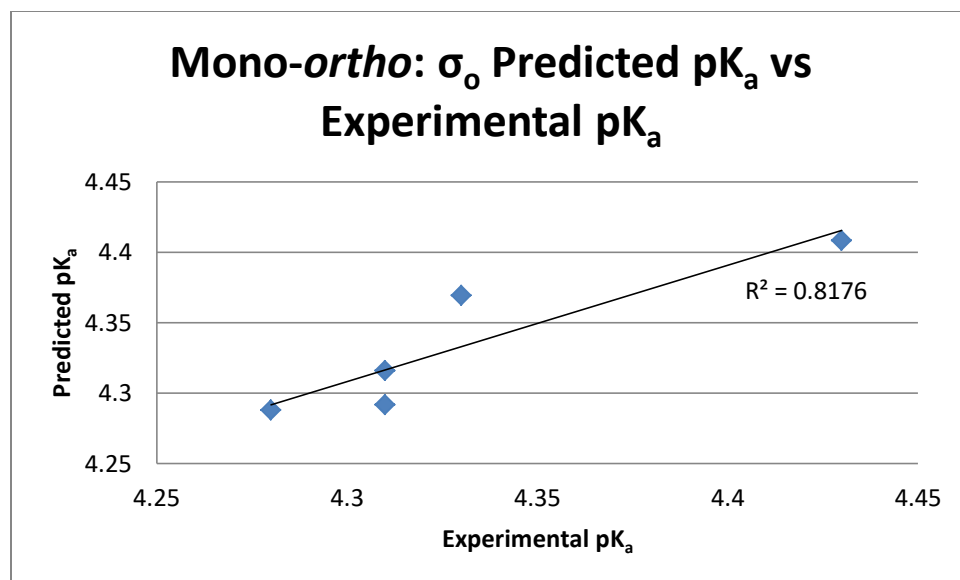


**Figure 21.** RB  $\sigma_o$  regression predicted pK<sub>a</sub> versus pK<sub>a</sub> of mono-*ortho* derivatives

---

group, which proved to increase the contribution from steric parameters as compared to the RB derivatives in the di-*ortho* analysis. However, since the mono-*ortho* RB derivatives only rely on electronics and do not vary substantially, it is clear that they are not well suited for our desired purpose as they are not high enough to work well in the acidic region.

### Section III. Crystal structure and Gaussian modeling

#### A. Crystal Structure for RB-DIA

Our interest in determining the 3D structure of our compounds arose from noting non-equivalent isopropyl protons in RB-DIA and R6G-DIA. This indicated that the compound was twisting so as to create non-equivalence with certain substituents.

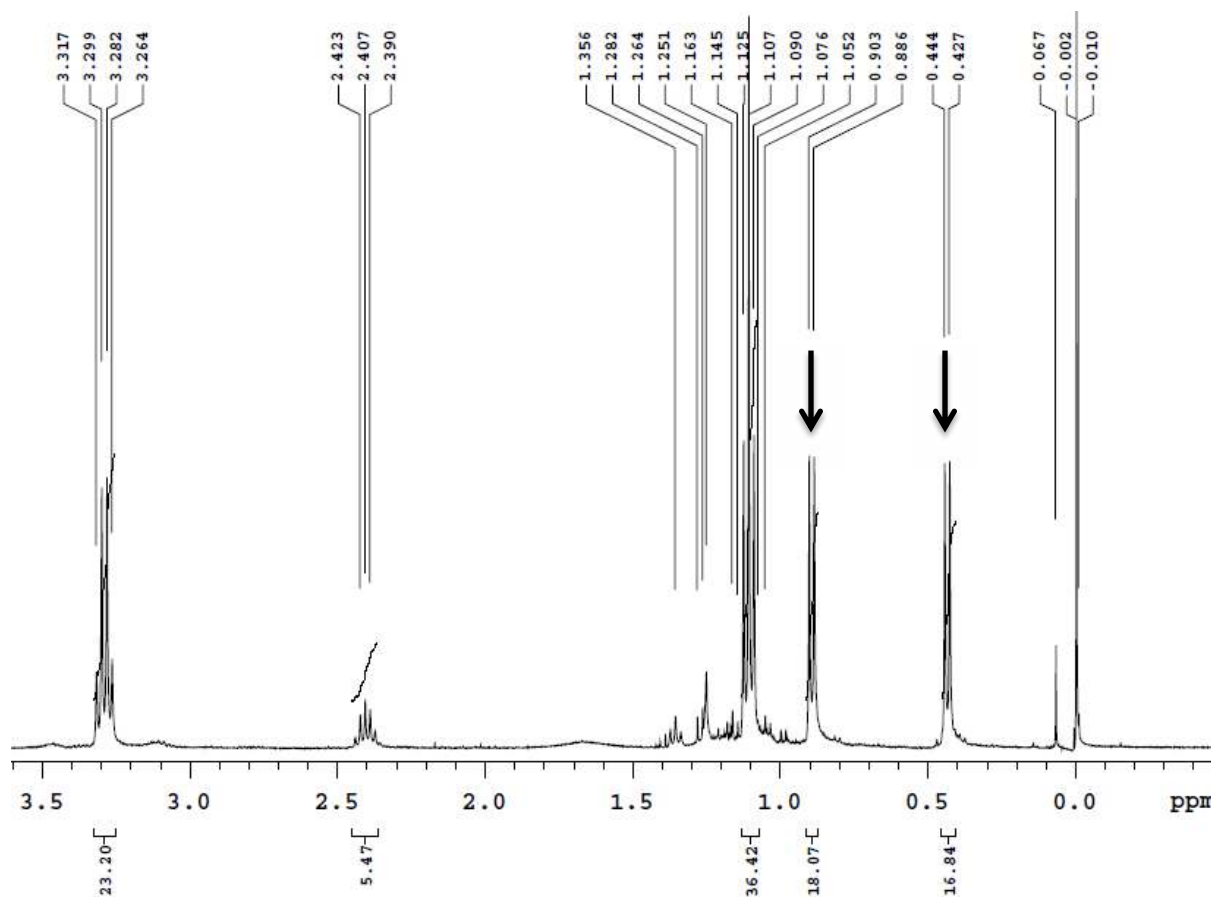


**Figure 22.** RB-DIA aliphatic region with arrows pointing to the non-equivalent isopropyl peaks

Several samples of RB-DIA were dissolved into various solvents and left covered in an NMR tube at room temperature for approximately seven months in order to grow crystals (see **Table 12**). The amount of solvent used was about 2.5 mL. Only one sample was successful, RB-DIA in 5:1 DCM:MeOH. Other suggestions include dissolving the rhodamines in a compound that they aren't very soluble in and leaving in the freezer. This slows the rate of solvent



Compound	Solutions	Crystals
RB-DIA	CDCl <sub>3</sub>	No
RB-DIA	1:1 EtOH:H <sub>2</sub> O	No
RB-DIA	5:1 DCM:MeOH	Yes
RB-DCPA	5:1 DCM:MeOH	No (powder)
RB-DIA	EtOH	No

**Table 12.** Crystal growing experiment results based on solution

evaporation which allows the big crystals needed for x-ray diffraction to form. Mixtures of solvents work best, particularly a combination of a solvent which rhodamine dissolves in and one which it doesn't with a ratio favoring the solvent rhodamine is not soluble in. Once again the intention is to slow the rate of evaporation so that the environment is hospitable for crystal growth. I found that smaller diameter tubes, approximately the size of NMR tubes, covered with a cap were useful to grow crystals. The cap helped slow the rate of evaporation and the tube could be covered in tin foil to protect the rhodamine crystals from light.

X-ray crystallography of the crystal was performed and analyzed by Dr. Robert D. Pike (see **Figure 23**). The full data from the analysis is available in **Appendix D**. The crystal structure clearly shows a xanthene bend, caused by the positioning of the aniline substituent out of the spiro lactam ring plane. The interplanar angle between the xanthene and spiro lactam rings is 32.15 degrees. In essence, the spiro lactam ring sits perpendicular to the xanthene ring. However, due to the xanthene bend the xanthene ring is not entirely planar. This xanthene twist is 154.8 degrees, which makes it 25.2 degrees off from completely planar (planar being 180 degrees).

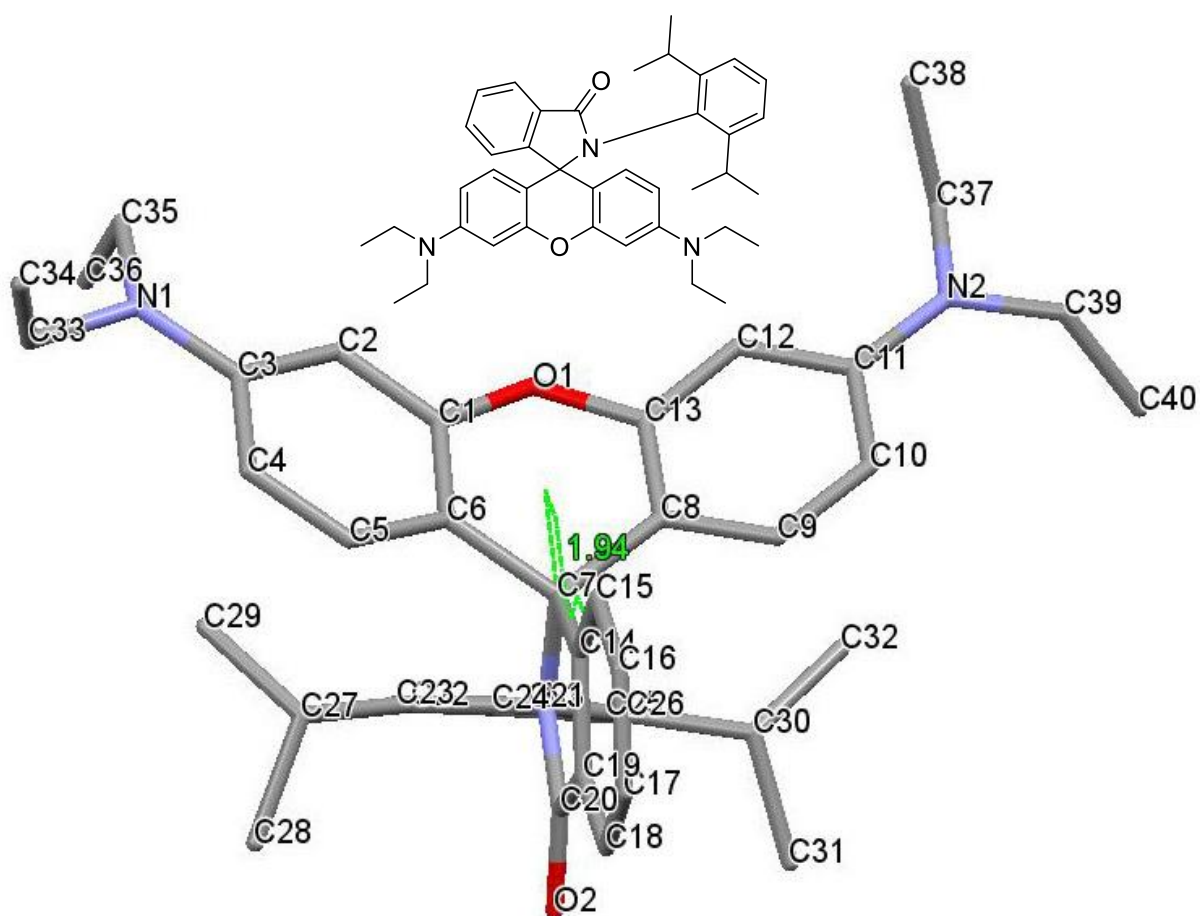


**Figure 23.** Crystal structure of RB-DIA

The N-phenyl sits at a 93.67° angle from the spiro lactam ring. As I was unable to grow any other crystals, these values were used to test the accuracy of a theoretical model of RB-DIA so as to determine the best calculations for computational models of the di-*ortho* RB and R6G series. The xanthene twist and N-phenyl coplanarity with the carbonyl can then be compared to determine how those angles affect the  $pK_a$ . The structures will certainly model steric parameters which we already proved had a significant impact for both RB and R6G di-*ortho* compounds. Given that sterics played a greater role in the  $pK_a$  of the R6G derivatives, I suspect the angles for those compounds will demonstrate a greater correlation with the  $pK_a$ .

### *B. Computation models of RB and R6G di-ortho substituted derivatives*

First, the crystal structure for RB-DIA was compared to the computation model of RB-DIA to test the accuracy of the optimization to the HF/6-311(d,p) level when run using Gaussian. The actual angle of the xanthene twist was 152.363 degrees whereas the calculated angle was 152.435 degrees. The values were close enough to declare this computation model accurate for rhodamine compounds. Of course, actual crystal structures would be preferred but given the difficulties in growing rhodamine crystals of the correct properties for x-ray diffraction

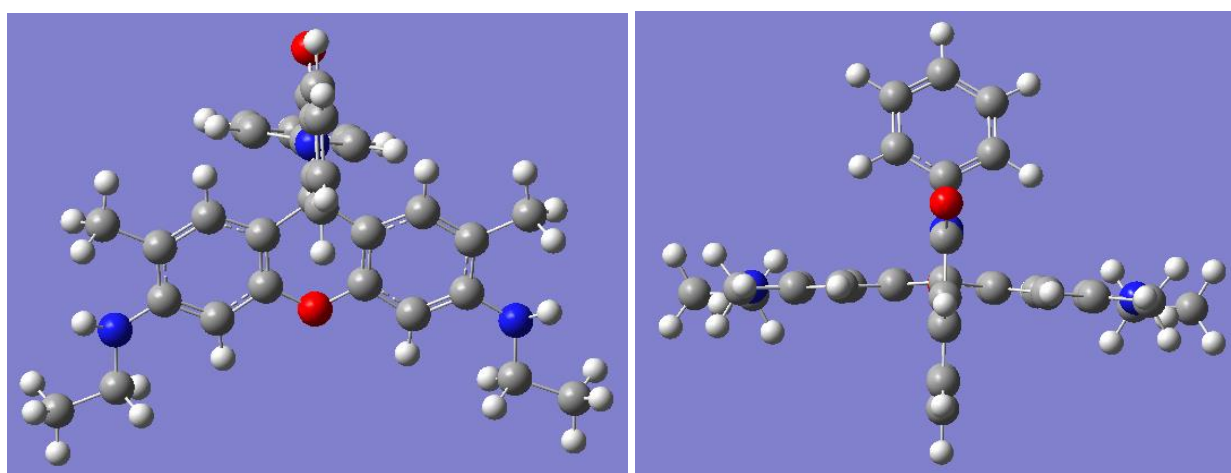


**Figure 24.** Optimized structure of R6G-A (left) front view and (right) bird's eye view

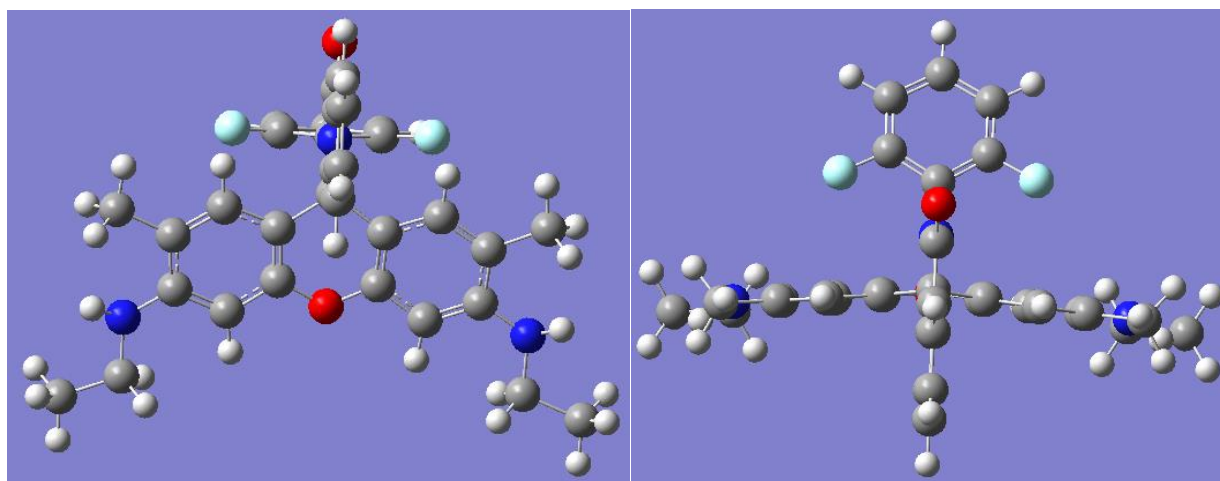


**Figure 25.** Optimized structure of R6G-DFA (left) front view and (right) bird's eye view

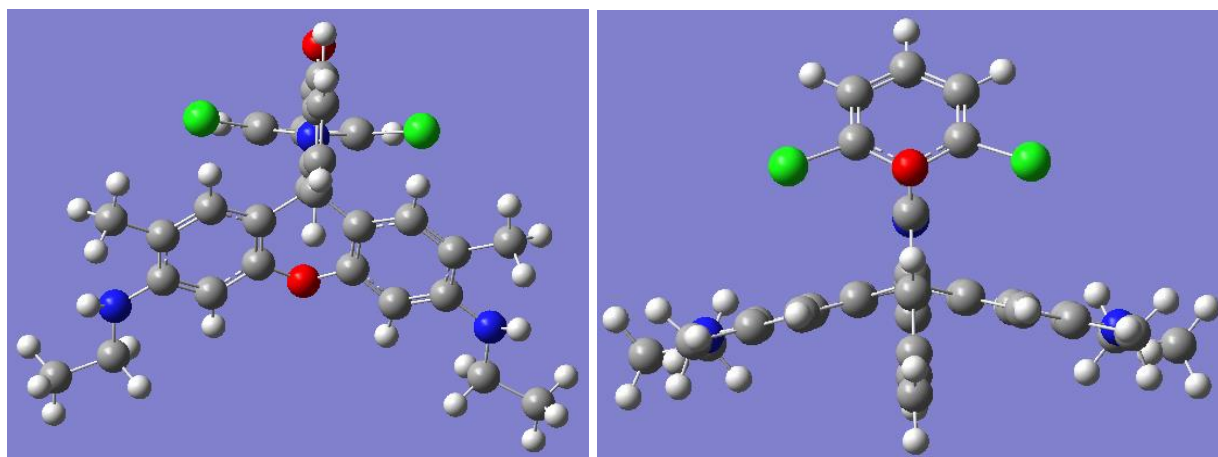


**Figure 26.** Optimized structure of R6G-DCA (left) front view and (right) bird's eye view

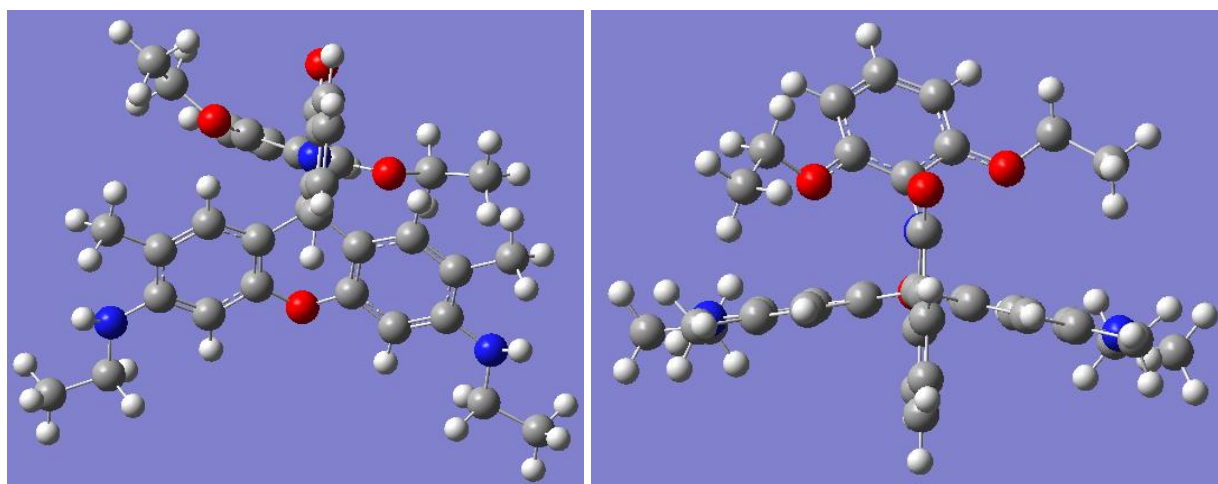


**Figure 27.** Optimized structure of R6G-DEA (left) front view and (right) bird's eye view

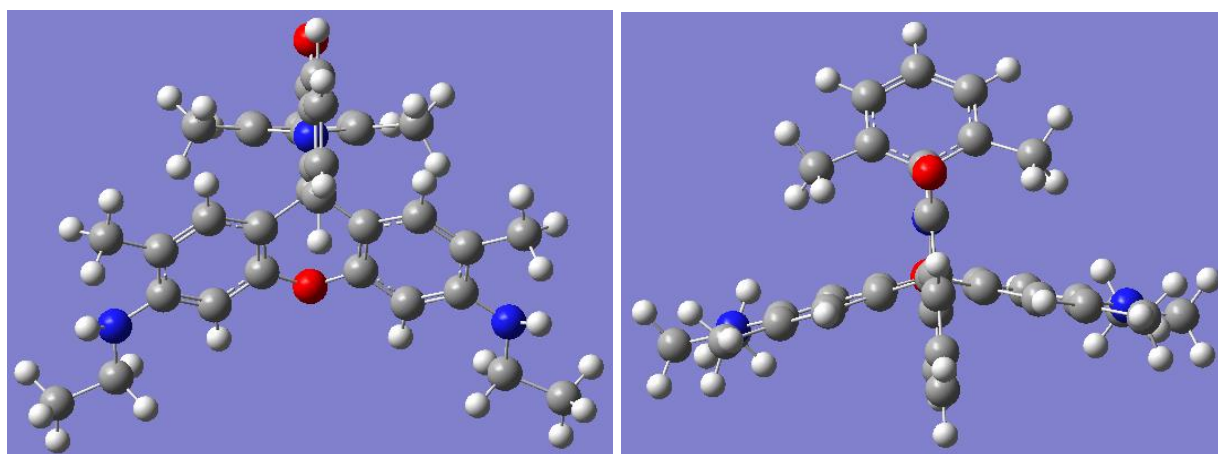


**Figure 28.** Optimized structure of R6G-DMA (left) front view and (right) bird's eye view

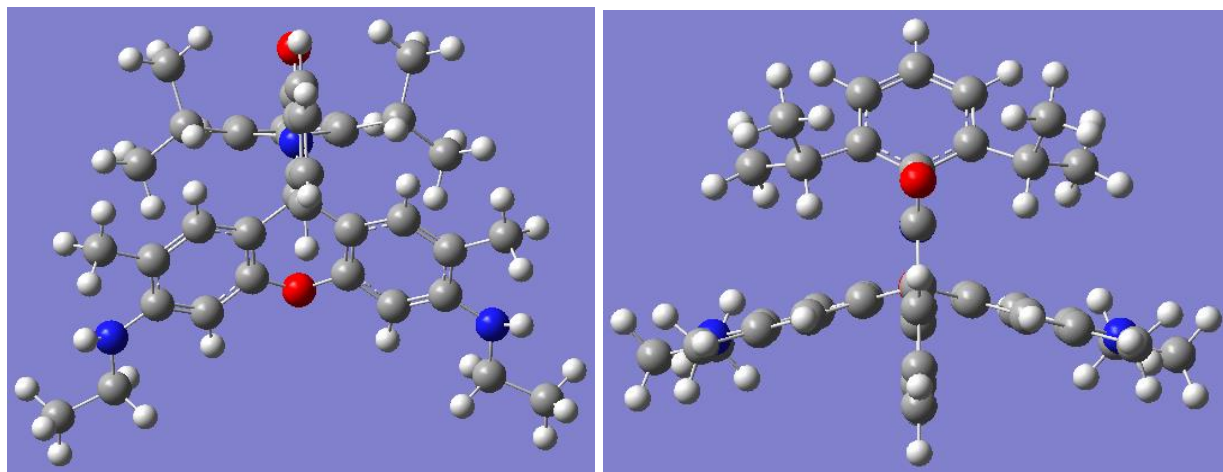


**Figure 29.** Optimized structure of R6G-DIA (left) front view and (right) bird's eye view

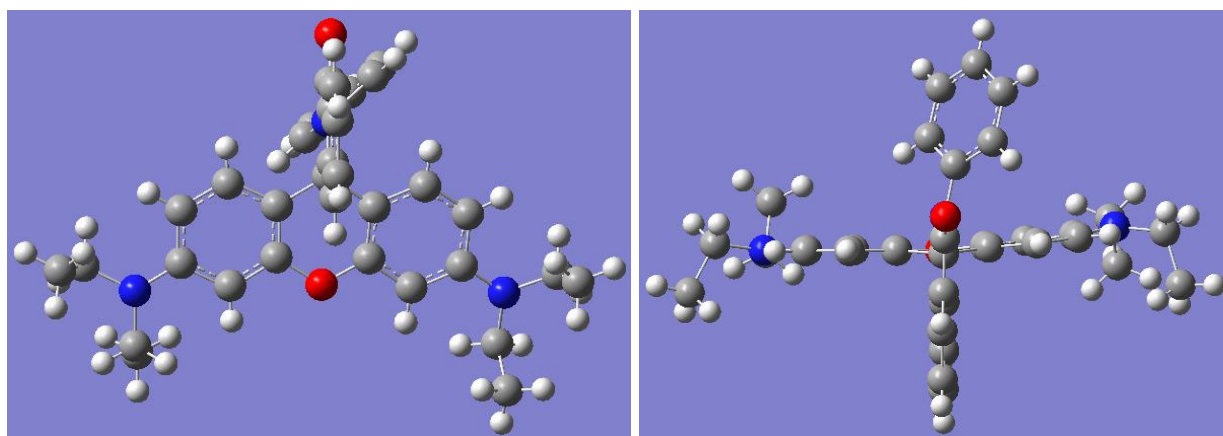


**Figure 30.** Crystal structure of RB-A (left) front view and (right) bird's eye view<sup>28</sup>

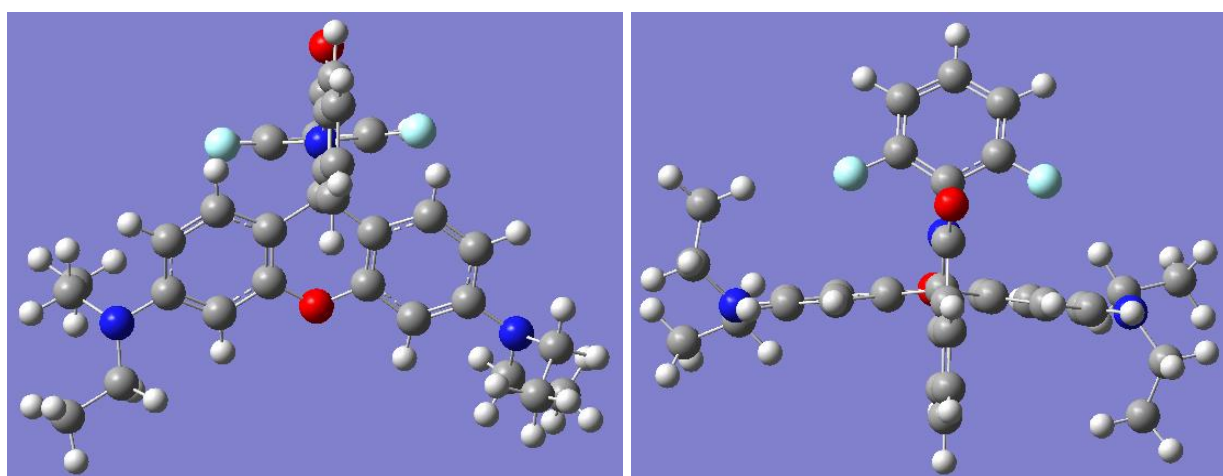


**Figure 31.** Optimized structure of RB-DFA (left) front view and (right) bird's eye view<sup>14</sup>

<sup>14</sup> Calculated by Grace E. Purnell

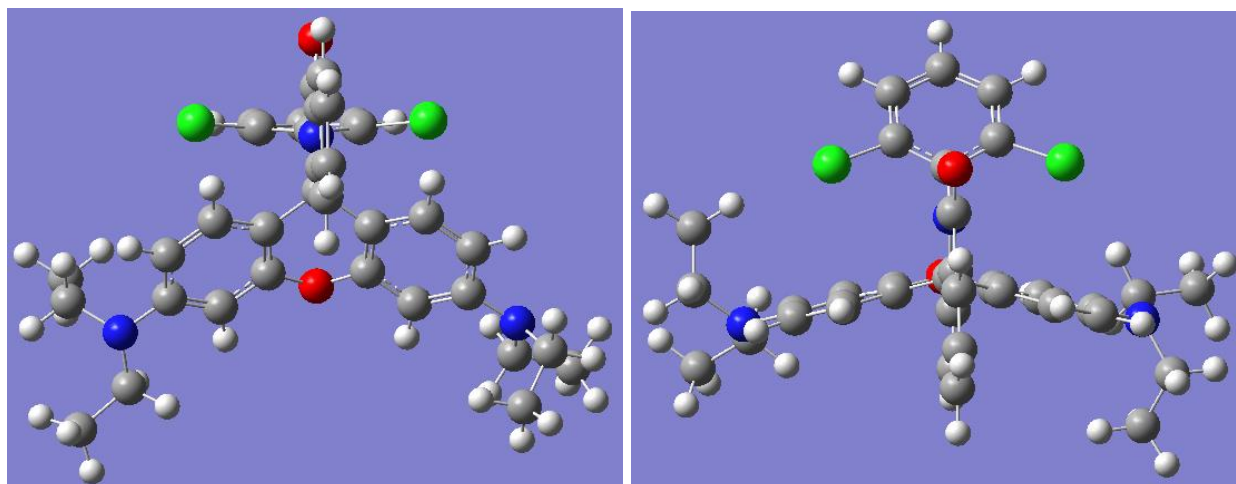


**Figure 32.** Optimized structure of RB-DCA (left) front view and (right) bird's eye view<sup>14</sup>

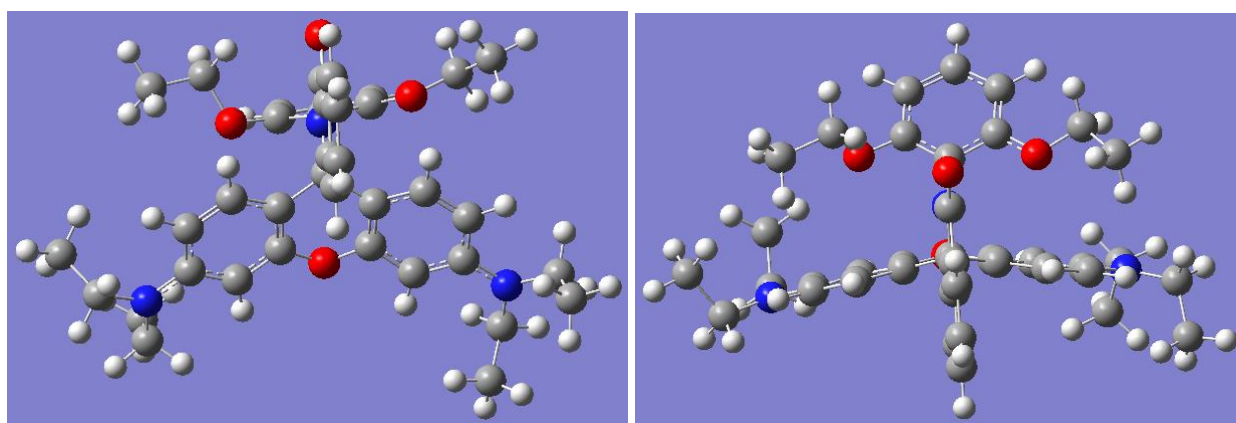


**Figure 33.** Optimized structure of RB-DEA (left) front view and (right) bird's eye view

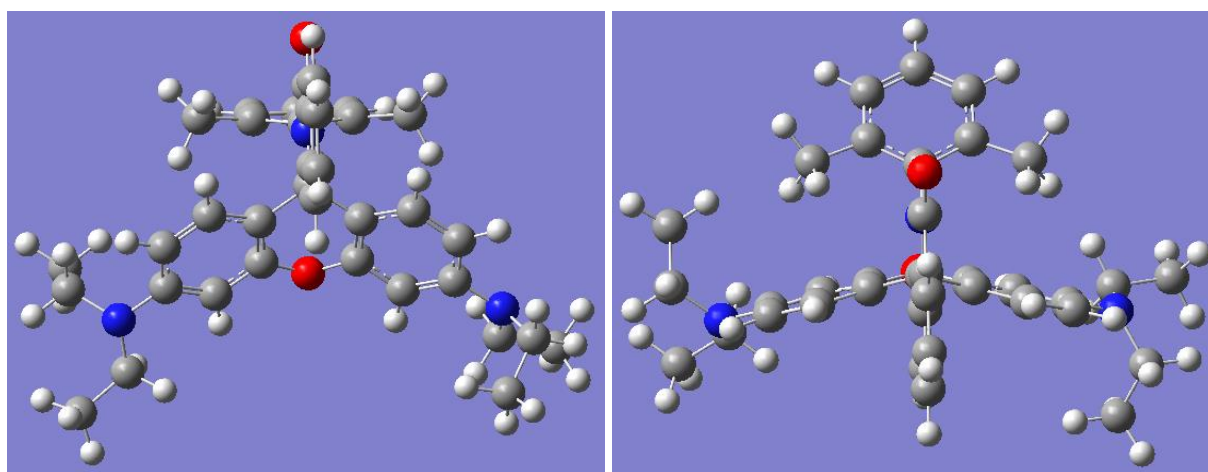


**Figure 34.** Optimized structure of RB-DMA (left) front view and (right) bird's eye view<sup>14</sup>

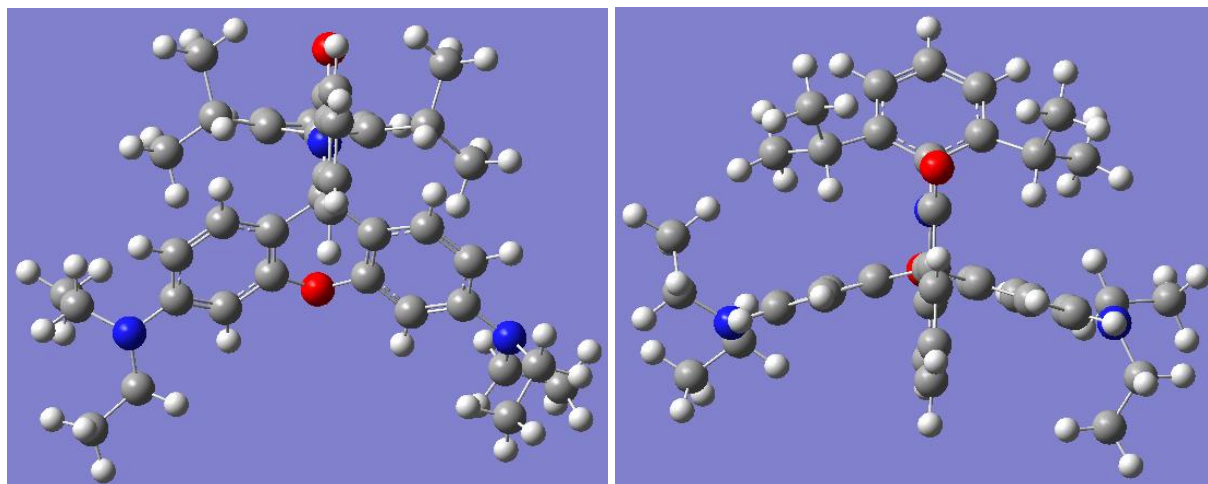


**Figure 35.** Optimized structure of RB-DIA (left) front view and (right) bird's eye view<sup>14</sup>

crystallography, these computation models are easier to generate. Grace Purnell calculated the majority of the RB set, with the exception of RB-DEA and RB-A, which was obtained from Deng and colleagues' crystal structure.<sup>28</sup> 2D structures are available in **Table 18**.

Xanthene torsion found by averaging the value of the angle between C1-O1-C13-C12, C13-O1-C1-C2, C5-C6-C7-C8, and C9-C8-C7-C6 (see **Figure 36**). In terms of the xanthene twist, RB and R6G derivatives were essentially equal, which implies that the additional methyl group in R6G compounds does not impact the xanthene angle. As such, the xanthene angle is

**Table 13.** RB and R6G derivatives by pK<sub>a</sub>, xanthene ring twist, A value,  $\sigma_p$  value, and E<sub>s</sub>

Substituent	RB pK <sub>a</sub>	Xanthene	R6G pK <sub>a</sub>	Xanthene	A value	$\sigma_p$ value	E <sub>s</sub>
H	4.31	172.576	3.81	172.964	0	0	0
F	4.52	168.967	4.3	169.409	0.3	0.12	-0.92
Cl	5.38	154.971	5.62	155.613	0.86	0.46	-1.94
OEt	4.03	161.924	4.15	160.957	1.8	-0.48	-1.1
Me	4.9	155.297	5.32	155.634	3.4	-0.34	-2.48
iPr	5.72	152.435	5.87	153.234	4.3	-0.3	-3.42

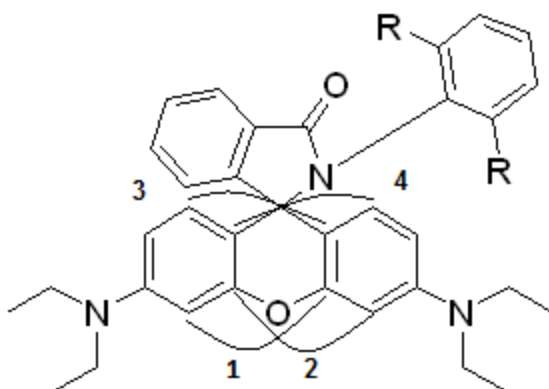


**Figure 36.** The angles measured to calculate the xanthene twist

most likely due to the substituent group. Theoretically, the xanthene angle should be the result of sterics, particularly the van der Waals repulsion. However, while the graph of xanthene angle versus  $E_s$  was fairly linear (**Figure 37**), the graph versus  $A$  values (**Figure 38**) was much more so, with the exception of RB-DCA and R6G-DCA. As I mentioned in the previous chapter,  $A$  values had more of a relationship with the electronic measure  $\sigma_p$  than  $E_s$ . So, that the xanthene twist is more linear plotted against  $A$  values implies that there is some relationship with

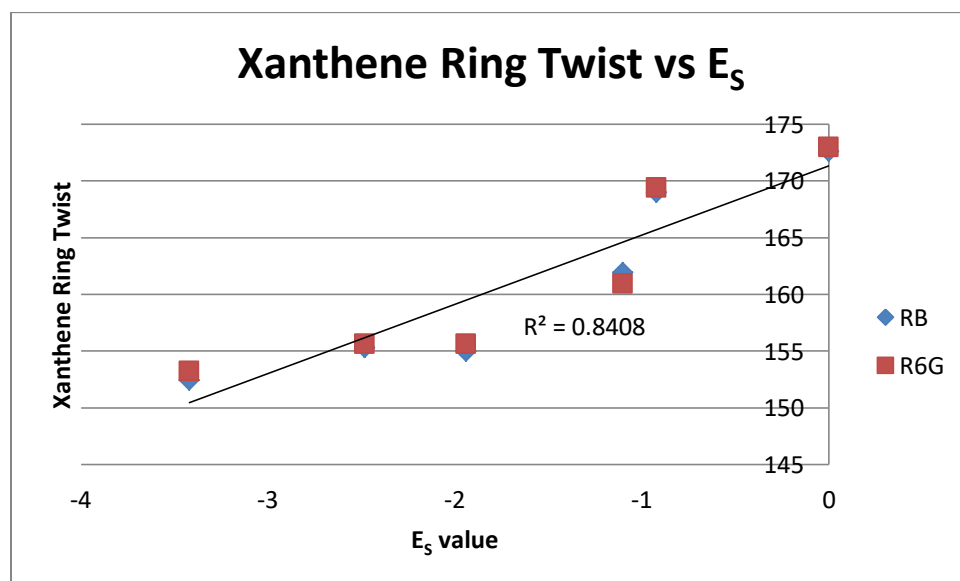


**Figure 37.** Xanthene ring torsion for RB and R6G derivatives versus the  $E_s$  parameter



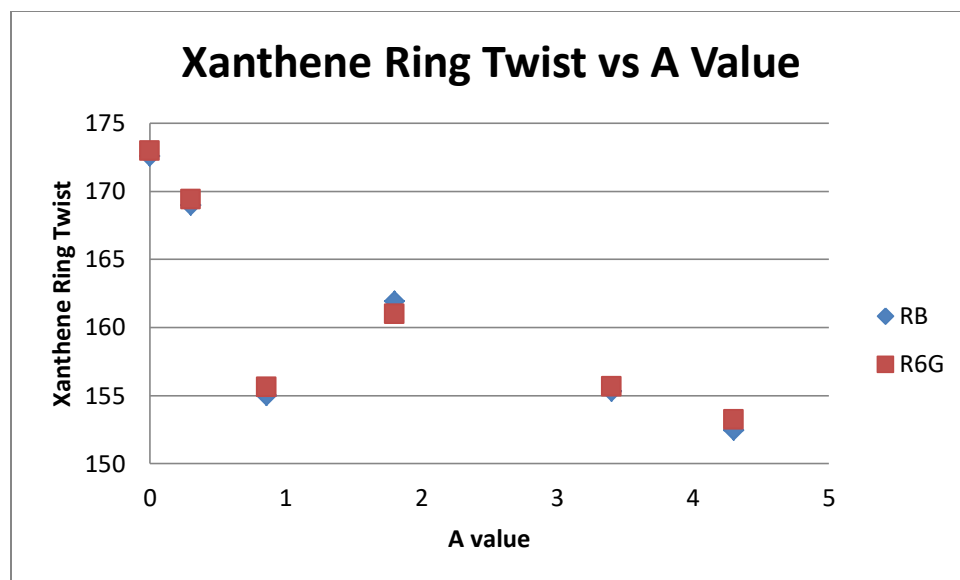


**Figure 38.** Xanthene ring torsion for RB and R6G derivatives versus the A value parameter

electronics which influences the angle twist. Only RB and R6G-DCA lie off of the line. This is likely due to the long bond length associated with chlorine and carbon. In R6G, this bond is 1.735 Å as compared to the fluorine-carbon bond length of 1.317 Å. Since the angle of both groups off of the phenyl ring is approximately the same, it stands to reason that, due to its longer bond length, the chlorine group pushes the xanthene ring further away due to repulsion effects. Therefore, the xanthene ring angle is less when the rhodamine has DCA substituents.

There is also clear distinction between the electron withdrawing and electron donating groups when graphed versus  $\sigma_p$ , thereby supporting the presence of electronic effects in the xanthene ring torsion. In fact, **Figure 39** is nearly identical to the graph of  $\sigma_p$  versus  $pK_a$ , only with a different slope. Within each electronic grouping, an increase in planarity induces ring opening, resulting in increasing  $pK_a$ .

As shown in the graph above, the xanthene ring twist was a fairly good model for  $pK_a$ . A regression analysis showed that R6G was better predicted by the xanthene angle than RB,

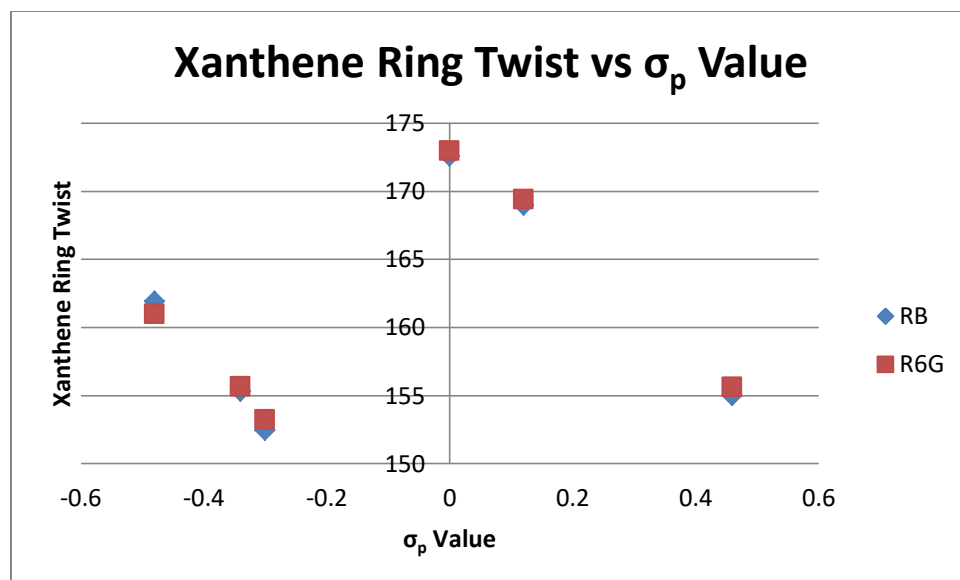


**Figure 39.** Xanthene ring torsion for RB and R6G derivatives versus the  $\sigma_p$  parameter

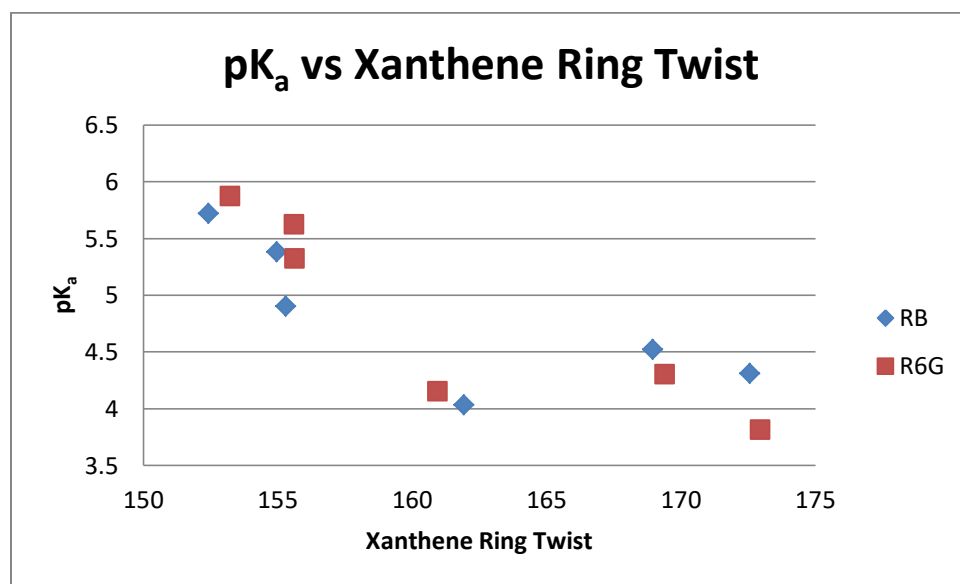


**Figure 40.** RB and R6G derivatives  $pK_a$  values versus their respective xanthene ring torsion

which suggests that though the angle does incorporate some electronic effects it is primarily steric. Since R6G has a greater dependence on sterics, the prediction suits those derivatives better. Both the RB and R6G model overestimates the  $pK_a$  for DEA and DMA, while underestimating all other  $pK_a$  values. This trend does suggest that the model is primarily steric in

**Table 14.** Regression analysis on R6G and RB using xanthene twist as a parameter

	<b>R6G</b>	<b>RB</b>
Intercept	20.137 ( $\pm$ 0.942)	14.455 ( $\pm$ 1.152)
P-value	1.73e-23	3.94e-16
Xanthene Angle Parameter	-0.094 ( $\pm$ 0.006)	-0.0597 ( $\pm$ 0.007)
P-value	3.41e-19	1.27e-10
Adjusted R <sup>2</sup>	0.865	0.604
F	263.254	69.731
P-value	3.41e-19	1.27e-10

nature. We know the DIA substituents are large enough to overcome the stabilizing factor of an electron donating side group, however DEA and DMA are not. Hence, they have a lower  $pK_a$  than would otherwise be expected based on their steric bulk alone.

Another factor looked at in the computational models was the coplanarity of the phenyl ring with the carbonyl group. This angle was measured as the angle between C20-N3-C21-C22 (see **Figure 41**). As shown in the front views of the computational models, there is a distinct twist in the phenyl ring off the spiroctam ring which is dependent upon the substituents off of the phenyl ring. When graphed versus  $pK_a$  (**Figure 42**) it is apparent that the majority of the compounds have an approximately 90° angle with the spiroactam ring, most likely due to the repulsion factors for their substituents. The exceptions are A and DEA for R6G and A, DFA, and DEA for RB. The angle for RB-A is substantially smaller than the angle for R6G-A. Either the methyl groups on the R6G do not allow the phenyl ring to twist as much or else our computational models are not as accurate as we would like them to be. Regardless, we can still determine that both RB-A and R6G-A do not lie close to a 90° angle with the carbonyl group.

These trends are also evident when graphed against both  $E_s$  and  $\sigma_p$  with little change (**Figures 44** and **45**). R6G, as noted before with the regressions, follows the trend more closely. If we assume that R6G-A is not a right angle because it has no bulky side groups to force a twist,

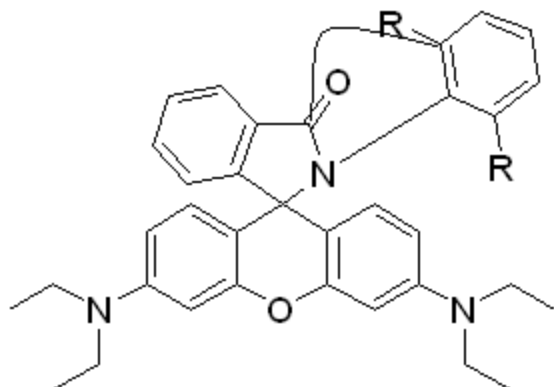


**Figure 41.** The angle between C20-N3-C21-C22

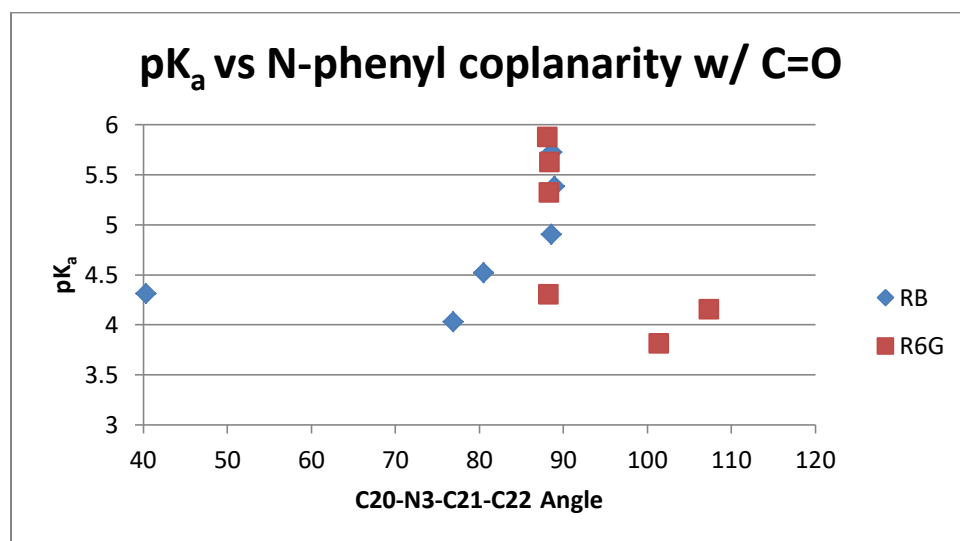


**Figure 42.**  $pK_a$  versus RB and R6G derivatives measure of coplanarity with the carbonyl

Substituent	RB pKa	C20-N3-C21-C22	R6G pKa	C20-N3-C21-C22
H	4.31	40.31	3.81	101.452
F	4.52	80.519	4.3	88.268
Cl	5.38	89.008	5.62	88.412
OEt	4.03	76.917	4.15	107.42
Me	4.9	88.628	5.32	88.351
iPr	5.72	88.646	5.87	88.148

**Table 15.** RB and R6G derivatives by  $pK_a$  and coplanarity with the carbonyl

then R6G-DEA is the main outlier. Both of these compounds also possess the lowest  $pK_a$  values. Perhaps than the more coplanar the phenyl ring is, the greater the strain is placed on the spirolactam ring. Unfortunately, this does not explain the variation in RB-DFA, other than the fact that the regression makes it clear that RB is less mathematically compliant. There appears to be some other factor in the RB model, most likely an electronic one, which would account for this difference.

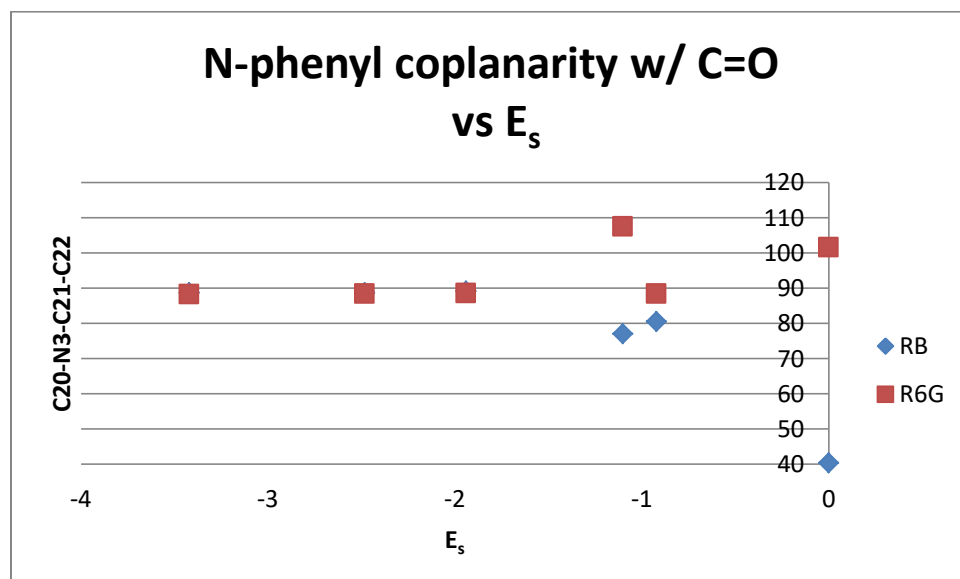


**Figure 43.** RB and R6G derivatives measure of coplanarity with the carbonyl versus the  $E_s$  parameter

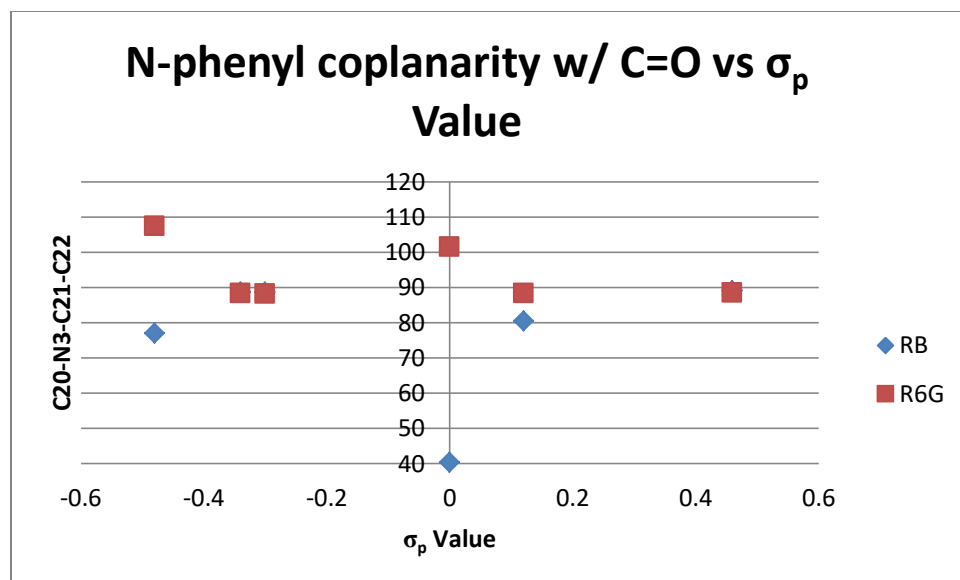


**Figure 44.** RB and R6G derivatives measure of coplanarity with the carbonyl versus the  $\sigma_p$  parameter

*C. Computational models of RB mono-ortho substituted derivatives*

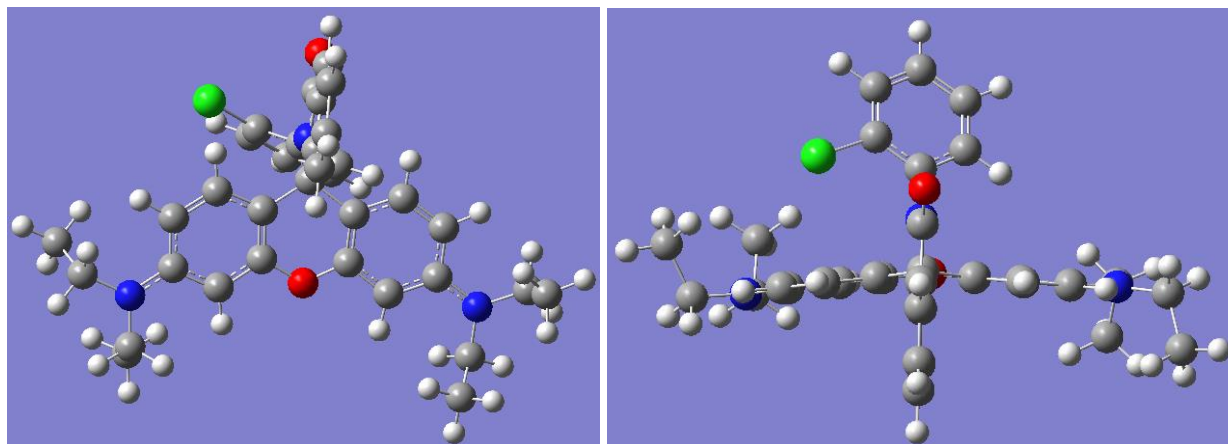


**Figure 45.** Optimized structure of RB-2CA (left) front view and (right) bird's eye view

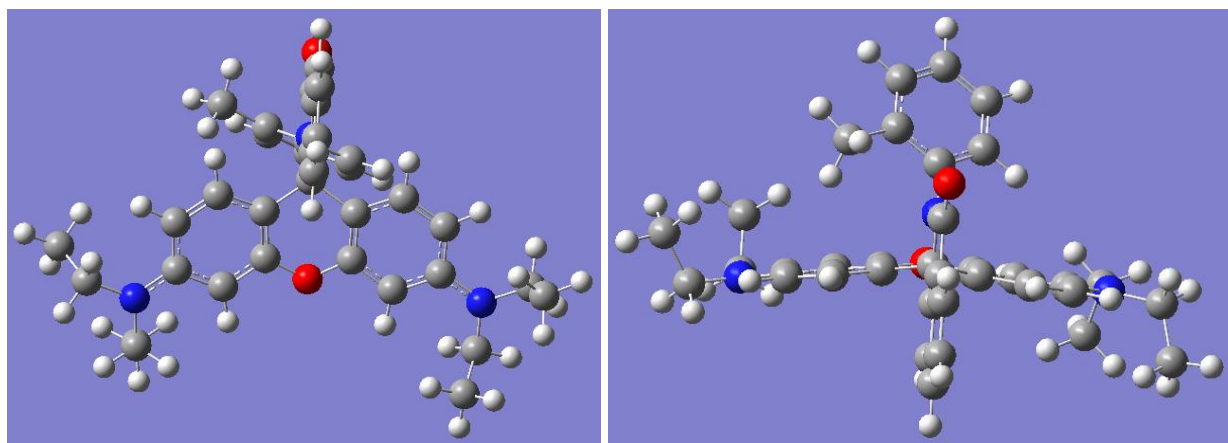


**Figure 46.** Optimized structure of RB-2MA (left) front view and (right) bird's eye view

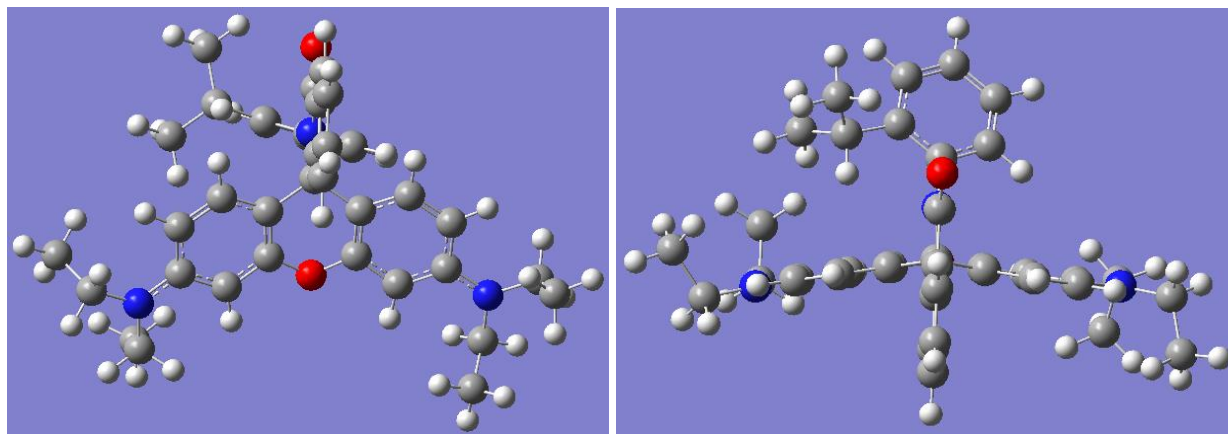


**Figure 47.** Optimized structure of RB-2IA (left) front view and (right) bird's eye view

Since the mono-*ortho* compounds were best modeled by electronic parameters only, it stands to reason that they won't have much correlation with either xanthene ring twist or coplanarity with the carbonyl. The mono-*ortho* substitution does mean that the phenyl ring can twist to avoid steric strain with the xanthene ring so as expected, the xanthene ring is more planar in structure (**Table 16**). As with the di-*ortho* derivatives, the mono-*ortho* compounds are extremely linear in nature when graphed against A values (**Figure 48**) and slightly less linear when graphed against  $E_s$  (**Figure 49**). This supports the theory that the xanthene ring twist is primarily a steric parameter but has some electronic contributions as well. Indeed, the graph of the mono-*ortho* compounds versus  $\sigma_p$  (**Figure 50**) is very similar to that of the di-*ortho*

**Table 16.** RB mono-*ortho* derivatives by  $pK_a$ , xanthene ring twist, A value,  $\sigma_p$  value, and  $E_s$

Substituent	RB $pK_a$	Xanthene	A value	$\sigma_p$ value	$E_s$
H	4.31	172.576	0	0	0
Me	4.31	165.987	1.7	-0.17	-1.24
iPr	4.28	164.369	2.15	-0.15	-1.71
Cl	4.43	169.494	0.43	0.23	-0.97

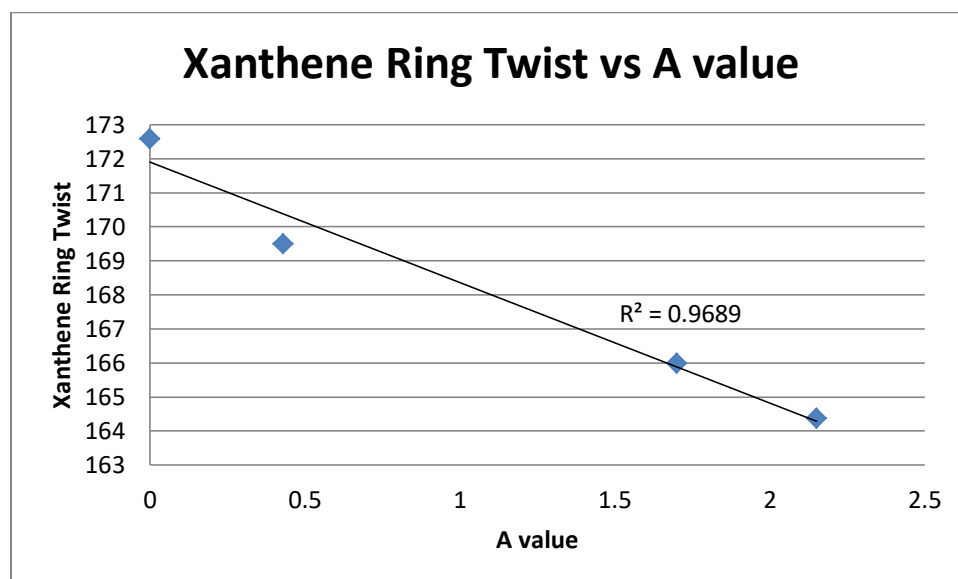


**Figure 48.** Xanthene ring torsion for RB mono-*ortho* derivatives versus A values



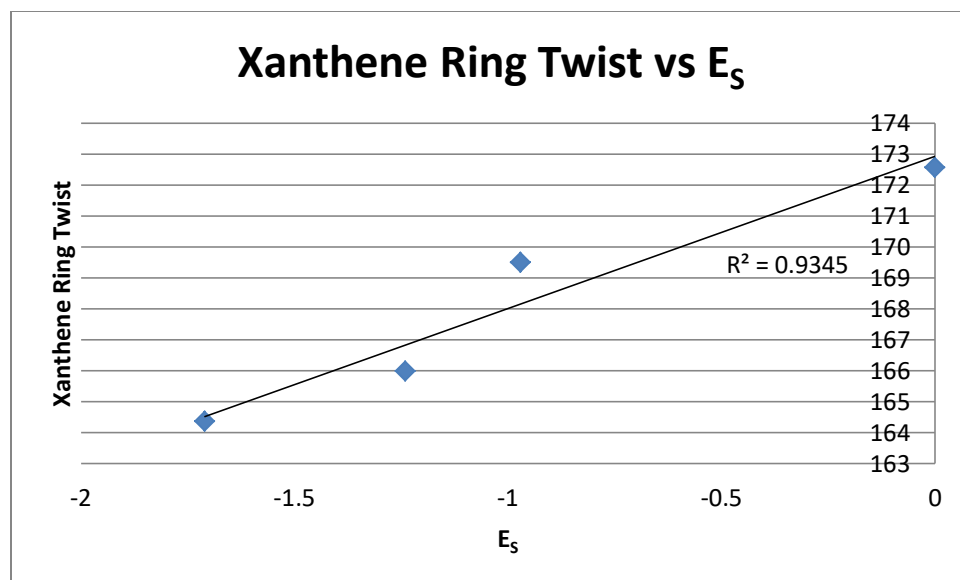


**Figure 49.** Xanthene ring torsion for RB mono-*ortho* derivatives versus the  $E_s$  parameter

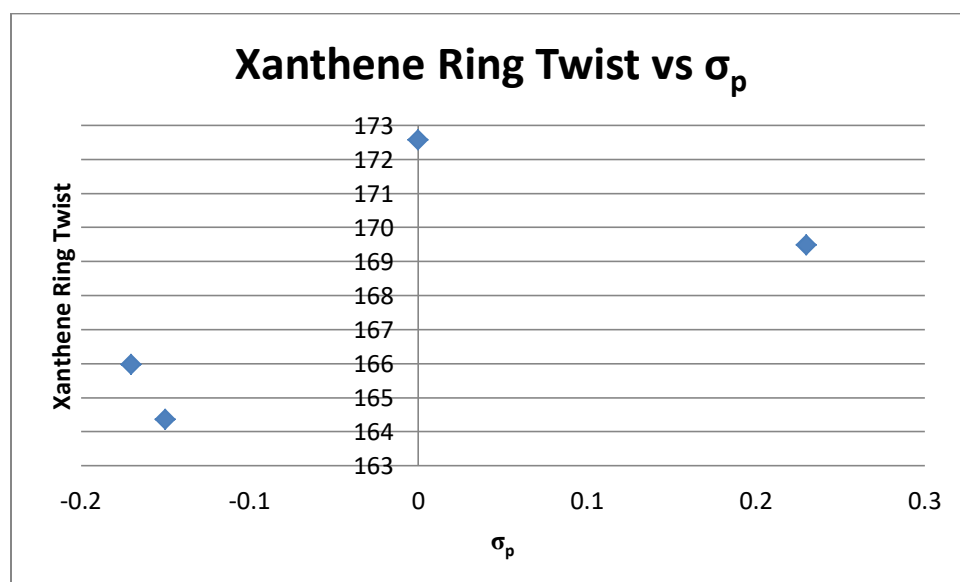


**Figure 50.** Xanthene ring torsion for RB mono-*ortho* derivatives versus the  $\sigma_p$  parameter

compounds, where the trends are split for electron withdrawing and donating groups. Of course, it is hard to make any definitive statement about these trends as only two compounds from each group were included in this analysis. As we have determined that the xanthene ring torsion is primarily the result of steric effects and the mono-*ortho* compounds were best modeled with only

**Table 17.** RB mono-*ortho* derivatives by pK<sub>a</sub> and coplanarity with the carbonyl

Substituent	RB pK <sub>a</sub>	C20-N3-C21-C22
H	4.31	40.31
Me	4.31	71.966
iPr	4.28	76.942
Cl	4.43	71.794

electronic effects, the xanthene ring twist does not correlate well with pK<sub>a</sub>.

Even though the pK<sub>a</sub> of RB-A is the same as for RB-2MA, it is clear from their respective angles with regards to the spiro lactam ring that there is a distinct difference in their orientation. Once again, it is possible that our computational models vary in some manner from the actual crystal structures of the molecules. However, the RB-2MA has a methyl group off the phenyl ring which would prohibit it twisting too much or else risk interference with the carbonyl itself. Since RB-A only has hydrogens in the *ortho* positions it doesn't have this same concern. That explanation also accounts for why RB-2IA lies closer to a right angle with the spiro lactam ring as it has the greatest steric bulk.

As shown on the next page in **Figure 51**, there is a slight linearity between steric bulk and the coplanarity with the carbonyl. The bigger the side group, the closer to a 90° angle the phenyl ring is with the spiro lactam ring. Once again though, as this is a steric parameter it does not explain the pK<sub>a</sub> differences. Just as with the xanthene ring, there appear to be clear trends when the coplanar angle is graphed against the electronic parameter of  $\sigma_p$  (**Figure 52**). This indicates that there is a strong electronic effect, which we already knew from the regression. However, since there are only two points for electron withdrawing and electron donating groups

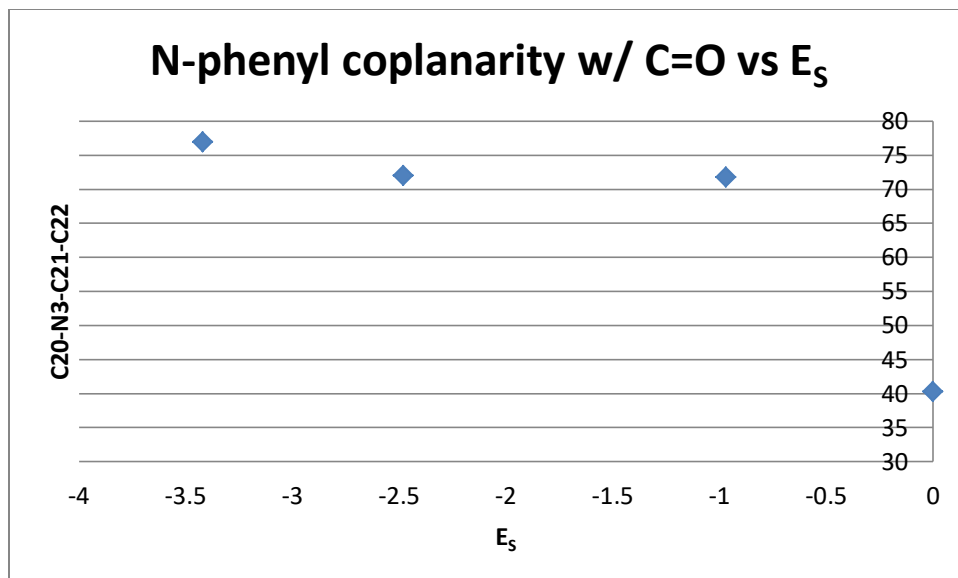


**Figure 51.** RB mono-*ortho* derivatives measure of coplanarity with the carbonyl versus  $E_s$  parameter

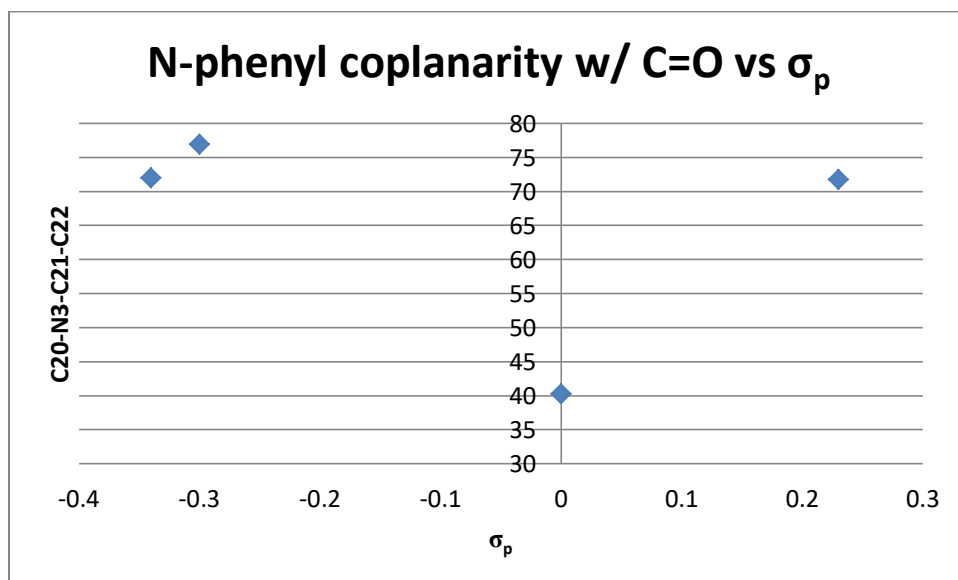


**Figure 52.** RB mono-*ortho* derivatives measure of coplanarity with the carbonyl versus  $\sigma_p$  parameter

respectively we are unable to reach support any conclusion. Unfortunately, there is no evidence to support the theory that the more coplanar the phenyl ring is, the greater the strain is placed on the spirolactam ring. RB-2IA has a lower  $pK_a$  than RB-A yet RB-A is more coplanar. It is possible that explanation only accounts for the di-*ortho* series, where sterics is a more important

factor. Therefore, computational modeling provides better insight into  $pK_a$  for the di-*ortho* series, given that it is a primarily steric indicator.

#### Section IV. Nano incorporation of RB-DIA dyes

As mentioned in the introduction, conjugated polymer nanoparticles (CPN) can serve as a vector for transmission of the rhodamine dyes to cancer cells or other targets. The particular polymer I used with my rhodamine dyes was poly[(9,9-dioctylfluorenyl-2,7-diyl)-alt-co-(1,4-benzo-{2,1',3}-thiadiazole)], called PFBT from here on (**Figure 53**). This polymer was combined with a protective coating polymer poly(vinyl butyral-co-vinyl alcohol-co-vinyl acetate), also known as PVCoCo (**Figure 54**).

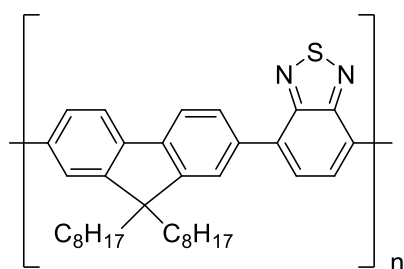


**Figure 53.** Structure of PFBT

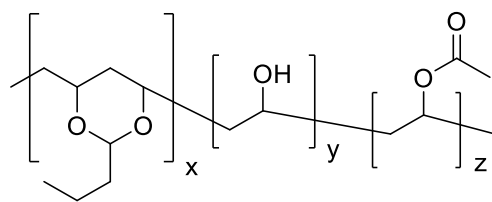


**Figure 54.** Structure of PVCoCo

While the coating polymer is non-fluorescent and only serves to protect the nanoparticle, PFBT is fluorescent. By incorporating a dye molecule into the nanoparticle we aim to intensify its fluorescence by exciting the dye through the polymer through a process known as fluorescence resonance energy transfer (FRET). The fluorescence emission spectrum of PFBT overlaps with the absorbance spectrum of RB. As such, the donor, PFBT, can transfer its energy to the acceptor, the rhodamine dye, thereby increasing the rhodamine's fluorescence. Since the PFBT's absorbed energy is being transferred to the rhodamine, the fluorescence intensity of the PFBT will drop. FRET depends on distance; the donor and acceptor molecules must be close together for FRET to occur. Therefore it is necessary to have the rhodamine molecules in or on the nanoparticle. The goal for this project was to incorporate RB-DIA, one of our higher  $pK_a$  dyes, into a nanoparticle so that FRET can occur. Since the FRET amplifies the intensity of the

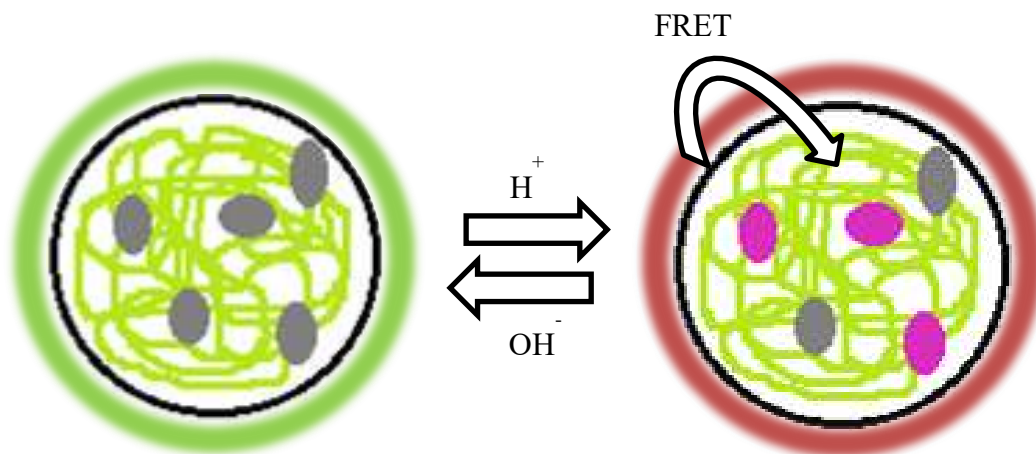


**Figure 55.** The addition of acid switches the fluorescence of the CPNs from the green region to the red as FRET occurs between PFBT and RB-DIA

acceptor molecule, we can use smaller concentrations of RB-DIA, which would reduce the risk of toxicity.

Our lab has modified its nanos procedure since the first testing of one of our di-*ortho* RB compounds in a nano particle. A major component of this change involves the method of tetrahydrofuran (THF) removal. The polymers are first dissolved into THF to make the pre-nanos solution. Nanos are not formed until water is added, whereupon the hydrophobic PFBT curls to form a spherical nanoparticle. The THF must then be removed from the sample. Our old procedure used high vacuum pumping to remove the THF however we were finding that there was still a distinctive smell of THF from the nano solution even after the water was beginning to be removed from the sample. As a result, Matthew McCarron developed a method of removing the THF through argon bubbling. This method is more regulated than the previous procedure, where the nano solution was placed under high vacuum pumping until THF could no longer be smelled. Now, the solution is weighed before and after to help quantify the amount of liquid lost. Since the high vacuum pump's pressure depended on how many solutions were on the line and

the seals of that line, the argon bubbling is also more consistent as we are able to control the bubbling rate.

#### Old Nanos Procedure:

- Prepare pre-nano solution with PFBT and PVCoco. PFBT is dissolved in THF in a 1 mg:1 mL ratio and stirred under argon gas for 2 hours. PVCoco is also dissolved in THF in a 1:1 ratio and stirred for 20 minutes.
- Filter PFBT solution with 0.7  $\mu\text{m}$  filter.
- Take 0.45 mL PFBT solution and add 24.1 mL THF and 0.45 mL of 1 mg dye in 10 mL THF solution.
- Place 1 mL of this solution into 8 mL of ultrapure water and sonicate for 2 minutes (after sonicating both separately for 30 seconds first).
- High vacuum pumping to remove THF.
- Filter nano solution with 0.2  $\mu\text{m}$  and 0.7  $\mu\text{m}$  filter.

#### New Nanos Procedure:

- Prepare 1:1 stock of PFBT and 1:1 stock of PVCoco. Stock of PVCoco needs to stir for at least 24 hours prior while stock of PFBT needs to stir for 2 hours prior.
- Best ratio of PVCoco stock to PFBT stock is 1:2.6 so take 1000  $\mu\text{L}$  of stock PFBT, 390  $\mu\text{L}$  of PVCoco, and 2361  $\mu\text{L}$  THF (anhydrous) (diluting to 25 mL with THF) and filtered with 0.7  $\mu\text{m}$  paper. Note that the total amount can be halved or quartered so long as the ratios of PFBT and PVCoco are kept the same and THF is still used to dilute to the desired amount. Reducing the amounts used reduces waste as only 2  $\mu\text{L}$  are used for the tested sample.
- Sonicate 1 mL of this pre-nano solution and 8 mL of nano-pure water separately for 30 seconds before pouring the ultrapure water into the pre-nano solution and sonicating for 2 minutes.
- Pour nanos into a dark vial and mass.
- Remove THF with argon bubbling for 30 minutes while heating to 65°C. Mass vial again to ensure the complete removal of THF.
- Add 3.6  $\mu\text{L}$  of dye solution (10 mg dye in 1 mL THF).
- Filter with 0.2  $\mu\text{m}$  and 0.7  $\mu\text{m}$  filter paper.

Using the new procedure, the nanoparticles should have a formula of 400 ppm PFBT, 90 wt%

RB-DIA, and 2.6:1 PFBT:PVCoco.

$$400 \text{ ppm PFBT in solution} = 0.04 \text{ mg PFBT/mL} * 25 \text{ mL total solution} = 1 \text{ mL PFBT}$$

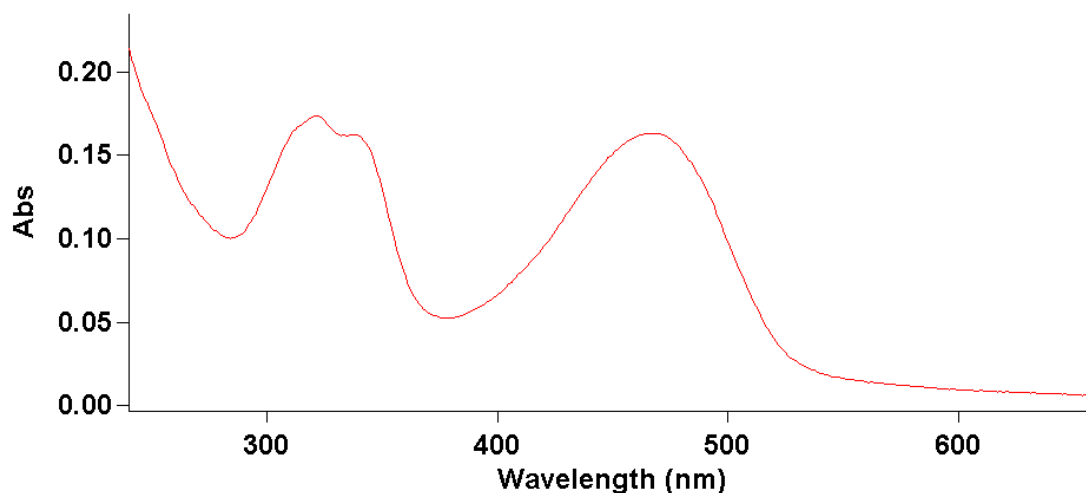


**Figure 56.** PFBT UV-Vis spectrum

$$1 \text{ mL PFBT}/2.6 = 0.385 \text{ mL PVCoCo}$$

$$0.9 * 0.04 \text{ mL PFBT} = 0.036 \text{ mL RB-DIA}/(10 \text{ mg/mL}) = 0.0036 \text{ mL RB-DIA}$$

This ratio of dye to polymer is rather large, which could indicate that not all the dye is in or on the nanos. Also, since we are injecting THF with the dye, the THF could be stabilizing the nano further or keeping the dye solution suspended instead of incorporating the dyes into the nanos.

I created a different set of nanos, adding the dye before the first filter step. In this set, all the THF should be removed from the sample as opposed to the first procedure.

Pre-Argon Bubbling Dye Addition:

250  $\mu\text{L}$  of PFBT  
 96  $\mu\text{L}$  PVCoCo  
 5904  $\mu\text{L}$  THF  
 2.5  $\mu\text{L}$  RB-DIA (10 mg/1 mL THF)

This new set of nanos also has less dye, with 10 wt% RB-DIA instead of 90 wt%. Otherwise, the formula was not changed.

$$400 \text{ ppm PFBT in solution} = 0.04 \text{ mg PFBT/mL} * 6.25 \text{ mL total solution} = 0.250 \text{ mL PFBT}$$



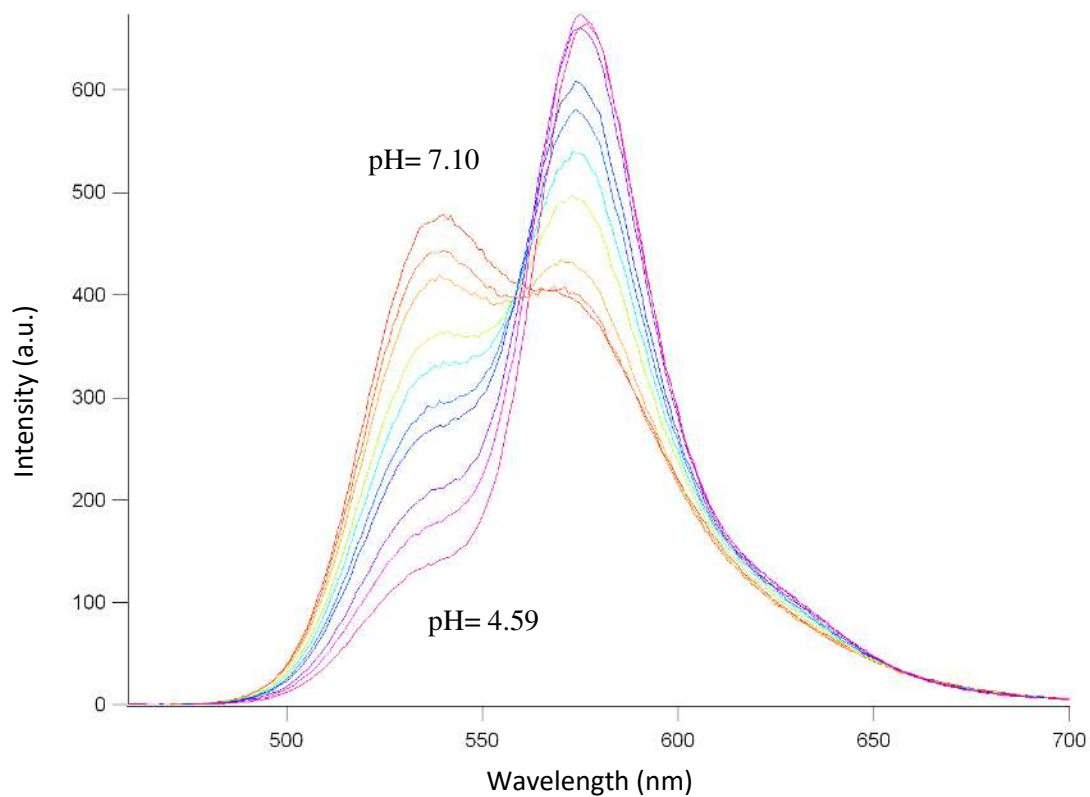


**Figure 57.** Post-argon bubbling addition of dye fluorescence, excitation at 450 nm (polymer peak on left, rhodamine on right) (red is pH 7.10 and pink is 4.59)

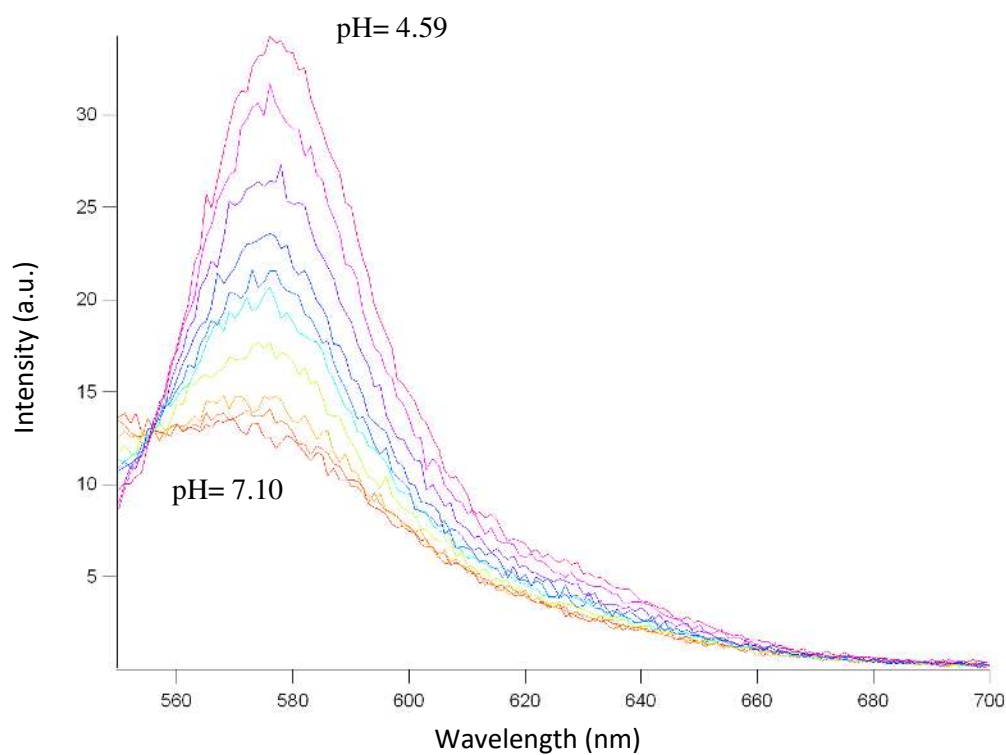


**Figure 58.** Post-argon bubbling addition of dye fluorescence, excitation at 535 nm

$$0.250 \text{ mL PFBT}/2.6= 0.096 \text{ mL PVCoCo}$$

$$0.1 * 0.250 \text{ mL PFBT}= 0.025 \text{ mL RB-DIA} / 10 \text{ mg/mL}= 0.0025 \text{ mL RB-DIA}$$

To test whether or not the nanos were on or in the nanoparticle, we ran fluorescent scans at 450 nm, exciting the polymer, and 535 nm, exciting RB-DIA. If the dyes are in the nano particle and undergoing FRET, the intensity of the rhodamine peak should be greater than if just the rhodamine is excited. For both the pre and post argon bubbling dye addition, the rhodamine peak was distinctly less intense when not excited through the nanoparticle. There appears to be very little difference between the two processes, though the ratio of polymer peak to rhodamine peak is greater for the post argon bubbling addition, as expected given the higher weight percent of RB-DIA. There was little difference seen in the UV-Vis spectrum for the dyes as well, though the point at which the rhodamine peak began to appear varied slightly. With the post-Ar addition of dye, the RB-DIA peak began to appear around a pH of 4.82, just before the nano began to degrade at 4.59 as evidenced by the bathochromic shift in the UV-Vis and fluorescence spectra. In comparison, the pre-Ar addition of dye had the RB-DIA peak appearing at 5.19 with the bathochromic shift beginning at 4.87. It appears that the THF does stabilize the nano slightly.

While the process was reversible so that the addition of base increased the intensity of the polymer peak and decreased the intensity of the dye peak, the overall intensity was diminished at lower pH values, likely due to the degradation of the nano and this loss could not be restored. As can be seen in **Figures 62** and **63** the overall intensity of the peaks are diminished after the first titration down with acid to a pH of 5.24. The intensity also noticeably decreases on the addition of base to change the pH from 8.49 to 9.21. The ratio of the peaks does remain approximately the same though. The nano set for **Figures 62** and **63** also was a post-Ar addition of dye; the presence of THF could explain the remarkable stability of the nanos as this set was tested after two days. Both previous sets mentioned were used within a day of making the nano solution.

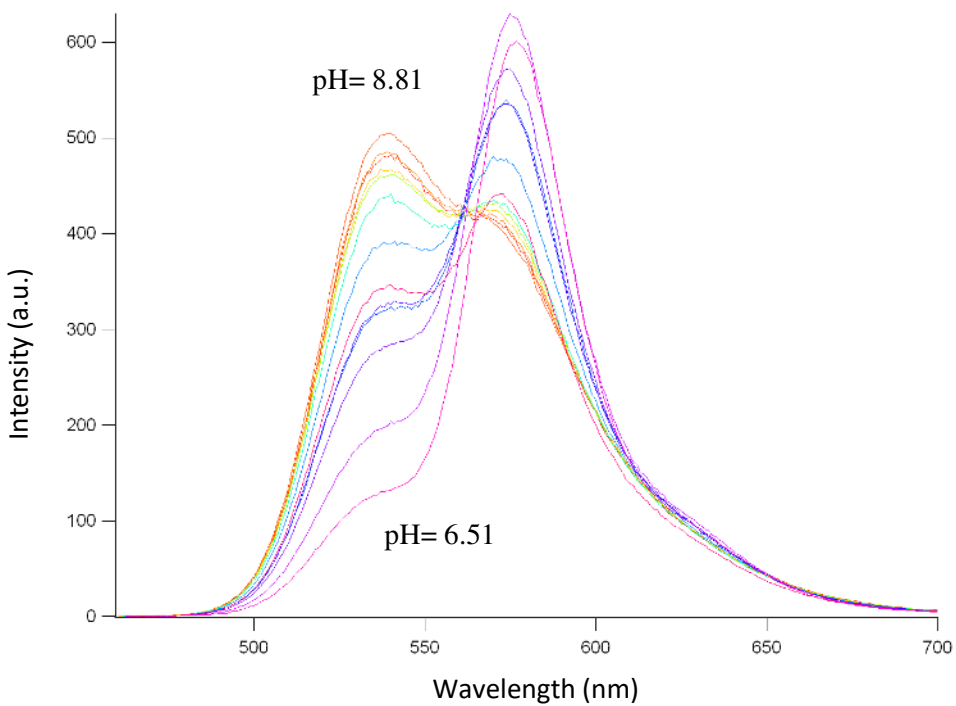


**Figure 59.** Pre-argon bubbling addition of dye fluorescence, excitation at 450 nm (polymer peak on left, rhodamine on right) (red line is pH 8.81 and pink line is 6.51)

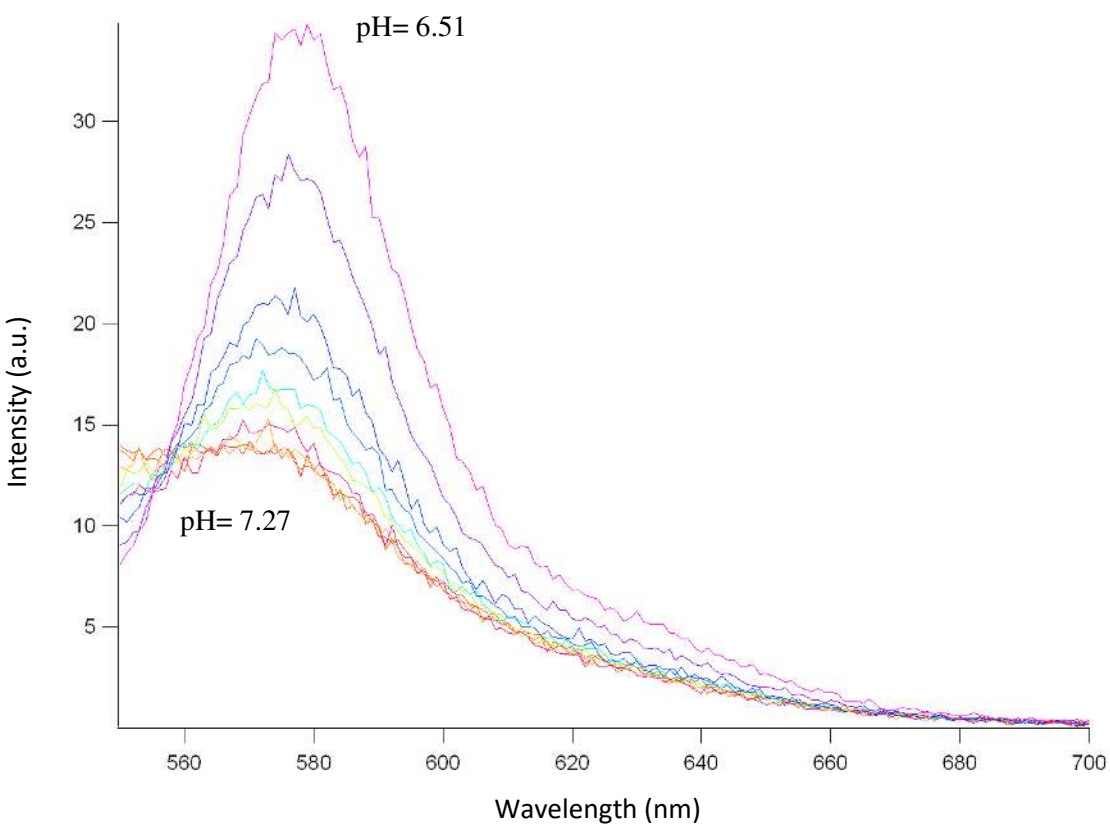


**Figure 60.** Pre-argon bubbling addition of dye fluorescence, excitation at 535 nm

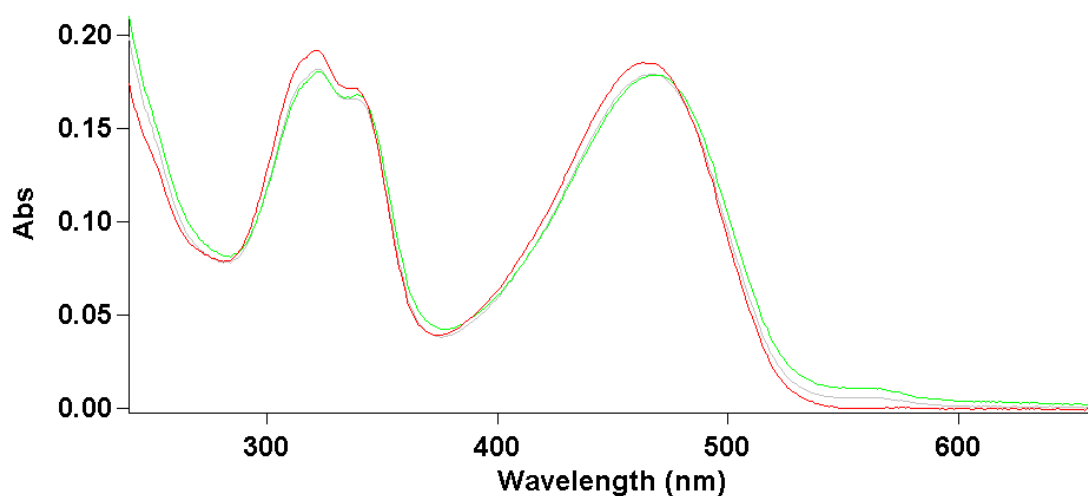


**Figure 61.** Post-argon bubbling addition of dye UV-Vis spectra (red line is pH of 7.10, grey is 4.82, and green is 4.59); the small bump just below 600 nm is the rhodamine peak

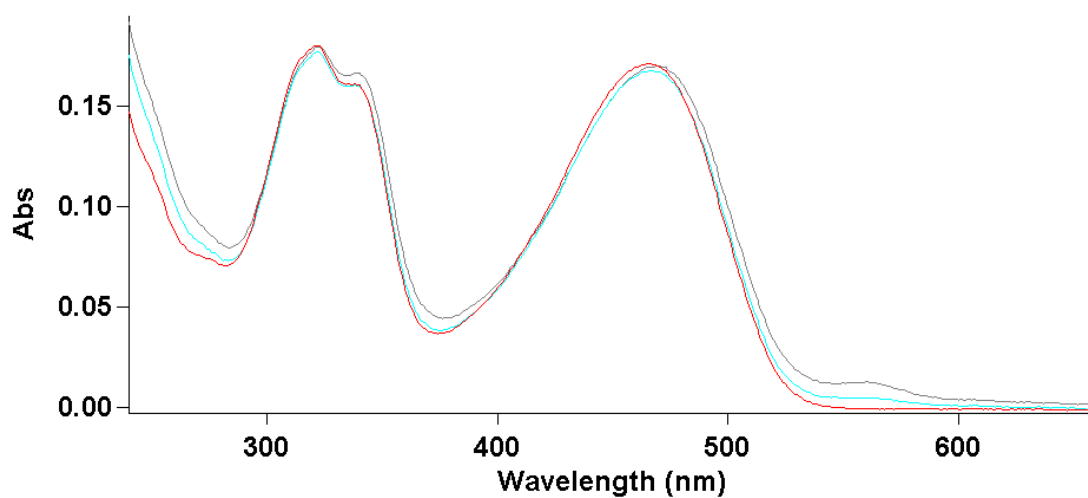


**Figure 62.** Pre-argon bubbling addition of dye UV-Vis spectra (red line is pH of 8.81, blue is 5.19, and grey is 4.87); the small bump just below 600 nm is the rhodamine peak

---

This age stability would be interesting to test further as the longer the nano stays stable for the easier it will be to use. To store these nanos for use I merely kept them in a dark vial, sealed the cap with Parafilm, and covered in tin foil before storing in the fridge. This protected the nanos from possibly degrading in the light. Unfortunately, while the THF does seem to

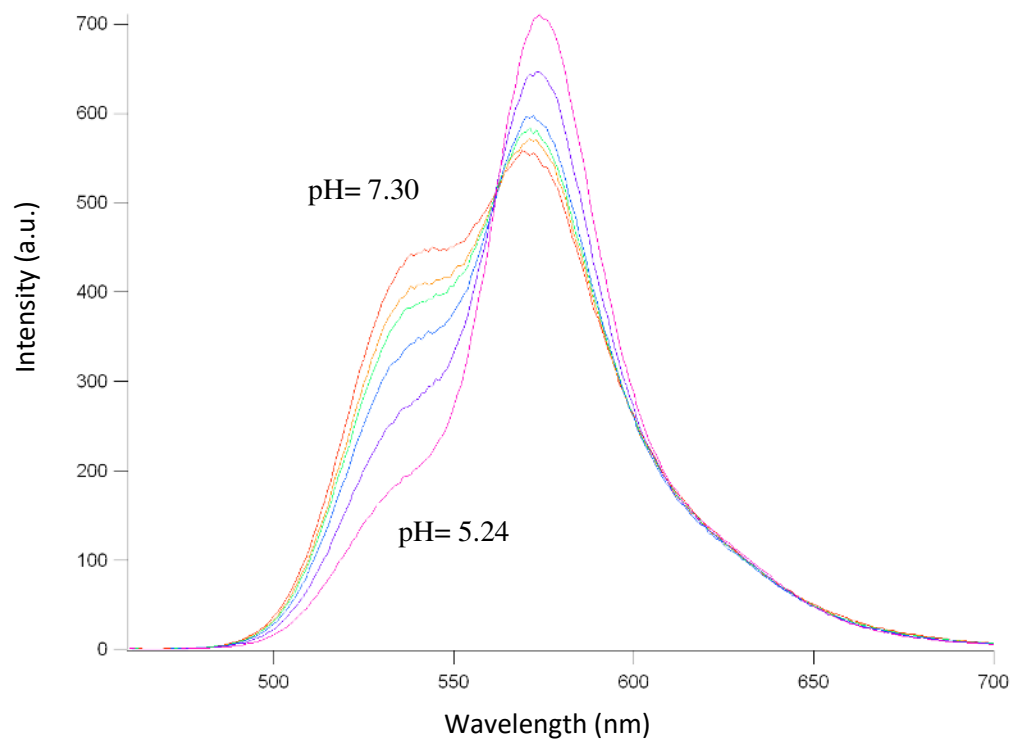


**Figure 63.** Two-day old nanos addition of acid fluorescence, excitation at 450 nm (polymer peak on left, rhodamine on right) (red is pH 7.30 and pink is 5.24)

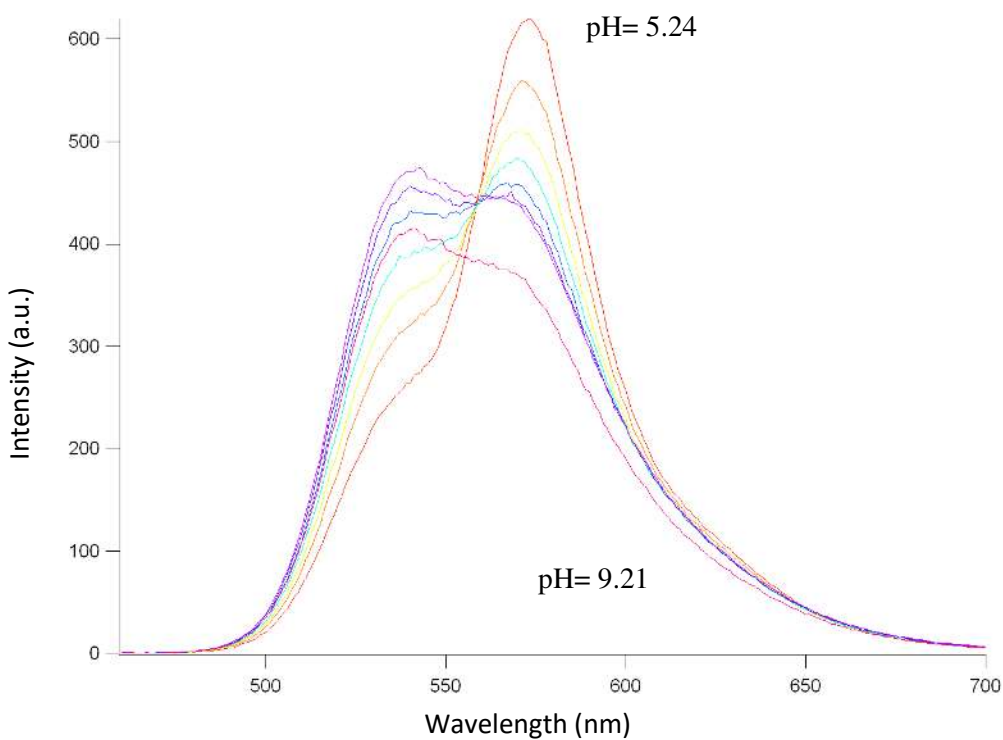


**Figure 64.** Two-day old nanos addition of base fluorescence, excitation at 450 nm (polymer peak on left, rhodamine on right) (red is pH is 5.24 and pink is 9.21)

positively affect stability of the nanos, it is not recommended for use in living biological systems.

Since we cannot use THF to stabilize the nano, we must determine at what acidic pH the nanoparticle begins to degrade. To this end, we made a nano solution without any dye added and used argon bubbling to remove all the THF. We used the bathochromic shift in the UV-Vis spectra to mark the degradation of the nano, though intensity was lost prior to that as well. As can be seen in the fluorescence spectra (**Figure 64**), the intensity at first increased. Presumably the protonation from the acid addition at first increased the size of the nanos, thereby increasing the surface area of fluorescence. However, in the UV-Vis spectra the intensity of absorbance begins decreasing immediately. The fluorescence intensity began to drop before the bathochromic shift appeared in the UV-Vis spectrum at a pH of 4.70. This result appears fairly consistent with previous titrations of the nanoparticle with the RB-DIA dye where the shift began in the upper to mid 4.00 region. Unfortunately, this made accurately determining a  $pK_a$  value difficult, particularly since the dye peak continued to increase in intensity at a pH of less than 5. Such an increase was expected as the dye used, RB-DIA, had a  $pK_a$  of 5.72. With the bathochromic shift occurring at just below the  $pK_a$ , the titration curve could not be completed by simply measuring the intensities of the rhodamine peak as we did in determining the  $pK_a$  values for our compounds in solution. While the ratio between polymer and dye peak could be used to determine the  $pK_a$  I would recommend an investigation into other polymers which overlap with the rhodamine spectra to see if there are any others which might be more stable at lower pH values.

The size of the nanoparticle was determined through dynamic light scattering (DLS). The number-weight Nicomp distribution gave 12.7 nm, 15.3 nm, and 14.4 nm diameters for an

average of 14.1 (see **Figure 67**). Based on previous tests in our lab on nanoparticle sizes, this sizing was what we would expect for these nanoparticles.

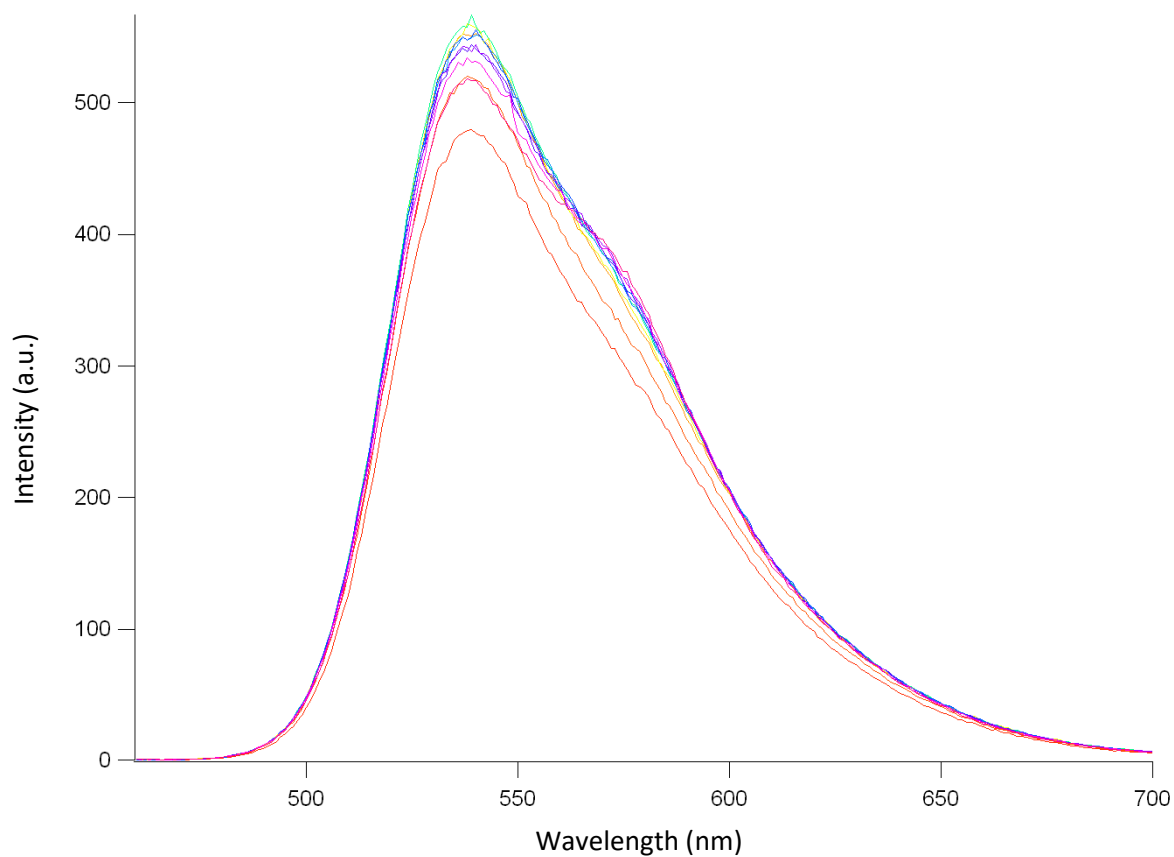


**Figure 65.** PFBT and PVCoCo with no dye, addition of acid fluorescence, excitation at 450 nm (pH range of 6.60 to 3.93; red to pink line)

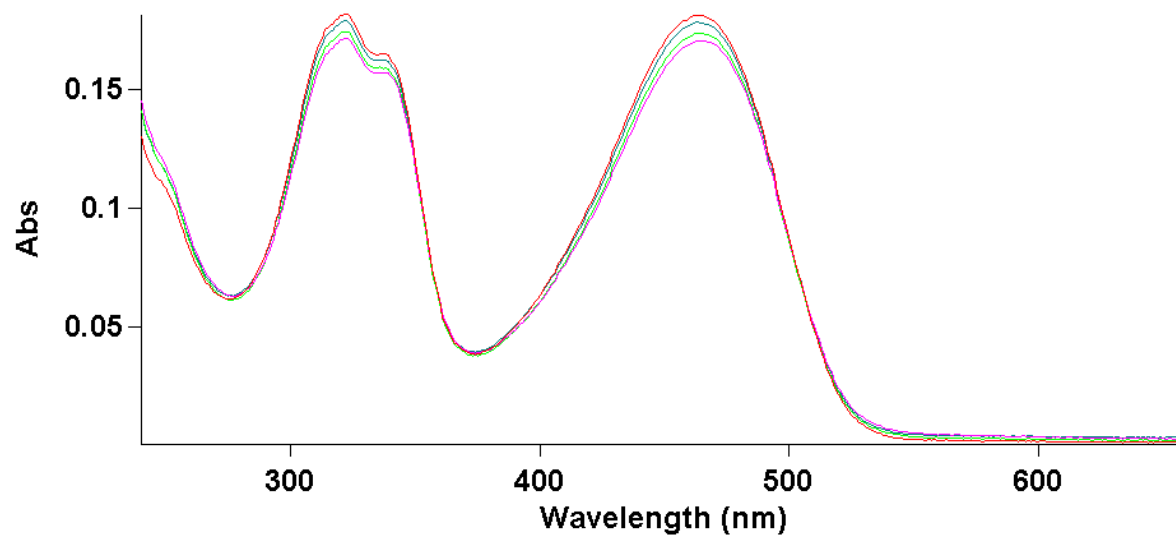


**Figure 66.** PFBT and PVCoco with no dye, addition of acid UV-Vis spectra (red line is 6.60 pH, dark green is 4.70, 4.29 is the light green line, and 3.93 is the pink line)

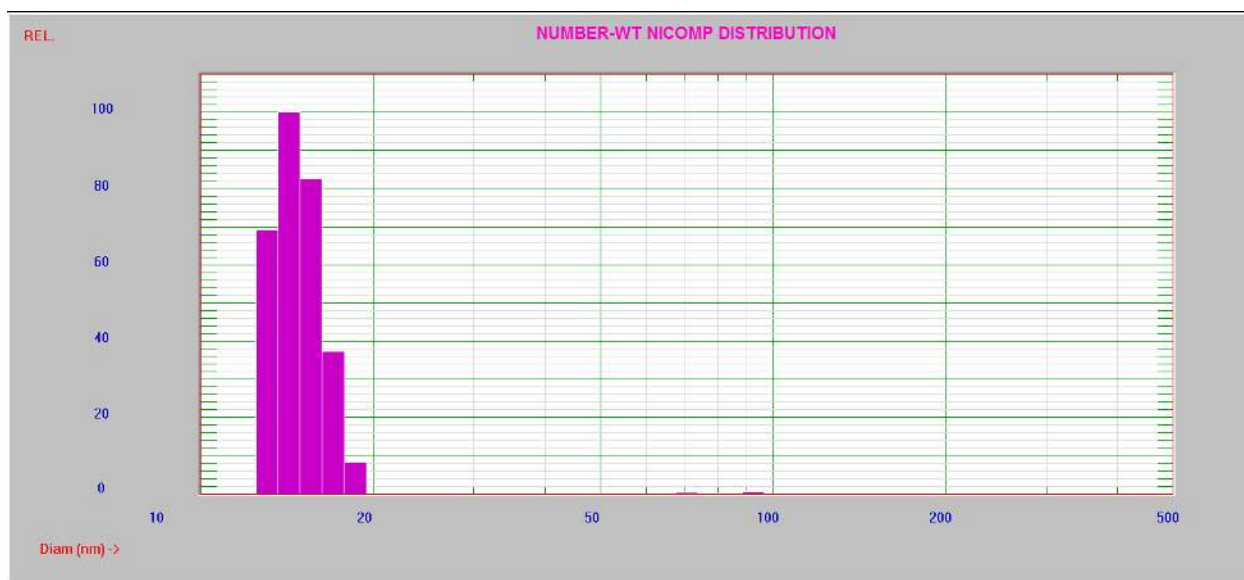


**Figure 67.** Sample particle sizing of the PFBT and PVCoco nanoparticle containing RB-DIA for a diameter of 14.4 nm using a DLS machine



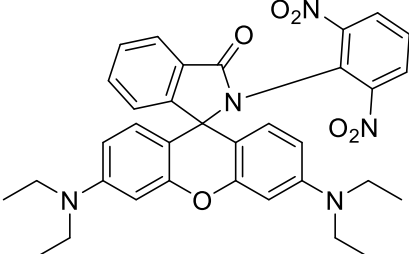
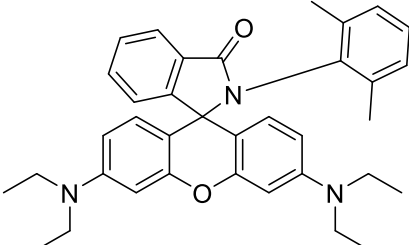
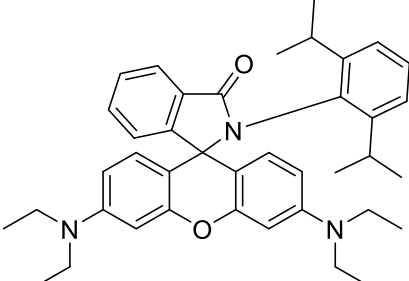
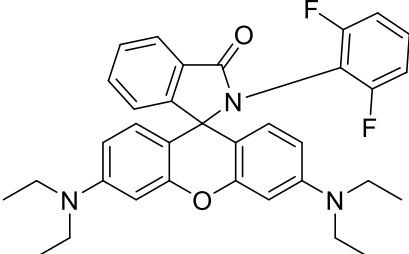
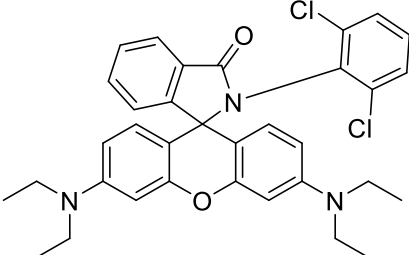
## Conclusions

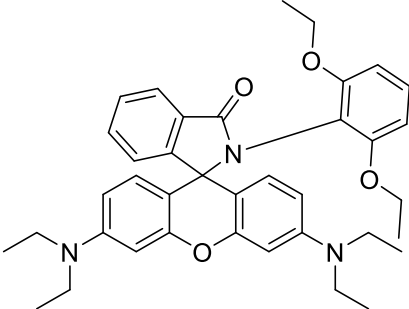
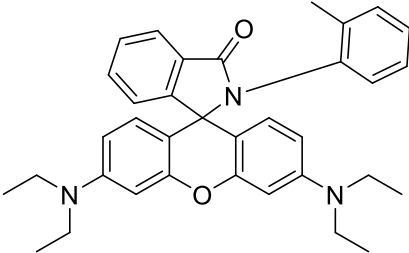
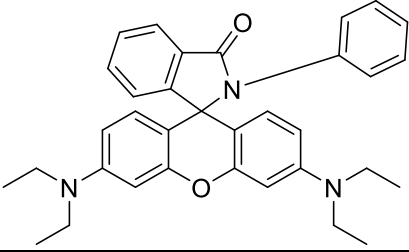
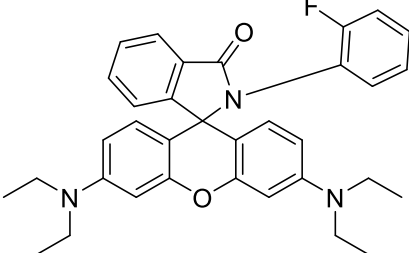
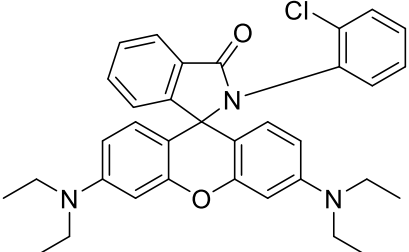
While the synthesis procedure for R6G di-*ortho* derivatives is already optimized, the RB di-*ortho* synthesis procedure could use some modifications, chiefly a reduction in the amount of POCl<sub>3</sub> used. This change should hopefully increase the percent yields. Otherwise, di-*ortho* compounds are clearly preferred to *meta*, *para*, and mono-*ortho* compounds for use in the acidic region of 4.5 to 6. R6G compounds in particular should be the focus of future research despite their synthetic hurdles as they have greater intensity than their RB counterparts and are more easily modeled mathematically. Their compliance with the mathematical model is likely due to the greater role of steric effects in their pK<sub>a</sub> values. RB appears to have an additional electronic parameter which is not fully accounted for in our models, hence its comparable lack of agreement with the mathematical model.

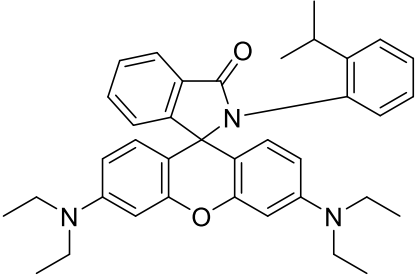
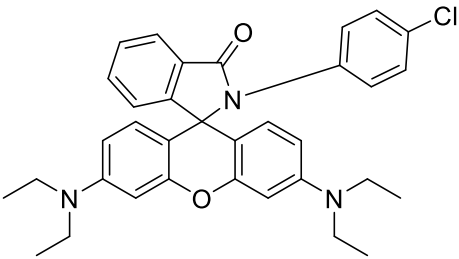
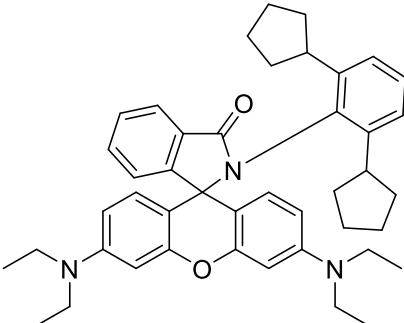
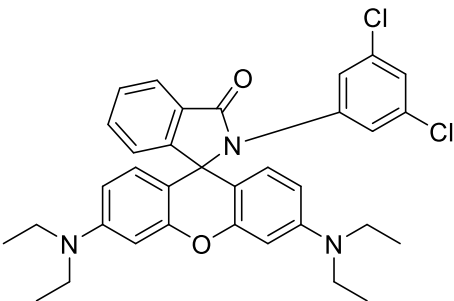
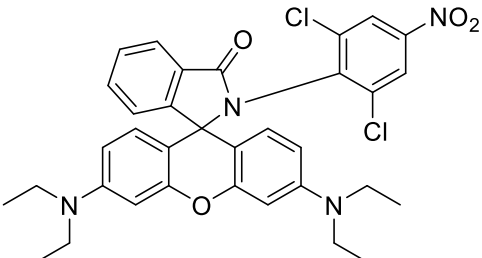
For both compounds, a variation on the Fujita-Nishioka equation in which R is substituted for F is the best model ( $pK_a = \rho\sigma_p + \delta E_s + rR + c$ ). The mono-*ortho* compounds were best modeled by a sole electronic parameter of  $\sigma_o$  however, as they were also RB compounds, there remained an unexplained effect, presumably electronic in nature. Since the pK<sub>a</sub> of the mono-*ortho* compounds was dependent on electronic effects, their computational models did not give as much insight into their nature as the computational models for the di-*ortho* compounds.

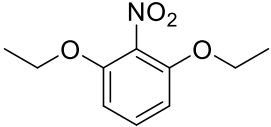
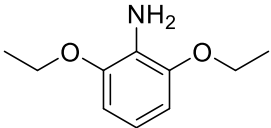
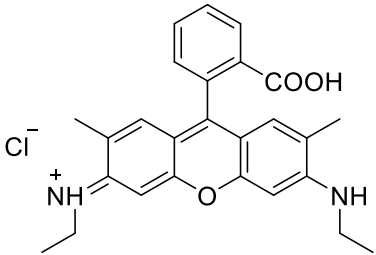
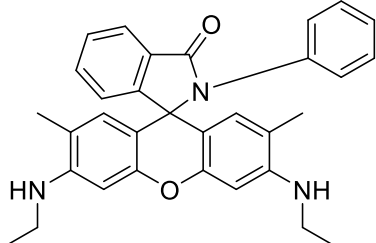
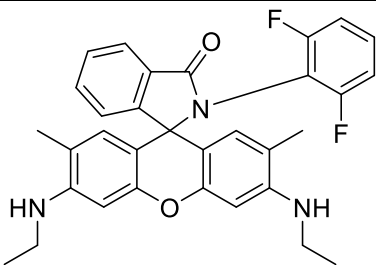
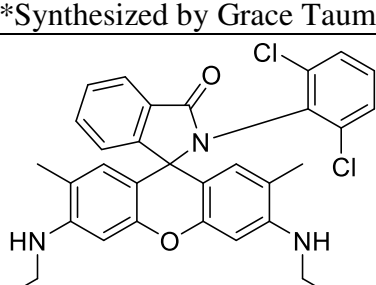
Rhodamine dyes were successfully incorporated into a PFBT and PVCoCo nanoparticle and demonstrated FRET. However, the CPN was not as stable in low pK<sub>a</sub> values as this system would prefer. An investigation into other potential CPN systems is recommended for future studies.

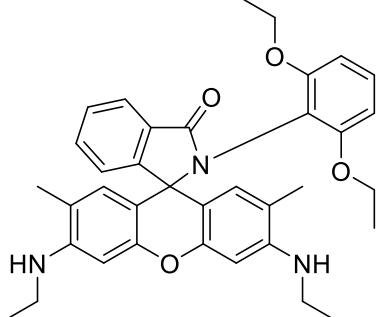
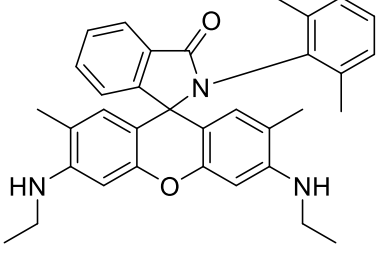
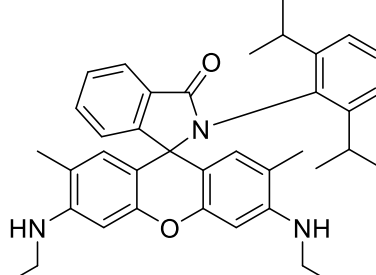
## Experimental

RB-DNA	
RB-DMA	
RB-DIA	
RB-DFA	 <p data-bbox="824 1367 1219 1398">*Synthesized by Grace Purnell</p>
RB-DCA	 <p data-bbox="824 1675 1219 1707">*Synthesized by Grace Purnell</p>

RB-DEA	
RB-2MA	
RB-A	
RB-2FA	 <p data-bbox="824 1297 1230 1333">*Synthesized by Mona Rasooly</p>
RB-2CA	 <p data-bbox="824 1602 1230 1638">*Synthesized by Mona Rasooly</p>

RB-2IA	 <p>*Synthesized by Mona Rasooly</p>
RB-4CA	 <p>*Synthesized by Grace Purnell</p>
RB-DCPA	 <p></p>
RB-3,5CA	 <p>*Synthesized by Grace Purnell</p>
RB-DCNA	 <p>*Synthesized by William Czaplyski</p>

2,6-diethoxynitrobenzene	 <chem>CCOC1=CC=C(C(=O)N)C=C1OCC</chem>
2,6-diethoxyaniline	 <chem>CCOC1=CC=C(N)C=C1OCC</chem>
R6G-Acid	 <chem>CCNc1cc2c(c1)oc3cc(C)cc(NCC)c3c2C1=CC=C(C(=O)O)C=C1.[Cl-]</chem>
R6G-A	 <chem>CCNc1cc2c(c1)oc3cc(C)cc(NCC)c3c2C1=CC=C(C(=O)Nc2ccccc2)C=C1</chem>
R6G-DFA	 <chem>CCNc1cc2c(c1)oc3cc(C)cc(NCC)c3c2C1=CC=C(C(=O)Nc2cc(F)c(F)cc2)C=C1</chem> <p>*Synthesized by Grace Taumoefolau</p>
R6G-DCA	 <chem>CCNc1cc2c(c1)oc3cc(C)cc(NCC)c3c2C1=CC=C(C(=O)Nc2cc(Cl)c(Cl)cc2)C=C1</chem> <p>*Synthesized by Grace Taumoefolau</p>

R6G-DEA	
R6G-DMA	 <p data-bbox="824 787 1299 814">*Synthesized by Grace Taumoefolau</p>
R6G-DIA	

**Table 18.** Structures and abbreviations for the rhodamine derivatives and precursors

The fluorescence spectra were recorded on a Varian Cary50 while the absorbance spectra were recorded on a Varian Eclipse. NMR studies were recorded on a Varian DD2 ( $^1\text{H}$  400 MHz,  $^{13}\text{C}$  100 MHz) and referenced to TMS ( $^1\text{H}$ ) or  $\text{CDCl}_3$  at 77.0 ( $^{13}\text{C}$ ). MS analyses were performed on a Bruker 12.0 Tesla APEX-Qe FTICR-MS with an Apollo II ion source with positive electrospray ionization. These analyses were run by COSMIC Lab at Old Dominion University.

**Synthesis of RB-DNA:** Rhodamine B (0.204 g) was dissolved in approximately 8 mL of 1,2-dichloroethane (DCE) before being placed on magnetic stir plate while 0.3 mL of  $\text{POCl}_3$  was added drop-wise over the course of two minutes. Refluxed for four hours before rotovapping off the solvents. Sonicated for ten minutes after redissolving in 10 mL of DCE with top covered with

rubber stopper and needle to vent. Massed out 0.501 g of 2,6-dinitroaniline and added DCE to dissolve. Added this mixture drop-wise via syringe to the RB-acid chloride in the round bottom flask over the course of five minutes. Swirled occasionally while adding. Refluxed for twenty-three hours and ten minutes. Rinsed with three washes of acid (2 M HCl) and four washes of base (2 M NaOH). Then rinsed with two washes of brine saturated solution. The aqueous layer was discarded after every wash. Several large scoops of magnesium sulfate (anhydrous) were added to the solution until the powder no longer clumped, forming a 'snow globe' effect when swirled. This step removed excess water. The solution was then funneled through filter paper into a round bottom and concentrated *in vacuo*. A semisolid substance formed in the solution before the solution formed a powder which coated the entire round bottom. After an NMR confirmed product, determined that 60:40 ethyl acetate (EtOAc) to hexane provided the best separation. Started a column at this separation before gradually increasing to 65:35 EtOAc to hexanes, then 70:30, and finally 80:20 right before the second band exited the column.

Triethylamine was added to the column consistently in order to keep the rhodamine in its closed form as the acidic nature of the silica induced a ring opening. The first band was bright yellow (most likely aniline) while the second was a dark red, and the third a light pink. The second band indicated the possible presence of product on TLC. Concentrated *in vacuo* however had water enter the round bottom so also had to evaporate out the water. Dissolved in pure triethylamine with some acetone. At first this sample was a tan/yellow colored solution but as it was rotovapped it turned dark pink, indicating that the rhodamine had opened. NMR determined that this was likely product. Percent yield of 50.21% but could not get to stay closed at a pH lower than about 15.  $^1\text{H}$  NMR (400MHz,  $\text{CDCl}_3$ ) 8.00-7.98 (d, 1H), 7.61-7.54 (m, 2H), 7.20-7.18 (d, 1H), 6.59-6.57 (d, 2H), 6.44 (s, 2H), 6.35-6.32 (dd, 2H), 3.37-3.32 (m, 3H), 2.96-2.92 (m, 1H),

1.22-1.07 (m, 6H).  $^{13}\text{C}$  NMR (100 MHz,  $\text{CDCl}_3$ ) 170.0, 153.6, 149.8, 134.2, 129.2, 129.1, 125.0, 124.4, 108.2, 106.3, 97.4, 45.0, 44.5, 12.5, 8.8.

**Synthesis of RB-DMA:** Rhodamine B (0.2047 g) was dissolved in approximately 6 mL of DCE. Covered top with rubber stopper with needle to vent before adding 0.3 mL of  $\text{POCl}_3$  drop-wise over three minutes and swirled, followed by 0.15 mL DMA added drop-wise over two minutes. Refluxed for twenty-three hours and fifty-five minutes. The solution in the round bottom had separated into a lighter aqueous layer and a dark red lower layer. Concentrated *in vacuo*. Once the majority of the solution was removed, added chloroform and allowed to sit five minutes after mixing in a separatory funnel. Washed three times with acid (2 M HCl), three times with base (2 M NaOH), and twice with brine. Added magnesium sulfate (anhydrous) and filtered to get a very light orange-tan solution. Rotovapped and took NMR to find strange anomalies. Dried under high vacuum pumping before taking another NMR to find pure product with some water. Percent yield was 23.50%.  $^1\text{H}$  NMR (400MHz,  $\text{CDCl}_3$ ) 8.09-8.07 (d,  $J= 7.4$  Hz, 1H), 7.68-7.64 (m, 2H), 7.43-7.42 (d,  $J= 7.4$  Hz, 1H), 7.05-7.01 (t,  $J= 7.4$  Hz, 1H), 6.84-6.82 (d,  $J= 7.4$  Hz, 2H), 6.57-6.55 (d,  $J= 9.0$  Hz, 2H), 6.30-6.27 (dd,  $J= 8.8, 2.5$  Hz, 2H), 6.23 (d,  $J= 2.4$  Hz, 2H), 3.34-3.29 (q,  $J= 7.03$ , 8H), 1.35 (s, 6H), 1.14-1.11 (t,  $J= 7.03$ , 12H);  $^{13}\text{C}$  NMR (100 MHz,  $\text{CDCl}_3$ ) 166.0, 155.9, 149.0, 148.6, 139.0, 132.1, 129.4, 128.7, 127.9, 127.7, 124.8, 123.9, 109.0, 107.4, 98.4, 44.5, 18.3, 12.4; Exact mass calculated for  $\text{C}_{36}\text{H}_{39}\text{FN}_3\text{O}_2\text{H}^+$ , 546.311504 m/z. Found 546.310670 m/z.

**Synthesis of RB-2FA:** Mona Rasooly synthesized RB-2FA. Measured out 0.2011 g RB and dissolved in 8 mL DCE. Added 0.3 mL  $\text{POCl}_3$  dropwise over five minutes and 0.18 mL 2-fluoroaniline over one minute. Refluxed for twenty-three hours and twenty-five minutes. Added 30 mL chloroform and washed with three times with acid (2 M HCl), three times with base (2 M



NaOH), and twice with brine. Concentrated *in vacuo* before running a column in 20:80 EtOAc:Hexanes. Second band was product. Dried under high vacuum pumping.  $^1\text{H}$  NMR (400MHz,  $\text{CDCl}_3$ ) 8.04-8.02 (m, 1H), 7.55-7.49 (m, 2H), 7.19-7.17 (m, 1H), 7.15-7.10 (m, 1H), 6.97-6.92 (t, J= 8.2, 1.2Hz, 1H), 6.86-6.83 (t, J= 7.65, 1.3 Hz, 1H), 6.72-6.69 (d, J= 9.0, 1.2 Hz, 2H), 6.40-6.36 (td, J= 7.63, 5.5 Hz, 1H), 6.34-6.31 (dd, J= 9.0, 2.7 Hz, 2H), 6.24-6.23 (sd, J= 2.7 Hz, 2H), 3.35-3.29 (m, 8H), 1.17-1.14 (t, J=7.05 Hz, 12H);  $^{13}\text{C}$  NMR (100 MHz,  $\text{CDCl}_3$ ) 166.9, 153.5, 153.3, 148.8, , 132.8, 130.9, 129.3, 129.0/129.0, 128.2, 124.2, 123.8, 123.4, 116.3, 116.0, 108.1, 106.0, 97.6, 67.6, 45.8, 44.3, 29.7, 12.5, 8.6. Exact mass calculated for  $\text{C}_{34}\text{H}_{34}\text{N}_3\text{O}_2\text{H}^+$ , 536.270782 m/z. Found 536.270232 m/z.

**Synthesis of RB-2CA:** Mona Rasooly synthesized RB-2CA. Massed out 0.2064 g RB and dissolved in 8 mL DCE. Added 0.3 mL  $\text{POCl}_3$  dropwise over five minutes and 0.12 mL 2-CA dropwise over three minutes. Refluxed for twenty-four hours. Added 30 mL chloroform and washed three times with acid (2 M HCl), three times with base (2 M NaOH), and twice with brine. Concentrated *in vacuo* before running a column in 10:90 EtOAc:Hexanes. Second band was product. Dried under high vacuum pumping.  $^1\text{H}$  NMR (400MHz,  $\text{CDCl}_3$ ) 8.06-8.04 (m, 1H), 7.58-7.52 (m, 2H), 7.25-7.22 (m, 2H), 7.11-7.07 (td, J= 7.63, 1.43 Hz 1H), 6.96-6.92 (td, J= 7.63, 1.43 Hz, 1H), 6.75-6.73 (d, J=9.0 Hz, 1H), 6.64-6.62 (d, J= 8.6 Hz, 1H), 6.39-6.37 (dd, J= 6.6, 2.4 Hz, 1H), 6.31-6.30 (sd, J= 2.4 Hz, 1H), 6.27-6.22 (td, J= 8.23, 1.83 Hz, 2H), 6.15-6.14 (sd, J= 2.3 Hz, 1H), 3.38-3.35 (m, 4H), 3.29-3.25 (m, 4H), 1.26-1.10 (m, J= 6.95 Hz, 12H);  $^{13}\text{C}$  NMR (100 MHz,  $\text{CDCl}_3$ ) 166.0, 152.4, 134.3, 133.8, 132.7, 131.8, 130.9, 130.1, 129.5, 129.0, 128.7, 128.3, 126.6, 124.3, 108.3, 107.5, 97.9, 97.4, 68.2, 44.4, 44.3, 29.7, 12.5. Exact mass calculated for  $\text{C}_{34}\text{H}_{34}\text{ClN}_3\text{O}_2\text{H}^+$ , 552.241232 m/z. Found 552.241146 m/z.

**Synthesis of RB-2IA:** Mona Rasooly synthesized RB-2IA. Massed out 0.2077 g RB and dissolved in 8 mL DCE. Added 0.3 mL  $\text{POCl}_3$  dropwise over five minutes and 0.2 mL 2-IA

dropwise over three minutes. Refluxed for forty hours and forty-five minutes. Added 30 mL chloroform and washed three times with acid (2 M HCl), three times with base (2 M NaOH), and twice with brine. Concentrated *in vacuo* before running a column. Dried under high vacuum pumping.  $^1\text{H}$  NMR (400MHz,  $\text{CDCl}_3$ ) 8.06-8.03 (m, 1H), 7.63-7.56 (m, 2H), 7.33-7.31 (m, 1H), 7.21-7.13 (m, 2H), 6.85-6.81 (td, J= 6.85, 1.95 Hz, 1H), 6.62-6.57 (t, J= 10.4 Hz, 2H), 6.40-6.38 (dd, J= 8.8, 2.5 Hz, 1H), 6.31-6.28 (dd, J= 9.0, 2.8 Hz, 1H), 6.26-6.25 (sd, J= 2.7 Hz, 1H), 6.16-6.16 (sd, J= 2.4 Hz, 1H), 6.00-5.97 (dd, J= 7.85, 1.15 Hz, 1H), 3.44-3.21 (m, 8H), 2.59-2.52 (qu, J= 6.85 Hz, 1 H), 1.19-1.16 (t, J= 7.05 Hz, 6H), 1.14-1.08 (m, 9H), 0.44-0.43 (d, J= 6.6 Hz, 3H);  $^{13}\text{C}$  NMR (100 MHz,  $\text{CDCl}_3$ ) 166.7, 155.0, 154.3, 151.1, 148.9/148.9, 148.6, 133.0, 132.7, 132.4, 129.4, 129.1, 128.9, 128.4/128.4, 126.1, 125.4, 124.5, 123.4, 108.2, 108.0, 107.9, 106.8, 98.0, 97.8, 68.2, 44.5, 44.4, 28.3, 24.8, 23.1, 12.6, 12.5. Exact mass calculated for  $\text{C}_{35}\text{H}_{41}\text{N}_3\text{O}_2\text{H}^+$ , 560.327154 m/z. Found 560.326818 m/z.

**Synthesis of RB-4CA:** Grace Purnell synthesized RB-4CA. This compound was reported previously<sup>13</sup>.

**Synthesis of RB-DCPA:** Rhodamine B (0.2036 g) was dissolved in 5 mL of DCE. Covered the top with a rubber stopper with needle to vent before adding 0.3 mL  $\text{POCl}_3$  drop-wise over the course of three minutes while swirling constantly. Dissolved 0.54 g 2,6-dicyclopentylaniline in 5 mL DCE and added this mixture to the rhodamine solution drop-wise over the course of fifteen minutes. Added approximately 3 mL more DCE since the solution was now a thick sludge. Refluxed for twenty-four hours and ten minutes. Very thick consistency, similar to that of a melted crayon, so concentrated *in vacuo*. Added 50 mL chloroform before using Buchner filtration to separate out the gelatin like solid. Washed with 5 mL of chloroform four times before leaving under vacuum for an hour. Took the liquid and added 40 mL chloroform before washing with three washes of 2 M HCl, three washes 2 M NaOH, and two washes of brine.

Added magnesium sulfate anhydrous and filtered before rotovapping to get a dark red substance. Ran column in 60:40 EtOAc: Hexanes but had bands one and two run together to form a tan/white powder which later turned into a pinkish, cotton candy like powder. Ran another column in 80:20 EtOAc: Hexanes to get a tan and pink band. The tan band was run through a third column in the same ratio of solvents and concentrated *in vacuo* to get a tan powder which eventually turned white with a slightly pink tint. Yield was 7%.

**Synthesis of RB-A:** This compound was reported previously.<sup>13</sup> Rhodamine B (0.2024 g) dissolved in approximately 6 mL of DCE. Covered the top with a rubber stopper with a needle to vent prior to adding 0.3 mL POCl<sub>3</sub> drop-wise over the course of three minutes, while swirling. Added 0.15 aniline drop-wise over the course of two minutes, while swirling. Refluxed for twenty-four hours and fifteen minutes. Over the course of the reflux the mixture went from light/bubblegum pink to light red. Washed three times with 2M HCl, three times with 2M NaOH, and twice with brine. Added magnesium sulfate anhydrous before filtering and concentrated *in vacuo* to form a waxy red substance. Ran a column in 60:40 EtOAc: Hexanes and concentrated *in vacuo* the first band (tan) to form a yellow-tan solid with a bubbly appearance. Percent yield was 28.98%

**Synthesis of RB-DIA:** Rhodamine B (0.2793 g) was dissolved in approximately 8 mL DCE before covering with a rubber stopper and needle to vent. Placed on a stir plate prior to adding 0.3 mL POCl<sub>3</sub> over the course of three minutes while stirring. Then added 0.25 mL 2,6-diisopropylaniline drop-wise over the course of two minutes while stirring. Refluxed twenty-four hours and five minutes. Washed three times with 2M HCl, three times with 2M NaOH, and twice with brine. Added magnesium sulfate anhydrous and filtered before concentrating *in vacuo*. Ran a column in 70:30 EtOAc:Hexanes and collected the first band, which showed up pink on the

TLC. Concentrated *in vacuo* to get large quantities of white powder. Ran another column in 60:40 EtOAc: Hexanes and got tan crystals with a faint white ring around the edge of the round bottom. Ran a third column in 40:60 EtOAc: Hexanes and collected the second band which formed a large amount of white powder. Dried under high vacuum pumping. Percent yield was 19.87%. <sup>1</sup>H NMR (400MHz, CDCl<sub>3</sub>) 8.07-8.05 (m, 1H), 7.63-7.60 (m, 2H), 7.30-7.28 (m, 1H), 7.24-7.20 (t, J= 7.8 Hz, 1H), 6.99-6.97 (d, J= 7.4 Hz, 2H), 6.56-6.54 (d, J= 9.0 Hz, 2H), 6.30-6.28 (dd, J= 9.0, 2.7 Hz, 2H), 6.20 (d, J= 2.3 Hz, 2H), 3.32-3.26 (q, J= 7.0 Hz, 8H), 2.42-2.37 (qui, J= 6.7 Hz, 2H), 1.13-1.09 (t, J= 7.1 Hz, 12H), 0.90-0.89 (d, J= 6.6 Hz, 6H), 0.44-0.43 (d, J= 6.6 Hz, 6H); <sup>13</sup>C NMR (100 MHz, CDCl<sub>3</sub>) 167.3, 156.5, 149.4, 148.9, 148.7, 133.2, 132.0, 129.5, 128.8, 128.5, 125.0, 123.7, 123.1, 108.9, 107.5, 98.4, 69.9, 44.4, 29.7, 26.7, 21.8, 12.6

**Synthesis of 2,6-Diethoxynitrobenzene:** Using the synthesis developed by Carrol et al<sup>29</sup>, made a threefold reaction by dissolving 1.5252 2-nitroresorcinol into 30 mL of dimethylformamide (DMF) in a 100 mL round bottom. Added 2.7246 g of potassium carbonate, anhydrous. Placed under argon gas at room temperature with a needle to vent as started stirring. Dropwise addition of 1.7 mL ethyl iodine over the course of five minutes. Stirred for twenty-four hours before adding cold de-ionized water to the round bottom until the round bottom was full. A white/tan foam began appearing in the solution. Filtered using a Buchner funnel. The liquid was brown with white powder collecting in the funnel. Washed with cold water until there was approximately 175 mL in the filter flask. Let sit with vacuum for thirty minutes after the last drop of clear liquid into the filter flask. Massed into a clean glass vial by scooping powder in with a spatula. Percent yield was 96.18%.

**Synthesis of 2,6-Diethoxyaniline:** Once again using the Carrol paper as the basis for the synthesis, massed out 0.3 g of 2,6-diethoxynitrobenzene into a small 50 mL round bottom.

Added 10 mL of de-ionized water and stirred while adding 0.42 mL acetic acid. Then massed out 0.83 g purified iron and added. [The iron was purified using the process given in Purification of Laboratory Chemicals.<sup>30</sup> This process consisted of cleaning iron powder in 6M HCl using Buchner filtration before rinsing in a lot of de-ionized water. The last rinse was done with acetone and the powder was left to dry for an hour. Removed the powder than had turned orange and placed the grey/green powder in a glass vial.] Heated to reflux for one and a half hours at 68°C. Took off reflux and added 20 mL saturated NaHCO<sub>3</sub>. Then extracted three times with 30 mL ethyl acetate. Top layer was yellow and clear while the bottom layer was dark. This top layer was concentrated *in vacuo* to form black oil with an almost blue-grey sheen to it. Dried overnight. Percent yield of 56.2%.

**Synthesis of RB-DEA:** Massed out 0.2377 g RB and dissolved in 5 mL DCE. Added 0.3 mL POCl<sub>3</sub> dropwise over two minutes while swirling. Dissolved 0.265 g DEA in 4 mL DCE. Added dropwise over five minutes. Refluxed for twenty-five hours and fifty minutes. Added 30 mL chloroform and washed three times with 2M HCl, three times with 2M NaOH, and twice with brine. Added magnesium sulfate and filtered before concentrating *in vacuo* to get a purple oil. Ran column in 60:40 EtOAc:Hexanes. First band was product. Formed a tan solid. Percent yield was 28.61%. <sup>1</sup>H NMR (400MHz, CDCl<sub>3</sub>) 8.05-8.02 (m, 1H), 7.58-7.55 (m, J= 5.1, 1.15 Hz, 2H), 7.29-7.27 (m, 1H), 7.05-7.01 (t, J= 8.4 Hz, 1H), 6.59-6.57 (d, J= 9 Hz, 2H), 6.26-6.22 (m, J= 8.6, 2.7 Hz, 4H), 6.19-6.18 (d, J= 2.8 Hz, 2H), 3.68-3.61 (m, J= 7.0, 2.3 Hz, 4H), 3.33-3.26 (m, 8H), 1.13-1.10 (t, J= 7.0 Hz, 12H), 1.04-1.01 (t, J= 6.9 Hz, 6H); <sup>13</sup>C NMR (100 MHz, CDCl<sub>3</sub>) 167.2, 157.5, 154.8, 151.2, 148.2, 130.8, 130.7, 129.3, 128.0, 124.5, 123.3, 108.7, 106.8, 105.2, 103.9, 97.4, 65.2, 63.1, 44.4, 14.5, 14.4, 12.6. Exact mass calculated for C<sub>38</sub>H<sub>43</sub>N<sub>3</sub>O<sub>4</sub>H<sup>+</sup>, 606.332633 m/z. Found 606.332228 m/z.

**Synthesis of R6G-acid:** Massed out 1.022 g of R6G and 1.970 g of NaOH. Added 10 mL EtOH (absolute) and 20 mL DIH<sub>2</sub>O. Hooked up to condenser and heated to 90°C with an oil bath. Refluxed for twenty hours and fifty minutes. Left to stir for two days. Added 10 mL 6M HCl slowly before placing in an ice bath to cool. Buchner filtered and left to sit in hood for an hour and a half before transferring to a glass vial using a spatula. Very wet, oily red product. Percent yield was 39.82%.

**Synthesis of R6G-A:** Got a 100 mL round bottom and added ~4 scoops molecular sieves to it. Covered top with rubber stopper after adding a stir bar. Added needle to vent. Flame dried for approximately 3 minutes while hooked up to argon gas. The heat from the flame activates the molecular sieves. Left to cool as massed out 0.2003 g R6G-acid (prepared by Grace T.) into a small Erlenmeyer. Crushed the R6G-acid with a spatula and added 20 mL anhydrous 1,2-dichloroethane before sonicating. Added 10 mL of anhydrous 1,2-dichloroethane to the round bottom while stirring before adding the 20 mL from the Erlenmeyer. Added another 20 mL of 1,2-dichloroethane to the Erlenmeyer, once again crushing the R6G-acid and sonicating. Added to the round bottom. Crushed the remaining R6G-acid as much as possible, then added 10 mL 1,2-dichloroethane and sonicated. Added to round bottom. Left the mixture in the round bottom to stir overnight under argon. After approximately 24 hours placed the solution in an ice bath. While still stirring and under argon, added 0.3 mL aniline and left to stir for 30 minutes. After 30 minutes, added 0.05 ml POCl<sub>3</sub> dropwise. Product almost instantly formed as tested by TLC plates. Left mixture to stir overnight under argon in the ice bath. Mixture went from bubblegum pink to orangish with the addition of POCl<sub>3</sub>. The next day, removed the melted ice bath and left to stir for another 24 hours. Removed from stir plate and shut off argon gas before setting up a Buchner filtration. Washed with 1,2-dichloroethane (not dry) until liquid dripping into flask was

clear. Transferred the liquid to a large (500 mL) separatory funnel. Rinsed the flask with 1,2-dichloroethane and continued transferring to the separatory funnel until the liquid in the flask was clear. Added 50 mL of chilled 2 M NaOH to the sep funnel and gently swirled while occasionally venting. Then took the bottom layer and discarded the top layer. Repeated three times. The mixture turned more orange in color with each wash. Started peach color and turned light orange. Then added 50 mL of brine to the sep funnel and gently swirled. Once again collected the bottom layer and repeated. Added several heaping scoops of anhydrous sodium sulfate to the product solution to dry. Did another Bunchner filtration, scooping the wet sodium sulfate onto the filter and rinsing with chloroform. Transferred to a large (500 mL) round bottom. Concentrated *in vacuo* to form red, oily ring on round bottom. Started column at 40:60 EtOAc:Hexane and graduated to 90:10 EtOAc:Hexanes. Product was orangey-brown powder. Percent yield was 5.12%. <sup>1</sup>H NMR (400MHz, CDCl<sub>3</sub>) 8.04-8.02 (dd, J= 5.5, 2.6 Hz, 1H), 7.52-7.48 (dt, J= 8.6, 3.6 Hz, 2H), 7.12-7.06 (m, 4H), 6.77-6.74 (dd, J= 7.8, 2.0 Hz, 2H), 6.44 (s, 2H), 6.22 (s, 2H), 3.18-3.13 (q, J= 7.1 Hz, 4H), 1.93 (s, 6H), 1.32-1.28 (t, J= 7.1 Hz, 6H), 1.25 (s, 3H); <sup>13</sup>C NMR (100 MHz, CDCl<sub>3</sub>) 167.7, 153.3, 151.5, 147.3, 136.6, 132.9, 131.0, 128.6, 128.5, 128.1, 127.2, 126.6, 124.0, 123.4, 117.8, 106.9, 96.6, 67.5, 38.3, 29.7, 16.8, 14.7. Exact mass calculated for C<sub>32</sub>H<sub>31</sub>N<sub>3</sub>O<sub>2</sub>H<sup>+</sup>, 490.248904 m/z. Found 490.248945 m/z.

**Synthesis of R6G-DEA:** Added 4 scoops of molecular sieves and stir bar to 100 mL round bottom before stopping with a rubber stopper and needle to vent. Flame dried under argon gas. While cooling, massed out a little over 0.2 g R6G-acid into a small Erlenmeyer. Added 20 mL dichloroethane (DCE) and sonicated. Added 10 mL DCE to round bottom under argon. Starting stirring as added the 20 mL from the Erlenmeyer. Added another 20 mL DCE to Erlenmeyer, sonicated, and added to round bottom. Added 10 mL DCE to Erlenmeyer, sonicated, and added

to round bottom. Left mixture to stir overnight under argon. The next day, stuck the mixture in an ice bath while dissolved 0.27 g DEA in 5 mL DCE anhydrous. Added to the round bottom and after thirty minutes added 0.05 mL POCl<sub>3</sub> dropwise. Left to stir for four days while monitoring with TLC but the TLCs didn't change much. Turned off argon and set up Buchner filtration, washing with DCE. Worked up using four washes of 2 M NaOH and two washes of brine. Added several scoops of sodium sulfate anhydrous and did another Buchner filtration. Concentrated *in vacuo* to get a red oil. Ran a column in 30:70 EtOAc:Hexanes. Ran a second column in 10:90 EtOAc:Hexanes with a gradient to 40:60 EtOAc:Hexanes. Ran a third column in 10:90 EtOAc:Hexanes with gradient to 30:70 EtOAc:Hexanes. Ran a fourth column in 10:90 EtOAc:Hexanes to get product. Percent yield was 9.65%. <sup>1</sup>H NMR (400MHz, CDCl<sub>3</sub>) 8.07-8.05 (m, 1H), 7.60-7.56 (m, J= 3.6 Hz, 2H), 7.25-7.21 (m, 1H), 7.04-7.00 (t, J=8.4 Hz, 1H), 6.39 (s, 2H), 6.25-6.23 (d, J= 8.7 Hz, 2H), 6.17 (s, 2H), 3.65-4.59 (m, J= 9.2, 2.4 Hz, 2H), 3.39-3.29 (m, J= 9.4, 2.3 Hz, 2H), 3.17-3.12 (m, J= 7.1, 2.8 Hz, 4H), 1.92 (s, 6H), 1.30-1.26 (t, J= 7.1 Hz, 6H), 0.98-0.950 (t, J= 6.9 Hz, 6H); <sup>13</sup>C NMR (100 MHz, CDCl<sub>3</sub>) 167.3, 157.5, 153.3, 151.8, 146.8, 133.4, 132.0, 130.7, 129.1, 128.0, 124.6, 123.2, 115.9, 109.1, 104.4, 96.2, 68.4, 63.4, 38.4, 29.7, 16.9, 14.8, 14.2. Exact mass calculated for C<sub>36</sub>H<sub>39</sub>N<sub>3</sub>O<sub>4</sub>H<sup>+</sup>, 578.301333 m/z. Found 578.301291 m/z.

**Synthesis of R6G-DIA:** Added 4 scoops of molecular sieves and stir bar to round bottom before stopping with a rubber stopper and needle to vent. Flame dried under argon gas for four minutes. Massed out 0.2067 g R6G-acid to which was added 20 mL of anhydrous DCE. Mixture was sonicated and 10 mL anhydrous DCE was added to round bottom. Added the 20 mL from the R6G-acid mixture than added 20 mL anhydrous DCE to the R6G-acid and sonicated again. Added to round bottom. Added 10 mL anhydrous DCE to R6G-acid, sonicated, and added to



round bottom. Left mixture to stir for twenty-four hours under argon gas. Placed in an ice bath and added 0.3 mL DIA. Allowed to stir under argon for thirty minutes before adding 0.05 mL POCl<sub>3</sub> dropwise. Left to stir for forty-five hours, removing the ice bath once it had melted. Buchner filtered then washed with 2 M NaOH three times and brine once. Added anhydrous sodium sulfate and did another Buchner filtration. Concentrated *in vacuo*. Ran column in 40:60 EtOAc:Hexanes to 90:10 EtOAc:Hexanes. Ran a second column with 40:60 EtOAc:Hexanes. Concentrated *in vacuo* to get white powder. Percent yield was 17.99%. <sup>1</sup>H NMR (400MHz, CDCl<sub>3</sub>) 8.10-8.07 (m, 1H), 7.65-7.62 (m, J= 3.5 Hz, 2H), 7.25-7.24 (m, 1H), 7.22-7.18 (t, J= 7.9 Hz, 1H), 6.96-6.94 (d, J= 7.8 Hz, 2H), 6.33 (s, 2H), 6.17 (s, 2H), 3.46 (s, 2H), 3.15-3.10 (q, J= 6.8 Hz, 4H), 2.42-2.35 (qui, J= 6.6 Hz, 2H), 1.93 (s, 6H), 1.28-1.24 (t, J= 7.1 Hz, 6H), 0.89-0.87 (d, J= 6.6 Hz, 6H), 0.37-0.35 (d, J= 6.7 Hz, 6H); <sup>13</sup>C NMR (100 MHz, CDCl<sub>3</sub>) 167.3, 154.9, 150.0, 149.5, 147.3, 133.0, 132.1, 129.6, 128.8, 128.5, 125.0, 123.6, 123.0, 117.2, 109.0, 97.1, 50.9, 38.3, 29.8, 26.8, 21.3, 16.8, 14.7. Exact mass calculated for C<sub>36</sub>H<sub>39</sub>N<sub>3</sub>O<sub>4</sub>H<sup>+</sup>, 574.342804 m/z. Found 574.342140 m/z.

**Synthesis of RB-o-toluidine (aka RB-2MA):** Massed out 0.2056 g RB into a 50 mL round bottom. Added 7 mL 2,6-dichloroethane (DCE) to dissolve before adding 0.3 mL POCl<sub>3</sub> dropwise over two minutes. Added 0.15 mL o-toluidine dropwise over one minute. Refluxed for forty-nine hours and ten minutes. Added 30 mL chloroform and washed with 2x 2M HCl, 3x 2M NaOH, and 2x brine. Added anhydrous magnesium sulfate and filtered before concentrating *in vacuo* to get a pinkish-purple sludge which was waxy in consistency. Ran column in 30:70 EtOAc:Hexanes to get product in the second band. Percent yield is 40.84%. <sup>1</sup>H NMR (400 MHz, CDCl<sub>3</sub>) 8.06-8.04 (m, 1H), 7.62-7.55 (m, 2H), 7.32-7.29 (m, 1H), 7.10-7.02 (m, 2H), 6.87-6.83 (td, J= 7.45, 1.55 Hz, 1H), 6.62-6.59 (dd, J= 8.8, 2.4 Hz, 2H), 6.40-6.38 (dd, J= 8.8, 2.5 Hz, 1H),

6.28-6.25 (dd, J= 9.0, 2.7 Hz, 2H), 6.17-6.16 (sd, J= 2.7 Hz, 1H), 6.06-6.04 (dd, J= 7.8, 1.2 Hz, 1H), 3.40-3.26 (m, 8H), 1.26-1.16 (t, J= 7.05 Hz, 6H), 1.14-1.10 (t, J= 7.05 Hz, 6H);  $^{13}\text{C}$  NMR (100 MHz,  $\text{CDCl}_3$ ) 165.9, 154.7, 154.0, 151.4, 149.0, 148.2, 138.1, 134.3, 132.8, 132.5, 130.5, 130.5, 129.7, 128.9, 128.6, 128.4, 128.4, 127.8, 127.8, 125.6, 125.6, 124.4, 123.4, 123.4, 108.2, 107.9, 107.4, 106.7, 98.0, 97.8, 97.8, 68.1, 44.5, 44.4, 44.3, 18.4, 18.4, 12.5, 12.5. Exact mass calculated for  $\text{C}_{35}\text{H}_{37}\text{N}_3\text{O}_2\text{H}^+$ , 532.295854 m/z. Found 532.295977 m/z.

**RB-DCNA:** Synthesized by William Czaplyski and previously reported<sup>13</sup>.

**RB-3,5CA:** Synthesized by Grace Purnell.

**RB-DCA:** Synthesized by Grace Purnell using the procedure outlined in the synthesis chapter.

$^1\text{H}$  NMR (400 MHz,  $\text{CDCl}_3$ ) 8.08-8.07 (d, J= 6.6 Hz, 1H), 7.70-7.60 (td, J= 7.5, 1.4, 1.2 Hz, 2H), 7.41-7.39 (d, J= 7.4 Hz, 1H), 7.14-7.05 (m, 3H), 6.61-6.59 (d, J= 8.6 Hz, 2H), 6.29-6.26 (dd, J= 9.0, 2.7 Hz, 2H), 6.23 (d, J= 2.4 Hz, 2H), 3.34-3.29 (q, J= 7.1 Hz, 8H), 1.14-1.11 (t, J= 7.1 Hz, 12H);  $^{13}\text{C}$  NMR (100 MHz,  $\text{CDCl}_3$ ) 166.2, 155.5, 149.6, 149.1, 137.3, 132.7, 132.6, 131.6, 130.6, 129.6, 128.6, 128.3, 124.9, 123.9, 108.1, 107.6, 98.1, 70.2, 44.5, 12.4

**RB-DFA:** Synthesized by Grace Purnell using the procedure outlined in the synthesis chapter.

$^1\text{H}$  NMR (400MHz,  $\text{CDCl}_3$ ) 8.04-8.01 (m, 1H), 7.60-7.53 (m, J= 7.4, 1.6, 1.2 Hz, 2H), 7.25-7.24 (d, J= 1.6 Hz, 1H), 7.15-7.08 (tt, J= 8.5, 5.9 Hz, 1H), 6.71-6.67 (t, 8.5 Hz, 2H), 6.65-6.62 (dd, J= 8.8, 1.7 Hz, 2H), 6.32-6.29 (dd, J= 9.0, 2.7 Hz, 2H), 6.21 (d, J= 2.3 Hz, 2H), 3.34-3.28 (qd, J= 7.0, 2.3 Hz, 8H), 1.15-1.12 (t, J= 7.0 Hz, 12 H);  $^{13}\text{C}$  NMR (100 MHz,  $\text{CDCl}_3$ ) 167.3, 153.7, 152.6, 148.8, 133.0, 131.3, 130.2, 130.1, 129.7, 128.4, 124.6, 123.4, 111.8, 111.5, 107.8, 106.0, 97.4, 68.5, 44.4, 12.5

**R6G-DCA:** Synthesized by Grace Taumoefolau using the procedure outlined in the synthesis chapter<sup>19</sup>. Percent yield 10-15%.  $^1\text{H}$  NMR (400MHz,  $\text{CDCl}_3$ ) 8.10-8.08 (dd, J= 6.3, 1.2 Hz, 1H),

7.70-7.62 (m, J= 7.4, 1.6 Hz, 2H), 7.35-7.33 (dd, J= 6.5, 1.0 Hz, 1H), 7.12-7.02 (m, 3H), 6.40 (s, 2H), 6.19 (s, 2H), 3.39-3.11 (m, 4H), 1.92 (s, 6H), 1.31-1.27 (t, J= 7.3, 6H);  $^{13}\text{C}$  NMR (100 MHz,  $\text{CDCl}_3$ ) 166.3, 153.9, 150.1, 147.6, 137.1, 132.8, 132.5, 130.8, 129.5, 128.6, 128.4, 124.9, 123.9, 116.8, 108.2, 96.5, 70.3, 38.4, 16.7, 14.7. Exact mass calculated for  $\text{C}_{32}\text{H}_{29}\text{Cl}_2\text{N}_3\text{O}_2\text{H}^+$ , 580.152904 m/z. Found 580.152346 m/z.

**R6G-DFA:** Synthesized by Grace Taumoefolau using the procedure outlined in the synthesis chapter<sup>19</sup>. Percent yield was 5%.  $^1\text{H}$  NMR (400MHz,  $\text{CDCl}_3$ ) 8.06-8.04 (m, 1H), 7.60-7.55 (m, J= 5.1, 1.3 Hz, 2H), 7.21-7.19 (m, 1H), 7.12-7.08 (m, J= 8.4, 2.3 Hz, 1H), 6.69-6.65 (t, J= 8.9 Hz, 2H), 6.45 (d, J= 1.2 Hz, 2H), 6.18 (s, 2H), 3.48 (s, 2H), 3.18-3.13 (q, J= 7.1 Hz, 4H), 1.94 (s, 6H), 1.31-1.28 (t, J= 7.0 Hz, 6H);  $^{13}\text{C}$  NMR (100 MHz,  $\text{CDCl}_3$ ) 167.4, 161.6, 159.0, 159.0, 152.9, 152.1, 147.4, 133.1, 130.0/ 130.0, 129.7/ 129.6/ 129.5, 128.4, 124.5, 123.4, 117.25, 111.8/111.6/111.5, 106.4, 96.0, 68.6, 38.3, 16.7, 14.7. Exact mass calculated for  $\text{C}_{32}\text{H}_{29}\text{F}_2\text{N}_3\text{O}_2\text{H}^+$ , 526.230060 m/z. Found 526.229075 m/z.

**R6G-DMA:** Synthesized by Grace Taumoefolau using the procedure outlined in the synthesis chapter.<sup>19</sup> Percent yield was 5%.  $^1\text{H}$  NMR (400MHz,  $\text{CDCl}_3$ ) 8.10-8.08 (m, 1H), 7.69-7.64 (m, J= 6.6, 1.2 Hz, 2H), 7.38-7.36 (dd, J= 6.1, 1.8 Hz, 1H), 7.03-7.00 (t, J= 7.5 Hz, 1H), 6.81-6.79 (d, J= 7.5 Hz, 2H), 6.35 (s, 2H), 6.19 (s, 2H), 3.46 (s, 2H), 3.18-3.12 (m, J= 7.9 Hz, 4H), 1.93 (s, 6H), 1.32 (s, 6H), 1.31-1.27 (t, J= 7.1 Hz, 6H);  $^{13}\text{C}$  NMR (100 MHz,  $\text{CDCl}_3$ ) 166.0, 154.3, 149.1, 147.5, 138.9, 133.5, 132.2, 129.6, 128.7, 127.9, 127.8, 124.9, 123.8, 116.8, 109.2, 96.9, 69.5, 38.4, 18.3, 16.8, 14.6. Exact mass calculated for  $\text{C}_{36}\text{H}_{39}\text{N}_3\text{O}_2\text{H}^+$ , 546.311504 m/z. Found 546.310670 m/z.

**Drying Chloroform:** Due to the continued presence of contaminants in the  $\text{CDCl}_3$ , a new procedure was developed to purify the solvent. The stock solution (100 mL, Sigma-Aldrich) was

sealed with Parafilm and stored in the fridge. A pipet was used as a column, stuffed with glass wool then filled with anhydrous magnesium sulfate ( $\text{MgSO}_4$ , Sigma-Aldrich) and potassium carbonate ( $\text{K}_2\text{CO}_3$ , Sigma-Aldrich). The potassium carbonate was used to interact with the hydrochloric acid (HCl) byproducts formed by the  $\text{CDCl}_3$  with the anhydrous magnesium sulfate removing the water produced by the acid-base reaction. Approximately six milliliters of the stock  $\text{CDCl}_3$  was run through this column into a small, dark vial filled halfway with molecular sieves. This vial was then sealed with Parafilm and covered with foil before being placed in a desiccator at room temperature for storage. The stock solution:  $^1\text{H}$  NMR (400MHz,  $\text{CDCl}_3$ ) 7.23 (s), 3.47-3.46 (d,  $J=4.3$  Hz), 2.16 (s), 1.82 (s), 1.33 (s). The purified  $\text{CDCl}_3$ :  $^1\text{H}$  NMR (400MHz,  $\text{CDCl}_3$ ) 7.52 (s), 7.26 (s), 6.99 (s), 3.50 (br s), 1.54 (s). Only the chloroform and water peaks were of any significant height within the purified  $\text{CDCl}_3$  which was an improvement upon the chloroform and four additional peaks in the stock solution. However, the chloroform to water ratio was approximately equal (1:0.16) in both solutions. This amount of water was acceptable for NMR usage as it would be drowned out by dry compounds dissolved in the  $\text{CDCl}_3$ .

## Acknowledgements

Chiefly, I wish to thank Dr. Elizabeth Harbron, who has been my PI since freshman year. She has funded me through several summers of research and I've grown a lot as a chemist under her tutelage. While she has encouraged me to think independently about various problems I've encountered throughout the course of my project, she was always there to answer any questions I had, no matter how silly they seemed to me. My years as a member of her research group have only solidified my love of laboratory work and I feel that they were instrumental in providing me with the confidence I needed to know where I want my future path to lead.

I would also like to thank my fellow members of Harbron lab. While everyone in lab has been supportive and extremely helpful in guiding me as my project shifted into the world of nanoparticles, I would in particular like to thank Mona Rasooly, Matthew McCarron, Grace Tamoefolau, and Grace Purnell. Grace Purnell mentored me when I first entered lab, teaching me all the basics I needed to know. After she left lab, Grace Tamoefolau took over and helped me figure out any difficulties I had regarding synthesis, purification, and NMR interpretation. They've both made the majority of the di-*ortho* compounds I tested for RB and R6G and Grace Tamoefolau spent a lot of time improving upon the R6G synthesis technique so that by the time I started making R6G compounds the process was fairly straight forward. Matthew McCarron assisted me when I began making nanoparticles by patiently teaching me a new process I with which I was unfamiliar. Mona Rasooly, my own mentee, has proved a stalwart member of this project and the mono-*ortho* series would not be complete without her efforts. Though I've never met him, William Czaplyski mentored my mentor and has been the foundation of the rhodamine project. Our work would not be what it is today without him. Harbron lab has always been a tight knit group and the fun I've had with them will never be forgotten.

I would also like to thank the other members of my committee, Dr. Robert Hinkle, Dr. John Poutsma, and Dr. John Conlee, as well as the rest of the Chemistry Department. I've always been able to find someone to assist me with a question as my project has expanded into areas in which the rest of Harbron lab does not specialize in. I would especially like to thank Dr. Robert Pike for his assistance with x-ray crystallography and tips for growing better crystals. Dr. Robert Hinkle has also been essential with aiding me in my struggles to synthesize and purify my compounds as well as helping me get publication worthy NMRs.

Last but not least, I would like to thank my friends and family. My parents and sister have been especially supportive. My sister, Debbie Stratton, helped with proofreading. My dad, Jim Stratton, helped me organize my graphs. Though none of them understand the intricacies of my research they are always willing to listen to me talk about it. My mom, Dr. Leslie Stratton, has helped me understand the deeper statistical side of my research and has spent hours of her time discussing regressions with me. Their support has meant the world to me and their confidence in me has encouraged me to try things I would never have dared attempt otherwise. Thank you all.

## References

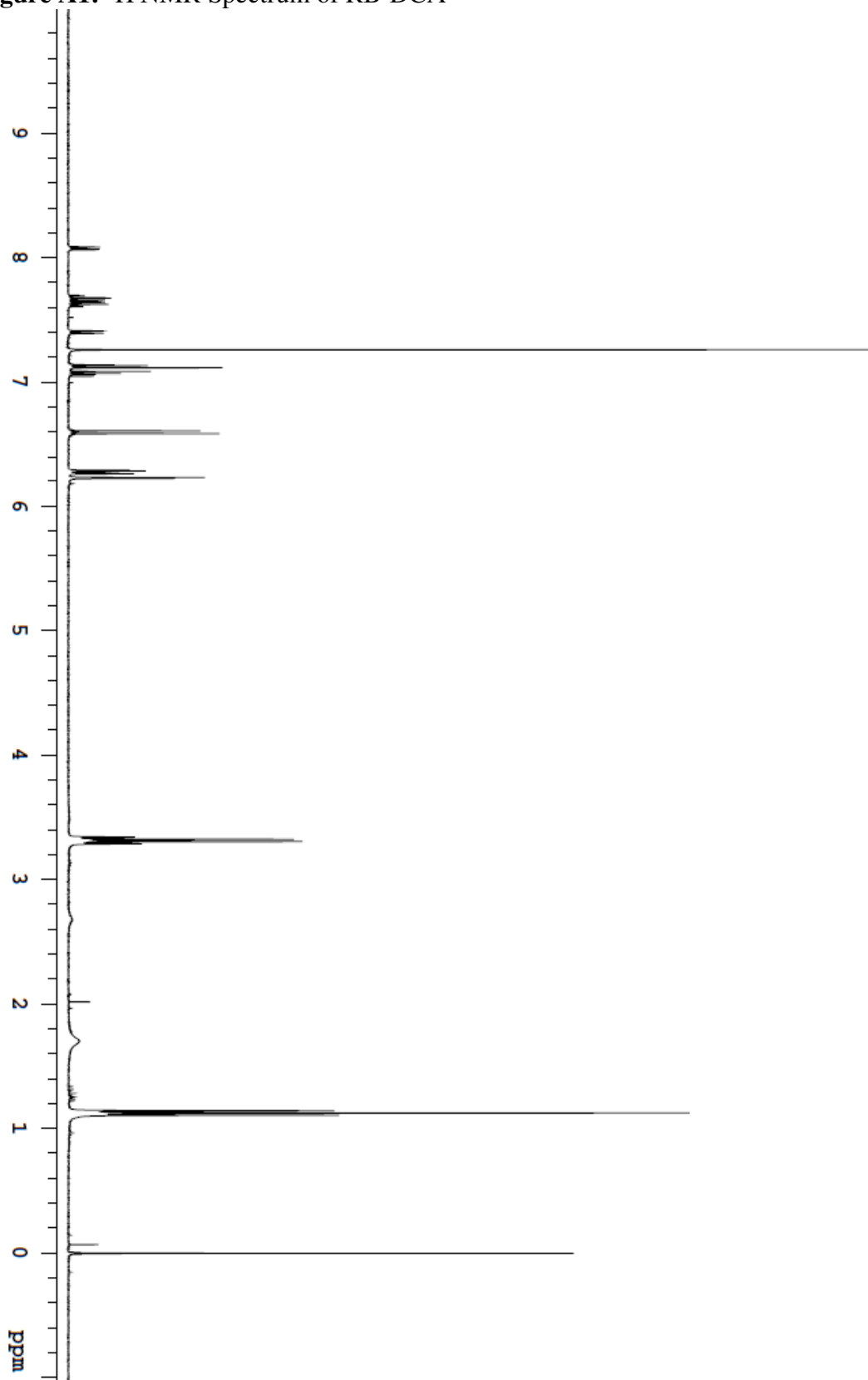
1. Yu, K.-K. *et al.* A Single Design Strategy for Dual Sensitive PH Probe with a Suitable Range to Map PH in Living Cells. *Sci. Rep. Scientific Reports*. **2015**, 5, 15540. doi: 10.1038/srep15540
2. Wolfe, D. M. *et al.* Autophagy Failure in Alzheimer's Disease and the Role of Defective Lysosomal Acidification. *European Journal of Neuroscience Eur J Neurosci*. **2013**, 37, 1949–1961. doi: 10.1111/ejn.12169
3. Esteves, R. A.; Oliveira, C. R.; and Cardoso, S. M. (2013). Autophagy, the “Master” Regulator of Cellular Quality Control: What Happens when Autophagy Fails?, Authophagy- A Double-Edged Sword- Cell Survival or Death?, Dr. Yannick Bailly (Ed.), InTech, doi: 10.5772/55196
4. Tung, C.-H.; Qi, J.; Hu, L.; Han, M. S.; and Kim, Y. A Quick Responsive Fluorogenic pH Probe for Ovarian Tumor Imaging. *Theranostics*. **2015**, 5(10), 1166-1174. doi: 10.7150/thno.12813
5. Khan, M. A.; Misra, A.; Trivedi, A.; Srivastava, AN. Effect Of Alkalinity on Cancerous Cells at Different PH and Morphological Variations In-Vitro. *International Journal of Bioassays*. **2014**, 3(09), 3297–3302.
6. Liu, L. *et al.* Fluorescent And Colorimetric Detection of PH by a Rhodamine-Based Probe. *Sensors and Actuators B: Chemical*. **2014**, 194, 498–502. doi: 10.1016/j.snb.2013.12.023
7. *Fluorescence-Based Biosensors: from Concepts to Applications*; Morris, M. C., Ed.; Elsevier/Academic Press: Amsterdam, 2013; Vol. 113.
8. Chen, X., Pradhan, T., Wang, F., Kim, J. S., and Yoon, J. Development of Reversible Fluorescence Probes Based on Redox Oxoammonium Cation for Hypobromous Acid Detection in Living Cells. *Chem. Rev*. **2012**, 112, 1910.
9. Urano, Y. *et al.* Selective Molecular Imaging of Viable Cancer Cells with pH-Activatable Fluorescence Probes. *Nat. Med*. **2009**, 15(1), 104-109. doi: 10.1038/nm.1854
10. Liu, J. and Zhu, X. Ionic Liquid-immobilized Silica Solid Phase Extraction Coupled with High Performance Liquid Chromatography for the Analysis Rhodamine B. *Open Science Journal of Analytical Chemistry*. **2014**, 1(2), 10-16.
11. Lakowicz, J. R. *Principles Of Fluorescence Spectroscopy*; 2nd ed.; Springer Science Business Media, LLC: Boston, MA, 2006.
12. Yuan, L.; Lin, W.; Feng, Y. A Rational Approach to Tuning the PKa Values of Rhodamines for Living Cell Fluorescence Imaging. *Organic & Biomolecular Chemistry Org. Biomol. Chem*. 2011, 9, 1723–1726. doi: 10.1039/c0ob01045f

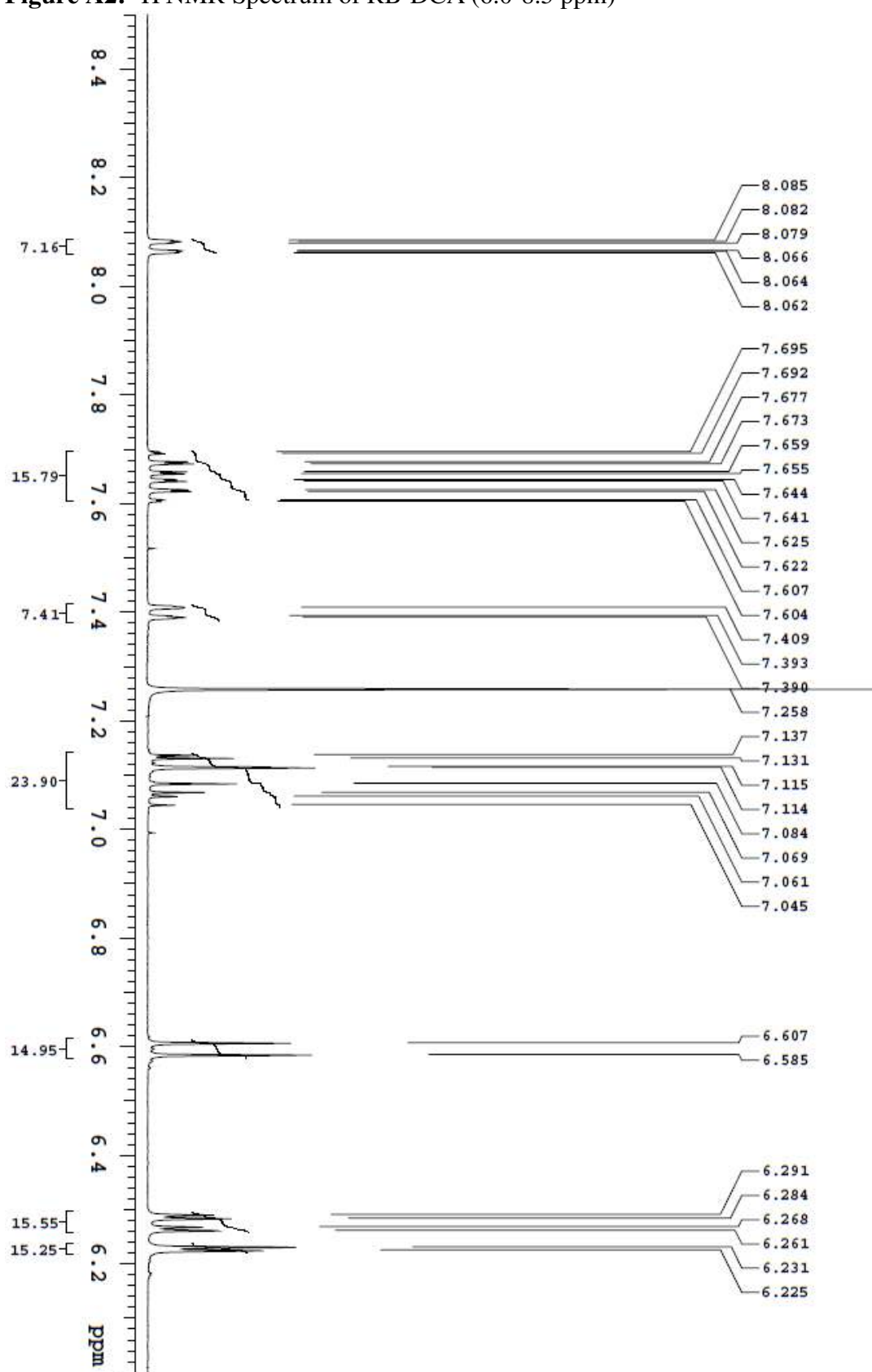
13. Czaplyski, W. L.; Purnell, G. E.; Roberts, C. A.; Allred, R. M.; Harbron, E. J. Substituent Effects on the Turn-on Kinetics of Rhodamine-Based Fluorescent PH Probes. *Org. Biomol. Chem.* **2014**, *12*, 526–533. doi: 10.1039/c3ob42089b
14. Li, H. *et al.* An Acid Catalyzed Reversible Ring-Opening/Ring-Closure Reaction Involving a Cyano-Rhodamine Spirolactam. *Org. Biomol. Chem.* **2013**, *11*, 1805–1809. doi: 10.1039/c3ob27356c
15. Kubin, R. F. and Fletcher, A. N. Fluorescence Quantum Yields of Some Rhodamine Dyes. *Journal of Luminescence.* **1982**, *27(4)*, 455-462. doi: 10.1016/0022-2313(82)90045-X
16. Feng, L.; Zhu, C.; Yuan, H.; Liu, L.; Lv, F.; and Wang, S. Conjugated Polymer Nanoparticles: Preparation, Properties, Functionalization, and Biological Applications. *Chem. Soc. Rev.* **2013**, *42*, 6620-6633. doi: 10.1039/c3cs60036j
17. Yang, L. *et al.* Single Chain Epidermal Growth Factor Receptor Antibody Conjugated Nanoparticles for in vivo Tumor Targeting and Imaging. *Small.* **2009**, *5(2)*, 235-243. doi: 10.1002/sml.200800714
18. Best, Q. A.; Liu, C.; van Hoveln, P. D.; McCarroll, M. E.; and Scott, C. N. AnilinoMethylRhodamines: pH Sensitive Probes with Tunable Photophysical Properties by Substituent Effect. *J. Org. Chem.* **2013**, *78(20)*, 10134-10143. doi: 10.1021/jo401323g
19. Taumoefolau, G. H. Synthesis and Characterization of pH-Sensitive Rhodamine 6G Spirolactam Structures. *Undergraduate Honors Theses.* **2015**, Paper 220. <http://publish.wm.edu/honorstheses/220>
20. Muller, P. Glossary of Terms Used in Physical Organic Chemistry. *Pure and Appl. Chem.* **1994**, *66(5)*, 1077–1184.
21. Smith, M. B. and March, J. March's Advanced Organic Chemistry: Reactions, Mechanisms, and Structure. *John Wiley & Sons.* **2007**.
22. Fujita, T. and Nishioka, T. The Analysis of the Ortho Effect. *Prog. Phys. Org. Chem.* **1976**, *12*, 49-89.
23. Bott, G.; Field, L. D.; and Sternhell, S. Steric Effects. A Study of a Rationally Designed System. *J. Am. Chem. Soc.* **1980**, *102*, 5618-5626.
24. Tribble, M. T. and Traynham, J. G. Nuclear Magnetic Resonance Studies of *ortho* Substituted Phenols in Dimethyl Sulfoxide Solutions. Electronic Effects of *ortho* Substituents. *Journal of the American Chemical Society.* **1969**, *91(1)*, 379-388.
25. Charton, M. The Application of the Hammett Equation to Ortho-Substituted Benzene Reaction Series. *Can. J. Chem.* **1960**, *38*, 2493-2499.



26. Bijloo, G. J. and Rekker, R. F. Some Critical Remarks Concerning the Inductive Parameter  $\sigma_1$  Part IV: Parametrization of the Ortho Effect in Anilines and Pyridines. *Quant. Struct. Act. Relat.* **1984**, *3*, 111-115.
27. D'Anna, F.; Ferroni, F.; Frenna, V.; Guernelli, S.; Lanza, C. Z.; Macaluso, G.; Pace, V.; Petrillo, G.; and Spinelli, D. On the Application of the Extended Fujita-Nishioka Equation to Polysubstituted Systems. A Kinetic Study of the Rearrangement of Several Poly-substituted Z-arylhydrazones of 3-benzoyl-5-phenyl-1, 2, 4-oxadiazole into 2-aryl 4-benzoylamino-5-phenyl-1,2,3-triazoles in Dioxane/water. *Tetrahedron.* **2005**, *61(1)*, 167-178. doi: 10.1016/j.tet.2004.10.054
28. Deng, W.-J.; Sun, D.; Su, B.-Y.; Wang, S.-P.; and Zheng, H. CCDC 729554: Experimental Crystal Structure Determination. *Acta Crystallogr. Sect. E: Struct. Rep. Online.* **2009**, *65*, o1464. doi: 10.1107/S1600536809020248
29. Carrol, W. R. *et al.* A torsional molecular balance for measuring aliphatic CH- $\pi$  interactions. *Org. Lett.* **2011**, *13(16)*, 4320-4323.
30. *Purification of Laboratory Chemicals*; Armarego, W. L. F. and Chai, C. L. L. 2009. Retrieved through EBSCOHost

## Appendix A

Figure A1:  $^1\text{H}$  NMR Spectrum of RB-DCA

**Figure A2:**  $^1\text{H}$  NMR Spectrum of RB-DCA (6.0-8.5 ppm)

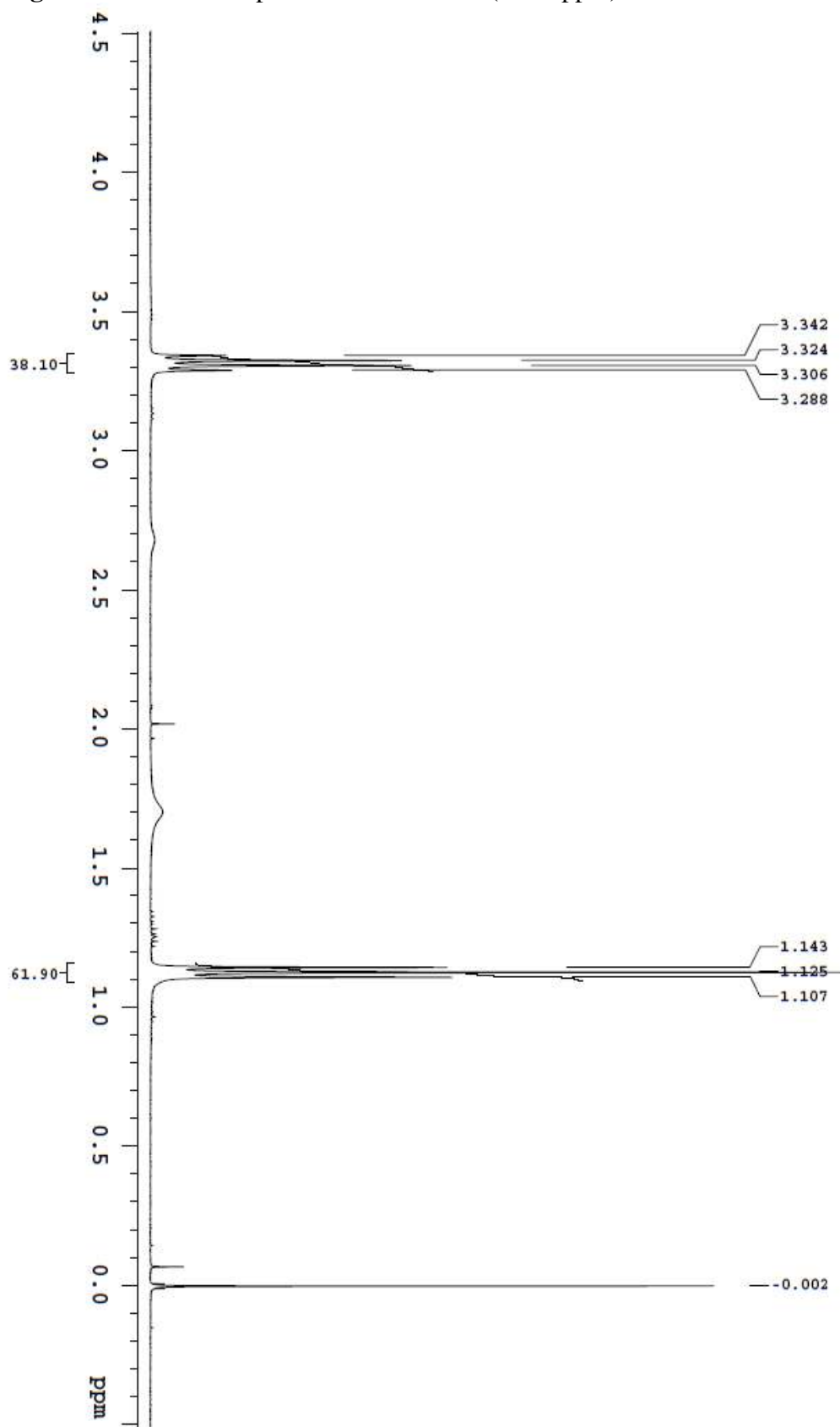
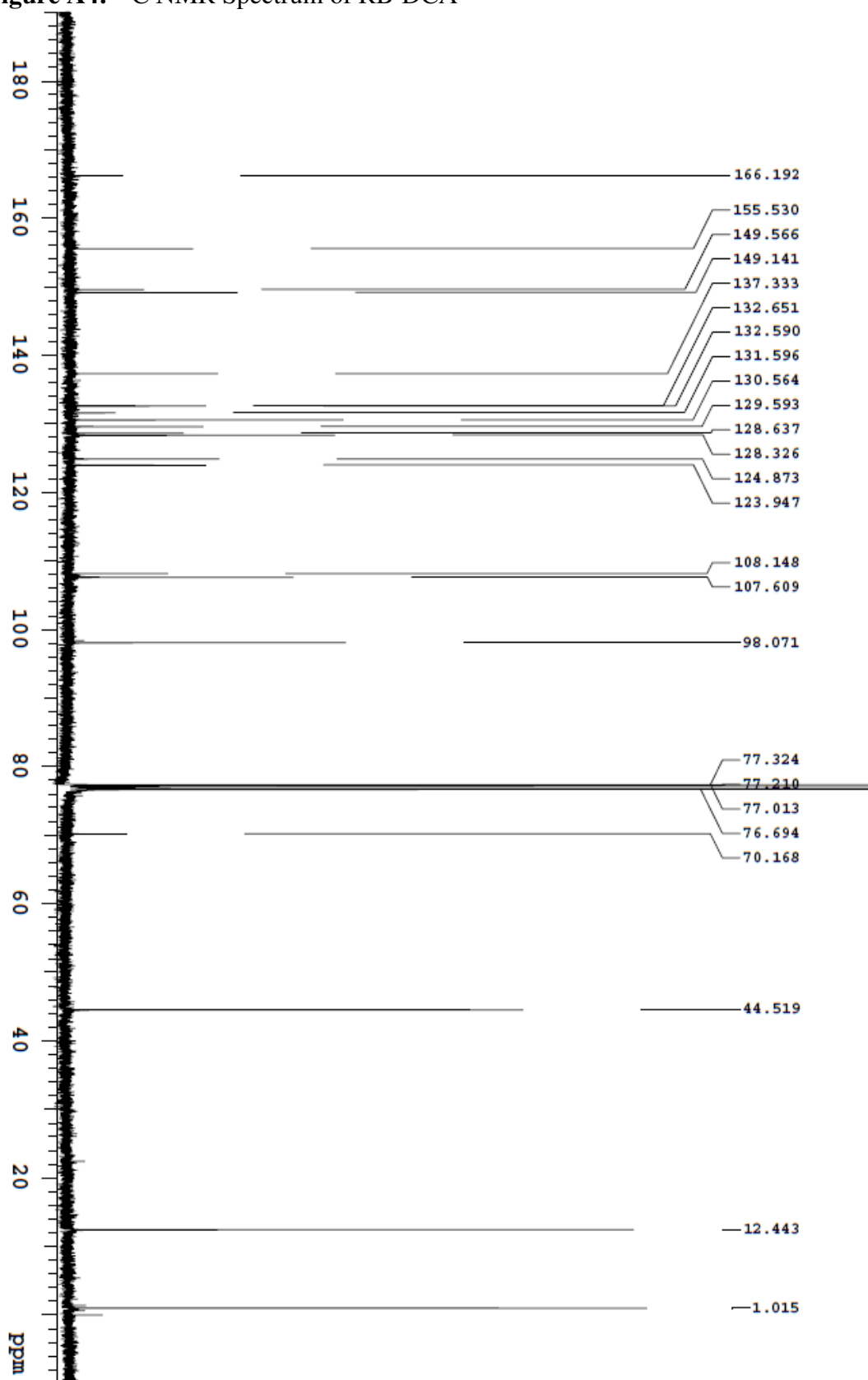
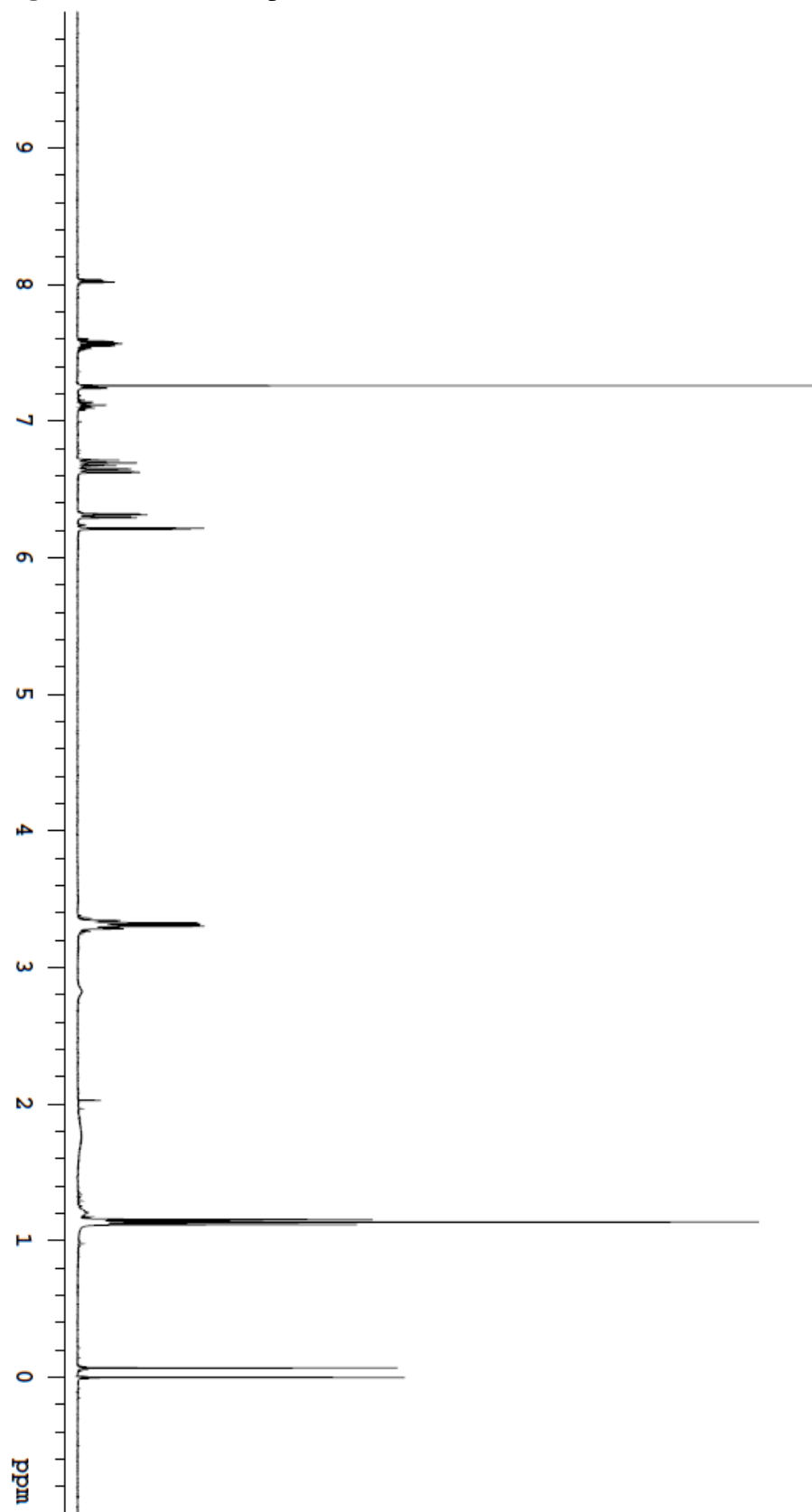
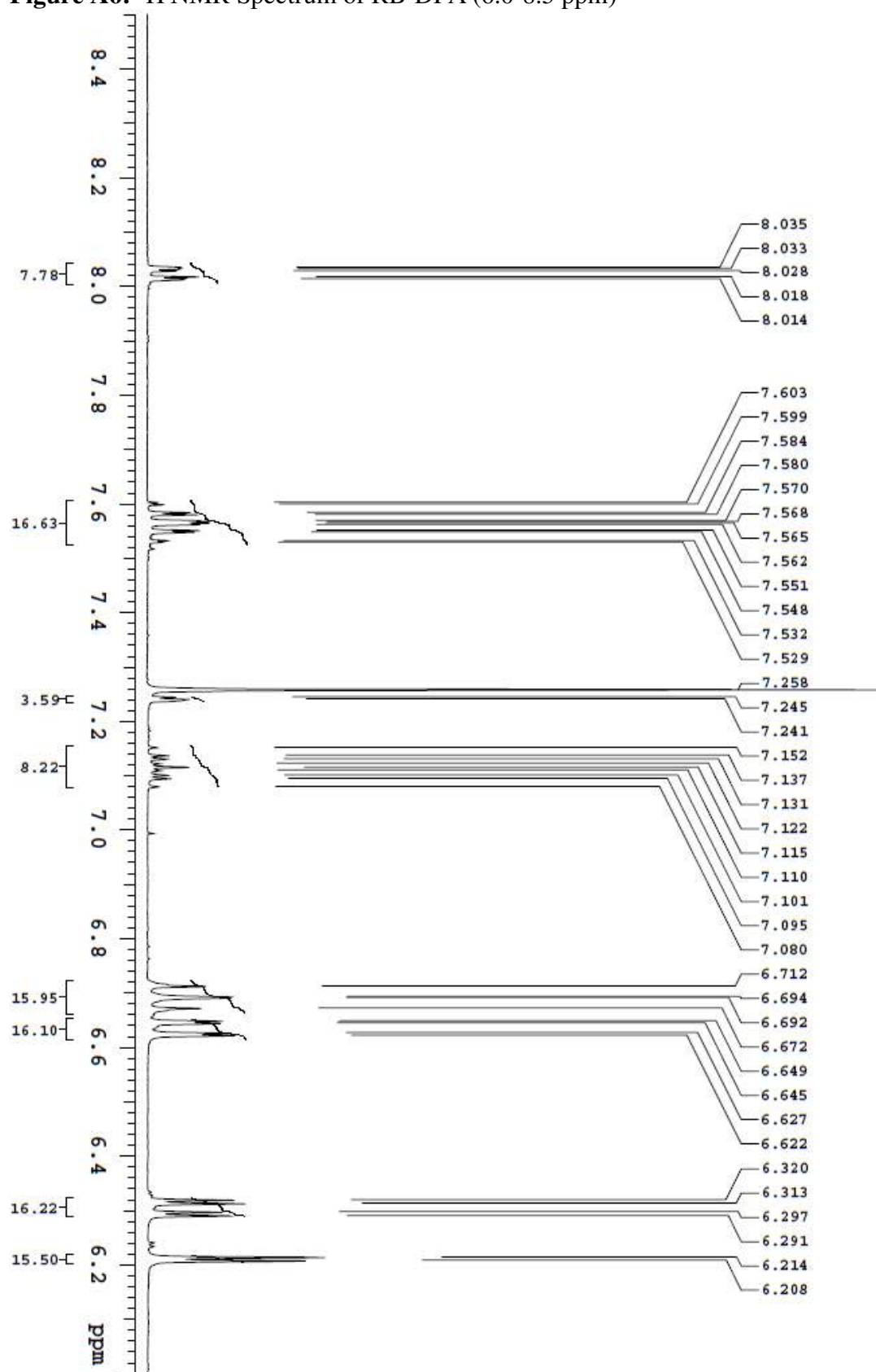
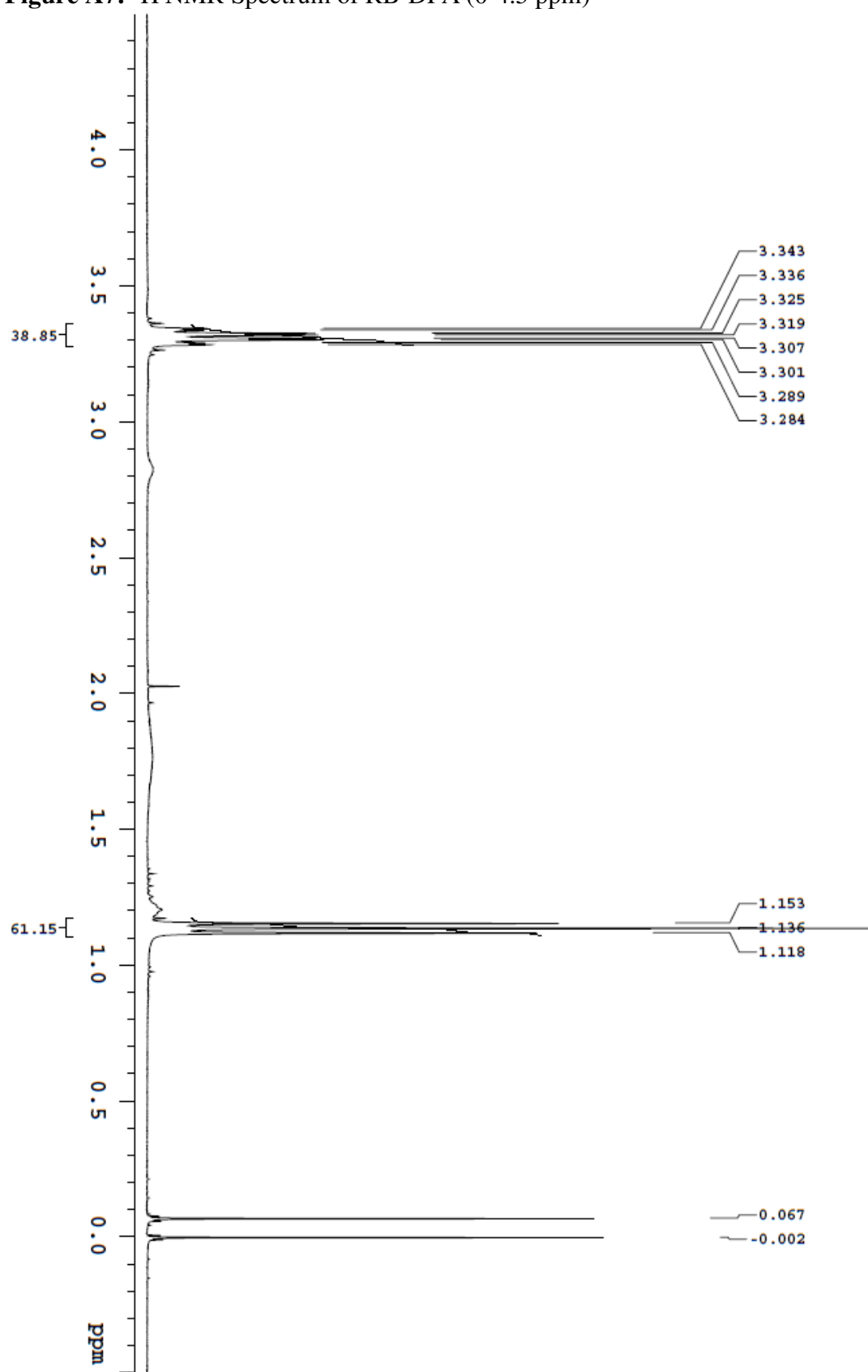
**Figure A3:**  $^1\text{H}$  NMR Spectrum of RB-DCA (0-4.5 ppm)

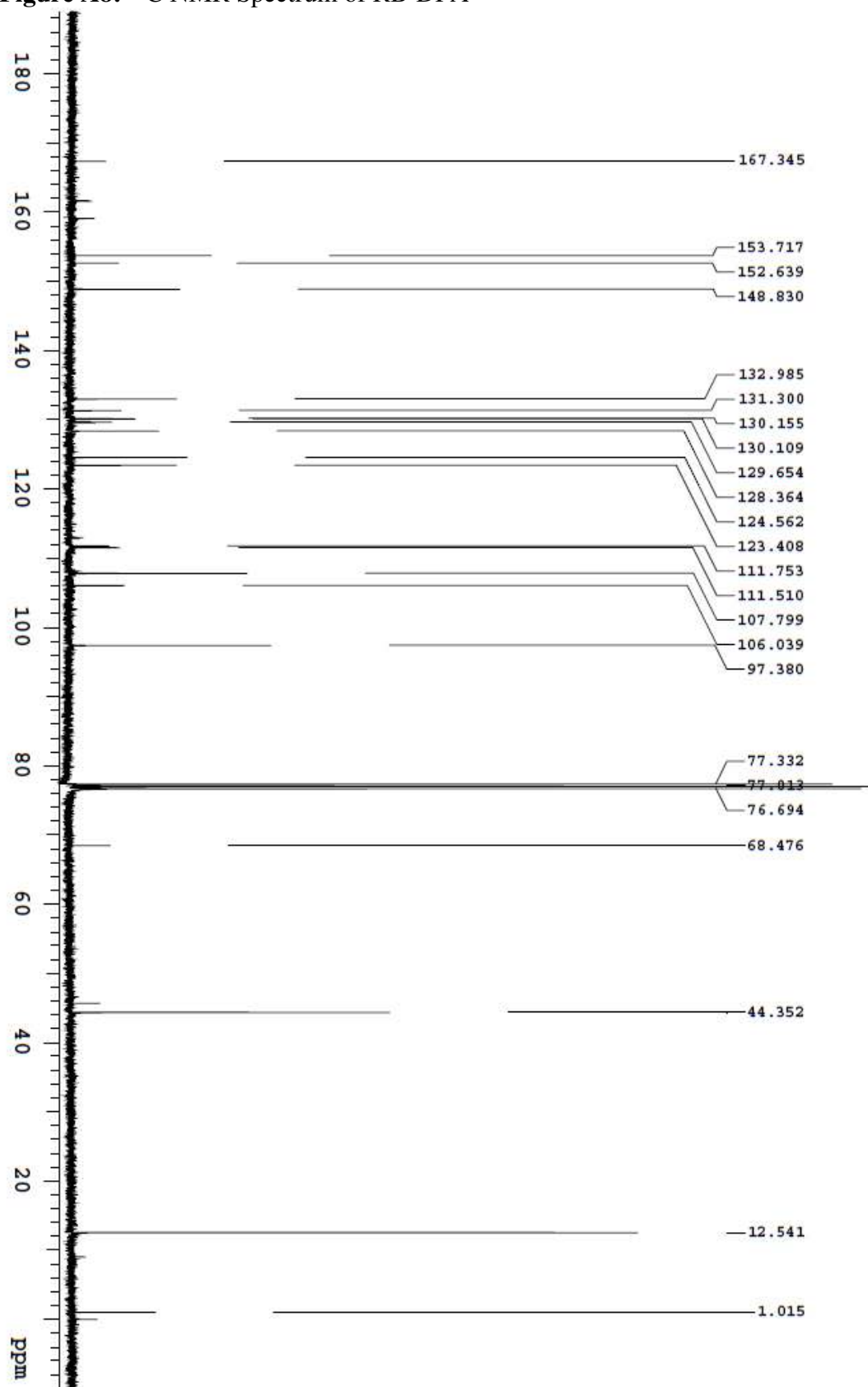
Figure A4:  $^{13}\text{C}$  NMR Spectrum of RB-DCA

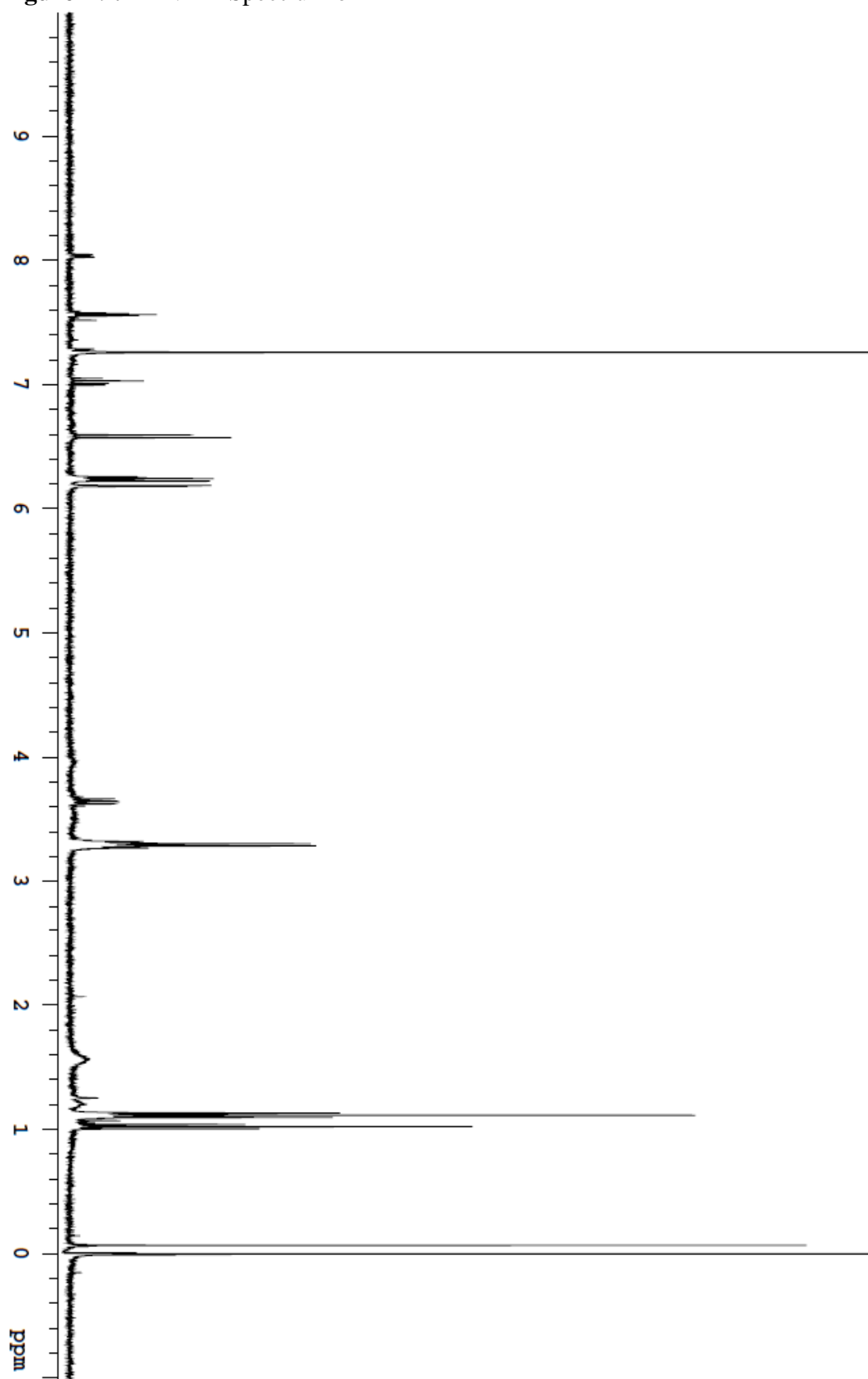
**Figure A5:**  $^1\text{H}$  NMR Spectrum of RB-DFA

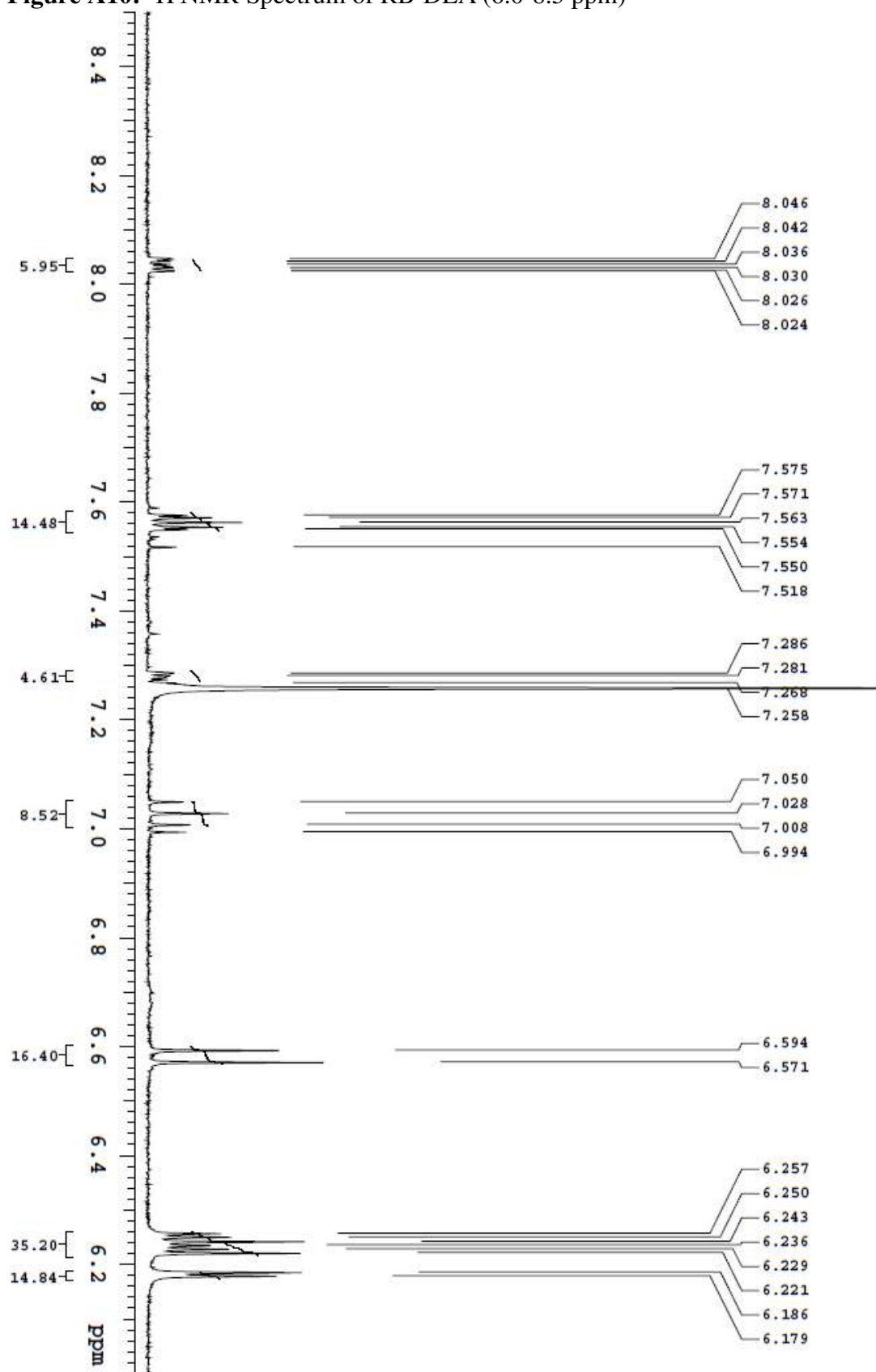
**Figure A6:**  $^1\text{H}$  NMR Spectrum of RB-DFA (6.0-8.5 ppm)

**Figure A7:**  $^1\text{H}$  NMR Spectrum of RB-DFA (0-4.5 ppm)



**Figure A8:**  $^{13}\text{C}$  NMR Spectrum of RB-DFA

**Figure A9:**  $^1\text{H}$  NMR Spectrum of RB-DEA

**Figure A10:**  $^1\text{H}$  NMR Spectrum of RB-DEA (6.0-8.5 ppm)

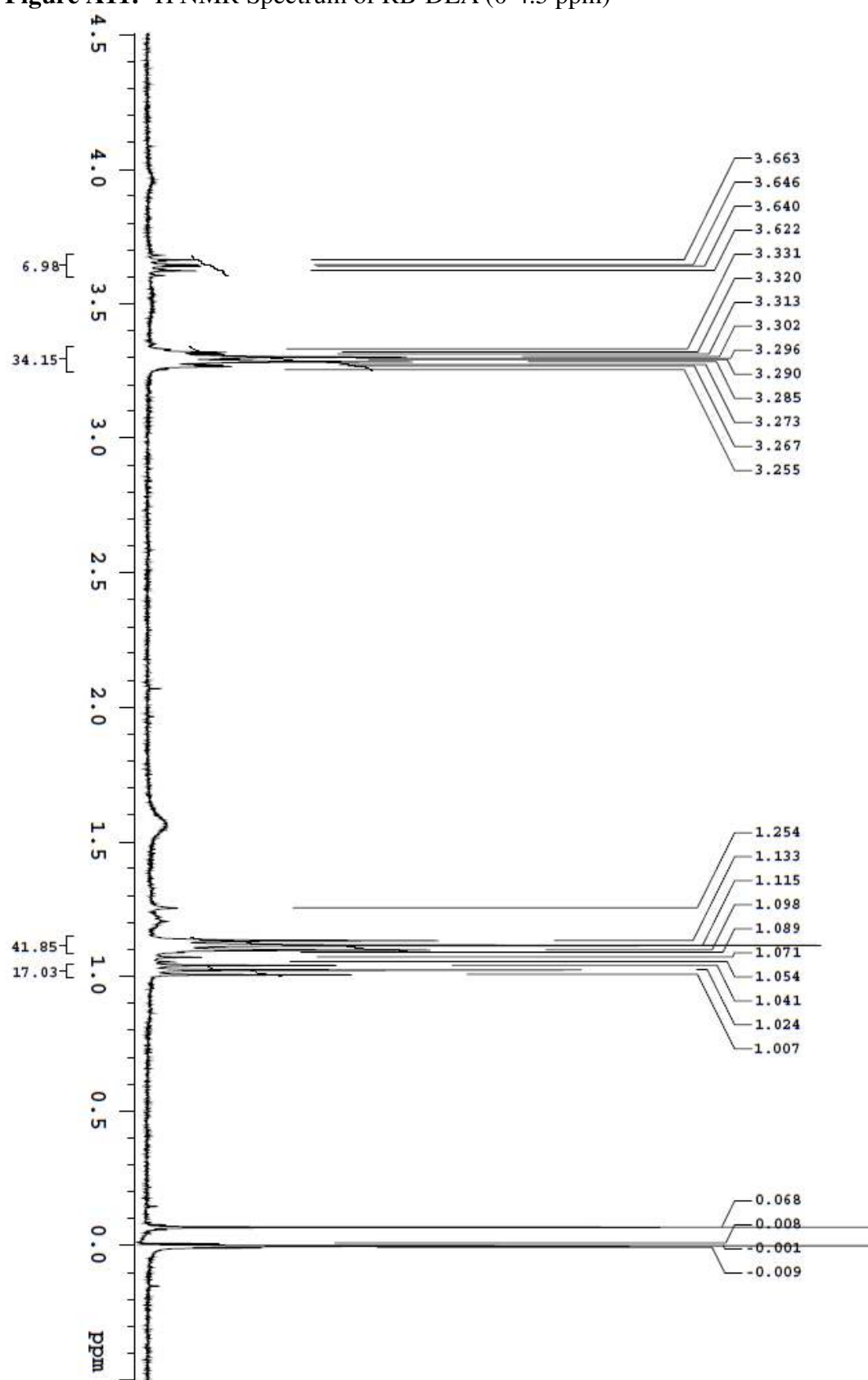
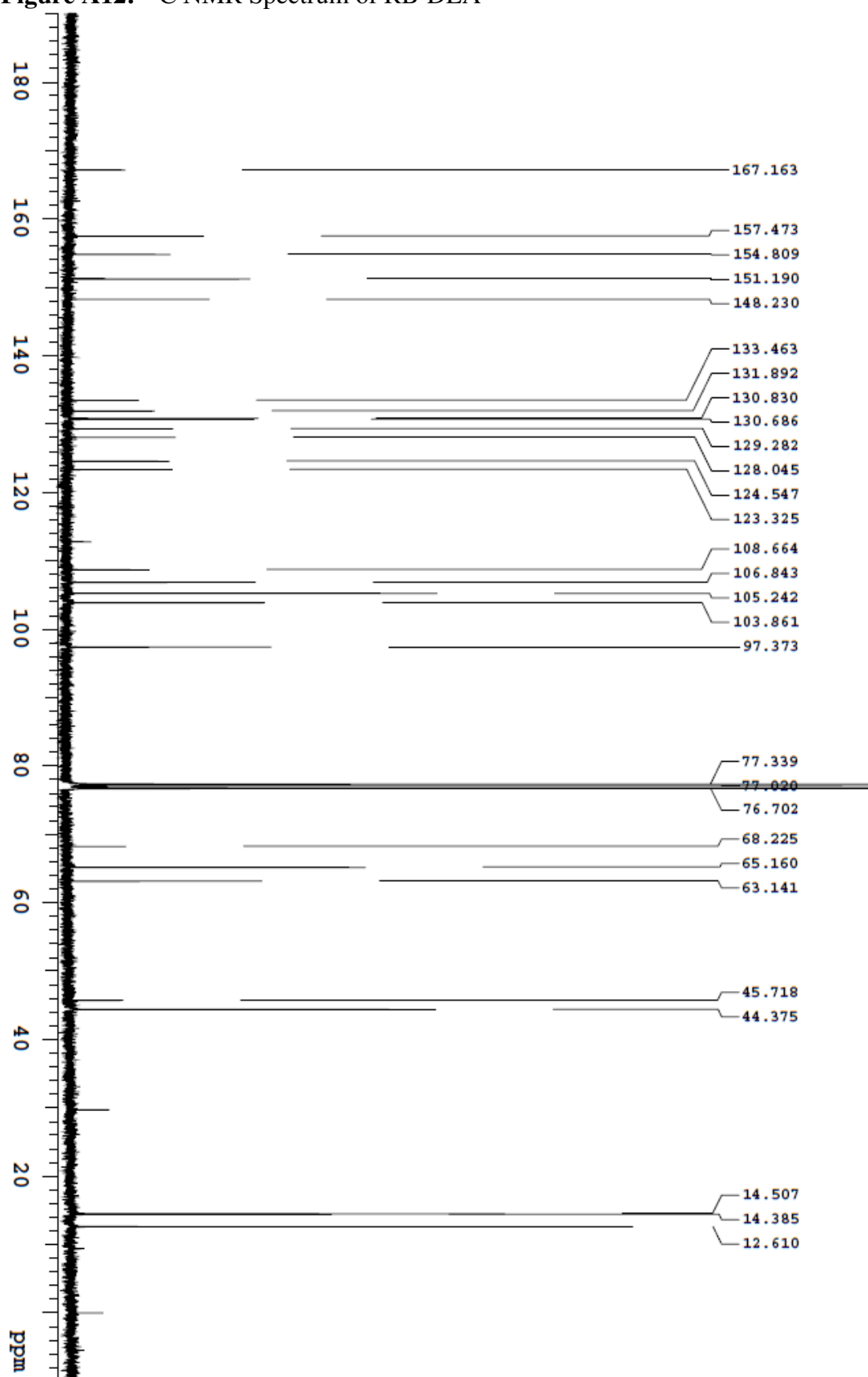
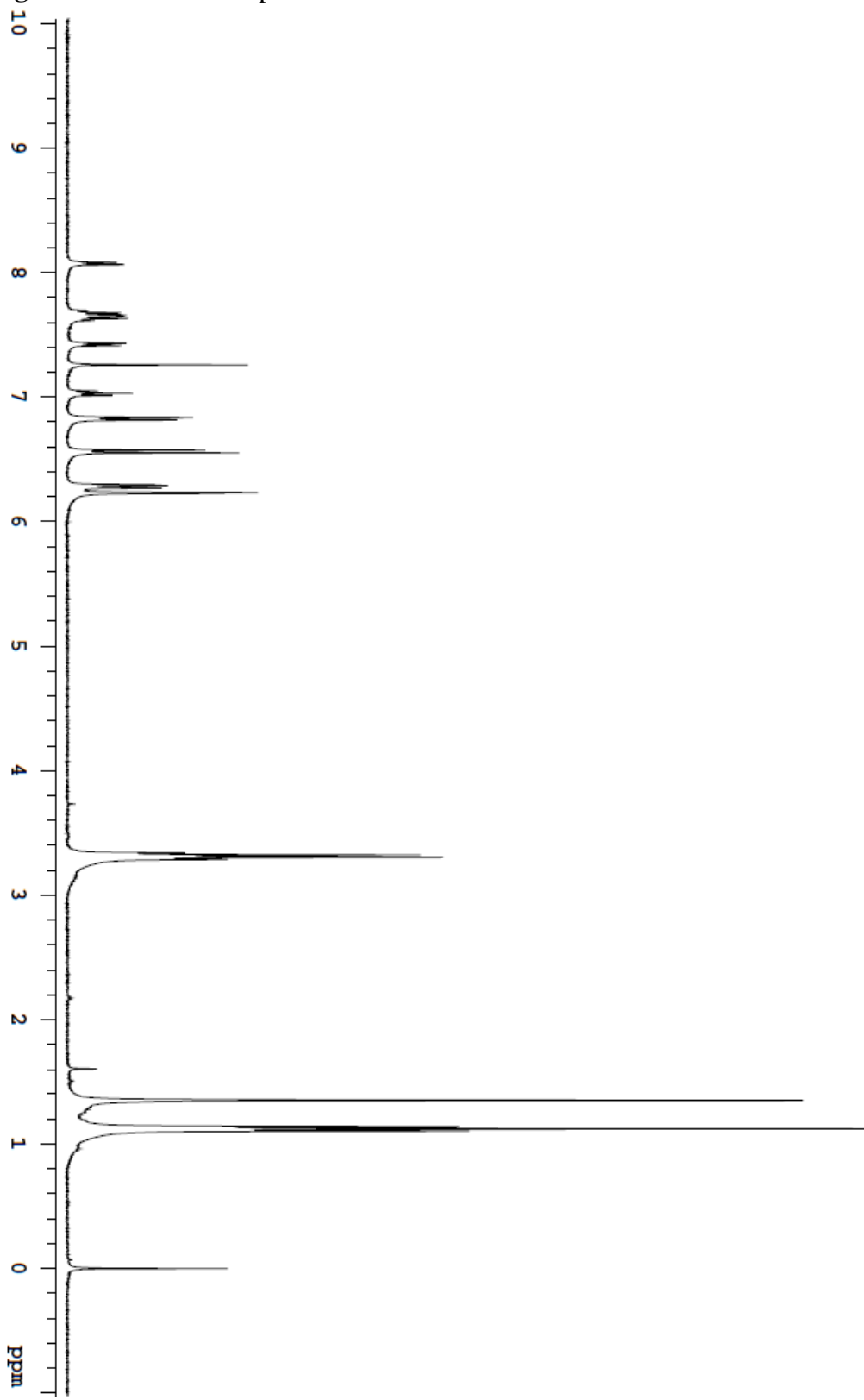
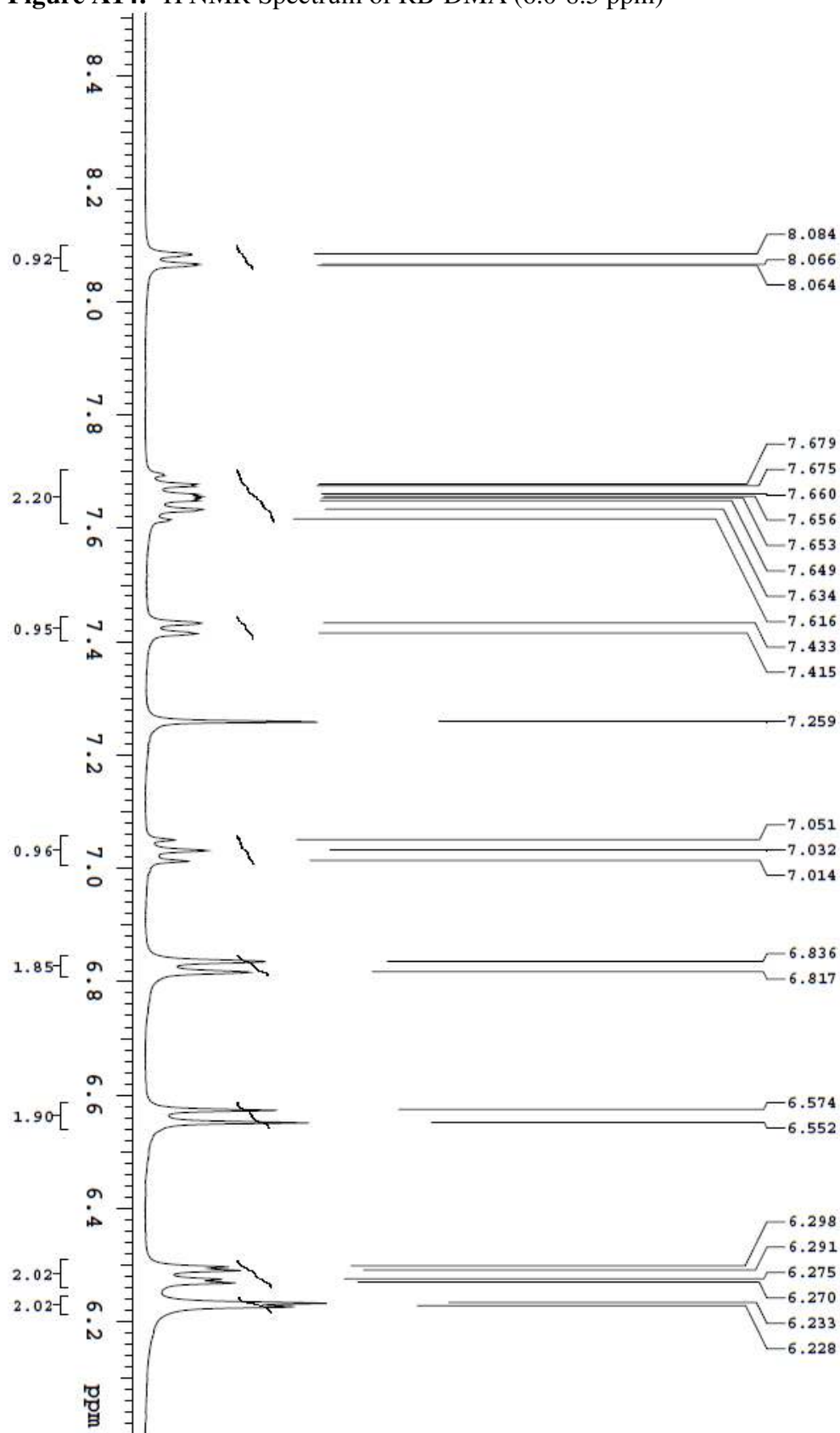
**Figure A11:**  $^1\text{H}$  NMR Spectrum of RB-DEA (0-4.5 ppm)

Figure A12:  $^{13}\text{C}$  NMR Spectrum of RB-DEA

**Figure A13:**  $^1\text{H}$  NMR Spectrum of RB-DMA<sup>15</sup>

<sup>15</sup> NMR by Grace Purnell

**Figure A14:**  $^1\text{H}$  NMR Spectrum of RB-DMA (6.0-8.5 ppm)<sup>15</sup>

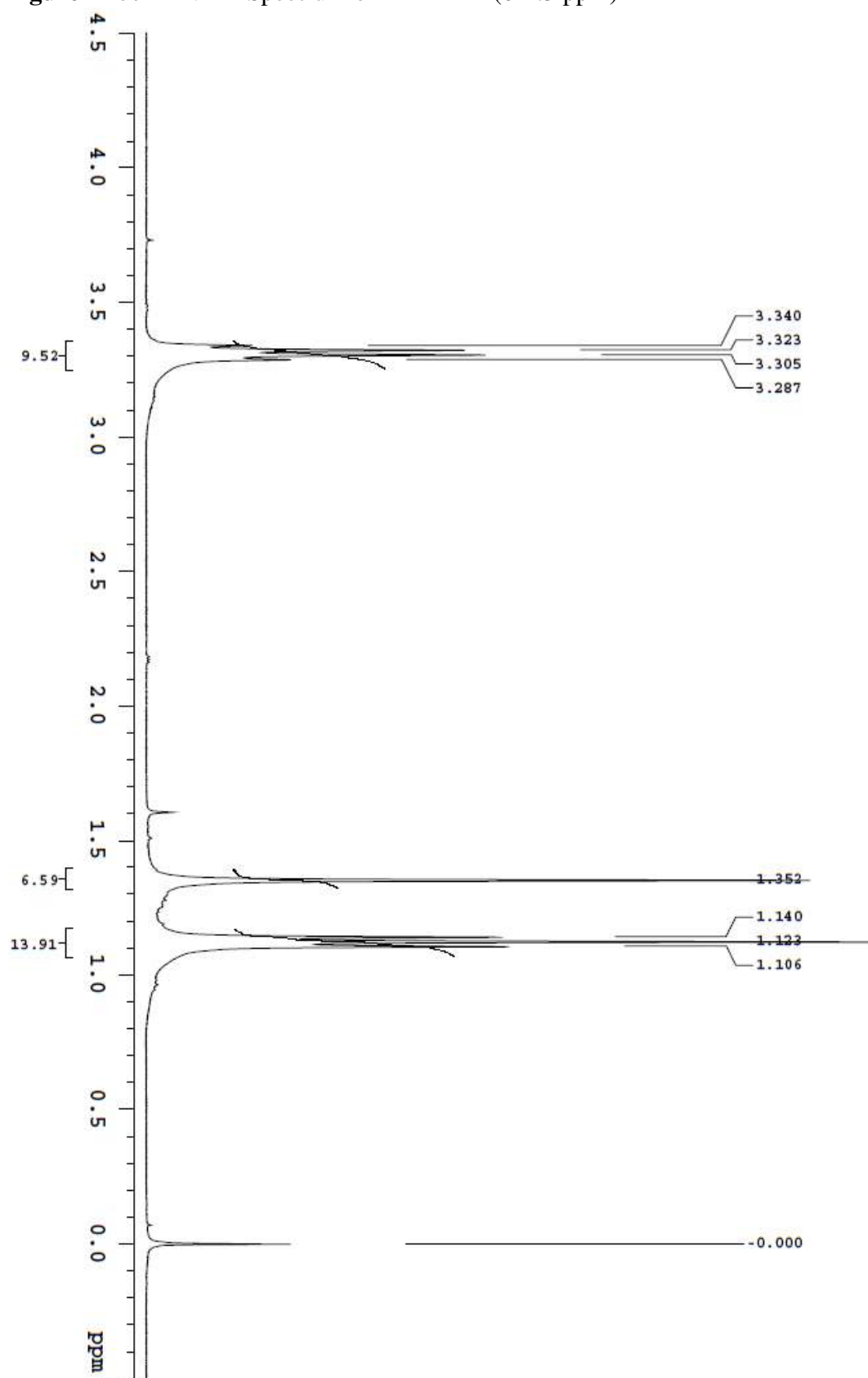
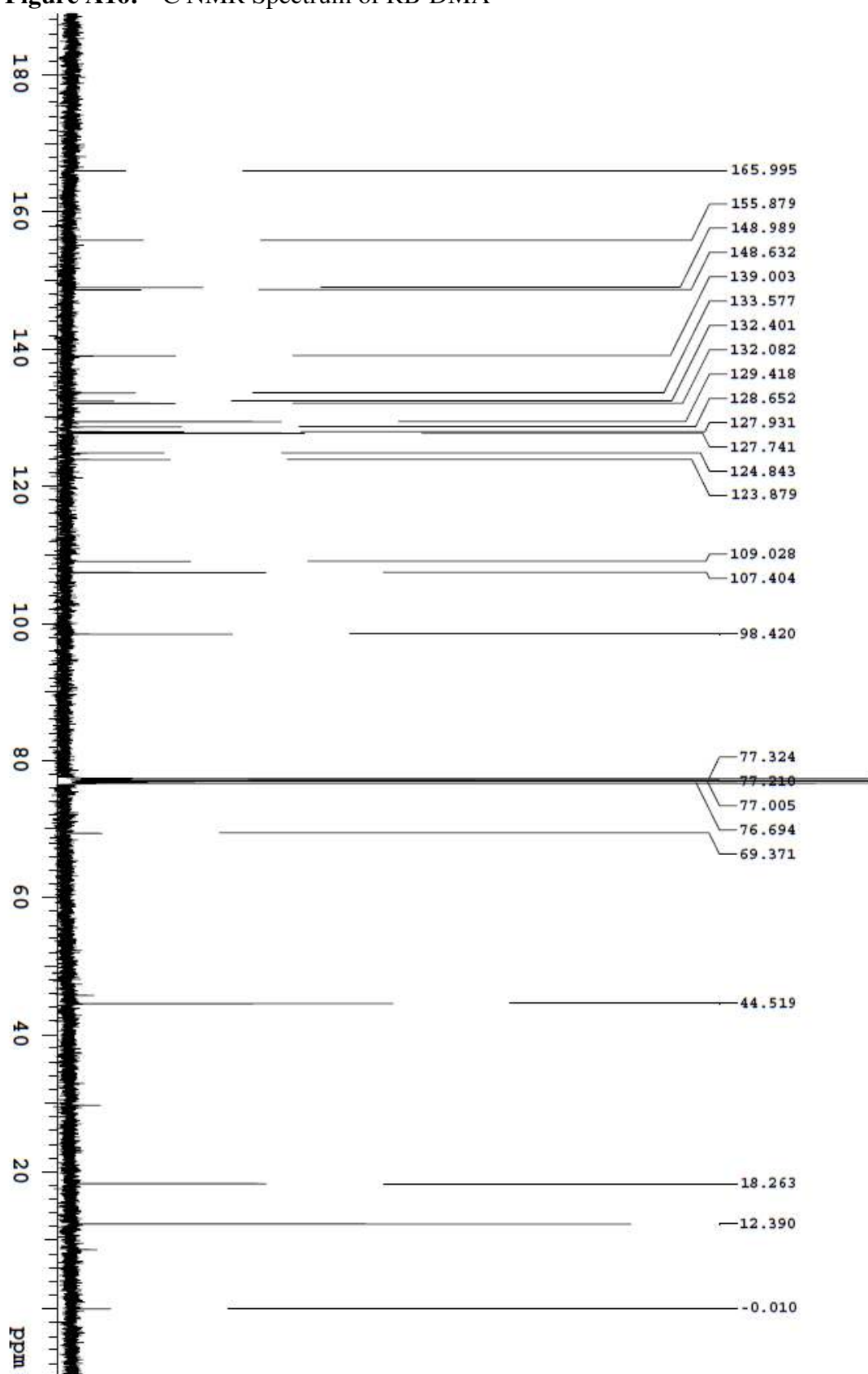
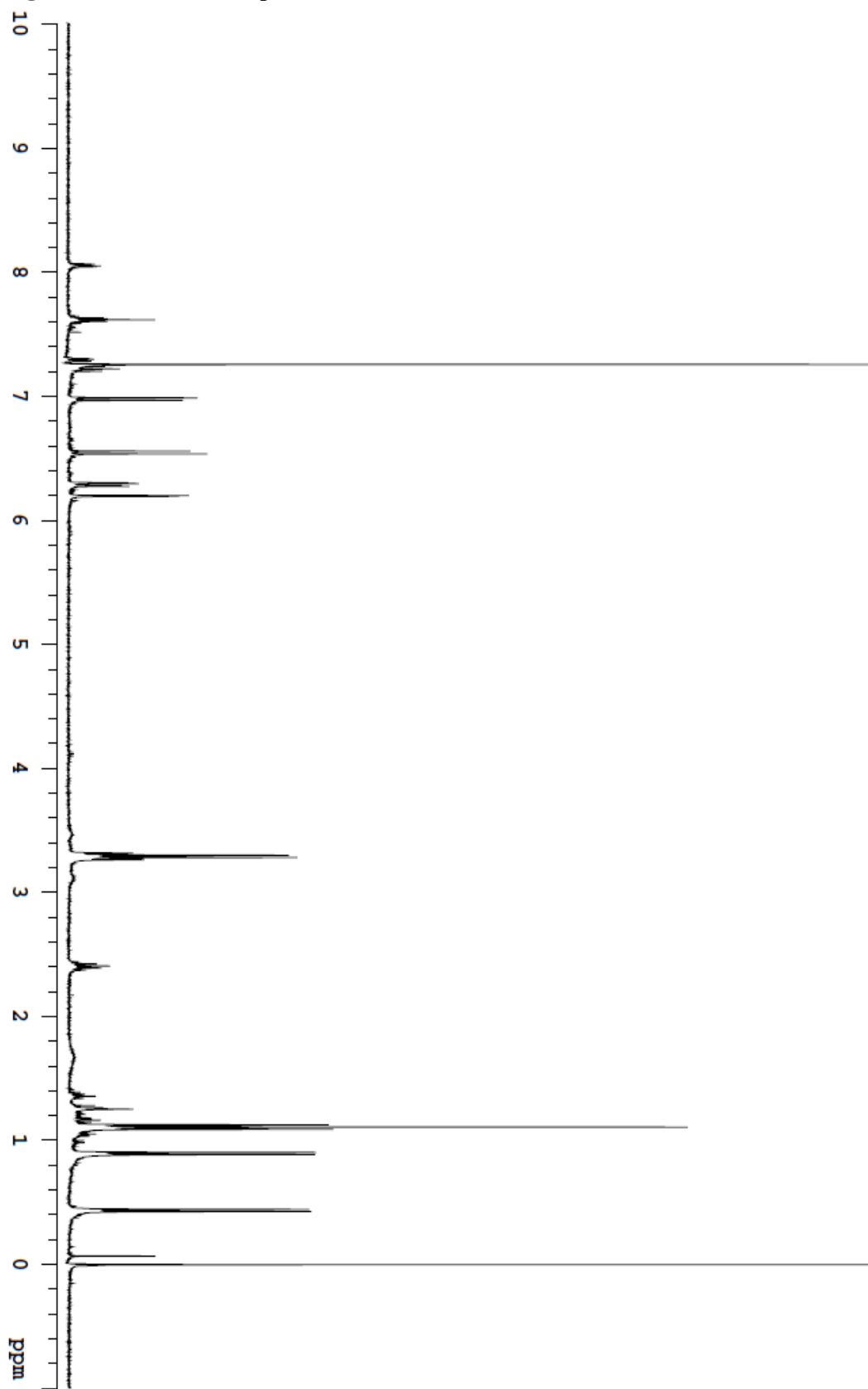
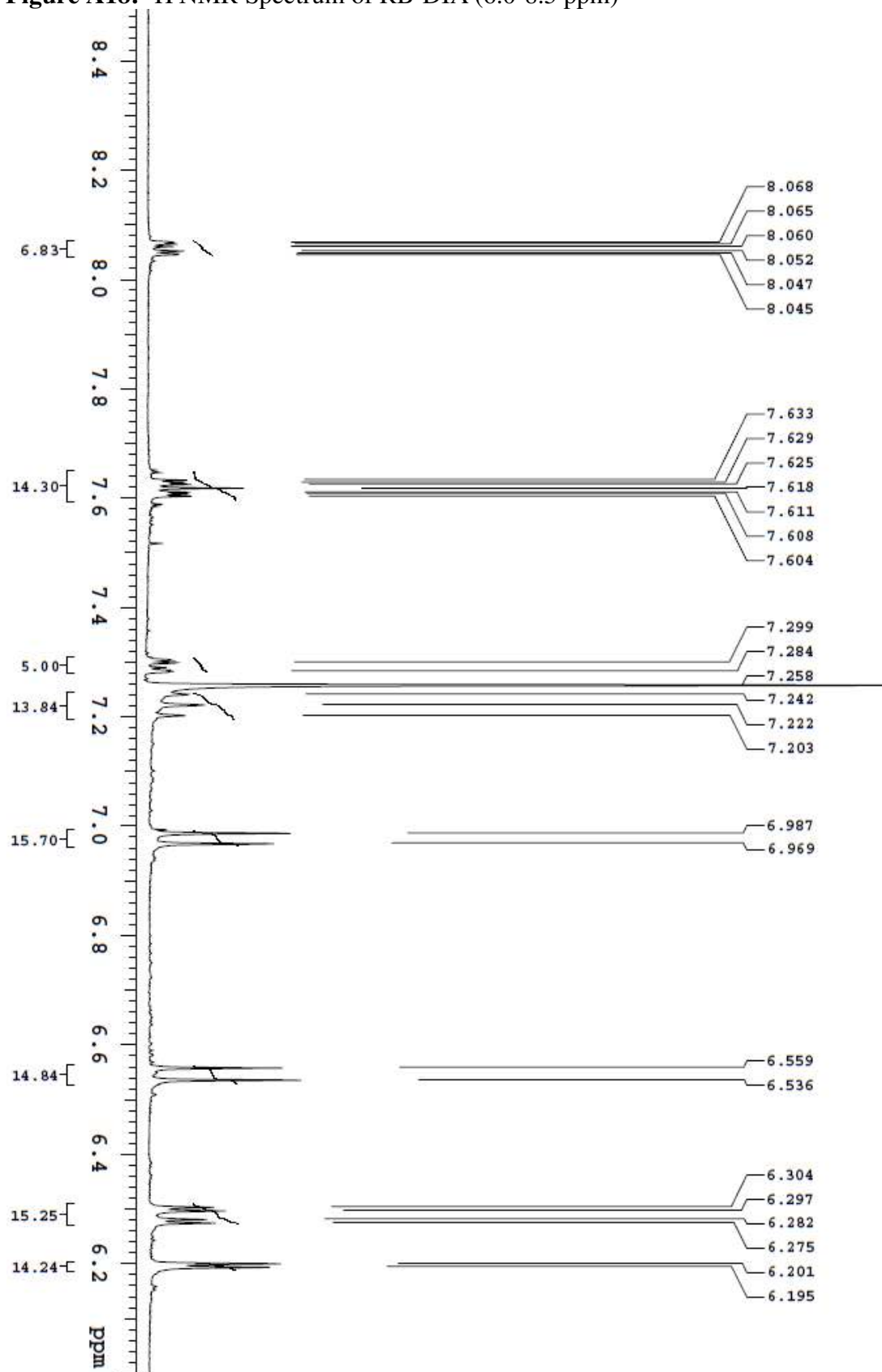
**Figure A15:**  $^1\text{H}$  NMR Spectrum of RB-DMA (0-4.5 ppm)<sup>15</sup>



Figure A16:  $^{13}\text{C}$  NMR Spectrum of RB-DMA

**Figure A17:**  $^1\text{H}$  NMR Spectrum of RB-DIA

**Figure A18:**  $^1\text{H}$  NMR Spectrum of RB-DIA (6.0-8.5 ppm)

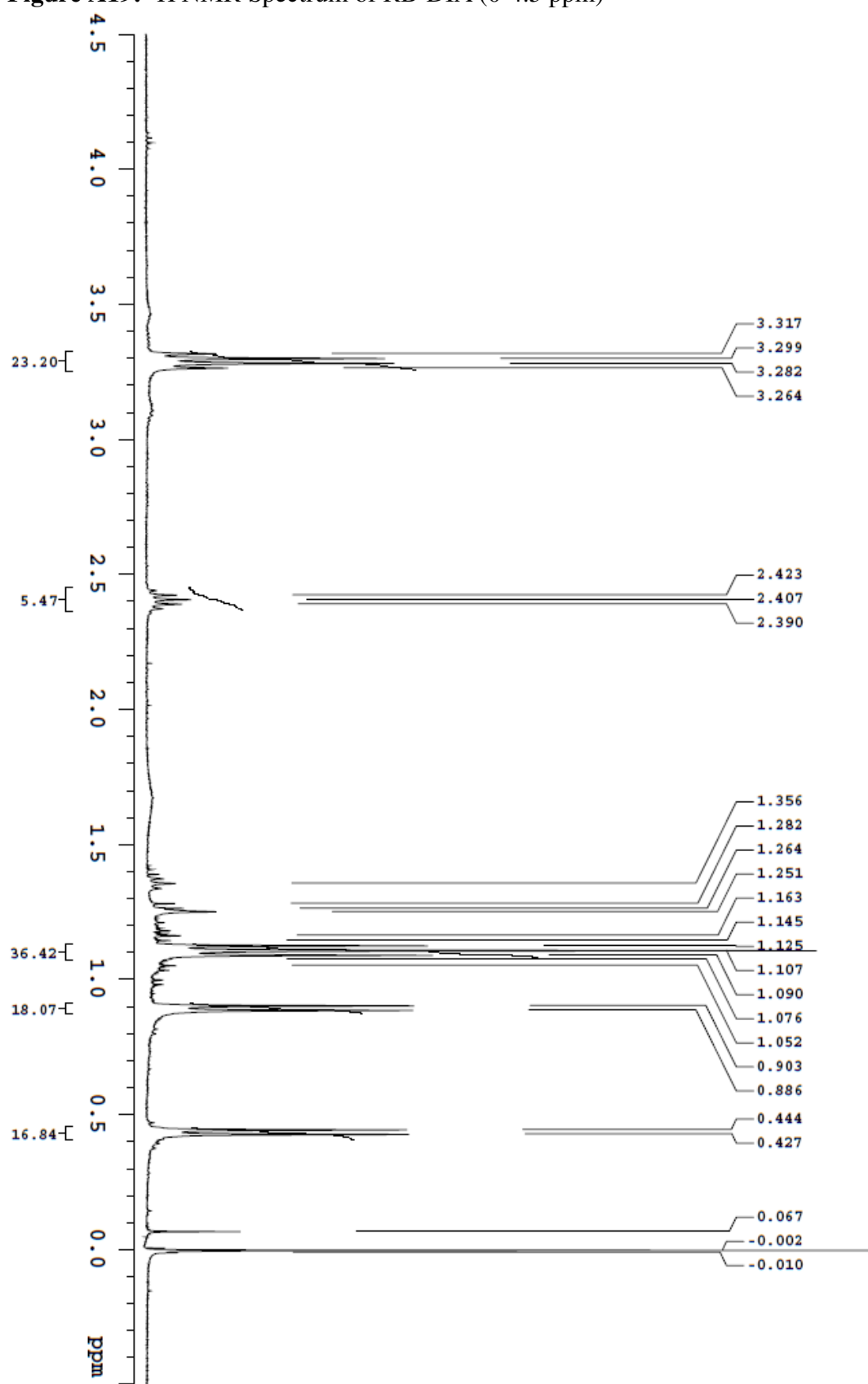
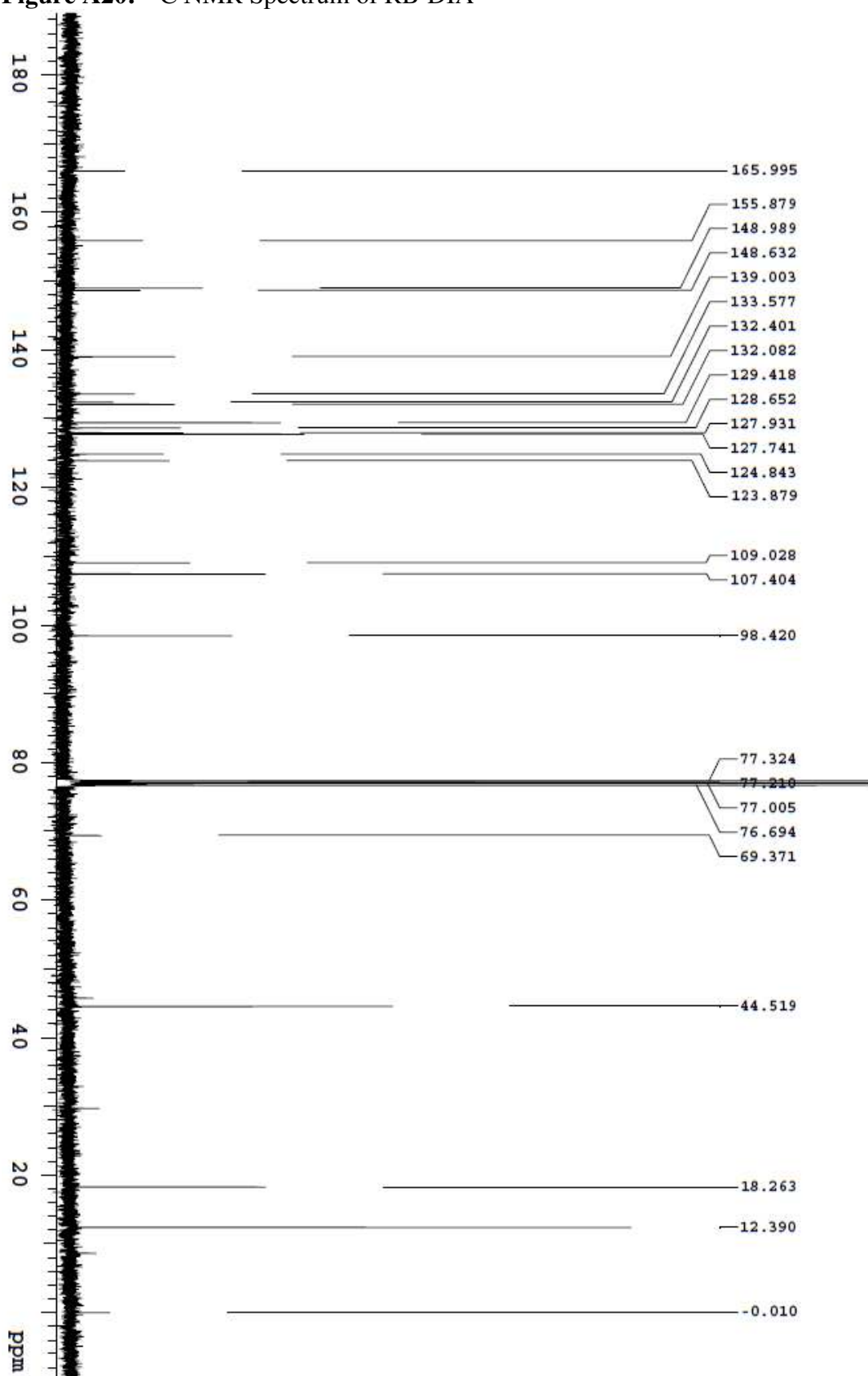
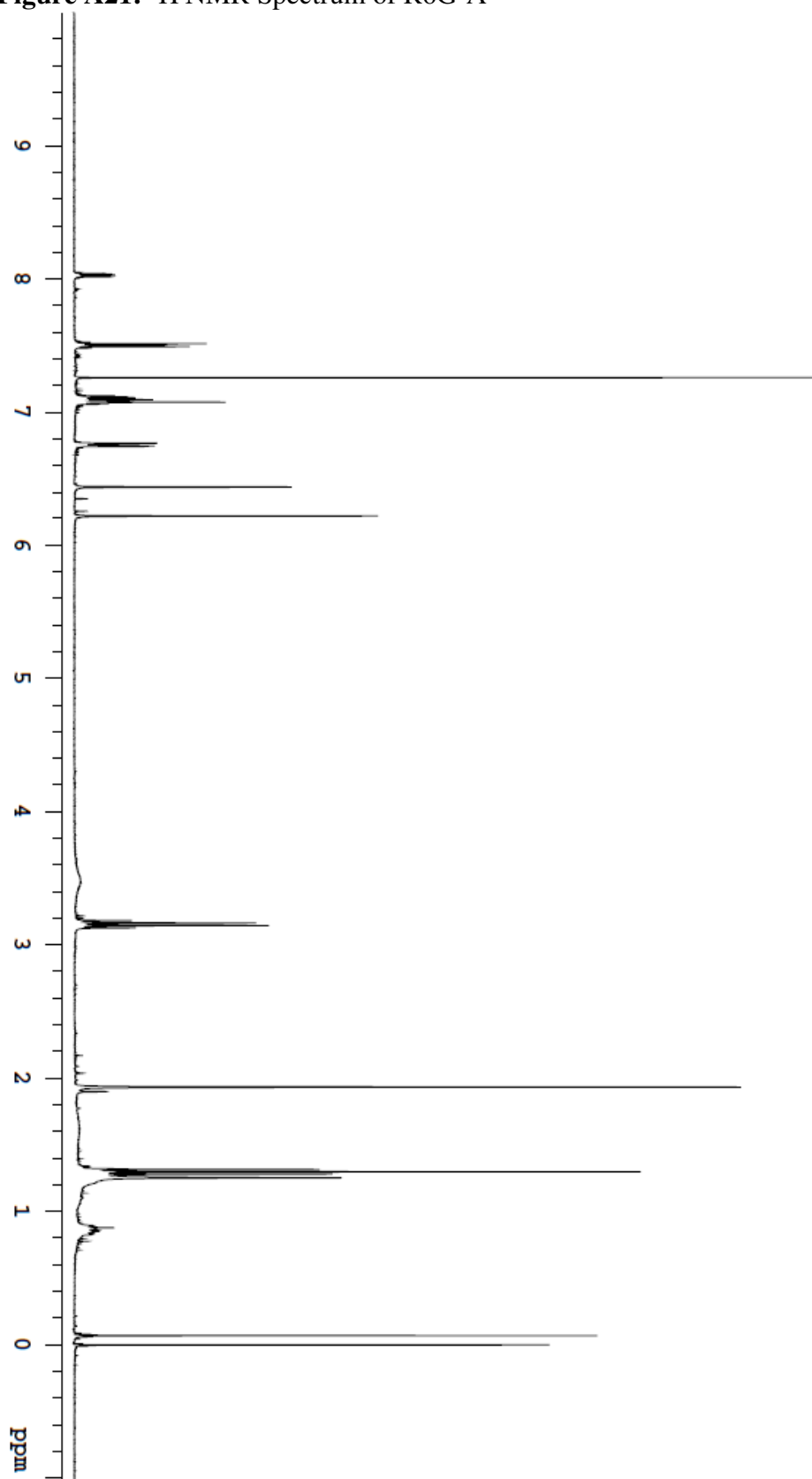
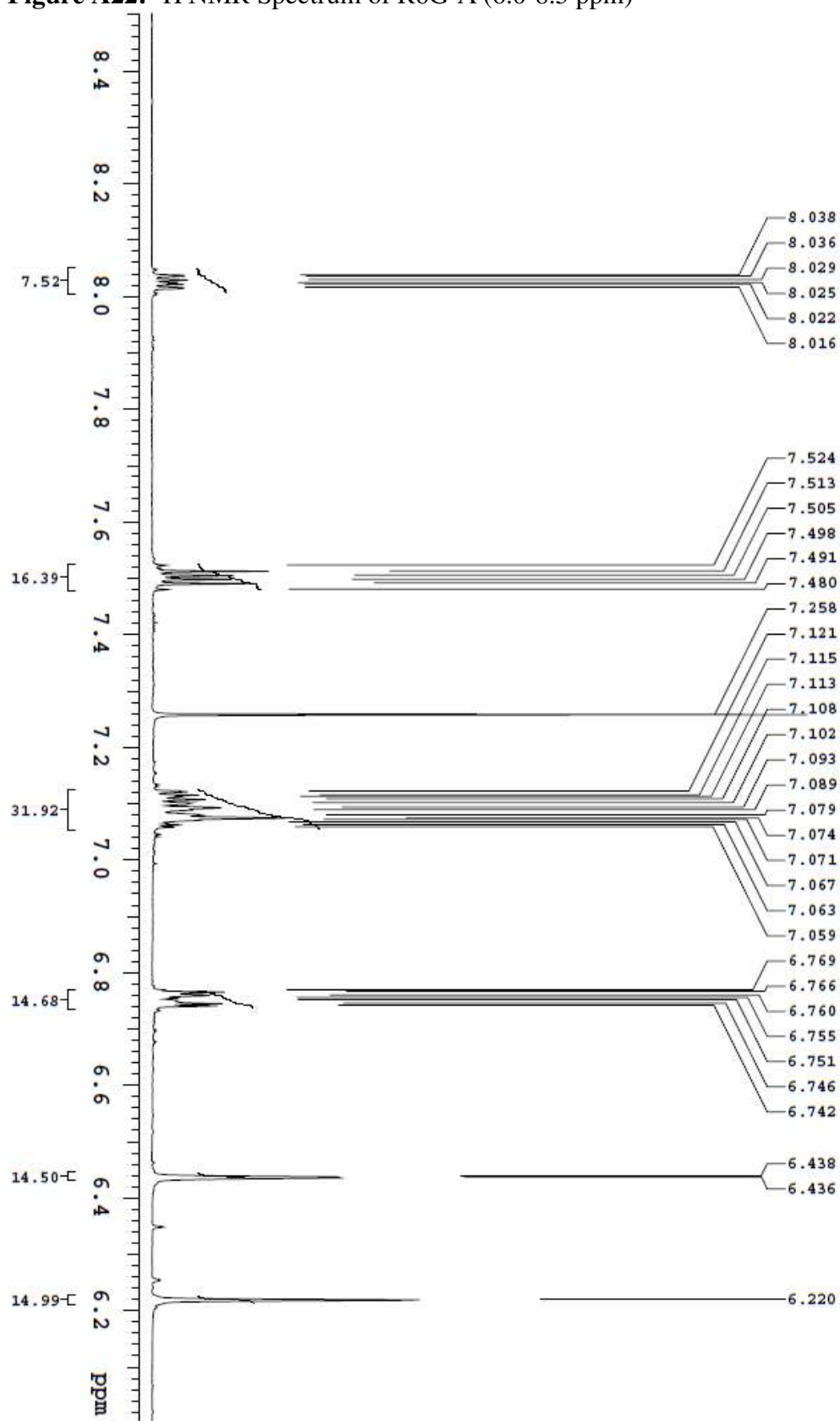
**Figure A19:**  $^1\text{H}$  NMR Spectrum of RB-DIA (0-4.5 ppm)

Figure A20:  $^{13}\text{C}$  NMR Spectrum of RB-DIA

**Figure A21:**  $^1\text{H}$  NMR Spectrum of R6G-A

**Figure A22:**  $^1\text{H}$  NMR Spectrum of R6G-A (6.0-8.5 ppm)

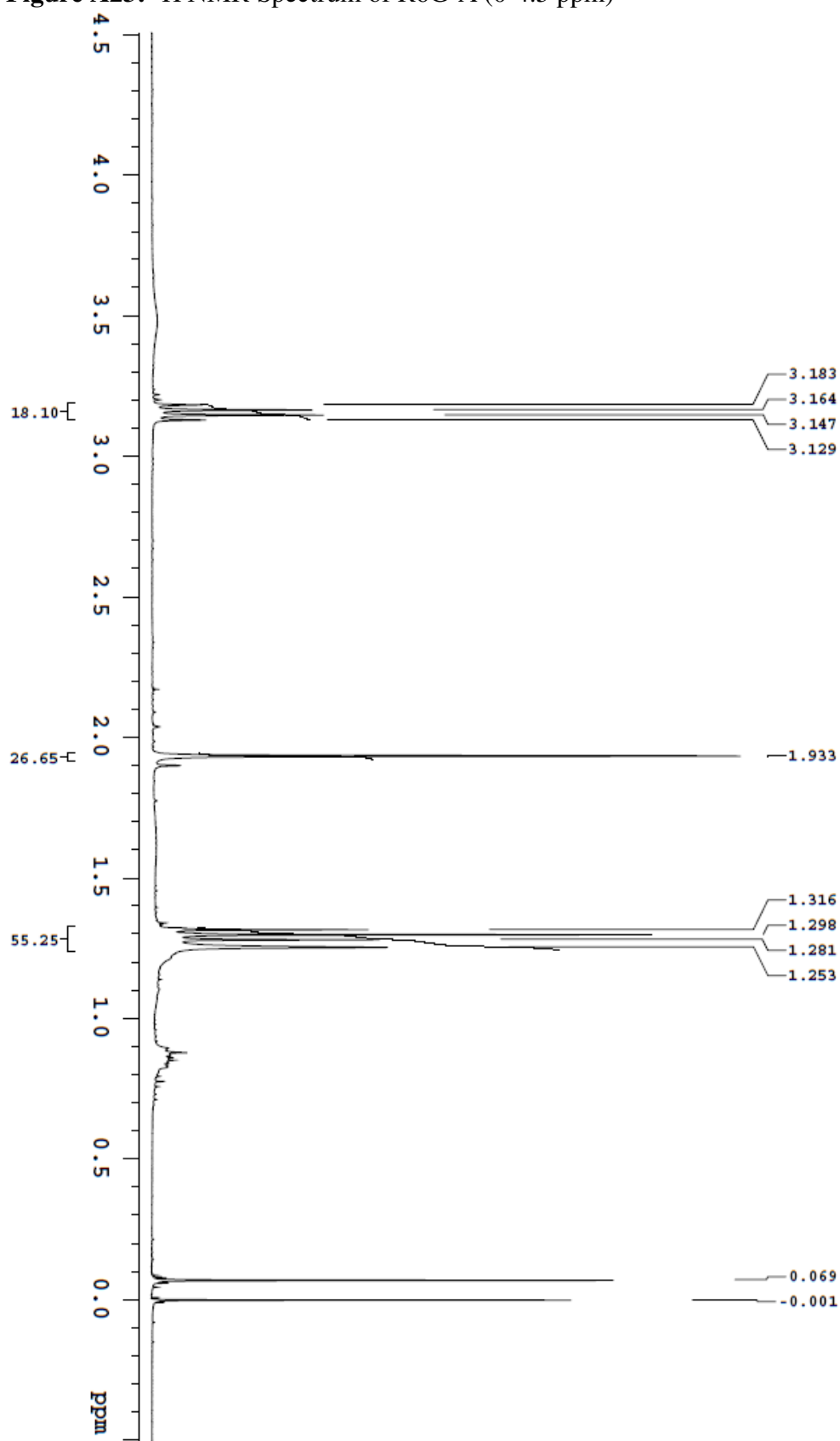
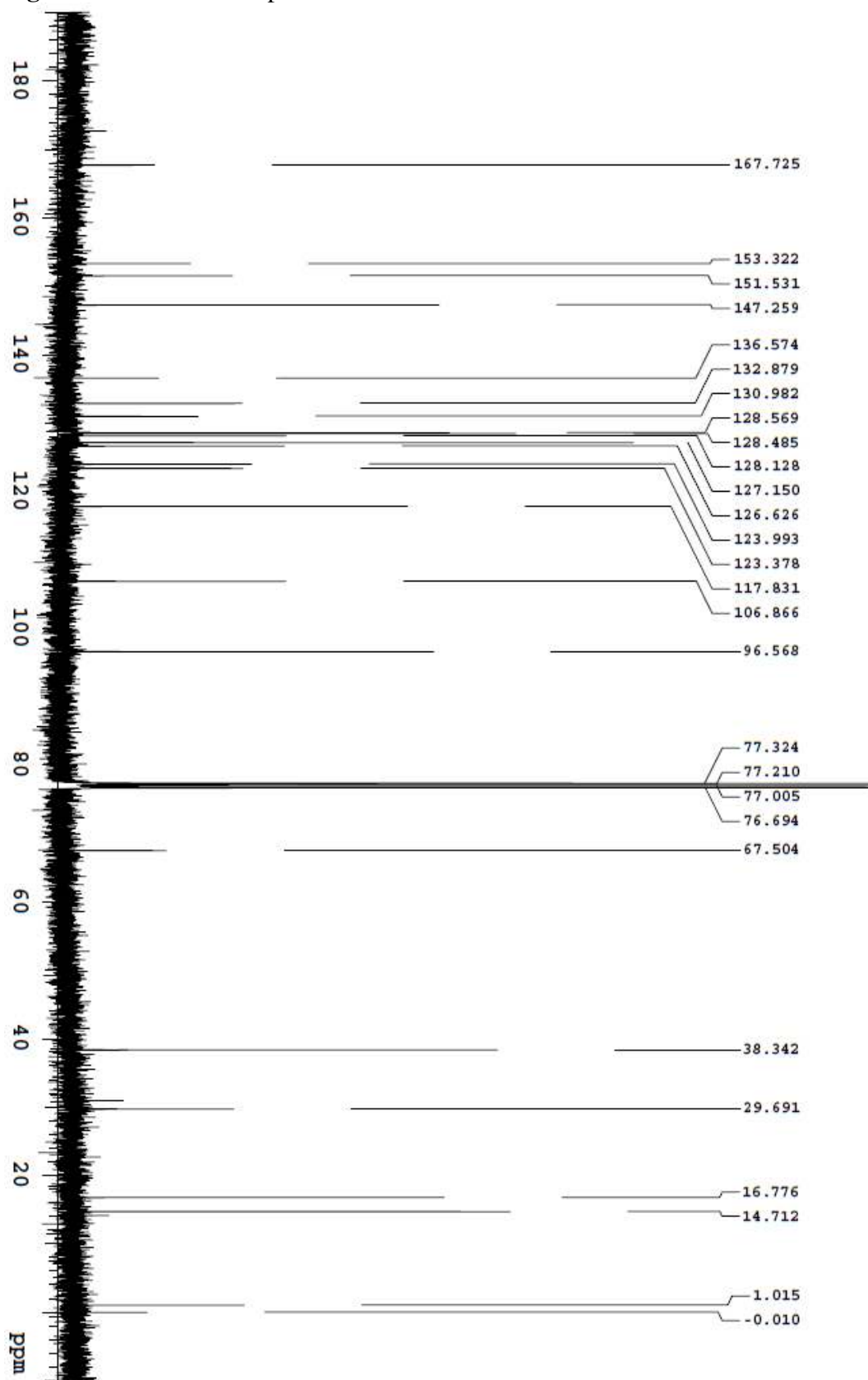
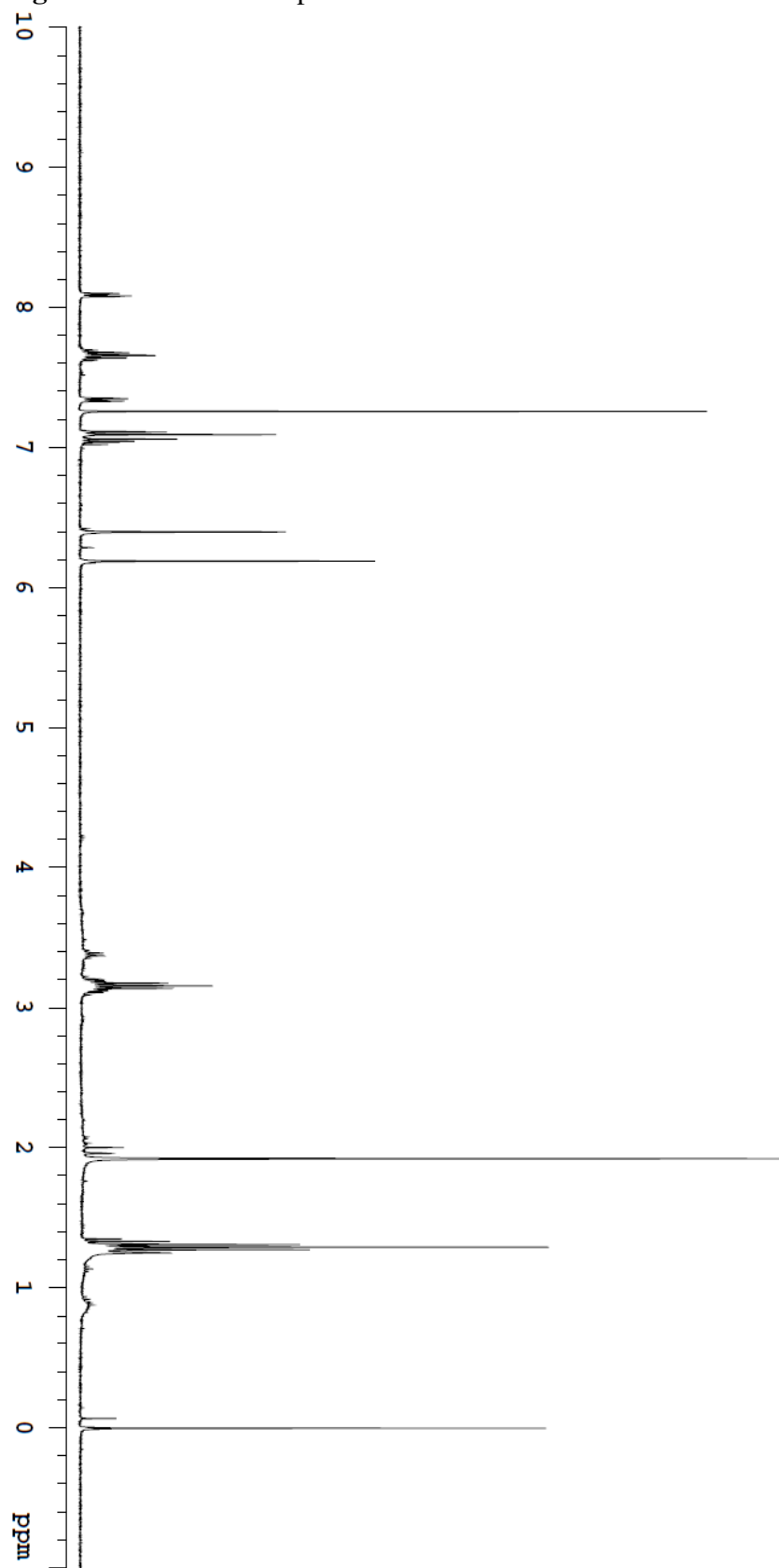
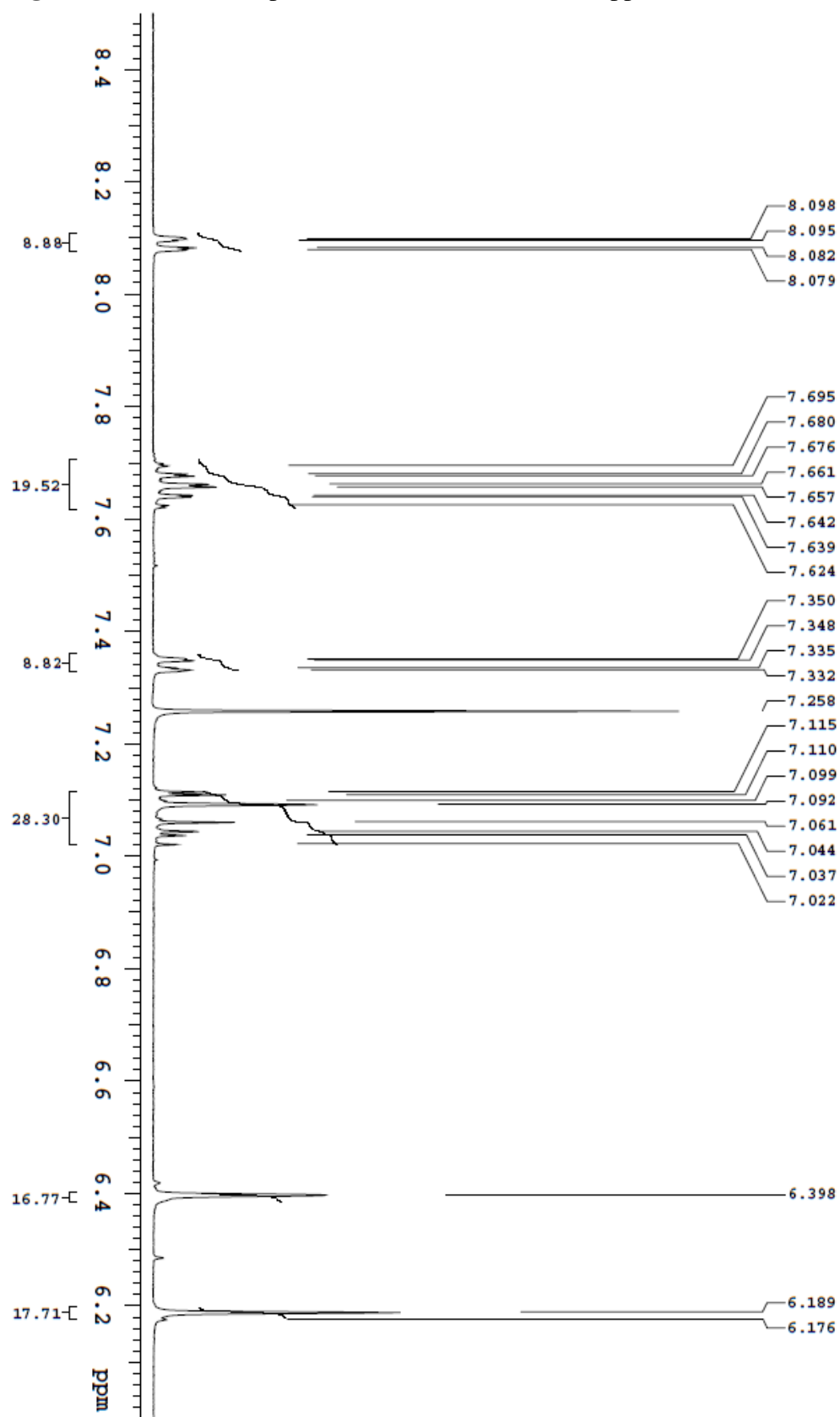
**Figure A23:**  $^1\text{H}$  NMR Spectrum of R6G-A (0-4.5 ppm)



Figure A24:  $^{13}\text{C}$  NMR Spectrum of R6G-A

**Figure A25:**  $^1\text{H}$  NMR Spectrum of R6G-DCA

**Figure A26:**  $^1\text{H}$  NMR Spectrum of R6G-DCA (6.0-8.5 ppm)

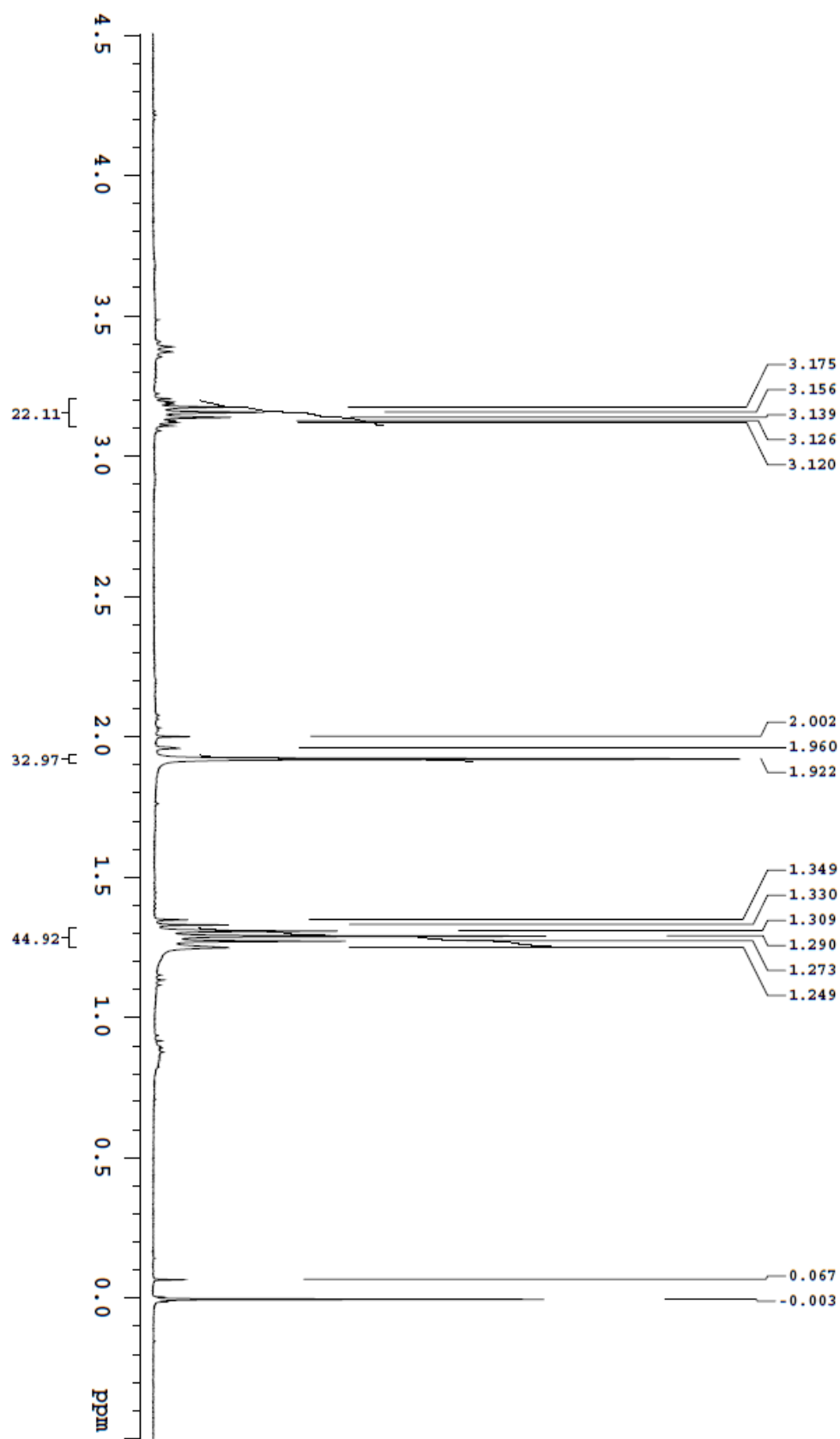
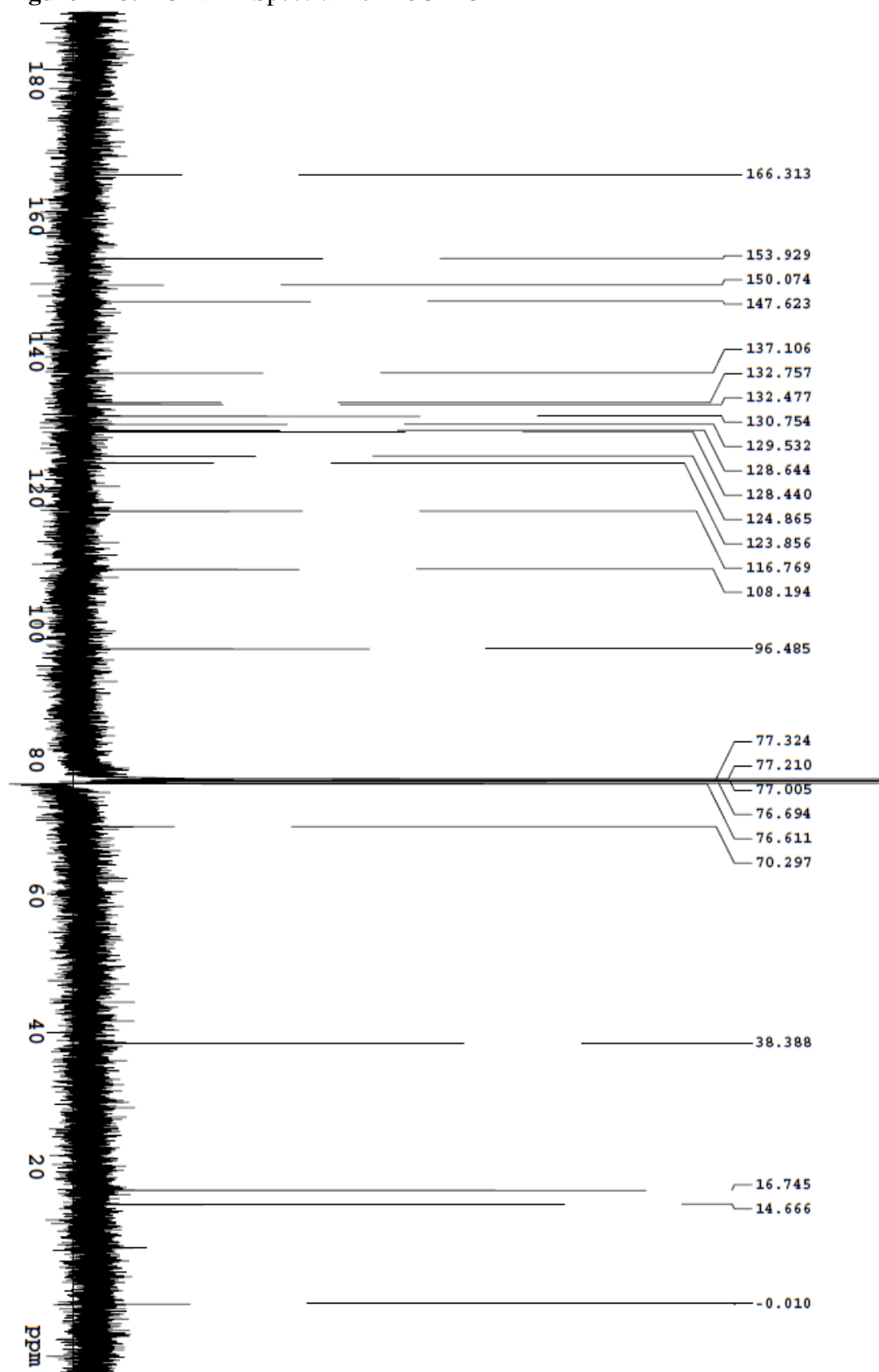
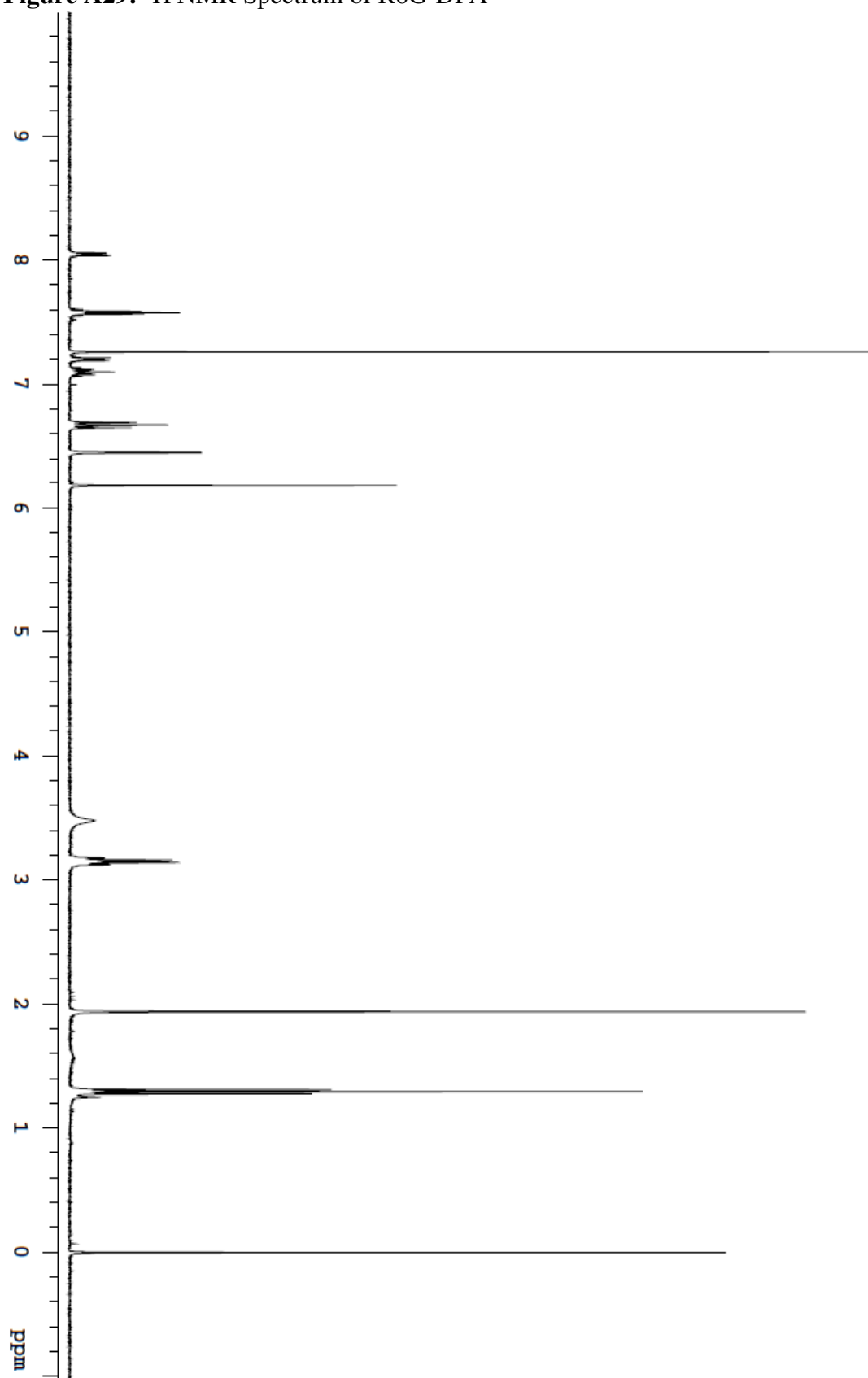
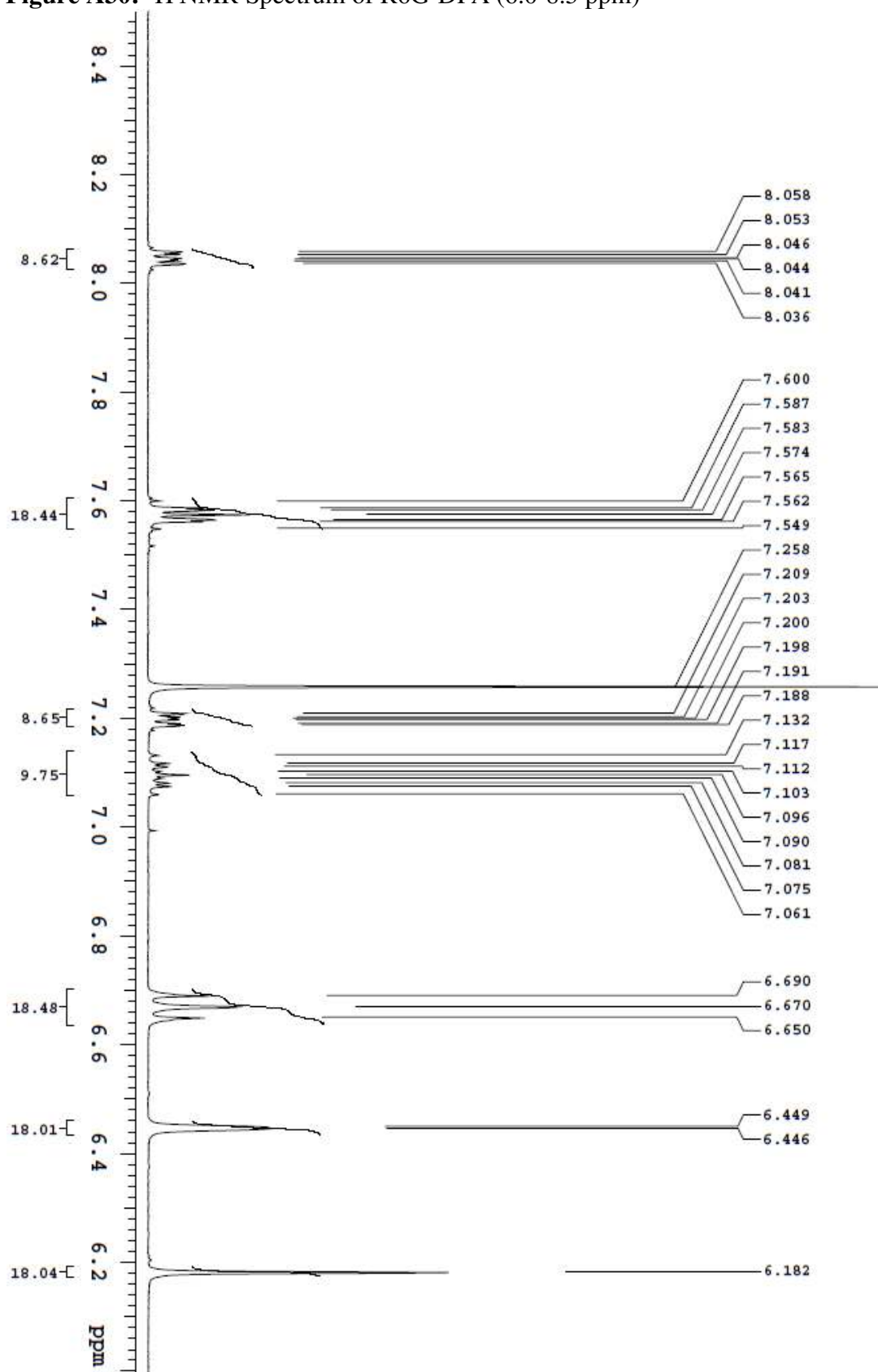
**Figure A27:**  $^1\text{H}$  NMR Spectrum of R6G-DCA (0-4.5 ppm)

Figure A28:  $^{13}\text{C}$  NMR Spectrum of R6G-DCA

**Figure A29:**  $^1\text{H}$  NMR Spectrum of R6G-DFA

**Figure A30:**  $^1\text{H}$  NMR Spectrum of R6G-DFA (6.0-8.5 ppm)

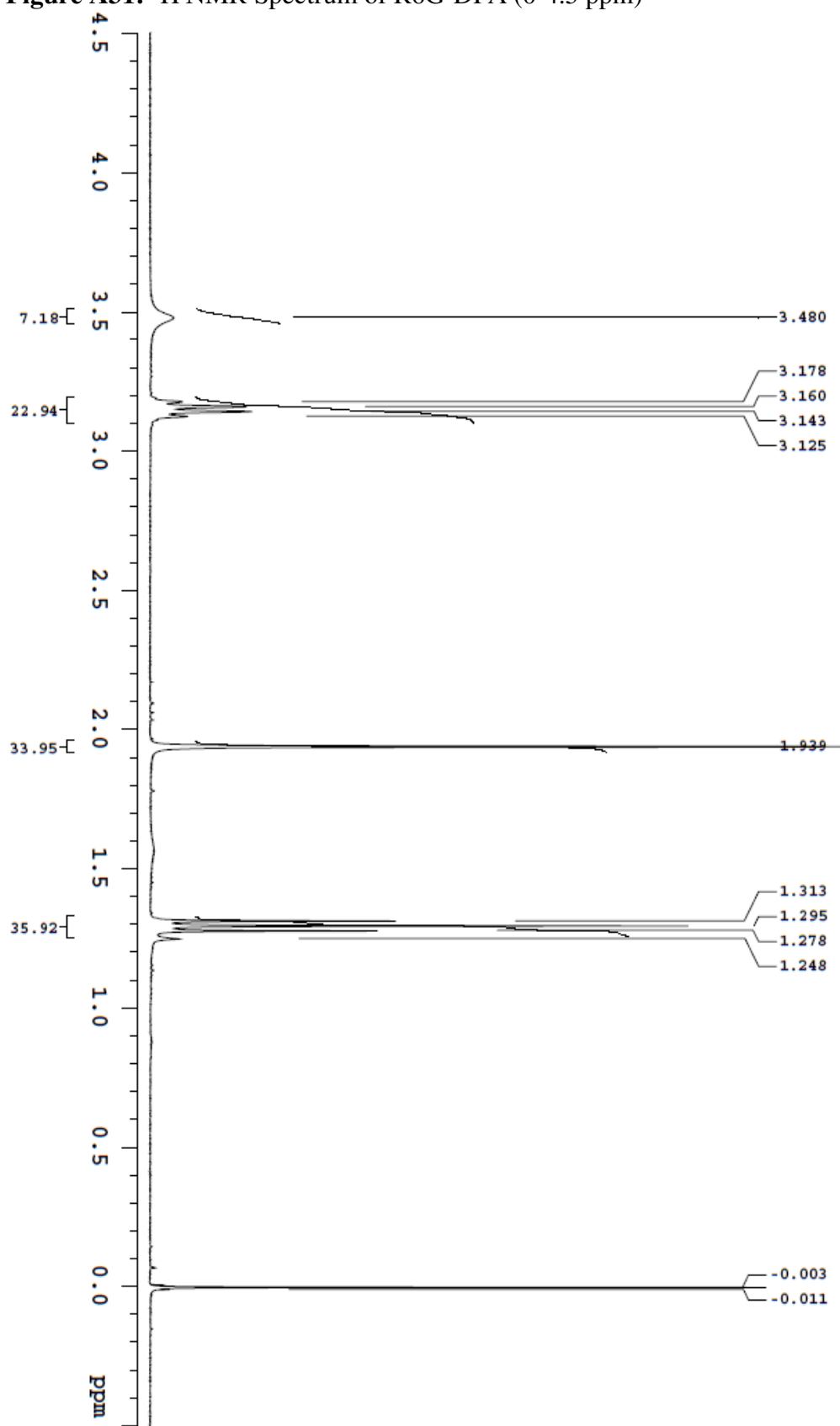
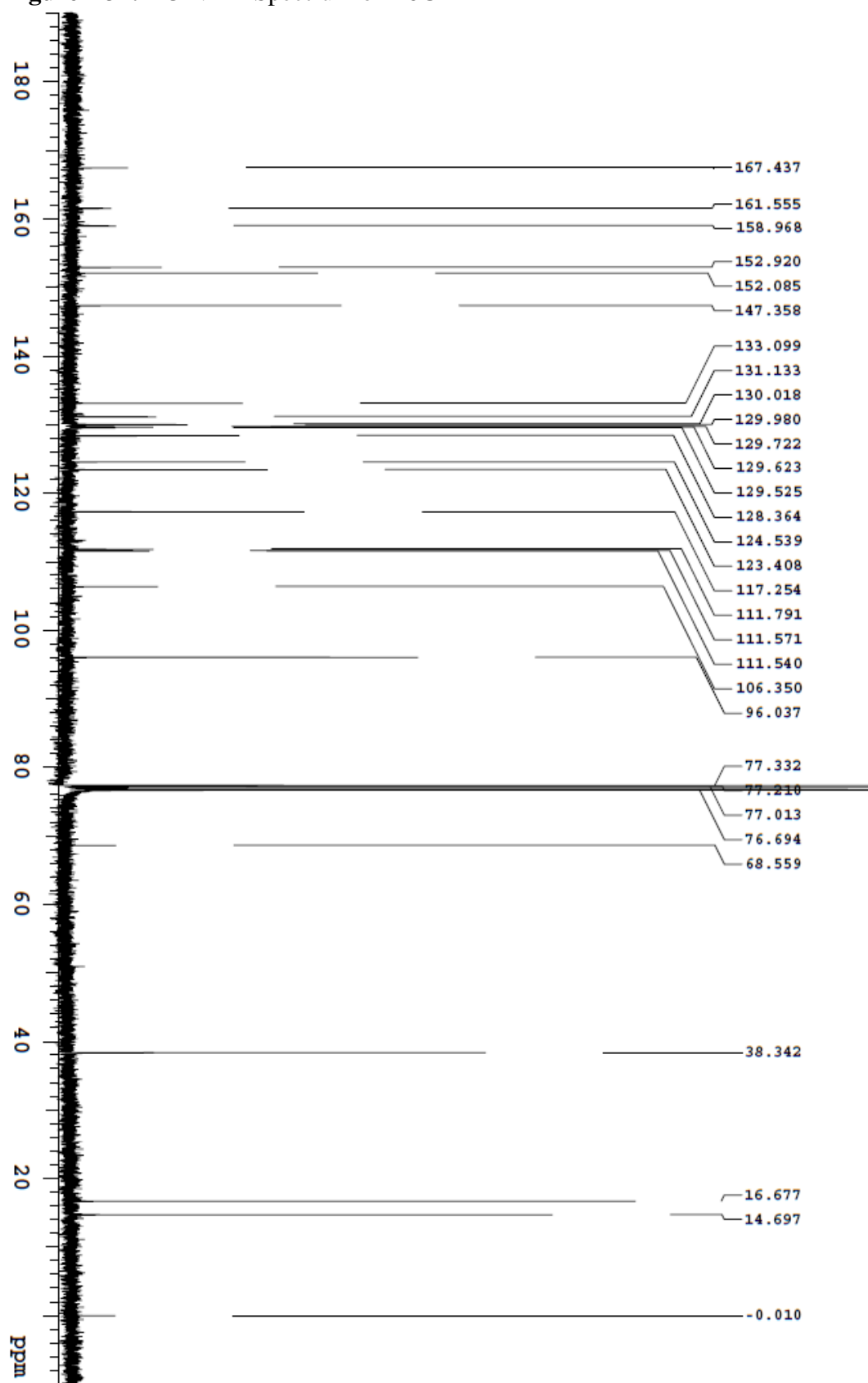
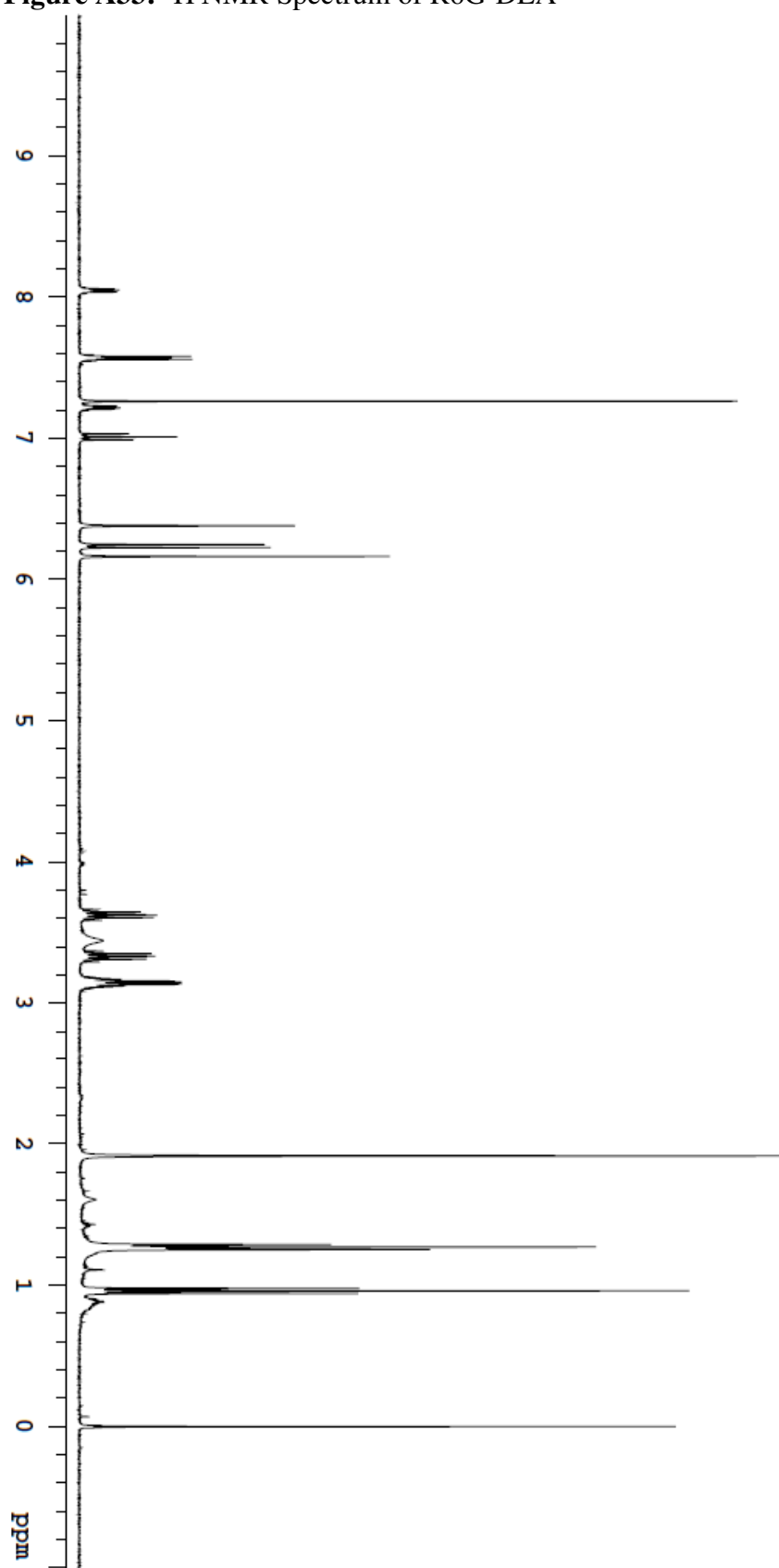
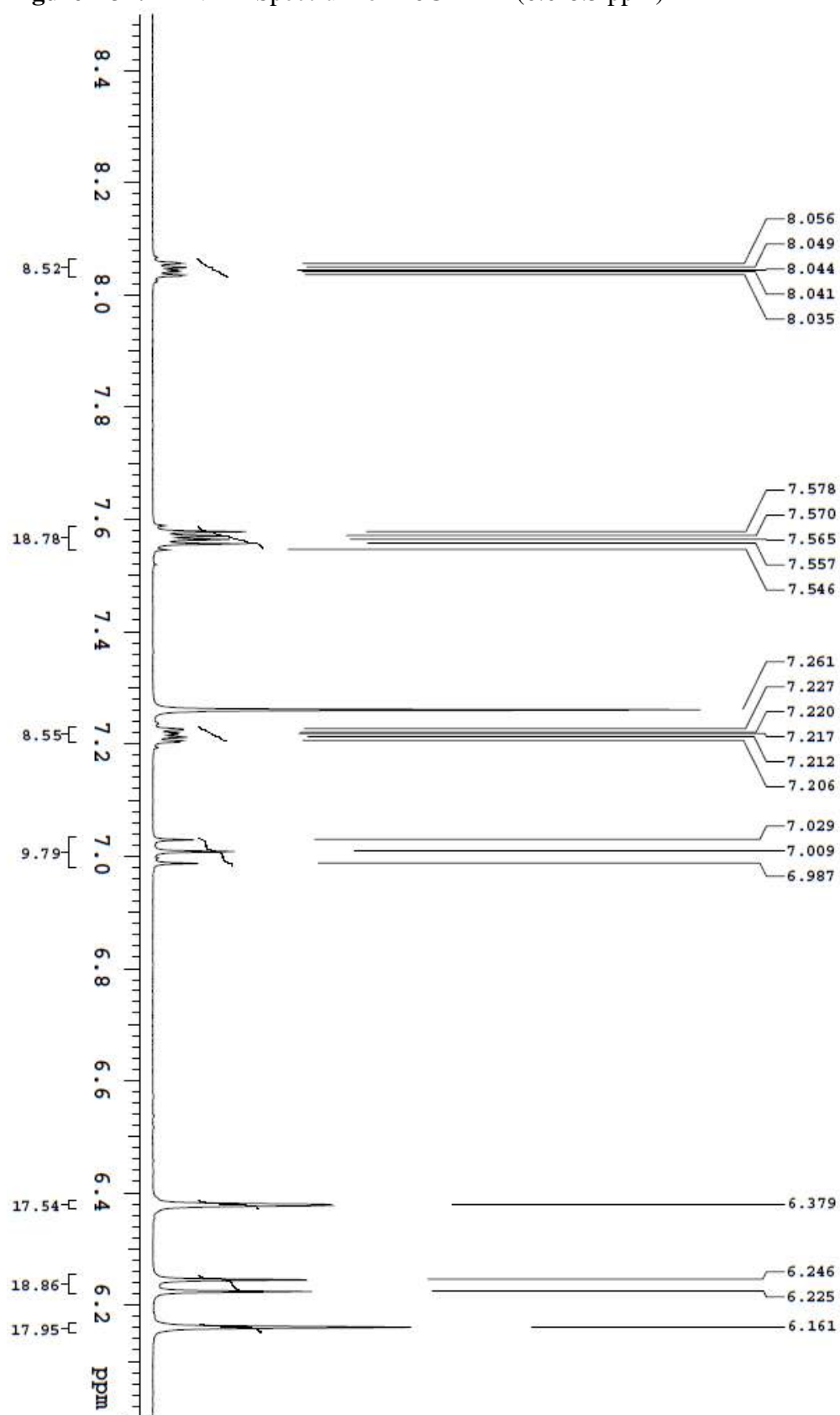
**Figure A31:**  $^1\text{H}$  NMR Spectrum of R6G-DFA (0-4.5 ppm)



Figure A32:  $^{13}\text{C}$  NMR Spectrum of R6G-DFA

**Figure A33:**  $^1\text{H}$  NMR Spectrum of R6G-DEA

**Figure A34:**  $^1\text{H}$  NMR Spectrum of R6G-DEA (6.0-8.5 ppm)

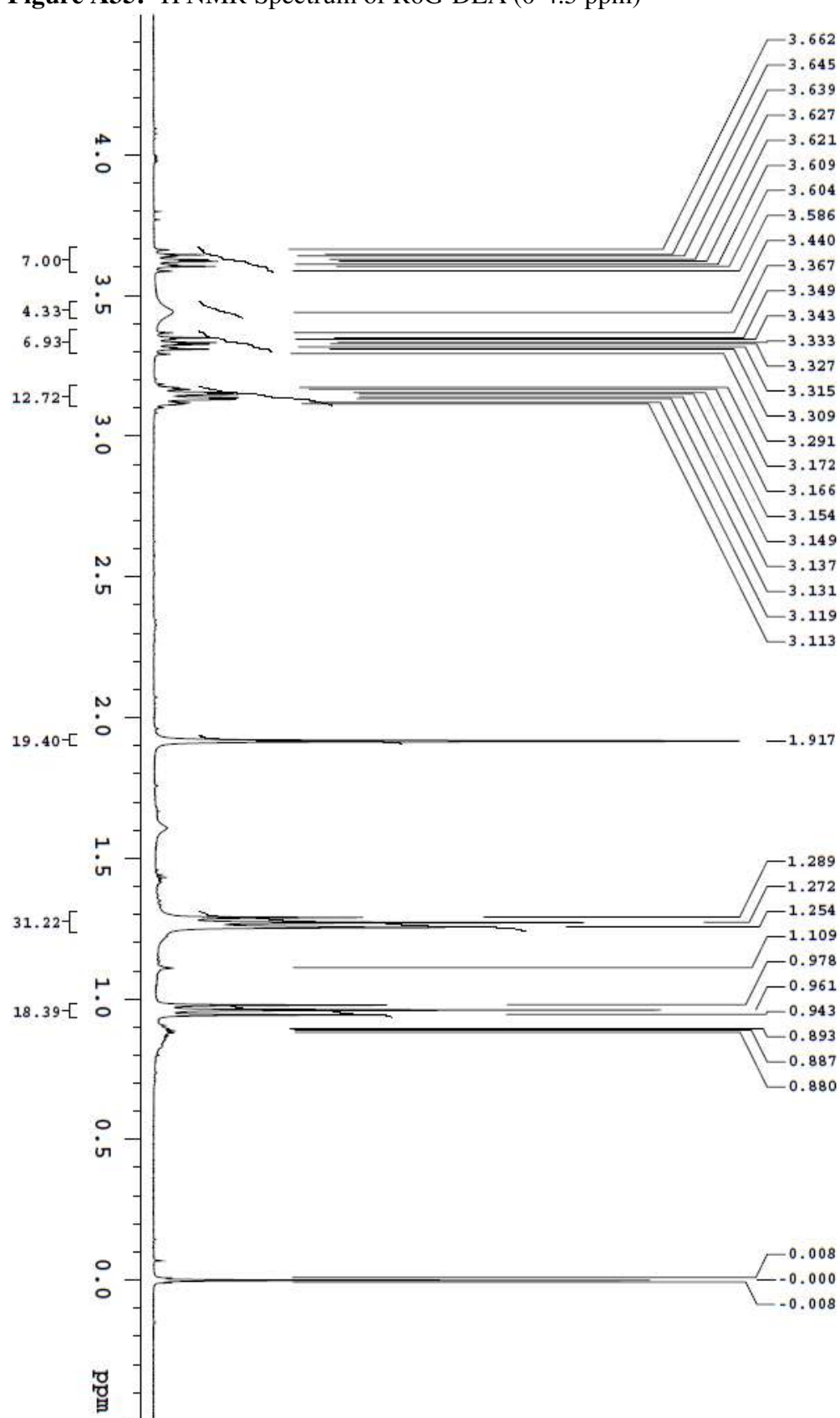
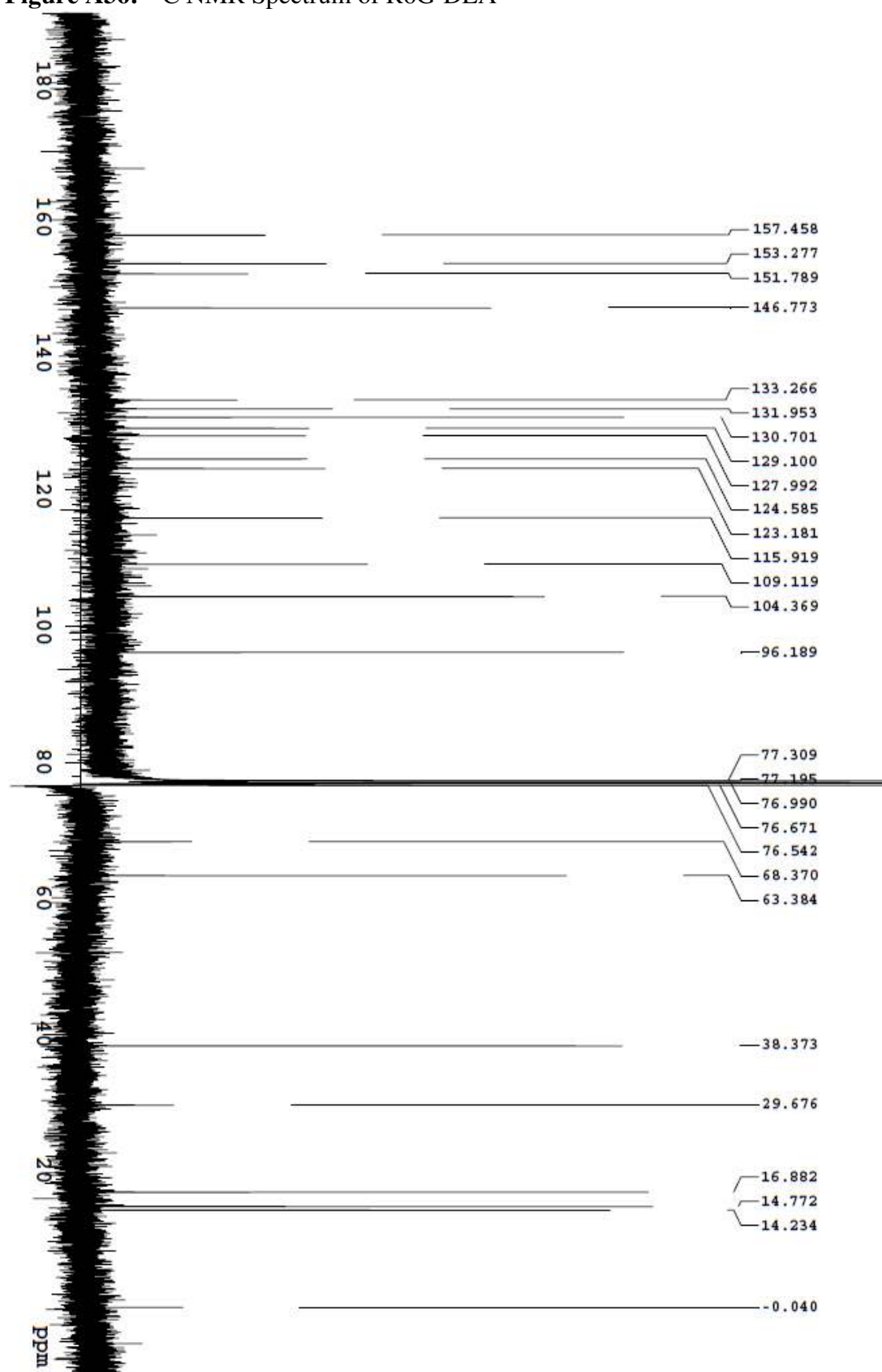
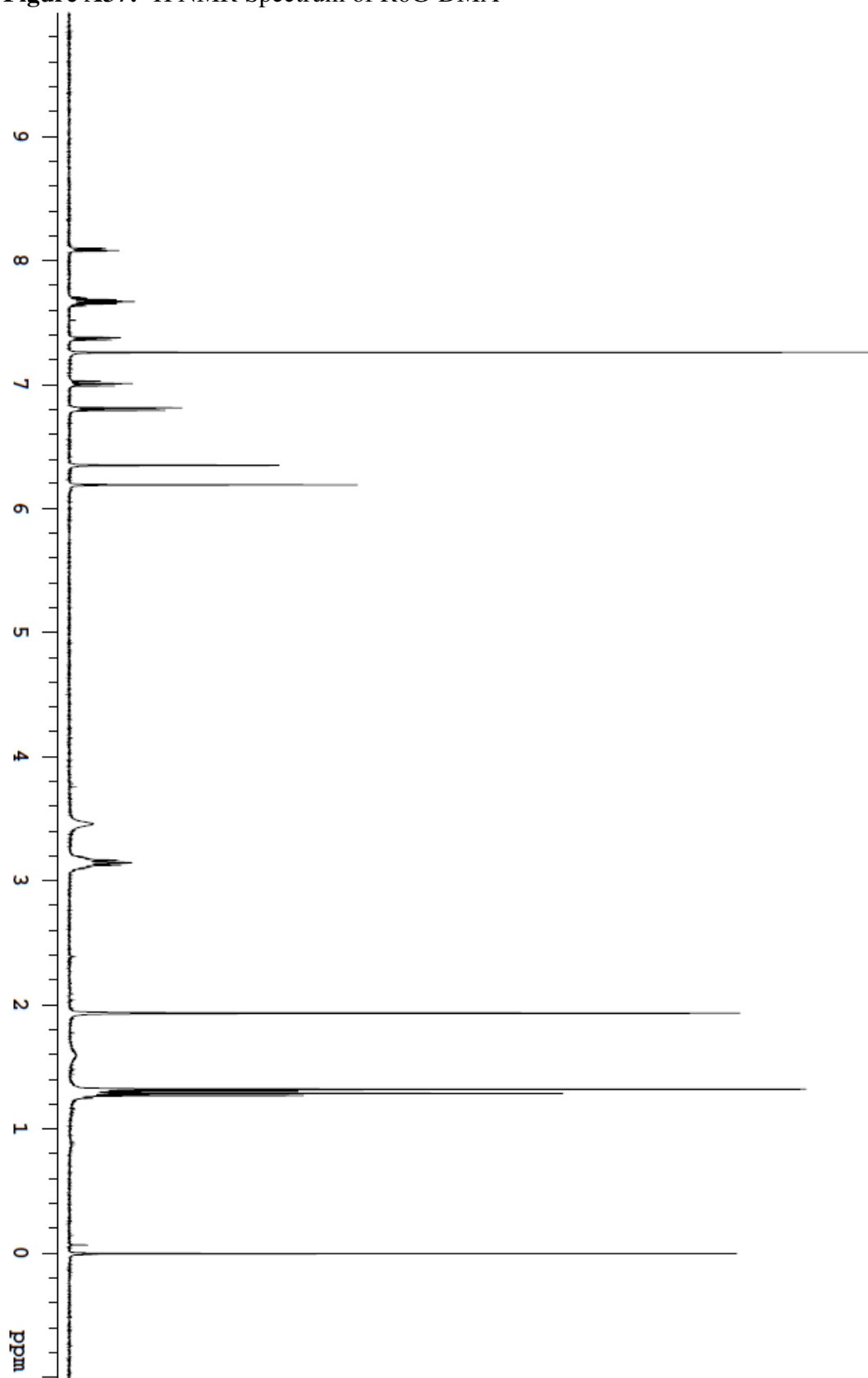
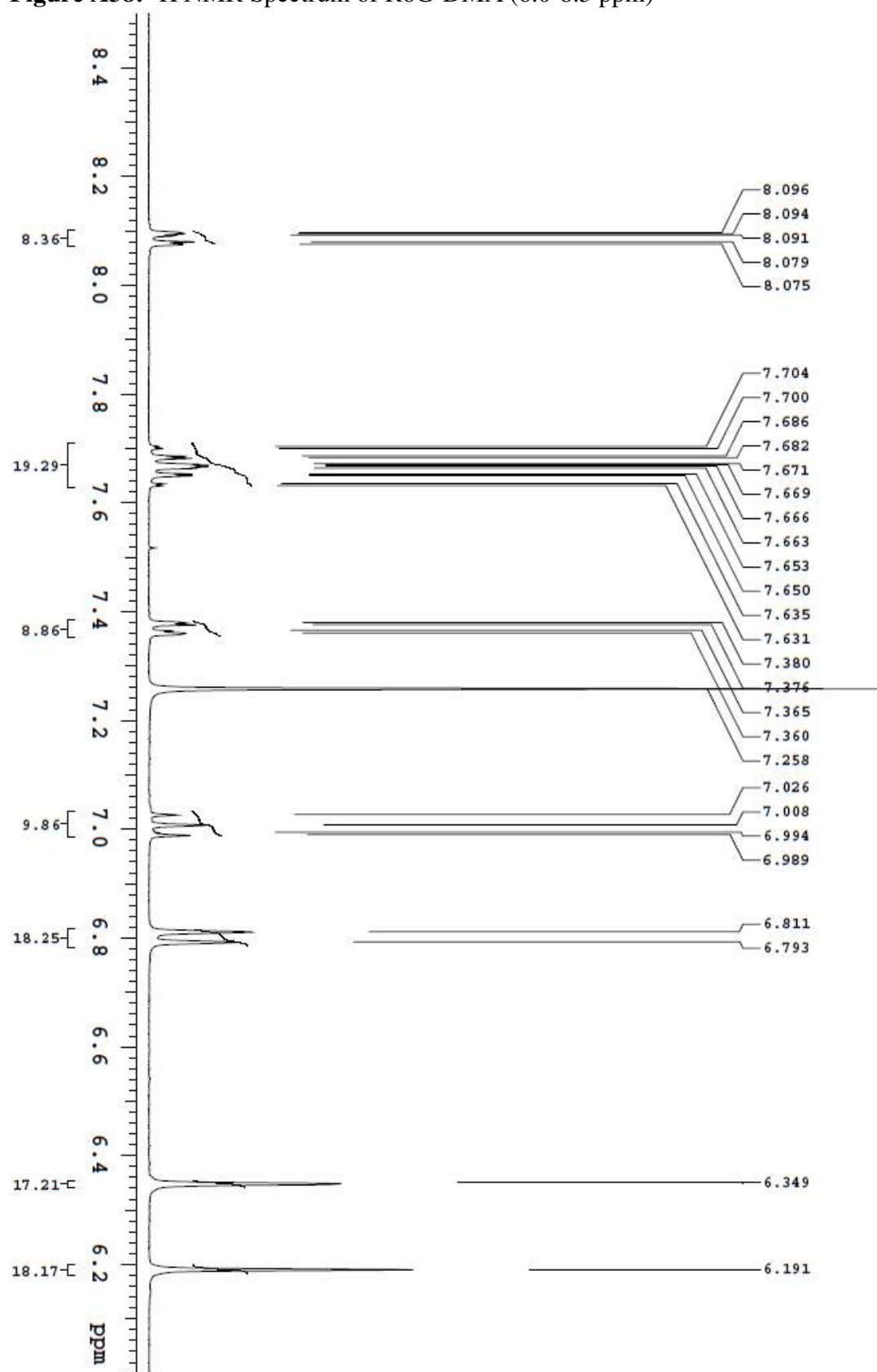
**Figure A35:**  $^1\text{H}$  NMR Spectrum of R6G-DEA (0-4.5 ppm)

Figure A36:  $^{13}\text{C}$  NMR Spectrum of R6G-DEA

**Figure A37:**  $^1\text{H}$  NMR Spectrum of R6G-DMA

**Figure A38:**  $^1\text{H}$  NMR Spectrum of R6G-DMA (6.0-8.5 ppm)

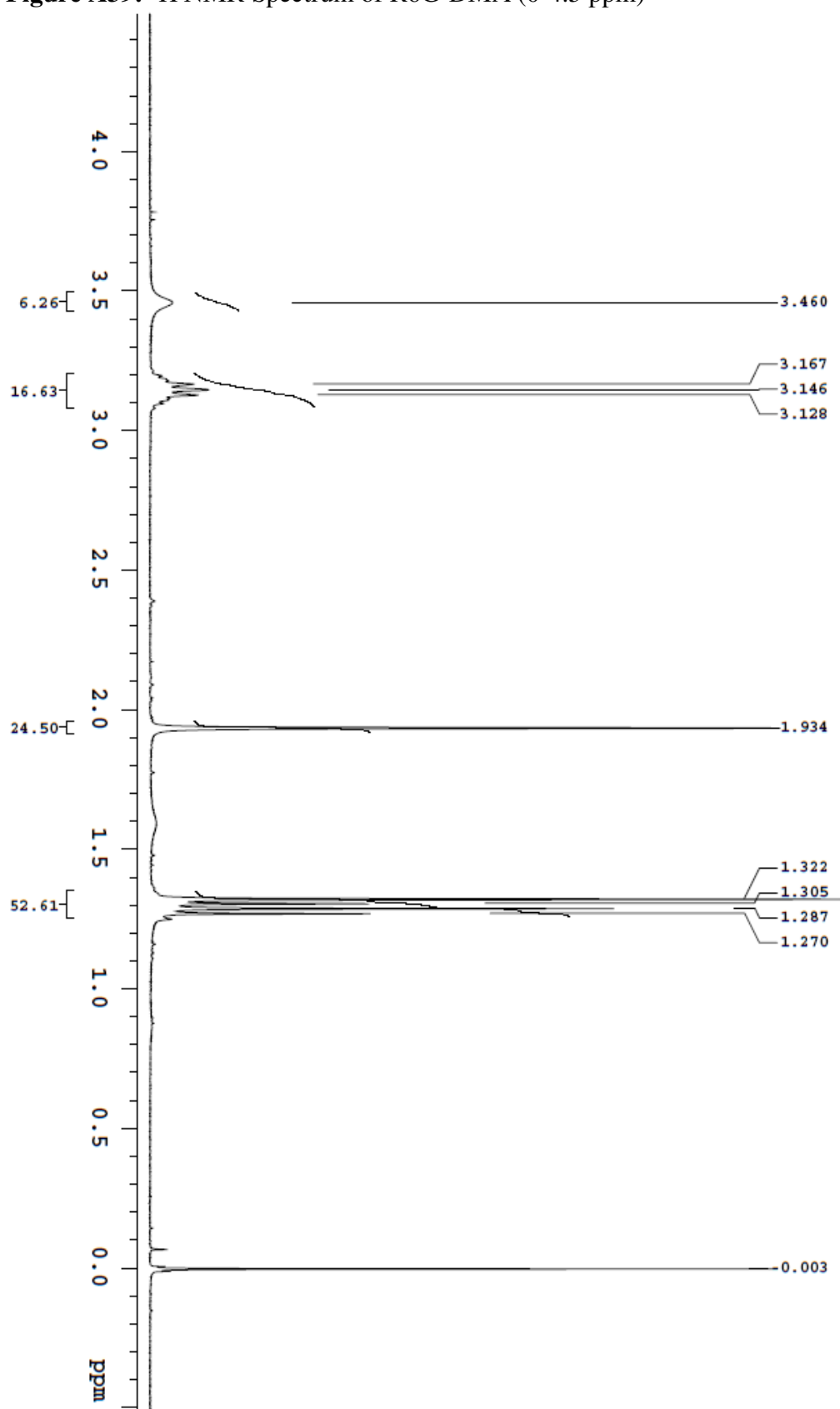
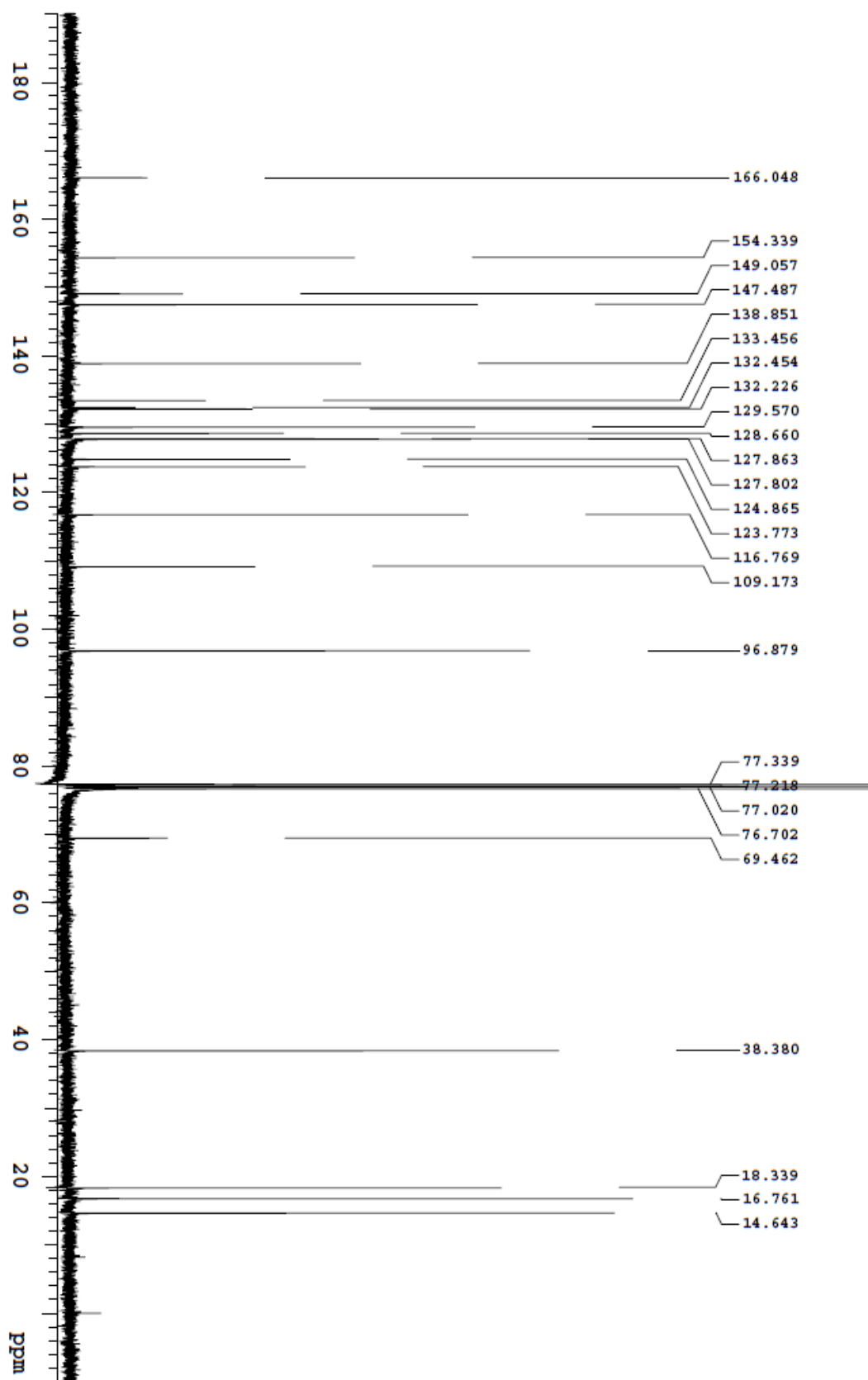
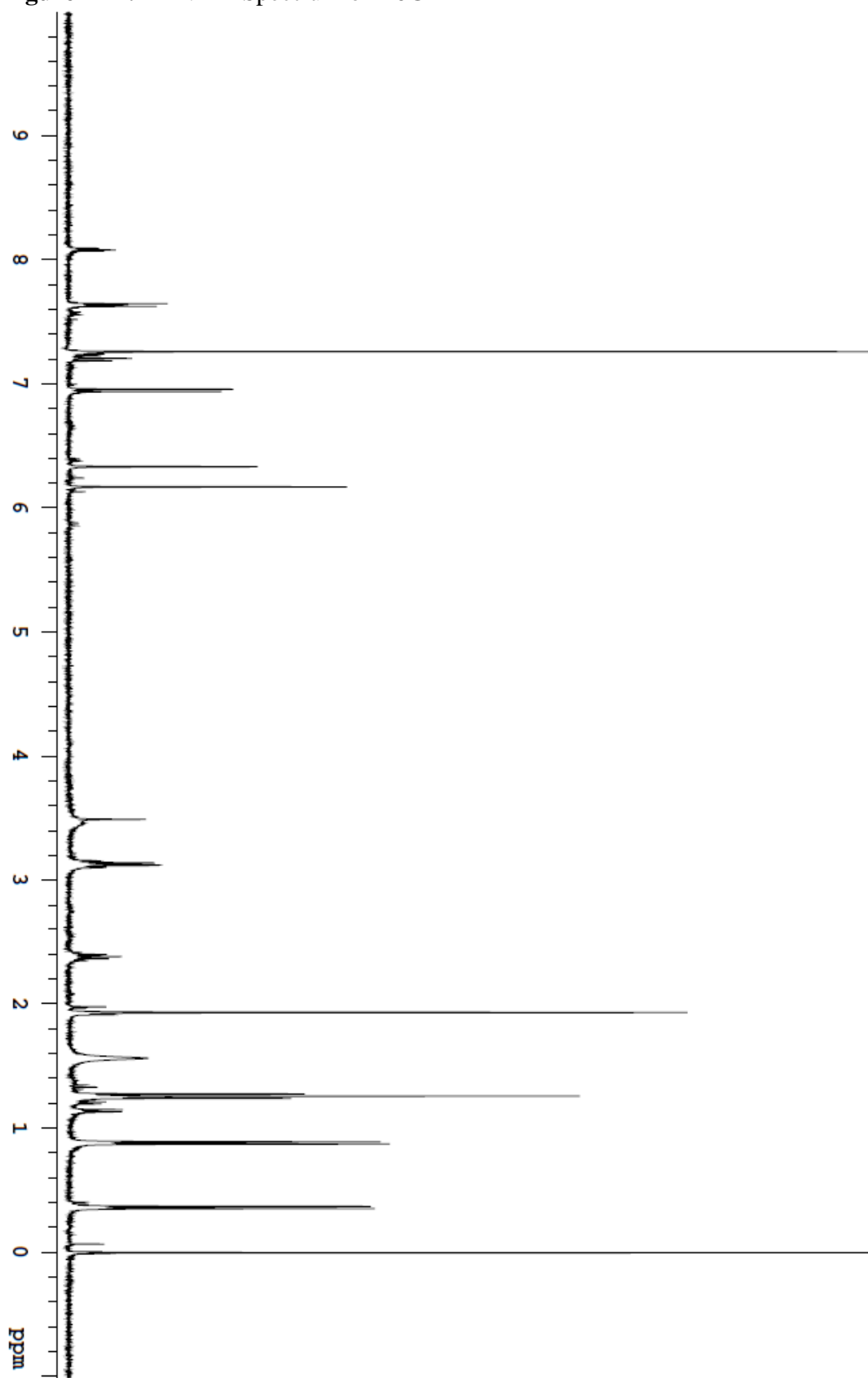
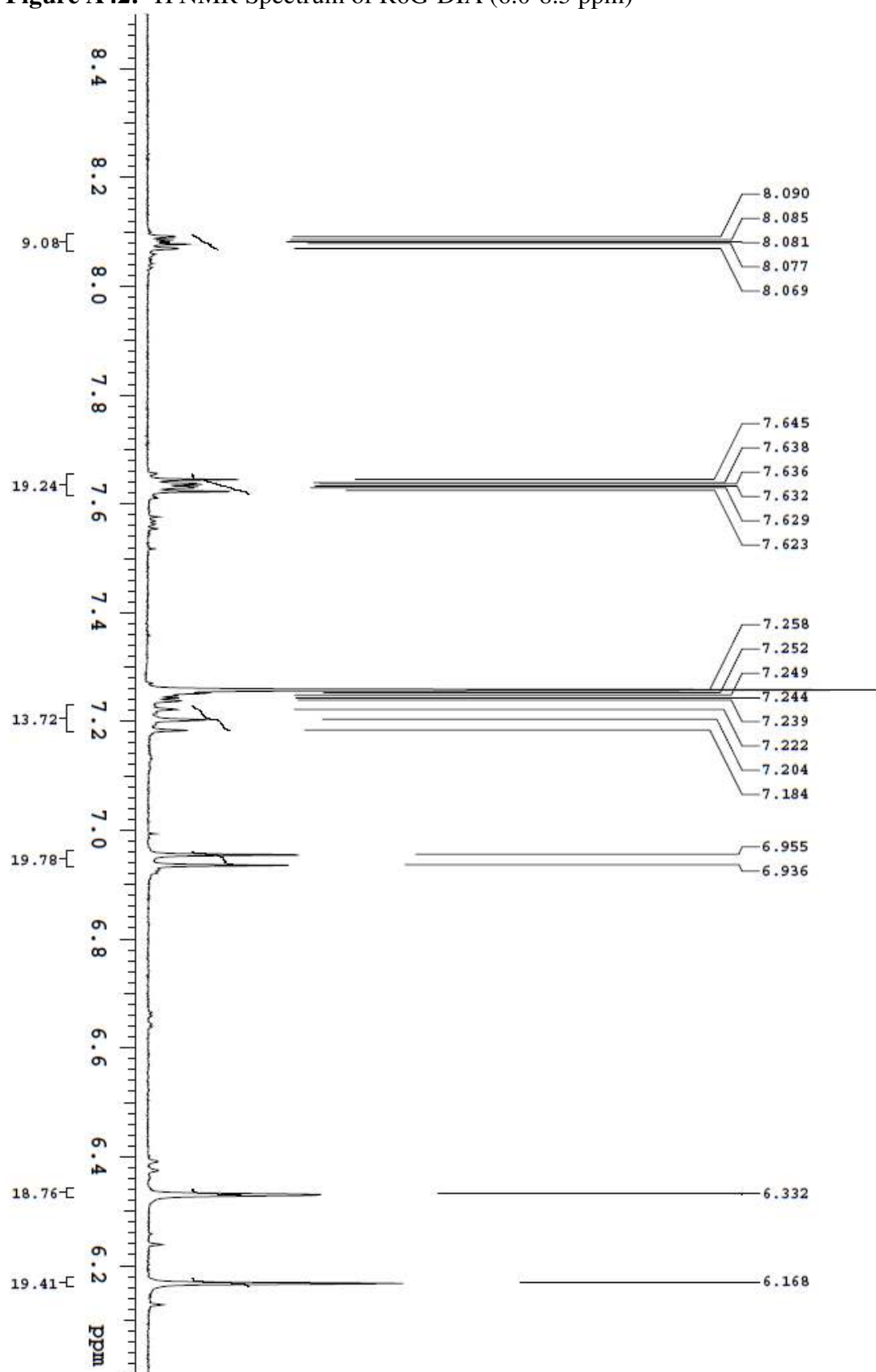
**Figure A39:**  $^1\text{H}$  NMR Spectrum of R6G-DMA (0-4.5 ppm)



Figure A40:  $^{13}\text{C}$  NMR Spectrum of R6G-DMA

**Figure A41:**  $^1\text{H}$  NMR Spectrum of R6G-DIA

**Figure A42:**  $^1\text{H}$  NMR Spectrum of R6G-DIA (6.0-8.5 ppm)

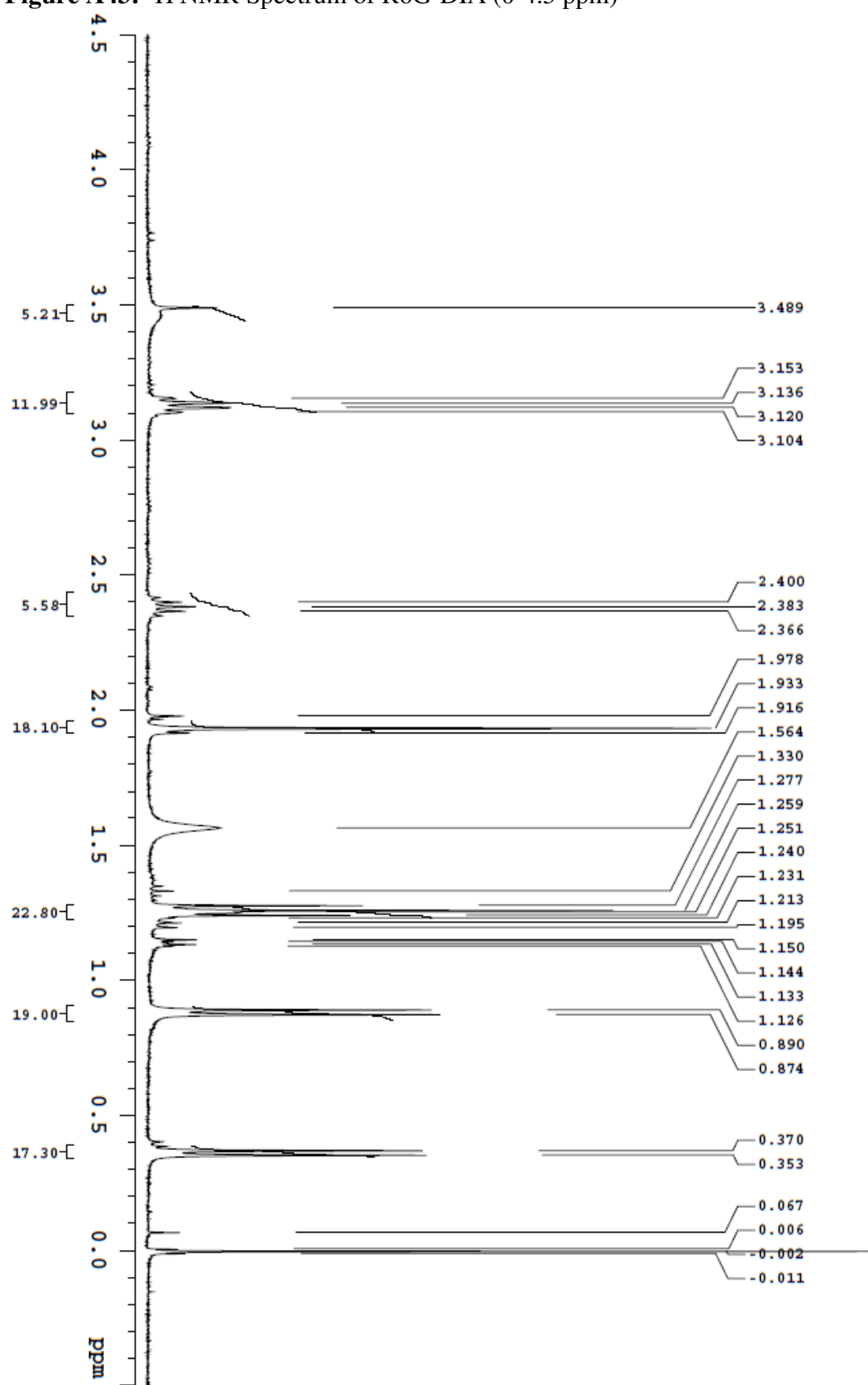
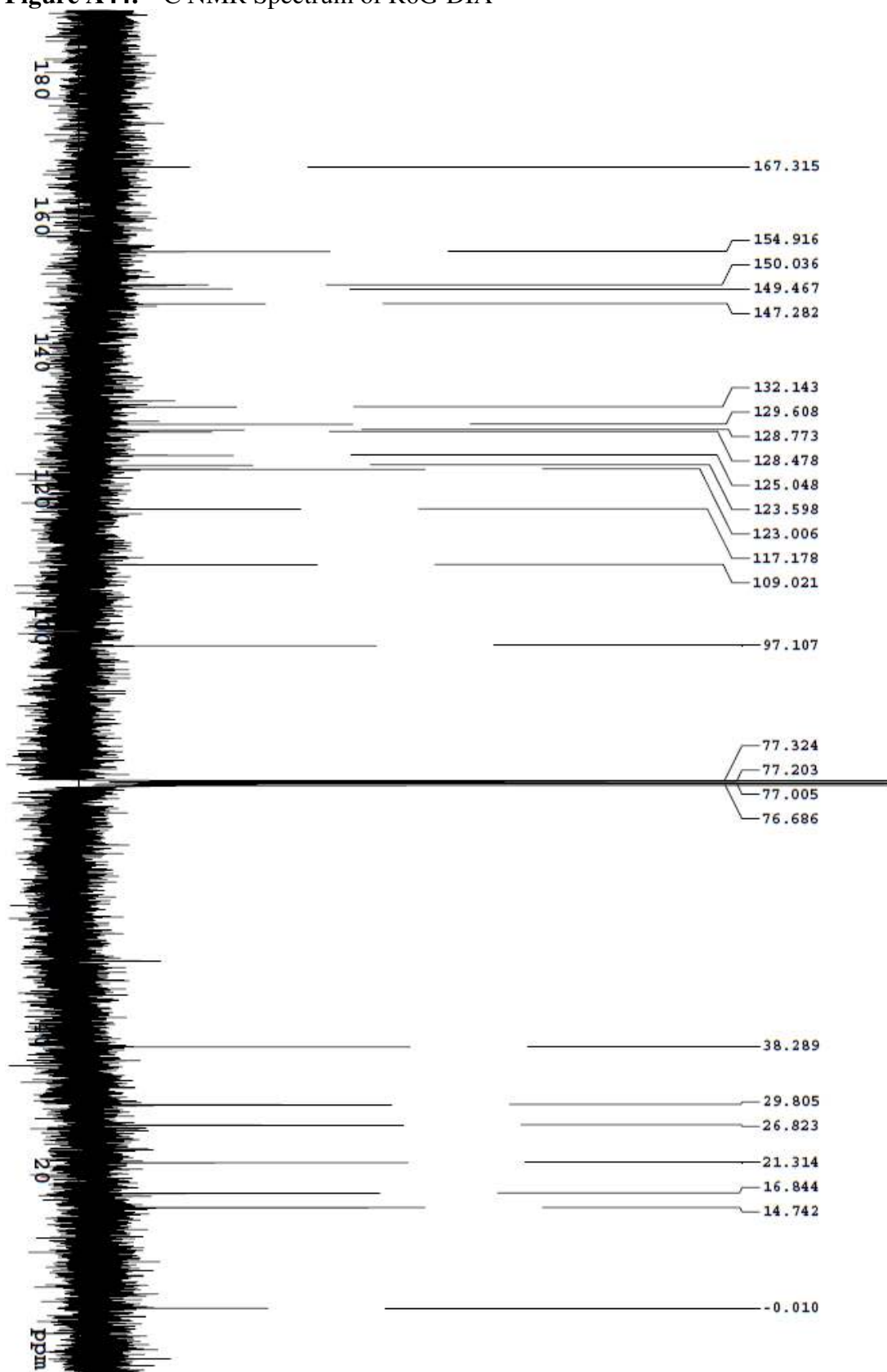
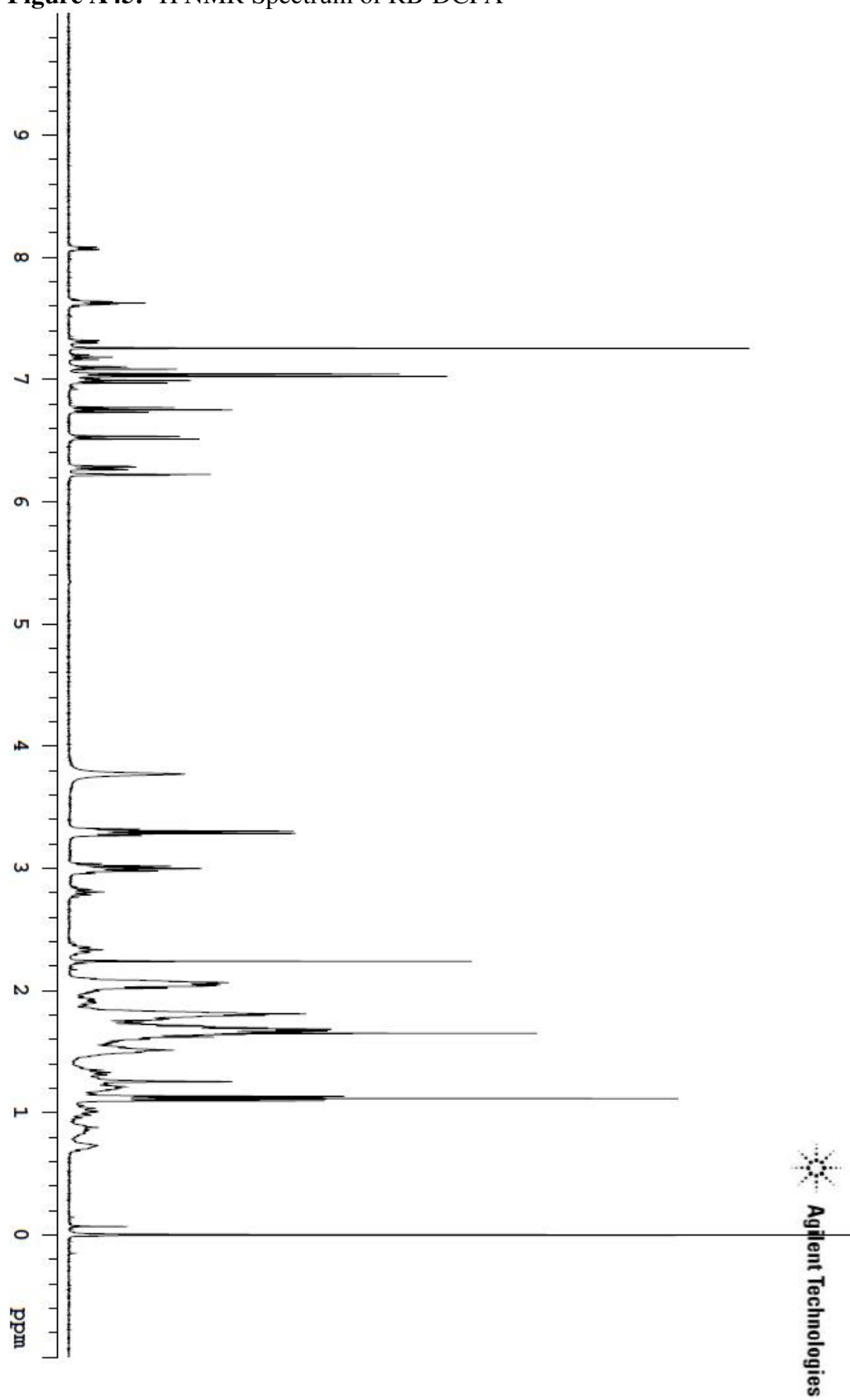
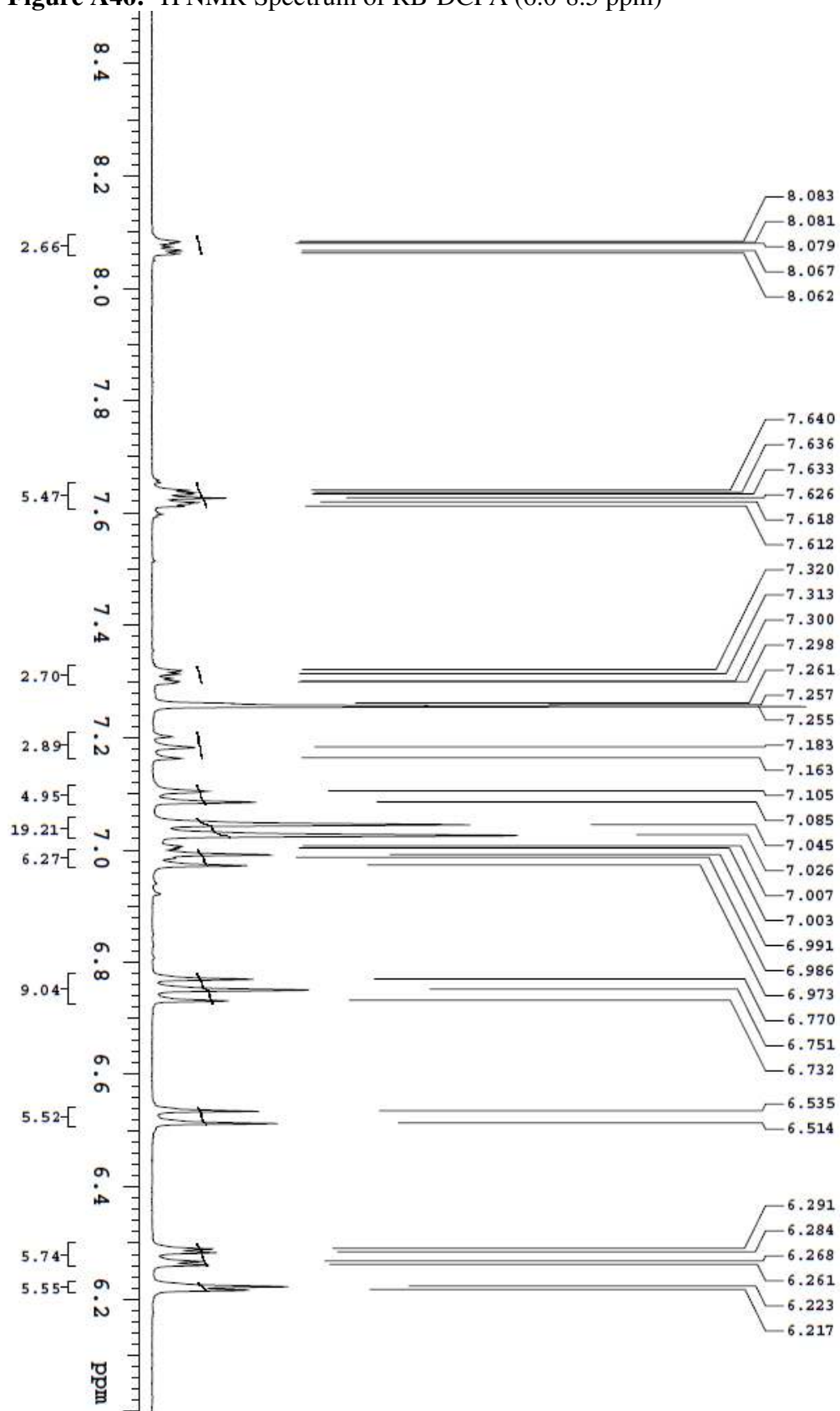
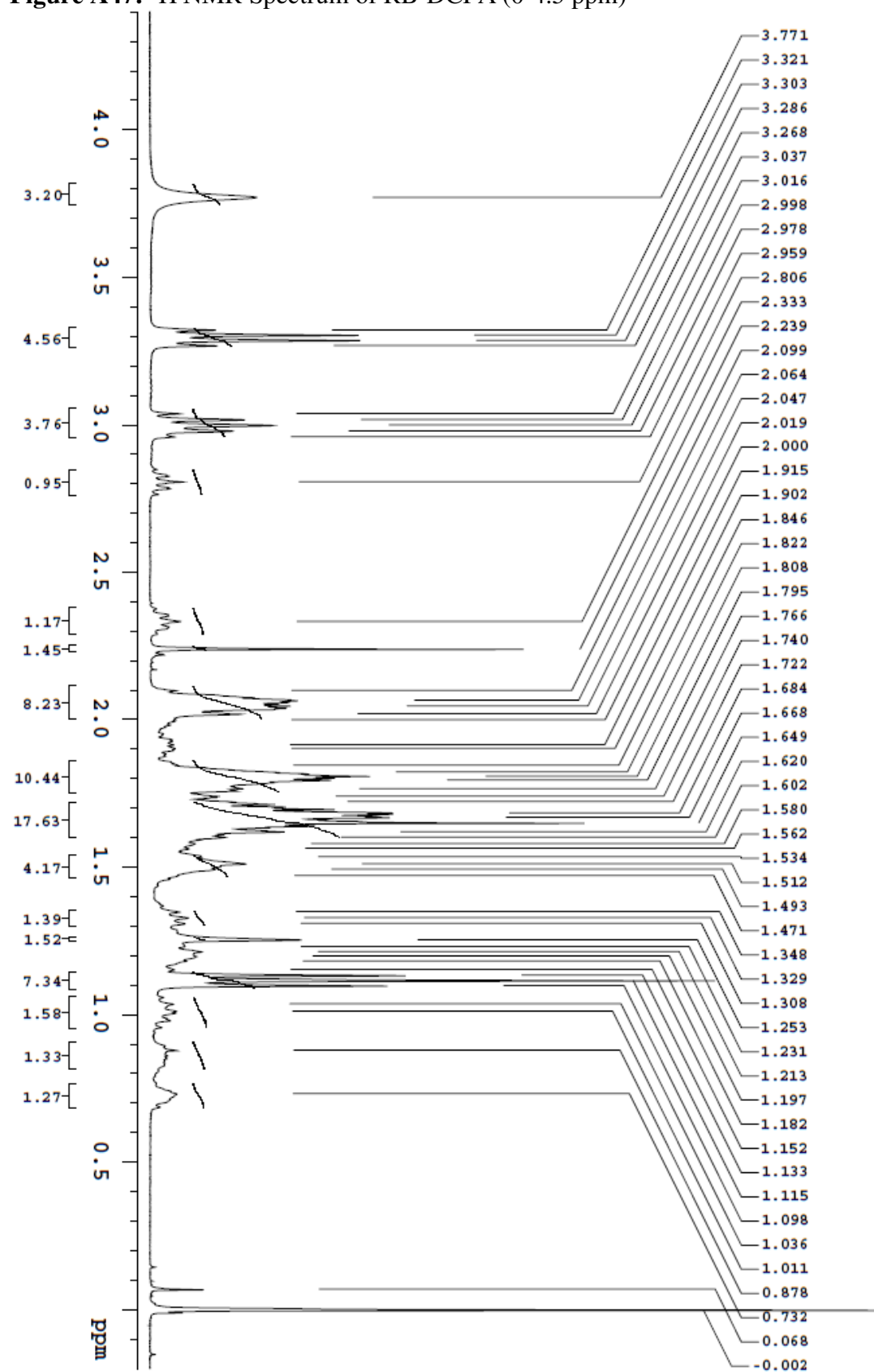
**Figure A43:**  $^1\text{H}$  NMR Spectrum of R6G-DIA (0-4.5 ppm)

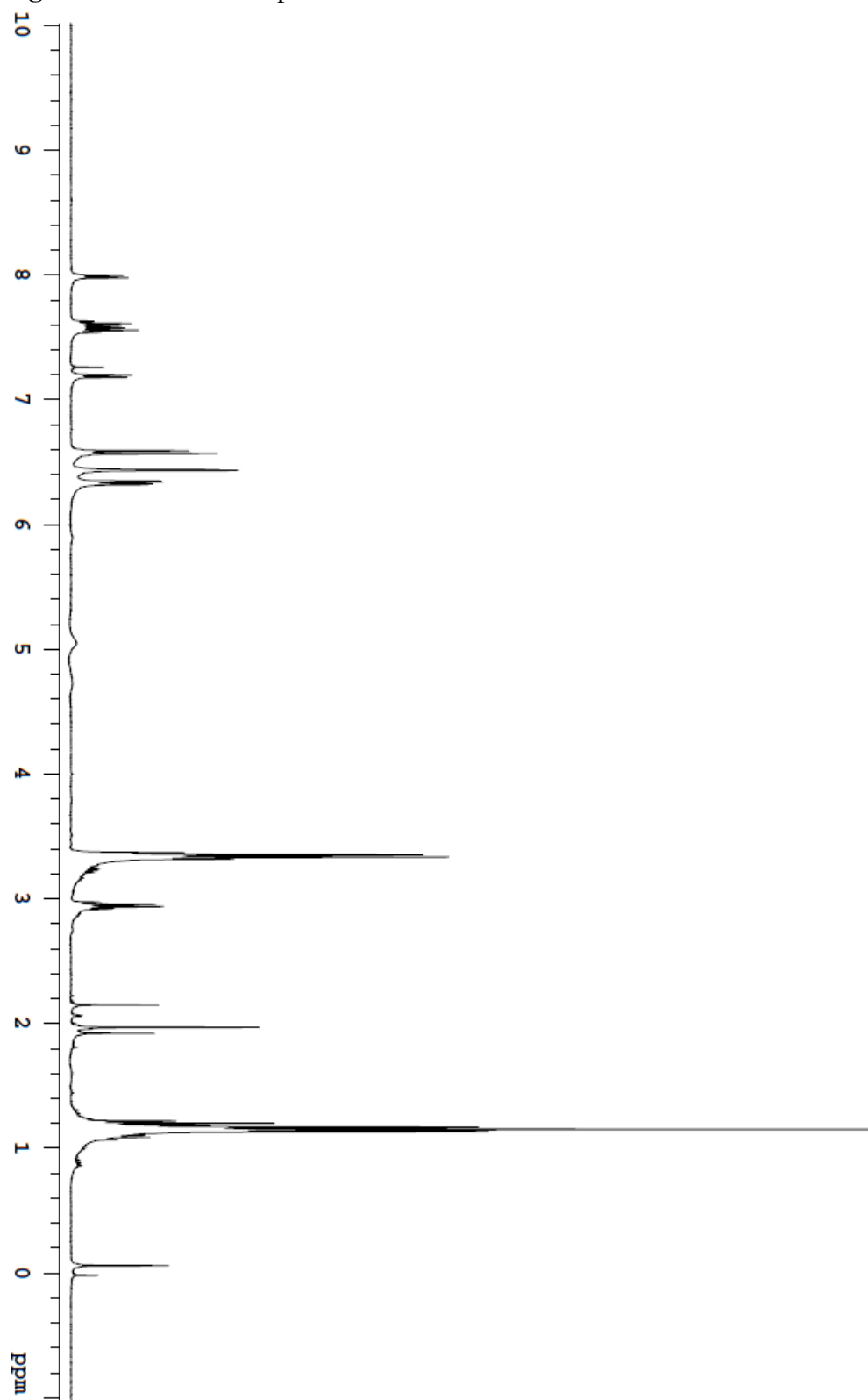
Figure A44:  $^{13}\text{C}$  NMR Spectrum of R6G-DIA

**Figure A45:**  $^1\text{H}$  NMR Spectrum of RB-DCPA

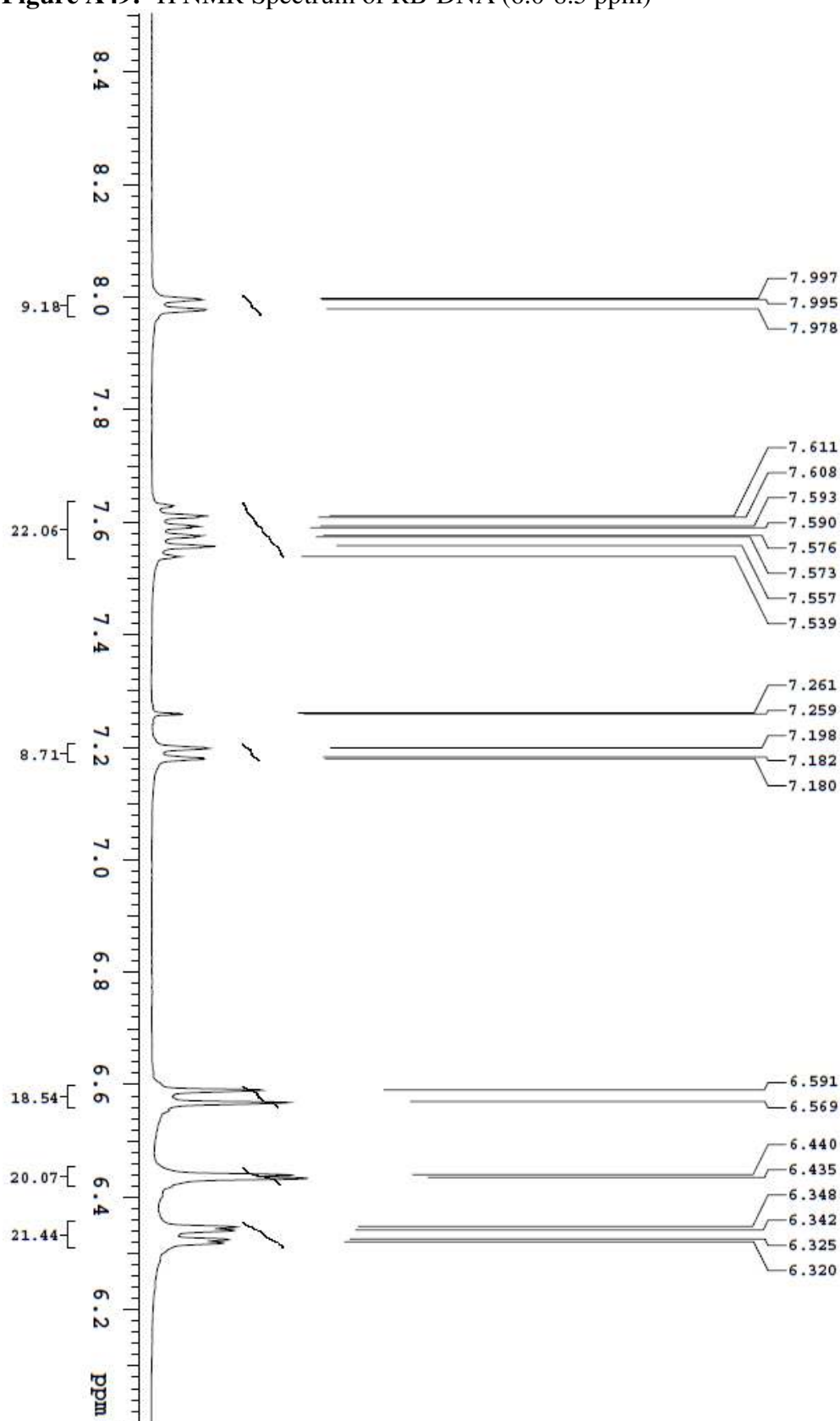
**Figure A46:**  $^1\text{H}$  NMR Spectrum of RB-DCPA (6.0-8.5 ppm)

**Figure A47:**  $^1\text{H}$  NMR Spectrum of RB-DCPA (0-4.5 ppm)



**Figure A48:**  $^1\text{H}$  NMR Spectrum of RB-DNA<sup>16</sup>

<sup>16</sup> NMR by Grace Purnell

**Figure A49:**  $^1\text{H}$  NMR Spectrum of RB-DNA (6.0-8.5 ppm)<sup>16</sup>

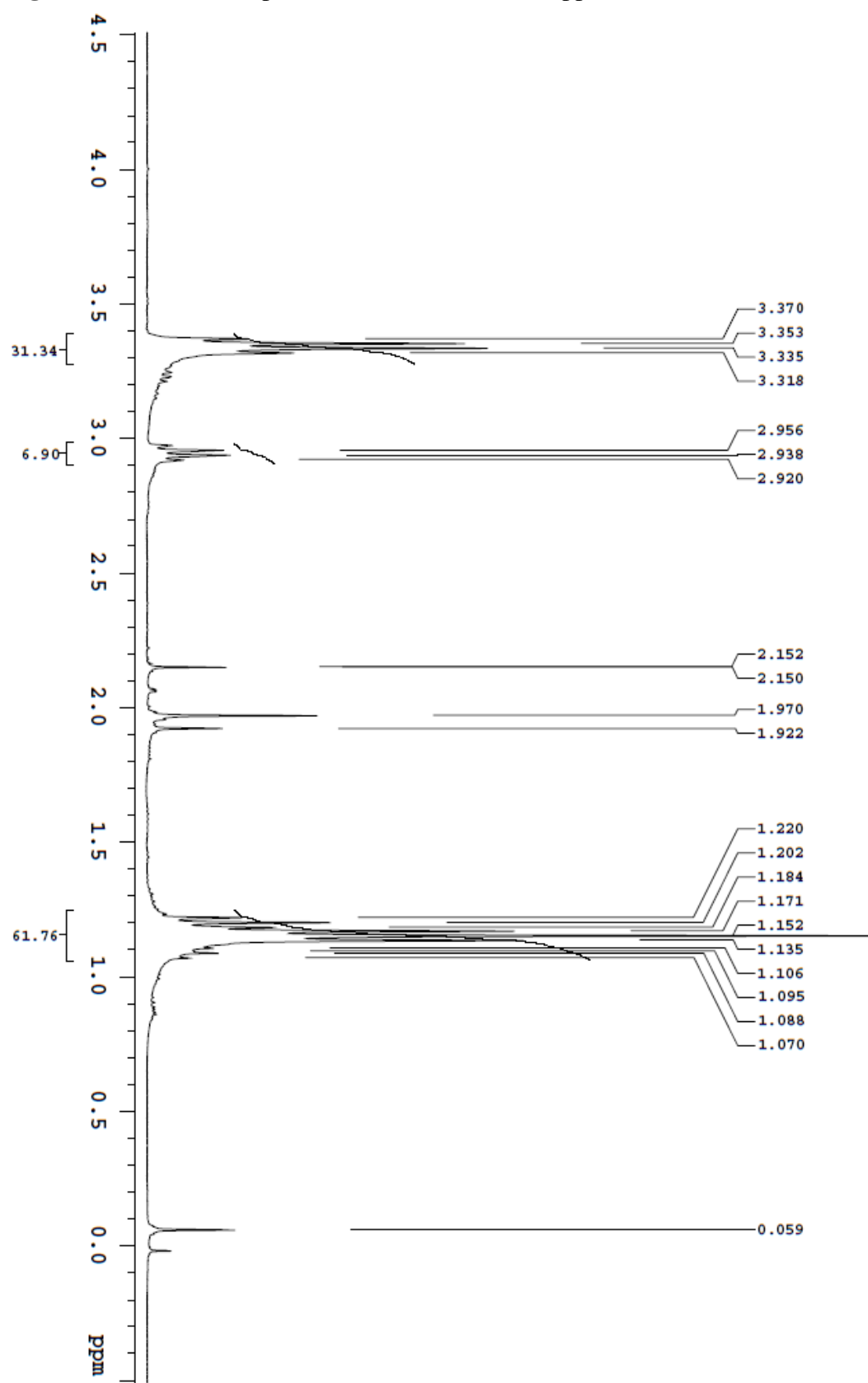
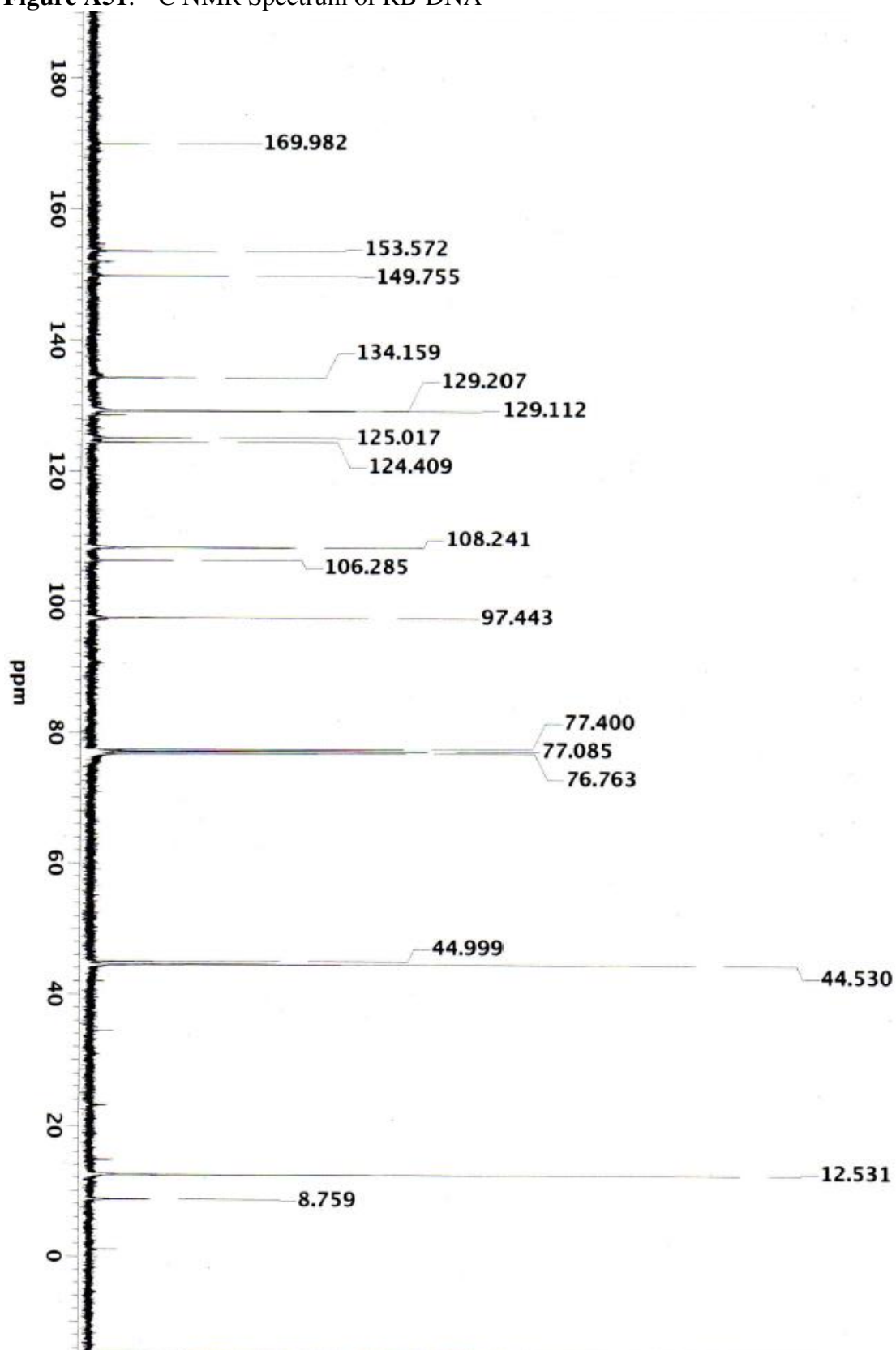
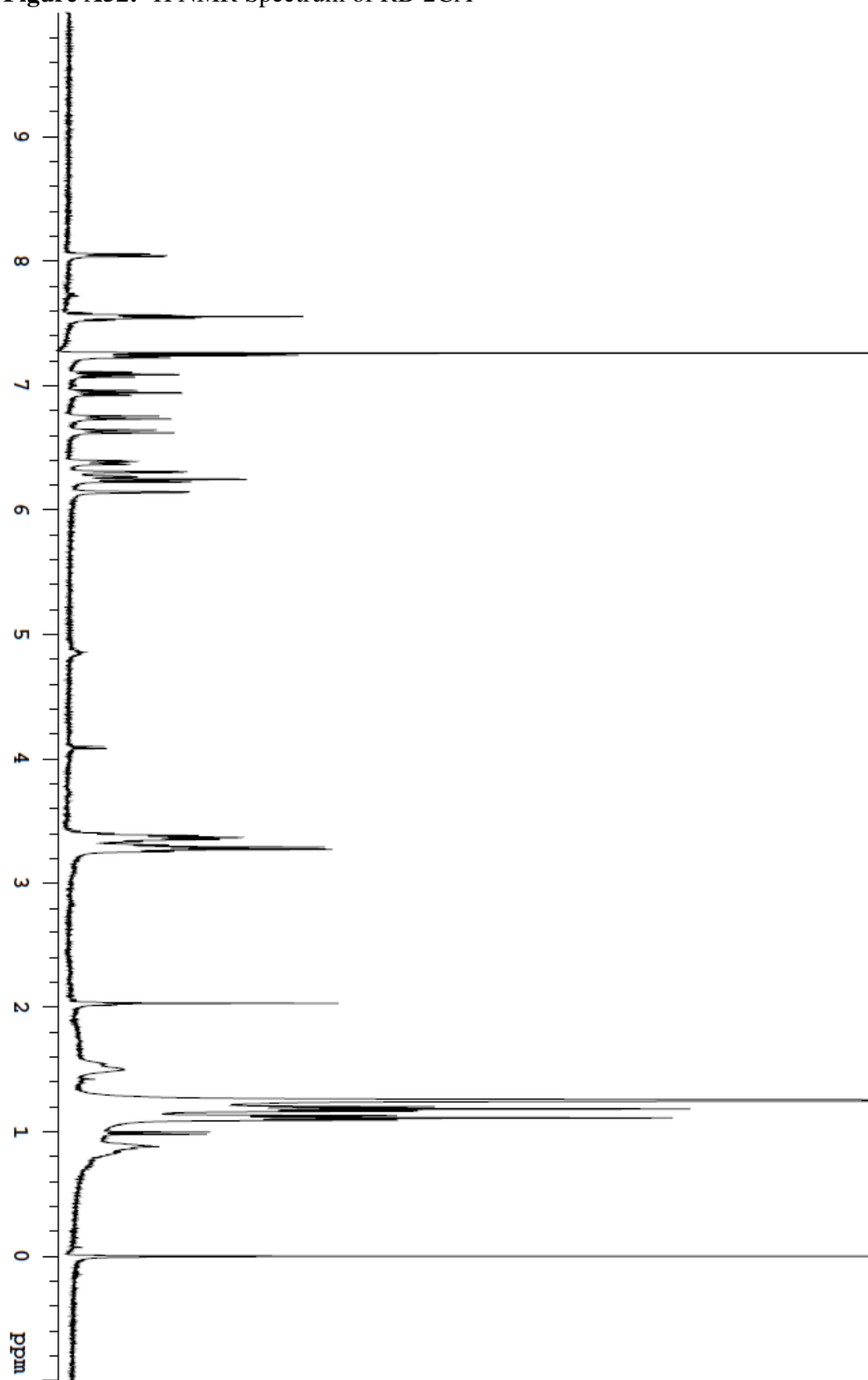
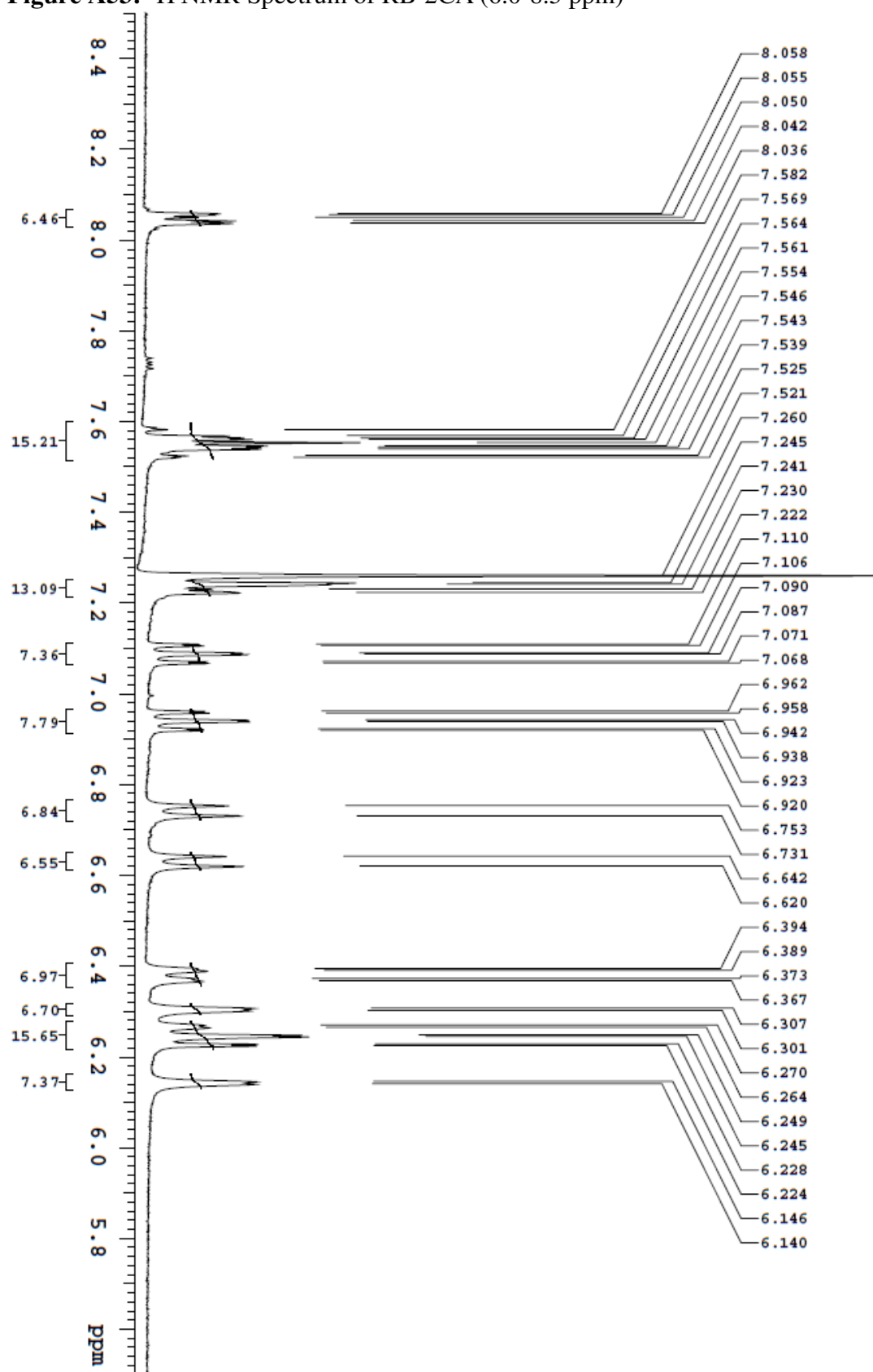
**Figure A50:**  $^1\text{H}$  NMR Spectrum of RB-DNA (0-4.5 ppm)<sup>16</sup>

Figure A51:  $^{13}\text{C}$  NMR Spectrum of RB-DNA<sup>16</sup>

**Figure A52:**  $^1\text{H}$  NMR Spectrum of RB-2CA

**Figure A53:**  $^1\text{H}$  NMR Spectrum of RB-2CA (6.0-8.5 ppm)

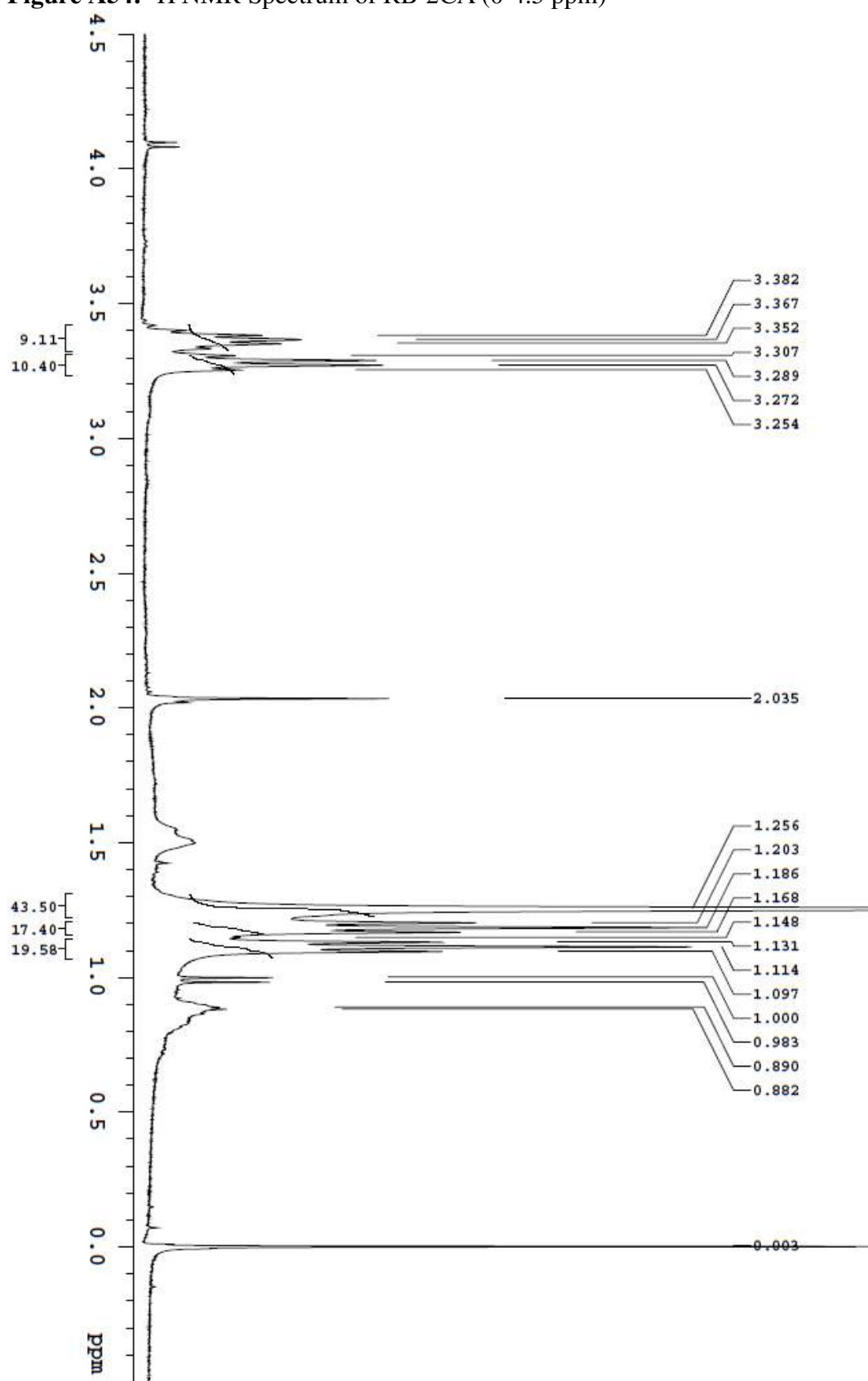
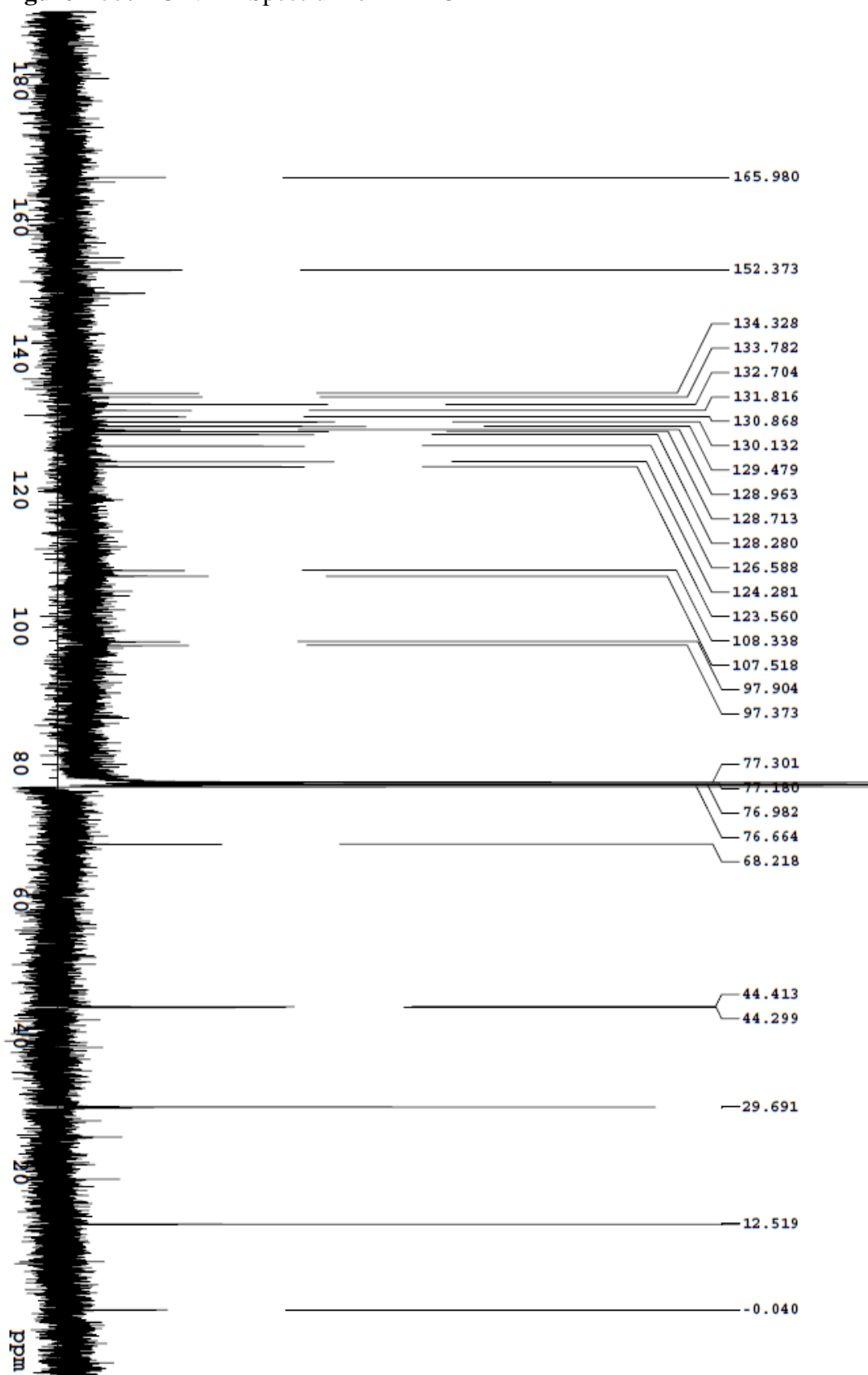
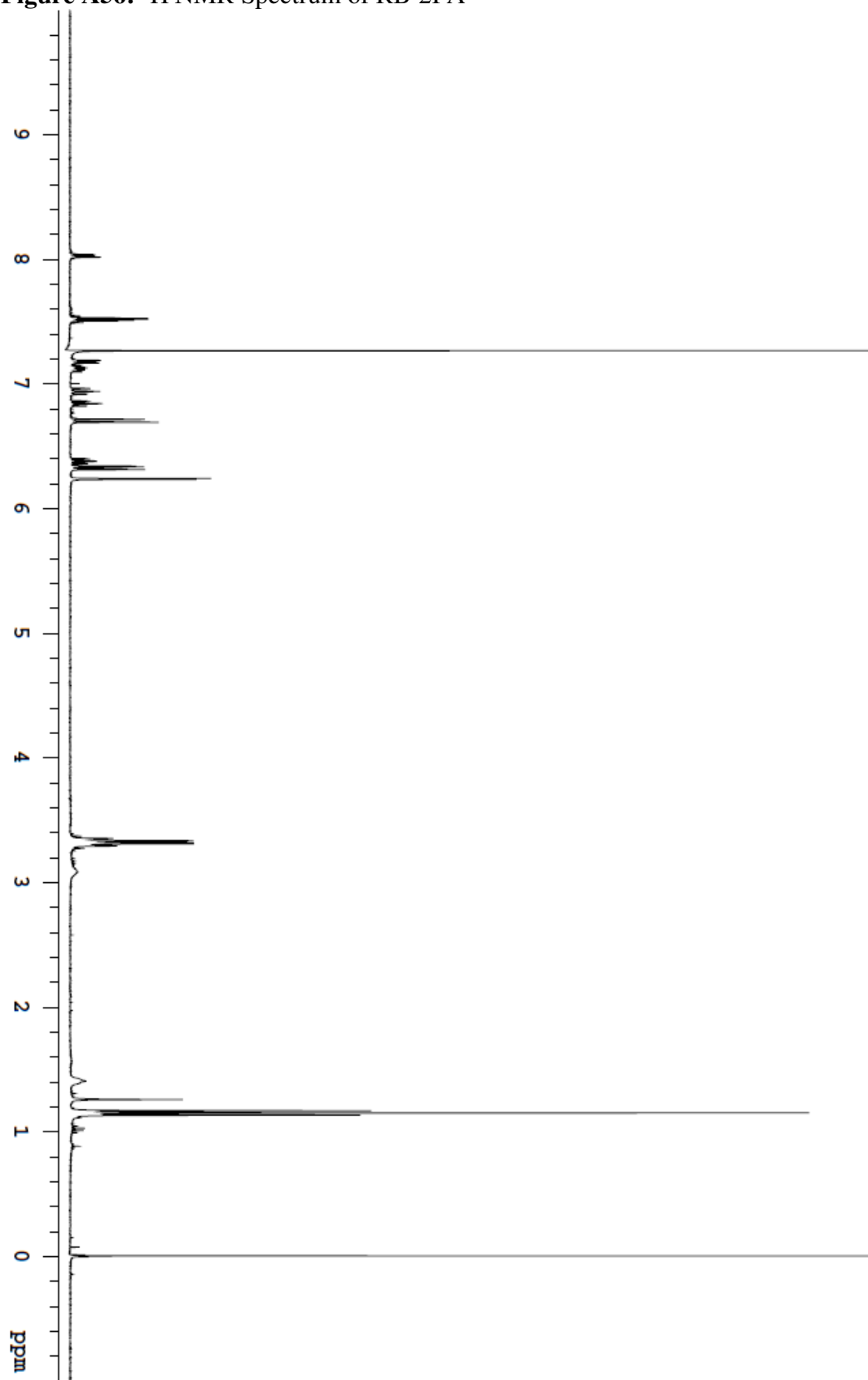
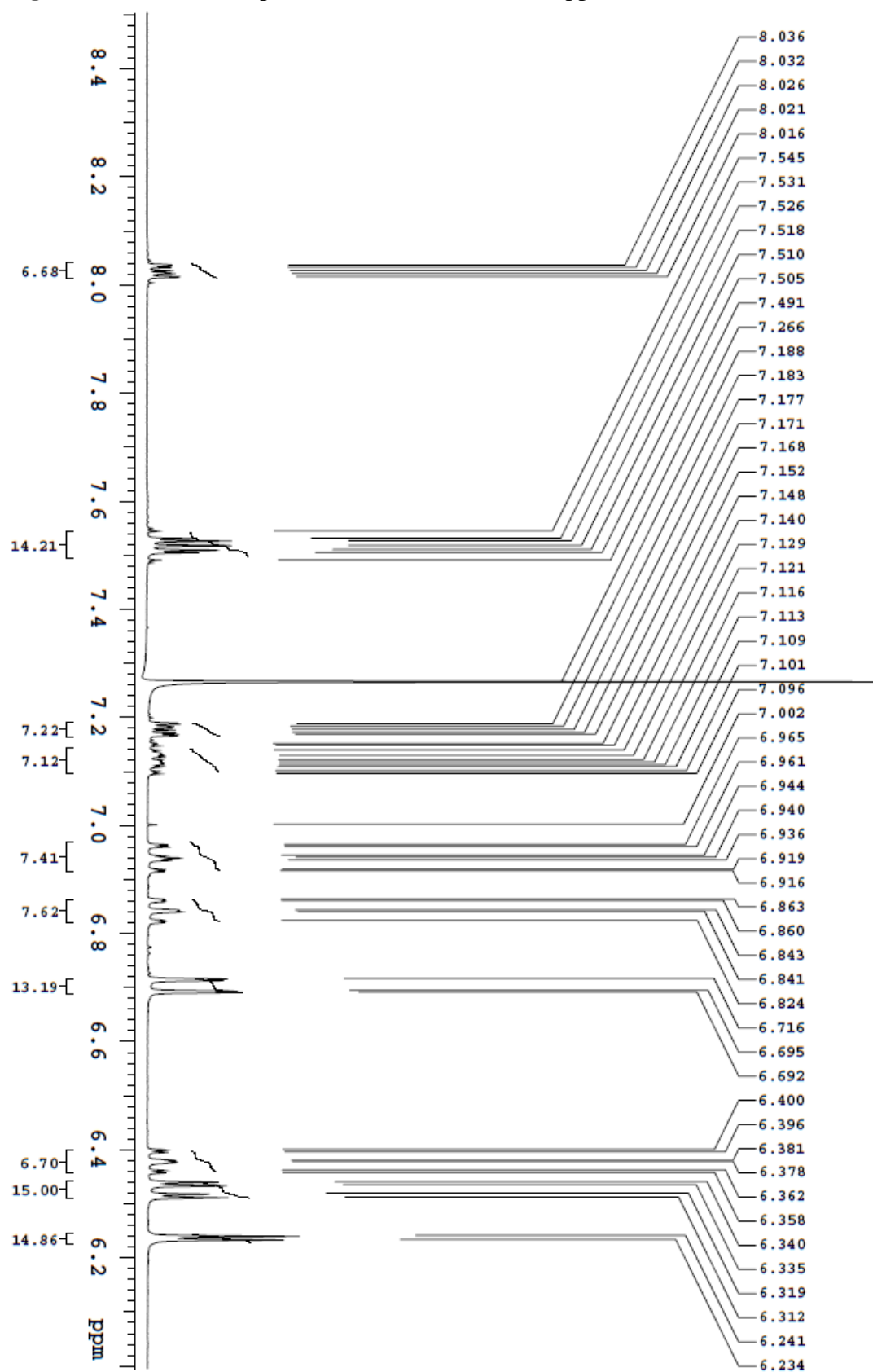
**Figure A54:**  $^1\text{H}$  NMR Spectrum of RB-2CA (0-4.5 ppm)

Figure A55:  $^{13}\text{C}$  NMR Spectrum of RB-2CA



**Figure A56:**  $^1\text{H}$  NMR Spectrum of RB-2FA

**Figure A57:**  $^1\text{H}$  NMR Spectrum of RB-2FA (6.0-8.5 ppm)

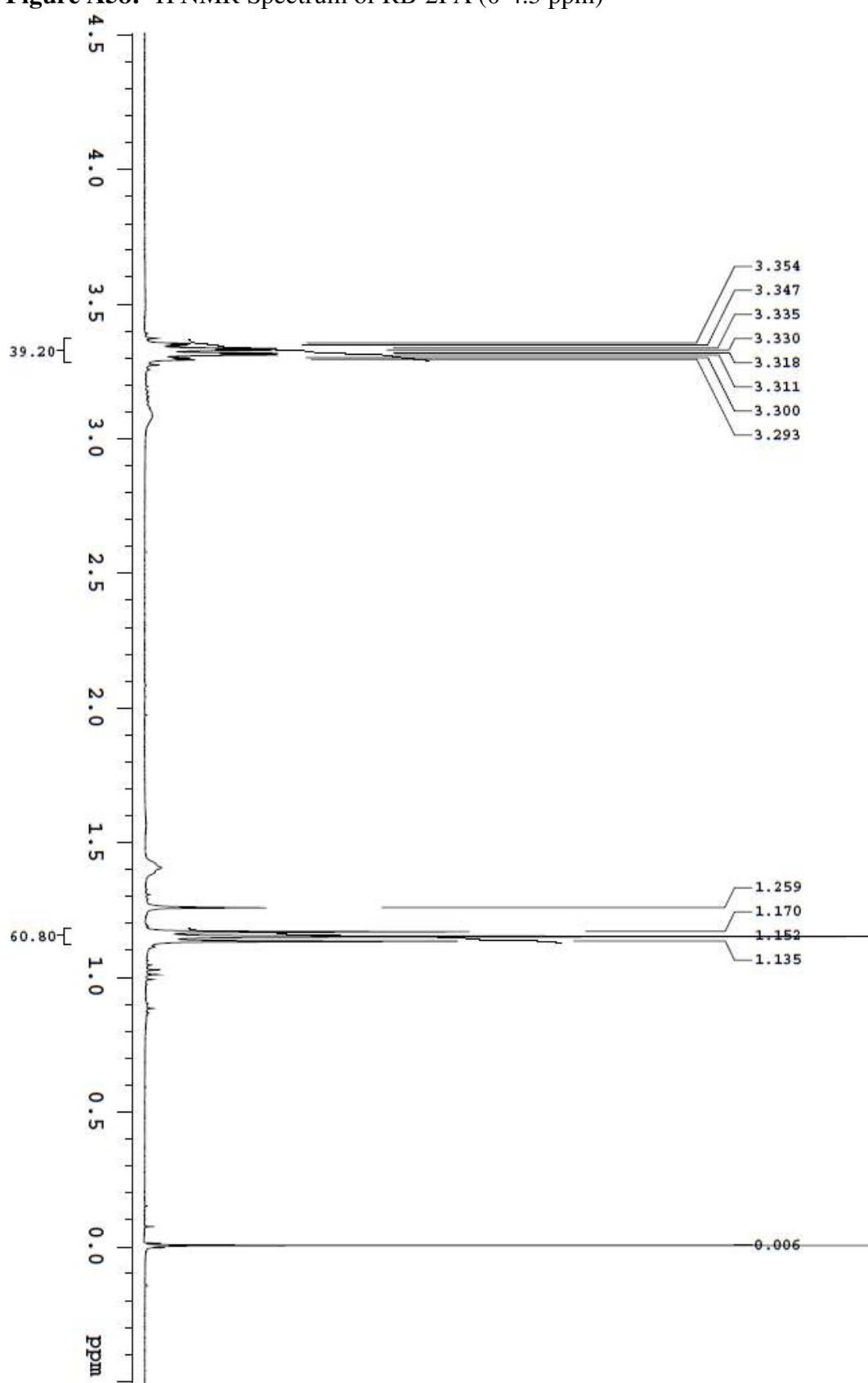
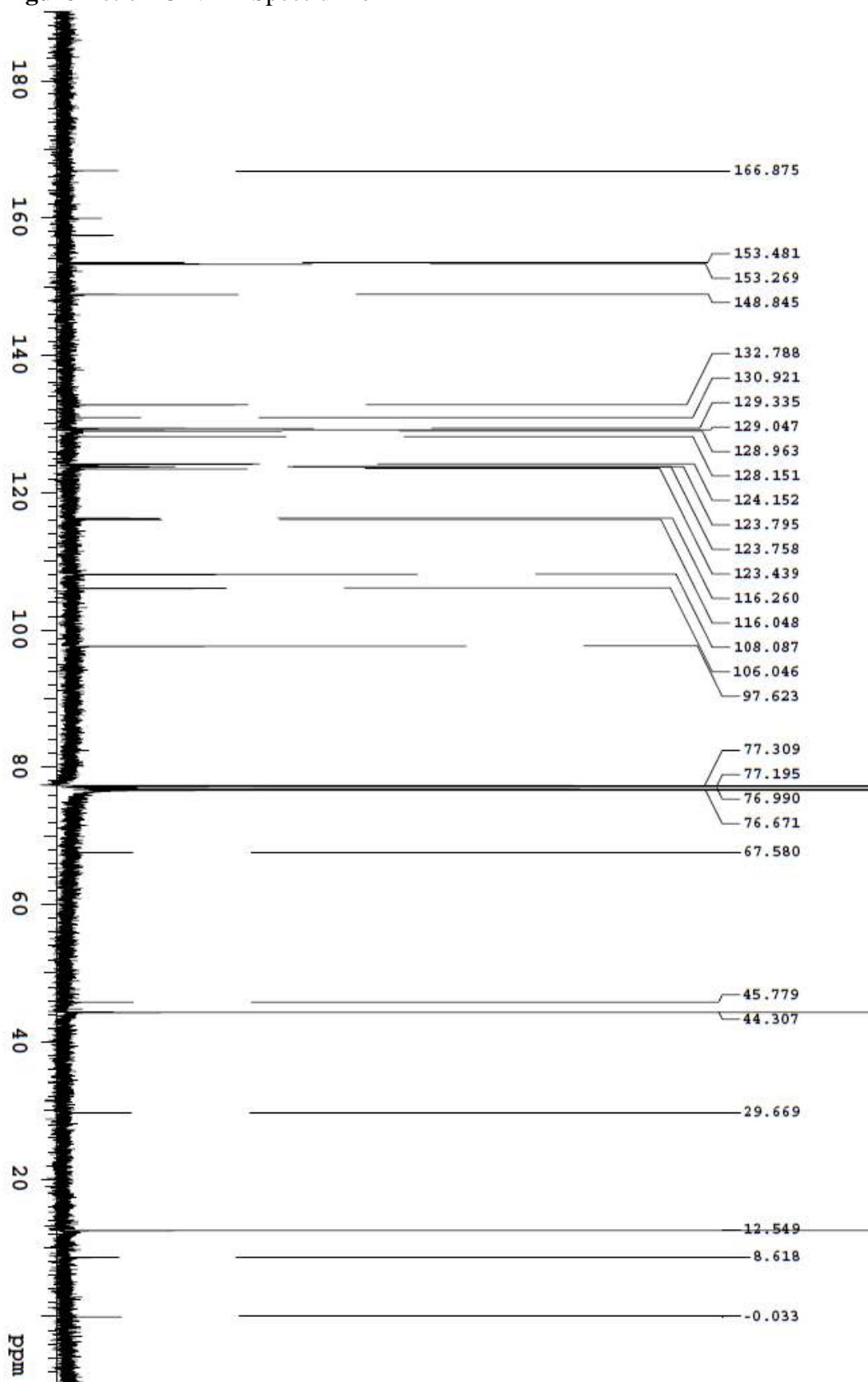
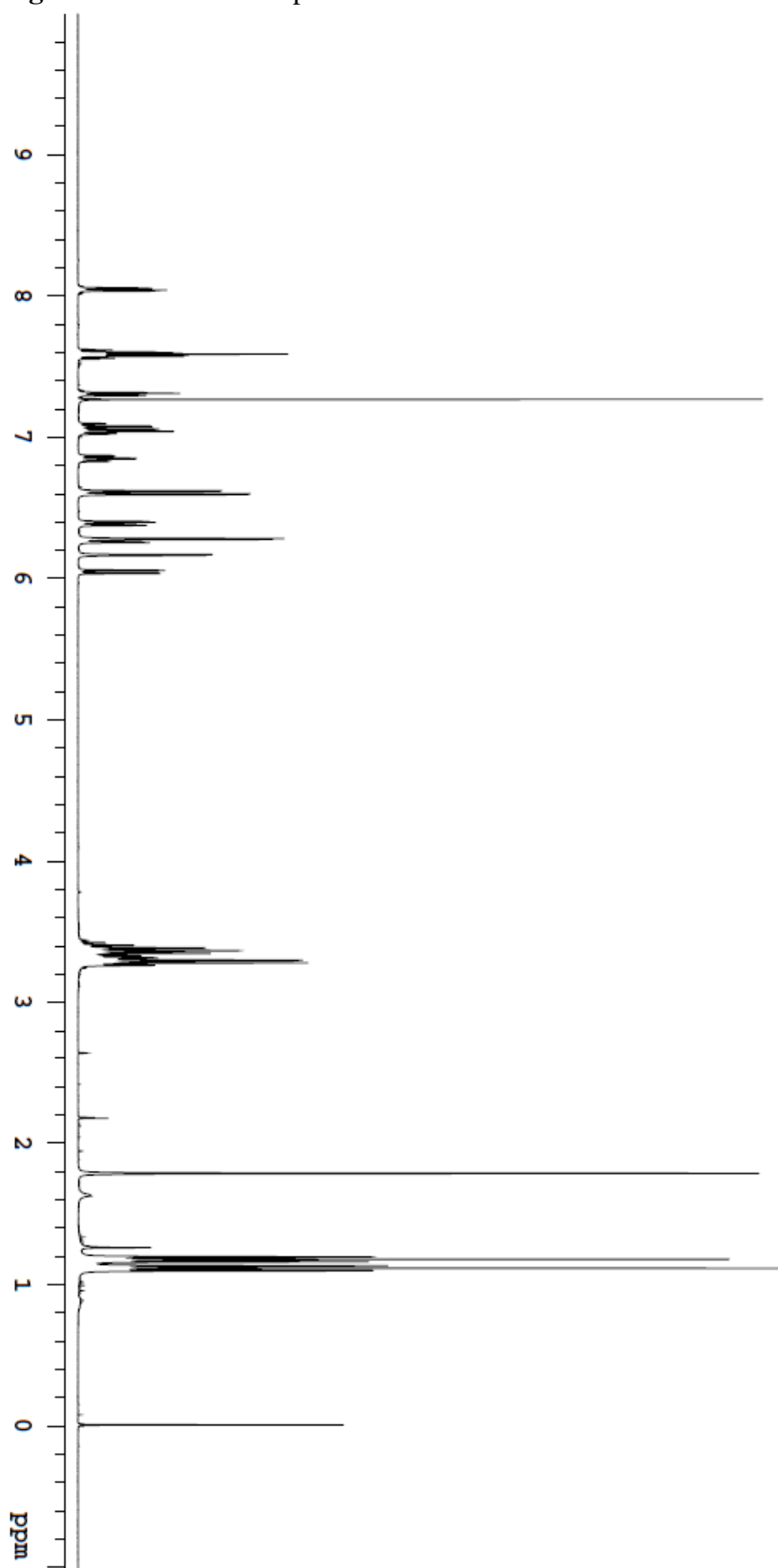
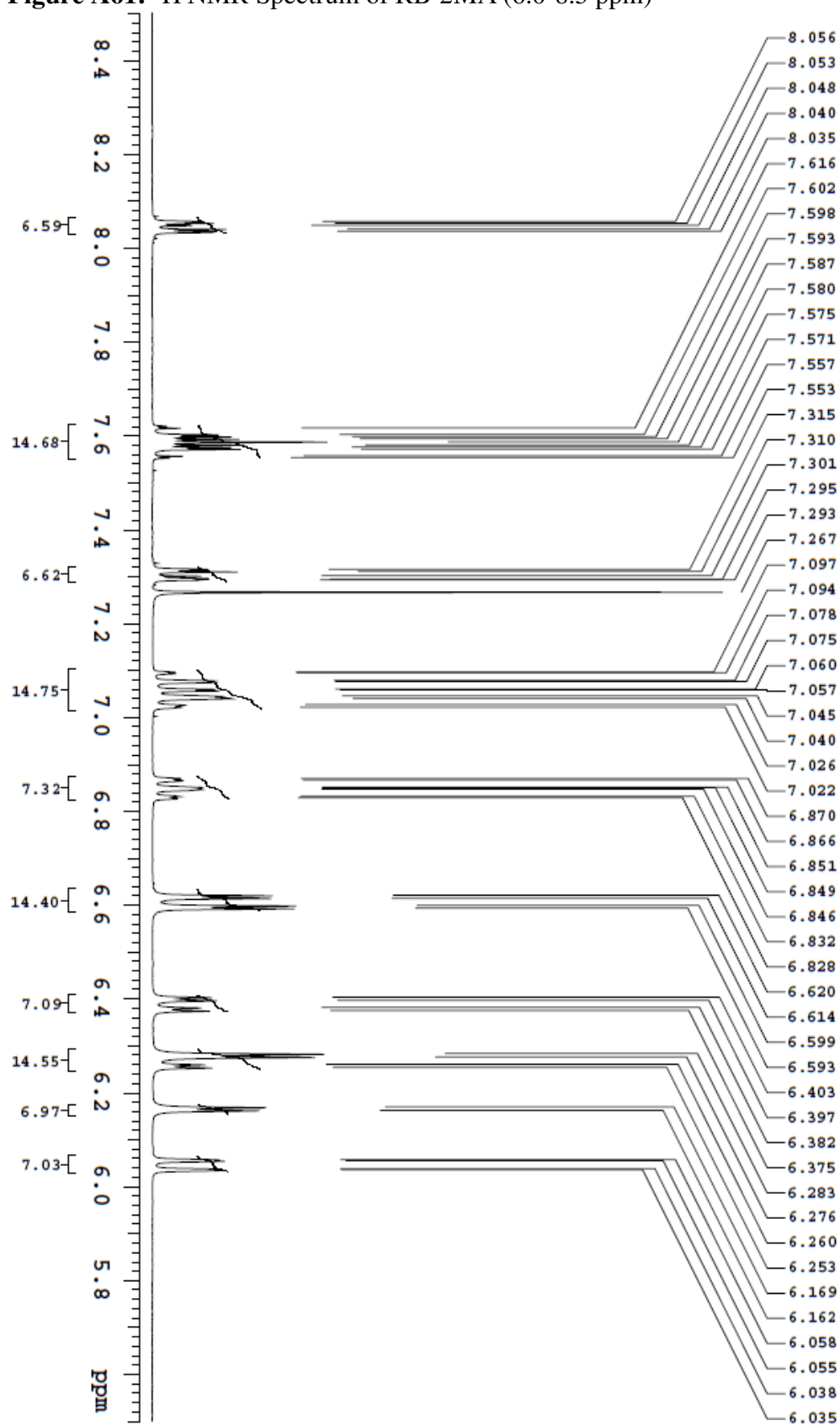
**Figure A58:**  $^1\text{H}$  NMR Spectrum of RB-2FA (0-4.5 ppm)

Figure A59:  $^{13}\text{C}$  NMR Spectrum of RB-2FA

**Figure A60:**  $^1\text{H}$  NMR Spectrum of RB-2MA

**Figure A61:**  $^1\text{H}$  NMR Spectrum of RB-2MA (6.0-8.5 ppm)

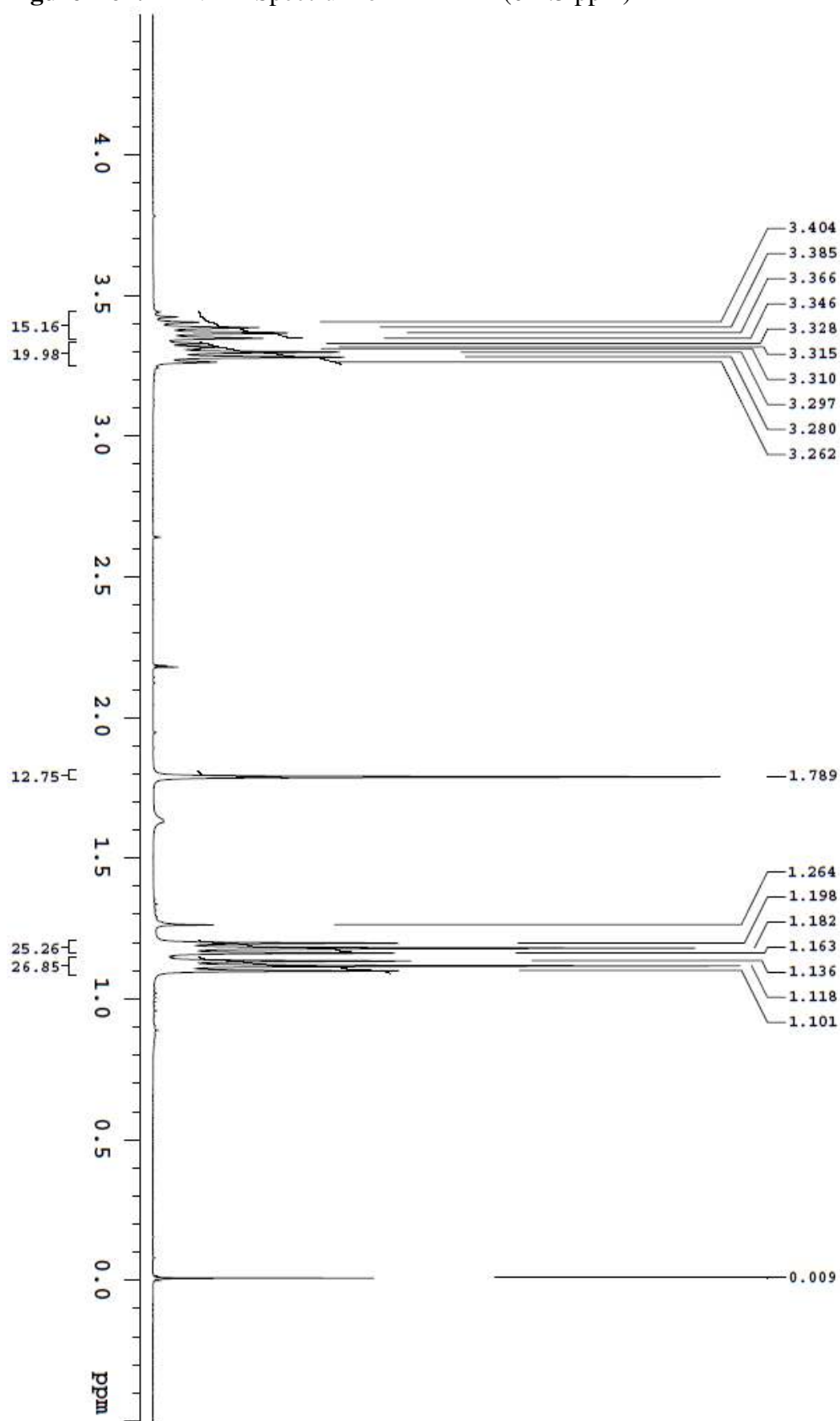
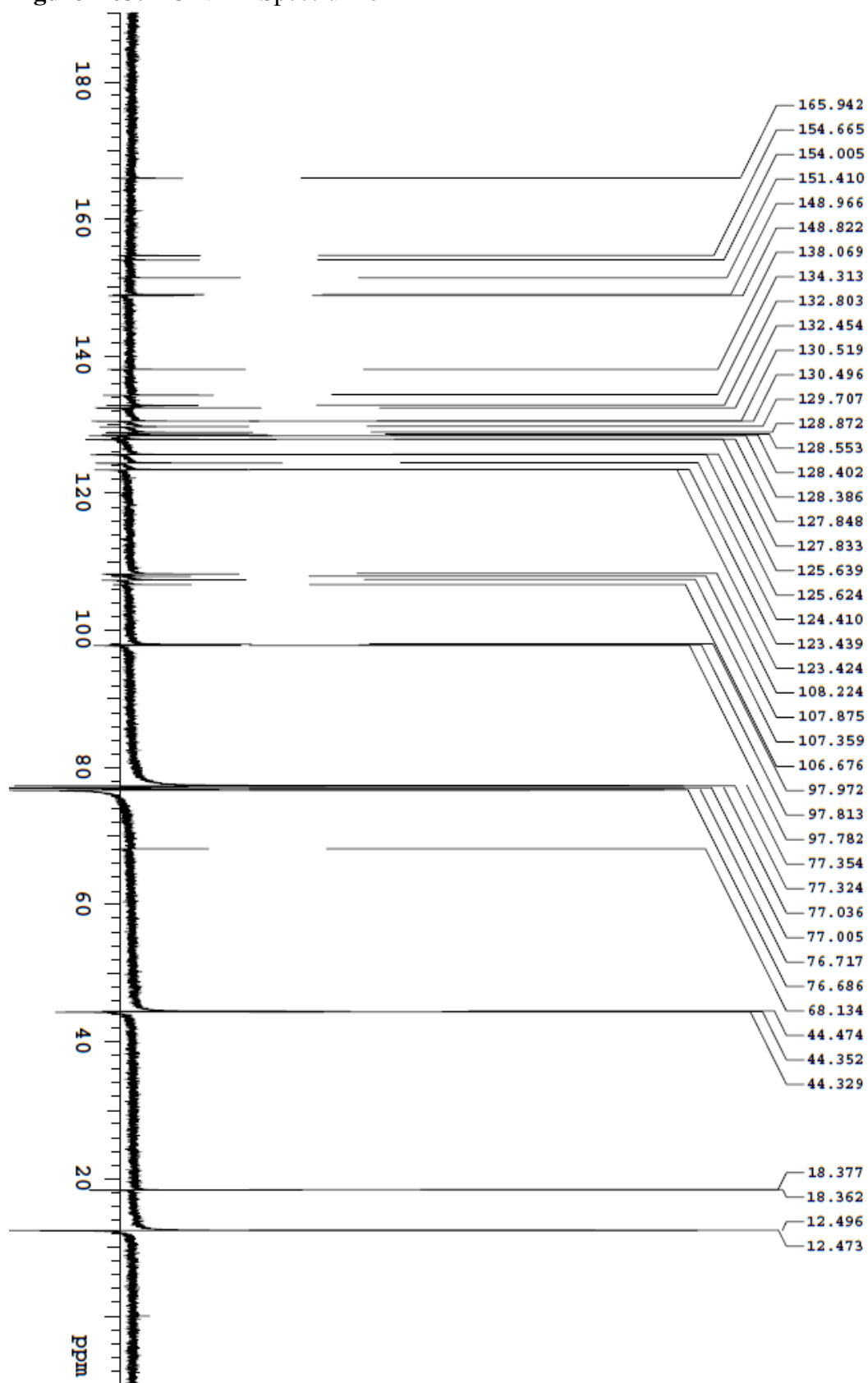
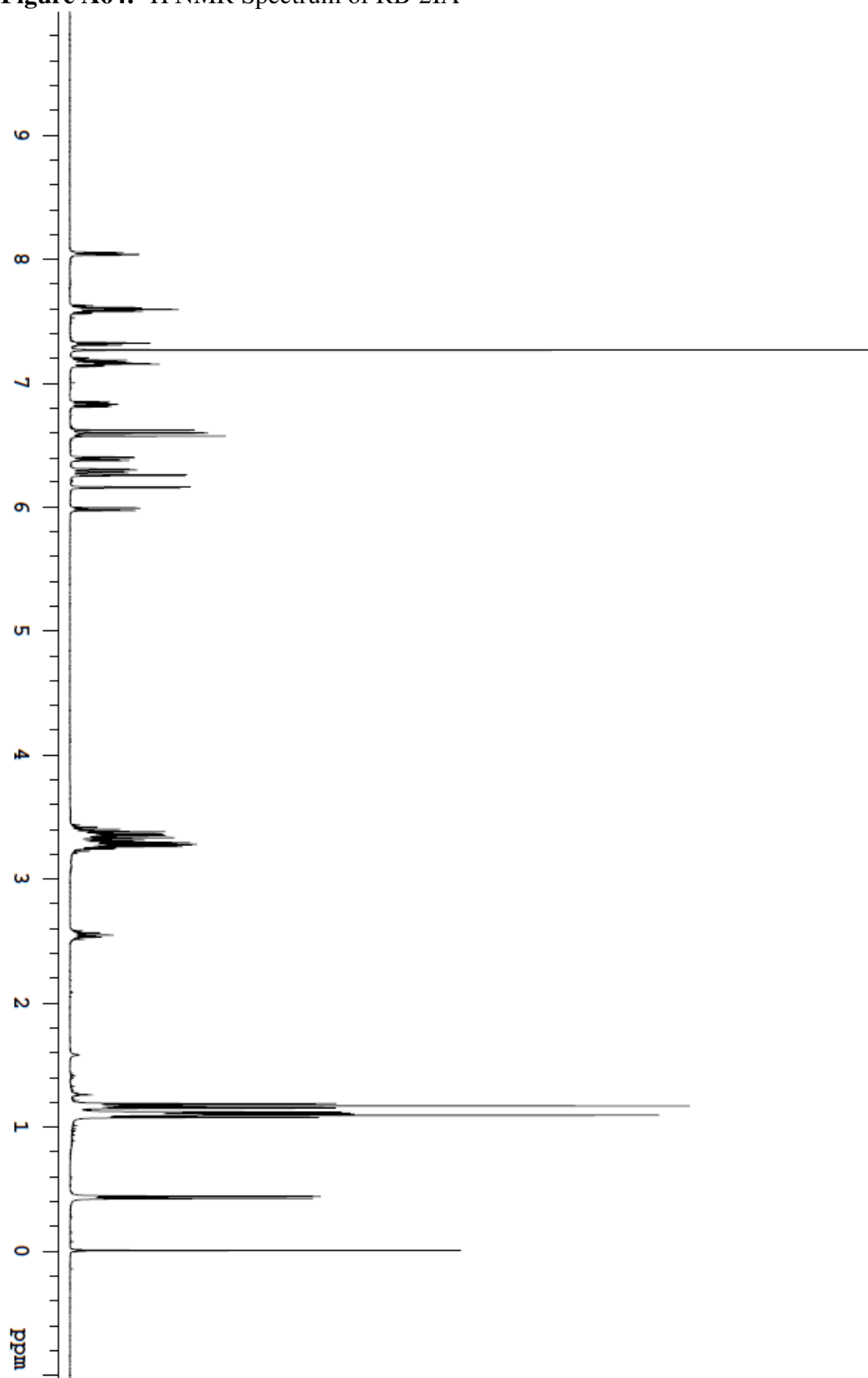
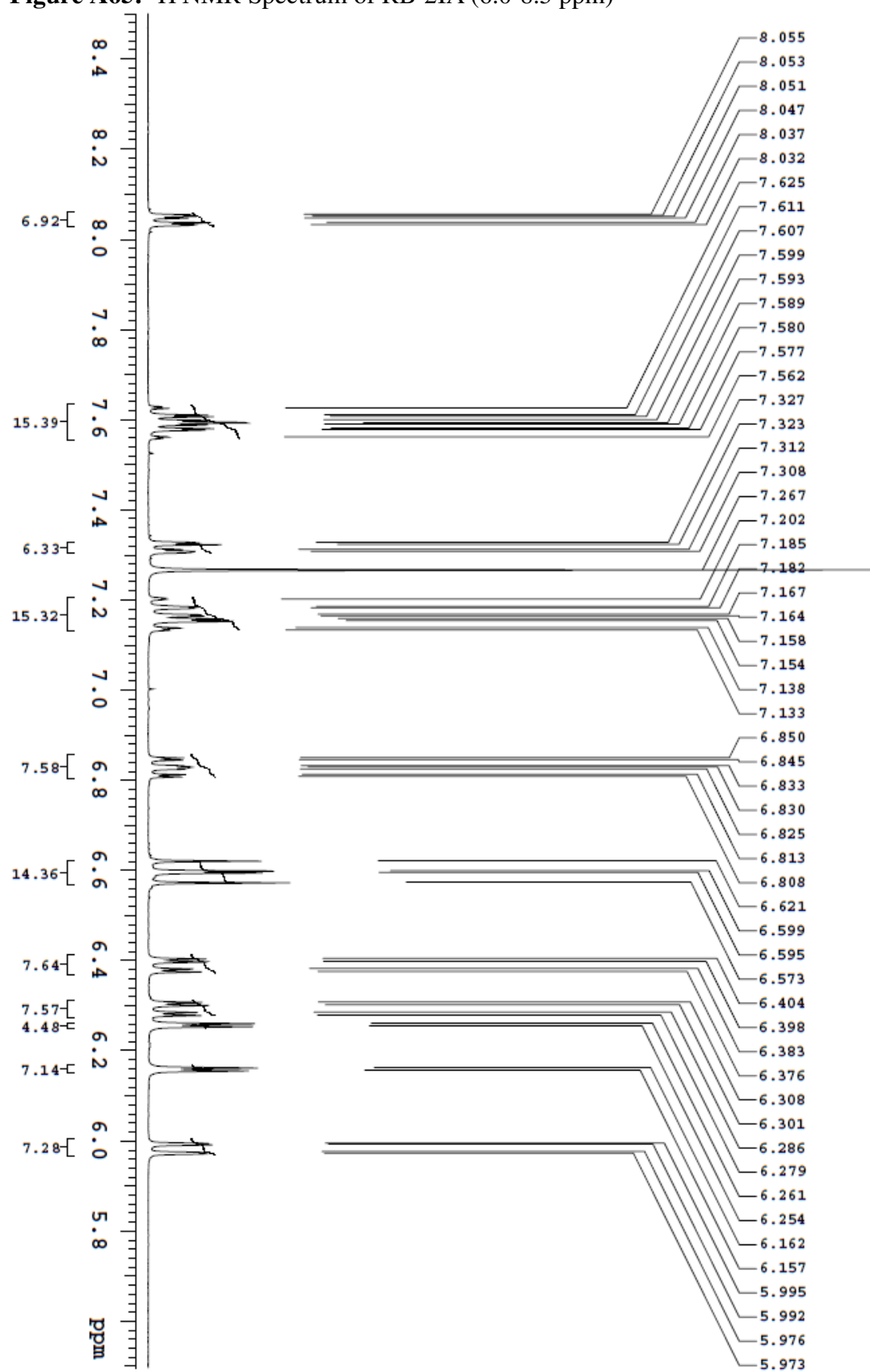
**Figure A62:**  $^1\text{H}$  NMR Spectrum of RB-2MA (0-4.5 ppm)

Figure A63:  $^{13}\text{C}$  NMR Spectrum of RB-2MA



**Figure A64:**  $^1\text{H}$  NMR Spectrum of RB-2IA

**Figure A65:**  $^1\text{H}$  NMR Spectrum of RB-2IA (6.0-8.5 ppm)

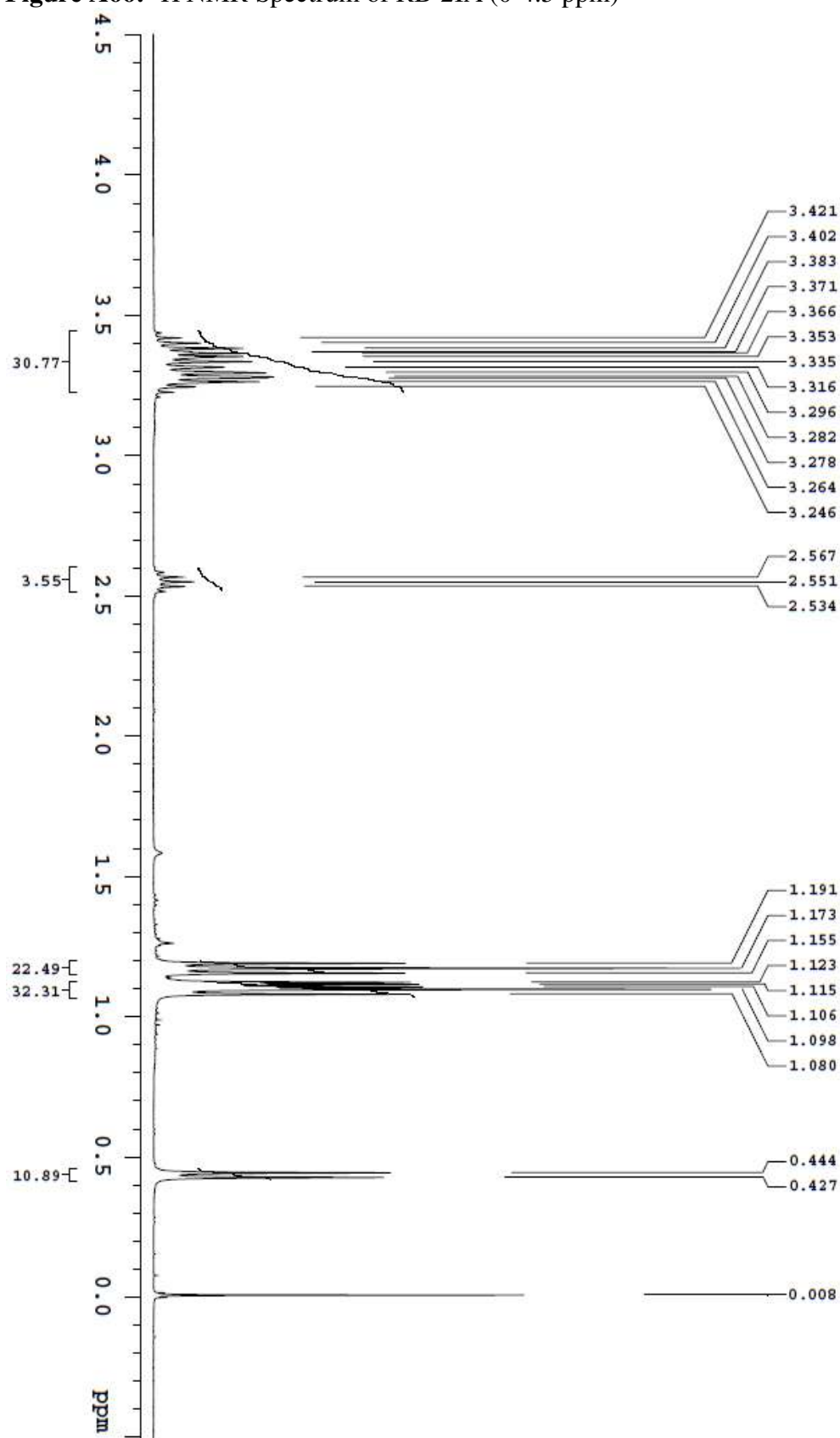
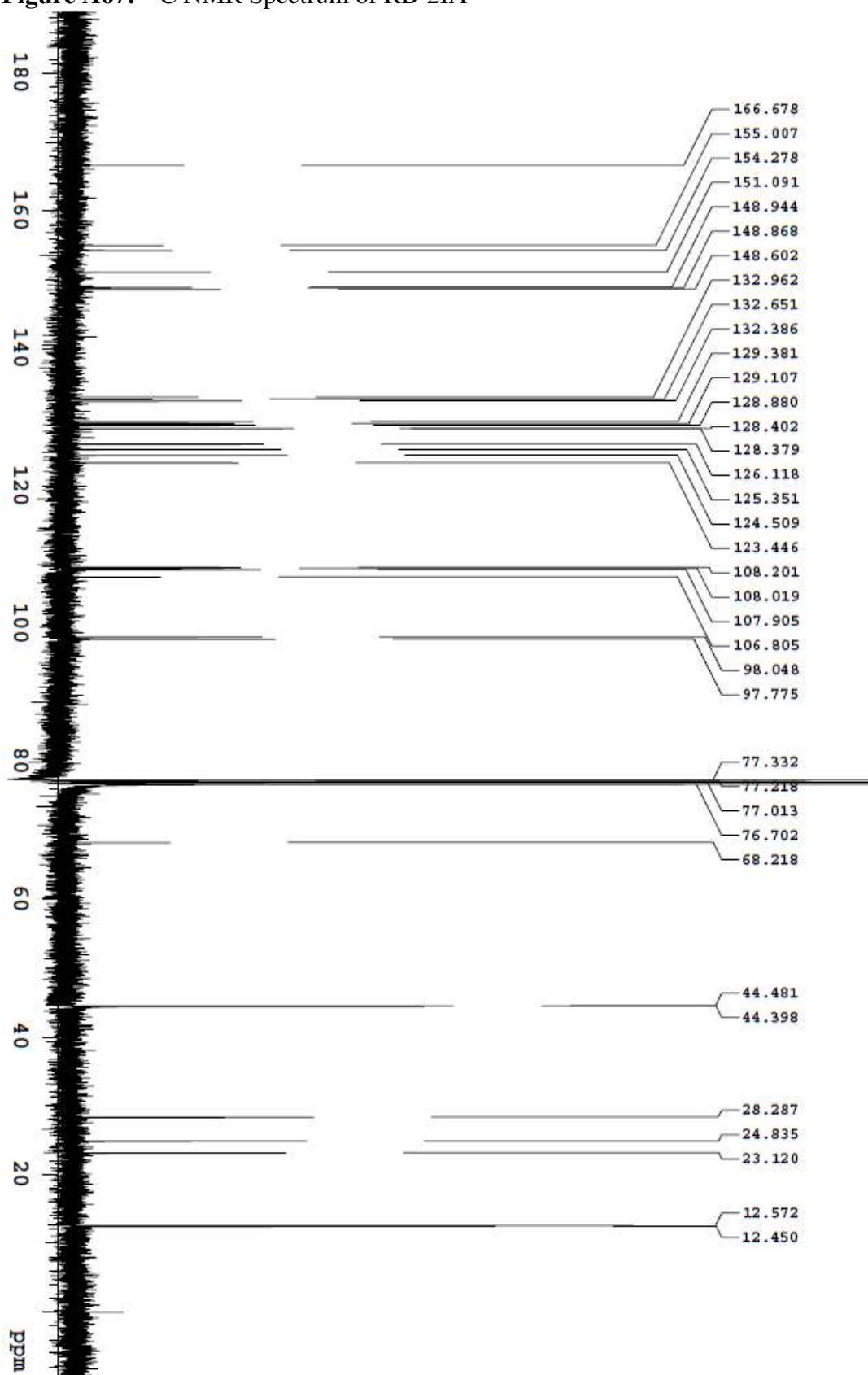
**Figure A66:**  $^1\text{H}$  NMR Spectrum of RB-2IA (0-4.5 ppm)

Figure A67:  $^{13}\text{C}$  NMR Spectrum of RB-2IA

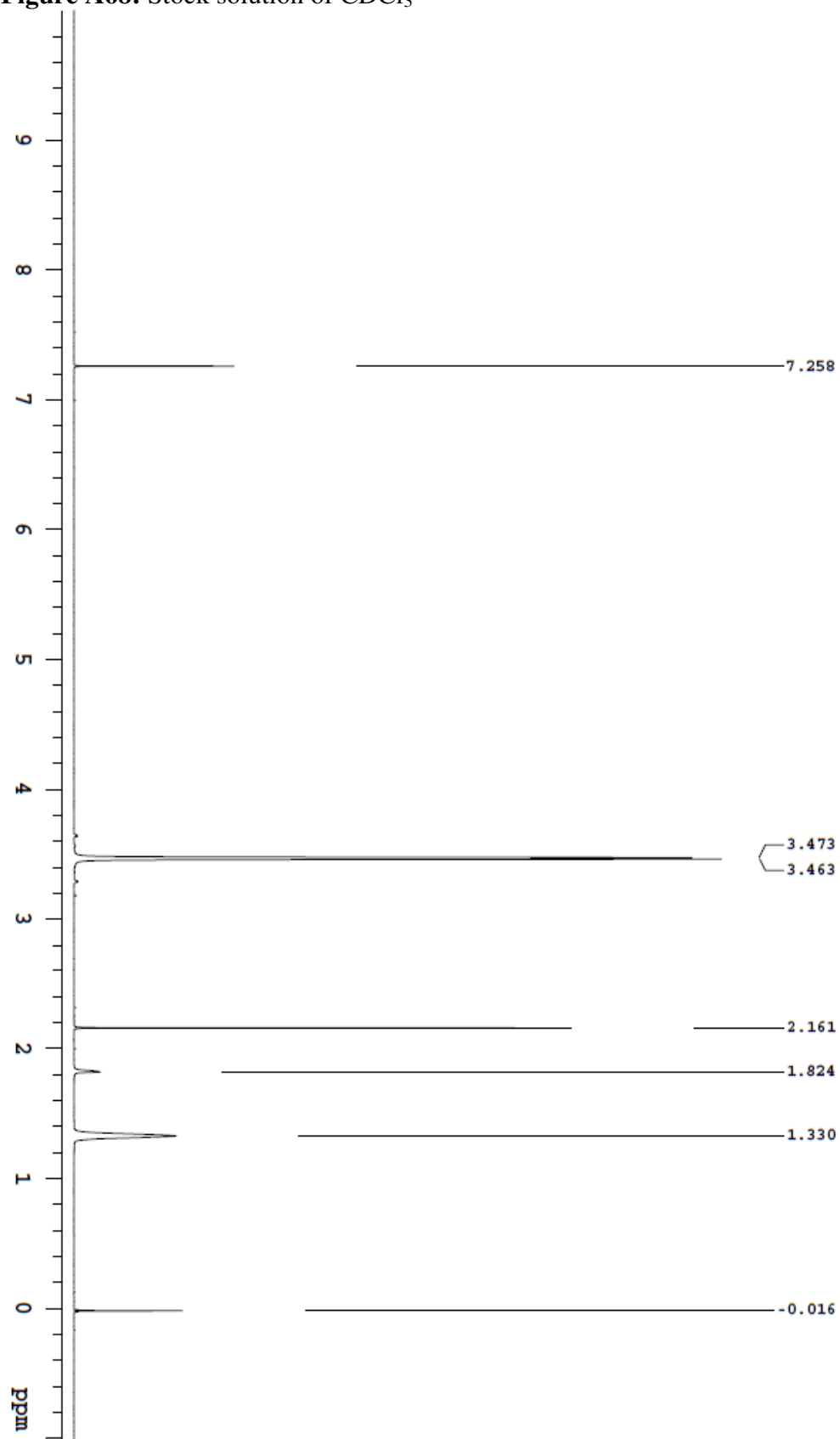
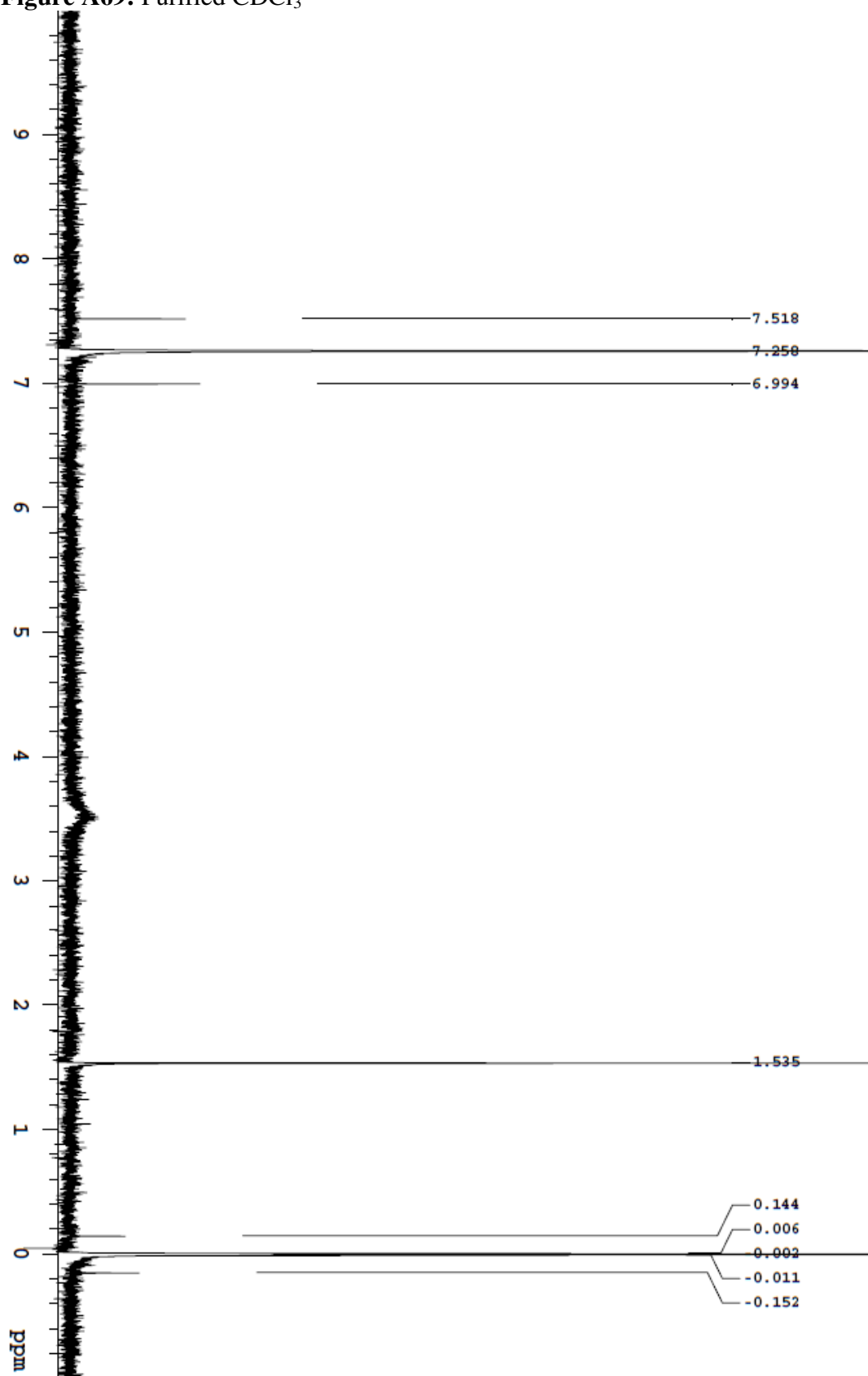
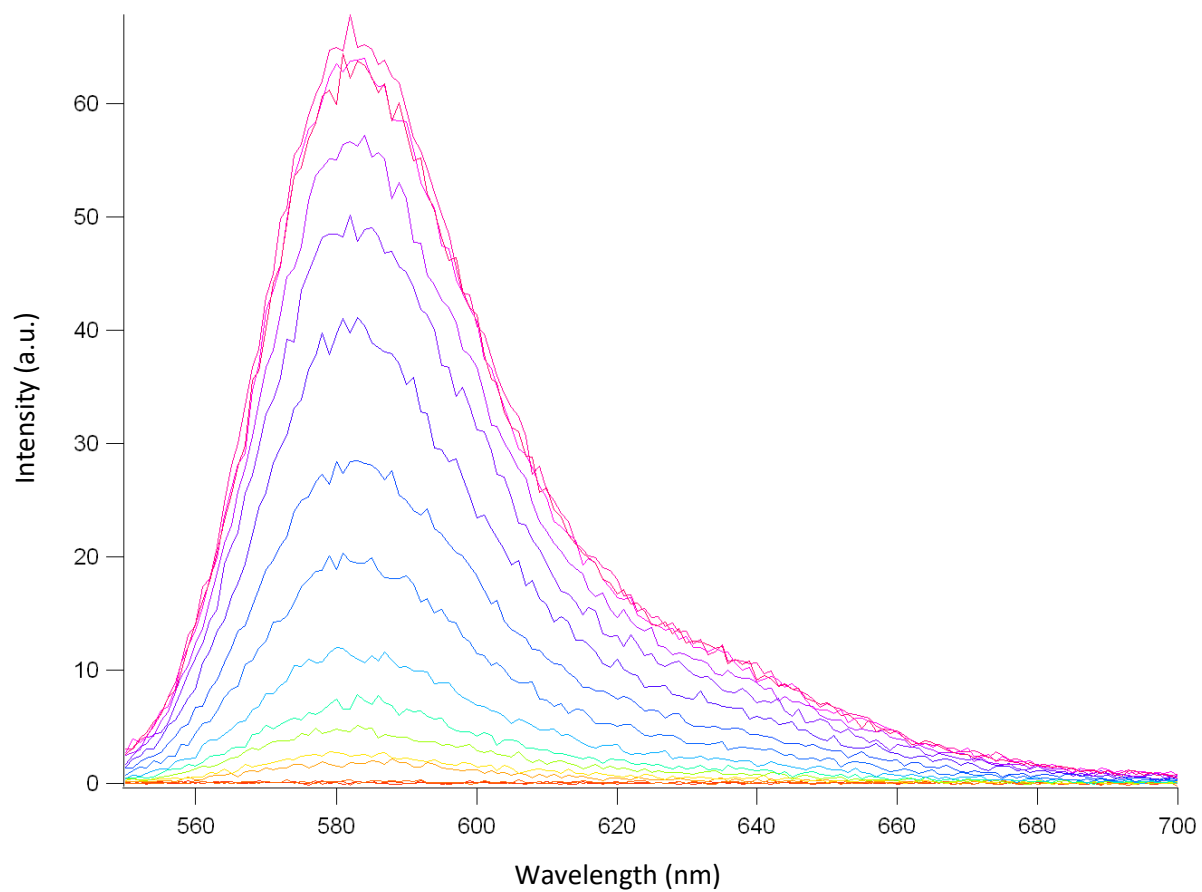
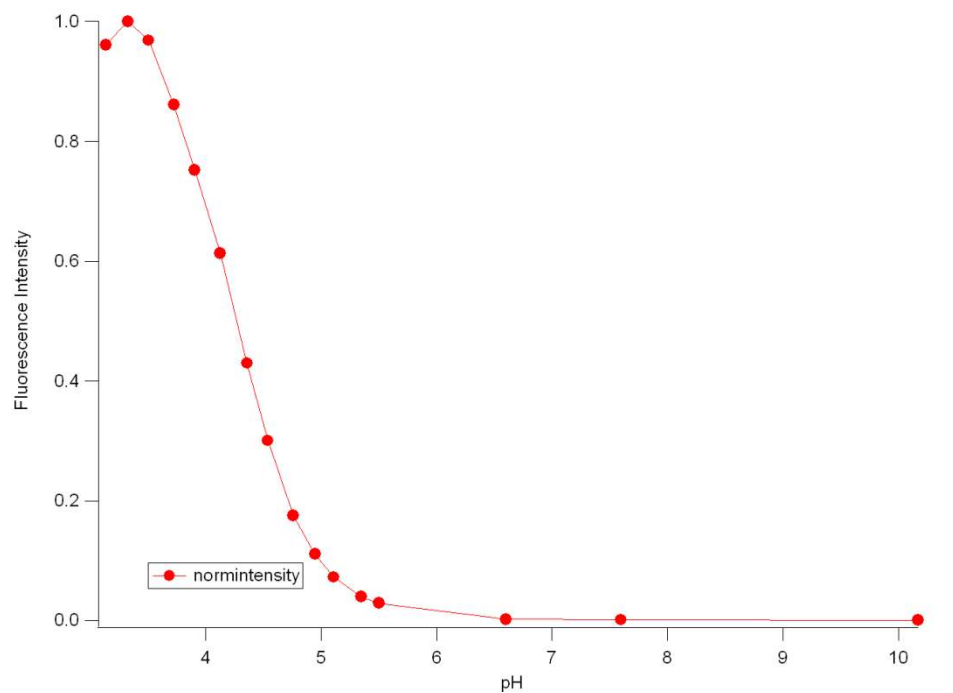
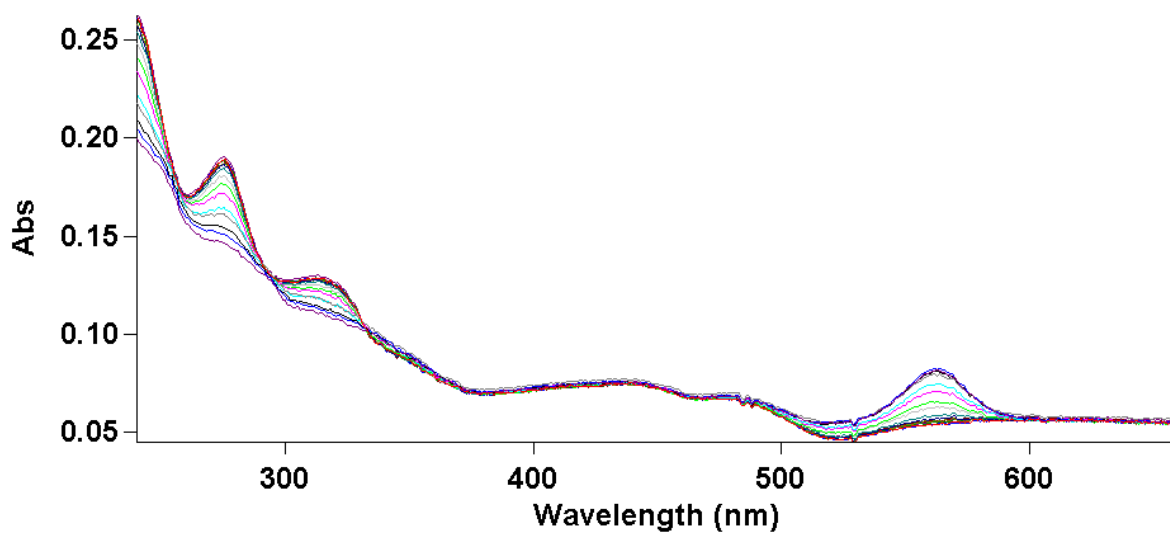
**Figure A68:** Stock solution of  $\text{CDCl}_3$ 

Figure A69: Purified  $\text{CDCl}_3$ 

**Appendix B****Figure B1:** Sample fluorescence spectra for RB-A



**Figure B2:** Sample titration curve for RB-A



**Figure B3:** Sample UV-Vis spectra for RB-A



<b>RB-A</b>	<b>pK<sub>a</sub></b>	<b>Max fl intensity</b>	<b>Fl lmax</b>
	4.36	176	583
	4.31	176	583
	4.31	220	583
	4.34	218	583
	4.30	106	583
	4.31	97	583
	4.27	66	583
Mean	4.314	151.286	
Std dev	0.024	24.839	

**Table B1:** pK<sub>a</sub> values for RB-A

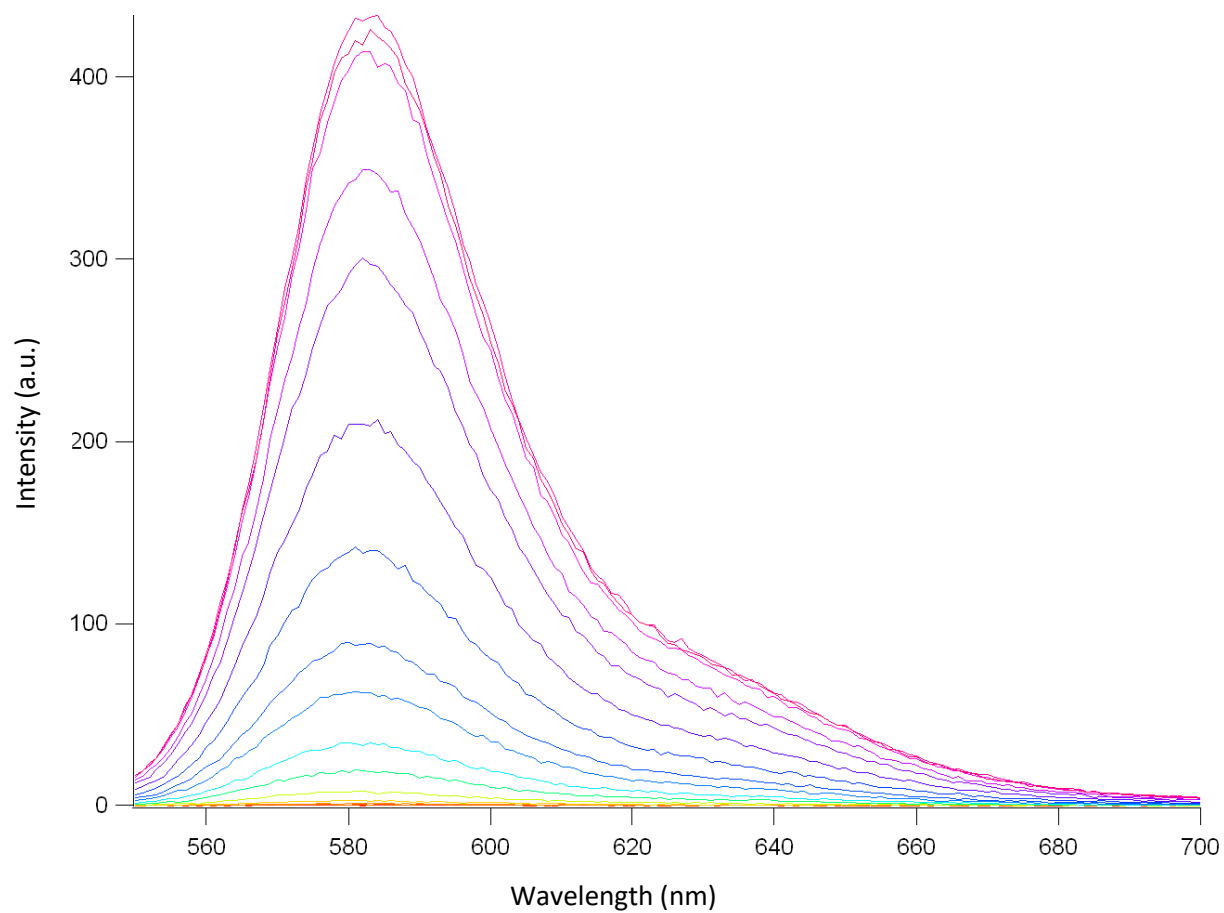


**Figure B4:** Sample fluorescence spectra for RB-DFA

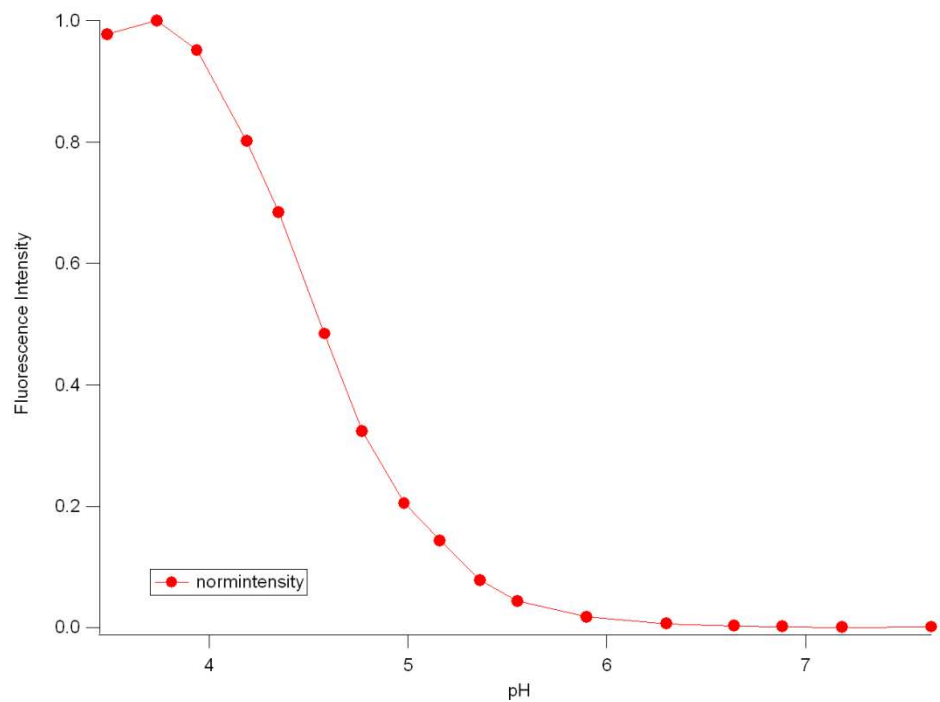


**Figure B5:** Sample titration curve for RB-DFA

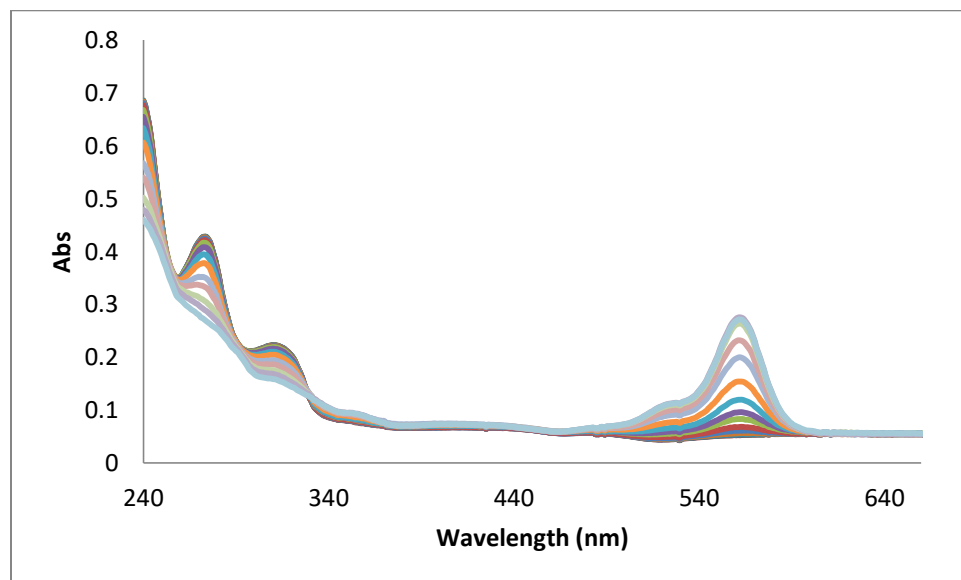


**Figure B6:** Sample UV-Vis spectra for RB-DFA

<b>RB-DFA</b>	<b>pKa</b>	<b>Max fl intensity</b>	<b>Fl lmax</b>
	4.41	333	582
	4.44	368	582
	4.46	267	582
	4.50	349	582
	4.62	280	582
	4.58	309	582
	4.54	353	582
	4.58	434	582
Mean	4.516	336.625	
Std dev	0.076	53.074	

**Table B2:** pKa values for RB-DFA

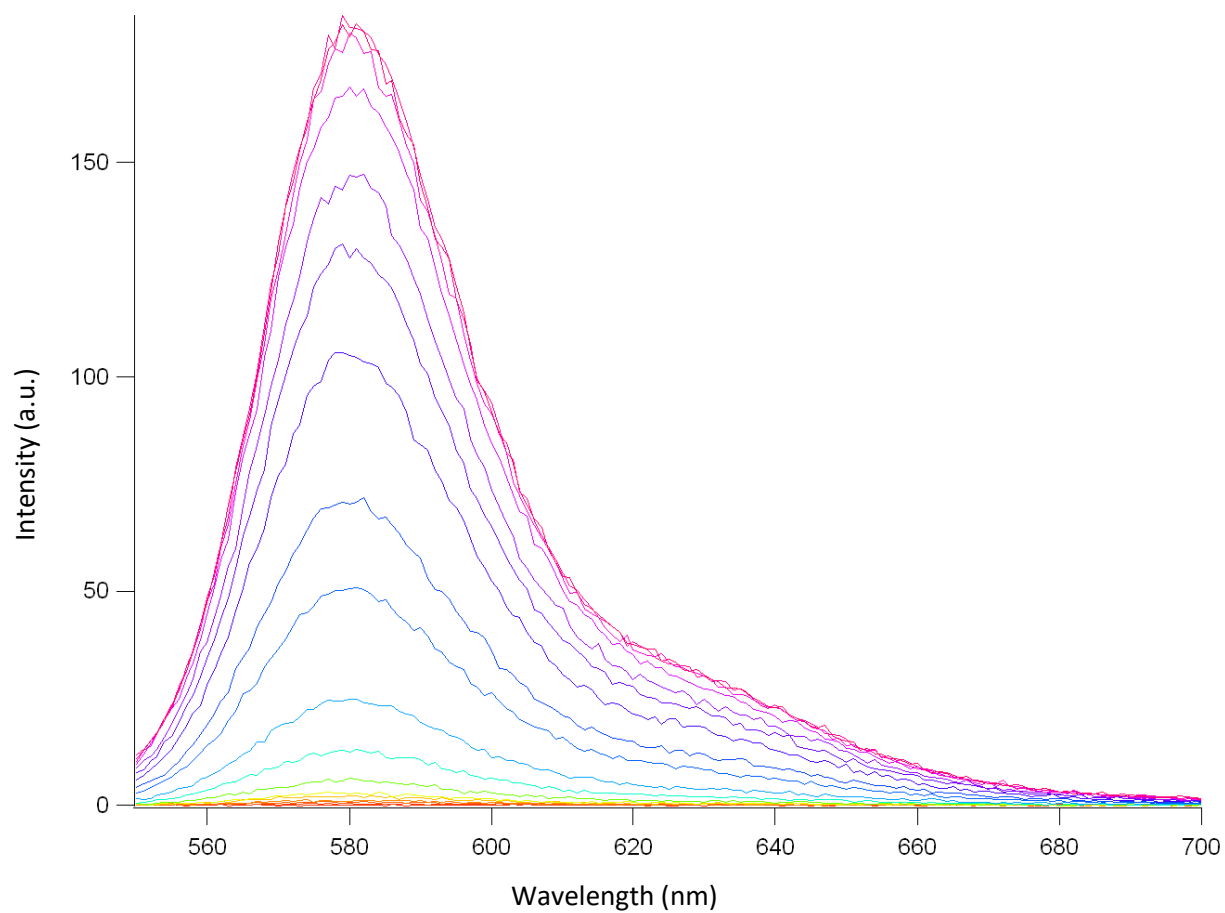


**Figure B7:** Sample fluorescence spectra for RB-DCA

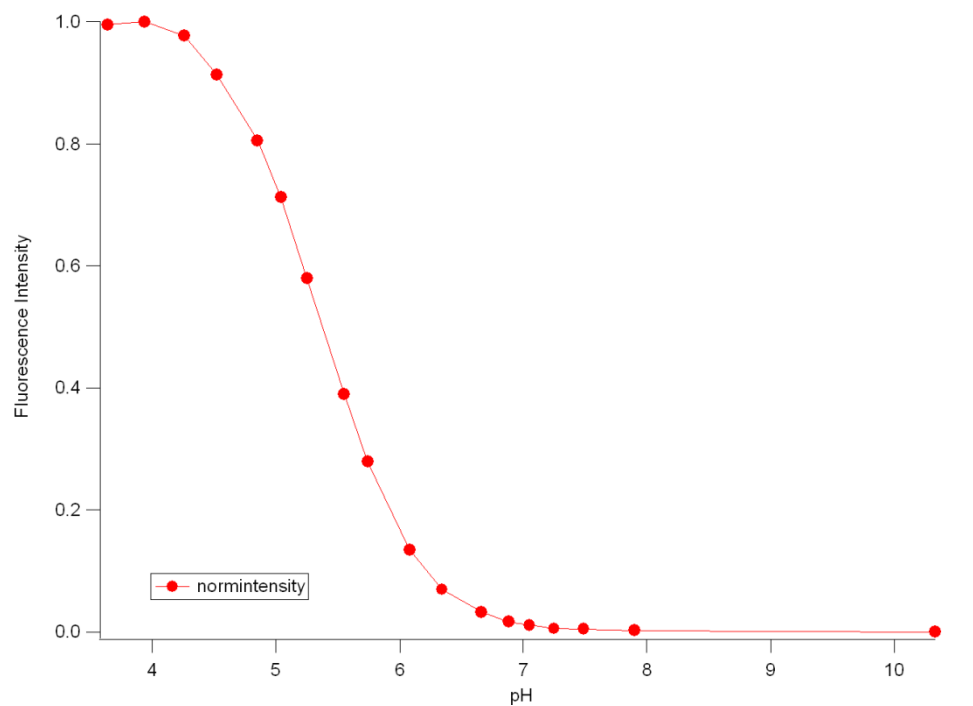


**Figure B8:** Sample titration curve for RB-DCA

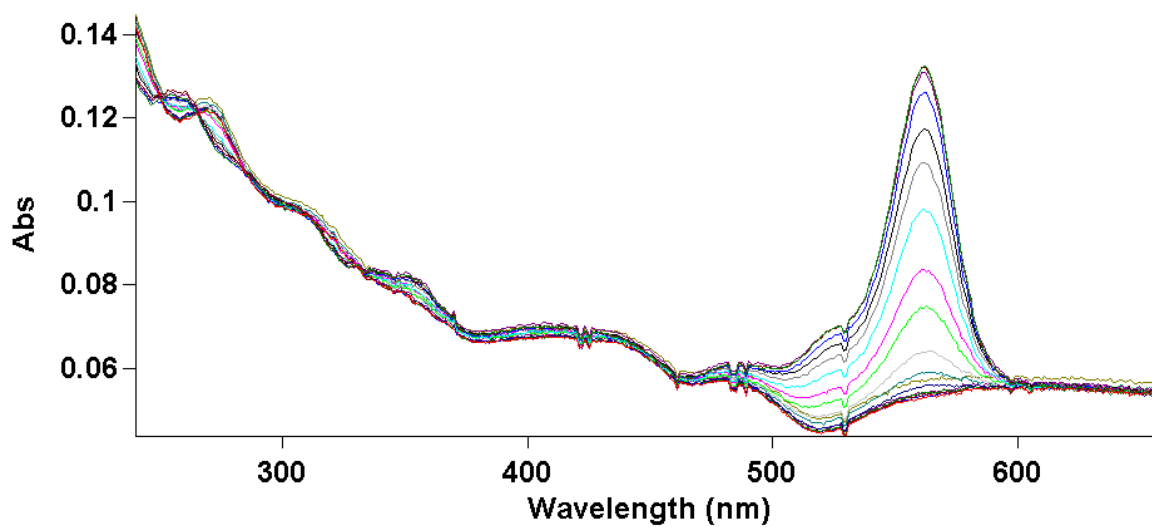


**Figure B9:** Sample UV-Vis spectra for RB-DCA

<b>RB-DCA</b>	<b>pKa</b>	<b>Max fl intensity</b>	<b>Fl lmax</b>
	5.19	282	581
	5.39	292	581
	5.42	336	581
	5.43	241	581
	5.41	193	581
	5.39	188	581
	5.39	255	581
	5.42	182	581
Mean	5.38	246.125	
Std dev	0.078	55.917	

Note: Diluted 2x

**Table B3:** pKa values for RB-DCA

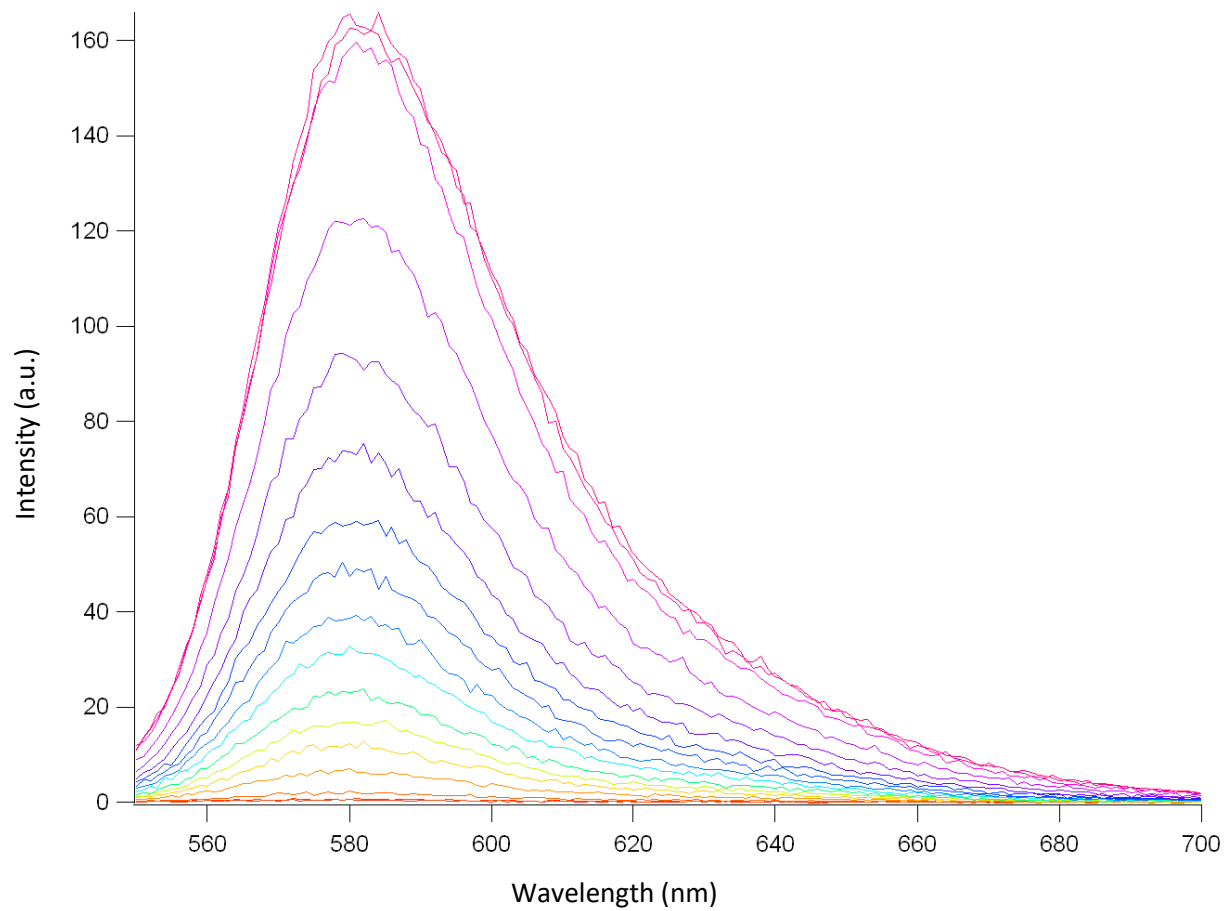


**Figure B10:** Sample fluorescence spectra for RB-DEA



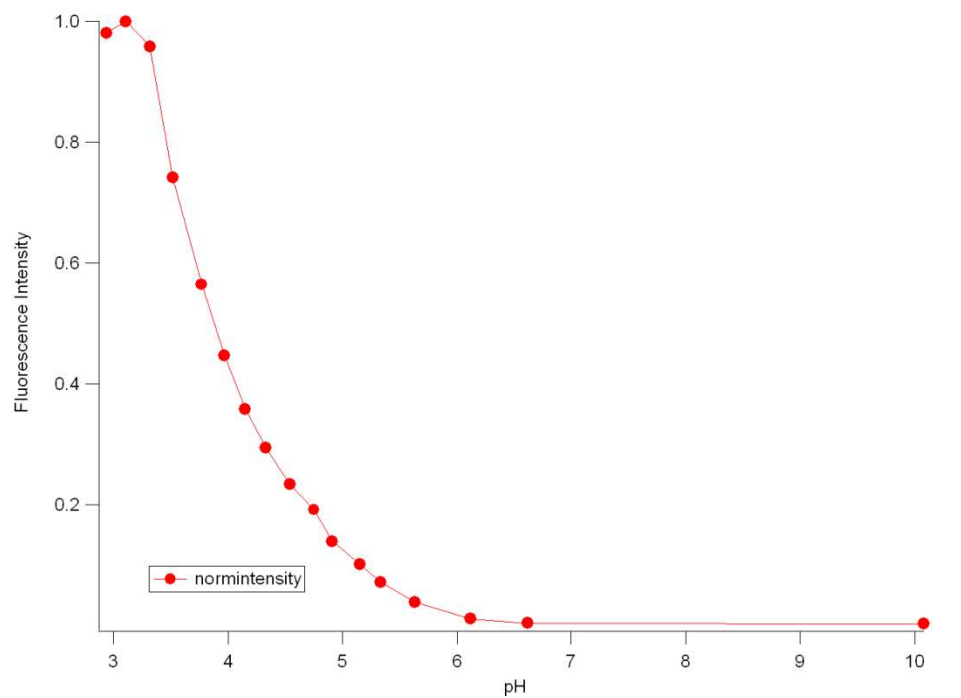


**Figure B11:** Sample titration curve for RB-DEA

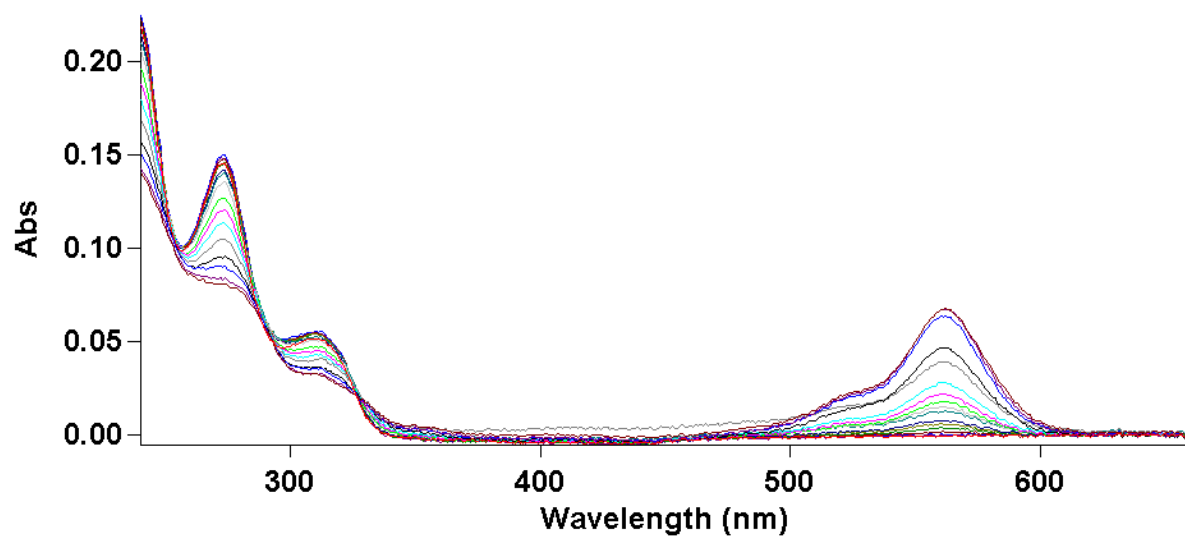


**Figure B12:** Sample UV-Vis spectra for RB-DEA

<b>RB-DEA</b>	<b>pKa</b>	<b>Max fl intensity</b>	<b>Fl lmax</b>
	3.96	210	583
	4.03	215	583
	4.12	166	583
	4.09	171	583
	4.04	167	583
	3.93	166	583
Mean	4.028	182.5	583
Std dev	0.073	23.365	

**Table B4:** pKa values for RB-DEA

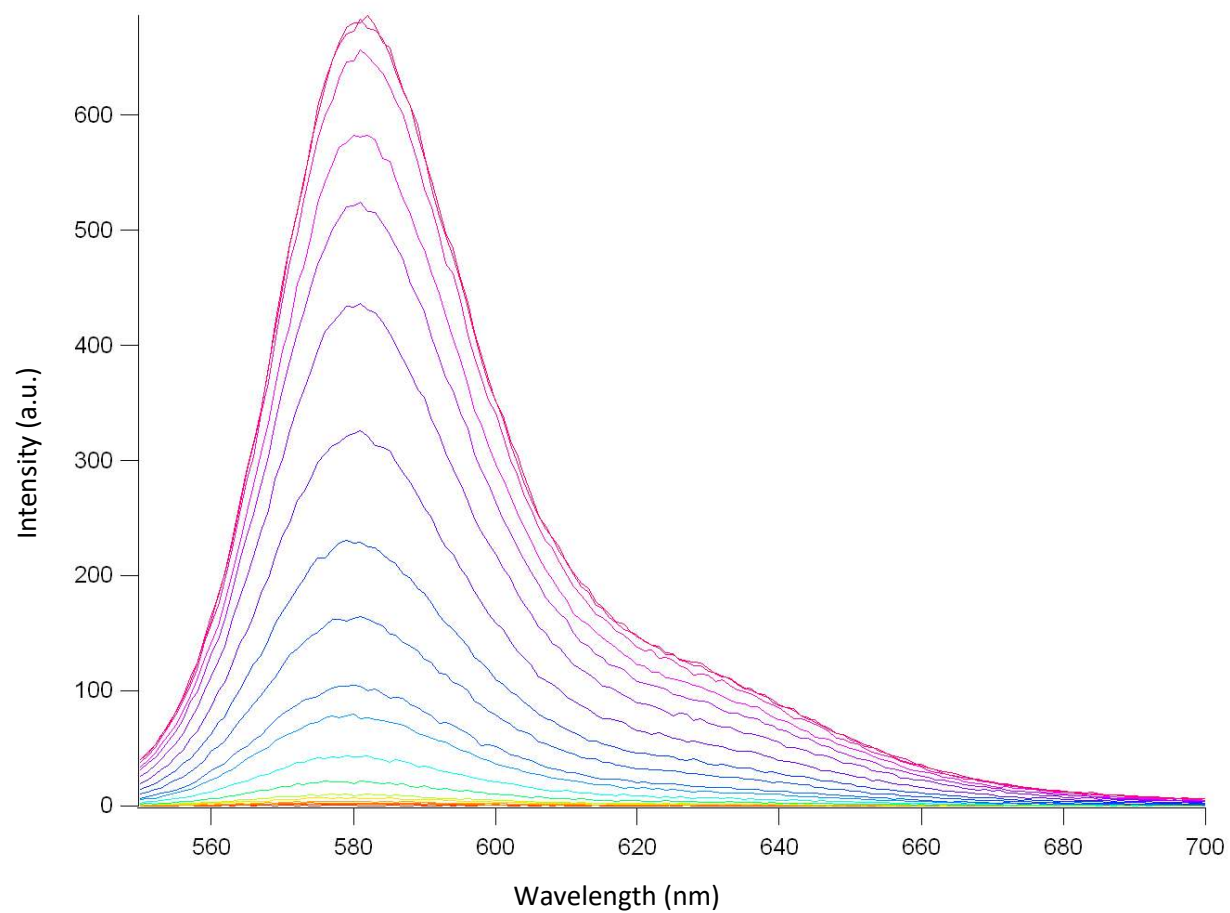


**Figure B13:** Sample fluorescence spectra for RB-DMA

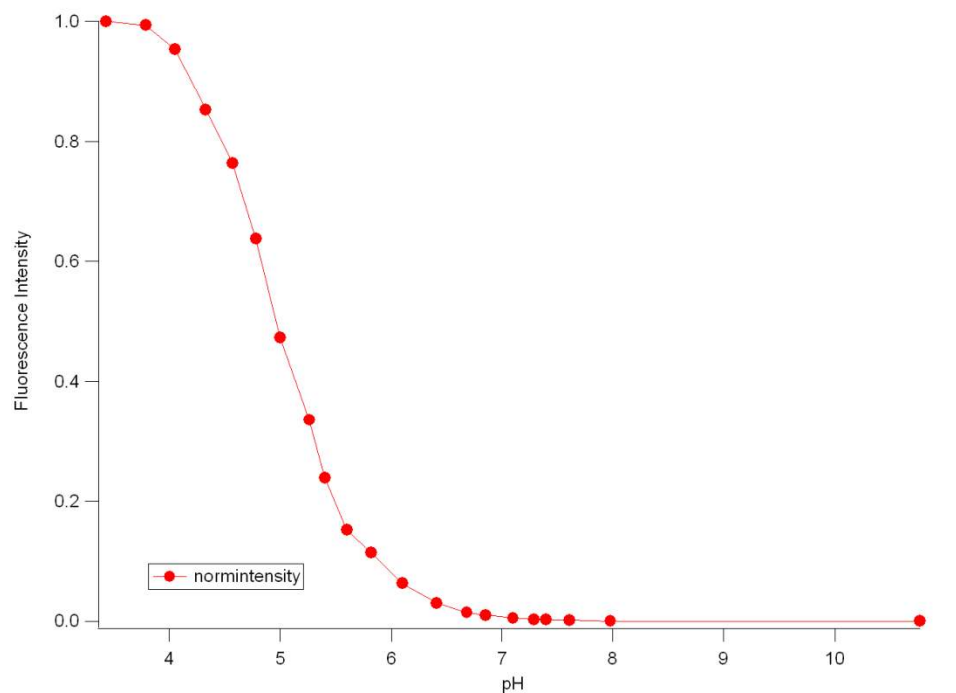


**Figure B14:** Sample titration curve for RB-DMA

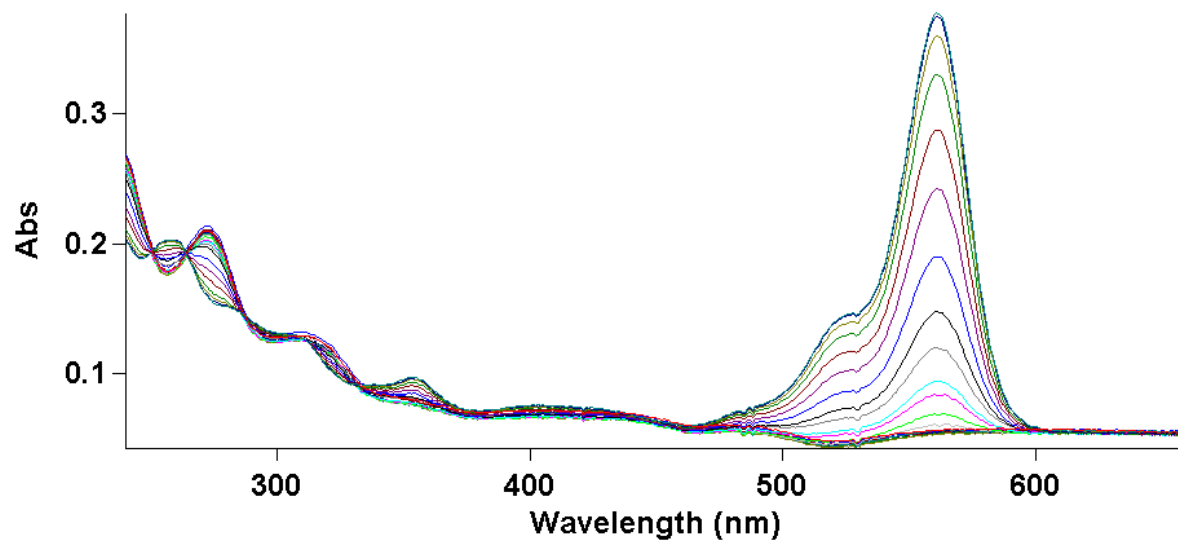


**Figure B15:** Sample UV-Vis spectra for RB-DMA

<b>RB-DMA</b>	<b>pKa</b>	<b>Max fl intensity</b>	<b>Fl lmax</b>
	4.82	204	581
	4.68	220	581
	4.88	187	581
	4.94	257	581
	4.92	304	581
	5.04	93	581
	4.95	105	581
	4.99	683	581
Mean	4.903	256.625	
Std dev	0.112	186.226	

Note: Diluted 2x

**Table B5:** pKa values for RB-DMA

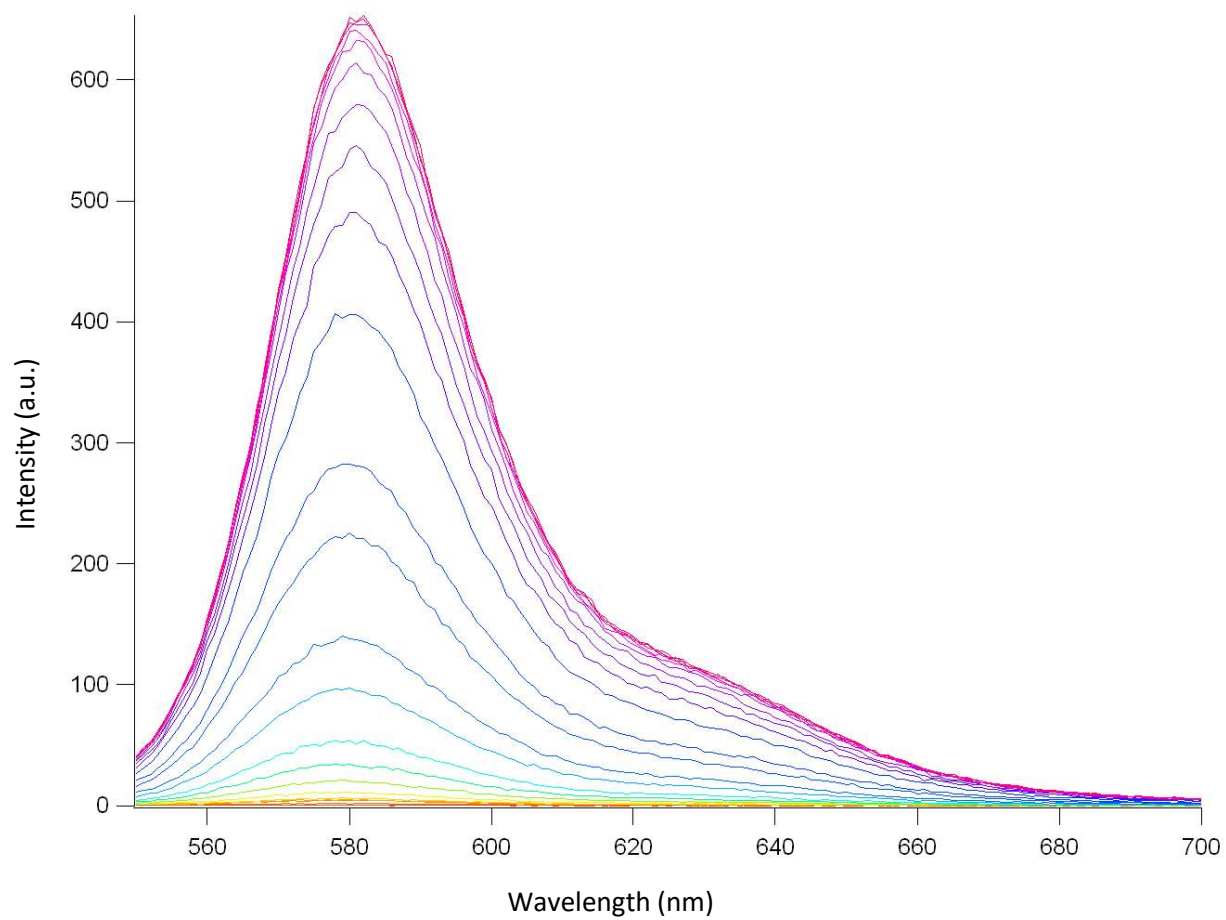


**Figure B16:** Sample fluorescence spectra for RB-DIA

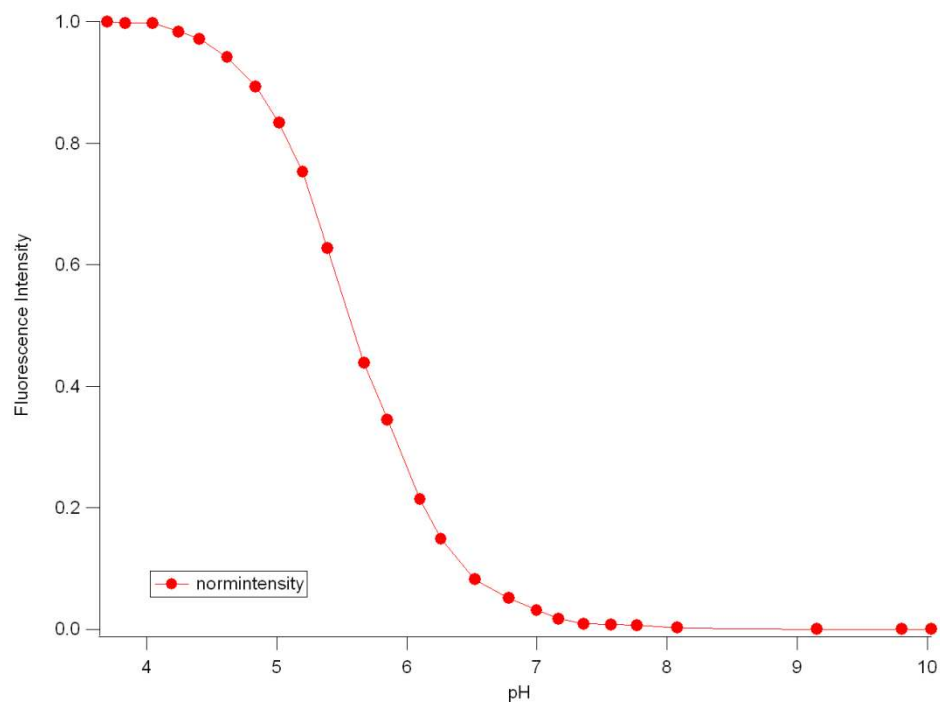


**Figure B17:** Sample titration curve for RB-DIA

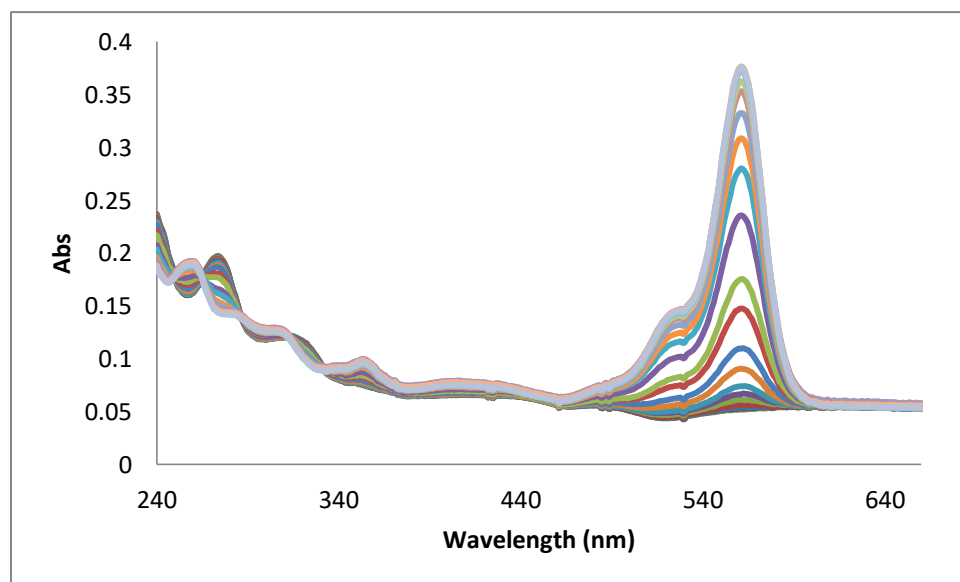


**Figure B18:** Sample UV-Vis spectra for RB-DIA

<b>RB-DIA</b>	<b>pKa</b>	<b>Max fl intensity</b>	<b>Fl lmax</b>
	5.87	898	582
	5.75	620	582
	5.67	552	582
	5.74	549	582
	5.53	586	582
	5.64	611	582
	5.93	562	582
	5.61	647	582
Mean	5.718	628.125	
Std dev	0.134	114.487	

**Table B6:** pKa values for RB-DIA



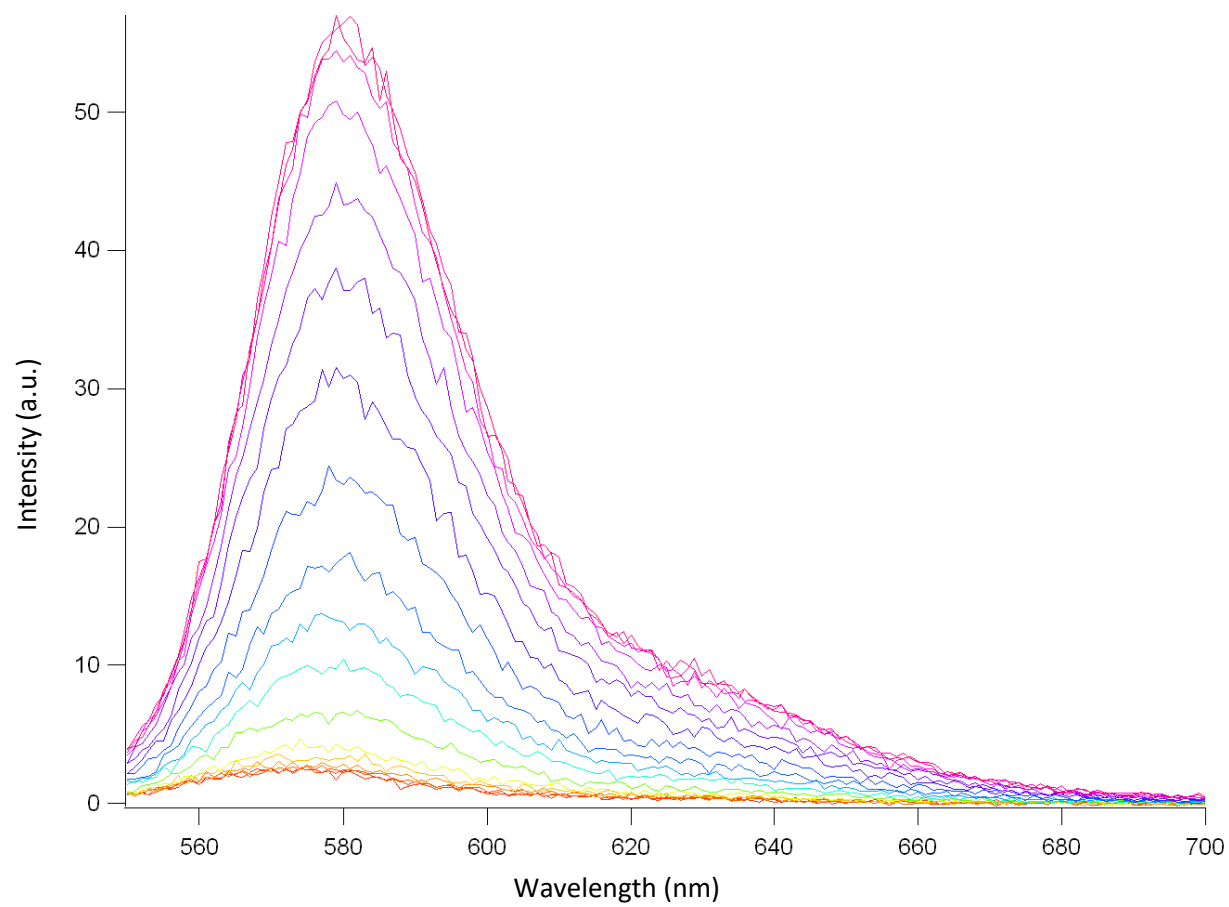


**Figure B19:** Sample fluorescence spectra for RB-DCPA

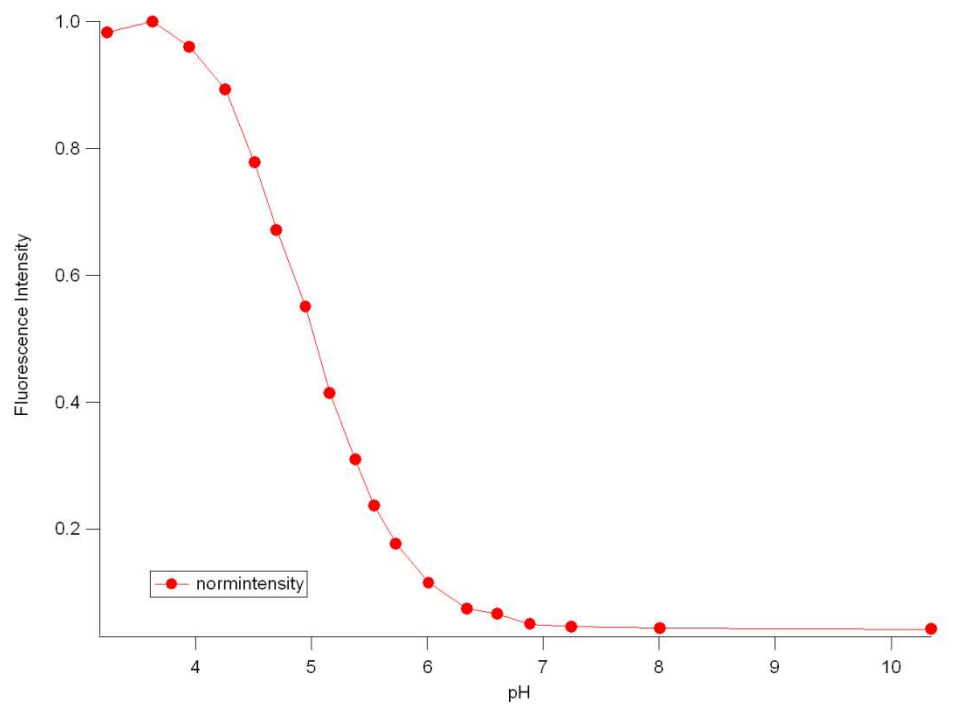


**Figure B20:** Sample titration curve for RB-DCPA

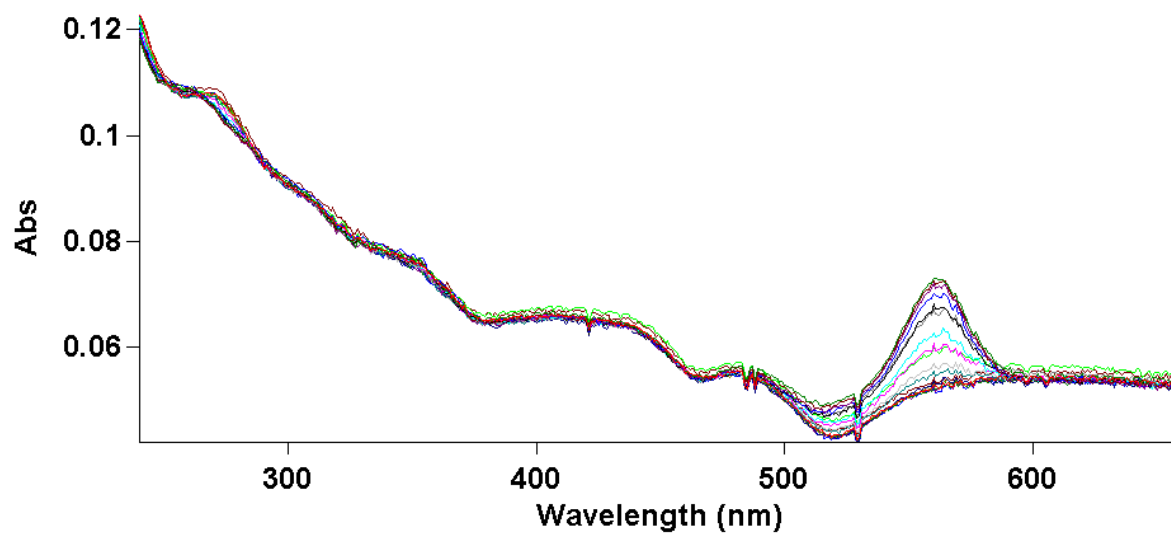


**Figure B21:** Sample UV-Vis spectra for RB-DCPA

<b>RB-DCPA</b>	<b>pKa</b>	<b>Max fl intensity</b>	<b>Fl lmax</b>
	4.96	10	580
	4.92	10	580
	5.04	57	580
Mean	4.973	25.667	
Std dev	0.061	27.135	

**Table B7:** pKa values for RB-DCPA

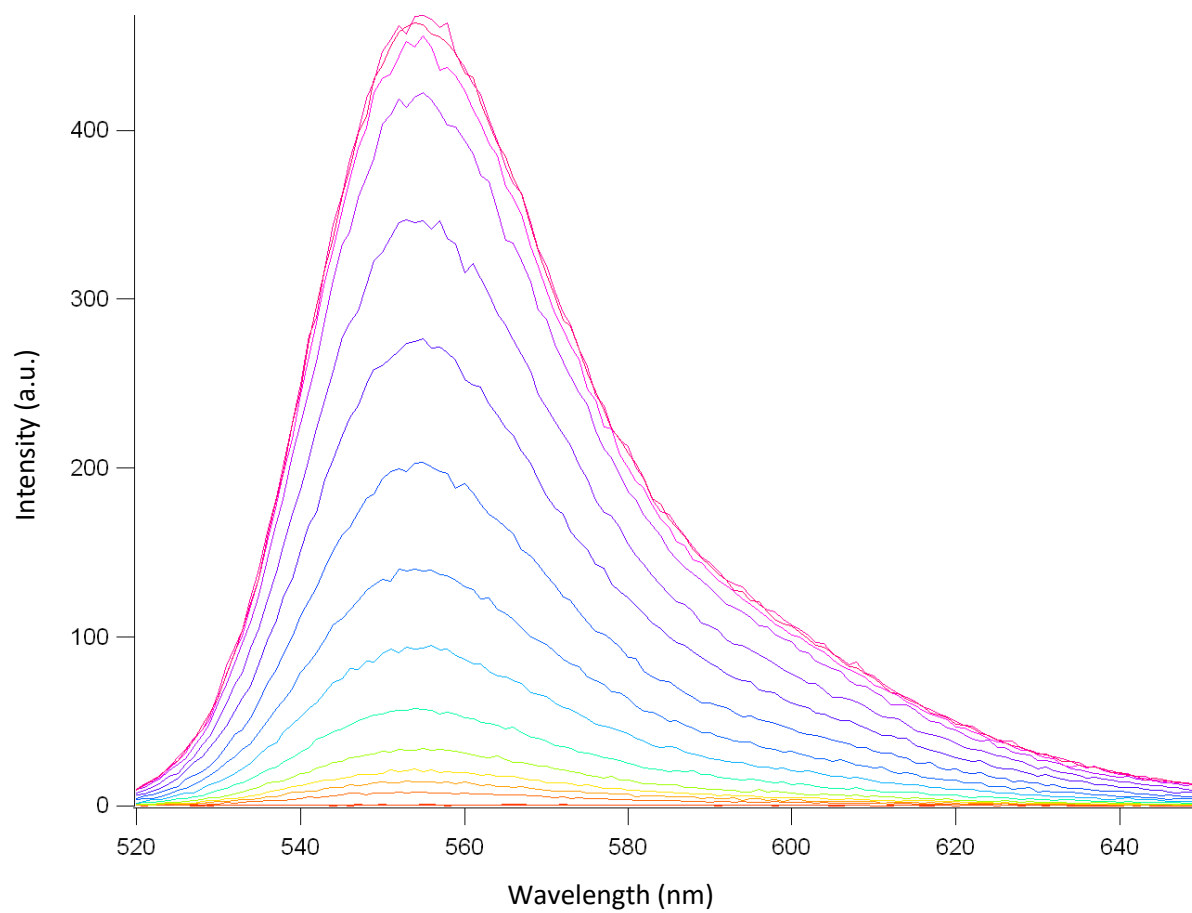


**Figure B22:** Sample fluorescence spectra for R6G-A

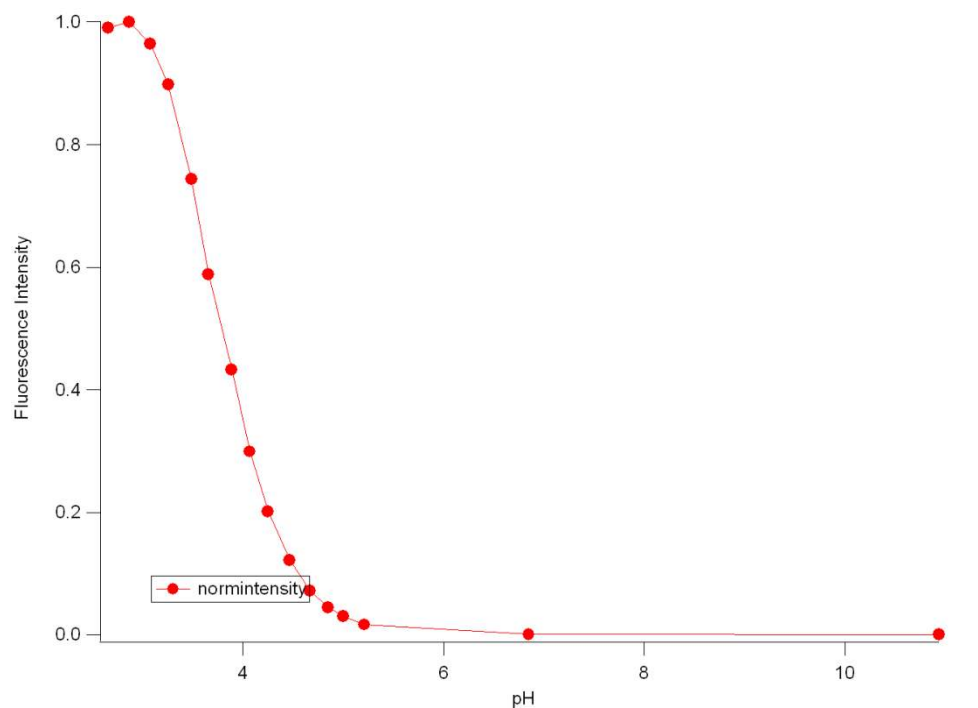


**Figure B23:** Sample titration curve for R6G-A

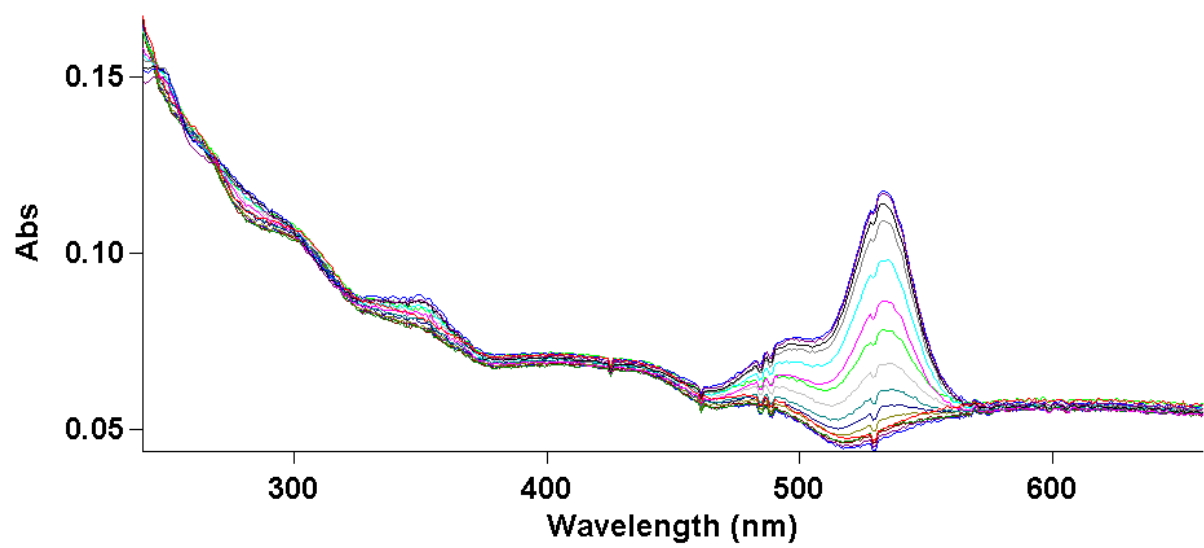


**Figure B24:** Sample UV-Vis spectra for R6G-A

<b>R6G-A</b>	<b>pKa</b>	<b>Max fl intensity</b>	<b>Fl lmax</b>
	3.83	431	555
	3.83	500	555
	3.83	267	555
	3.79	295	555
	3.80	340	555
	3.79	355	555
	3.81	467	555
	3.82	421	555
Mean	3.813	384.5	
Std dev	0.018	83.073	

Note: Diluted 2x

**Table B8:** pKa values for R6G-A

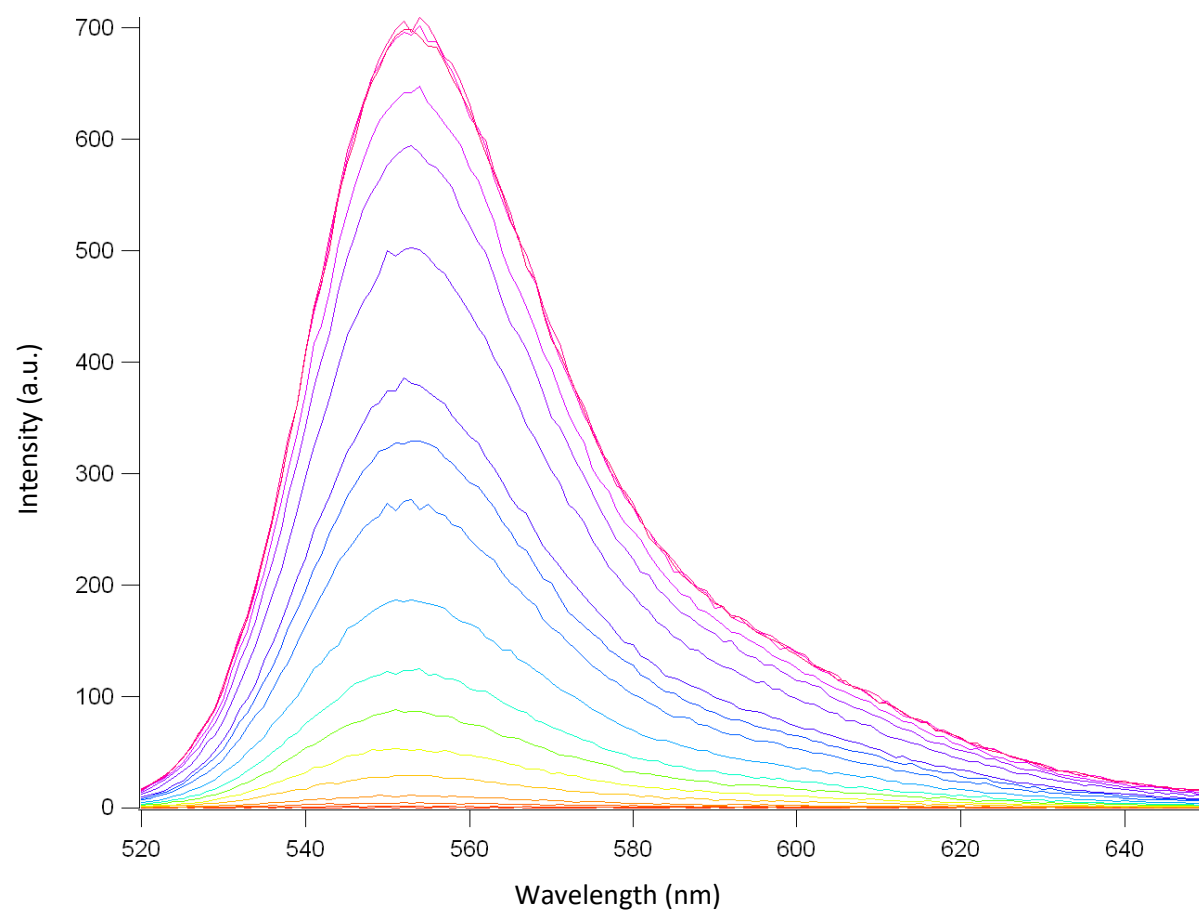


**Figure B25:** Sample fluorescence spectra for R6G-DFA

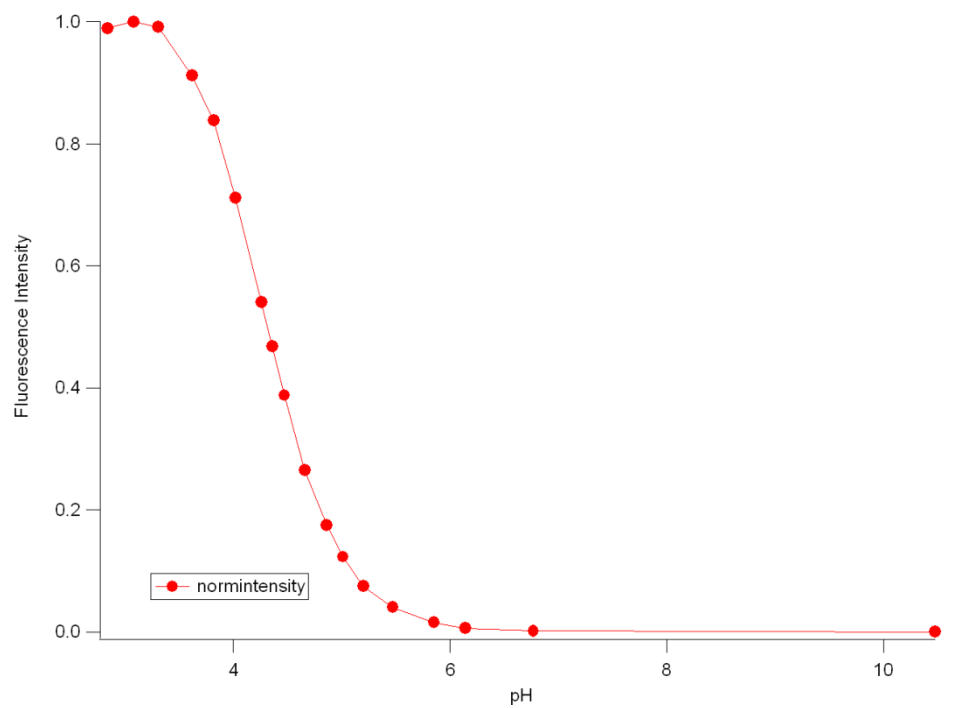


**Figure B26:** Sample titration curve for R6G-DFA

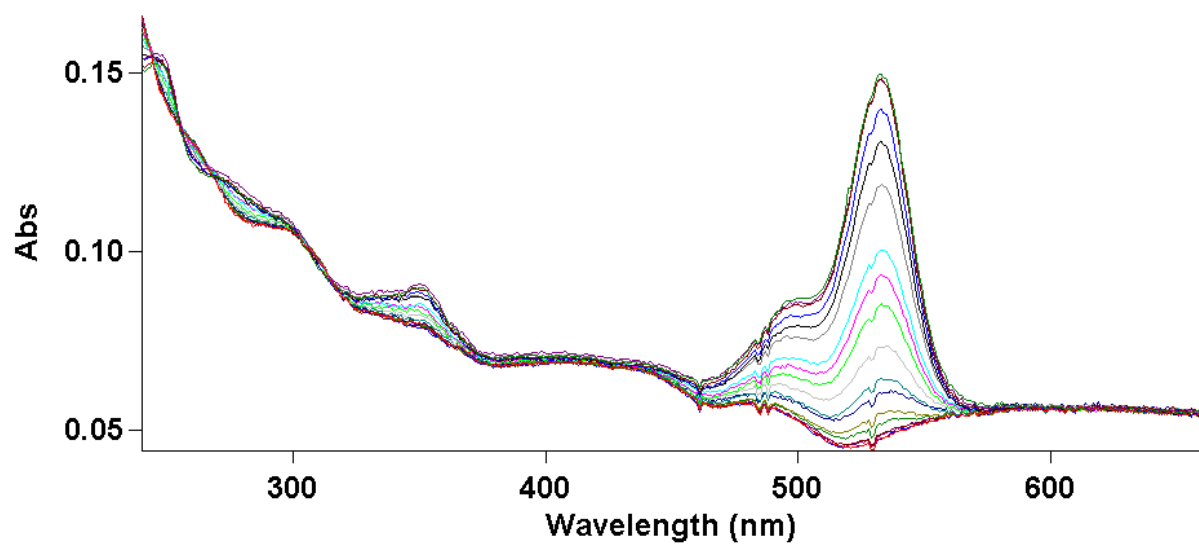


**Figure B27:** Sample UV-Vis spectra for R6G-DFA



<b>R6G-DFA</b>	<b>pKa</b>	<b>Max fl intensity</b>	<b>Fl lmax</b>
	4.26	607	553
	4.27	683	553
	4.30	591	553
	4.29	601	553
	4.32	551	553
	4.28	564	553
	4.37	584	553
	4.33	704	553
Mean	4.303	610.625	
Std dev	0.036	54.623	

Note: Diluted 2x

**Table B9:** pKa values for R6G-DFA

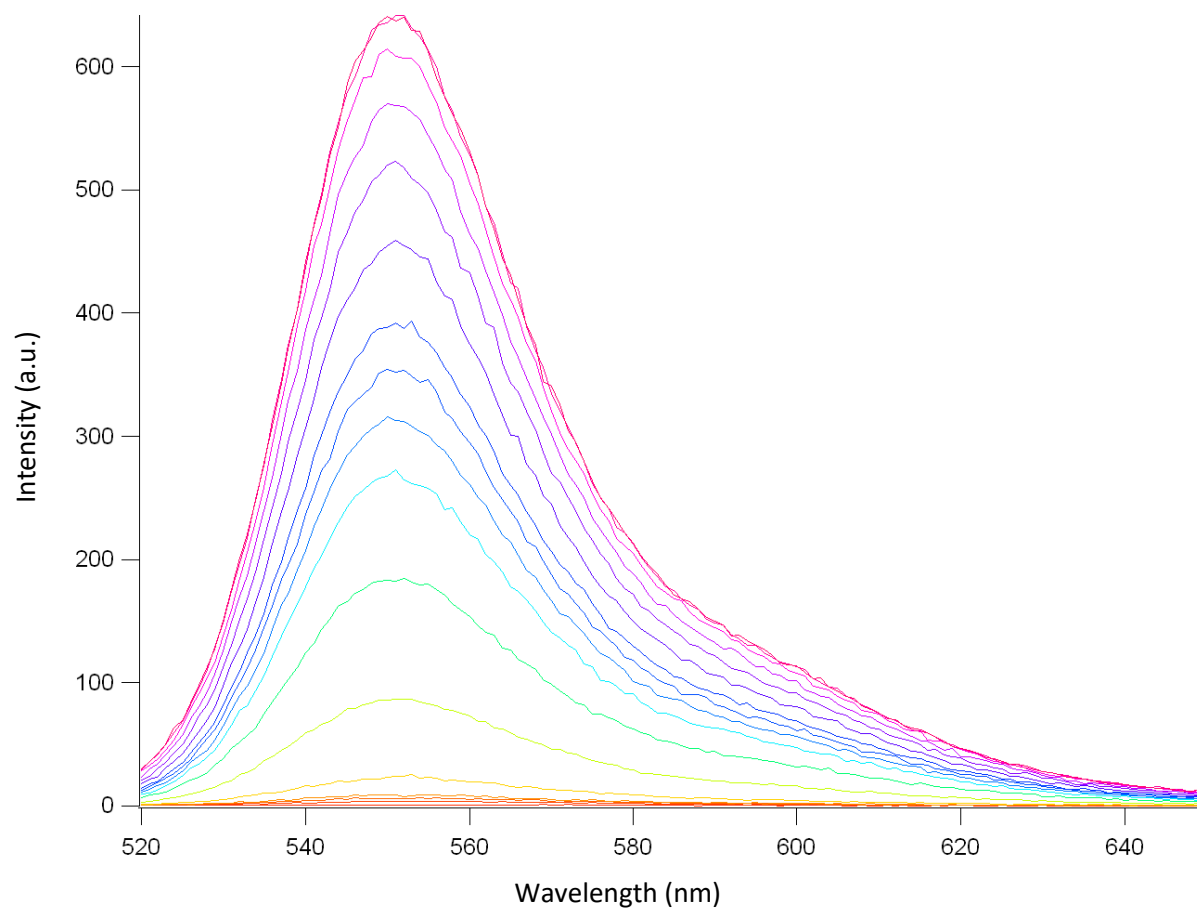


**Figure B28:** Sample fluorescence spectra for R6G-DCA

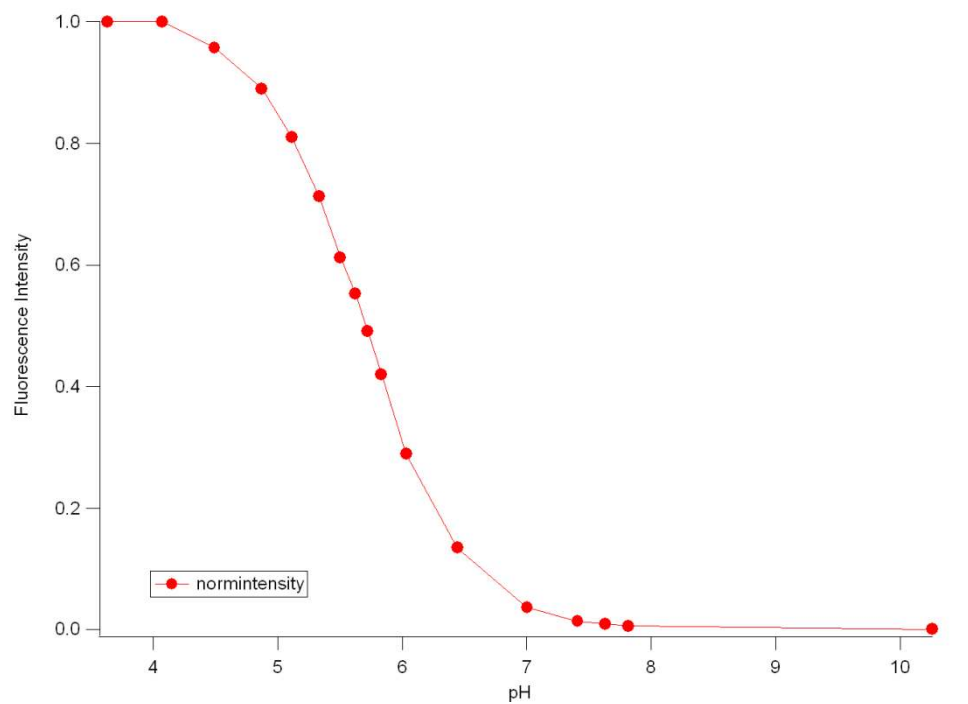


**Figure B29:** Sample titration curve for R6G-DCA

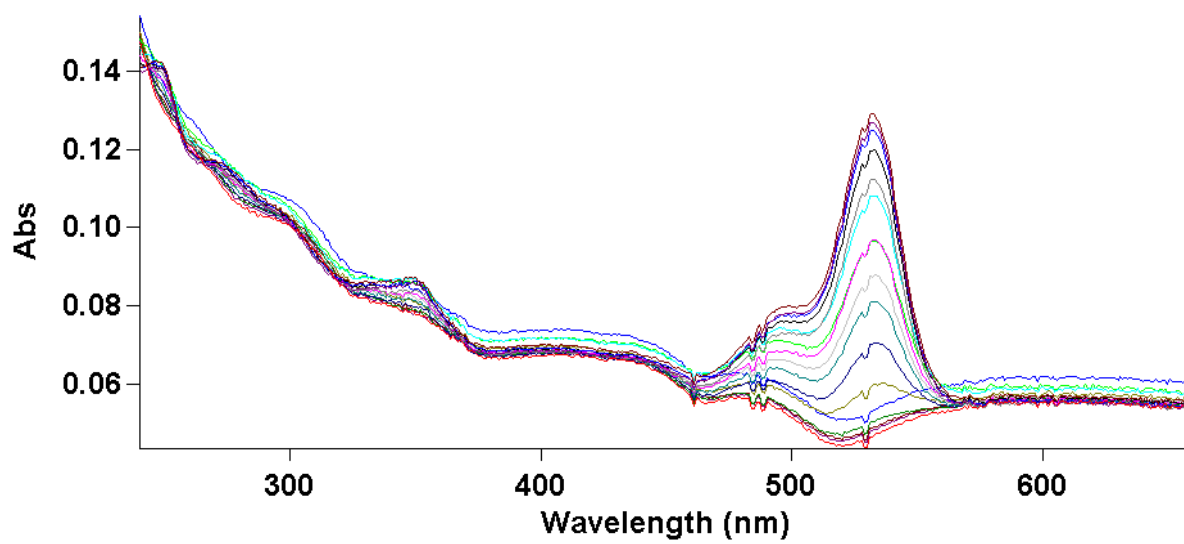


**Figure B30:** Sample UV-Vis spectra for R6G-DCA

<b>R6G-DCA</b>	<b>pKa</b>	<b>Max fl intensity</b>	<b>Fl lmax</b>
	5.64	644	551
	5.59	590	551
	5.58	656	551
	5.64	663	551
	5.58	650	551
	5.64	463	551
	5.59	647	551
	5.69	639	551
Mean	5.619	619	
Std dev	0.040	66.817	

Note: Diluted 2x

**Table B10:** pKa values for R6G-DCA

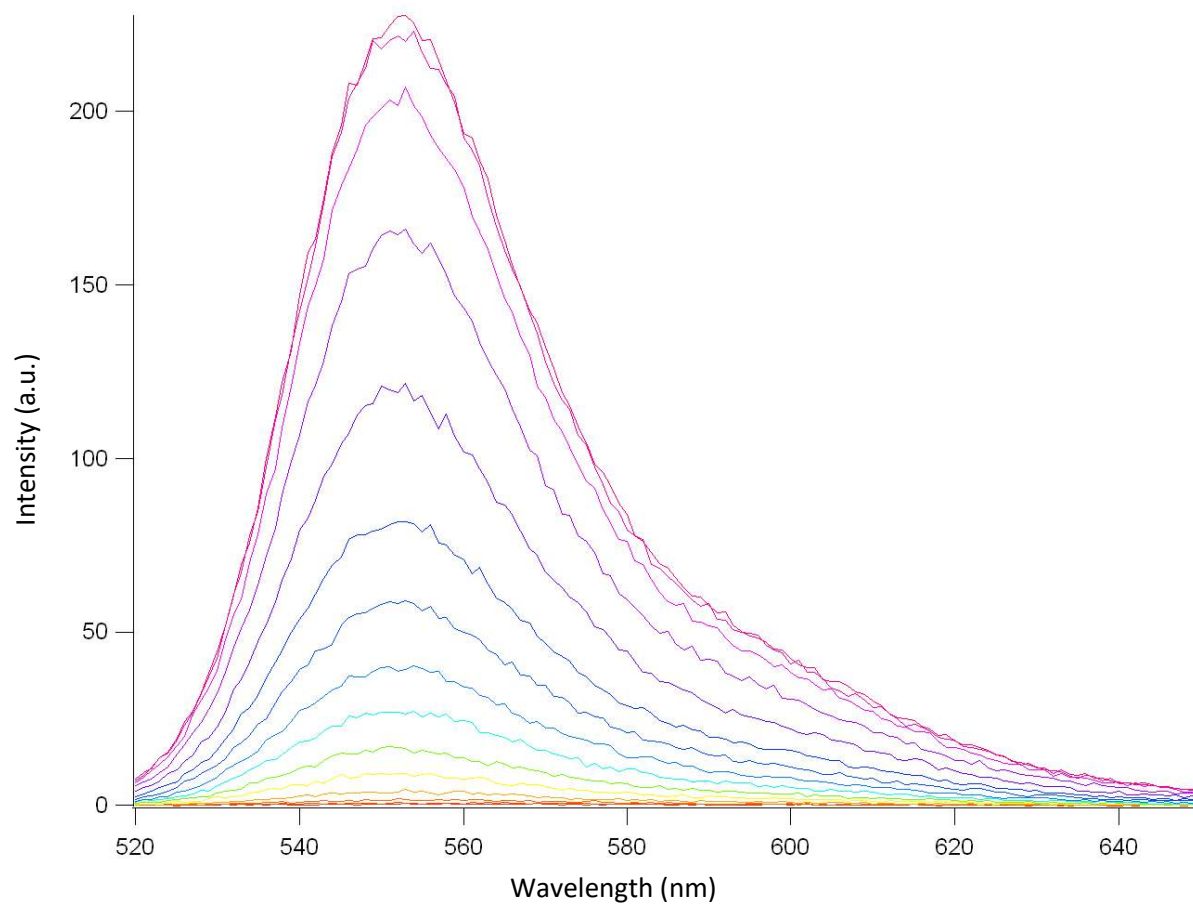


**Figure B31:** Sample fluorescence spectra for R6G-DEA

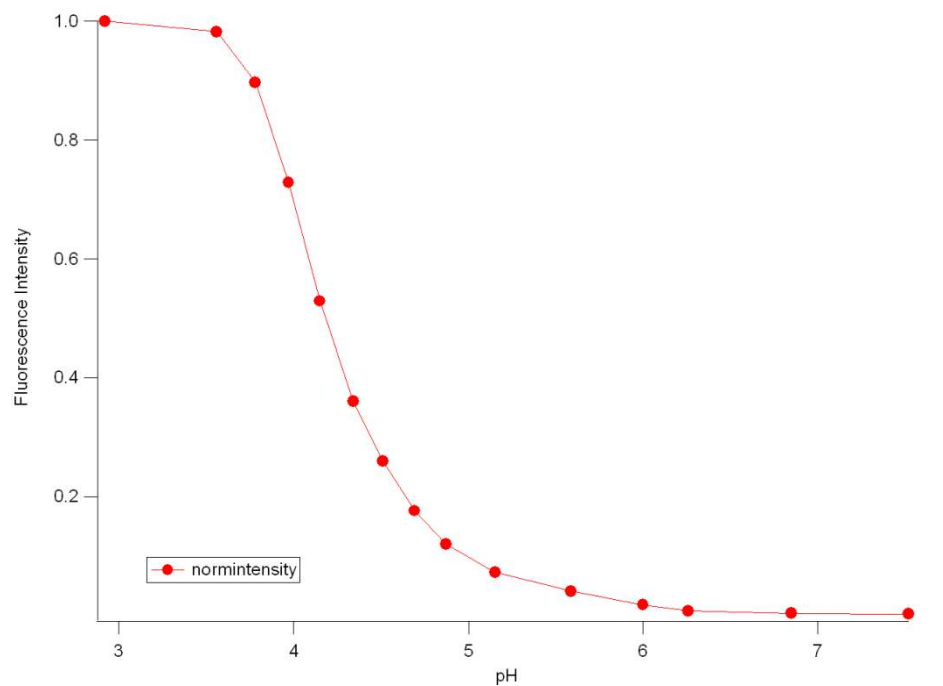


**Figure B32:** Sample titration curve for R6G-DEA

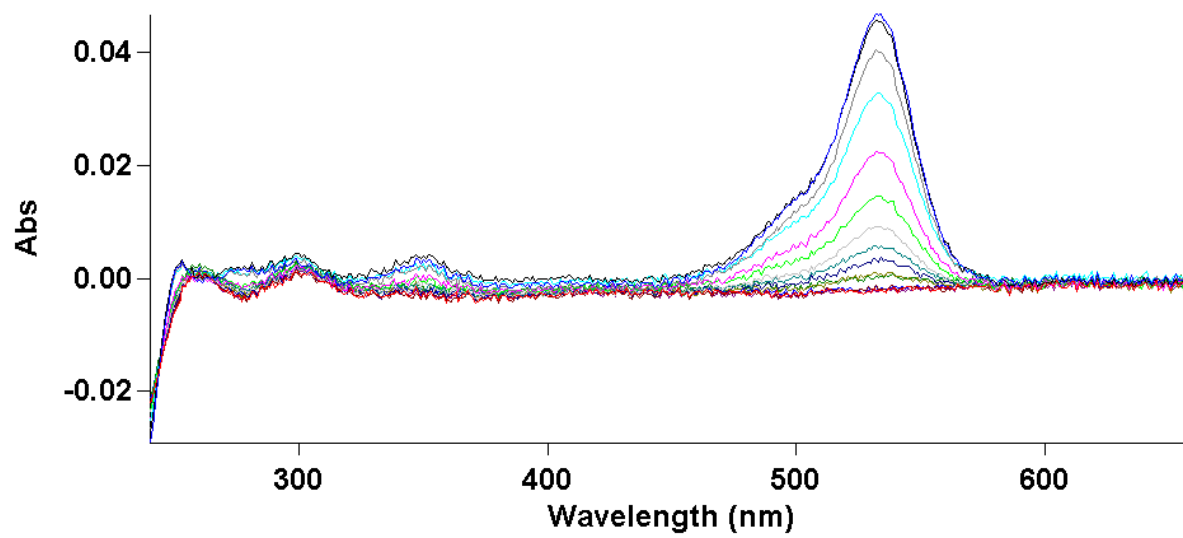


**Figure B33:** Sample UV-Vis spectra for R6G-DEA

<b>R6G-DEA</b>	<b>pKa</b>	<b>Max fl intensity</b>	<b>Fl lmax</b>
	4.13	136	552
	4.10	133	552
	4.21	227	552
	4.15	83	552
Mean	4.148	144.75	552
Std dev	0.046	59.980	

Note: Diluted 2x

**Table B11:** pKa values for R6G-DEA

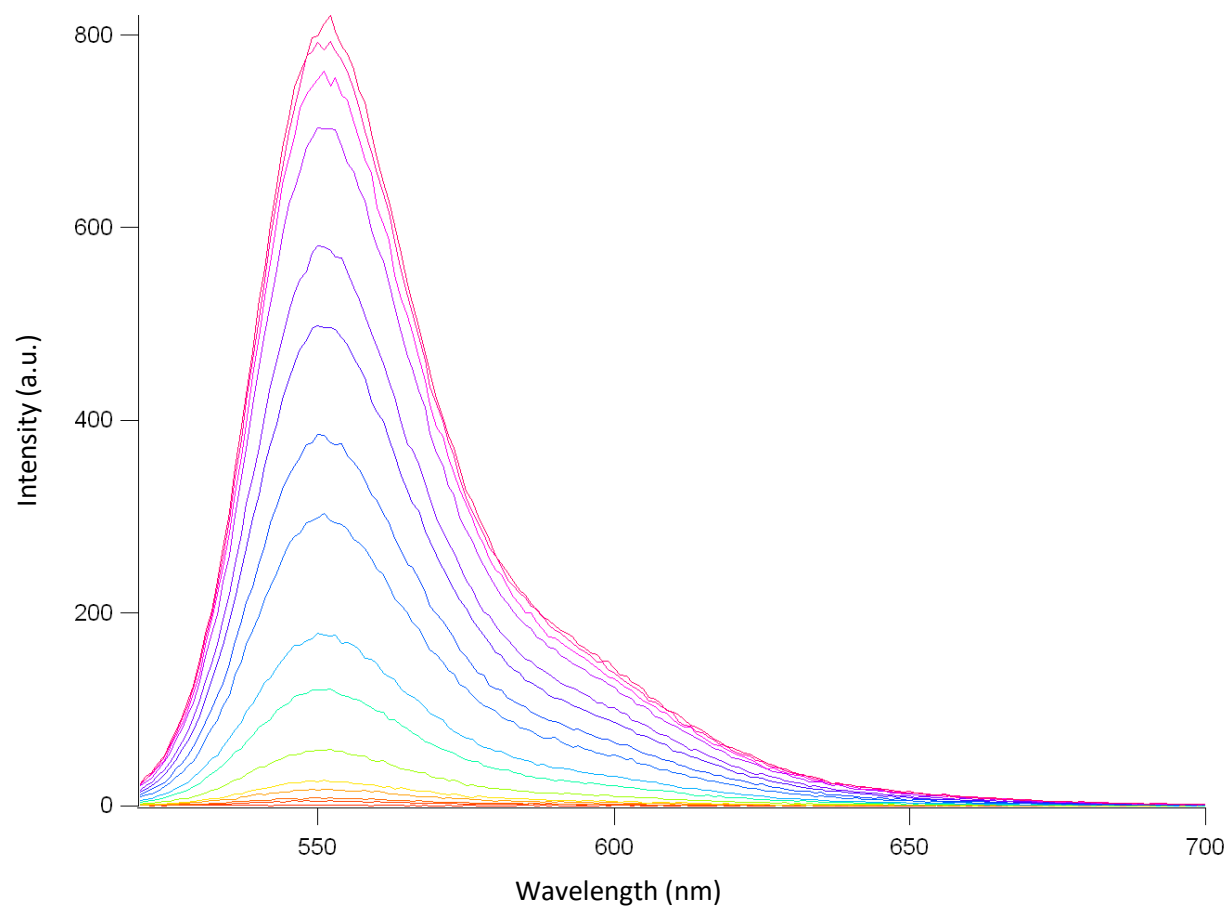


**Figure B34:** Sample fluorescence spectra for R6G-DMA



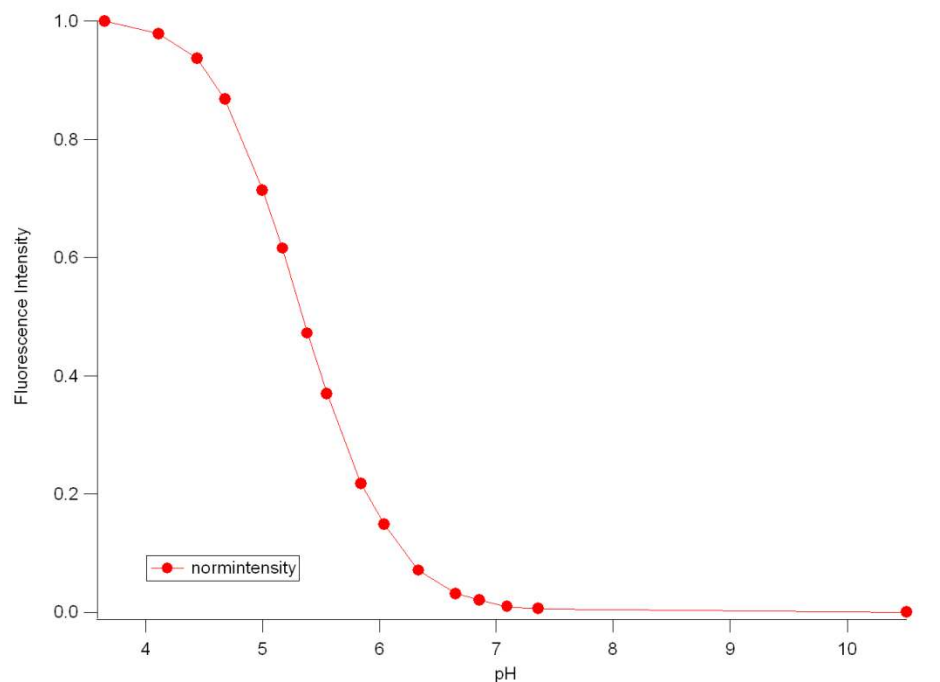


**Figure B35:** Sample titration curve for R6G-DMA

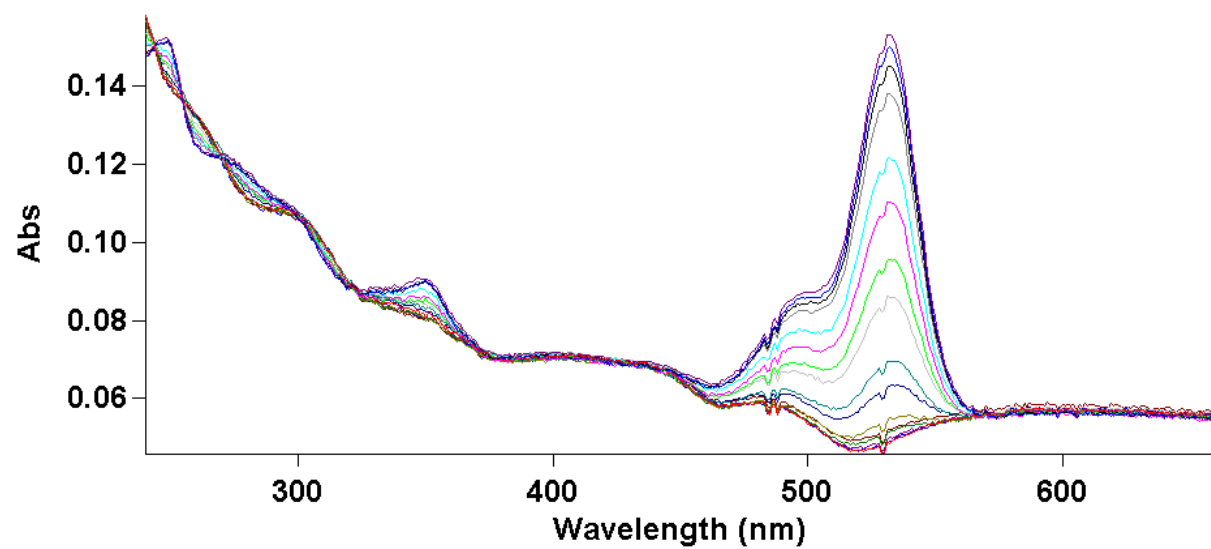


**Figure B36:** Sample UV-Vis spectra for R6G-DMA

<b>R6G-DMA</b>	<b>pKa</b>	<b>Max fl intensity</b>	<b>Fl lmax</b>
	5.29	882	552
	5.21	824	552
	5.28	537	552
	5.33	495	552
	5.30	551	552
	5.44	503	552
	5.36	809	552
	5.36	763	552
Mean	5.321	670.5	
Std dev	0.0683	163.442	

Note: Diluted 2x

**Table B12:** pKa values for R6G-DMA

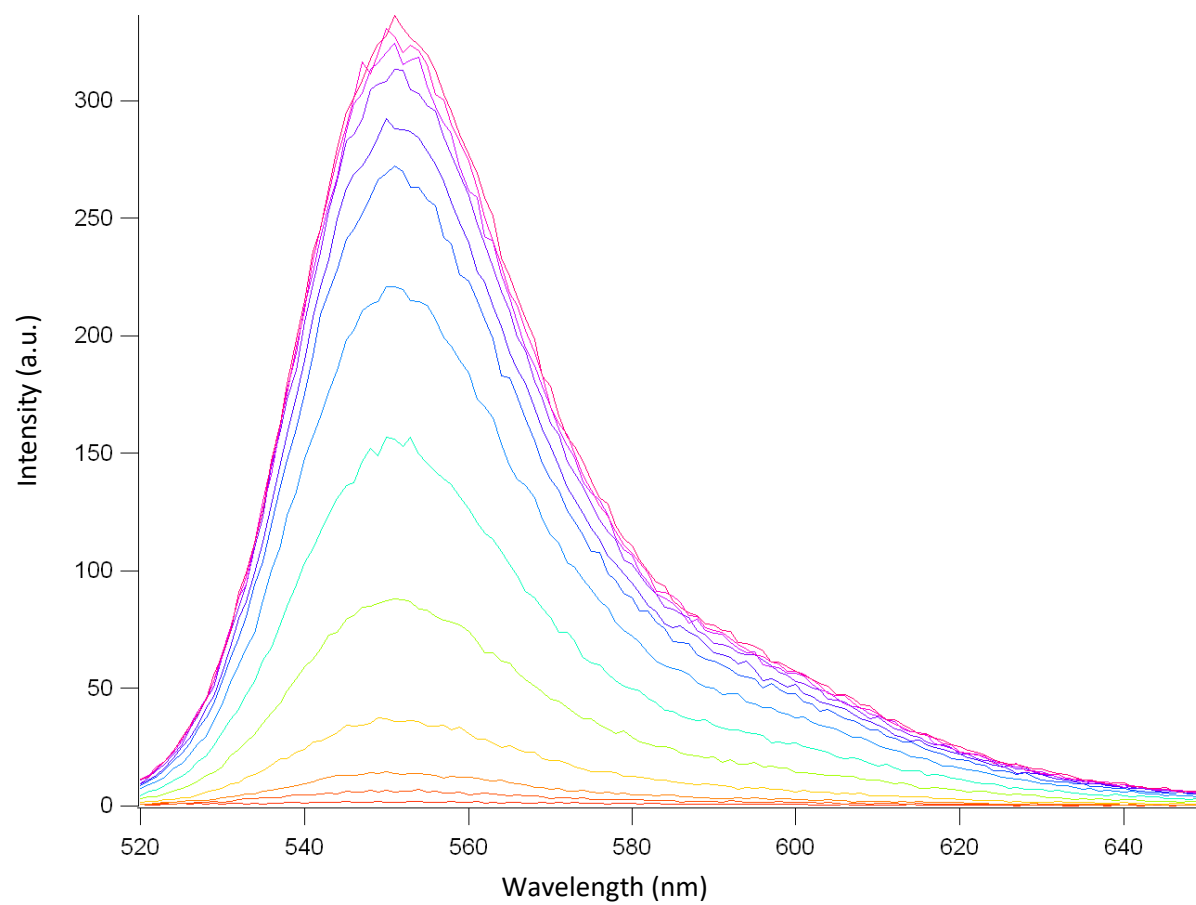


**Figure B37:** Sample fluorescence spectra for R6G-DIA

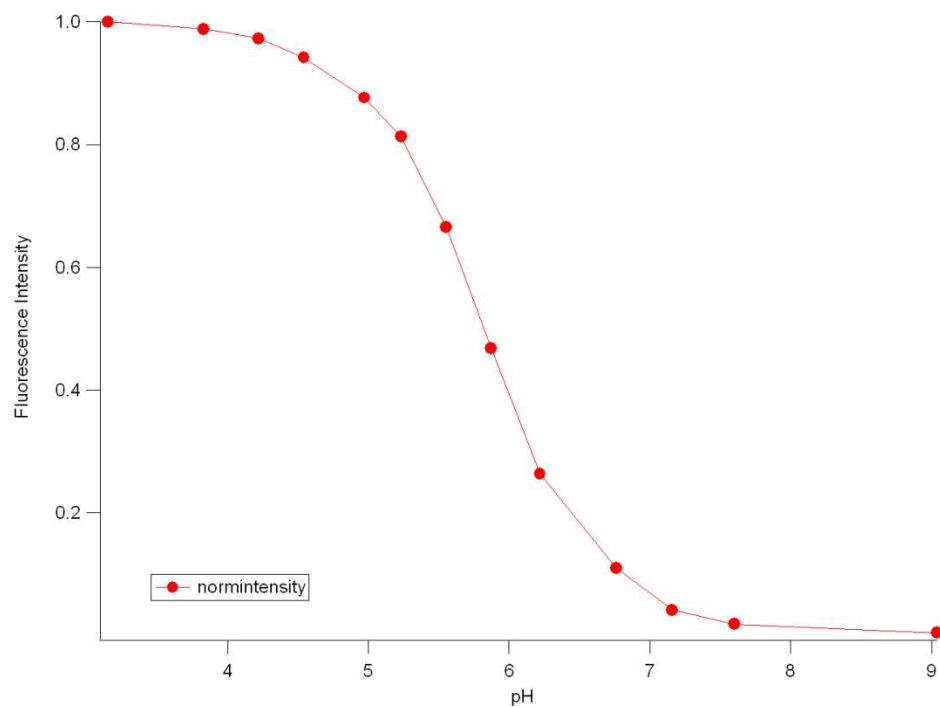


**Figure B38:** Sample titration curve for R6G-DIA

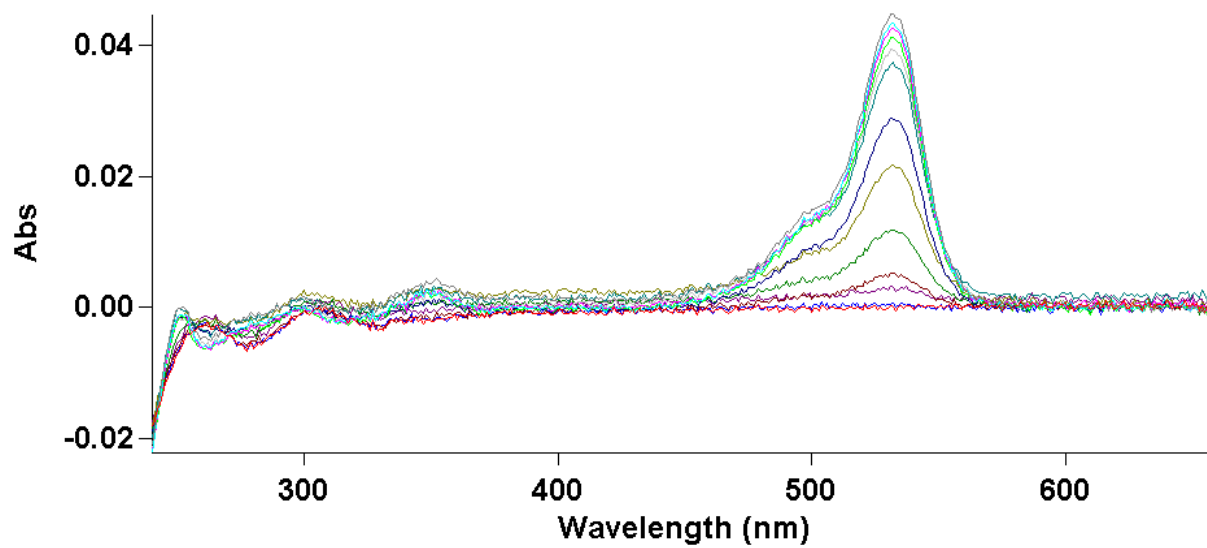


**Figure B39:** Sample UV-Vis spectra for R6G-DIA

<b>R6G-DIA</b>	<b>pKa</b>	<b>Max fl intensity</b>	<b>Fl lmax</b>
	5.86	299	552
	5.79	221	552
	5.90	299	552
	5.81	330	552
	5.96	420	552
	5.91	374	552
Mean	5.872	323.833	
Std dev	0.064	68.718	

Note: Diluted 2x

**Table B13:** pKa values for R6G-DIA

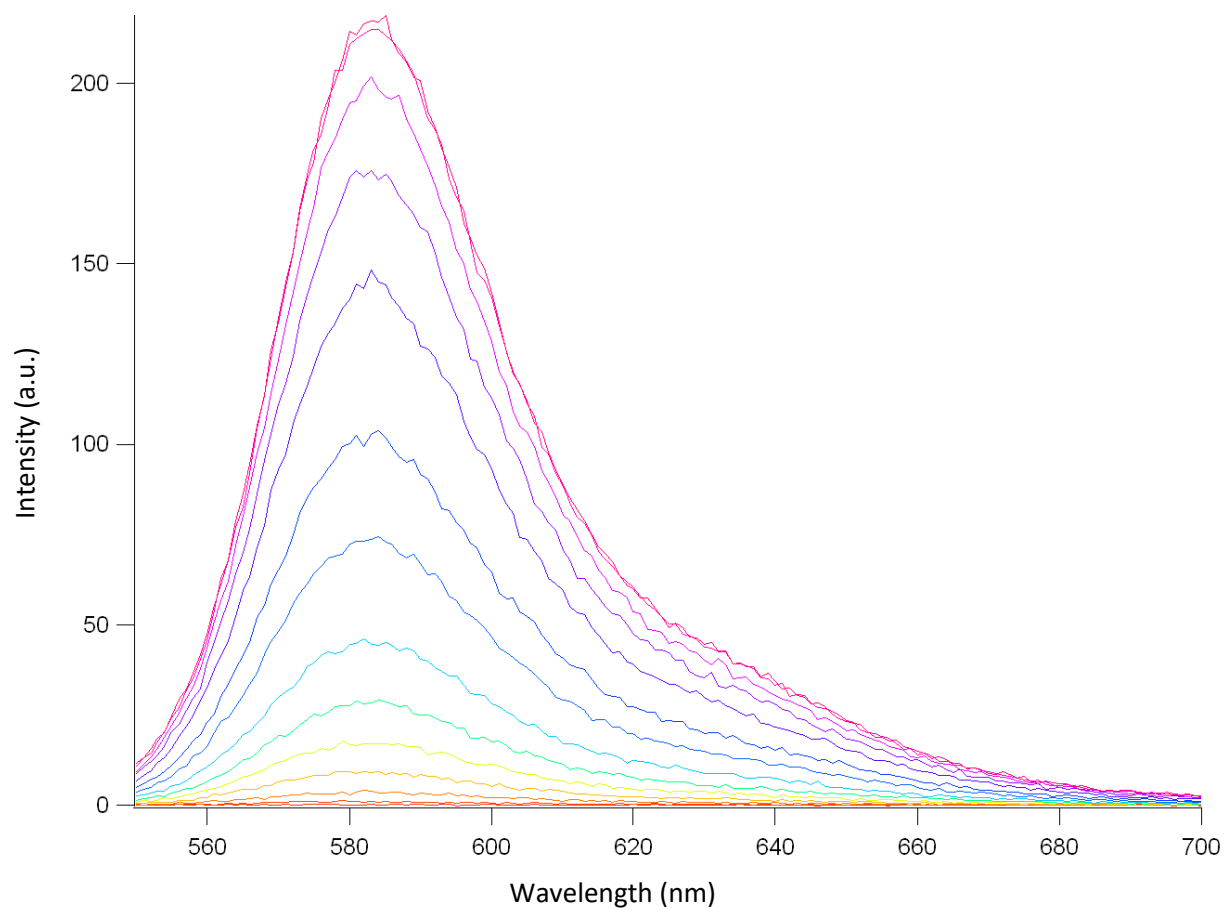


**Figure B40:** Sample fluorescence spectra for RB-4CA

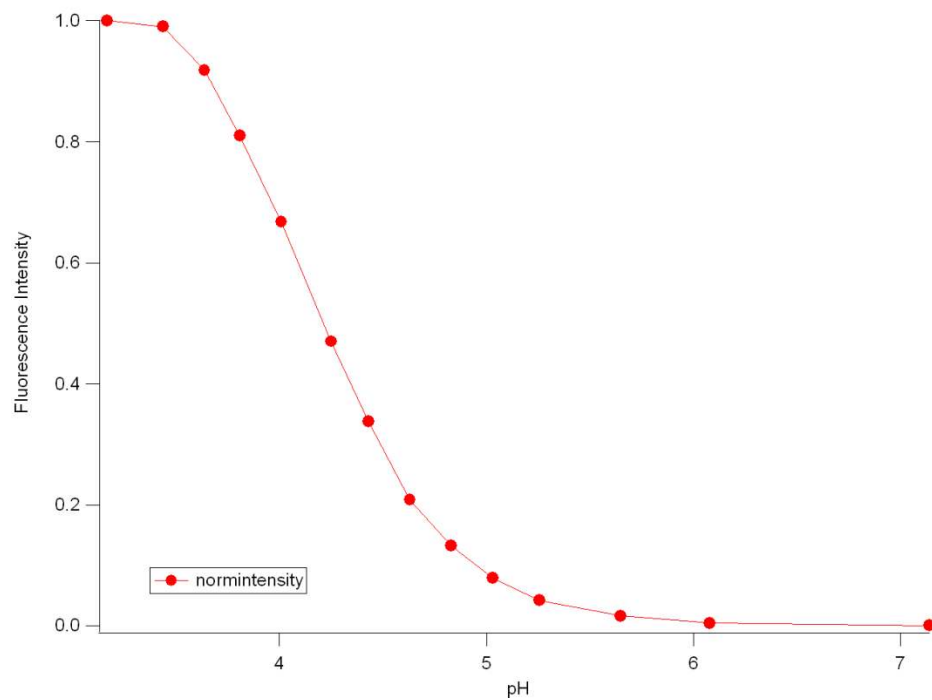


**Figure B41:** Sample titration curve for RB-4CA

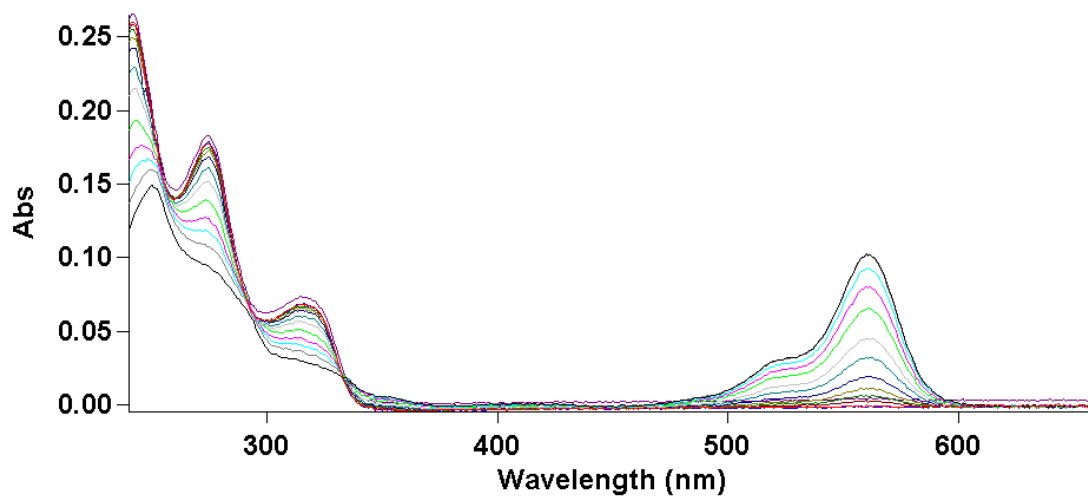


**Figure B42:** Sample UV-Vis spectra for RB-4CA

<b>RB-4CA</b>	<b>pKa</b>	<b>Max fl intensity</b>	<b>Fl lmax</b>
	4.20	270	583
	4.21	270	583
	4.20	215	583
	4.23	215	583
Mean	4.21	242.500	
Std dev	0.014	31.754	

**Table B14:** pKa values for RB-4CA



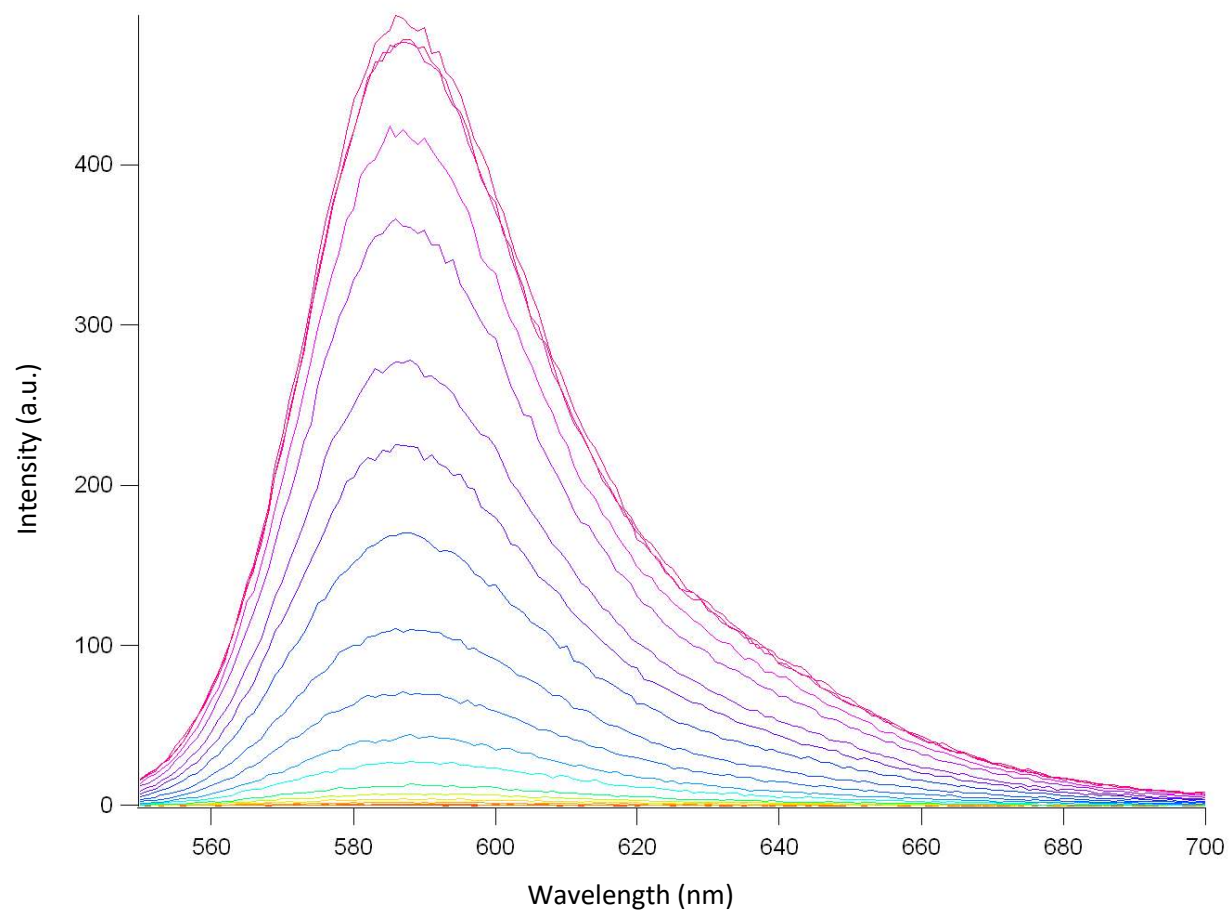


**Figure B43:** Sample fluorescence spectra for RB-3,5CA

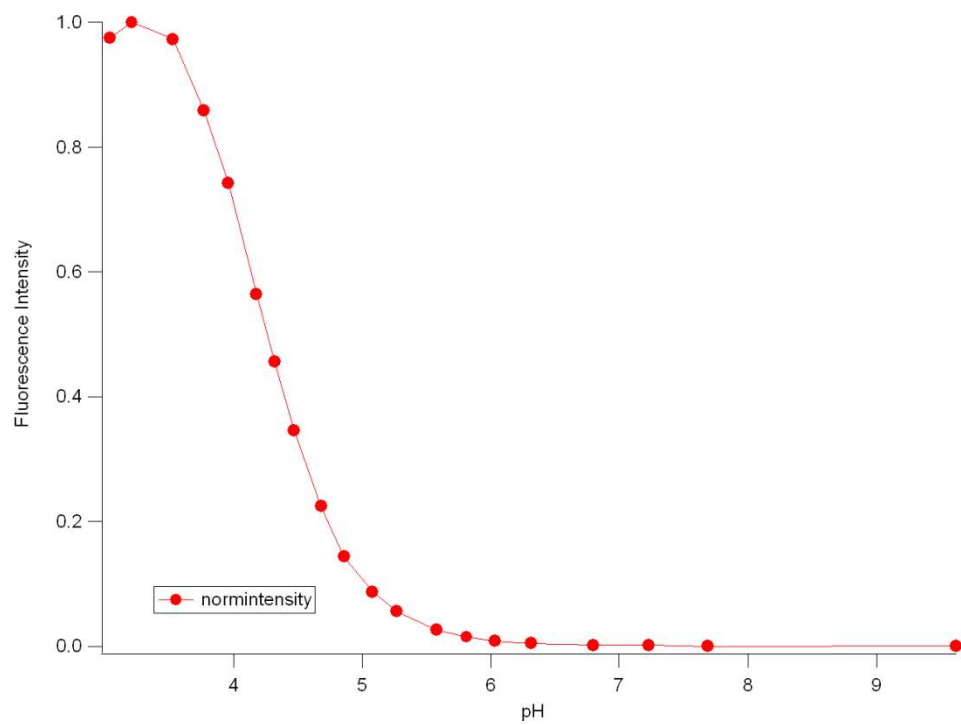


**Figure B44:** Sample titration curve for RB-3,5CA

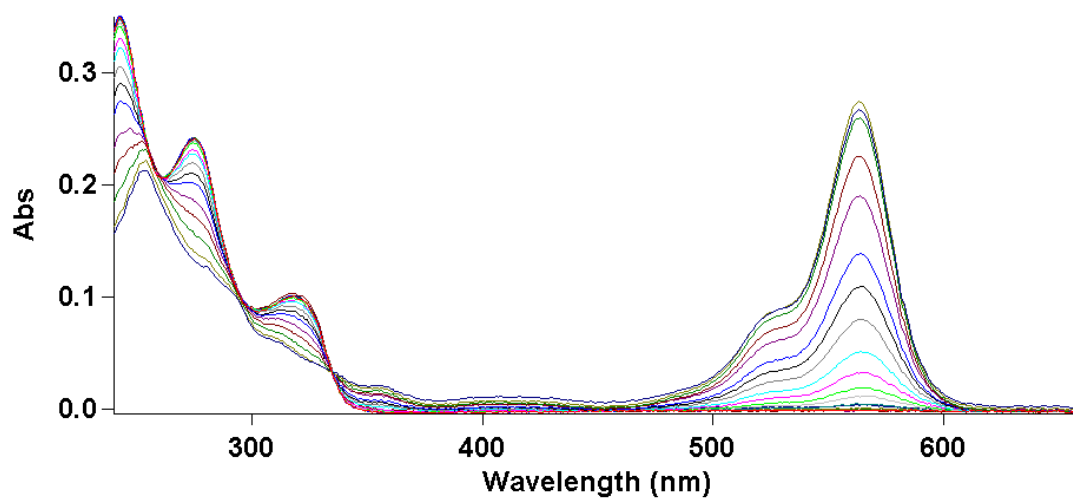


**Figure B45:** Sample UV-Vis spectra for RB-3,5CA

<b>RB-3,5CA</b>	<b>pKa</b>	<b>Max fl intensity</b>	<b>Fl lmax</b>
	4.30	485	587
	4.36	478	587
	4.35	291	587
	4.36	493	587
Mean	4.343	436.750	
Std dev	0.050	97.360	

**Table B15:** pKa values for RB-3,5CA

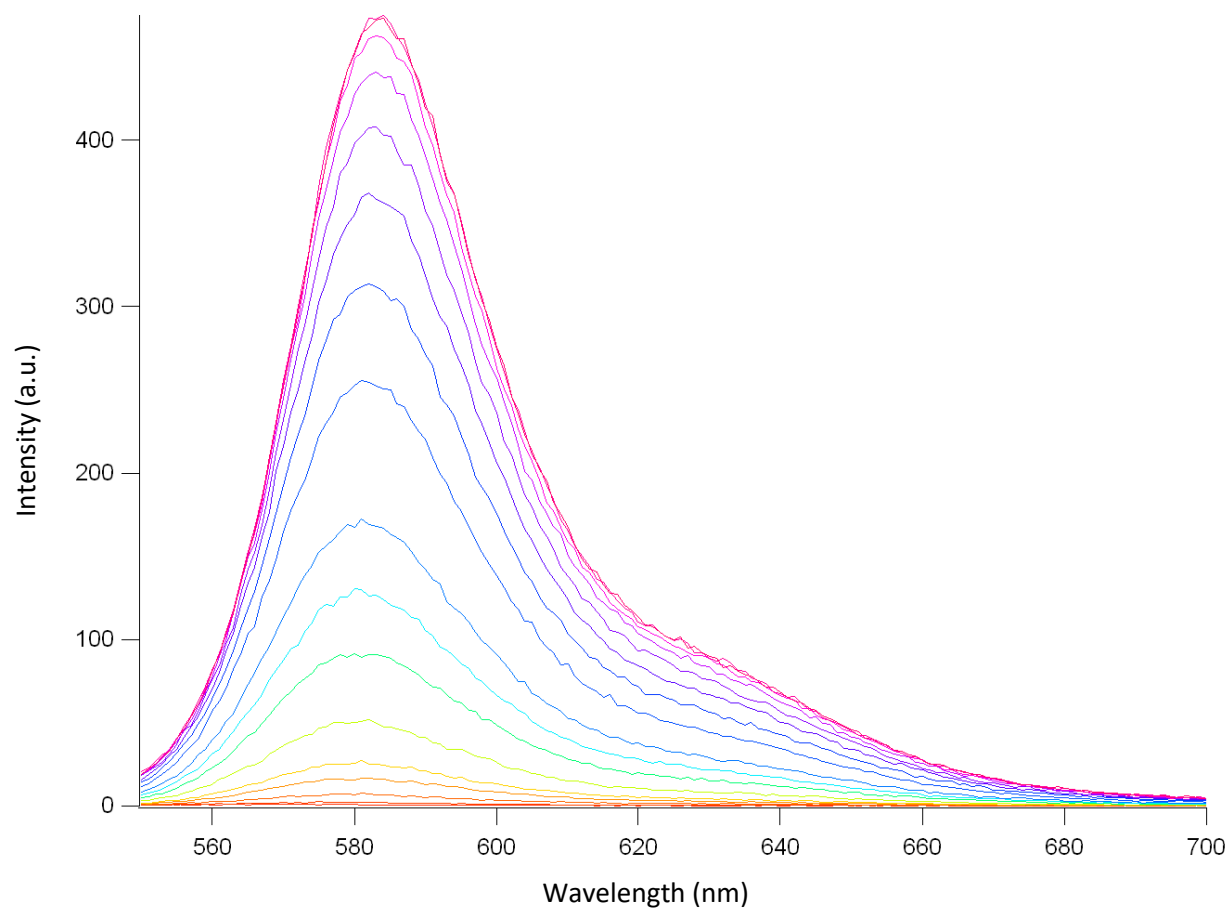


**Figure B46:** Sample fluorescence spectra for RB-DCNA

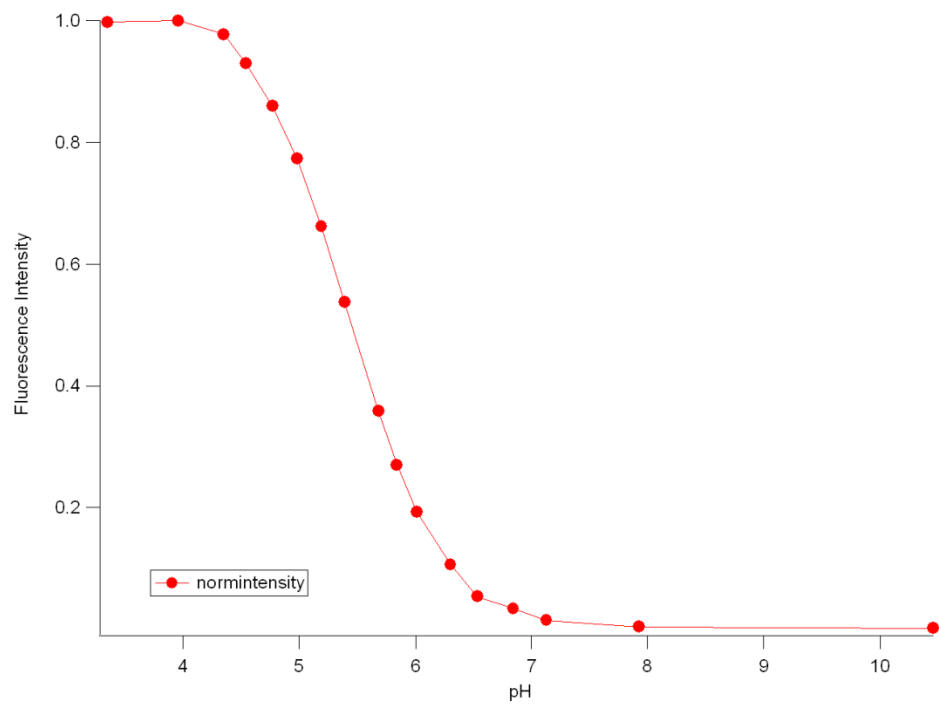


**Figure B47:** Sample titration curve for RB-DCNA

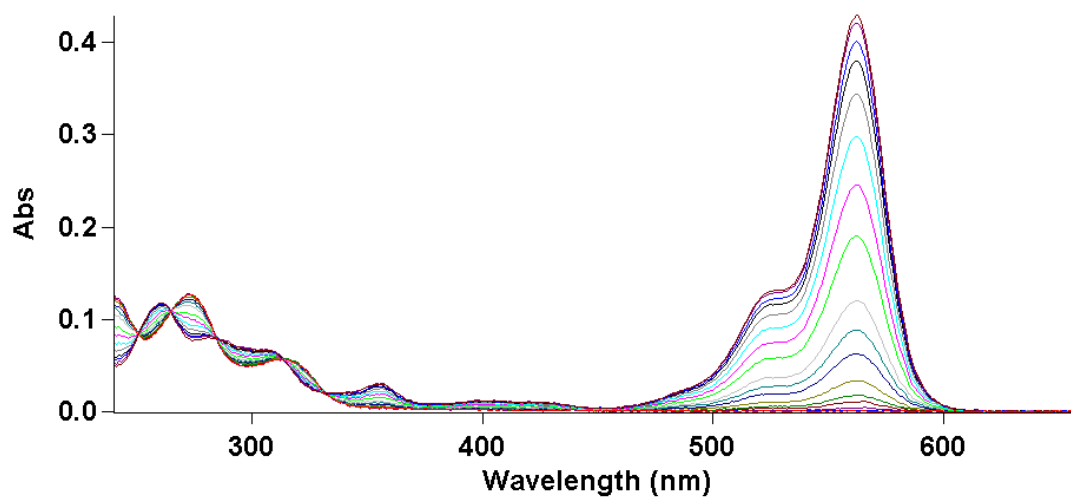


**Figure B48:** Sample UV-Vis spectra for RB-DCNA

RB-DCNA	pKa	Max fl intensity	Fl lmax
	5.43 <sup>17</sup>	-	-
	5.46	475	583
	5.44	456	583
	5.50	475	583
Mean	5.458	468.667	
Std dev	0.031	10.970	

**Table B16:** pKa values for RB-DCNA

---

<sup>17</sup> Titration by William L. Czaplyski

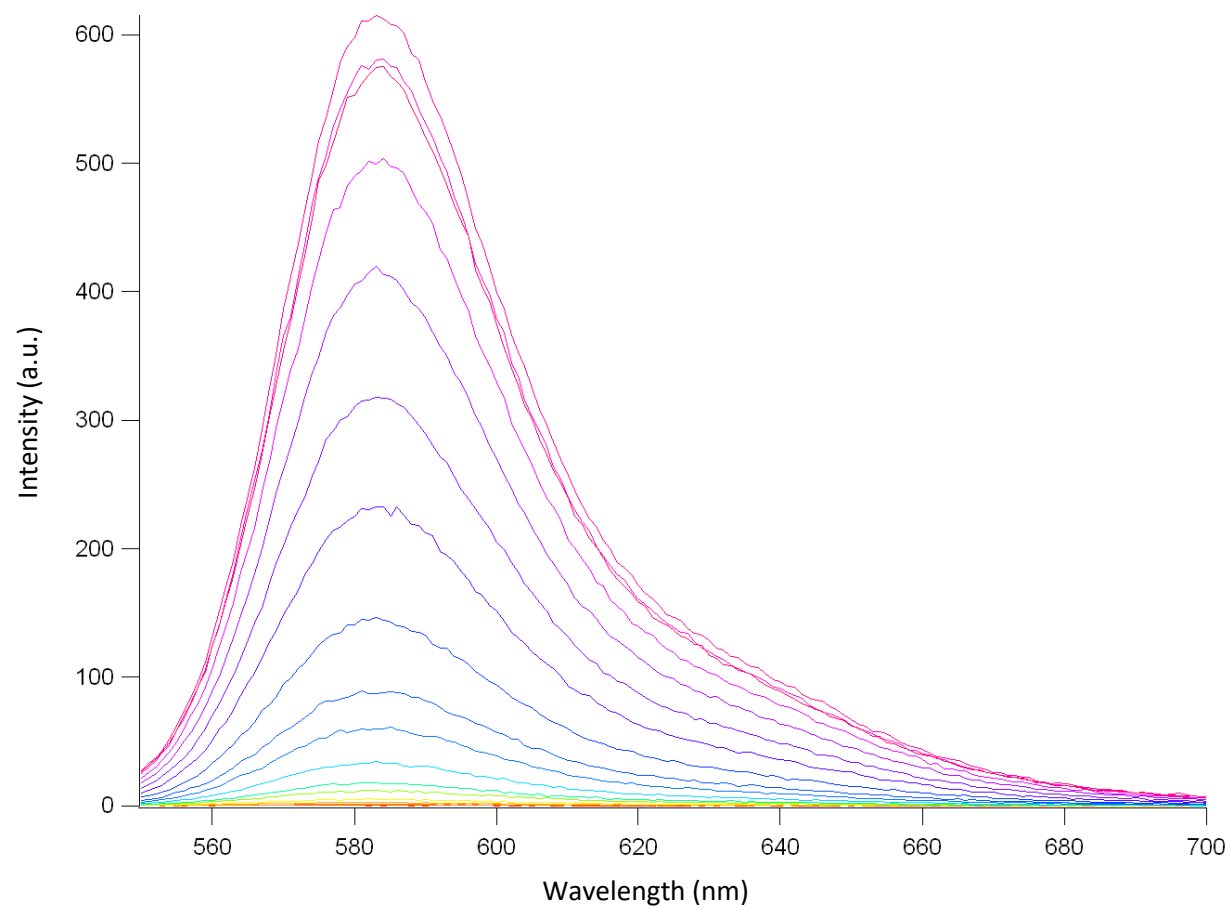


**Figure B49:** Sample fluorescence spectra for RB-2FA

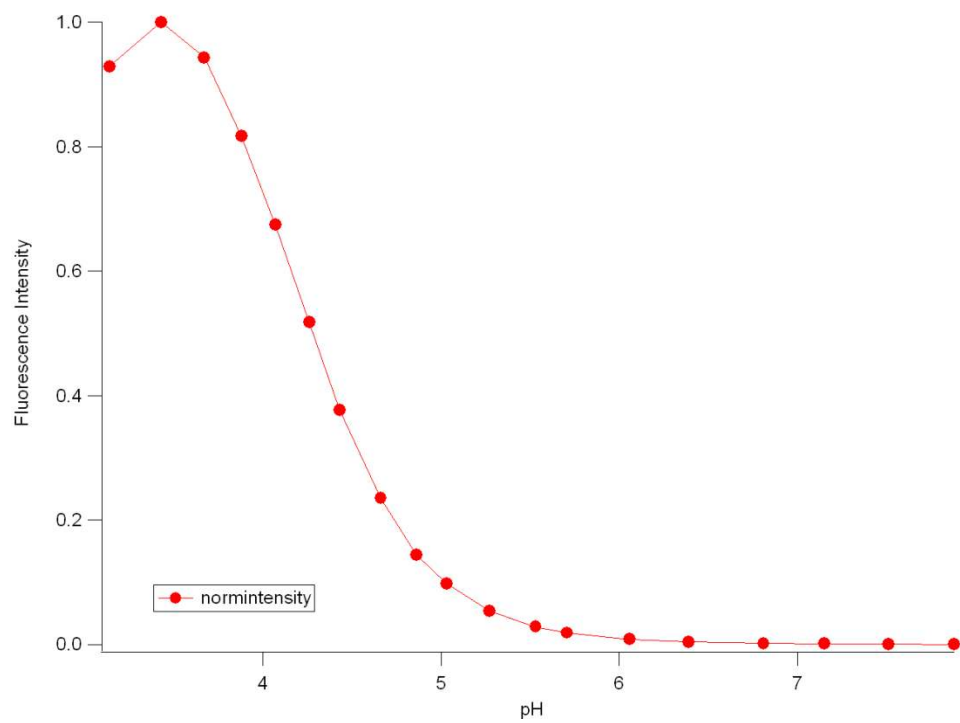


**Figure B50:** Sample titration curve for RB-2FA

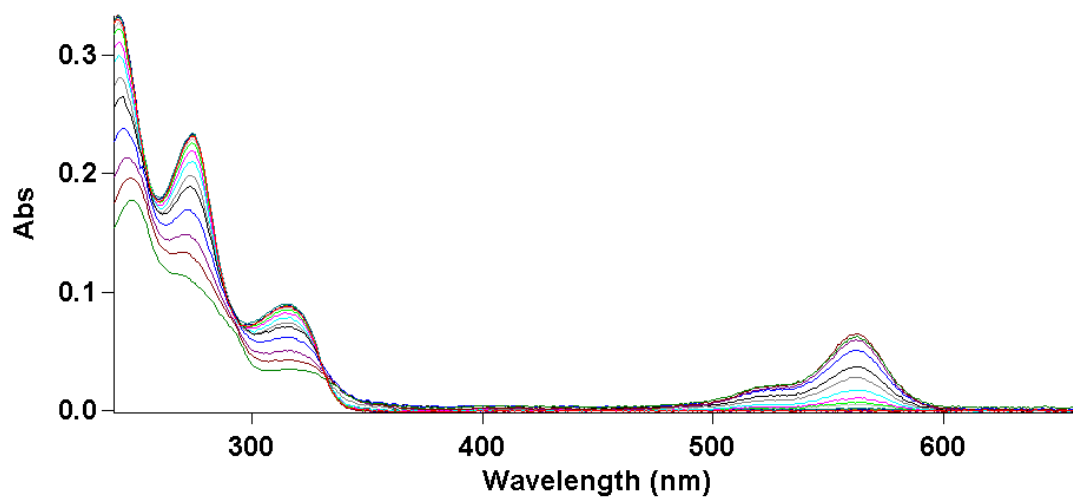


**Figure B51:** Sample UV-Vis spectra for RB-2FA



<b>RB-2FA</b>	<b>pKa</b>	<b>Max fl intensity</b>	<b>Fl lmax</b>
	4.33	70	583
	4.34	615	583
	4.32	132	583
Mean	4.33	272.333	
Std dev	0.01	298.373	

**Table B17:** pKa values for RB-2FA

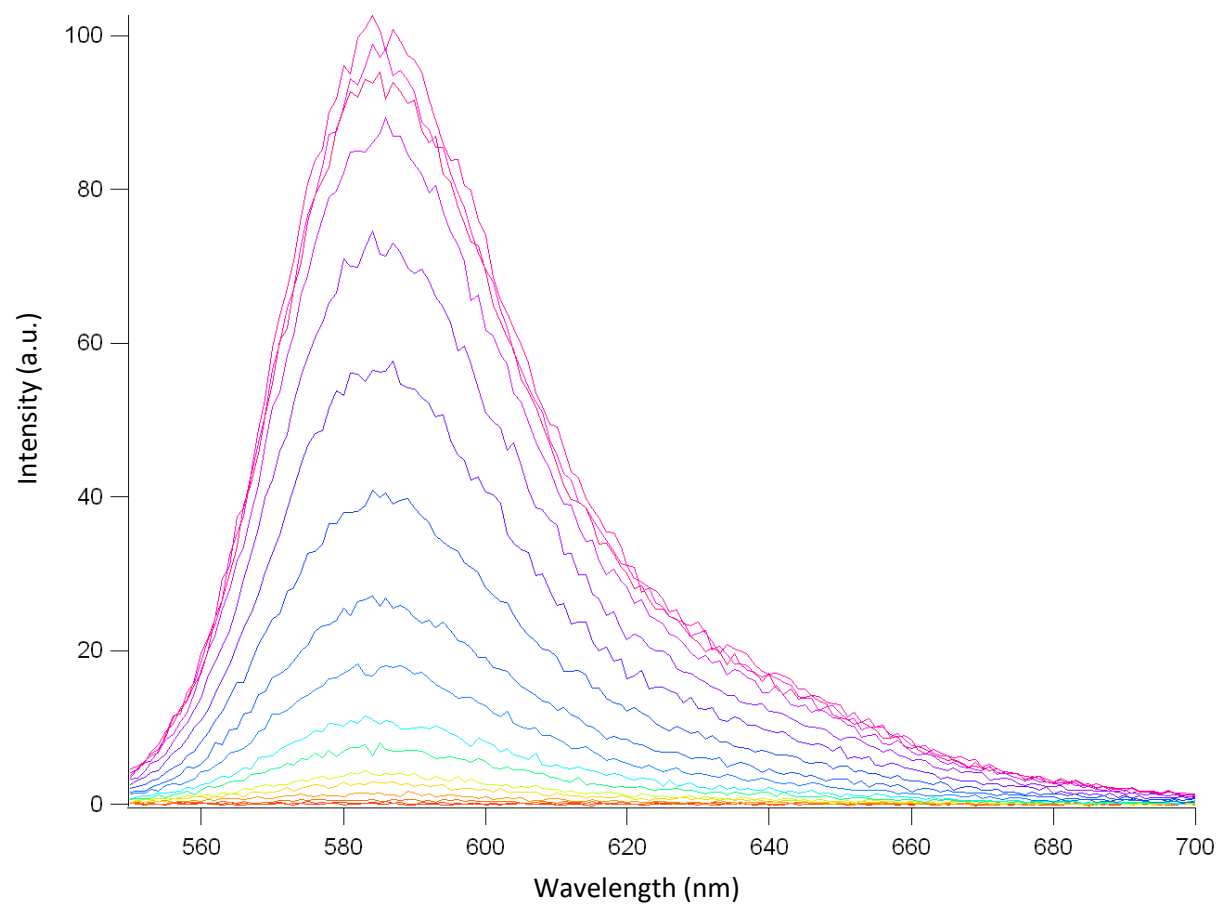


**Figure B52:** Sample fluorescence spectra for RB-2CA

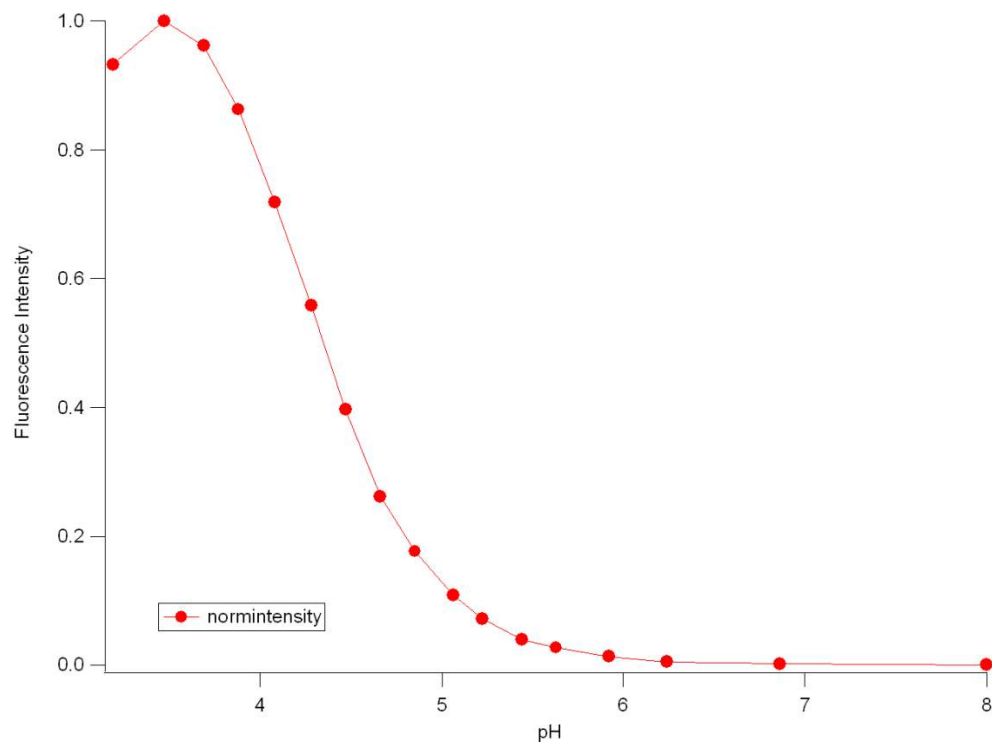


**Figure B53:** Sample titration curve for RB-2CA

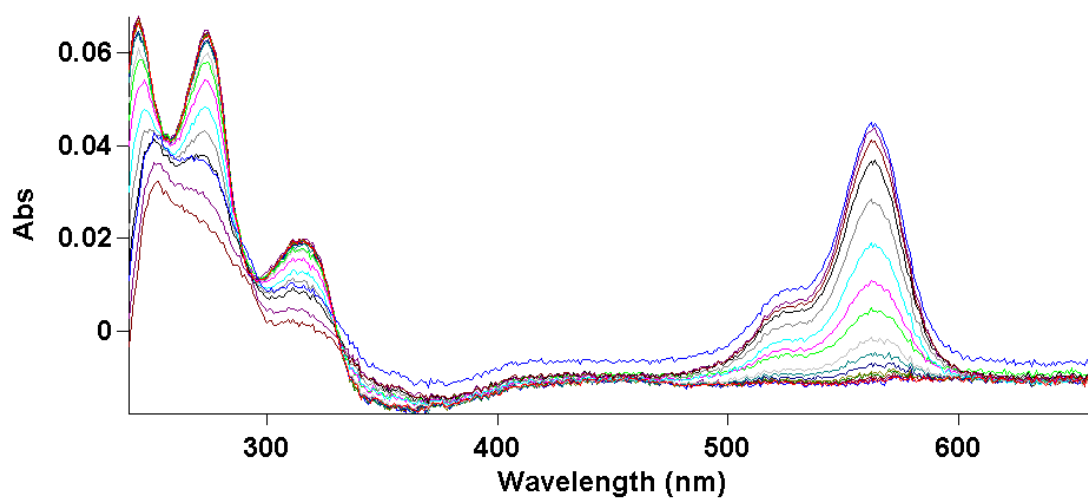


**Figure B54:** Sample UV-Vis spectra for RB-2CA

<b>RB-2CA</b>	<b>pKa</b>	<b>Max fl intensity</b>	<b>Fl lmax</b>
	4.35	79	585
	4.45	103	585
	4.49 <sup>18</sup>	220	585
Mean	4.43	134.000	
Std dev	0.072	75.439	

**Table B18:** pKa values for RB-2CA

---

<sup>18</sup> Titrated by Mona Rasooly

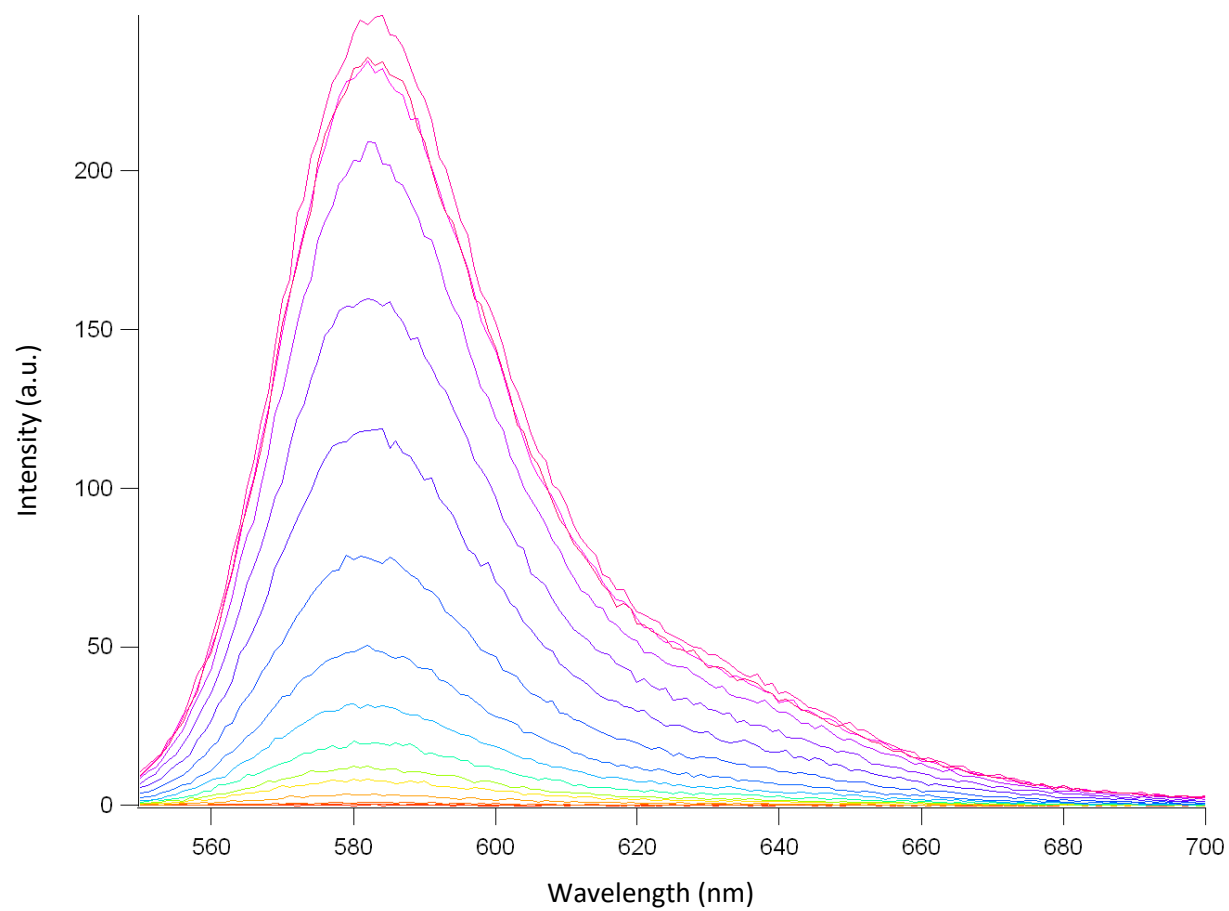


**Figure B55:** Sample fluorescence spectra for RB-2MA

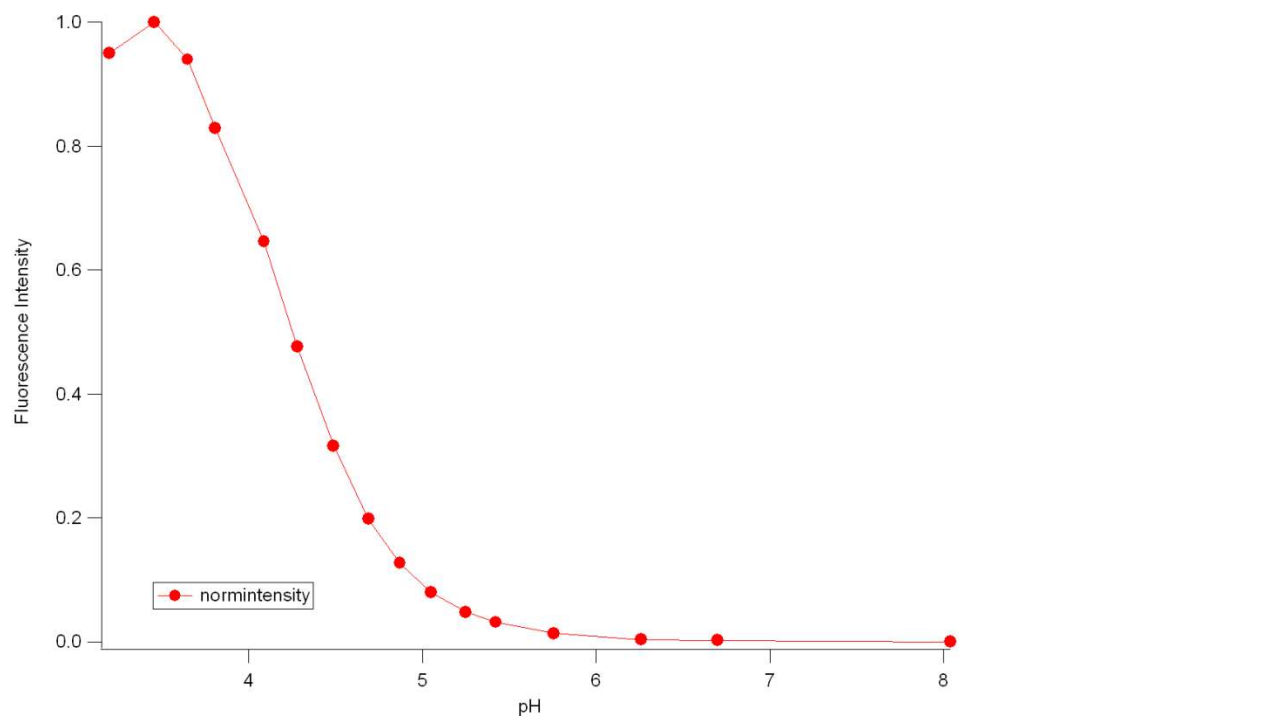


**Figure B56:** Sample titration curve for RB-2MA

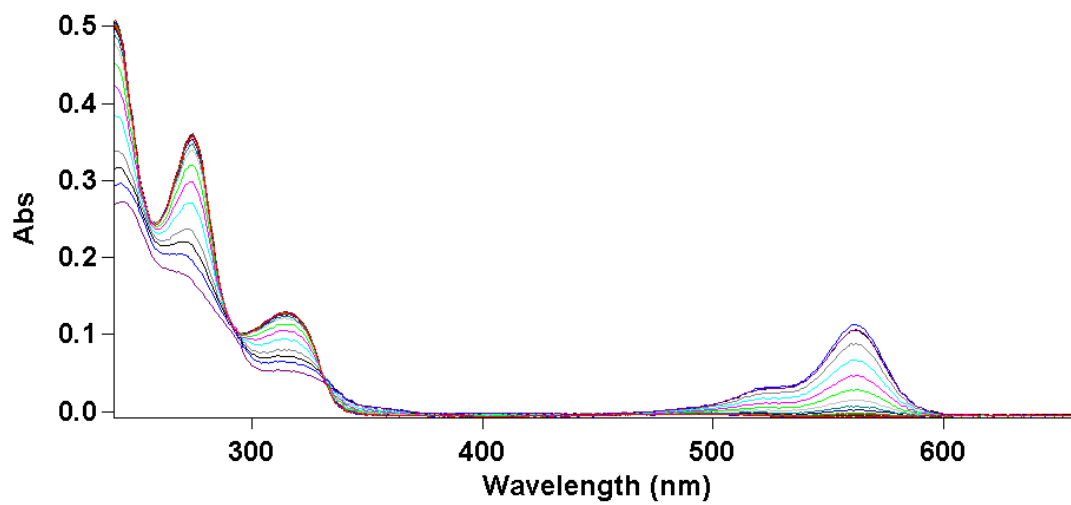


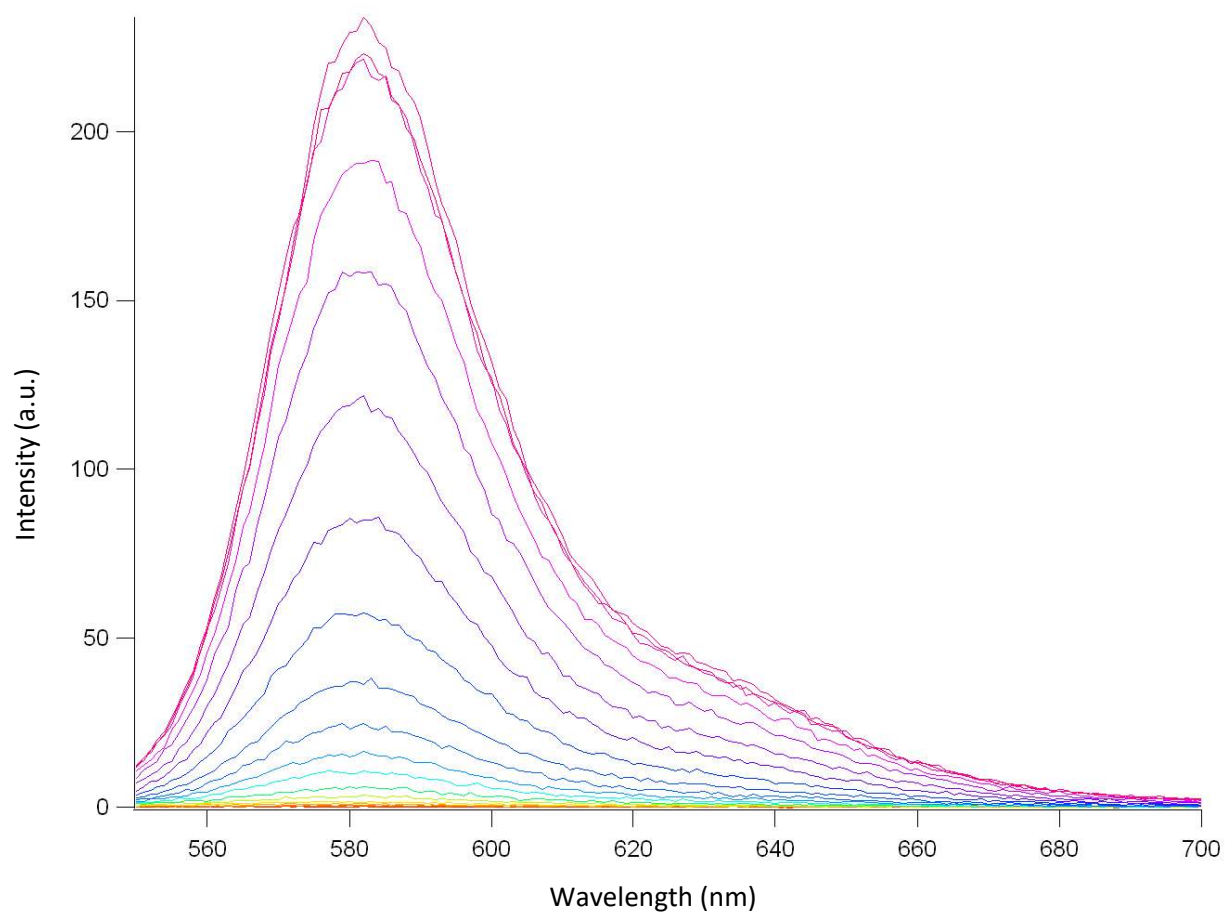
**Figure B57:** Sample UV-Vis spectra for RB-2MA

<b>RB-2MA</b>	<b>pKa</b>	<b>Max fl intensity</b>	<b>Fl lmax</b>
	4.32 <sup>19</sup>	249	583
	4.31 <sup>19</sup>	204	583
	4.27 <sup>19</sup>	219	583
	4.32	191	583
Mean	4.305	215.75	
Std dev	0.021	24.945	

**Table B19:** pKa values for RB-2MA

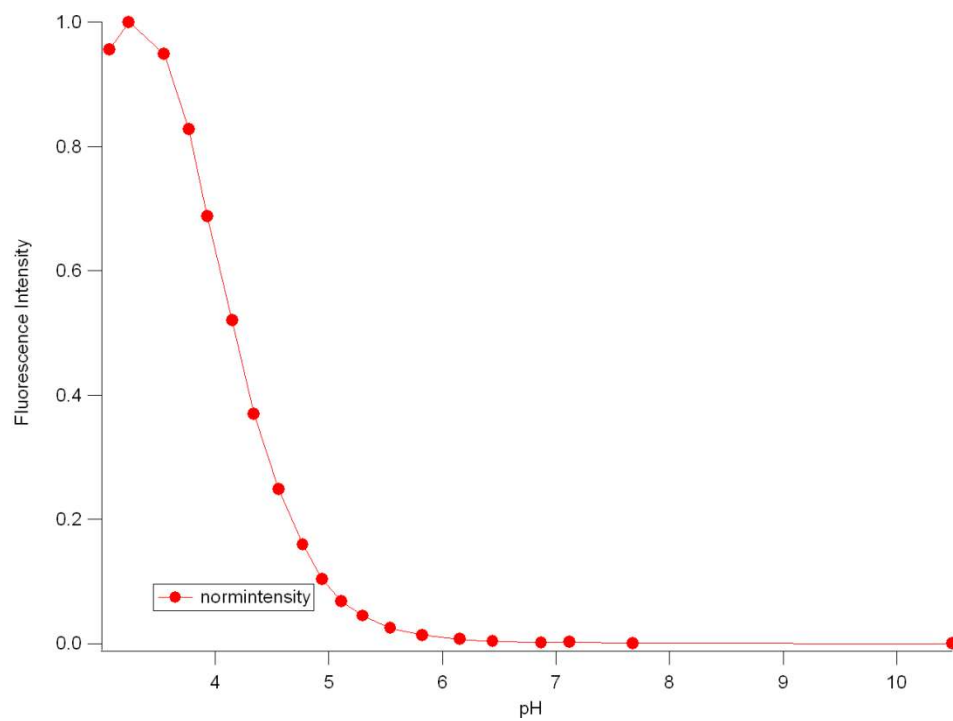
---

<sup>19</sup> Titrated by Mona Rasooly

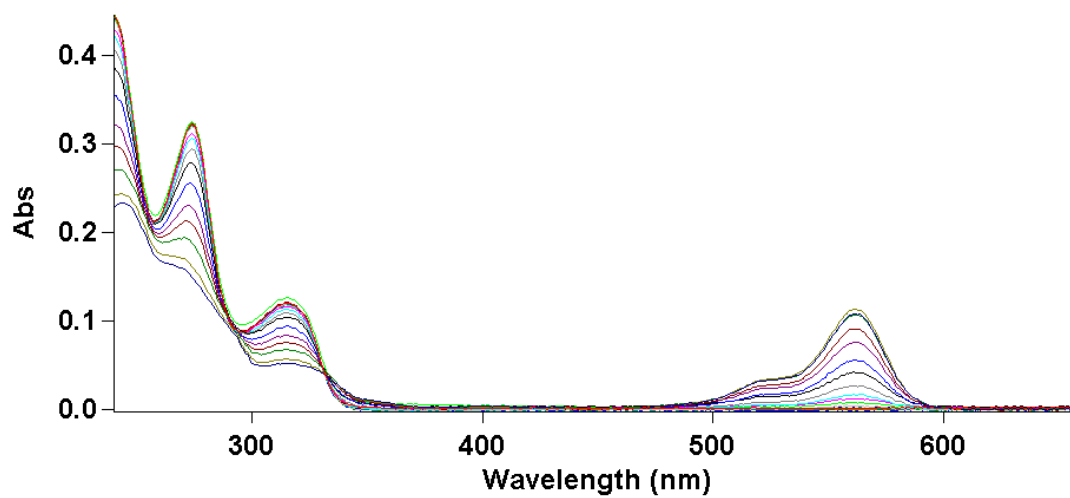


**Figure B58:** Sample fluorescence spectra for RB-2IA





**Figure B59:** Sample titration curve for RB-2IA

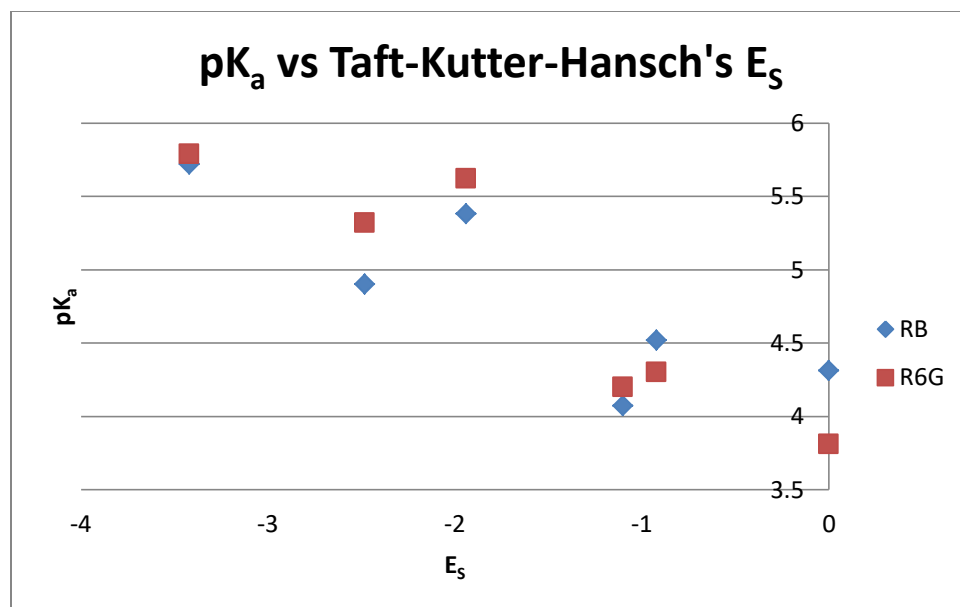
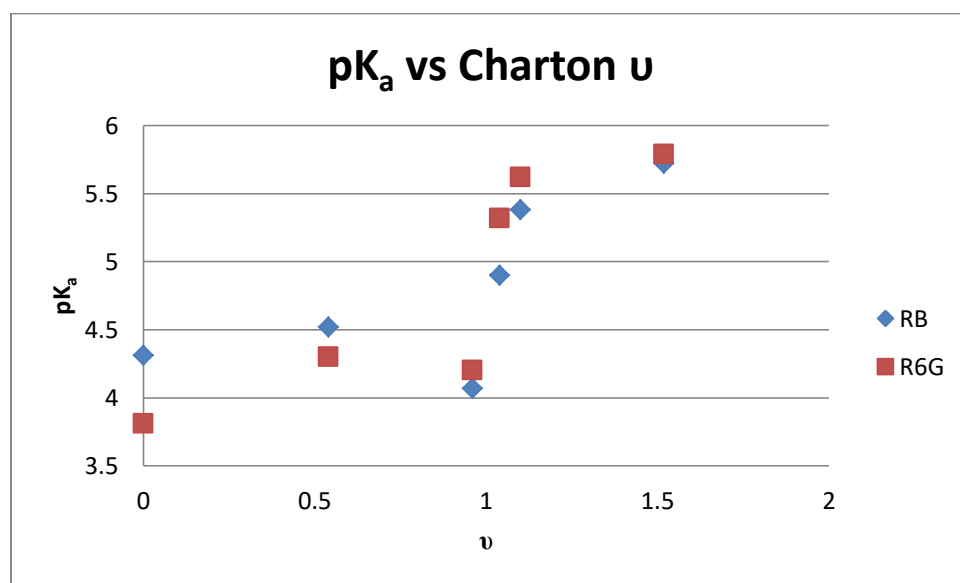


**Figure B60:** Sample UV-Vis spectra for RB-2IA

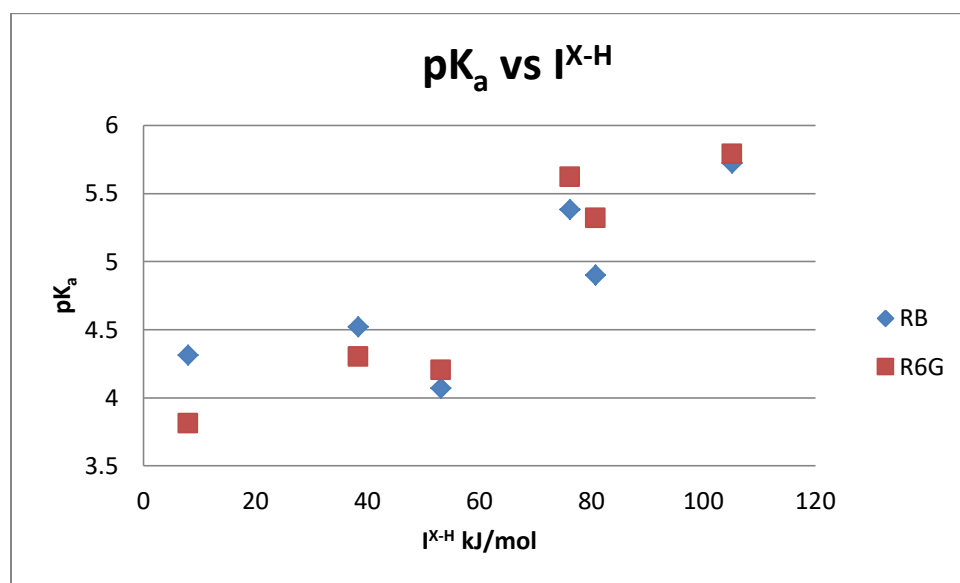
<b>RB-2IA</b>	<b>pKa</b>	<b>Max fl intensity</b>	<b>Fl lmax</b>
	4.28	245	582
	4.30	234	582
	4.26	234	582
Mean	4.280	237.667	
Std dev	0.020	6.351	

**Table B20:** pKa values for RB-2IA

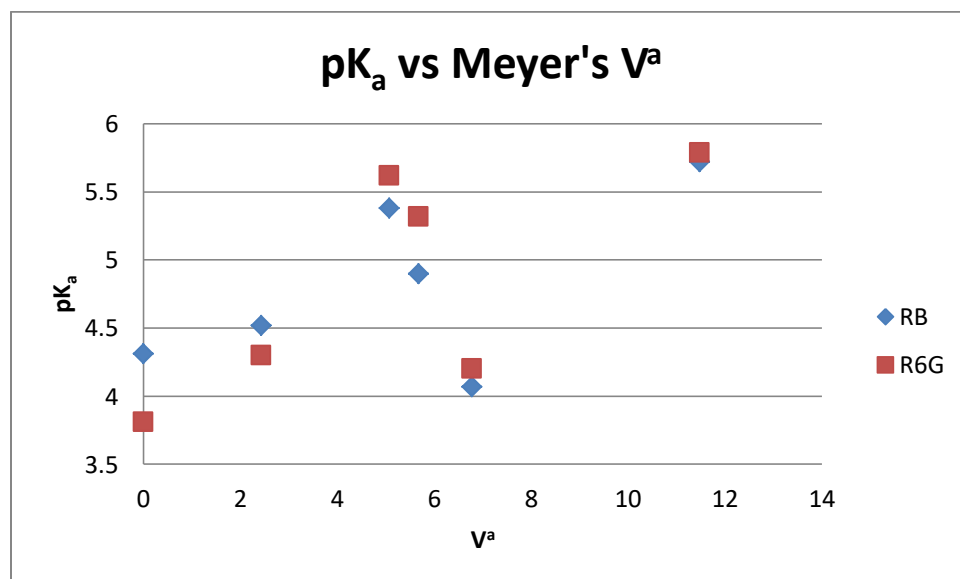
## Appendix C

**Figure C1.** RB and R6G pK<sub>a</sub> data for di-*ortho* substituents versus their Taft-Kutter-Hansch's E<sub>s</sub> values**Figure C2.** RB and R6G pK<sub>a</sub> data for di-*ortho* substituents versus their Charton  $\nu$  values

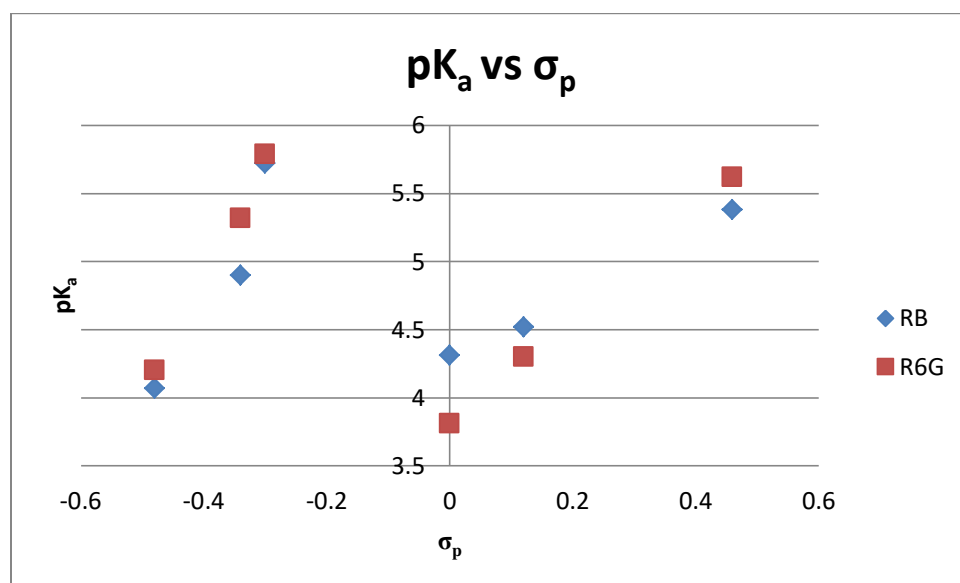
**Figure C3.** RB and R6G  $pK_a$  data for di-*ortho* substituents versus their  $I^{X-H}$  kJ/mol values



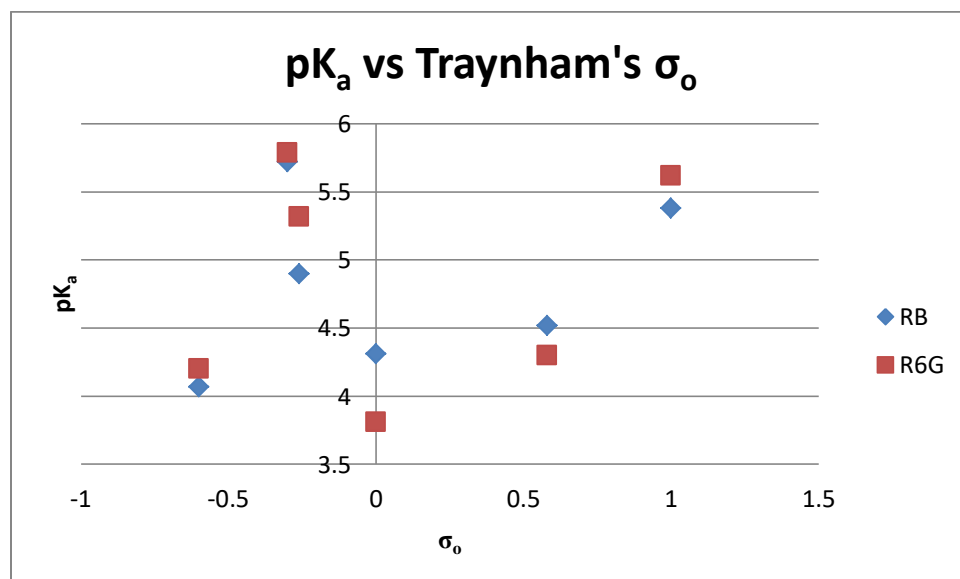
**Figure C4.** RB and R6G  $pK_a$  data for di-*ortho* substituents versus their Meyer's  $V^a$  values



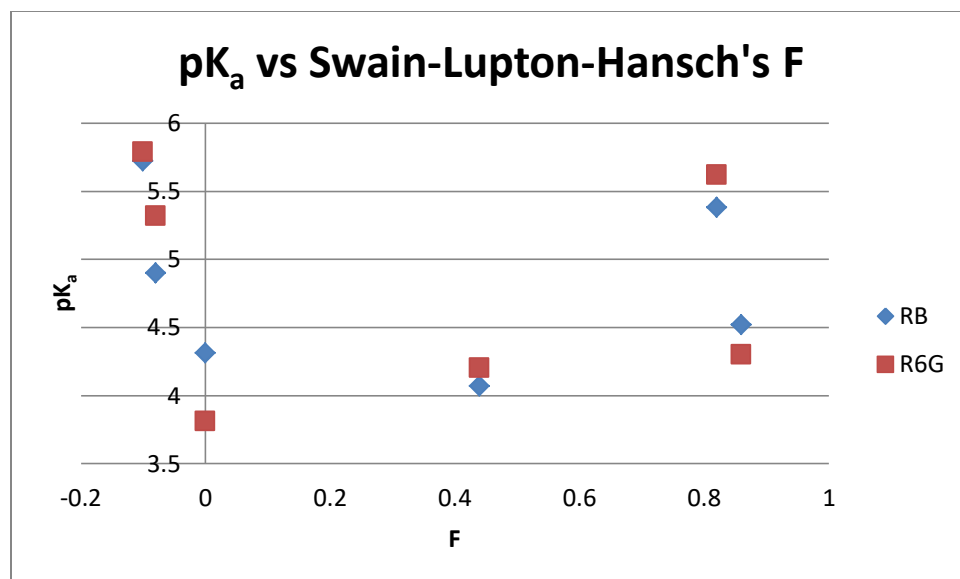
**Figure C5.** RB and R6G  $pK_a$  data for di-*ortho* substituents versus their  $\sigma_p$  values



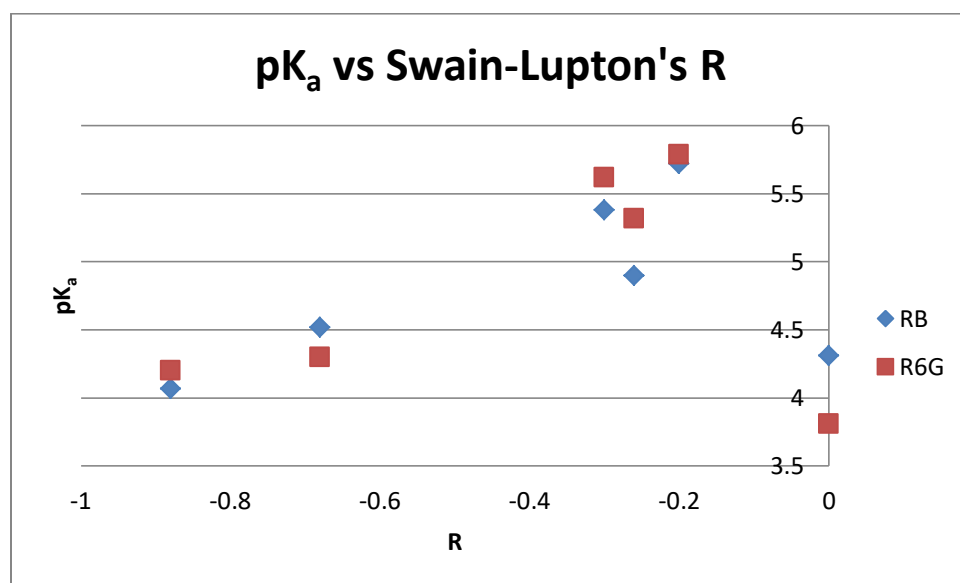
**Figure C6.** RB and R6G  $pK_a$  data for di-*ortho* substituents versus their Traynham's  $\sigma_o$  values



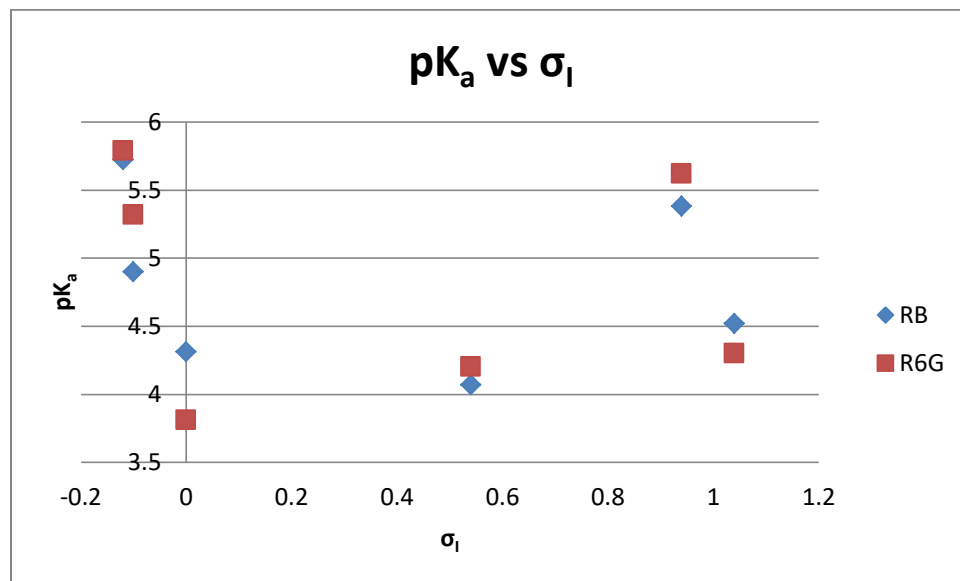
**Figure C7.** RB and R6G  $pK_a$  data for di-*ortho* substituents versus their Swain-Lupton-Hansch's F values



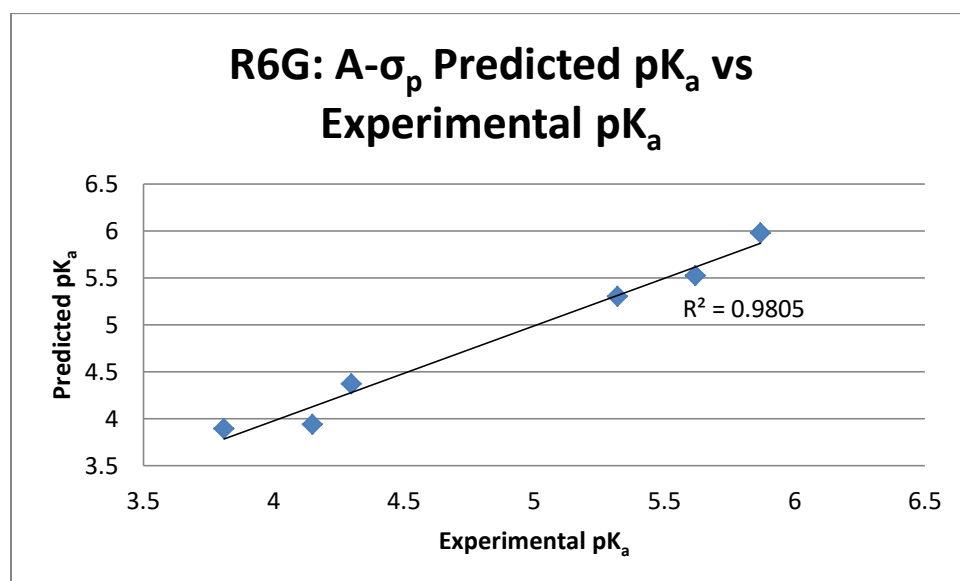
**Figure C8.** RB and R6G  $pK_a$  data for di-*ortho* substituents versus their Swain-Lupton's R values



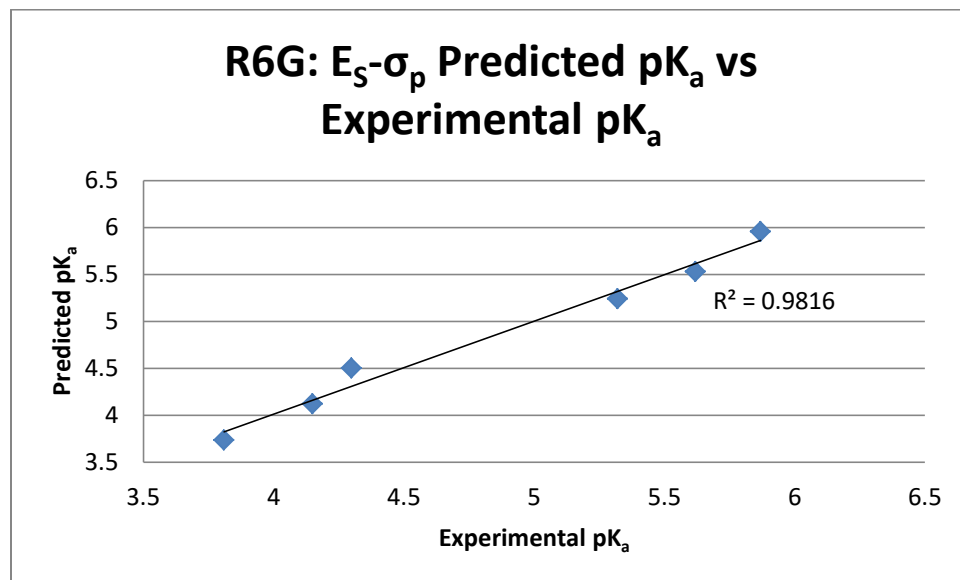
**Figure C9.** RB and R6G  $pK_a$  data for di-*ortho* substituents versus their  $\sigma_1$  values



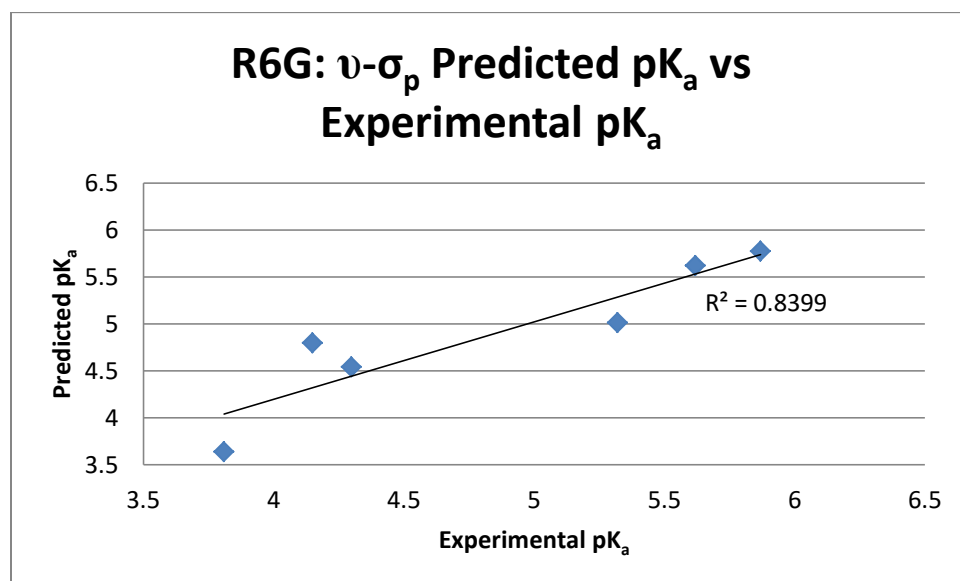
**Figure C10.** R6G A- $\sigma_p$  regression predicted  $pK_a$  versus  $pK_a$  of di-*ortho* derivatives



**Figure C11.** R6G  $E_s$ - $\sigma_p$  regression predicted  $pK_a$  versus  $pK_a$  of di-*ortho* derivatives

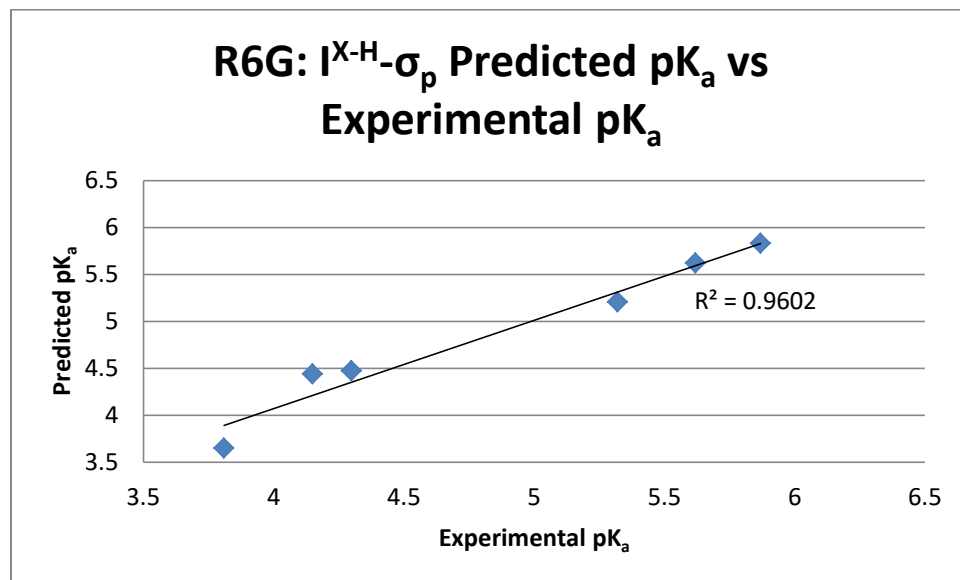


**Figure C12.** R6G  $\nu$ - $\sigma_p$  regression predicted  $pK_a$  versus  $pK_a$  of di-*ortho* derivatives

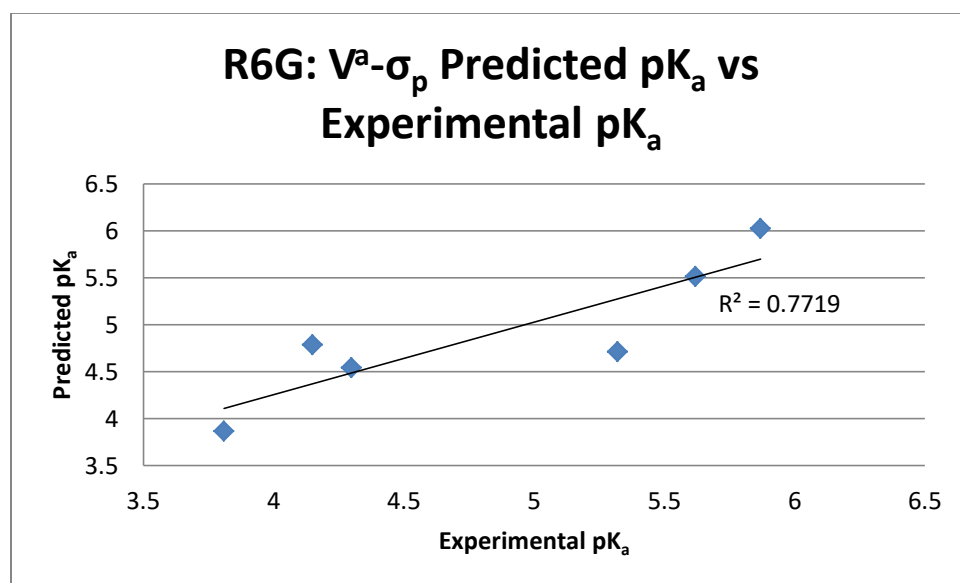




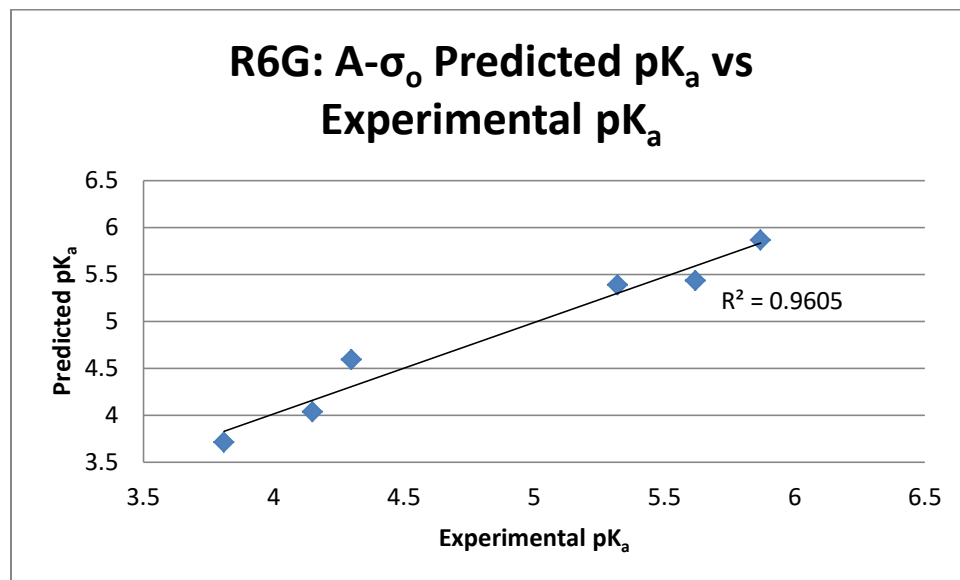
**Figure C13.** R6G  $I^{X-H}-\sigma_p$  regression predicted  $pK_a$  versus  $pK_a$  of di-*ortho* derivatives



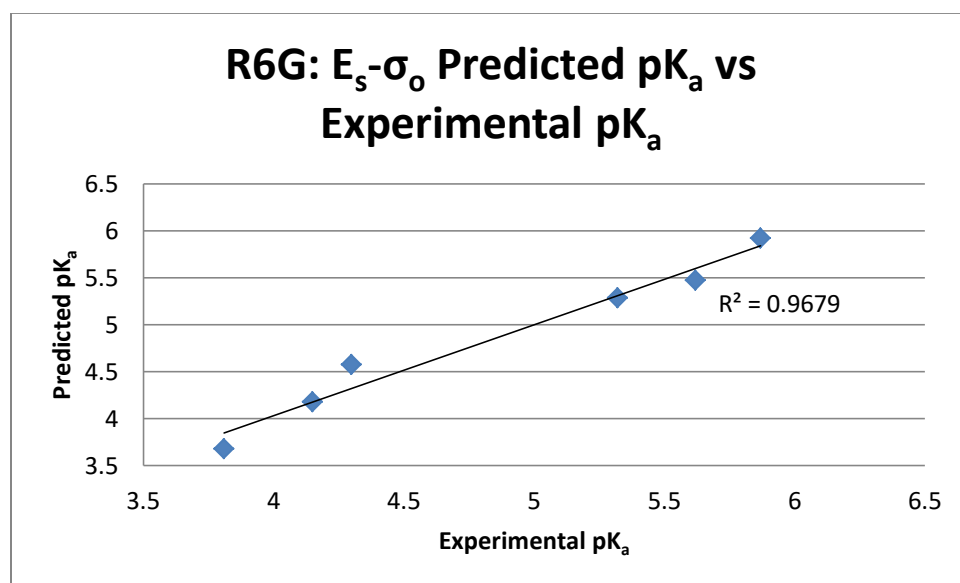
**Figure C14.** R6G  $V^a-\sigma_p$  regression predicted  $pK_a$  versus  $pK_a$  of di-*ortho* derivatives



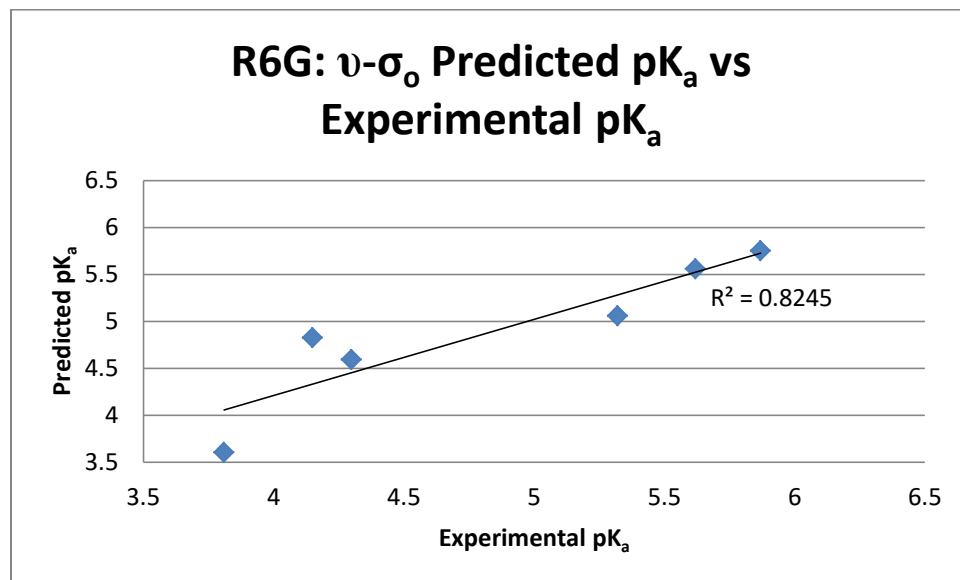
**Figure C15.** R6G A- $\sigma_o$  regression predicted  $pK_a$  versus  $pK_a$  of di-*ortho* derivatives



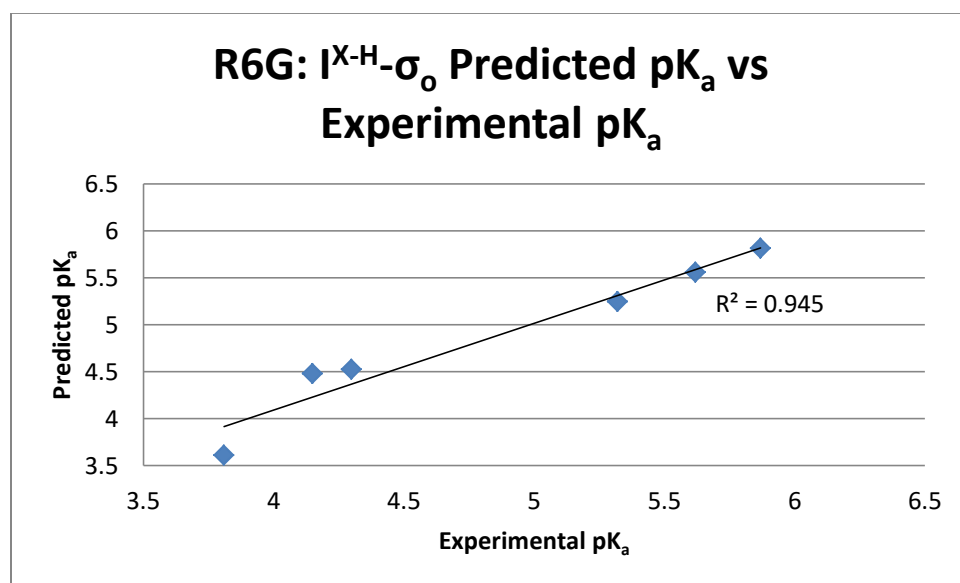
**Figure C16.** R6G  $E_s$ - $\sigma_o$  regression predicted  $pK_a$  versus  $pK_a$  of di-*ortho* derivatives



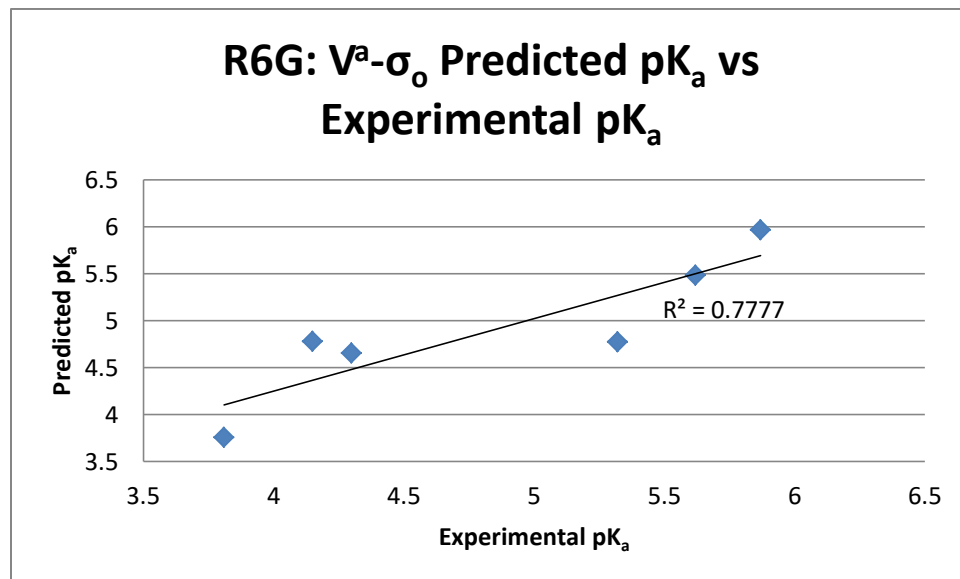
**Figure C17.** R6G  $\nu-\sigma_o$  regression predicted  $pK_a$  versus  $pK_a$  of di-*ortho* derivatives



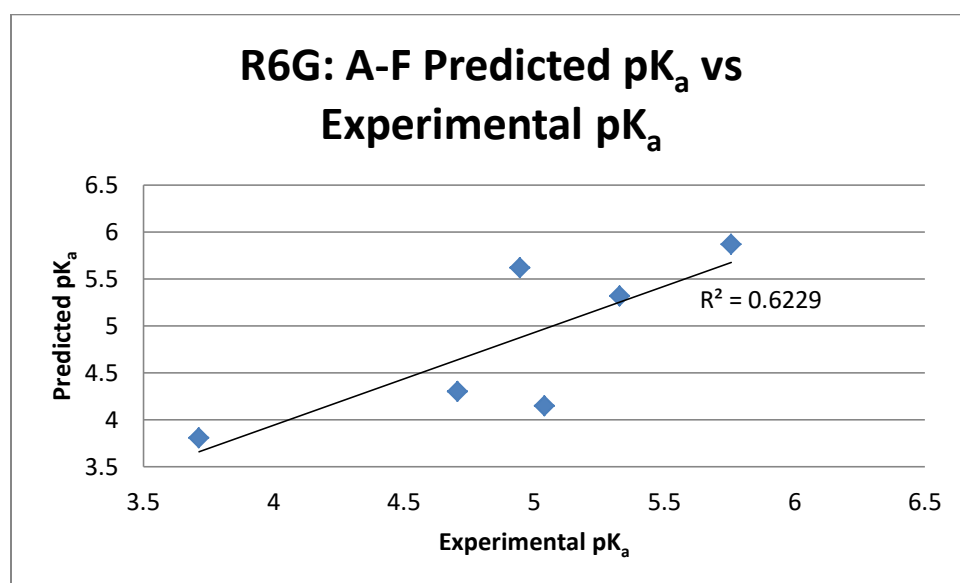
**Figure C18.** R6G  $I^{X-H}-\sigma_o$  regression predicted  $pK_a$  versus  $pK_a$  of di-*ortho* derivatives

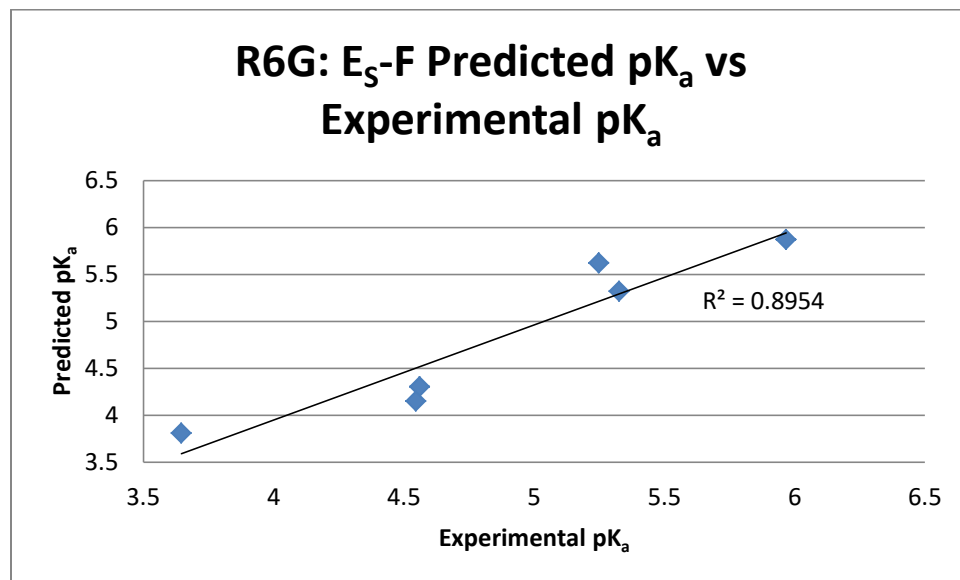
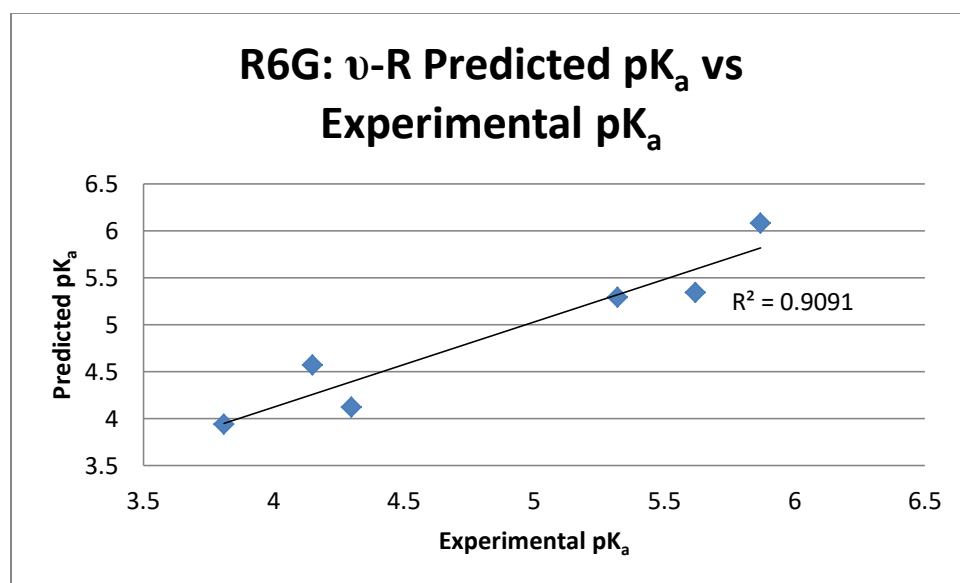


**Figure C19.** R6G  $V^a - \sigma_o$  regression predicted  $pK_a$  versus  $pK_a$  of di-*ortho* derivatives



**Figure C20.** R6G A-F regression predicted  $pK_a$  versus  $pK_a$  of di-*ortho* derivatives



**Figure C21.** R6G E<sub>s</sub>-F regression predicted pK<sub>a</sub> versus pK<sub>a</sub> of di-*ortho* derivatives**Figure C22.** R6G v-R regression predicted pK<sub>a</sub> versus pK<sub>a</sub> of di-*ortho* derivatives

**Figure C23.** R6G I<sup>X-H</sup>-R regression predicted pK<sub>a</sub> versus pK<sub>a</sub> of di-*ortho* derivatives

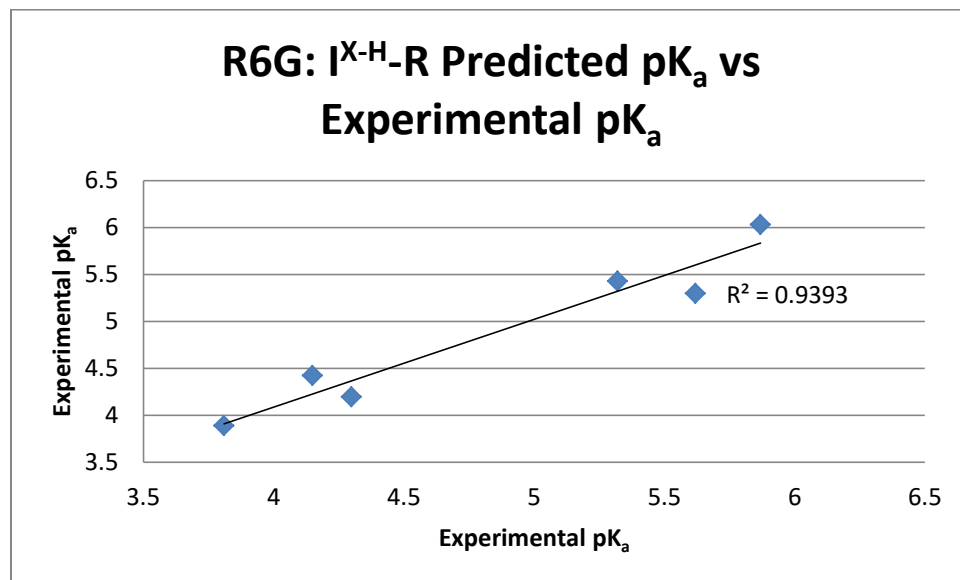


**Figure C24.** R6G V<sup>a</sup>-R regression predicted pK<sub>a</sub> versus pK<sub>a</sub> of di-*ortho* derivatives

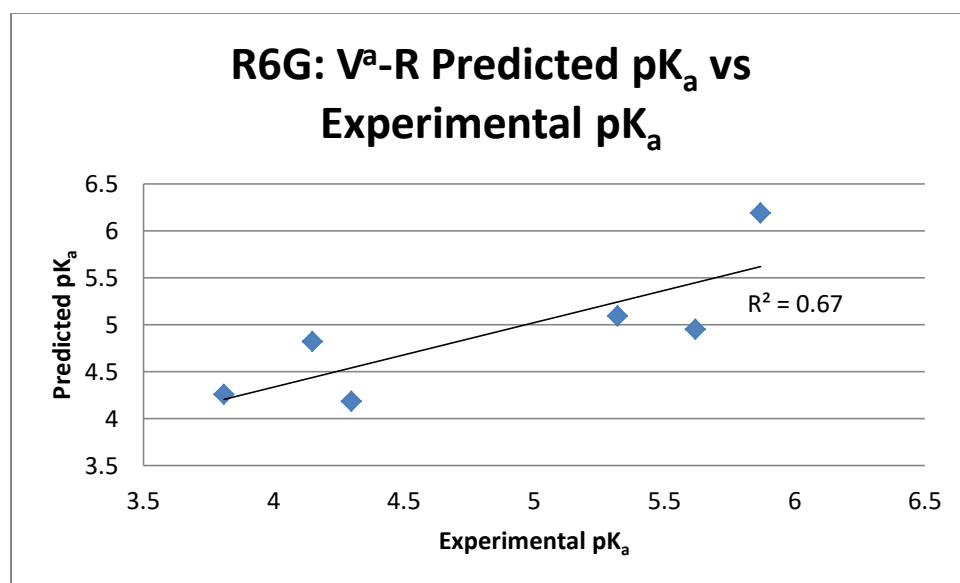


**Figure C25.** R6G A- $\sigma_1$  regression predicted  $\text{pK}_a$  versus  $\text{pK}_a$  of di-*ortho* derivatives

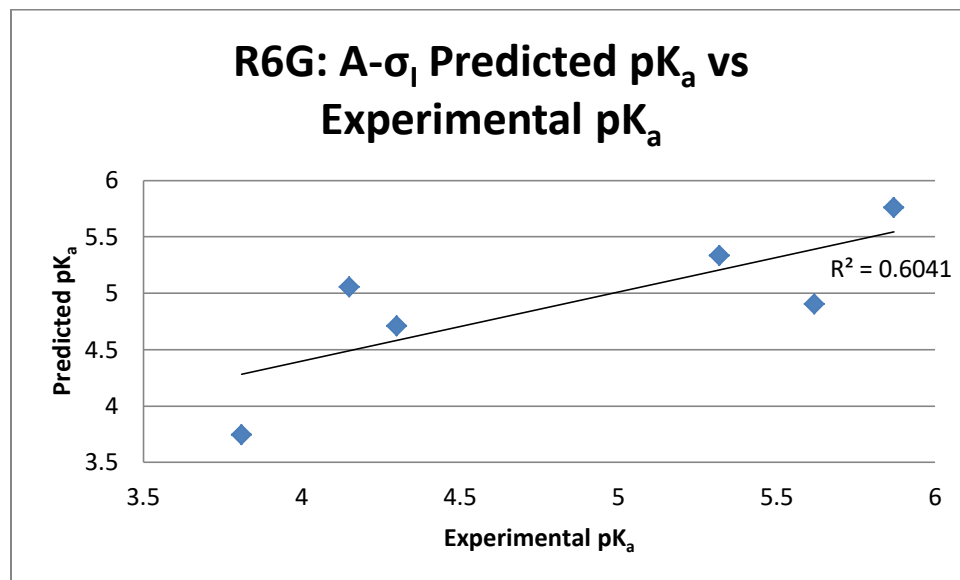


**Figure C26.** R6G  $E_s$ - $\sigma_1$  regression predicted  $\text{pK}_a$  versus  $\text{pK}_a$  of di-*ortho* derivatives

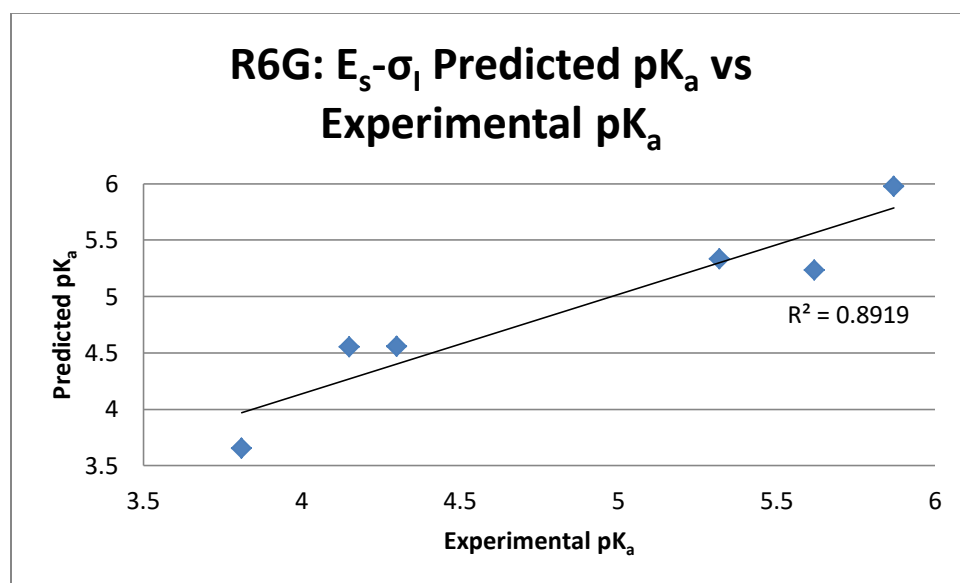


**Figure C27.** R6G  $E_S$ -F-R regression predicted  $pK_a$  versus  $pK_a$  of di-*ortho* derivatives

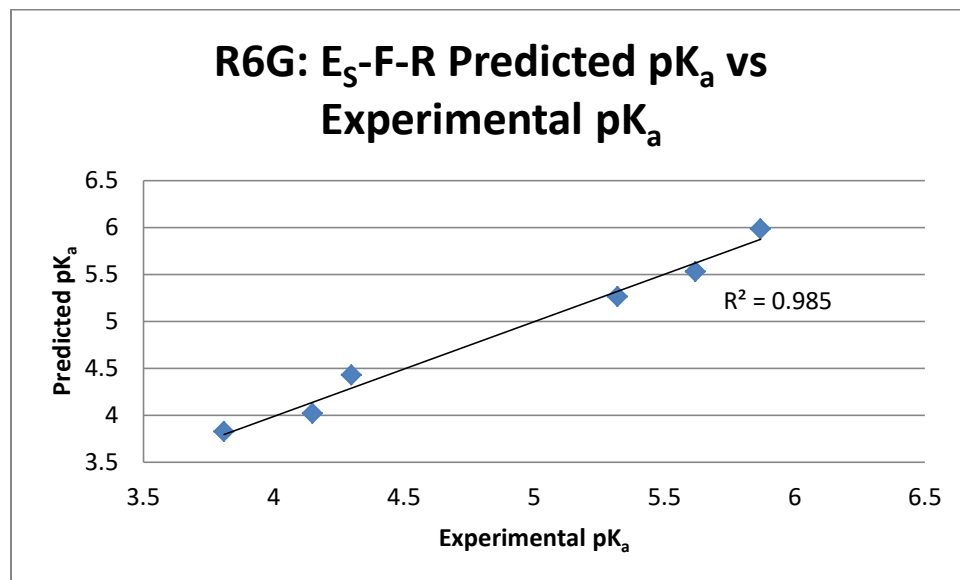


**Figure C28.** R6G  $E_S$ - $\sigma_I$ -R regression predicted  $pK_a$  versus  $pK_a$  of di-*ortho* derivatives

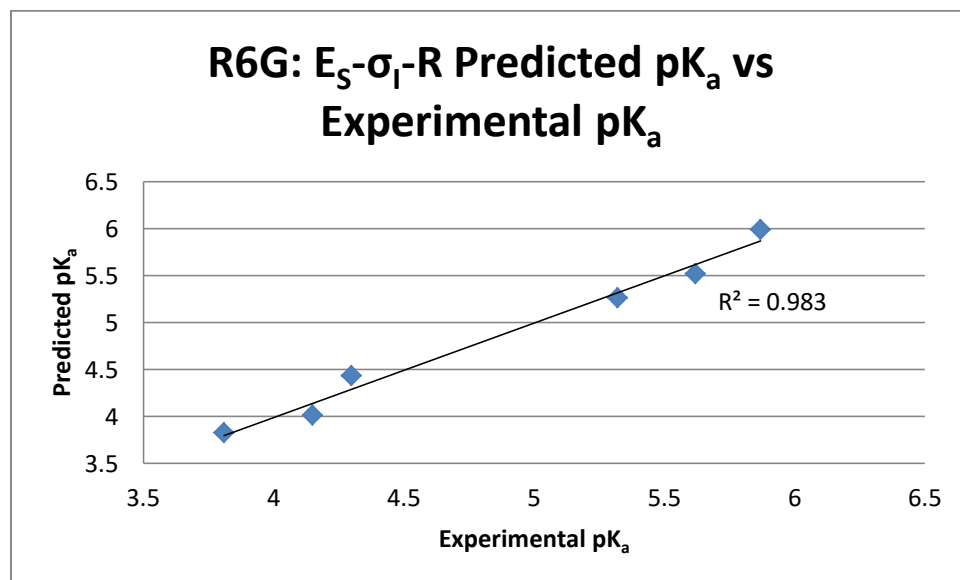




**Figure C29.** R6G  $E_s$ - $\sigma_I$ -F-R regression predicted  $pK_a$  versus  $pK_a$  of di-*ortho* derivatives

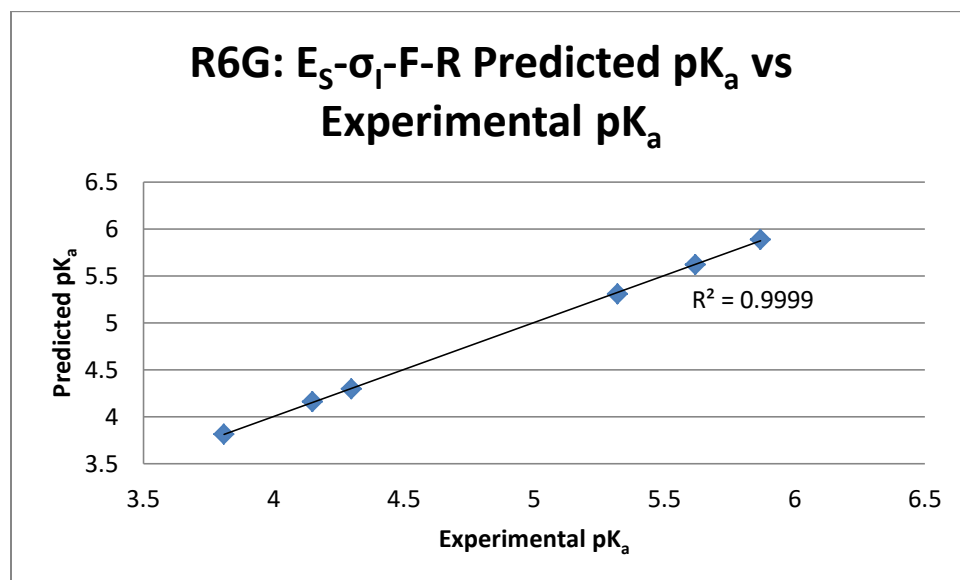


**Figure C30.** R6G  $E_s$ - $\sigma_I^{\text{mod}}$ -F-R regression predicted  $pK_a$  versus  $pK_a$  of di-*ortho* derivatives

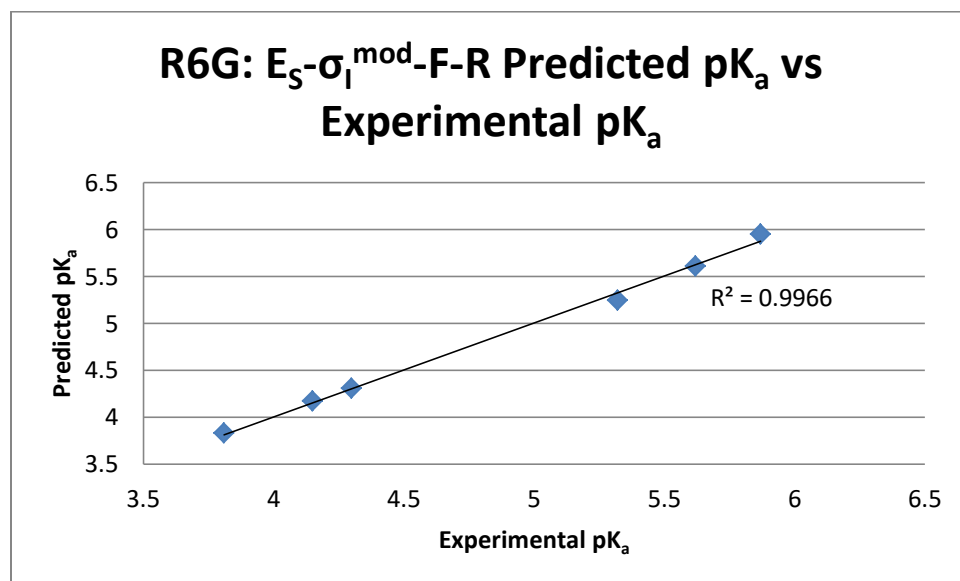


**Figure C31.** RB  $A-\sigma_p$  regression predicted  $pK_a$  versus  $pK_a$  of di-*ortho* derivatives

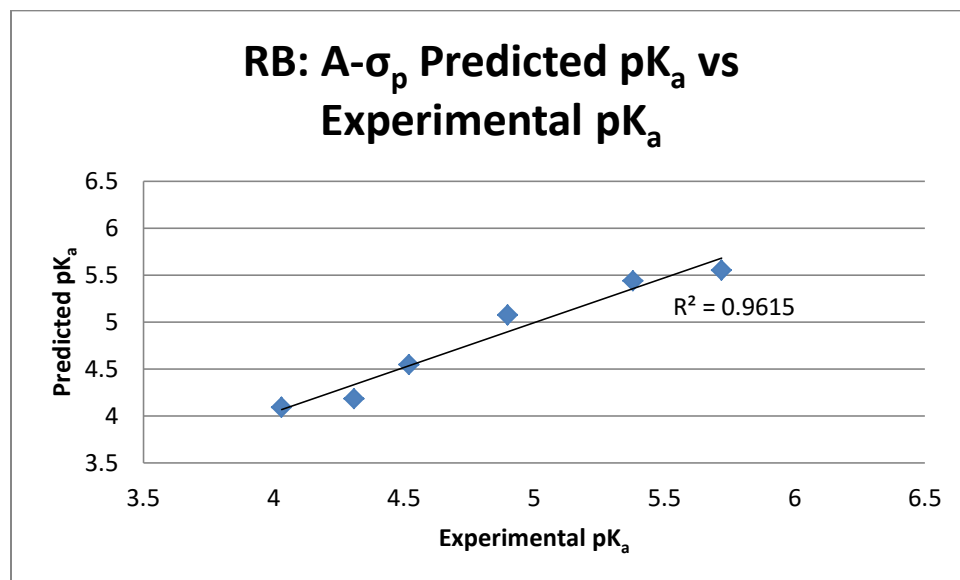


**Figure C32.** RB  $E_s-\sigma_p$  regression predicted  $pK_a$  versus  $pK_a$  of di-*ortho* derivatives

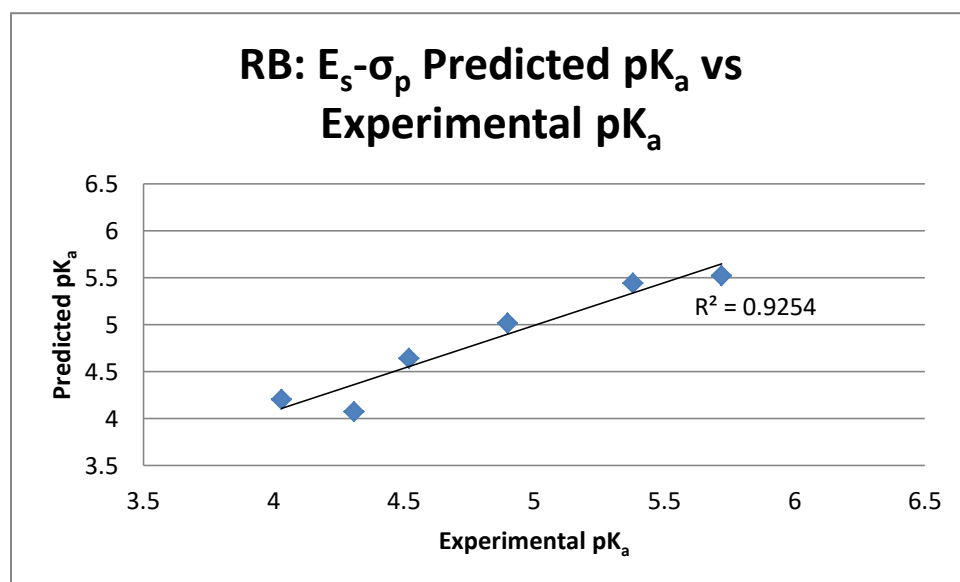


Figure C33. RB  $I^{X-H}-\sigma_p$  regression predicted  $pK_a$  versus  $pK_a$  of di-*ortho* derivatives

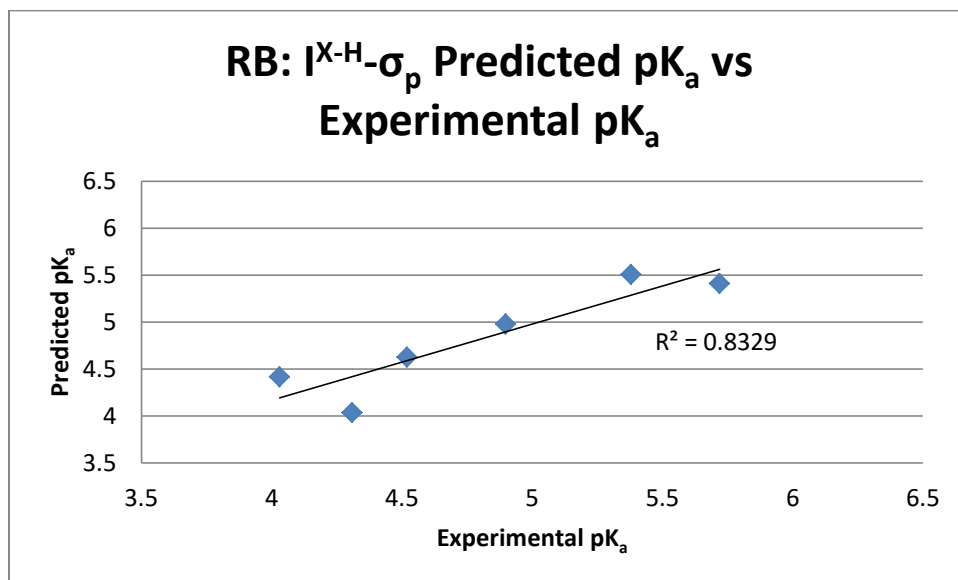
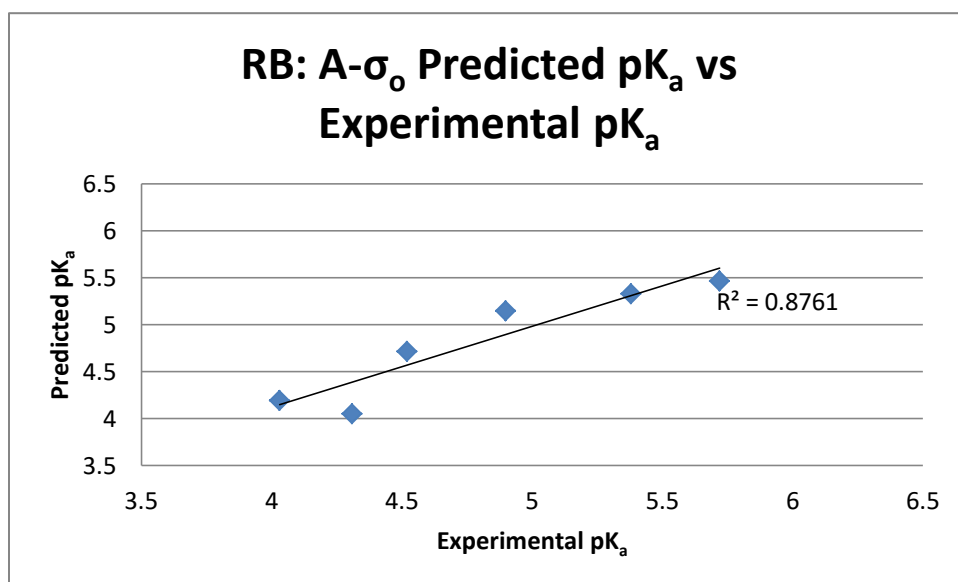
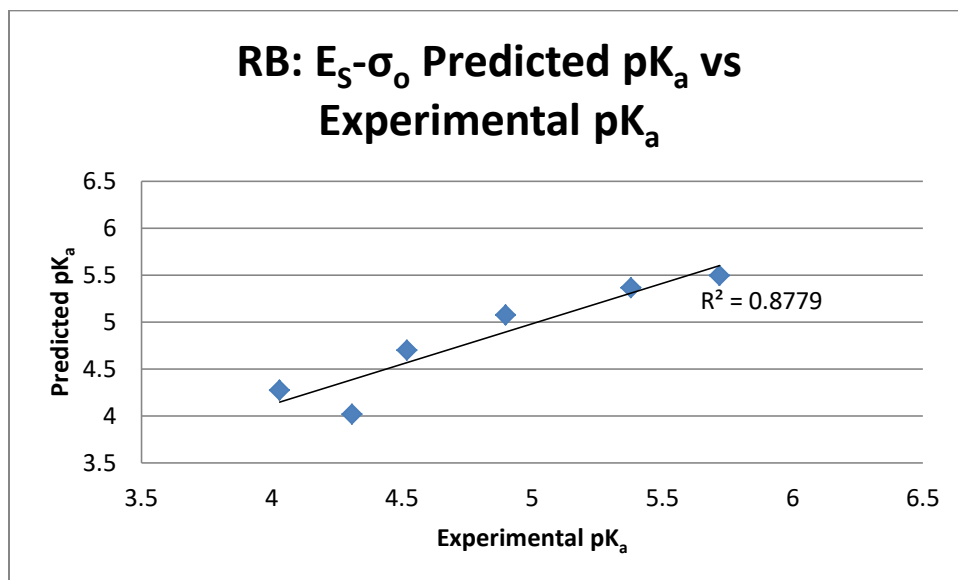


Figure C34. RB  $A-\sigma_o$  regression predicted  $pK_a$  versus  $pK_a$  of di-*ortho* derivatives



**Figure C35.** RB  $E_S$ - $\sigma_o$  regression predicted  $pK_a$  versus  $pK_a$  of di-*ortho* derivatives



**Figure C36.** RB  $I^{X-H}$ - $\sigma_o$  regression predicted  $pK_a$  versus  $pK_a$  of di-*ortho* derivatives

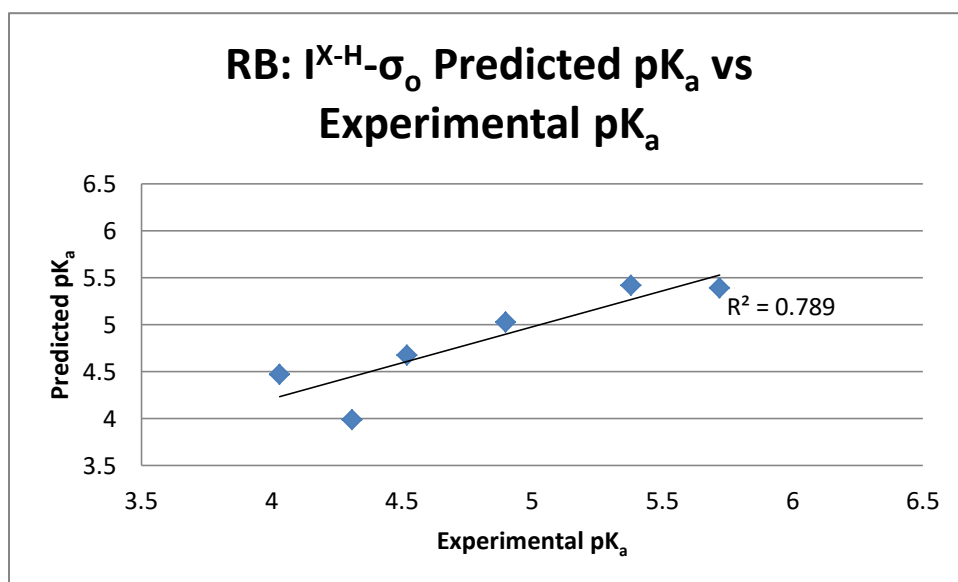


**Figure C37.** RB  $\nu$ -R regression predicted  $\text{pK}_a$  versus  $\text{pK}_a$  of di-*ortho* derivatives

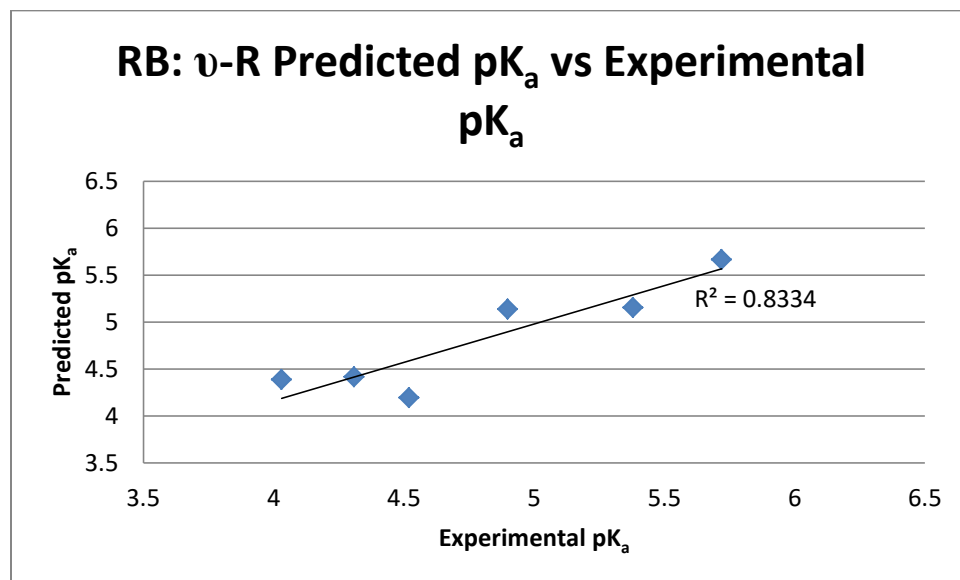


**Figure C38.** RB  $I^{X-H}$ -R regression predicted  $\text{pK}_a$  versus  $\text{pK}_a$  of di-*ortho* derivatives

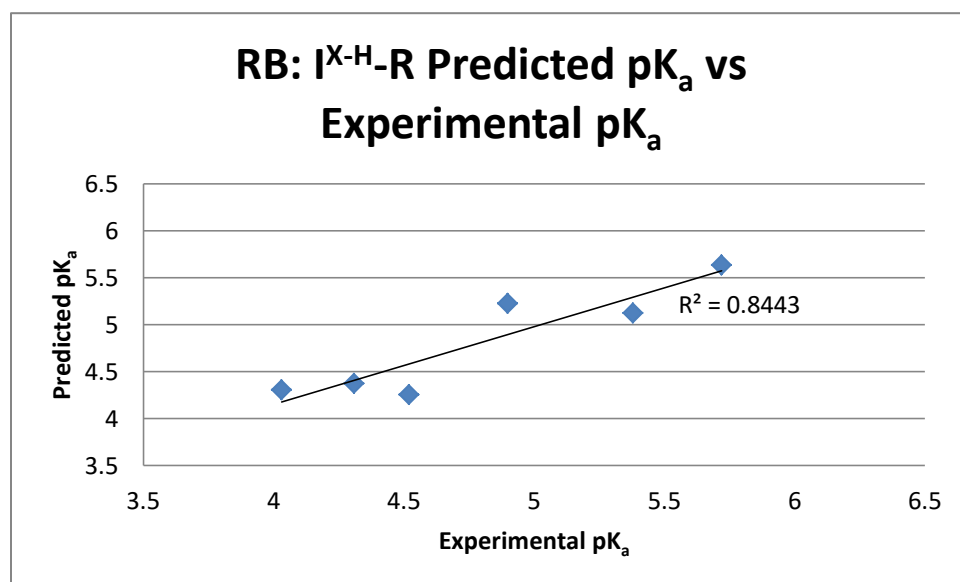


**Figure C39.** RB  $E_s$ - $\sigma_p$ -F regression predicted  $pK_a$  versus  $pK_a$  of di-*ortho* derivatives

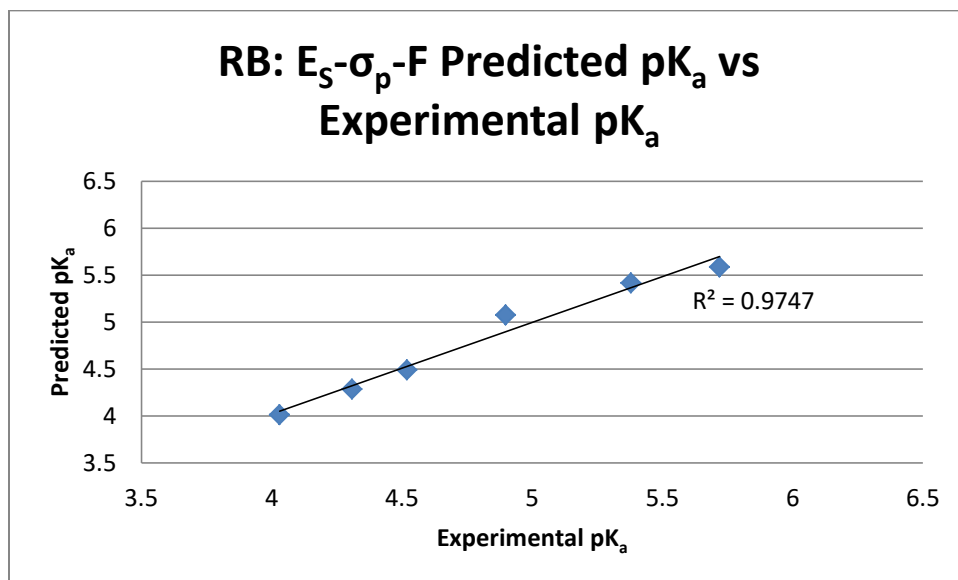


**Figure C40.** RB  $E_s$ -F-R regression predicted  $pK_a$  versus  $pK_a$  of di-*ortho* derivatives

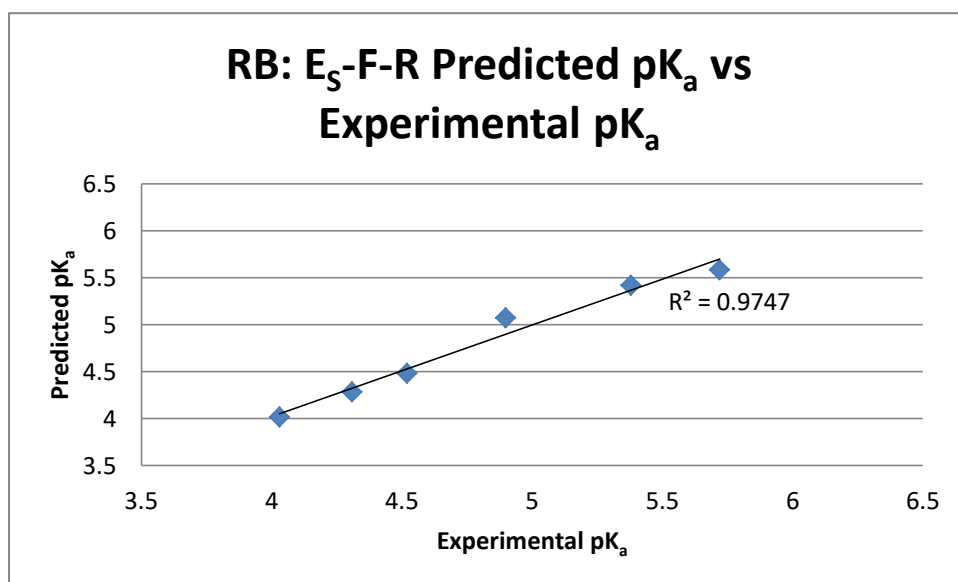


**Figure C41.** RB  $E_S$ - $\sigma_I$ -R regression predicted  $pK_a$  versus  $pK_a$  of di-*ortho* derivatives

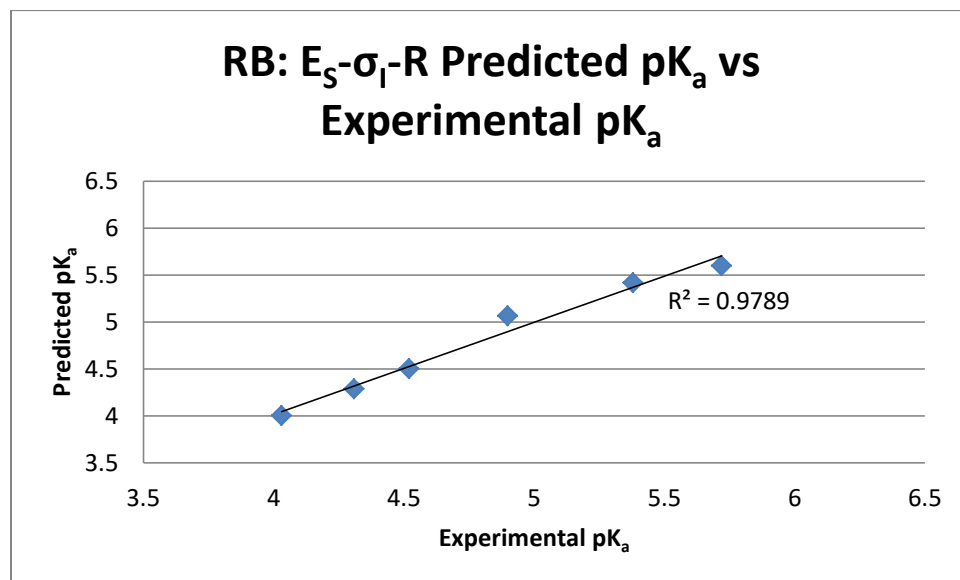


**Figure C42.** RB  $E_S$ - $\sigma_I$ -F-R regression predicted  $pK_a$  versus  $pK_a$  of di-*ortho* derivatives

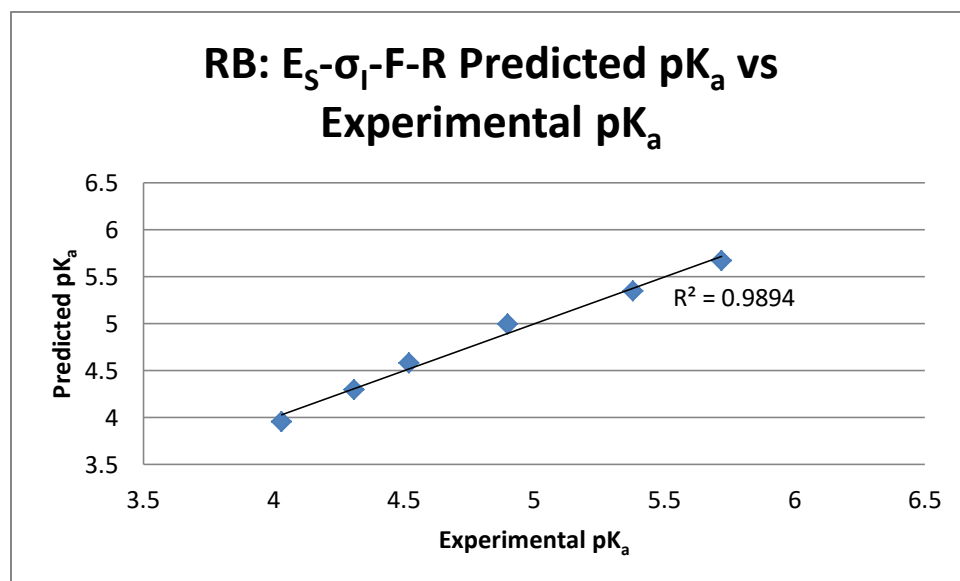


**Figure C43.** RB  $pK_a$  data for mono-*ortho* substituents versus their  $\sigma_1$  values

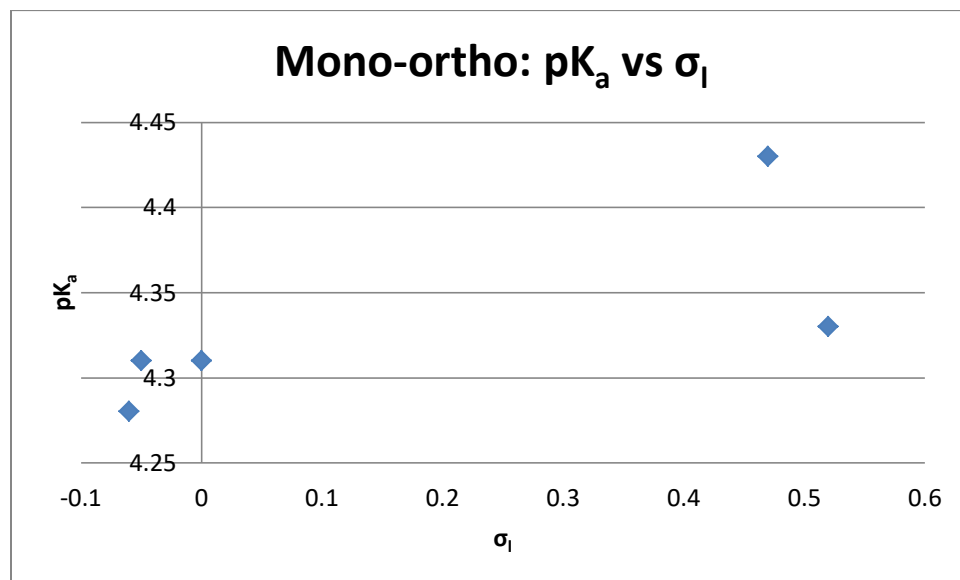


**Figure C44.** RB  $pK_a$  data for mono-*ortho* substituents versus their F values

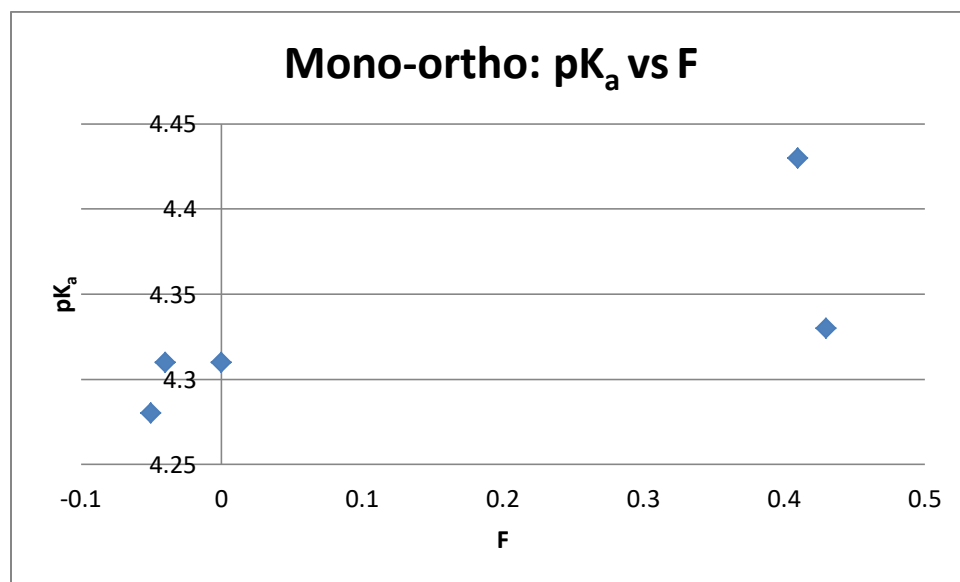




**Figure C45.** RB  $pK_a$  data for mono-*ortho* substituents versus their R values

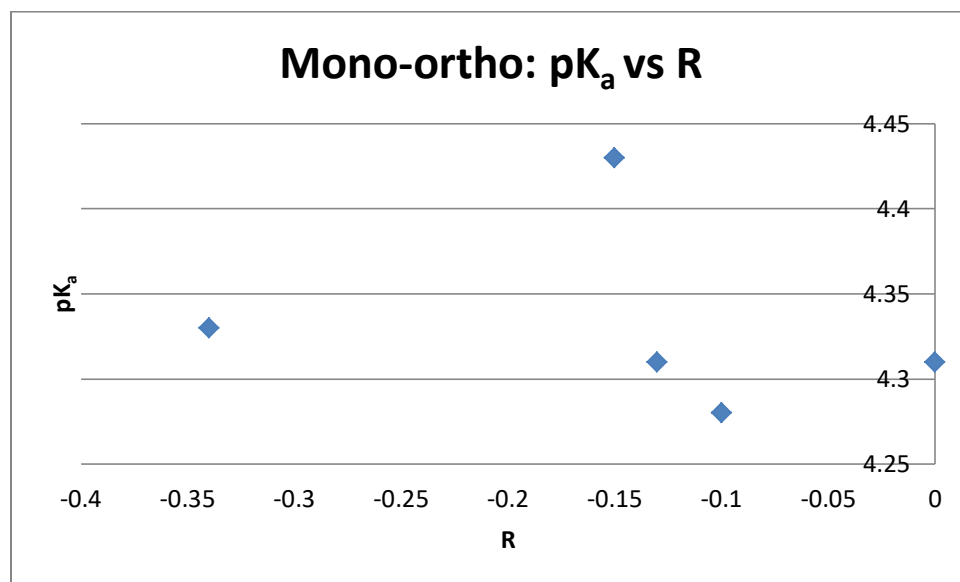


**Figure C46.** RB  $pK_a$  data for mono-*ortho* substituents versus their  $V^a$  values

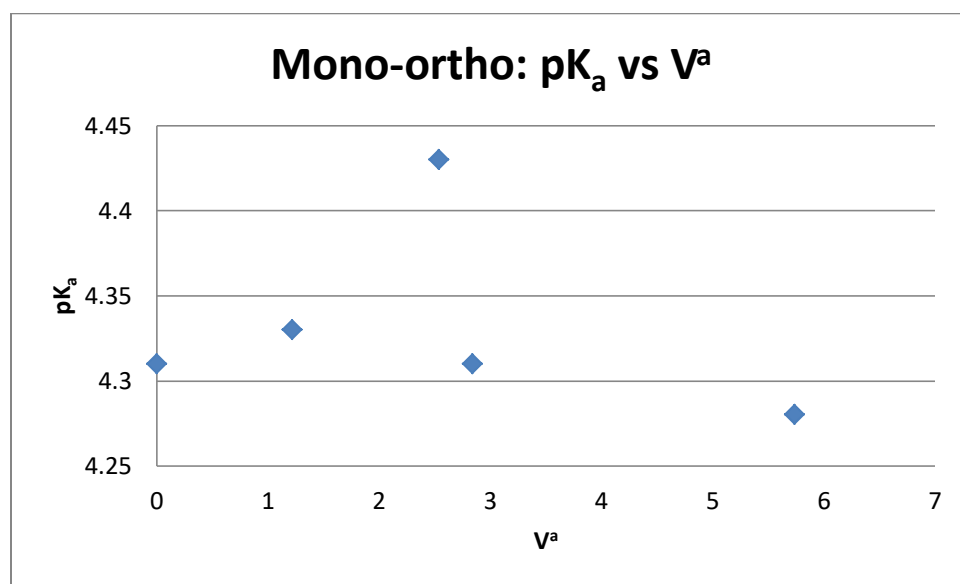


**Figure C47.** RB  $pK_a$  data for mono-*ortho* substituents versus their  $E_s$  values

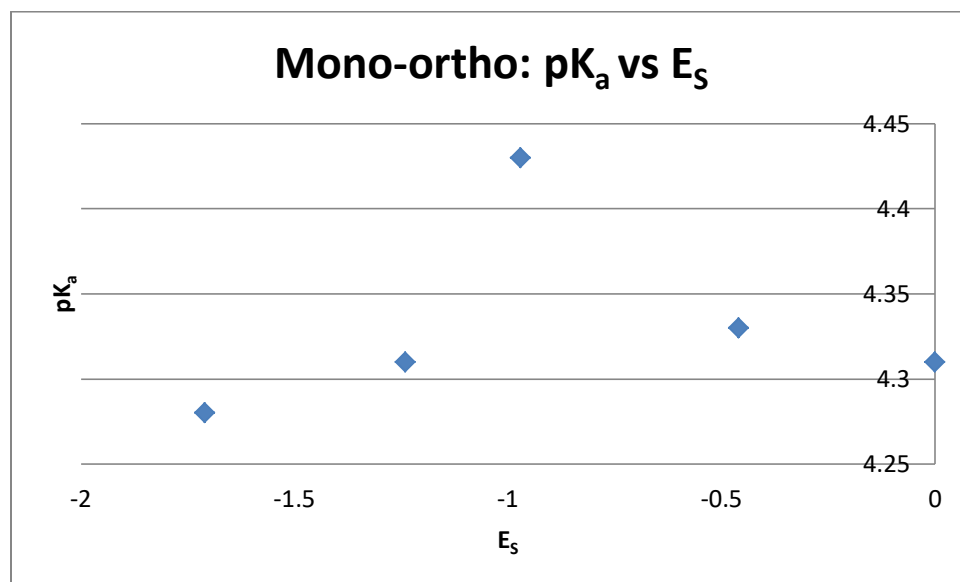


**Figure C48.** RB  $pK_a$  data for mono-*ortho* substituents versus their A values

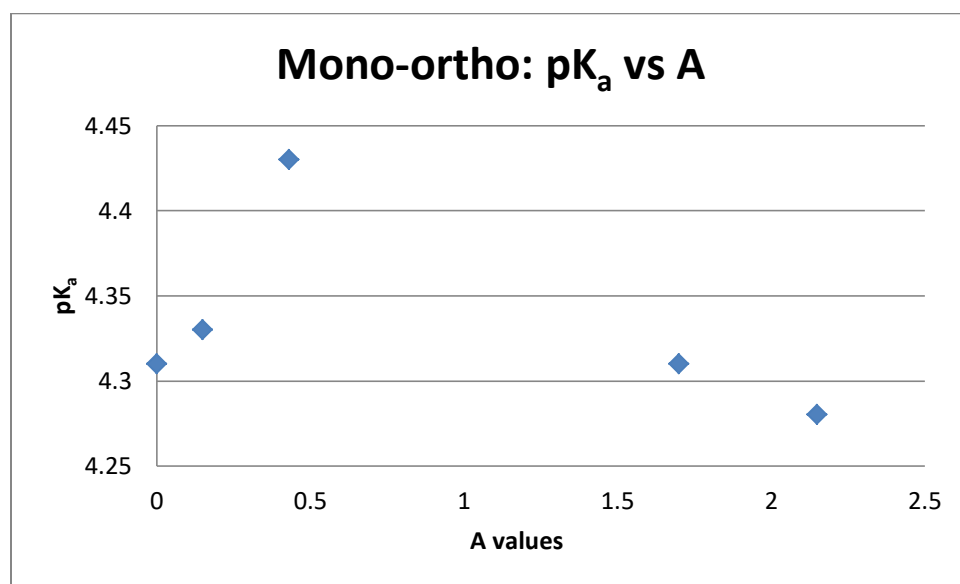


**Figure C49.** RB  $pK_a$  data for mono-*ortho* substituents versus their  $\nu$  values

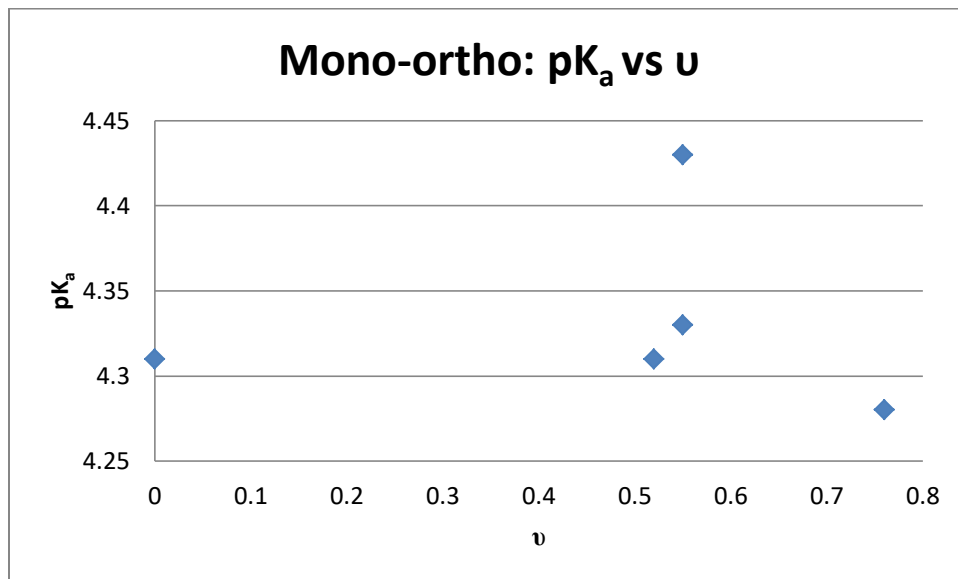


**Figure C50.** RB  $pK_a$  data for mono-*ortho* substituents versus their  $I^{X-H}$  values

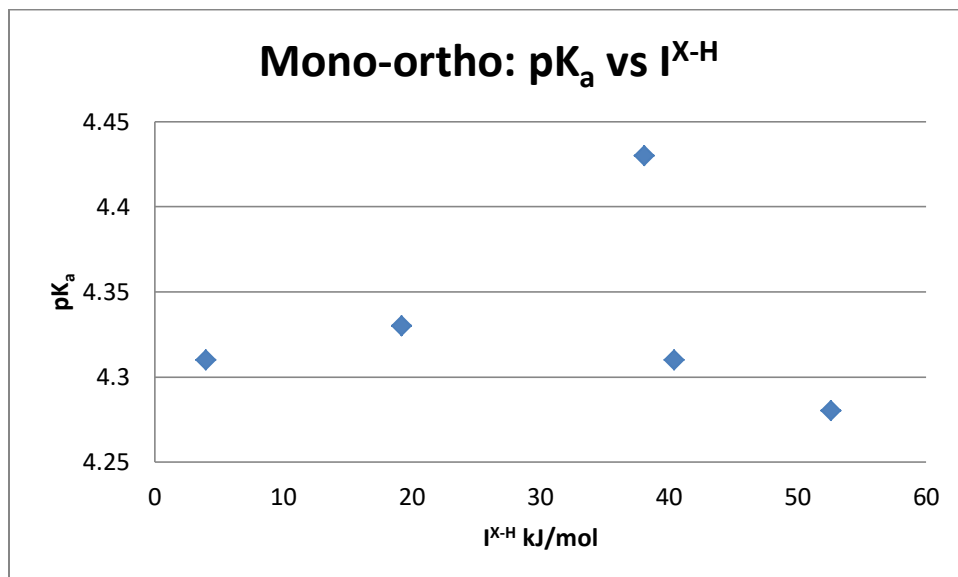


**Figure C51.** RB  $\sigma_p$  regression predicted  $\text{pK}_a$  versus  $\text{pK}_a$  of mono-*ortho* derivatives

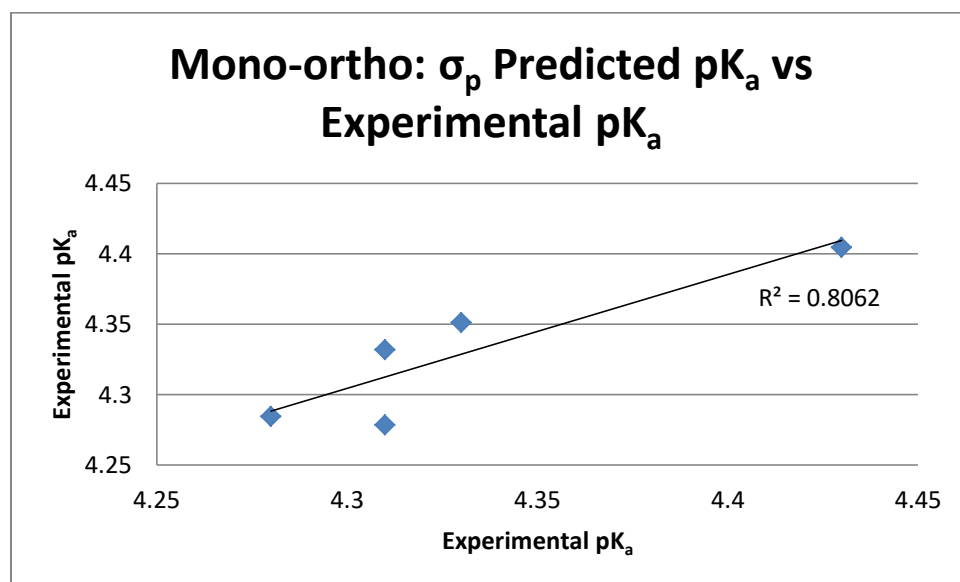


**Figure C52.** RB  $\sigma_I$  regression predicted  $\text{pK}_a$  versus  $\text{pK}_a$  of mono-*ortho* derivatives

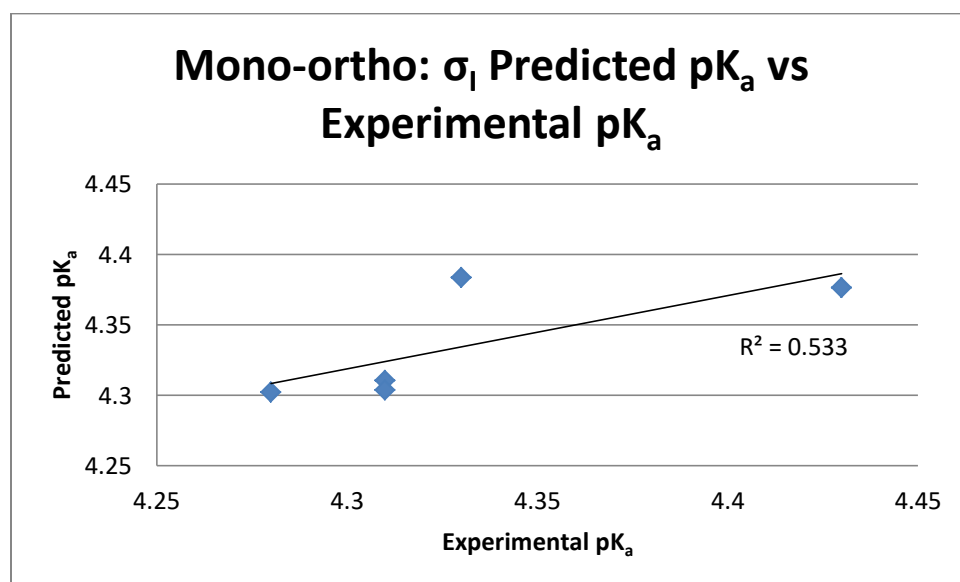


**Figure C53.** RB  $\sigma_I^{\text{mod}}$ -R regression predicted  $\text{pK}_a$  versus  $\text{pK}_a$  of mono-*ortho* derivatives

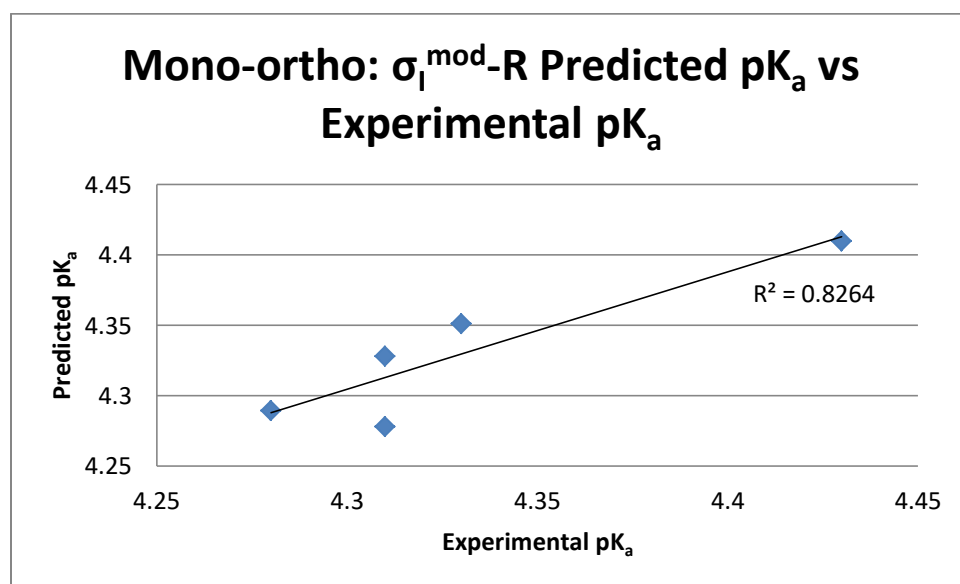
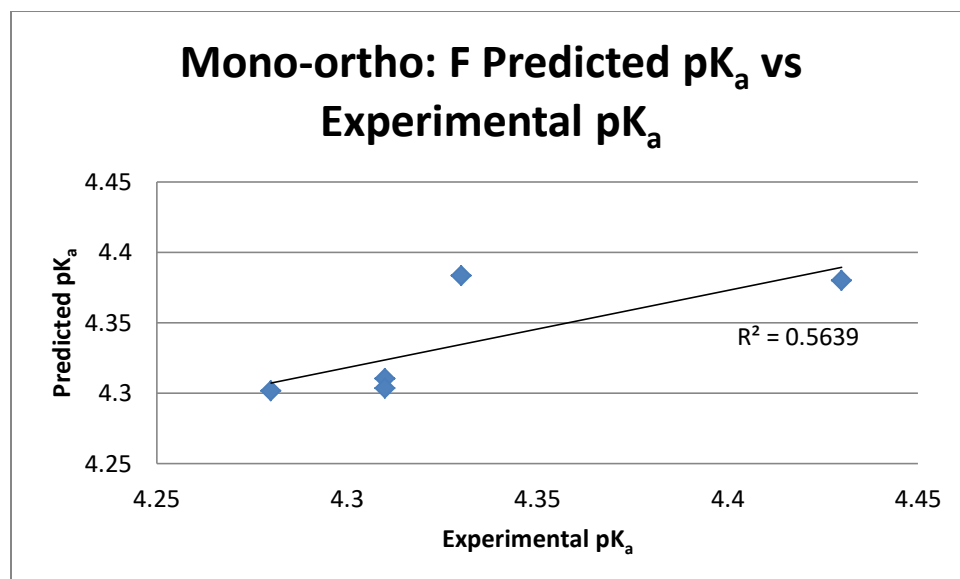


**Figure C54.** RB F regression predicted  $\text{pK}_a$  versus  $\text{pK}_a$  of mono-*ortho* derivatives



## Appendix D

Note: All analyses performed by Dr. Robert D. Pike

**Table D1.** Atomic coordinates (  $\times 10^4$ ) and equivalent isotropic displacement parameters ( $\text{\AA}^2 \times 10^3$ ) for RB-DIA.  $U(\text{eq})$  is defined as one third of the trace of the orthogonalized  $U^{ij}$  tensor.

	x	y	z	U(eq)
O(1)	-1044(1)	284(1)	3277(1)	17(1)
O(2)	2396(1)	2825(1)	4558(1)	27(1)
N(1)	-2332(1)	-3025(1)	3970(1)	22(1)
N(2)	-2623(1)	3331(1)	2449(1)	24(1)
N(3)	905(1)	1864(1)	4087(1)	15(1)
C(1)	-1310(1)	-194(1)	3637(1)	15(1)
C(2)	-1646(2)	-1328(1)	3628(1)	18(1)
C(3)	-2004(1)	-1897(1)	3972(1)	18(1)
C(4)	-2047(2)	-1262(1)	4319(1)	18(1)
C(5)	-1679(1)	-142(1)	4318(1)	17(1)
C(6)	-1275(1)	426(1)	3979(1)	15(1)
C(7)	-845(1)	1652(1)	3974(1)	15(1)
C(8)	-1297(1)	2105(1)	3572(1)	15(1)
C(9)	-1761(1)	3211(1)	3508(1)	16(1)
C(10)	-2195(2)	3612(1)	3144(1)	18(1)
C(11)	-2191(2)	2917(1)	2812(1)	18(1)
C(12)	-1759(2)	1795(1)	2873(1)	17(1)
C(13)	-1344(1)	1417(1)	3246(1)	15(1)
C(14)	-1636(2)	2306(1)	4294(1)	15(1)
C(15)	-3254(2)	2436(1)	4354(1)	17(1)
C(16)	-3700(2)	3110(1)	4661(1)	19(1)
C(17)	-2551(2)	3644(1)	4902(1)	20(1)
C(18)	-937(2)	3507(1)	4841(1)	19(1)
C(19)	-506(2)	2824(1)	4535(1)	17(1)
C(20)	1117(2)	2532(1)	4408(1)	18(1)
C(21)	2240(1)	1463(1)	3871(1)	16(1)
C(22)	2903(1)	413(1)	3965(1)	17(1)

C(23)	4197(2)	47(1)	3752(1)	19(1)
C(24)	4829(2)	703(1)	3465(1)	19(1)
C(25)	4215(2)	1753(1)	3390(1)	19(1)
C(26)	2915(2)	2159(1)	3591(1)	17(1)
C(27)	2398(2)	-281(1)	4309(1)	23(1)
C(28)	3636(2)	-151(1)	4646(1)	31(1)
C(29)	2165(2)	-1512(1)	4205(1)	31(1)
C(30)	2384(2)	3356(1)	3518(1)	20(1)
C(31)	3601(2)	4161(1)	3710(1)	28(1)
C(32)	2127(2)	3610(1)	3082(1)	27(1)
C(33)	-2494(2)	-3640(1)	4335(1)	23(1)
C(34)	-4208(2)	-3713(1)	4458(1)	30(1)
C(35)	-2032(2)	-3698(1)	3629(1)	23(1)
C(36)	-266(2)	-3971(1)	3590(1)	29(1)
C(37)	-2495(2)	2682(1)	2095(1)	33(1)
C(38)	-4002(3)	2062(2)	1978(1)	61(1)
C(39)	-3278(2)	4454(1)	2405(1)	25(1)
C(40)	-2017(2)	5355(1)	2386(1)	33(1)

---

**Table D2.** Bond lengths [ $\text{\AA}$ ] and angles [ $^\circ$ ] for RB-DIA

---

O(1)-C(13)	1.3850(15)
O(1)-C(1)	1.3869(14)
O(2)-C(20)	1.2229(16)
N(1)-C(3)	1.3805(17)
N(1)-C(35)	1.4515(17)
N(1)-C(33)	1.4611(17)
N(2)-C(11)	1.3744(17)
N(2)-C(37)	1.4488(18)
N(2)-C(39)	1.4596(17)
N(3)-C(20)	1.3663(16)
N(3)-C(21)	1.4452(15)
N(3)-C(7)	1.5239(15)
C(1)-C(6)	1.3850(17)
C(1)-C(2)	1.3887(18)
C(2)-C(3)	1.4039(18)
C(2)-H(2)	0.9500
C(3)-C(4)	1.4133(18)
C(4)-C(5)	1.3779(18)
C(4)-H(4)	0.9500
C(5)-C(6)	1.3987(17)
C(5)-H(5)	0.9500
C(6)-C(7)	1.5131(17)
C(7)-C(8)	1.5141(16)
C(7)-C(14)	1.5201(16)
C(8)-C(13)	1.3891(17)
C(8)-C(9)	1.3965(17)
C(9)-C(10)	1.3734(18)
C(9)-H(9)	0.9500
C(10)-C(11)	1.4108(18)
C(10)-H(10)	0.9500
C(11)-C(12)	1.4073(18)
C(12)-C(13)	1.3871(17)
C(12)-H(12)	0.9500
C(14)-C(19)	1.3808(18)



C(14)-C(15)	1.3867(17)
C(15)-C(16)	1.3894(18)
C(15)-H(15)	0.9500
C(16)-C(17)	1.3992(19)
C(16)-H(16)	0.9500
C(17)-C(18)	1.3854(18)
C(17)-H(17)	0.9500
C(18)-C(19)	1.3887(18)
C(18)-H(18)	0.9500
C(19)-C(20)	1.4852(17)
C(21)-C(26)	1.4064(18)
C(21)-C(22)	1.4083(18)
C(22)-C(23)	1.3996(18)
C(22)-C(27)	1.5164(18)
C(23)-C(24)	1.3795(19)
C(23)-H(23)	0.9500
C(24)-C(25)	1.3802(19)
C(24)-H(24)	0.9500
C(25)-C(26)	1.3971(18)
C(25)-H(25)	0.9500
C(26)-C(30)	1.5202(18)
C(27)-C(29)	1.529(2)
C(27)-C(28)	1.531(2)
C(27)-H(27)	1.0000
C(28)-H(28A)	0.9800
C(28)-H(28B)	0.9800
C(28)-H(28C)	0.9800
C(29)-H(29A)	0.9800
C(29)-H(29B)	0.9800
C(29)-H(29C)	0.9800
C(30)-C(32)	1.5305(19)
C(30)-C(31)	1.5342(19)
C(30)-H(30)	1.0000
C(31)-H(31A)	0.9800
C(31)-H(31B)	0.9800
C(31)-H(31C)	0.9800

C(32)-H(32A)	0.9800
C(32)-H(32B)	0.9800
C(32)-H(32C)	0.9800
C(33)-C(34)	1.5149(19)
C(33)-H(33A)	0.9900
C(33)-H(33B)	0.9900
C(34)-H(34A)	0.9800
C(34)-H(34B)	0.9800
C(34)-H(34C)	0.9800
C(35)-C(36)	1.5262(19)
C(35)-H(35A)	0.9900
C(35)-H(35B)	0.9900
C(36)-H(36A)	0.9800
C(36)-H(36B)	0.9800
C(36)-H(36C)	0.9800
C(37)-C(38)	1.507(3)
C(37)-H(37A)	0.9900
C(37)-H(37B)	0.9900
C(38)-H(38A)	0.9800
C(38)-H(38B)	0.9800
C(38)-H(38C)	0.9800
C(39)-C(40)	1.514(2)
C(39)-H(39A)	0.9900
C(39)-H(39B)	0.9900
C(40)-H(40A)	0.9800
C(40)-H(40B)	0.9800
C(40)-H(40C)	0.9800
C(13)-O(1)-C(1)	116.06(9)
C(3)-N(1)-C(35)	120.53(11)
C(3)-N(1)-C(33)	121.09(11)
C(35)-N(1)-C(33)	115.62(10)
C(11)-N(2)-C(37)	122.60(11)
C(11)-N(2)-C(39)	120.74(11)
C(37)-N(2)-C(39)	116.64(11)
C(20)-N(3)-C(21)	121.77(10)

C(20)-N(3)-C(7)	113.40(9)
C(21)-N(3)-C(7)	124.75(10)
C(6)-C(1)-O(1)	122.04(11)
C(6)-C(1)-C(2)	122.92(11)
O(1)-C(1)-C(2)	115.02(11)
C(1)-C(2)-C(3)	120.36(11)
C(1)-C(2)-H(2)	119.8
C(3)-C(2)-H(2)	119.8
N(1)-C(3)-C(2)	121.46(11)
N(1)-C(3)-C(4)	121.31(11)
C(2)-C(3)-C(4)	117.22(11)
C(5)-C(4)-C(3)	120.63(11)
C(5)-C(4)-H(4)	119.7
C(3)-C(4)-H(4)	119.7
C(4)-C(5)-C(6)	122.59(12)
C(4)-C(5)-H(5)	118.7
C(6)-C(5)-H(5)	118.7
C(1)-C(6)-C(5)	116.17(11)
C(1)-C(6)-C(7)	120.65(11)
C(5)-C(6)-C(7)	123.17(11)
C(6)-C(7)-C(8)	107.87(10)
C(6)-C(7)-C(14)	112.51(10)
C(8)-C(7)-C(14)	111.61(10)
C(6)-C(7)-N(3)	112.74(9)
C(8)-C(7)-N(3)	112.17(9)
C(14)-C(7)-N(3)	99.90(9)
C(13)-C(8)-C(9)	115.94(11)
C(13)-C(8)-C(7)	121.12(11)
C(9)-C(8)-C(7)	122.88(11)
C(10)-C(9)-C(8)	122.57(11)
C(10)-C(9)-H(9)	118.7
C(8)-C(9)-H(9)	118.7
C(9)-C(10)-C(11)	121.17(11)
C(9)-C(10)-H(10)	119.4
C(11)-C(10)-H(10)	119.4
N(2)-C(11)-C(12)	122.52(11)

N(2)-C(11)-C(10)	120.55(11)
C(12)-C(11)-C(10)	116.91(11)
C(13)-C(12)-C(11)	120.24(11)
C(13)-C(12)-H(12)	119.9
C(11)-C(12)-H(12)	119.9
O(1)-C(13)-C(12)	115.43(11)
O(1)-C(13)-C(8)	121.39(11)
C(12)-C(13)-C(8)	123.12(11)
C(19)-C(14)-C(15)	120.84(11)
C(19)-C(14)-C(7)	110.85(10)
C(15)-C(14)-C(7)	128.30(11)
C(14)-C(15)-C(16)	118.02(12)
C(14)-C(15)-H(15)	121.0
C(16)-C(15)-H(15)	121.0
C(15)-C(16)-C(17)	120.91(12)
C(15)-C(16)-H(16)	119.5
C(17)-C(16)-H(16)	119.5
C(18)-C(17)-C(16)	120.77(12)
C(18)-C(17)-H(17)	119.6
C(16)-C(17)-H(17)	119.6
C(17)-C(18)-C(19)	117.74(12)
C(17)-C(18)-H(18)	121.1
C(19)-C(18)-H(18)	121.1
C(14)-C(19)-C(18)	121.71(12)
C(14)-C(19)-C(20)	109.46(11)
C(18)-C(19)-C(20)	128.83(12)
O(2)-C(20)-N(3)	126.30(12)
O(2)-C(20)-C(19)	127.34(12)
N(3)-C(20)-C(19)	106.35(10)
C(26)-C(21)-C(22)	121.40(11)
C(26)-C(21)-N(3)	119.38(11)
C(22)-C(21)-N(3)	119.08(11)
C(23)-C(22)-C(21)	117.90(11)
C(23)-C(22)-C(27)	118.47(11)
C(21)-C(22)-C(27)	123.33(11)
C(24)-C(23)-C(22)	121.18(12)

C(24)-C(23)-H(23)	119.4
C(22)-C(23)-H(23)	119.4
C(23)-C(24)-C(25)	120.14(12)
C(23)-C(24)-H(24)	119.9
C(25)-C(24)-H(24)	119.9
C(24)-C(25)-C(26)	121.23(12)
C(24)-C(25)-H(25)	119.4
C(26)-C(25)-H(25)	119.4
C(25)-C(26)-C(21)	118.01(12)
C(25)-C(26)-C(30)	118.48(11)
C(21)-C(26)-C(30)	123.35(11)
C(22)-C(27)-C(29)	112.65(11)
C(22)-C(27)-C(28)	109.25(11)
C(29)-C(27)-C(28)	110.60(12)
C(22)-C(27)-H(27)	108.1
C(29)-C(27)-H(27)	108.1
C(28)-C(27)-H(27)	108.1
C(27)-C(28)-H(28A)	109.5
C(27)-C(28)-H(28B)	109.5
H(28A)-C(28)-H(28B)	109.5
C(27)-C(28)-H(28C)	109.5
H(28A)-C(28)-H(28C)	109.5
H(28B)-C(28)-H(28C)	109.5
C(27)-C(29)-H(29A)	109.5
C(27)-C(29)-H(29B)	109.5
H(29A)-C(29)-H(29B)	109.5
C(27)-C(29)-H(29C)	109.5
H(29A)-C(29)-H(29C)	109.5
H(29B)-C(29)-H(29C)	109.5
C(26)-C(30)-C(32)	112.22(11)
C(26)-C(30)-C(31)	109.73(11)
C(32)-C(30)-C(31)	111.03(11)
C(26)-C(30)-H(30)	107.9
C(32)-C(30)-H(30)	107.9
C(31)-C(30)-H(30)	107.9
C(30)-C(31)-H(31A)	109.5

C(30)-C(31)-H(31B)	109.5
H(31A)-C(31)-H(31B)	109.5
C(30)-C(31)-H(31C)	109.5
H(31A)-C(31)-H(31C)	109.5
H(31B)-C(31)-H(31C)	109.5
C(30)-C(32)-H(32A)	109.5
C(30)-C(32)-H(32B)	109.5
H(32A)-C(32)-H(32B)	109.5
C(30)-C(32)-H(32C)	109.5
H(32A)-C(32)-H(32C)	109.5
H(32B)-C(32)-H(32C)	109.5
N(1)-C(33)-C(34)	112.77(11)
N(1)-C(33)-H(33A)	109.0
C(34)-C(33)-H(33A)	109.0
N(1)-C(33)-H(33B)	109.0
C(34)-C(33)-H(33B)	109.0
H(33A)-C(33)-H(33B)	107.8
C(33)-C(34)-H(34A)	109.5
C(33)-C(34)-H(34B)	109.5
H(34A)-C(34)-H(34B)	109.5
C(33)-C(34)-H(34C)	109.5
H(34A)-C(34)-H(34C)	109.5
H(34B)-C(34)-H(34C)	109.5
N(1)-C(35)-C(36)	112.71(12)
N(1)-C(35)-H(35A)	109.0
C(36)-C(35)-H(35A)	109.0
N(1)-C(35)-H(35B)	109.0
C(36)-C(35)-H(35B)	109.0
H(35A)-C(35)-H(35B)	107.8
C(35)-C(36)-H(36A)	109.5
C(35)-C(36)-H(36B)	109.5
H(36A)-C(36)-H(36B)	109.5
C(35)-C(36)-H(36C)	109.5
H(36A)-C(36)-H(36C)	109.5
H(36B)-C(36)-H(36C)	109.5
N(2)-C(37)-C(38)	113.61(15)

N(2)-C(37)-H(37A)	108.8
C(38)-C(37)-H(37A)	108.8
N(2)-C(37)-H(37B)	108.8
C(38)-C(37)-H(37B)	108.8
H(37A)-C(37)-H(37B)	107.7
C(37)-C(38)-H(38A)	109.5
C(37)-C(38)-H(38B)	109.5
H(38A)-C(38)-H(38B)	109.5
C(37)-C(38)-H(38C)	109.5
H(38A)-C(38)-H(38C)	109.5
H(38B)-C(38)-H(38C)	109.5
N(2)-C(39)-C(40)	113.71(12)
N(2)-C(39)-H(39A)	108.8
C(40)-C(39)-H(39A)	108.8
N(2)-C(39)-H(39B)	108.8
C(40)-C(39)-H(39B)	108.8
H(39A)-C(39)-H(39B)	107.7
C(39)-C(40)-H(40A)	109.5
C(39)-C(40)-H(40B)	109.5
H(40A)-C(40)-H(40B)	109.5
C(39)-C(40)-H(40C)	109.5
H(40A)-C(40)-H(40C)	109.5
H(40B)-C(40)-H(40C)	109.5

---

**Table D3.** Torsion angles [°] for RB-DIA

---

C(13)-O(1)-C(1)-C(6)	-23.79(16)
C(13)-O(1)-C(1)-C(2)	154.80(11)
C(6)-C(1)-C(2)-C(3)	1.28(18)
O(1)-C(1)-C(2)-C(3)	-177.30(10)
C(35)-N(1)-C(3)-C(2)	11.42(18)
C(33)-N(1)-C(3)-C(2)	171.79(11)
C(35)-N(1)-C(3)-C(4)	-169.95(12)
C(33)-N(1)-C(3)-C(4)	-9.58(18)
C(1)-C(2)-C(3)-N(1)	-179.58(11)
C(1)-C(2)-C(3)-C(4)	1.73(18)
N(1)-C(3)-C(4)-C(5)	178.43(12)
C(2)-C(3)-C(4)-C(5)	-2.88(18)
C(3)-C(4)-C(5)-C(6)	1.10(19)
O(1)-C(1)-C(6)-C(5)	175.44(10)
C(2)-C(1)-C(6)-C(5)	-3.04(17)
O(1)-C(1)-C(6)-C(7)	-3.67(17)
C(2)-C(1)-C(6)-C(7)	177.85(11)
C(4)-C(5)-C(6)-C(1)	1.85(18)
C(4)-C(5)-C(6)-C(7)	-179.07(11)
C(1)-C(6)-C(7)-C(8)	27.40(15)
C(5)-C(6)-C(7)-C(8)	-151.65(11)
C(1)-C(6)-C(7)-C(14)	150.94(11)
C(5)-C(6)-C(7)-C(14)	-28.11(16)
C(1)-C(6)-C(7)-N(3)	-97.01(13)
C(5)-C(6)-C(7)-N(3)	83.95(14)
C(20)-N(3)-C(7)-C(6)	-120.66(11)
C(21)-N(3)-C(7)-C(6)	62.67(14)
C(20)-N(3)-C(7)-C(8)	117.32(11)
C(21)-N(3)-C(7)-C(8)	-59.34(15)
C(20)-N(3)-C(7)-C(14)	-1.03(13)
C(21)-N(3)-C(7)-C(14)	-177.69(10)
C(6)-C(7)-C(8)-C(13)	-26.99(15)
C(14)-C(7)-C(8)-C(13)	-151.07(11)
N(3)-C(7)-C(8)-C(13)	97.76(13)



C(6)-C(7)-C(8)-C(9)	149.95(11)
C(14)-C(7)-C(8)-C(9)	25.87(16)
N(3)-C(7)-C(8)-C(9)	-85.30(13)
C(13)-C(8)-C(9)-C(10)	-1.82(18)
C(7)-C(8)-C(9)-C(10)	-178.92(11)
C(8)-C(9)-C(10)-C(11)	-0.11(19)
C(37)-N(2)-C(11)-C(12)	-7.2(2)
C(39)-N(2)-C(11)-C(12)	171.26(12)
C(37)-N(2)-C(11)-C(10)	174.02(13)
C(39)-N(2)-C(11)-C(10)	-7.50(19)
C(9)-C(10)-C(11)-N(2)	-179.78(12)
C(9)-C(10)-C(11)-C(12)	1.38(18)
N(2)-C(11)-C(12)-C(13)	-179.49(12)
C(10)-C(11)-C(12)-C(13)	-0.68(18)
C(1)-O(1)-C(13)-C(12)	-153.04(10)
C(1)-O(1)-C(13)-C(8)	24.21(16)
C(11)-C(12)-C(13)-O(1)	175.84(11)
C(11)-C(12)-C(13)-C(8)	-1.35(19)
C(9)-C(8)-C(13)-O(1)	-174.47(10)
C(7)-C(8)-C(13)-O(1)	2.67(17)
C(9)-C(8)-C(13)-C(12)	2.56(17)
C(7)-C(8)-C(13)-C(12)	179.71(11)
C(6)-C(7)-C(14)-C(19)	121.63(11)
C(8)-C(7)-C(14)-C(19)	-116.94(11)
N(3)-C(7)-C(14)-C(19)	1.82(12)
C(6)-C(7)-C(14)-C(15)	-59.82(16)
C(8)-C(7)-C(14)-C(15)	61.61(16)
N(3)-C(7)-C(14)-C(15)	-179.63(12)
C(19)-C(14)-C(15)-C(16)	0.60(18)
C(7)-C(14)-C(15)-C(16)	-177.83(11)
C(14)-C(15)-C(16)-C(17)	0.20(18)
C(15)-C(16)-C(17)-C(18)	-0.5(2)
C(16)-C(17)-C(18)-C(19)	0.06(19)
C(15)-C(14)-C(19)-C(18)	-1.10(19)
C(7)-C(14)-C(19)-C(18)	177.58(11)
C(15)-C(14)-C(19)-C(20)	179.31(11)

C(7)-C(14)-C(19)-C(20)	-2.01(14)
C(17)-C(18)-C(19)-C(14)	0.75(19)
C(17)-C(18)-C(19)-C(20)	-179.75(12)
C(21)-N(3)-C(20)-O(2)	-3.4(2)
C(7)-N(3)-C(20)-O(2)	179.78(12)
C(21)-N(3)-C(20)-C(19)	176.72(10)
C(7)-N(3)-C(20)-C(19)	-0.06(14)
C(14)-C(19)-C(20)-O(2)	-178.56(13)
C(18)-C(19)-C(20)-O(2)	1.9(2)
C(14)-C(19)-C(20)-N(3)	1.28(14)
C(18)-C(19)-C(20)-N(3)	-178.27(12)
C(20)-N(3)-C(21)-C(26)	-82.17(15)
C(7)-N(3)-C(21)-C(26)	94.23(14)
C(20)-N(3)-C(21)-C(22)	93.66(14)
C(7)-N(3)-C(21)-C(22)	-89.94(14)
C(26)-C(21)-C(22)-C(23)	-4.13(18)
N(3)-C(21)-C(22)-C(23)	-179.87(11)
C(26)-C(21)-C(22)-C(27)	169.47(12)
N(3)-C(21)-C(22)-C(27)	-6.27(18)
C(21)-C(22)-C(23)-C(24)	1.45(18)
C(27)-C(22)-C(23)-C(24)	-172.47(11)
C(22)-C(23)-C(24)-C(25)	1.69(19)
C(23)-C(24)-C(25)-C(26)	-2.26(19)
C(24)-C(25)-C(26)-C(21)	-0.37(18)
C(24)-C(25)-C(26)-C(30)	175.12(11)
C(22)-C(21)-C(26)-C(25)	3.61(18)
N(3)-C(21)-C(26)-C(25)	179.33(11)
C(22)-C(21)-C(26)-C(30)	-171.65(11)
N(3)-C(21)-C(26)-C(30)	4.08(18)
C(23)-C(22)-C(27)-C(29)	-50.71(16)
C(21)-C(22)-C(27)-C(29)	135.72(13)
C(23)-C(22)-C(27)-C(28)	72.63(15)
C(21)-C(22)-C(27)-C(28)	-100.94(14)
C(25)-C(26)-C(30)-C(32)	51.45(15)
C(21)-C(26)-C(30)-C(32)	-133.32(12)
C(25)-C(26)-C(30)-C(31)	-72.49(15)

C(21)-C(26)-C(30)-C(31)	102.74(14)
C(3)-N(1)-C(33)-C(34)	93.38(15)
C(35)-N(1)-C(33)-C(34)	-105.35(13)
C(3)-N(1)-C(35)-C(36)	76.94(15)
C(33)-N(1)-C(35)-C(36)	-84.44(14)
C(11)-N(2)-C(37)-C(38)	92.72(17)
C(39)-N(2)-C(37)-C(38)	-85.82(17)
C(11)-N(2)-C(39)-C(40)	84.85(15)
C(37)-N(2)-C(39)-C(40)	-96.58(15)

---